

PGI Interim Report 2009 – 2012

Peter Grünberg Institute

Imprint

Peter Grünberg Institute (PGI)
Interim Report 2009 – 2012

Published by:
Forschungszentrum Jülich GmbH
52425 Jülich, Germany

Editors:
Prof. Dr. Claus M. Schneider, Managing Director PGI
Dr. Wolfgang Speier, JARA-FIT
Prof. Dr. Rainer Waser, Programme Spokesman FIT

Technical Editing:
Dr. L. Baumgarten
S. Schilling
Dr. W. Speier
A. Wenzik

Printed by:
Forschungszentrum Jülich, Grafische Medien
September 2012

**Peter Grünberg Institute
(PGI)**

Research for the Fundamentals of Future
Information Technology

Interim Report 2009-2012

Contents

I. Peter Grünberg Institute: Research for the Fundamentals of Future Information Technology.....	1
II. The Helmholtz Research Programme FIT	3
III. The Jülich-Aachen Research Alliance JARA-FIT.....	9
IV. Divisions	11
PGI-1/IAS-1: Quantum Theory of Materials.....	13
Scientific Staff.....	14
Research Highlights	15
Selected Publications	31
Indicators	32
PGI-2/IAS-3: Theoretical Nanoelectronics	35
Scientific Staff.....	36
Research Highlights	37
Selected Publications	47
Indicators	48
PGI-3: Functional Nanostructures at Surfaces	49
Scientific Staff.....	50
Research Highlights	51
Selected Publications	65
Indicators	66
PGI-4/JCNS-2: Scattering Methods.....	67
Scientific Staff.....	68
Research Highlights	69
Selected Publications	83
Indicators	84
PGI-5: Microstructure Research	85
Scientific Staff.....	86
Research Highlights	87
Selected Publications	101
Indicators	102
PGI-6: Electronic Properties.....	103
Scientific Staff.....	104
Research Highlights	105
Selected Publications	119
Indicators	120
PGI-7: Electronic Materials.....	121
Scientific Staff.....	122
Research Highlights	123
Selected Publications	137
Indicators	138

PGI-8/ICS-8: Bioelectronics	139
Scientific Staff	140
Research Highlights.....	141
Selected Publications	159
Indicators	160
PGI-9: Semiconductor Nanoelectronics	161
Scientific Staff	162
Research Highlights.....	163
Selected Publications	177
Indicators	178
V. Major Facilities and Scientific-Technical Infrastructure	179
Helmholtz Nanoelectronic Facility (HNF)	181
Ernst Ruska-Centre (ER-C)	183
Research Highlights.....	185
Selected Literature.....	189
Jülich Centre for Neutron Science (JCNS)	191
List of instruments.....	192
Research Highlights.....	193
Selected Literature.....	197
Jülich Synchrotron Radiation Laboratory (JSRL)	199
Research Highlights.....	201
Selected Literature.....	205
Scientific Infrastructure of the PGI	207

Introduction

I. Peter Grünberg Institute:

Research for the Fundamentals of Future Information Technology

The Peter Grünberg Institute (PGI) was established in 2011 as a merger of the Institute of Solid State Research (IFF) and the Institute for Bio- and Nanosystems (IBN) which have been dealing with electronic phenomena, materials, and devices. Named after Peter Grünberg, the first Nobel laureate in the Forschungszentrum Jülich, the institute dedicates itself to fundamental research in the field of information technology and related areas. The main focus is on the exploration of novel physical concepts and new materials with a future emphasis on energy efficiency – „Green IT“. The research activities bridge from contemporary semiconductor nanoelectronics via spintronics to bioelectronics and quantum information processing. The PGI also not only features a broad basis of state-of-the-art condensed matter theory, but also an experimental platform for the development of highly specialized instruments, procedures and innovative material systems for nanoelectronics. This unique combination permits the PGI to develop new ideas also in application-oriented directions. The scientific challenges are pursued along three main axes: (i) exploring novel electronic phenomena in condensed matter physics, (ii) investigating specific aspects of material science in complex electronic systems and devices, (iii) development of new theoretical and experimental concepts, methods and strategies.

Quantum mechanics forms the fundamental framework of the main research activities in the PGI. On a microscopic scale it determines the interactions of electrons and atomic building blocks, and their response to external stimuli on a broad range of time and length scales. Particular strengths of the PGI lie in the theory of electronic structures and processes, phenomena and materials for nano-, molecular, bio- and spinelectronics, and electron microscopy and spectroscopy. This is paired with a long-standing expertise in the development of instruments at synchrotron radiation and neutron sources for detailed investigations of complex material systems.

Major topics of the PGI research are the electronic properties of solid state structures ranging from crystals down to single molecules as well as biological systems. The PGI research is carried out in close collaboration with the RWTH Aachen in the framework of the Jülich-Aachen Research Alliance (JARA), particularly within the section „Fundamentals of Future Information Technology“ (JARA-FIT). Further links exist to the section „High-Performance Computing“ (JARA-HPC).

The PGI operates state-of-the-art laboratories and facilities for the preparation of semiconductors, oxides, and metals, as well as the synthesis of molecular systems and the growth of thin films and crystals. In particular, the Helmholtz Nanoelectronic Facility (HNF) is going to serve as a major cleanroom facility, which offers the entire range of micro- and nanotechnological fabrication methods on wafer-size level. The HNF will start its operation in mid-2013. In addition to the utilization of standard techniques in condensed matter physics and material sciences we develop and implement new highly specialized approaches. These range from superconducting microscopy and femtosecond laser spectroscopy to spinpolarized electron spectroscopies and –microscopies. In close contact with the PGI, the JCNS operates a variety of state-of-the-art instruments at external laboratories, which are continuously improved. This encompasses neutron facilities at the reactor FRM II in Munich, the ILL in Grenoble, and the spallation source SNS in Oak Ridge (USA), which are complemented by portfolio of dedicated instruments at the synchrotron radiation sources BESSY, DELTA, Elettra (Italy) and the APS, Argonne (USA). All of these end stations are accessible for external users as well. The Ernst Ruska-Centre for Microscopy and Spectroscopy provides a variety of powerful electron microscopy devices and since 2012 operates as world-wide leading facility the PICO, the first transmission microscope in Europe with a chromatic and spherical aberration correction with a resolution of 50 pm.

The PGI is a valuable collaboration partner for more than 100 universities and research institutes world-wide. Within Germany the PGI has established close relations to scientists and research groups throughout the country, and takes a leading position as scientific partner in cooperations with industry companies such as Agilent, Bosch, Daimler-Chrysler, ExxonMobil, Infineon, Intel, Micron, Philips, Samsung and Thomson.

Interdisciplinarity is a central scheme in our research activities (cf. chapter II). Therefore, the boundaries between the divisions and research groups in the PGI are very permeable and permit multiple interactions between the various areas ranging from the preparation of material systems through their characterization up to their theoretical description and prediction.

In order to carry out their research programmes the scientists in the PGI take advantage of the various central facilities of the Forschungszentrum Jülich, in particular also the Jülich Supercomputing Centre, JSC. Moreover, the PGI can also rely on its own highly specialized technical and administrative infrastructure, which is an important precondition for the design and the construction of scientific instruments, such as synchrotron beamlines, monochromators, neutron spectrometers, sputtering systems and crystal growth systems.

The PGI organizes on a regular basis the internationally recognized IFF spring school and the Nanoelectronics Lab-course.

The Peter Grünberg Institute comprises the divisions:

PGI-1/IAS-1	Quantum Theory of Materials	Prof. Dr. Stefan Blügel
PGI-2/IAS-3	Theoretical Nanoelectronics	Prof. Dr. David DiVincenzo
PGI-3	Functional Nanostructures at Surfaces	Prof. Dr. Stefan Tautz
PGI-4/JCNS-2	Scattering Methods	Prof. Dr. Thomas Brückel
PGI-5	Microstructure Research	Prof. Dr. Rafal Dunin-Borkowski
PGI-6	Electronic Properties	Prof. Dr. Claus M. Schneider
PGI-7	Electronic Materials	Prof. Dr. Rainer Waser
PGI-8/ICS-8	Bioelectronics	Prof. Dr. Andreas Offenhäusser
PGI-9	Semiconductor Nanoelectronics	Prof. Dr. Detlev Grützmacher
PGI-TA	Technical Services and Administration	Dirk Schlotmann

II. The Helmholtz Research Programme FIT

In the next decade, the development of information technology systems will be dominated by two major trends – a continuation of the exponential increase in performance and efficiency (“Moore’s law”) by further down-scaling, new materials, novel device concepts, and additional functionalities (“More than Moore”) by the emergence of advanced concepts in e.g. sensors and bioelectronics. The Helmholtz Programme *Fundamentals of Future Information Technology (FIT)* conducts exploratory research in nanoelectronics by focusing on medium-term and long-term tasks, on emerging far-reaching concepts, and on issues of physics and technology well ahead of the mainstream development of the nanoelectronics industry. Our mission and objective is to approach the ultimate limits of the scaling of nanoelectronics, to search for fundamentally different state variables for information processing and storage, and to open up new pathways for additional functionalities.

A. Programme Structure

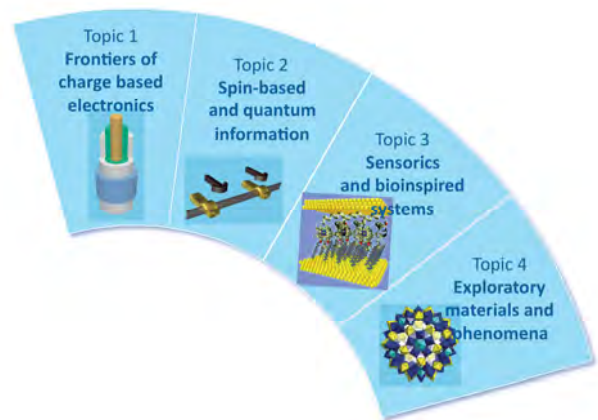
The programme FIT is conducted by the PGI and is organized in four scientific topics and the customization and advancement of major infrastructure facilities.

Topic 1 *Frontiers of charge-based electronics* explores potential extensions of Si-CMOS and beyond-CMOS concepts.

Topic 2 *Spin-based and quantum information* aims at an exploitation of the electron spin as an alternative state variable in information technology.

The goal of **Topic 3 *Sensorics and bioinspired systems*** is to develop new technologies and concepts for the interconnection of biological matter to electronic probes.

In **Topic 4 *Exploratory materials and phenomena*** we explore alternative concepts for future electronics which are as yet far removed from prospects of actual application, but which are nevertheless promising enough to warrant a concerted research effort now.



The topics make extensive use of the excellent scientific-technical infrastructure provided by Jülich and its partners, including the exceptional supercomputer facility, the Neutron sources in Munich, in Grenoble, and in Oak Ridge, and the synchrotron radiation sources in Dortmund, Berlin and Trieste (Italy). The PGI also runs the Ernst Ruska-Centre for Microscopy and Spectroscopy together with the RWTH Aachen, a world-wide leading facility. A particular development for the programme will be the establishment of the Helmholtz Nanoelectronic Facility next year. For more details about these facilities see below. The Peter Grünberg Institute has also set up a variety of dedicated medium-sized facilities and specialized laboratory instruments for contemporary condensed matter physics, such as the Nanospintronics Facility or an ultra-low vibration laboratory for precision scanning tunnelling microscopy, also described more specifically below.

The research activities of the Helmholtz programme FIT are closely interlinked with further Helmholtz research programmes and other institutes in the Forschungszentrum Jülich. This is also indicated by a „double membership“ of several PGI divisions with the Institute for Advanced Simulation (IAS), the Institute of Complex Systems (ICS) and the Jülich Center for Neutron Science (JCNS).

B. Programme Topics, joint research efforts, and interdisciplinary cooperation

The programme FIT defines the research strategy and directions of the Peter Grünberg Institute and its two theoretical and seven experimental departments. Interdisciplinary cooperation is an essential prerequisite for achieving advances in this challenging research area, which encompasses disciplines that include solid-state and surface physics, inorganic and organic chemistry, cellular and molecular biology, electrical engineering and information technology. Several PGI departments contribute to each of the four research topics, with scientific interactions fostered through frequent topical discussions, collaborative projects and joint supervision of PhD students. Complementary expertise is provided by

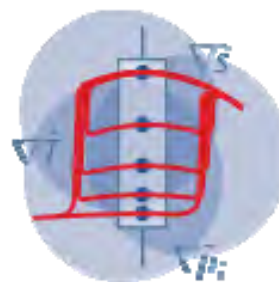
partner institutes at RWTH Aachen University, within the framework of JARA-FIT (see chapter III). One measure that is designed to promote close collaborations is the creation of joint appointments with working capacity in both Jülich and Aachen.

Topic 1 “Frontiers of Charge-Based Electronics” deals with phenomena and devices that utilize the electron charge as the classical state variable for information processing and storage. As a general guiding rule, research aims at the exploitation of ideas to reach the ultimate physical limits of charge-based information technology, which are in turn defined by

- geometrical scaling limits associated with the onset of tunnelling currents between lateral structures
- thermodynamic limits in energy consumption per logic operation based on Boltzmann statistics
- power dissipation limits due to the finite heat conductivity of materials.

Here, theoretical and experimental contributions are primarily from PGI-1, PGI-5, PGI-7 and PGI-9, and address semiconductor nanowire transistors, various novel non-volatile memory concepts, such as redox-based resistive switching systems, and alternative chip architecture concepts, which allow for the fusion of information processing and storage..

A prominent collaboration activity in this topic is embedded into the new Collaborative Research Center (SFB 917) “Nanoswitches” funded by the DFG since July 2011. Eight JARA-FIT institutes at the RWTH Aachen and four PGI institutes focus on the fundamental aspects of resistive switching phenomena based on phase change and redox effects in oxides and higher chalcogenides. Theoretical contributions on electronic structure and switching kinetics in various material classes come from PGI-1 and PGI-2, whereas PGI-7 explores resistive oxides and their microscopic switching mechanisms. Studies in PGI-6 make use of dedicated synchrotron-radiation microscopy and spectroscopic techniques to unravel switching dynamics on ultrashort time scales in the same materials.



Topic 2 “Spin-Based and Quantum Information” explores phenomena and materials that may lead to devices that utilize the properties of electron spins as state variables or information carriers for storing or processing information in two main directions. Firstly, an improved control of spin currents and spin-transfer processes is required to bring about the next generation of devices with added functionalities. This includes studies on incoherent or coherent ensemble of electron spins as well as on the static and dynamic properties of strongly correlated many-electron spins. Secondly, the long term goal aims to manipulate individual spins and tune their interactions in a condensed matter environment – this is both a precondition and a major step on the way to a future solid-state-based quantum-information-processing approach. Contributing departments to this topic are PGI-1, PGI-2, PGI-4, PGI-6, and PGI-9.

The division PGI-2 takes a special mission. Being inaugurated in 2011 it has a clear mandate to make a strong effort in the area of Quantum Information Science. Under the auspices of JARA, PGI-2's efforts have since then been developed in a coordinated way with the new Institute for Quantum Information of Prof. DiVincenzo at the RWTH. Strong progress has been made in a range of scientific directions in these two years, one of them being concerned with the modeling of qubits realized in single-electron quantum dots. Exciting developments in the achievement of highly coherent qubits are underway in the labs of Prof. Hendrik Bluhm (also arrived at RWTH in 2011). Another example concerns superconducting devices and transmon qubits. Many of these developments will be featured in the 44th annual IFF spring school, “Quantum Information Processing”, Feb 24-Mar 6, 2013 (www.iff-springschool.de), organized by Prof. DiVincenzo.



One example of joint activities in Topic 2 is in the new field of topological insulators. Thin film samples are grown in PGI-9 and investigated with respect to their spin-resolved electronic structure in PGI-6. Theoretical spin-transport concepts, materials design and the electronic structure calculations that are necessary to interpret the experimental data are performed in PGI-1. In the field of molecular and nanomagnetism, the chemistry group headed by Prof. Kögerler (RWTH Aachen/PGI-6) provides tailored molecular structures, which are characterized using neutron scattering techniques in PGI-4.

Collaborative activities in this topic concern the SFB 491 “Magnetic Heterostructures: Spin Structure and Spin Transport” together with the universities in Duisburg-Essen and Bochum (expired 31.12.2011), the FG 912 “Spin Coherence and Relaxation” together with the RWTH Aachen and EU-FP7 NMP- oxides

for electronics applications “IFOX – interfacing oxides. IFOX and the FG 912 both create a link between Topics 1 and 2.

Topic 3 “Sensorics and Bioinspired Systems” makes use of the fact that today’s electronic components are already scaled down to the size of biological molecules, which opens up exciting possibilities for combining electronic and biological functions. It addresses the development of new technologies and concepts for the interconnection of biological matter to electronic probes, which will provide novel approaches for studying cellular functions at the micro and nano-scale. From a fundamental perspective, these approaches aim at a better understanding of physiological behaviour and mechanisms of neuronal information processing. On the one hand, a major goal is to develop new tools for diagnostics and imaging materials, and devices. On the other hand the technological side can be inspired by biological systems leading to new cognitive and sensory approaches to information processing (e.g. sensory swarms). Within the Topic we take up this challenge and are developing bioelectronic devices that combine biological systems – from single biomolecules to living cells and organisms – with electronics. Participating departments include PGI-5, PGI-8 and PGI-9. The Topic also builds a scientific bridge to the activities within the Institute of Complex Systems (ICS).

Topic 4 “Exploratory Materials and Phenomena” explores alternative concepts for future electronics, which are currently far removed from prospects of actual application, but which are nevertheless promising enough to warrant an immediate concerted research effort. In addition to the approaches discussed in Topics 1 to 3, a number of innovative ideas are being explored in fields that include organic and molecular electronics and single-molecule switches. For instance, we investigate the self-organization, the chemical behaviour, and the electronic transport properties of molecules such as PTCDA and substituted coronenes on the individual molecule level. The coronene molecule can be regarded as a tiny flake of graphene paving the synthesis way from small molecules to graphene layers. This may establish a valuable link between ultimately scaled top-down technologies and molecular bottom-up approaches, which so-far not have been bridged. Thermoelectrics, molecular magnets and complex metallic alloys are also currently being investigated and may become important for electronic applications in the future. Transition metal oxides are addressed throughout the Programme. In the present Topic, we focus on their heterostructures and some of their fundamental properties, which are not yet exploited in devices. All PGI departments contribute to this topic. A particularly close link is formed between the divisions PGI-3 and PGI-6 by means of a joint PhD project which will address spin-dependent interactions between a molecule and a surface.

C. Future Directions

The overarching driving force for the future direction of our research programme is the quest for higher energy efficiency in computing, storage, and data transmission systems. This is triggered by the embarrassing energy consumption of today’s information technology meanwhile using about 10 % of the electrical power in industrialized nations, and further growing. This establishes one of the grand challenges of modern society. A 2011 competition between a human brain and the supercomputer Watson within the game show Jeopardy, where the brain operated with about 30 W, whereas the computer Watson used about 2 MW (and actually won the competition), reveals the enormous potential which still can be gained before approaching any universal physical limits.

In order to meet this challenge, we plan to pursue the major parts of our future programme along the following routes:

1. Beyond CMOS technologies
2. Spin and quantum information
3. Molecular and bioelectronic concepts
4. Exploiting electronic phenomena for energy technologies

1. Beyond CMOS technologies

Conventional MOSFETs suffer from the physically limited subthreshold slope. This limit does not exist in Tunnel (T)-FETs which are currently considered as the most promising choice of future FET devices. Due to their physical switching mechanisms different from conventional MOSFETs they potentially enable a drastic reduction of power consumption of tomorrow’s ICs. JARA-FIT scientists participated in the first experimental demonstration of a T-FET with a switching behaviour superior to conventional FETs, and the first grown in-situ doped silicon nanowire tunnel FET.

The phenomenon of redox-based resistive switching (“memristive” effects) may not only lead to non-volatile memories which are superior in energy efficiency to FLASH. In particular, electrochemical nanocells (also called “atomic switches”) built from an electrochemically active metal electrode such as Ag or Cu, a solid ion conductor of a few nanometre thickness and an inert counter electrode can be used to generate memristive switches, controlled by the *electrode* material. These cells show a particularly huge range of ON resistances which provides a particularly pronounced multilevel memristive characteristics. This makes the electrochemical atomic switches well suited for non-von Neumann field-programmable, crossbar based architectures as well as neuromorphic concepts and intelligent interconnects.

Oxidic heterostructures exhibit a number of exciting properties such as conductivity, superconductivity and magnetism, which are related to the formation of a quasi-2D electron gas at the interface. Understanding the microscopic mechanisms leading to these properties is paramount for unearthing the potential of such systems for nanoelectronics.

2. Spin-and Quantum Information

The use of spin-based and quantum phenomena in nanoelectronics promises not only memory and logic concepts with higher energy efficiency, but also added functionalities far beyond current imagination. Our research will follow two main directions. The first one continues our successful activities in the field of spintronics, exploring spin transport and transfer processes on the nanoscale down to molecular spin systems. Particular attention will be paid to the realization and control of pure spin currents. Another field of interest will concern spin-dependent transport processes on ultrashort time scales – i.e. ultrafast spin dynamics – which may open a new avenue to ultrafast optical modulation and control of spins.

The second direction will focus on selected quantum information aspects. One of them concerns qubits on the basis of single-electron quantum dots. We will continue with detailed modeling of noise sources in these systems, calculations of coherence times as determined by various mechanisms, and with developing architectural concepts to guide scaled-up experiments in Aachen and in other labs around the world. In the area of superconducting devices the continued strong ties with IBM research will permit high-impact theoretical research on optimal control methods for transmon qubits coupled to 2D and 3D cavities, development of new formal approaches to high-accuracy device modeling and deduction of optimal qubit-cavity geometries, and further exploration of fundamental mechanisms (e.g., quasiparticle dynamics) for decoherence in these systems. A third area of interest concerns Majorana physics, where we have leading ideas for the exploitation of newly observed phenomena in nanowire-superconductor hybrid devices. Basic modeling of the Delft experiments are being followed up by new concepts for Majorana array physics, and for the realization of quantum information processing in fermionic systems. Finally, we will address new developments in the fundamental theory of topological error correction and the properties of topological phases of matter, with attention to the techniques for efficient simulation of the entanglement properties and dynamics of such systems.

3. Molecular and bioelectronic concepts

The breathtaking development in chemistry during the last decade permits the synthesis of entirely novel classes of molecules with a wide variety of electronic and magnetic properties. Integrating such molecules into nanoelectronic devices and circuits opens the door to unique opportunities in molecular electronics ranging from logic and memory function encoded into individual molecules, chemical and biochemical sensors of ultimate sensitivity, advanced approaches in catalysis, to a tailored signal exchange between biological neurons and nanoelectronic circuits. Our research will cover different aspects and systems ranging from single small molecules on a surface through macromolecular structures such as polyoxometallates and DNA strands up to individual cells. The most crucial task in this research is the understanding and control of the organic-inorganic interface on the atomistic level. Based on this approach, we address the self-organization of molecular systems, the chemical and electronic structure of the interface and of the molecular system, as well as their electronic transport properties.

A fundamental aspect in molecular electronics concerns the contact of the molecule to a conductive electrode. Therefore, molecule-surface interactions and their role for the physical properties of a given molecule will be investigated as a first step. Based on this knowledge we expect to improve the understanding of electrical transport properties of molecular structures and their control by means of electrical, magnetic and electromagnetic fields. We will successively move from small molecules to more complex arrangements.

Bioelectronics research will focus on the connection of biology with electronic-based materials to detect minute changes (e.g. sensor arrays or neuron recording) and generate specific response (e.g. neuron stimulation or neurotransmitter release). The dynamic nature of the bio-electronic interface requires the development of electronic devices with micro- and nanoscale engineered surfaces and material properties ideally suited for optimal coupling to biological systems. Active bio-inorganic components will be developed based on biomolecules characterized by highly-specific surface recognition, analyte binding and, in some cases, electron tunneling.

A fundamental aspect in molecular electronics concerns the contact of the molecule to a conductive electrode. Therefore, molecule-surface interactions and their role for the physical properties of a given molecule will be investigated as a first step. This will be backed up by *ab initio* simulations. One of the foremost challenges in the field of molecular electronics is the insufficient structural and electronic contact definition in many of the single-molecule transport experiments reported up to date, demanding the performance and/or statistical analysis of hundreds of experiments to extract the relevant data. A focus of our work is the development of experimental platforms which allow structural control of molecular junctions and thus more reproducible current transport measurements through single molecules. One approach which we currently follow is the combination of scanning tunnelling microscopy (STM) with non-contact atomic force microscopy (AFM) to determine the electrical and mechanical properties of a given molecular junction simultaneously. Based on these novel experiments we expect to improve the understanding of electrical transport properties of molecular structures and their control by means of electrical, magnetic and electromagnetic fields. We will successively move from small molecules to more complex arrangements. The experiments will be complemented by *ab initio* simulations. Special emphasis will be placed on the inclusion of many body correlations into the transport calculations.

4. Exploiting electronic phenomena for energy technologies

Electronic phenomena studied within this Research Programme are of interest not only for applications in information technologies. They may provide a crucial benefit for all areas of energy technology, such as energy conversion, energy storage, and energy transformation, as well as for related areas such as sensorics and catalysis.

Redox-based resistive switches, for example, may be relevant for the entire range of electrochemical systems – from batteries and fuel cells to sensors. Owing to the extremely small thickness of the (inorganic) ion conductors studied for nanoelectronics, this leads to functioning cells at dimensions which are substantially smaller and work at temperatures which are significantly lower than for all conventional cells.

The epitaxial growth of III/V and III-nitride semiconductor nanostructures is not only a path to integrate novel electronic and optoelectronic devices on Si, but also opens attractive possibilities in photovoltaics and water splitting devices. Narrow band gap semiconductors like Bi_2Te_3 and Bi_2Se_3 , which became recently known as 3 dimensional topological insulators, are well known thermoelectric materials. Moreover, thermoelectric devices based on nanostructures, such as SiGe, Ge, GeSn and silicide quantum dots and wires, offer new possibilities for energy harvesting devices and in particular in combination with Si electronics also for the energy supply of small autonomous portable devices.

Electronic or magnetic materials such as thermoelectrics or magnetocalorics can be relevant for waste heat recovery or efficient energy conversion. Topological insulators support spin-currents that are protected from scattering events. The fundamental understanding of these materials requires the same experimental and theoretical approaches as for some materials relevant for information technologies.

The powerful facilities for atomic scale characterization and analysis (electron microscopes at the ER-C, synchrotron beam lines at the JSRL, neutron beam lines at the JCNS, as well as a multitude of scanning probe systems) are frequently used already for studying advanced materials and devices in energy technology.

III. The Jülich-Aachen Research Alliance JARA-FIT

RWTH Aachen University is one of Germany's Excellence Universities and is the strongest university within Germany with respect to third party funding. It is certainly one of the major technical universities within Europe. The RWTH sets out to develop into an integrated university with a particular strength in cross-disciplinary research in order to tackle the central global challenges of the future.

A key element of the overall strategic concept is the strengthening of the alliance between the RWTH Aachen University and the Forschungszentrum Jülich. The two institutions joined by contract in 2007 into a strategic alliance called Jülich-Aachen-Research Alliance, JARA, which includes the coordination of general strategies between the heads of both institutions, joint appointment procedures, joint infrastructure planning, and the establishment of joint research groups located at both places.

JARA is currently organized into five different sections, each concentrating on a different scientific topic. The PGI, and with it the Helmholtz-Programme FIT, is embedded into the section JARA-FIT. All together within JARA-FIT, 36 research groups each headed by a tenured professor and 10 additional groups headed by non-permanent junior professors are assembled from 32 institutes (21 from Aachen and 11 from Jülich). They all contribute to cross-disciplinary activities including physics, electrical engineering, mechanical engineering, mathematics, chemistry, and biology. The approach combines in an elegant fashion the advantages of a Helmholtz research center and a university, specifically the infrastructural strength and the program-oriented research focused on central questions at the research center with the multifaceted research based on brilliant students and the engineering competence at the RWTH Aachen.

Members of JARA-FIT listed according to faculties:

Physics

Prof. Dr. H. Bluhm, Aachen
 Prof. Dr. S. Blügel, Jülich
 Prof. Dr. T. Brückel, Jülich
 Prof. Dr. D. P. DiVincenzo, Aachen & Jülich
 Prof. Dr. R. Dunin-Borkowski, Jülich
 Prof. Dr. D. Grützmacher, Jülich
 Prof. Dr. C. Honerkamp, Aachen
 Prof. Dr. U. Klemradt, Aachen
 Prof. Dr. S. Mantl, Jülich
 Prof. Dr. R. Mazzarello, Aachen
 Prof. Dr. J. Mayer, Aachen
 Prof. Dr. V. Meden, Aachen
 Prof. Dr. Th. Schäpers, Aachen (interim) & Jülich
 Prof. Dr. M. Morgenstern, Aachen
 Prof. Dr. A. Offenhäusser, Jülich
 Prof. Dr. E. Pavarini, Jülich
 Prof. Dr. Claus M. Schneider, Jülich & Duisburg- Essen*
 Prof. Dr. H. Schoeller, Aachen
 Prof. Dr. J. Splettstößer, Aachen
 Prof. Dr. C. Stampfer, Aachen & Jülich
 Prof. Dr. T. Taubner, Aachen
 Prof. Dr. S. Tautz, Jülich
 Prof. Dr. B.M. Terhal, Aachen
 Prof. Dr. M. Wegewijs, Jülich
 Prof. Dr. M. Wuttig, Aachen

Mathematics

Prof. Dr. Chr. Melcher, Aachen

Chemistry

Prof. Dr. St. Appelt, Aachen & Jülich
 Prof. Dr. A. Böker, Aachen
 Prof. Dr. R. Dronskowski, Aachen
 Prof. Dr. P. Kögerler, Aachen & Jülich
 Prof. Dr. M. Martin, Aachen
 Prof. Dr. U. Simon, Aachen

Biology

Prof. Dr. S. Grün, Jülich

Elektrotechnical Engineering and Information Technology

Prof. Dr. J. Knoch, Aachen
 Prof. Dr. W. Mokwa, Aachen
 Prof. Dr. T. Noll, Aachen
 Prof. Dr. A. Vescan, Aachen
 Prof. Dr. R. Waser, Aachen & Jülich
 Prof. Dr. J. Witzens, Aachen

Mechanical Engineering

Prof. Dr. R. Poprawe, Aachen
 Prof. Dr. P. Loosen, Aachen

Geoessources and Material Engineering

Prof. Dr. G. Roth, Aachen

* UAMR-Professur der Universitätsallianz Metropole Ruhr

A major profit of the collaboration between Aachen and Jülich (besides cross-disciplinary interactions) is the development and running of a joint infrastructure as, e.g. the Ernst Ruska-Center for Electron Microscopy (ER-C), housing world-leading cutting-edge electron microscopes, or the joint development of state-of-the-art neutron scattering instruments.

The section JARA-FIT is now in its fifth year. The concept bears fruit, as either manifested in an increasing number of joint papers, prizes awarded to researchers or successes in project applications. This is now well recognized by internationally renowned scientists, who become attracted by the JARA concept and the unique possibilities offered in Aachen together with Jülich. Especially the field of Quantum Information has benefitted from this. David DiVincenzo joined the section. He received an Alexander von Humboldt Professorship which enables him to conduct cutting edge research at the RWTH Aachen in combination with the PGI on a sustainable basis. Together with Hendrik Bluhm, from Harvard University, Barbara Terhal, also from IBM, Norbert Schuch, from the California Institute of Technology, and Fabian Hassler, from Leiden, they set out together to establish a solid state-based quantum information processing approach, as described above.

As of today, the close alliance within JARA-FIT has already fostered many joint research projects, such as several Virtual Institutes funded by the Helmholtz Association, including the most recently accepted Virtual Institute for Topological Insulators (together with the University Würzburg), a DFG Research Group on spin coherence (FOR 912), and the DFG Collaborative Research Centre (Sonderforschungsbereich, SFB 917) on novel non-volatile memory concepts using chalcogenides (see above). Young members of the section have been highly successful in recruiting ERC starting grants: JARA Junior Professor C. Stampfer and, very recently, Prof. P. Kögerler, who is jointly appointed in Aachen and Jülich. Also, it is worth mentioning that Hendrik Bluhm received the Alfred Krupp award for young professors in 2011.

JARA-FIT received international recognition this summer, when the section hosted the first Nature Conference at a University in Germany organized by members of JARA-FIT led by Rainer Waser. From June 17th to June 20th around 500 scientists discussed “Frontiers in Electronic Materials” with a focus on correlation effects and memristive phenomena.

Building on the substantial achievements and mutual trust developed in the first phase of the Excellence Initiative, in phase II, the relationship and synergy between the RWTH Aachen University and Jülich will be fortified by establishing new formats of cooperation: JARA Institutes and JARA Professorships. The new JARA Institutes will consist of a small (three to five) group of JARA professors spearheading research on a joint mission towards a common goal, forming a dedicated “task-force”. They are organisations of both RWTH and Forschungszentrum Jülich. The institute’s achievements will be externally reviewed typically every five years. Each institute is to be financed as follows:

- Basic funding by the member JARA professors / principal investigators (>50%),
- Start-up funding from the Excellence Initiative,
- Additional funding by RWTH Aachen and Forschungszentrum Jülich matching the start-up,
- Joint third party funding.

In particular, JARA Institute members contractually commit to transfer a significant part of their individual resources to the common institute budget. This includes in kind contributions providing access to instrumentation to other institute members. The JARA Institutes will be included in the department structure of the PGI.

JARA plans to establish JARA Institutes in the section FIT with specific missions in the areas of

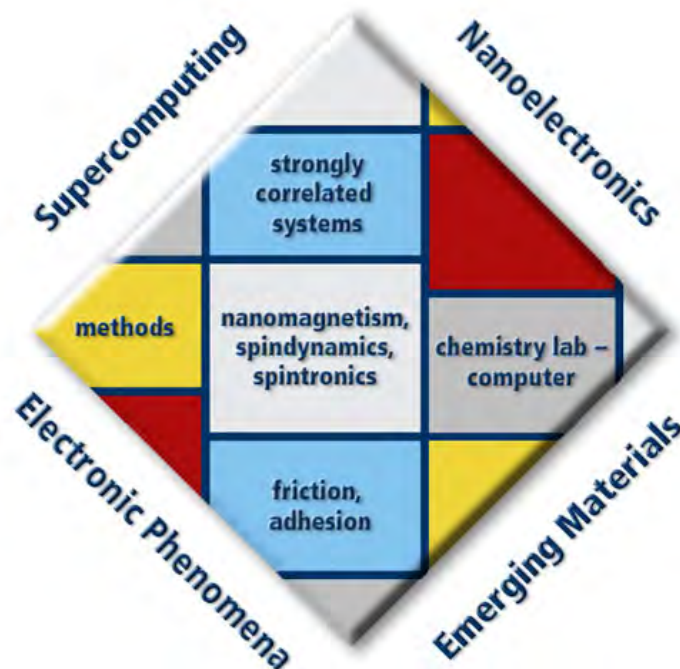
- (1) energy-efficient information technology (“Green IT”) and
- (2) quantum computing.

The mission of *JARA Institute “Green IT”* is the dedicated effort to reduce the energy consumption of computer hardware. The Institute will bring together the expertise from physics and electrical engineering situated in Aachen and Jülich with the aim to develop novel energy-efficient electronic nanometer-scale devices beyond CMOS technologies. Possible means to reduce energy may bring together the development of ultra low-power technologies based on novel semiconductor (Si) transistors with the memristive and non-volatile technologies based on transition metal oxides and chalcogenides. Since lower energy per bit may drastically increase bit error rates, a Reliability Lab will be established to explore possible failure mechanisms on all levels. The *JARA Institute of Quantum Computation* will target the development of a quantum computer as described above. The JARA Institute will bring together the researchers, both in theory and experimental physics, from Aachen and Jülich with the common goal to take the realization of qubits and quantum circuits to the next level.

IV. Divisions

PGI-1/IAS-1	Quantum Theory of Materials
PGI-2/IAS-3	Theoretical Nanoelectronics
PGI-3	Functional Nanostructures at Surfaces
PGI-4/JCNS-2	Scattering Methods
PGI-5	Microstructure Research
PGI-6	Electronic Properties
PGI-7	Electronic Materials
PGI-8/ICS-8	Bioelectronics
PGI-9	Semiconductor Nanoelectronics

PGI-1/IAS-1: Quantum Theory of Materials



The Institute PGI-1/IAS-1 – *Quantum Theory of Materials* computes and analyzes the microscopic properties of solids from the basic principles of quantum mechanics in terms of both basic research and practical applications. Our research covers key areas of condensed matter theory and computational materials science and interfaces closely with experiments. Emphasis is on effects, functionalities and materials relevant to nanoelectronics but also to energy related research.

We explore the electronic, structural, magnetic, ferroelectric, multiferroic and transport properties of complex solid systems such as large organic (including biological) molecules, graphene, low-dimensional magnets, nanostructures, interface materials, magnetic multilayers, oxide heterostructures, hybrid and phase-change materials. We study atom diffusion and large defects relevant for nanoionics. We consider electronic transport properties across interfaces, planar, transverse and topological transport phenomena, spin-relaxation mechanisms and spin-dynamics, electronic and magnetic excitations. We investigate the quasiparticle behavior of topological insulators, photovoltaic materials, oxides and transition metals that results from electronic correlations. We analyze the physics of strongly correlated materials such as transition-metal oxides. Other areas include nanoscale tribology, including friction, plastic deformation, adhesion and brittle fracture.

A major asset of our institute is the competence in developing conceptual and computational methods based on static and time-dependent density (DFT) and reduced density matrix functional theory (DMFT), many-body perturbation theory, and molecular and spin dynamics, paying particular attention to massively parallel high-performance computers that will provide petaflop performances.

Head of Institute:

Prof. Stefan Blügel, email: s.bluegel@fz-juelich.de, phone: +49-2461-61-4249.

Scientific Staff

On September 1st 2012, the staff of PGI-1/IAS-1 comprised 36 scientists, no technicians, 16 PhD students and 1 master student. The institute hosts 3 University-Helmholtz Young Investigator groups and an Emmy-Noether group.

Scientists

Atodiresei, Dr. Nicolae
Bihlmayer, Dr. Gustav
Blügel, Prof. Dr. Stefan
Friedrich, Dr. Christoph
Liebsch, Dr. Ansgar
Mavropoulos, Dr. Phivos
Persson, Dr. Bo
Wortmann, Dr. Daniel

Junior Research Group Leader

Helbig, Dr. Nicole
Lezaic, Marjana, Junior Prof. Dr.
Lounis, Samir Dr.
Mokrousov, Yuriy, Junior Prof. Dr.

Post-Docs

Baumeister, Dr. Paul
Burnus, Dr. Tobias
Betzinger, Dr. Markus
Caciuc, Dr. Vasile
Freimuth, Dr. Frank
Nguyen, Dr. Hoang Long

Lorenz, Dr. Boris
Rahmanizadeh, Dr. Kourosh
Rushchanskii, Dr. Konstantin
Sasioglu, Dr. Ersoy
Slipukhina, Dr. Ivetta
Tsukamoto, Dr. Shigeru
Xu, Dr. Pengxiang
Zhang, Dr. Hongbin
Bouhassoune, Dr. Mohammed
Kiselev, Dr. Nikolai
dos Santos Dias, Manuel
Theophilou, Dr. Iris
Kovacik, Dr. Roman
Al-Zubi, Dr. Ali
Lani, Dr. Giovanna

Guest Scientists

Lambrecht, Prof. Dr. Walter
(Fullbright Fellow)
Zanolli, Dr. Zeila
(Marie Curie)
Aguilera, Dr. Irene
(Alexander von Humboldt)

Research Highlights

Iron-Pnictides: strong Coulomb correlations via Hund's coupling

A. Liebsch

PGI-1 & IAS-1: Quantum Theory of Materials, Forschungszentrum Jülich

Hund's coupling in iron pnictides is shown to give rise to a significant depletion of spectral weight above E_F . DMFT calculations reveal that this pseudogap is associated with a collective mode in the self-energy caused by spin fluctuations. The pseudogap is remarkably stable over a wide range of Coulomb and exchange energies. The implications of this phenomenon for optical spectra of iron pnictides are discussed.

The discovery of superconductivity in iron pnictides has stimulated intense discussions concerning the role of correlation effects in these compounds. In contrast to high- T_c cuprates, which have antiferromagnetic Mott insulators as parent compounds, pnictides are correlated magnetic metals that show significant deviations from Fermi-liquid behavior. Moreover, as a result of the multi-band nature of pnictides, the interplay of Coulomb and exchange interactions gives rise to phenomena not found in cuprates. The importance of Hund coupling in pnictides has recently received wide attention. In particular, optical data on BaFe_2As_2 [1] reveal a high-energy pseudogap not compatible with normal metal behavior. This pseudogap differs from the low-energy gap in the antiferromagnetic spin-density wave phase. Also, ARPES data exhibit a depletion of spectral weight near E_F that differs from the superconducting gap.

To investigate the influence of Coulomb correlations on the electronic properties of iron pnictides, we use dynamical mean field theory (DMFT) combined with exact diagonalization (ED) as multi-orbital impurity solver [2]. As shown in Fig. 1(a), both the interacting and non-interacting Fe 3d density of states (DOS) reveal two main features separated by a minimum above E_F . Similar quasi-particle spectra were obtained by several groups for a variety of pnictides. It is not clear to what extent the pseudogap seen in these spectra is induced by Coulomb correlations or band structure effects.

To resolve this issue, we have performed DMFT calculations for five degenerate semi-elliptical bands [3]. Since in this case the DOS is featureless, correlation induced spectral modifications are easily identified. In addition, by scanning a wide range of Coulomb and exchange energies, it is feasible to investigate their respective roles. The main result of this work is that many-body effects are much more

sensitive to the magnitude of Hund's rule coupling J than to the intra-orbital Coulomb repulsion U . In particular, exchange interactions give rise to a pseudogap above E_F , which persists in the full range of realistic values of J , but disappears at small J . This is illustrated in Fig. 1(b) which shows DMFT spectra for $U = 3, \dots, 5$ eV and $J = 0.5$ eV. Spectra up to $J = 1.0$ eV are remarkably similar. Except in the limit $J = 0$, the interacting DOS exhibits peaks below

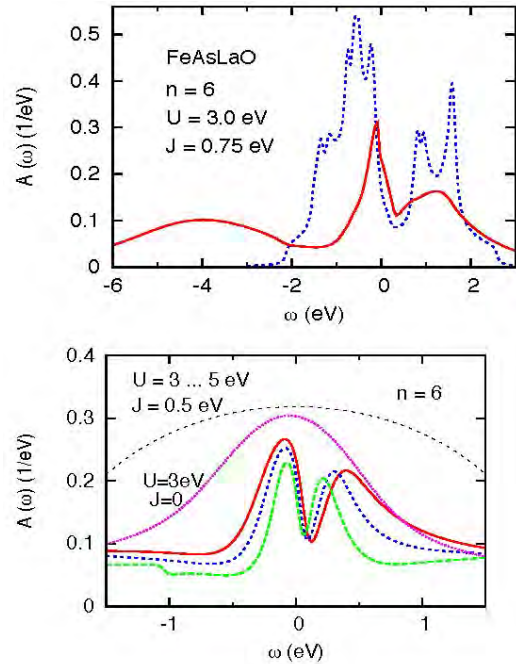


FIG. 1: (a) Fe 3d DOS of FeAsLaO. Solid curve: DMFT; dashed curve: LDA. (b) DMFT DOS of degenerate five-band model for several U and J . Black dashed curve: LDA.

and above E_F , separated by a pseudogap above E_F . The peak-dip structure near E_F is reminiscent of the one in the quasi-particle spectrum shown in panel (a). Since the bare DOS is smooth, the pseudogap is induced by the frequency-dependent selfenergy. These results suggest that the pseudogap above E_F is a generic feature caused by correlations within the 3d shell and that its existence depends crucially on realistic values of Hund's coupling. The quasi-particle spectra of actual pnictides should therefore consist of a combination of correlation features associated with J and signatures related to the bare density of states.

To illustrate the effect of Coulomb correlations on the self-energy, we show in Fig. 2 the imaginary part of $\Sigma(i\omega_n)$ for several occupancies. For $n \geq 6.2$, $\text{Im} \Sigma(i\omega_n) \sim \omega_n$ at low energies, so that the system is a correlated Fermi liquid with a doping dependent effective mass enhancement $m^*/m \approx 3, \dots, 6$. At smaller n , $\text{Im} \Sigma$ reveals a nonzero onset, associated with bad-metallic behavior. As shown previously [4], the spin correlation function then changes from Pauli to Curie Weiss behavior, indicating a spin freezing transition.

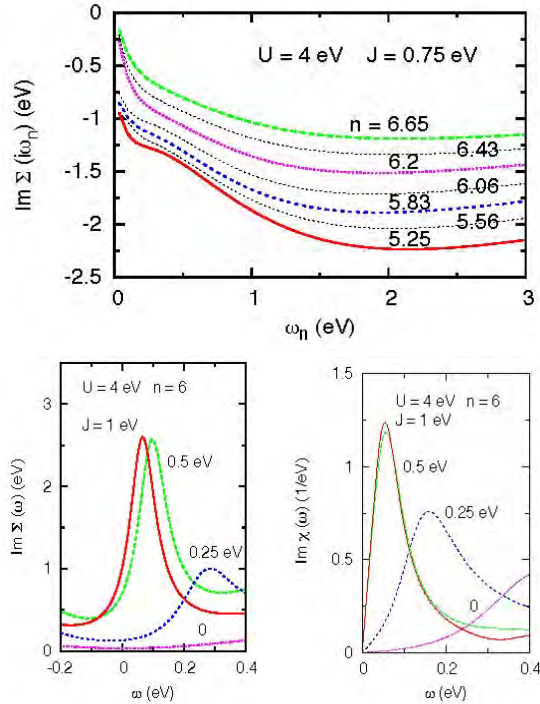


FIG. 2: (a) Self-energy for five-band model within ED DMFT for various occupancies. (b) Variation of self-energy (left) and spin susceptibility (right) with Hund's coupling.

In addition, $\text{Im} \Sigma(i\omega_n)$ exhibits a kink near $\omega_n \approx 0.1, \dots, 0.2$ eV, which is weak in the Fermi-liquid region, but becomes more intense at lower occupancy. As shown in panel (b), this kink is related to a resonance in $\text{Im} \Sigma(\omega)$, which is the origin of the pseudogap above E_F in the spectra shown in Fig. 1. Remarkably, the resonance disappears at small J . For $J = 0.5, \dots, 1.0$ eV, the local spin correlation function reveals a maximum below 0.1 eV, suggesting that the resonance in $\text{Im} \Sigma(\omega)$ corresponds to a collective mode induced by spin fluctuations associated with Hund's coupling. Thus, states in the resonance region have a greatly reduced lifetime. According to Kramers-Kronig relations, $\text{Re} \Sigma(\omega)$ exhibits a positive slope near the resonance, so that spectral weight is removed from the pseudogap region. Beyond this region, the slope of $\text{Re} \Sigma(\omega)$ becomes again negative, giving rise to a kink in the dispersion of energy bands.

A complementary understanding of the pseudogap can be achieved by realizing that the system at $n = 6$ occupancy exists in proximity to the $n = 5$ Mott insulator. As shown in Fig. 3, at half-filling the degenerate five-band model exhibits a Mott transition at a critical Coulomb energy that depends

sensitively on J , but is insensitive to U . In particular, U_c diminishes rapidly when J increases. Thus, for realistic U and J (see green box), the half-filled system is a Mott insulator composed of localized $S = 5/2$ spins. Upon doping, some of the localized states become itinerant, so that the DOS exhibits a narrow quasiparticle peak below E_F , and a minimum or pseudogap above E_F , in agreement with the spectra shown in Fig. 1. On the other hand, according to the phase diagram shown in Fig. 3, at small J the high orbital degeneracy yields a weakly correlated metal since $U \ll U_c$. This also holds at finite electron doping, so that the spectral distribution exhibits a broad quasi-particle peak, as indicated by the results for $U = 3$ eV, $J = 0$ in Fig. 1(b). It is evident, therefore, that the collective mode in the self-energy shown in Fig. 2 and the associated pseudogap obtained at realistic values of J are a consequence of Hund's coupling.

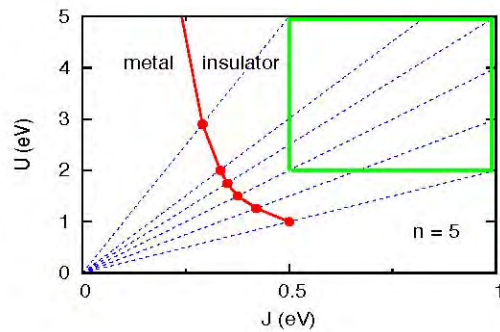


FIG. 3: Phase diagram of five-band model at half-filling. Dashed lines: fixed ratios $J/U = 1/10 \dots 1/2$. Dots: U_c of Mott transitions for these ratios. To the right (left) of the solid red curve, the system is insulating (metallic). Green box: range of U and J used in DMFT studies of iron pnictides.

At present there exists appreciable uncertainty concerning the experimentally determined values of U and J as well as their theoretical estimates. Nonetheless, the robustness of the pseudogap over a wide range of U and J and the persistence of the Mott phase at half-filling down to remarkably low Coulomb energies suggest that the characteristic peak-dip structure near E_F seen in many quasiparticle spectra of pnictides is partially caused by Coulomb correlations intimately related to Hund's coupling.

-
- [1] A.A. Schafgans et al., Phys. Rev. Lett. **108**, 147002 (2012), and references herein.
 - [2] A. Liebsch, H. Ishida, J. Phys. Condens. Matter **24**, 05320 (2012).
 - [3] A. Liebsch, Phys. Rev. B **84**, 180505(RC) (2011).
 - [4] H. Ishida, A. Liebsch, Phys. Rev. B **81**, 054513 (2010); A. Liebsch, H. Ishida, *ibid.* **82**, 155106 (2010).

Magnetic nano-skyrmions in an Fe monolayer on Ir(111)

G. Bihlmayer¹, S. Heinze², K. v. Bergmann³, S. Blügel¹

¹ Peter Grünberg Institut-1 & Institute for Advanced Simulation-1, Forschungszentrum Jülich

² Institut für Theoretische Physik und Astrophysik, Universität zu Kiel

³ Institut für Angewandte Physik, Universität Hamburg

Topological protection of a magnetic texture occurs when the stability of the structure is a consequence of the lattice as a whole, in contrast to other mechanisms, that rely on the properties of the individual magnetic moments. E.g., ferromagnetism in two dimensions can be stabilized by the magnetic anisotropy of single ions, while we report here on a magnetic skyrmion lattice that gains its robustness against external perturbations from its topological properties. In contrast to previously observed skyrmions, this example is of atomic dimensions, i.e. about 1 nm in diameter as experimentally observed by scanning-tunneling microscopy (STM). Density functional theory (DFT) elucidates the mechanisms that lead to the formation of these structures.

About 50 years ago, the English physicist Tony Skyrme was looking for stable mathematical solutions of field-theoretical equations that can be characterized by their topological properties [1] and are interpreted as particles. A simple, one-dimensional example in Fig. 1a can illustrate the principle: shown is a domain structure of a ferromagnetic chain of atoms. The direction of the magnetization of a single atom is symbolized by an arrow. To the left and right ends of the chain, these arrows point upwards, while in the middle we find a domain with opposite spin-orientations. In between, the magnetization rotates in so-called domain-walls. Both walls can rotate – as shown in Fig. 1a – either the same or (Fig. 1c) an opposite sense of rotation. Mathematically, this difference can be described by plotting the angle, θ of the spins with respect to the z-axis, on a unit circle. Then, it is observed that in the first case (Fig. 1a) the magnetization describes a full circle, while in the second case (Fig. 1c) it just describes a semicircle before the angle θ returns to zero. A winding number can be defined as

$$S = \frac{1}{2\pi} \int \frac{\partial\theta(x)}{\partial x} dx$$

to describe the two cases: in the first situation we find a winding number of unity, in the second case it is zero.

It can be easily seen, that a structure with finite winding number (i.e. a skyrmion) shows a stability that results from its topology. Suppose an external magnetic field in z-direction tries to remove the middle domain of the magnetic arrangement shown in Fig.1: while the inner domain shrinks, the domain

walls start moving towards each other. In the case shown in Fig. 1b, the angle θ will rotate around the unit circle in increasingly shorter spatial distances, but the inner domain cannot be removed due to a continuous deformation of the lattice in the (x,z) -plane. Quite different from this behaviour is the evolution of the magnetic structure shown in Fig. 1d: The curve described by θ contracts to a point and the middle domain disappears. We see that the skyrmion, with its non-zero winding number, is protected against continuous deformations caused by an external magnetic field.

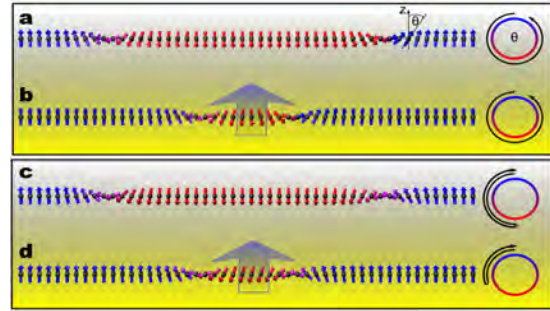


FIG. 1: One-dimensional example of a topologically protected magnetic structure (a,b) and of a topologically trivial one (c,d). On the right the orientation of the spins along the chain direction (x) is shown as a graph on the unit circle. In (a) the angle goes once around the circle and the winding number is unity, in (c) it is zero. Under the influence of a magnetic field (b,d) it can be seen that this difference in the topology of the magnetic structures results also in a difference of stability: while in the topologically trivial structure (c,d) the domain is removed, in the non-trivial one (a,b) it remains stable.

It is easily realized that the above discussion is only valid, if we the directions of the magnetic moments remain restricted to the shown (x,z) -plane. Spin rotations via the y -direction were not considered. An extension of the above discussion to three-dimensional magnetic structures on a two-dimensional lattice is straight forward: denoting the magnetization direction in the (x,y) -plane with the vector \vec{n} , we can define the winding number as

$$S = \frac{1}{4\pi} \int \vec{n} \cdot \left(\frac{\partial \vec{n}}{\partial x} \times \frac{\partial \vec{n}}{\partial y} \right) dx dy.$$

Without performing the integration, the above expression defines a skyrmion density, $S(x,y)$. In a similar fashion, Skyrme extended this concept to four dimensions. He was looking for Hamiltonians

that allow for solutions, which are characterized by non-trivial (non-zero) topological numbers. In field theory, many properties of such Hamiltonians are known, e.g. they have to contain higher (at least second) derivatives of the field variables for models in more than one spatial dimension [2].

Considering the particle nature of skyrmions there is a considerable interest to see, whether similar conditions can be realized in magnetic structures so that they can be used as units for information storage. Experimentalists in Hamburg found that a monolayer of iron on the hexagonal iridium (111) surface shows a square-like magnetic contrast in the spin-polarized STM images, like the one shown in the left inset of Fig. 2. A combination of these measurements and DFT calculations in Jülich could confirm that these structures are indeed skyrmions, which arrange on a lattice of atomic scale [3]. These nano-skyrmions are at least one order of magnitude smaller than the magnetic skyrmions found so far [4].

Commonly used models, like the Heisenberg Hamiltonian, describe the formation of one-dimensional spin-spirals that might be homogeneous or inhomogeneous as the structure shown in Fig.1a. The essential ingredient to form two-dimensionally modulated spin-structures is, in our example, a higher-order spin interaction, known as four-spin term

$$H_{4\text{-spin}} = \sum_{ijkl} K_{ijkl} \left((\vec{S}_i \cdot \vec{S}_j) (\vec{S}_k \cdot \vec{S}_l) + (\vec{S}_j \cdot \vec{S}_k) (\vec{S}_l \cdot \vec{S}_i) - (\vec{S}_i \cdot \vec{S}_k) (\vec{S}_j \cdot \vec{S}_l) \right)$$

that couples the one-dimensional (co-planar) spin-spirals to three-dimensional magnetic structures. But, as it turns out, such a superposition of two spin-spirals does not lead automatically to a topologically non-trivial spin structure, rather to a lattice of skyrmions and their anti-particles, the anti-skyrmions. Our calculations show that the finite winding number, the integral over the skyrmion density shown in the right inset of Fig.2, which is observed in the Fe films on Ir(111), result from the combination of the above-mentioned interactions with another, relativistic, two-spin term, the Dzyaloshinskii-Moriya (DM) interaction:

$$H_{\text{DM}} = \sum_{ij} \vec{D}_{ij} \cdot (\vec{S}_i \times \vec{S}_j)$$

This term favours skyrmions over anti-skyrmions and is, thus, responsible for the topological protection of this spin structure.

It should be noted that the DM interaction also selects a certain sense of rotation of the spin-spirals, e.g. a situation as shown in Fig. 1a can be more stable than the one shown in Fig.1c, where domain walls of different rotational sense occur. Recently, we have shown that this is indeed realized in ultrathin Fe films on a W(110) substrate [5]. In these one-dimensional examples, the left-rotating wall can be considered the “anti-particle” of the right-rotating wall. In two dimensions, structures with different

rotational sense (chirality) can have the same winding number, while the antiparticle is achiral.

Experiments confirmed a high stability of the skyrmion lattice in magnetic fields, as expected from its properties. Furthermore, careful analysis of the data shows that the magnetic structure is not exactly commensurate with the atomic lattice, thus being detached from the periodicity of the supporting atoms.

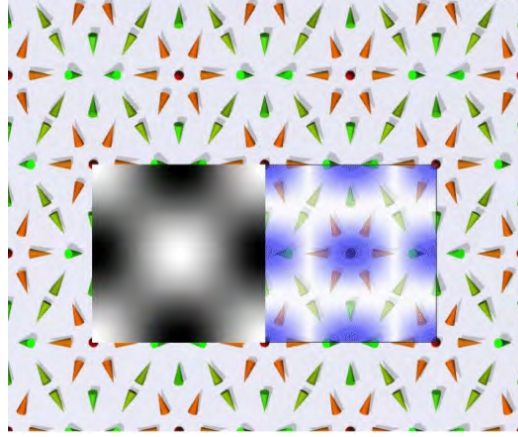


FIG. 2: The tiny vortices formed by only 15 atoms arrange in an almost square lattice. The colored cones indicate the orientation of the magnetic moments directions of the hexagonal iron layer. The inset on the left is a simulated image as it results from scanning tunneling microscopy with a spin-polarized tip with a polarization perpendicular to the film plane. The right inset shows the skyrmion-density, $S(x,y)$, in white (low) and blue (high).

For future applications, e.g. in the field of spintronics, these magnetic skyrmions open completely new possibilities: Nowadays, new storage concepts based on isolated skyrmions realizing a single bit are in the focus of research. But there are many questions that still have to be addressed, e.g. regarding the interaction of electrical currents with the skyrmions. Ideally this would offer a possibility to move and manipulate these magnetic entities. Our work [3] shows, that miniaturization of these concepts might be possible, down to the atomic scale.

We gratefully acknowledge insightful discussions with N. Kiselev and A. Bogdanov and the grant of computing time by the Jülich Supercomputing Centre (JSC).

-
- [1] T. H. Skyrme, A non-linear field theory. Proc. R. Soc. Lond. Ser. A 260, 127-138 (1961).
 - [2] G. H. Derrick, J. Math. Phys. 5, 1252 (1964).
 - [3] S. Heinze, K. von Bergmann, M. Menzel, J. Brede, A. Kubetzka, R. Wiesendanger, G. Bihlmayer, and S. Blügel, Spontaneous atomic-scale magnetic skyrmion lattice in two dimensions. Nature Physics 7, 713 (2011).
 - [4] S. Mühlbauer, B. Binz, F. Jonietz, C. Pfleiderer, A. Rosch, A. Neubauer, R. Georgii, und P. Böni, Science 323, 915-919 (2009).
 - [5] M. Heide, G. Bihlmayer and S. Blügel, Phys. Rev. B 78, 140403(R) (2008).

Two-dimensional topological insulators from first principles

G. Bihlmayer, F. Freimuth, H. Zhang, C. Friedrich, Y. Mokrousov, S. Blügel

Peter Grünberg Institut-1 & Institute for Advanced Simulation-1, Forschungszentrum Jülich

Edge states of topological insulators (TIs) carry dissipationless spin currents that are ideal for applications from spintronics to quantum computing. Employing density functional theory (DFT) and many-body perturbation theory, we study the electronic structure of TIs, the topological properties of the bulk as well as states at the boundaries under various conditions, e.g. in contact with substrates that may influence the material's structure or expose it to the presence of a magnetic (exchange) field. This opens the possibility to stabilize and tailor the properties of two-dimensional TIs like the Bi(111) bilayer.

Since the discovery of the Quantum Hall Effect (QHE) in silicon MOSFETs in 1980 it is clear that the surface of an insulator or semiconductor can host fundamentally new states of matter with fascinating properties like quantized charge conduction. While the QHE is only observed in the presence of extremely high magnetic fields, the Quantum Spin Hall Effect (QSHE), theoretically proposed around 2005, is carried by similar exotic states, existing at the edges of insulators, but without the external field. It is the relativistic effect of spin-orbit coupling (SOC) that leads to the quantized spin conduction at the surface of some materials, so called topological insulators, and can be understood as two copies of the QHE with different spin. Since the experimental confirmation of the QSHE in thin HgTe heterostructures, there is a continuous effort to find new, improved materials in this exotic state of matter.

When we break the translational invariance of a crystalline solid in z direction, k_z is no longer a good quantum number, and a continuum of states is formed in some regions of the (k_x, k_y) plane. This is the projected (bulk) bandstructure and in its gaps new states can form that are localized at the surface. If the gap is opened by SOC, there are always extra states in the gap. Even on a nonmagnetic surface these states are spin-split, since electrons move with wavevector k_{\parallel} in the potential gradient of the surface. In the rest-frame of the electrons, this electric field is experienced (Lorentz-transformed) as magnetic field. This is enhanced by atomic SOC, which is, as mentioned above, a basic ingredient to TIs. Strong SOC is induced by heavy atoms like Bi or Hg.

If, in addition, the (occupied) bulk states show special integral symmetry properties, one can also conclude that these edge states have to connect the valence and conduction band so that an odd number of Fermi contours forms in the Brillouin zone of the surface. For an edge of a two-dimensional (2D) TI

this means that, given a certain direction in k space, the number of spin-up and spin-down channels for transport in this direction do not match. As an example, Fig.1 shows the edge bandstructure of a Bi(111) bilayer ribbon [1].

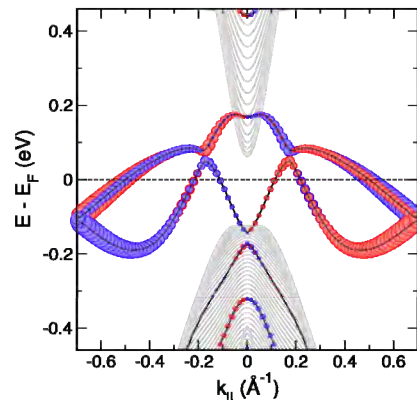


FIG. 1: Bandstructure of a Bi(111) bilayer ribbon and projected bandstructure of the bilayer (grey). Between valence and conduction band there is a 0.2 eV bandgap where the edge states (color) reside. The size of the symbols and the colour show the spin polarization and direction of the states, respectively. For a given spin direction, this also indicates the localization of the states on the left or right edge of the ribbon.

The special integral symmetry properties of the bulk can be mathematically cast into a number, denoted \mathbb{Z}_2 , and bears some similarity to the Chern numbers known from the theory of the QHE. In the absence of magnetic fields \mathbb{Z}_2 is well defined and edge currents are protected as the bandstructure (Fig.1) does not provide a spin-conserving backscattering channel. In the presence of magnetic fields a spin Chern number, C_s , was proposed, given by the difference of the Chern numbers of the spin-up and spin-down manifolds corresponding to the \mathbb{Z}_2 number. Our calculations show that a Bi(111) bilayer in an exchange field remains in a time-reversal broken (TRB) TI state with $C_s = -1$ before it transforms via a metallic phase to a Chern insulator that shows the Quantum Anomalous Hall (QAH) effect [2].

While the Bi(111) bilayer was one of the first proposed 2D TIs, it remained experimentally inaccessible: on Si(111) substrates, ultrathin Bi(111) layers undergo a structural transformation below a certain layer thickness and form thin layers of black-phosphorus type that are topologically trivial ($\mathbb{Z}_2=0$) [1]. But in the last years experimentalists succeeded in stabilizing these bilayers using Bi₂Te₃ as a substrate, which is itself a TI in the bulk. Our calculations show that the bandstructure of the Bi

bilayer is strongly influenced by the contact to the substrate, however, apart from some electron-transfer into the substrate the topological properties themselves remain unchanged [3].

It is interesting to compare Bi to Sb, which is chemically similar and crystallizes in the same structure, but as lighter element it shows smaller SOC effects. While the Sb(111) bilayer is topologically trivial, bulk Sb (in contrast to Bi) is a topological insulator ($\mathbb{Z}_2=1$). Therefore, it is of interest to investigate alloys of these two elements in low dimensions. We studied ultrathin films in (111) and (110) orientation assuming different chemical orderings. In their ground state the films turned out to be topologically trivial [4], showing a strong sensitivity to structural details: E.g. while a Bi(110) bilayer film is a TI in the A7 (bulk Bi) structure, upon relaxation some buckling occurs and the structure transforms to A17 (black P). In the course of this transition the bandgap closes and \mathbb{Z}_2 turns 0. Similar effects are seen for BiSb alloys [4].

The closing of the bandgap upon variation of a parameter is an indication (although not a proof) that the topology of the bandstructure changes. Like a polar domain wall in a ferroelectric indicates the change of the sign of polarization by formation of a metallic state, also the insulator cannot change \mathbb{Z}_2 without closing the bandgap. When SOC is gradually switched on in a calculation of a topological insulator, we can also observe the “exchange” of symmetry between valence and conduction band in this way. Therefore, whether a material is actually a TI or not depends not only on the strength of the SOC, but also on the bandgap (most TIs are in reality small gap semiconductors). Thus, the accurate description of the bandgap (that is usually underestimated in DFT) can be an important issue.

Many-body perturbation theory in the GW approximation for the electronic self-energy is a viable method to correct the DFT bandgap (more generally the full bandstructure). Apart from the excitation energies, one also obtains lifetime information. We have developed a fully spin-dependent formulation of the GW approximation [5], which allows to describe many-body renormalization effects arising from SOC, and implemented it in our GW code [6], which uses the same all-electron basis as the DFT code. This approach goes beyond a mere perturbative treatment and takes into account the spin off-diagonal elements of the Green function and the self-energy, which emerge as a result of the coupling of spatial and spin degrees of freedom.

Applying the scheme to quasiparticle calculations of HgS, HgSe, and HgTe, we find that the self-energy correction has a significant effect on their electronic bandstructures. These systems exhibit an inverted band structure due to strong relativistic effects. Figure 2 shows the bandstructure of HgTe as an example. While standard DFT functionals correctly predict the bandgaps to be negative, they turn out to be far too negative compared to experiment: The band inversion is overestimated. A considerable quantitative improvement is achieved by the fully

spin-dependent GW approximation, which brings the calculated bandgap much closer to experiment.

Furthermore, we find an unprecedented many-body renormalization of the spin-orbit splitting. The values change by about 0.1 eV, which corresponds to 10–50%. The resulting values compare very well with experiment. Another interesting finding is the reduction of the effective mass by a factor of 2 relative to the DFT value, which results from the strong k dependence of the GW self-energy.

The effect of the SOC on the screened interaction W is minor in the systems studied, implying that the spin-orbit induced changes originate mainly from the single-particle Green function G . This fact may allow for a simplification of the calculations. It would be interesting to investigate if this finding also applies to systems, in which SOC modifies the band structure considerably, e.g. Ir-based systems. The fully spin-dependent DFT and GW methods, in which SOC has been included in a consistent way, provide a reliable integrated computational approach to investigate the fine details of the electronic structure of TIs containing chemical elements with high nuclear number and strong SOC.

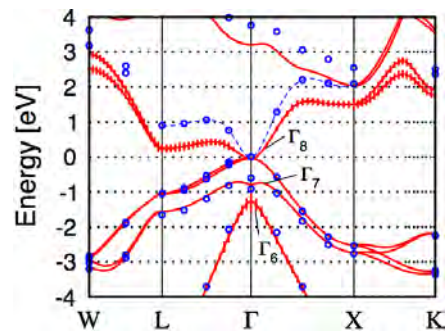


FIG. 2: Bandstructure of HgTe calculated within DFT using the local-density approximation (red lines) and with the GW approximation (blue dots). The vertical bars scale with the projection of the wavefunctions onto the Hg 6s state.

We gratefully acknowledge collaborations with the groups of S. Murakami, S. Hasegawa, E.V. Chulkov, and F. Aryasetiawan and the grant of computing time by the Jülich Supercomputing Centre (JSC).

-
- [1] M. Wada, S. Murakami, F. Freimuth, and G. Bihlmayer, Phys. Rev. B 83, 121310(R) (2011).
 - [2] H. Zhang, F. Freimuth, G. Bihlmayer, S. Blügel, and Y. Mokrousov, Phys. Rev. B 86, 035104 (2012).
 - [3] T. Hirahara, G. Bihlmayer, Y. Sakamoto, M. Yamada, H. Miyazaki, S.-i. Kimura, S. Blügel, and S. Hasegawa, Phys. Rev. Lett. 107, 166801 (2011).
 - [4] G. Bihlmayer, Yu. M. Koroteev, E. V. Chulkov, and S. Blügel, New J. Phys. 12, 065006 (2010).
 - [5] R. Sakuma, C. Friedrich, T. Miyake, S. Blügel, and F. Aryasetiawan, Phys. Rev. B 84, 085144 (2011).
 - [6] C. Friedrich, S. Blügel, and A. Schindlmayr, Phys. Rev. B 81, 125102 (2010).

Ferromagnetic spin coupling of N-impurities in N-doped MgO stabilized by intersite Coulomb interaction

Ivetta Slipukhina, Phivos Mavropoulos, Stefan Blügel, Marjana Ležaić

PGI-1 & IAS-1: Quantum Theory of Materials, Forschungszentrum Jülich

We conduct computational, first-principles studies of Nitrogen (N)-doped MgO. For a nitrogen dimer, a ferromagnetic coupling between spinpolarized 2p-holes is revealed by calculations based on the density functional theory amended by an on-site Coulomb interaction and corroborated by the Hubbard model. It is shown that the ferromagnetic coupling is facilitated by a T-shaped orbital arrangement of the 2p-holes, which is in its turn controlled by an intersite Coulomb interaction due to the directionality of the p-orbitals. We thus conjecture that this interaction is an important ingredient of ferromagnetism in band insulators with 2p dopants.

In the past decades, we have been witnessing a rapid development of various mechanisms and techniques for storing, manipulating and securing information. This is an important component in industrial development: the world-wide hard disk revenue is about to reach 30 billion Euros and is still rising. Ever increasing demands of the market are a great challenge for the information storage industry. The multifunctionality of the new devices puts stringent constraints on the materials that can be used: the higher the functionality, the more complicated the components. An example are the multifunctional oxides, in particular multiferroics, which are magnetic and ferroelectric in the same phase, offering the possibility of a multi-bit memory. However, these materials usually have a very complex crystal structure, with unit cells consisting of many atoms and strongly interacting magnetic and structural properties, that may further be modified or completely altered in conditions of strain (epitaxial or chemical) or reduced dimensionality [1, 2, 3]. Furthermore, these materials are scarce and a considerable effort is invested into computational design and experimental synthesis of new multiferroics. Note that especially useful in applications would be the ferromagnetic multiferroics which are unfortunately most difficult to find as ferromagnetism in insulating oxides does not occur frequently.

In the recent years, a new strategy in engineering ferromagnetic insulators is at work: instead of the traditional doping of nonmagnetic insulators with transition-metal ions, doping with *sp*-elements is explored. The observed magnetism is associated with the partially filled *p*-electronic states of the dopants

(or of Oxygen, induced by the dopants) and is usually referred to as *sp*-magnetism. For a nonmagnetic system to become magnetic due to doping, several conditions have to be fulfilled: (i) local magnetic moments have to be formed (usually, on dopants) (ii) the locally formed moments should interact with each other; note that the radius of such interaction is limited, and usually does not extend further than a couple of lattice constants in doped systems (iii) the magnetic moments should form a network spreading throughout the sample. In order to achieve ferromagnetism in the sample, the interaction of the local moments should be ferromagnetic, i.e. the atomic spins should be mutually parallel. Here we present our study of the driving force for the ferromagnetic interaction of the spins located on N-dopants in N-doped MgO [4, 5].

First, one should understand the origin of the local magnetic moment formed on N-dopants. Pure MgO is a nonmagnetic band insulator. Due to its large electronegativity, Oxygen attracts two electrons from the Mg outer electronic shell in order to complete its own outer shell with eight electrons. Six of these electrons are situated in *p*-orbitals, two in each one of p_x , p_y and p_z . In N-doped MgO, N substitutes one O atom in the crystal lattice. However, N has one electron less, which means that one of the three *p*-orbitals remains occupied with only one electron. The 2*p* wavefunctions are rather localized on the N atom and so the spin of one unpaired electron gives rise to the magnetic moment localized on this atom.

Next, we study the interaction of two N-impurities positioned next to each other in the MgO lattice. There are two points to pay attention to: (i) the mutual orientation of the half-filled orbitals on the two N atoms and (ii) the mutual orientation of spins on the two N atoms – ferromagnetic (FM) or antiferromagnetic (AFM). We define a coordinate system with the p_x and p_y orbitals pointing toward neighboring N (or O) atoms in the *xy* plane (Fig. 1), while the p_z orbital points out of plane, toward Mg. We omit Mg atoms from the discussion because they do not contribute to the magnetic interaction between the N-dopants.

The half-filled *p*-orbitals on two N atoms can be parallel to each other without any overlap (*yy* and *zz* configuration) or with a direct overlap (*xx* configuration); further in a T-configuration the half-occupied orbitals on the two Nitrogens are perpendicular to each other (*xy* and *xz* configuration).

Since the magnetic interaction is carried by the electrons that can move between the two N-sites, we can omit from our considerations the configurations in which only fully occupied Nitrogen orbitals overlap with each other, and we are left with only two configurations: xx (Fig. 1 top) and the T-configuration (Fig. 1 bottom). In order to understand what kind of magnetic interaction one can expect in these two configurations, three factors should be taken into account in a minimal model: the kinetic energy of the electrons (expressed by the so-called hopping matrix element, t), the onsite Coulomb-repulsion between the electrons U and the Hund's exchange J . Considering the FM and AFM spin-orientation in both of the two orbital configurations, one arrives at the conclusion that energetically the most favourable state should be the one with xx -orbital and AFM-spin configuration, i.e. one would expect no net magnetization in N-doped samples of MgO.

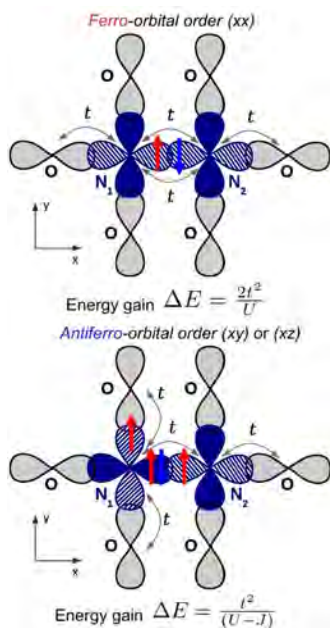


FIG. 1: Ferro-orbital (top) and antiferro-orbital (bottom) arrangement of the half-filled Nitrogen p -orbitals in N-doped MgO. The arrows indicate the preferred spin-arrangement: AFM for the ferro-orbital and FM for the antiferro-orbital arrangement. When the Coulomb intersite interaction is neglected, the configuration on the top is the ground state (as indicated by the corresponding energy gain). Firstprinciples calculations, however, identify the configuration on the bottom as the ground state.

Experimentally, however, the samples were found to be ferromagnetic. We also performed first-principles calculations looking for the answer to this puzzle. We used supercells of 64 atoms of host MgO and investigated all possible mutual orientations of orbitals and spins on the two N atoms (12 different spin-orbital configurations in total). The calculations yielded a ferromagnetic ground state with the T-orbital configuration, in contrast to our expectations relying on the minimal model. The only answer could be that the model was incomplete. Indeed, it turns out that the three factors mentioned above were not accounting for all the important interactions. Extending our model to take into account the

intersite Coulomb interaction, V , which favours the T-shaped configuration, we arrive to the conclusion in accordance to our first-principles findings (see Fig. 2) [5].

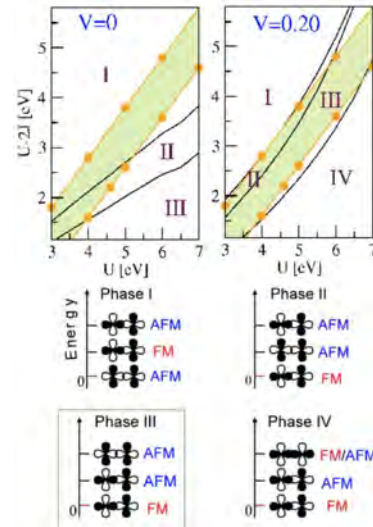


FIG. 2: Top: The $(U - 2J)$ vs. U phase diagram of the model at $V = 0$ and $V = 0.2$ eV. Orange circles denote the U and J values, considered in our *ab initio* calculations, outlining physically relevant (with physically acceptable U and J values) area in green. Bottom: The phases corresponding to different sequences of several orbitally arranged states in the order of energetic stability. Phase III is found in this system by the first-principles calculations. Clearly, in order to reproduce this result in the model, a finite Coulomb intersite repulsion V should be included.

The result that the FM spin-orientation is in fact stabilized by the intersite Coulomb interaction is rather exciting, as it is probably a characteristic of the systems presenting sp -magnetism exclusively, due to a larger spatial extent and directionality of the p -wavefunctions compared to the d -ones. However, further studies are needed in order to establish the role played by this interaction in insulators doped with $2p$ elements.

Support of research by the HGF-YIG Programme VH-NG-409 (Computational Nanoferronics Laboratory) and by a computing grant through the Jülich Supercomputing Centre (JSC) is greatly acknowledged.

- [1] C. Kadlec, V. Goian, K. Z. Rushchanskii, P. Kužel, M. Ležaić, K. Kohn, R. V. Pisarev, and S. Kamba, Phys. Rev. B **84**, 174120 (2011)
- [2] K. Z. Rushchanskii, S. Kamba, V. Goian, P. Vanek, M. Savinov, J. Prokleška, D. Nuzhnyy, K. Knižek, F. Laufek, S. Eckel, S. K. Lamoreaux, A. O. Sushkov, M. Ležaić and N. A. Spaldin, Nature Mater. **9**, 649 (2010)
- [3] M. Ležaić and N. A. Spaldin, Phys. Rev. B **83**, 024410 (2011)
- [4] Ph. Mavropoulos, M. Ležaić and S. Blügel, Phys. Rev. B **80**, 184403 (2009)
- [5] I. Slipukhina, Ph. Mavropoulos, S. Blügel, and M. Ležaić, Phys. Rev. Lett. **107**, 137203 (2011)

Heat Transfer between Solids and Graphene

B.N.J. Persson

Peter Grünberg Institut-1, Forschungszentrum Jülich

We have developed a general theory for the heat transfer between solid objects which includes both the phononic heat transfer and the radiative heat transfer associated with the evanescent electromagnetic waves which exist outside of all bodies. For the (weakly coupled) contact between graphene and a flat solid (amorphous SiO₂) the phononic heat transfer dominates, and the calculated heat transfer coefficient is in good agreement with the value deduced from experimental data.

Graphene, the recently isolated 2-dimensional (2D) carbon material with unique properties due to its linear electronic dispersion, is being actively explored for electronic applications. Important properties are the high mobilities reported especially in suspended graphene, the fact that graphene is the ultimately thin material, the stability of the carbon-carbon bond in graphene, the ability to induce a bandgap by electron confinement in graphene nanoribbons, and its planar nature, which allows established patterning and etching techniques to be applied.

Recently it has been found that the heat generation in graphene field-effect transistors can result in high temperature and device failure. Thus, it is important to understand the mechanisms which influence the heat flow. Understanding the energy relaxation and transfer channels are also important for optoelectronic devices and thermo photo voltaics.

Here we present a study of the different mechanisms which determine the heat transfer between graphene and an amorphous SiO₂ substrate. We first study the phononic contribution to the heat transfer.

Consider the interface between two solids, and assume that local thermal equilibrium occurs everywhere except close to the interface. The stress or pressure acting on the surface of solid 1 from solid 0 can be written as $\sigma(\mathbf{x},t) = K[u_0(\mathbf{x},t) - u_1(\mathbf{x},t)]$, where u_0 and u_1 are the (perpendicular) surface displacement of solid 0 and 1, respectively, and where K is a spring constant per unit area characterizing the interaction between the two solids. For weakly interacting solids the parallel interfacial spring constant K_{\parallel} is usually much smaller than the perpendicular spring constant $K_{\perp} = K$, and we will neglect the heat transfer resulting from the tangential interfacial stress associated with thermal vibrations (phonons). Using the fluctuation-dissipation theorem one can calculate the heat current $J_{0 \rightarrow 1}$ from solid 0 (temperature T_0) to solid 1 (temperature T_1) [1]:

$$J_{0 \rightarrow 1} = \frac{4}{(2\pi)^3} \int d^2q \int_0^{\infty} d\omega \Pi_0(\omega) \times \frac{K \text{Im} M_0(\mathbf{q}, \omega) K \text{Im} M_1(\mathbf{q}, \omega)}{|1 + K[M_0(\mathbf{q}, \omega) + M_1(\mathbf{q}, \omega)]|^2}, \quad (1)$$

where $M(\mathbf{q}, \omega) = u(\mathbf{q}, \omega)/\sigma(\mathbf{q}, \omega)$ and where

$$\Pi(\omega) = \hbar\omega \left(e^{\hbar\omega/k_B T} - 1 \right)^{-1}.$$

A similar equation with T_0 replaced by T_1 gives the energy transfer from solid 1 to solid 0, and the net energy flow $J = J_{0 \rightarrow 1} - J_{1 \rightarrow 0}$. The heat transfer coefficient $\alpha = J/\Delta T$ as $\Delta T = T_0 - T_1 \rightarrow 0$.

To proceed we need expressions for M_0 and M_1 . Here we give the M -function for membranes. We assume that the out-of-plane displacement $u(\mathbf{x},t)$ satisfies

$$\rho_0 \frac{\partial^2 u}{\partial t^2} = -\kappa \nabla^2 \nabla^2 u + \sigma,$$

where $\rho_0 = n_0 m_0$ is the mass density per unit area of the 2D-system (m_0 is the atom mass and n_0 the number of atoms per unit area), κ is the bending elasticity (for graphene, $\kappa \approx 1$ eV), and $\sigma(\mathbf{x},t)$ an external stress acting perpendicular to the membrane (or xy -plane). Using the definition $M(\mathbf{q}, \omega) = u(\mathbf{q}, \omega)/\sigma(\mathbf{q}, \omega)$ we get $1/M = \kappa q^4 - \rho_0 \omega^2 - i0^+$.

In the model above the heat transfer between the solids involves a single bending mode of the membrane or 2D-system. Because of the weak interaction (and large separation) between the graphene and the substrate, it is likely that the coupling between the in-plane vibrational modes of graphene and the substrate is negligible. The model above assumes implicitly that, due to lattice non-linearity (and defects), there exist phonon scattering processes which rapidly transfer energy to the bending mode involved in the heat exchange with the substrate. This requires very weak coupling to the substrate, so that the energy transfer to the substrate is so slow that the bending mode can be repopulated by phonon scattering processes in the 2D-system, e.g., from the inplane phonon modes, in such a way that its population is always close to what would be the case if complete thermal equilibrium occurs in the 2D-system.

This may require high enough temperature in order for multi-phonon scattering processes to occur with enough rates.

For the graphene - a-SiO₂ system one can calculate that at the graphene-substrate equilibrium separation ($d \approx 0.3$ nm) [1] $K \approx 1.8 \times 10^{20}$ N/m³, and from (1)

we obtain $\alpha \approx 3 \times 10^8 \text{ W/m}^2\text{K}$. This is very close to the measured the heat transfer coefficient: $\alpha \approx 2 \times 10^8 \text{ W/m}^2\text{K}$.

Let us now consider the radiative contribution to the heat transfer, which will dominate for separations $d > 1 \text{ nm}$ between the graphene and the substrate, e.g., for suspended graphene. The heat flux per unit area between two black-bodies separated by $d \gg d_T = c\hbar/k_B T$ is given by the Stefan-Boltzmann law

$$J = \frac{\pi^2 k_B^4}{60 \hbar^3 c^2} (T_0^4 - T_1^4). \quad (2)$$

In this limiting case the heat transfer between the bodies is determined by the propagating electromagnetic waves radiated by the bodies, and does not depend on the separation d . Electromagnetic waves (or photons) always exist outside a body due to thermal or quantum fluctuations of the current density inside the body. The electromagnetic field created by the fluctuating current density exists also in the form of evanescent waves, which are damped exponentially with the distance away from the surface of the body. For an isolated body, the evanescent waves do not give a contribution to the energy radiation. However, for two solids separated by $d < d_T$, the heat transfer may increase by many orders of magnitude due to the evanescent electromagnetic waves; this is often referred to as photon tunneling.

For short separation between two solids with flat surfaces ($d \ll d_T$), the heat current due to the evanescent electromagnetic waves is given by [2]

$$J_{0 \rightarrow 1} = \frac{4}{(2\pi)^3} \int d^2 q \int_0^\infty d\omega \Pi_0(\omega) \times e^{-2qd} \frac{\text{Im}R_0(\mathbf{q}, \omega) \text{Im}R_1(\mathbf{q}, \omega)}{|1 - e^{-2qd} R_0(\mathbf{q}, \omega) R_1(\mathbf{q}, \omega)|^2} \quad (3)$$

where the reflection factor $R(\mathbf{q}, \omega) = [\epsilon(\mathbf{q}, \omega) - 1] / [\epsilon(\mathbf{q}, \omega) + 1]$, where $\epsilon(\mathbf{q}, \omega)$ is the dielectric function. From (3) it follows that if $R_0(\mathbf{q}, \omega)$ and $R_1(\mathbf{q}, \omega)$ are independent of q , the heat current scale as $1/d^2$ with the separation between the solid surfaces.

We now apply (3) to graphene adsorbed on a nominally flat surface of amorphous SiO_2 . In this case the heat transfer is associated with thermally excited optical (surface) phonon's in SiO_2 and electron-hole pairs in the graphene. That is, the electric field of a thermally excited optical phonon in SiO_2 excites an electron-hole pair in the graphene, leading to energy transfer. The excitation transfer occurs in both directions but if one solid is hotter than the other, there will be a net transfer of energy from the hotter to the colder solid.

The graphene dielectric function was recently calculated using the mean field approximation where the electric field acting on an electron is the sum of the external electric field, and the induced field from the other electrons. In the calculation it was assumed that the one-particle energy eigenvalues are linearly

related to the wavevector \mathbf{k} via $\epsilon_{s\mathbf{k}} = s\gamma|\mathbf{k}|$, where $s = \pm 1$ indicate the conduction and valence bands, and where $\gamma \approx 6.5 \text{ eV}$ is a band parameter. In this model the Fermi wavevector $k_F = (\pi n)^{1/2}$, and the Fermi energy $E_F = \gamma k_F$, where n is the number of 2D carriers (electron or hole) per unit area. Note that in the absence of doping (and for vanishing gate voltage) $n = 0$. In the application below the excitation energy $\hbar\omega$ is of order the thermal energy $k_B T$ while the wavevector typically is of order $1/d$, where d is the average separation between the graphene and the substrate surface. Under these conditions $\hbar\omega \ll \gamma q$ which is equivalent to $q/k_F \gg \hbar\omega/E_F$. In this limit, for $q < 2k_F$ the dielectric function takes the following simple form:

$$\epsilon(\mathbf{q}, \omega) = 1 + \frac{4e^2 k_F}{\gamma q} \left(1 + i \frac{\hbar\omega}{\gamma q} \left[1 - \left(\frac{q}{2k_F} \right)^2 \right]^{1/2} \right).$$

For $q > 2k_F$ and $\hbar\omega \ll \gamma q$ the imaginary part of ϵ vanish so there will be no contribution to the heat transfer from $q > 2k_F$.

The optical properties of (amorphous) silicon dioxide (SiO_2) can be described using an oscillator model

$$\epsilon(\omega) = \epsilon_\infty + \frac{a}{\omega_a^2 - \omega^2 - i\omega\gamma_a} + \frac{b}{\omega_b^2 - \omega^2 - i\omega\gamma_b}$$

The frequency dependent term in this expression is due to optical phonon's. In the numerical calculations presented below we assume the graphene free carrier density $n = 10^{13} \text{ cm}^{-2}$, and the values for the optical phonon parameters in $\epsilon(\omega)$ are taken from experiment.

For graphene and an amorphous SiO_2 solid with a flat surface, at the temperatures $T = 500 \text{ K}$ and for the graphene-substrate separation $d \approx 1 \text{ nm}$, from (3) we obtain $\alpha \approx 3 \times 10^5 \text{ W/m}^2\text{K}$. This heat transfer coefficient is much smaller than the phononic contribution for graphene adsorbed on SiO_2 ($d \approx 0.3 \text{ nm}$), but for the non-contact case considered here (e.g., suspended graphene or graphene on rough surfaces [3]) the electromagnetic field coupling will dominate the heat transfer. Note that in this case the black-body radiation (2) gives (for $T = 500 \text{ K}$) $\alpha \approx 28 \text{ W/m}^2\text{K}$ i.e., 4 order of magnitude smaller heat transfer than the near-field contribution.

[1] B.N.J. Persson and H. Ueba, EPL 91, 56001 (2010); B.N.J. Persson, A.I. Volokitin and H. Ueba, J. Phys.: Condens. Matter 23, 045009 (2011).

[2] A.I. Volokitin and B.N.J. Persson, Reviews of Modern Physics 79, 1291 (2007); A.I. Volokitin and B.N.J. Persson, Phys. Rev. B83, 241407(R) (2011); B.N.J. Persson and H. Ueba, J. Phys.: Condens. Matter 22, 462201 (2010).

[3] B.N.J. Persson, B. Lorenz and A.I. Volokitin, The European Physics Journal E31, 3 (2010).

Theoretical probing of inelastic spin-excitations in adatoms on surfaces

S. Lounis¹, A. T. Costa², R. B. Muniz², and D. L. Mills³

¹ Peter Grünberg Institut and Institute for Advanced Simulation, Forschungszentrum Jülich & JARA

² Instituto de Física, Universidade Federal Fluminense, 24210-340 Niterói, Rio de Janeiro, Brazil

³ Department of Physics and Astronomy, University of California Irvine, California, 92697 USA

Within time-dependent density functional theory, combined with the Korringa-Kohn-Rostoker Green function method, we devised a real space method to investigate spin excitations, which are probed nowadays by state of the art inelastic scanning tunnelling spectroscopy. Our scheme enables the description and prediction of the main characteristics of these excitations, i.e. their resonance frequency, their lifetime and their behaviour upon application of external perturbations such as a magnetic field. We illustrate our method with application to 3d adatoms and dimers on several metallic substrates.

Magnetic atoms adsorbed on nonmagnetic substrates have been a topic of active study, both to provide insight into fundamental aspects of magnetism and as possible elements for future information technology. Scanning tunneling spectroscopy (STS) was, for example, utilized for atom-by-atom engineering and magnetometry of tailored nanomagnets [1]. It was also demonstrated, that such an experiment detects magnetic excitations by measuring the changes of the conductance (see e.g. [2,3]). The possibility to excite the substrate leads to an increase of the number of possible final channels for the tunneling electron when the STS bias matches an excitation energy threshold, leading to an abrupt increase of the conductance. Several parameters can affect the properties of these excitations, e.g. (i) the type of substrate, (ii) the details of the hybridization between the electronic states of the adsorbate and those of the substrate, (iii) and the symmetry, shape and size of the adsorbate. Describing such excitations from first-principles is a highly non-trivial task requiring access to dynamical response functions such as the transverse dynamical magnetic susceptibility χ that, in linear response, describes the amplitude of the transverse spin motion produced by an external magnetic field B_{ext} of frequency ω . The imaginary part of χ gives access to the local density of spin-excitations.

We developed a method that allows us to address magnetic excitations using the Korringa-Kohn-Rostoker single particle Green function (KKR-GF) within the framework of time-dependent density functional theory [4]. Our scheme is readily applied to bulk materials, to surfaces with adsorbed films, and it is a real space formalism ideal for diverse small nanostructures. To illustrate our scheme, we

explore spin-excitations of 3d adatoms (Cr, Mn, Fe and Co) on Cu(100), Cu(111) and Ag(111) surfaces.

We solve the following Dyson-like equation:

$$\chi = \chi_0(1 - U\chi_0)^{-1}, \quad (1)$$

where χ_0 , a convolution of Green function integrated over the energy, is the Kohn-Sham susceptibility and χ , the total susceptibility, is exact in principle if the full exchange and correlation kernel U is known. In practice, one often invokes the adiabatic local spin density approximation (ALDA); U can also be viewed as a Stoner parameter, i.e. ratio of the local exchange splitting divided by the magnetic moment, whose value is in the range of $1\text{eV}/\mu_B$ for 3d transition elements.

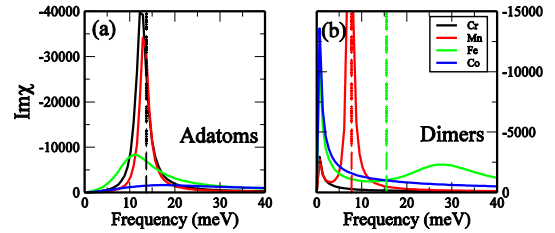


FIG. 1: In (a) the imaginary part of χ is plotted for every adatom when applying an additional magnetic field along the z -direction corresponding to a Larmor frequency of 13.6 meV (dashed line). In (b) are shown $\text{Im}\chi$ calculated for the four dimers. The optical modes, estimated for Mn and Fe from a Heisenberg model, are represented as dashed lines.

In Fig. 1(a), we show our calculations of the resonant response of the local moments for the four adatoms we have investigated on the Cu(001) surface [4]. If one applies an external magnetic field along the initial direction of the magnetic moments, we expect from a Heisenberg model a delta function in the response spectrum located at the Larmor frequency. For the field we have applied, a g value of 2 would provide a resonance at 13.6 meV. As can be seen in Fig.1(a), instead of delta functions we obtain resonances of different widths, i.e. resonances that are shifted differently from the ideal Larmor frequency depending on the chemical nature of the adatom. Cr and Mn are characterized by sharper resonances compared to Fe and Co, meaning that the former adatoms would be reasonably described by a Heisenberg model where the magnetic exchange interactions are evaluated within an adiabatic approach. The observed damping is induced by Stoner (electron-hole) excitations described by the Kohn-Sham susceptibility χ_0 and is related to the local density of states (LDOS) [3,4], and is thus

influenced by the position of the d levels relative to the Fermi energy. Consequently, the Co and Fe resonances are quite broad, since their minority spin levels intersect the Fermi level, whereas those for Mn and Cr are much sharper since for these adatoms the Fermi level lies between the majority and minority states.

The resonant (Larmor) frequency scales linearly with the applied magnetic field, as does the damping of the resonances for small frequencies, which is the regime of interest for STS. We have shown in a combined theoretical and experimental work [3] that such a behavior holds for an Fe adatom on Cu(111) and on Ag(111) surfaces (see e.g. Fig.2). The g -value on the latter, however, and contrary to the copper substrate, was surprisingly larger than 3, both experimentally and theoretically.

Fig.2 shows a nice agreement between theory and experiment, although the theoretical lifetimes are smaller compared to the experimental ones. One would think naively that since Cu and Ag have rather similar electronic properties, their impact on the magnetic response of the adatoms should be qualitatively the same. An important difference, though, between the two surfaces consist in the position of their surface states. For Ag, the bottom of the surface state is much closer to the Fermi energy (~ 60 meV) compared to the one of Cu (~ 500 meV).

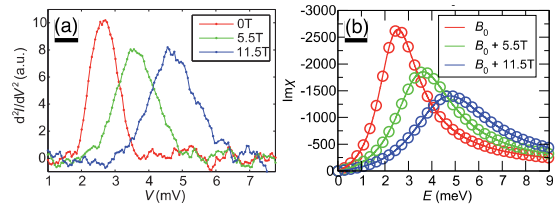


FIG. 2: Fe adatom on Ag(111) surface: The second derivative of the current with respect to the bias voltage measured experimentally by STS (left) and the calculated $\text{Im}\chi$ (right). Increasing the magnitude of an external magnetic field leads to a shift of the resonances to higher energies as well as a linear decrease in their lifetime. Stoner excitations create such a broadening.

A careful theoretical investigation was carried out considering several magnetic 3d adatoms at different locations: (i) on top of the surface, (ii) embedded in the last surface layer, (iii) and embedded in the center of the slab (30 Ag layers) employed to simulate the surface. The closer to the surface, the stronger should be the interaction between the impurity and the surface state. Among all investigated impurities, only the Fe adatom and Mn atom embedded in the surface layer exhibit a large g -value of ~ 3 . Additionally, a strong disturbance of the surface state can be achieved by reducing the thickness of the slab, which modifies the electronic properties of the surface at the Fermi energy and restores the usual g -value of Fe and Mn. This indicates, that the electronic properties of the surface state as well as details of the hybridization to the electronic states of the impurities play a crucial role in the observed g . We could relate this strong g -shift to the behavior of the real part of χ_0 [3].

We have also explored next nearest neighbor dimers of the 3d adatoms deposited on Cu(001) surface [4]

starting from a ferromagnetic configuration (Fig.1 b). For the dimer, there are two resonances, a zero frequency acoustical mode, and a high frequency optical mode that is damped by decay into Stoner excitations. The position of the optical mode provides information on the stability of the assumed ground state. For Cr and Co, we find the optical mode at negative frequency, which informs us that the ferromagnetic state is unstable, whereas for Fe and Mn dimer the modes reside at positive frequencies, so ferromagnetism is stable in total accordance with our static DFT ground-state calculations. The adiabatic approximation and a Heisenberg model gives optical mode frequencies (shown as dashed lines in Fig1.b) at -19.7 meV, 15.4 meV, 39.2 meV and -33.1 meV for respectively Cr, Mn, Fe and Co dimers. The same arguments used to describe the response of the single adatoms apply for the optical modes of dimers: compared to the optical resonance of Mn dimer, the one of Fe is substantially broader and more shifted from the mode expected in the adiabatic approximation.

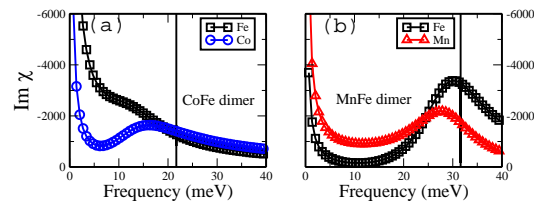


FIG. 3: Mixed dimers on Cu(001) surface: Local $\text{Im}\chi$ are shown in (a) for FeCo dimer and in (b) for MnFe dimer.

In the case of dimers made of different magnetic adatoms, i.e. FeCo dimer and FeMn dimer, we find the optical modes to occur at distinctly different frequencies (Fig. 3). This behavior, also explained from damping via Stoner excitations, is at variance with the Heisenberg description of the excitation spectrum of two well-defined localized spins where the optical mode is predicted to be unique for both adatoms. In the case of the FeMn dimer, the motion of Fe spin is damped far more strongly than that of Mn spin, but during its precession the latter feels the magnetic force of the heavily damped Fe spin which provides more damping on Mn.

Research supported by the HGF-YIG Programme VH-NG-717 (Functional nanoscale structure and probe simulation laboratory-Funsilab).

- [1] L. Zhou, J. Wiebe, S. Lounis, E. Vedmedenko, F. Meier, S. Blügel, P. H. Dederichs, R. Wiesendanger, Nature Physics 6, 187 (2010); A. A. Khajetoorians, J. Wiebe, B. Chilian, S. Lounis, S. Blügel, R. Wiesendanger, Nature Physics 8, 497 (2012).
- [2] A. A. Khajetoorians, S. Lounis, B. Chilian, A. T. Costa, L. Zhou, D. L. Mills, J. Wiebe, R. Wiesendanger, Phys. Rev. Lett. 106, 037205 (2011).
- [3] B. Chilian, A. A. Khajetoorians, S. Lounis, A. T. Costa, D.L. Mills, J. Wiebe, R. Wiesendanger, Phys. Rev. B 84, 212401 (2011).
- [4] S. Lounis, A. T. Costa, R. B. Muniz, D. L. Mills, Phys. Rev. Lett. 105, 187205 (2010); *ibid.* Phys. Rev. B 83, 035109 (2011).

Spin-polarized planar transport in transition metals from *ab initio*

H. Zhang, F. Freimuth, J. Weischenberg, Y. Mokrousov

Peter Grünberg Institut-1 & Institute for Advanced Simulation-1, Forschungszentrum Jülich

The prediction of transport properties of complex transition metals from first principles to an accuracy that allows reliable comparison to experiments has been a long-standing problem in condensed matter physics. Over the past years we have developed a number of techniques, which provide an ability to compute the transverse and longitudinal conductivity of metals in planar geometry. We have applied these techniques for first-principles studies of various transport phenomena, in particular anomalous, spin Hall and Nernst effects, anisotropic and domain-wall magneto-resistance. While in most of the cases based on our research we are able to describe and understand the measured trends in experiment, we suggest the occurrence of novel phenomena in known materials, which are yet to be tackled experimentally.

Within the linear response theory, the electrical current, which is generated in a crystal, is proportional to the applied electric field, and the constant of proportionality is the tensor of conductivity. In case of looking at the generated current transverse to the electric field direction, one talks about the family of Hall, or Nernst (if the role of electric field is replaced by a temperature gradient), effects. A typical example of such a phenomenon is the long-known anomalous Hall effect (AHE) in ferromagnets. While in the case of the AHE the transverse current is spin-polarized, one can also consider the situation of a purely *spin* transverse current, which is generated if an electric field is applied in a paramagnet, leading to the spin Hall effect (SHE). Both Hall effects are comparatively easily accessible experimentally, but on the theoretical side the understanding of the origins, which lead to transverse currents, are still intensively debated. Nowadays, the common consensus is that in good metals, very often the leading contribution to the Hall currents is coming from the so-called Berry curvature of Bloch electrons in a solid, related to the Berry phase physics of electrons exhibiting adiabatic dynamics. Accurate computation of the Berry curvature in transition metals has been for some time a cornerstone for the expertise of first-principles codes to expand into the area of transverse transport.

In our group we use the homemade technique for calculation of the Berry curvature, which is based on the sophisticated formalism of Wannier functions. We obtain the transverse conductivities as the integral of the Berry curvature over the occupied states in the Brillouin zone. In the past years, we

have performed various calculations of the anomalous and spin Hall effect in transition metals, and analyzed the microscopic origin of these phenomena from the detailed electronic structure of the materials [1]. Particularly relevant here were investigations of the ordered 3d-Pt alloys, which generated several experimental and theoretical studies [2]. Recently, we also extended our toolkit to evaluation of the Z_2 , Chern and spin Chern numbers in insulators, which play a crucial role in the field of topological insulators and insulators which exhibit a so-called quantum anomalous Hall effect. Having these functionalities at hand we were able to consider the topological phases in graphene doped with heavy transition-metal adatoms [3], see Fig. 1. According to our calculations, the adatoms on graphene display remarkable magnetic and magneto-electric properties. In particular, we predicted the occurrence of the quantization of the AHE in most of these systems, and suggested that this quantization can be observed experimentally up to room temperatures [3].

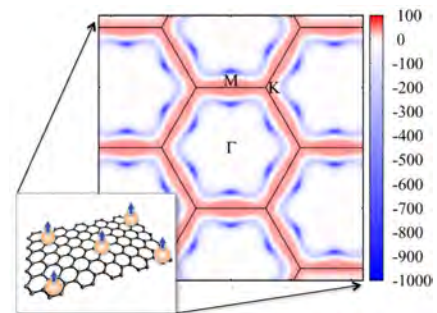


FIG. 1: Distribution of the Berry curvature (in bohr^2) in the reciprocal space of the graphene layer with tungsten adatoms deposited in 4×4 supercell geometry (inset). The non-trivial distribution of the Berry curvature has to be accurately taken into account in order to arrive at the values of the anomalous Hall conductivity. In the latter case this value is quantized, manifesting the occurrence of the quantum anomalous Hall effect in the system.

Of particular interest to our research was the subject of interplay of the crystal structure with the direction of the spin-polarization of the Hall current. While the origin of the SHE and the AHE lies in the spin-orbit interaction (SOI), in ferromagnets the SOI leads to an additional correlation of the structure and magnetism via the direction of the magnetization. This leads to the so-called anisotropy of the Hall effects [1]. Three years ago we demonstrated that the intrinsic, Berry curvature driven AHE exhibits a very large anisotropy as function of the magnetization direction in the crystal of uniaxial ferromagnets, appearing already in the first order with respect to

direction cosines. Taking as an example elemental hcp Co, we demonstrated from *ab initio* that the ratio of the Hall currents for the out-of-plane and in-plane directions of the magnetization constitutes a value as large as 4, in accordance to available experimental measurements for this material. It is necessary to take into account such strong angular dependences of the AHE when comparing to measurements performed on poly-crystalline samples. Further intensive calculations revealed that the anisotropy of the AHE in ferromagnets is rather a general feature than an exclusive phenomenon [1].

Moreover, our first-principles calculations indicated also the anisotropy of the SHE. Although completely absent in cubic metals, it can be very large in non-cubic materials, as can be clearly seen from Fig. 2, in which two different transverse components of the spin conductivity tensor are shown in red and blue (for the in-plane and out-of-plane spin-polarization of the spin current). We can clearly see from this figure that almost all non-cubic 3d, 4d and 5d transition metals exhibit a large anisotropy of the SHE. In this respect it seems particularly fruitful to underline that in antiferromagnets of any crystal structure and given direction of the local magnetization, the SHE is always anisotropic (c.f. case of Cr in Fig. 2) [4]. Later on, we were able to relate fundamentally the anisotropy of the Hall effects with anisotropy of spin-relaxation in paramagnets [1]. On a practical side, the anisotropic AHE and SHE could allow for an efficient control of the spin-polarized transport, with the possibility of even changing the sign of the conductivity, or flexibility in re-orientation of the Hall currents with respect to the electric field, spin polarization or the magnetization [1].

Among one of our latest developments is the explicit consideration of the effect of disorder on the transport properties of metals. It is known that disorder leads to two additional channels for transverse scattering: the skew-scattering and the side-jump. While the former is directly proportional to the impurity concentration and can be safely neglected at higher temperatures, the side-jump scattering provides a contribution to the AHE and SHE, which do not depend on the details of disorder. Owing to this scattering-independent feature, the side-jump is always measured experimentally together with the intrinsic contribution, making it almost impossible to separate the two [2]. Last year, we undertook an effort of computing the scattering-independent side-jump contribution to the AHE from first principles [5].

Within our treatment, motivated by the fact that the side-jump is independent of details of disorder, we assumed the simplified model for disorder, namely, the Gaussian short-range disorder model. Taking this model as a foundation, it was possible to derive the explicit expressions for the AHE and SHE, which relied only on the properties of the perfect crystal. Evaluating the side-jump contribution to the AHE from first principles resulted in essential improvements of the values for the conductivities in basic ferromagnets, as compared to solely intrinsic con-

tribution to the AHE [5], providing thus evidence that the disorder-independent side-jump is an important player in transverse transport properties of transition-metals. Characteristically, the side-jump

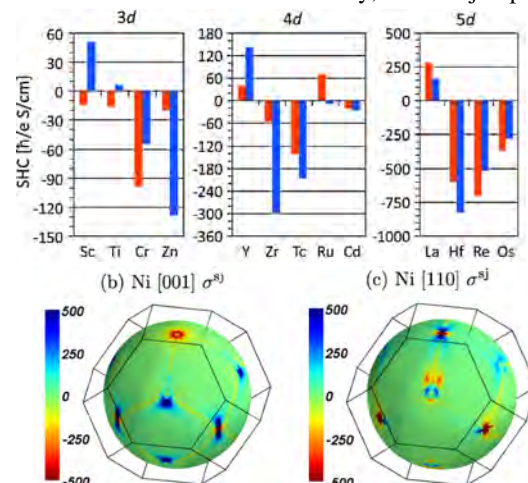


FIG. 2: Top: Spin Hall conductivity of 3d, 4d and 5d non-cubic transition-metals for the case of electric field applied along the *c*-axis and spin-polarization of the transverse current lying along the *x*-axis (red), and for the case of the electric field along the *y*-axis and spin-polarization of the current along the *c*-axis (blue). Strong difference between the two is visible. Bottom: Distribution of the side-jump contribution to the anomalous Hall effect in fcc Ni for two different magnetization directions calculated on the Fermi sphere.

also exhibits a very large magneto-crystalline anisotropy with respect to the direction of the magnetization, see e.g. Fig. 2. We have also successfully applied the short-range disorder model evaluating the longitudinal conductivity in case of transport through a Bloch domain-wall in FePt and FePd, allowing to distinguish different physical mechanisms which govern the domain-wall resistance in realistic samples [6]. On the way are applications of the developed technique to spin Nernst and anomalous Nernst effects, as well scattering on magnetic disorder.

Support of research by the HGF-YIG Programme VH-NG-513 (Topological Nanoelectronics Group) as well as a grant of computing time by the Jülich Supercomputing Centre (JSC) is greatly acknowledged.

-
- [1] Y. Mokrousov, H. Zhang, F. Freimuth, B. Zimmermann, N. H. Long, J. Weischenberg, I. Souza, Ph. Mavropoulos, S. Blügel, *Psi-k Highlight* 111 (2012)
 - [2] K.M. Seemann, Y. Mokrousov, A. Aziz, J. Miguel, F. Kronast, W. Kuch, M.G. Blamire, A.T. Hindmarch, B.J. Hickey, I. Souza, C.H. Marrows, *Phys. Rev. Lett.* 104, 076402 (2010)
 - [3] H. Zhang, C. Lazo, S. Blügel, S. Heinze, Y. Mokrousov, *Phys. Rev. Lett.* 108, 056802 (2012)
 - [4] F. Freimuth, S. Blügel, Y. Mokrousov, *Phys. Rev. Lett.* 105, 246602 (2010)
 - [5] J. Weischenberg, F. Freimuth, J. Sinova, S. Blügel, Y. Mokrousov, *Phys. Rev. Lett.* 107, 106601 (2011)
 - [6] K.M. Seemann, F. Garcia-Sanches, F. Kronast, J. Miguel, A. Kakay, C.M. Schneider, R. Hertel, F. Freimuth, Y. Mokrousov, S. Blügel, *Phys. Rev. Lett.* 108, 077201 (2012)

Ab Initio Design of Magnetic Properties at Hybrid Organic-Ferromagnetic Interfaces

N. Atodiresei¹, V. Caciuc², P. Lazic², and S. Blügel¹

¹ Peter Grünberg Institut and Institute for Advanced Simulation, Forschungszentrum Jülich & JARA

² Massachusetts Institute of Technology, Cambridge, 02139 Massachusetts, USA

Conceptual theoretical studies have been performed in order to understand how to precisely manipulate the local spin-polarization present at the interface formed between organic molecules and a ferromagnetic surface. Although adsorbed molecules might be nonmagnetic, due to an energy dependent spin-polarization, in a given energy interval the molecules have a net magnetic moment delocalized over the molecular plane. As a consequence, near the Fermi level, at the molecular site an inversion of the spin-polarization with respect to the ferromagnetic surface might occur. As a key result, we demonstrate the possibility to selectively and efficiently inject spin-up and spin-down electrons from a ferromagnetic-organic interface, an effect that can be exploited in future spintronic devices.

Merging the concepts of molecular electronics with spintronics opens the most exciting avenue in designing and building future nanoelectronic devices. In this context, the design of nanoscale spintronic elements in multifunctional devices relies on a clear theoretical understanding of the physics at the electrode-molecule interfaces and in particular, of the functionality of specific molecules in a given organic-metal surface environment. The density functional theory (DFT) provides a framework where a realistic understanding of these systems with predictive power can be expected.

In a first step, we performed ab initio calculations of prototype conjugated organic molecules adsorbed on a ferromagnetic 2 ML Fe/W(110) surface, a well-established substrate in spin-polarized scanning tunneling microscopy (SP-STM) experiments. We selected organic molecules containing $\pi(pz)$ -electron systems like benzene (Bz), cyclopentadienyl radical (Cp), and cyclooctatetraene (Cot), because they are representative of classes of organic molecules with significantly different reactivities. As a general characteristic of the adsorption geometry, we note that all adsorbed molecules have a nonplanar structure in which the H atoms are situated above C atoms (0.35 up to 0.45 Å). The shortest C-Fe bond is about 2.1 Å and corresponds to the C atoms sitting directly on top of Fe while the C atoms situated in bridge positions are 2.3 up to 2.5 Å away from Fe atoms. Furthermore, each of the molecules is nonmagnetic upon adsorption on the ferromagnetic

surface.

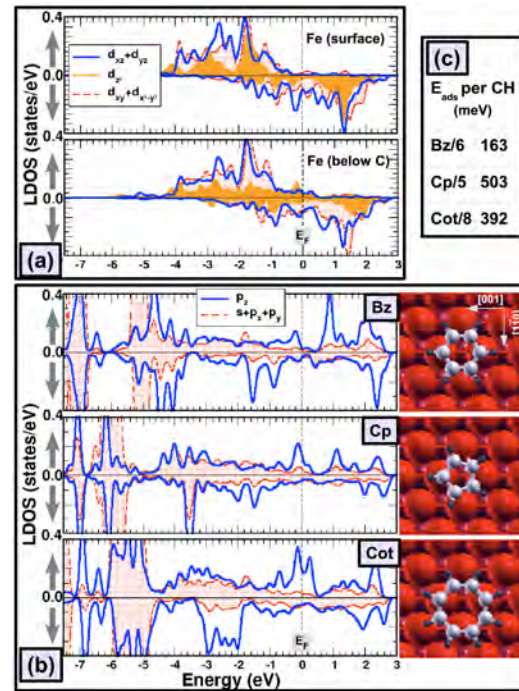


FIG. 1 (a) Spin-resolved local density of states of an Fe atom of the clean surface (upper panel) and an Fe atom below the C atom of the Cot molecule (lower panel); (b) adsorption geometries and the spin-resolved local density of states of the Bz, Cp and Cot molecules adsorbed on the 2ML Fe/W(110); (c) the adsorption energies of the Bz (C₆H₆), Cp (C₅H₅) and Cot (C₈H₈).

A general picture of the binding mechanism between Bz, Cp, and Cot molecules and the ferromagnetic surface can be extracted from the analysis of the spin-resolved local density-of-states (LDOS) of the calculated molecule-surface systems shown in Fig. 1. In the spin-up channel, the p_z atomic type orbitals, which originally form the π -molecular orbitals hybridize with the majority d states of the Fe atoms forming molecule-metal hybrid combinations with bonding and antibonding character. The bonding states are situated at low energies while the antibonding combinations appear at much higher energies, more precisely in an energy window situated around the Fermi level. The spin-polarized LDOS of the adsorbed Bz, Cp, and Cot molecules show a very intriguing feature: the energy dependent spin polarization.

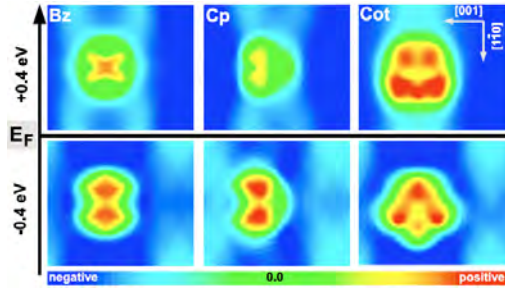


FIG. 2: The spin polarization above the Bz, Cp and Cot molecules adsorbed on the 2ML Fe/W(110) surface plotted for occupied $[-0.4, 0.0]$ eV and unoccupied $[0.0, 0.4]$ eV energy intervals around the Fermi level. All the organic molecules show a high, locally varying spin polarization ranging from attenuation to inversion with respect to the ferromagnetic Fe film.

As clearly visible in Fig. 1(b) for a given energy interval the number of spin-up and spin-down states is unbalanced. For that specific interval the molecule has a net magnetic moment delocalized over the molecular plane since it is carried mostly by the p_z states. Even more interesting, as depicted in the LDOS, around the Fermi level the states with large weight are in the spin-up channel at the molecular site, while on the clean Fe surface these states are in the spin down channel. As a consequence, at the molecular site an inversion of the spin polarization occurs with respect to the ferromagnetic surface. This effect is clearly seen in Fig. 2 which illustrates the spin polarization at 2.5 Å above the molecule in the energy intervals below $[-0.4, 0.0]$ eV and above $[0.0, 0.4]$ eV the Fermi level. A common characteristic for all the molecule-ferromagnetic surface systems is the high and locally varying spin polarization ranging from attenuation to inversion with respect to the ferromagnetic surface [1].

To demonstrate here the universal applicability of the theory driven concept, we apply in a second step spin polarized scanning tunneling microscopy [2] to directly observe with site sensitivity the spin polarization above a cobalt-phthalocyanine molecule (CoPc), adsorbed on out-of-plane magnetized 2 ML Fe/W(110).

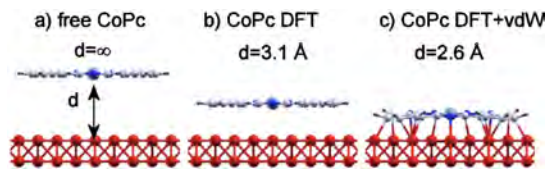


FIG. 3: The geometry and electronic structure for a isolated CoPc (a) and adsorbed on an Fe surface (b) without and (c) with vdW forces included during the relaxation.

Optimized molecule-surface geometries for the first-principles calculations were obtained by including long-range van der Waals interactions [2] during the relaxation, leading to an excellent agreement of theoretical and experimental data. The role of van der Waals forces is crucial as it brings the molecule 0.5 Å closer to the surface and distorts the molecular geometry (see Fig. 3). This new adsorption geometry has a drastically different electronic structure due to the overall changes of hybridization between

molecule and substrate. The newly formed molecule-surface hybrid states have, within a given energy interval, an unbalanced, locally varying electronic charge in the up and down channels which is mapped in SP-STM. For a direct comparison of the first-principles calculations with constant-current SP-STM images, isocharge surfaces above the CoPc are extracted from the spatial variation of the energy integrated spin polarized local density of states (SP-LDOS). This approach mimics the experimental situation of a local and spin-sensitive tip probing the charge density above the surface at constant current and thereby, accounts for the variation of decay lengths of the different states into vacuum (see Fig. 4). Only when the van der Waals relaxed adsorption geometry is used we find an excellent agreement of experimental findings and DFT calculations. Remarkably, not only reduction of but also inversion and amplification of the local spin polarization can equally be observed [3].

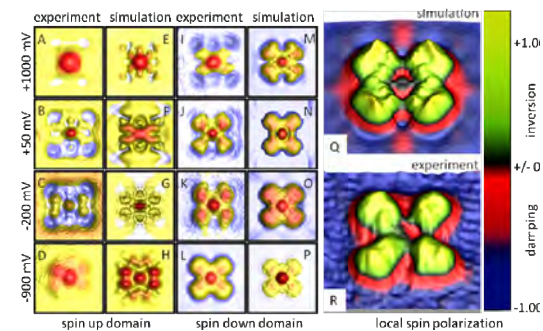


FIG. 4: Experimental and simulated SP-STM images at different bias voltages for both spin directions (A-P) and local spin polarization maps (Q,R).

To summarize, the spin polarization of a ferromagnetic surface can be locally tailored by flat adsorbing organic molecules containing $\pi(p_z)$ -electrons. Although adsorbed molecules are nonmagnetic, due to an energy dependent spin polarization, in a given energy interval the molecules have a net magnetization density delocalized over the molecular plane. Our first-principles study demonstrates that electrons of different spin [i.e., up and down] can selectively be injected from the same ferromagnetic surface by locally controlling the in-version of the spin polarization close to the Fermi level. Ultimately, this allows us to design the magnetic properties of hybrid organic-ferromagnetic interfaces that can be further exploited to design more efficient spintronic devices based on organic molecules.

We gratefully acknowledge a grant for computing time by the Jülich Supercomputing Center (JSC).

- [1] N. Atodiresei, J. Brede, P. Lazic, V. Caciuc, G. Hoffmann, R. Wiesendanger, S. Blügel, Phys. Rev. Lett. 105, 066601 (2010).
- [2] N. Atodiresei, V. Caciuc, P. Lazic, S. Blügel, Phys. Rev. Lett. 102, 136809 (2009).
- [3] J. Brede, N. Atodiresei, S. Kuck, P. Lazic, V. Caciuc, Y. Morikawa, G. Hoffmann, S. Blügel, R. Wiesendanger, Phys. Rev. Lett. 105, 047204 (2010).

Selected Publications

1. Hsieh, D.; Xia, Y.; Wray, L.; Qian, D.; Pal, A.; Dil, J. H.; Osterwalder, J.; Meier, F.; Bihlmayer, G.; Kane, C. L.; Hor, Y. S.; Cava, R. J.; Hasan, M. Z.
Observation of unconventional quantum spin textures in topological insulators
Science, **323** (2009), 919 – 922
2. Weismann, A.; Wenderoth, M.; Lounis, S.; Zahn, P.; Quaas, N.; Ulbrich, R.G.; Dederichs, P. H.; Blügel, S.
Seeing the Fermi-surface in Real Space by Nanoscale Electron Focusing
Science, **323** (2009) 5918, 1190 – 1193
3. Atodiresei, N.; Caciuc, V.; Lazic, P.; Blügel, S.
Chemical versus van der Waals Interaction: The Role of the Heteroatom in the Flat Absorption of Aromatic Molecules C_6H_6 , C_5NH_5 , and $C_4N_2H_4$ on the Cu(110) Surface
Physical Review Letters, **102** (2009) 13, 136809
4. Rushchanskii, K.; Kamba, S.; Goian, V.; Vanek, P.; Savinov, M.; Prokleska, J.; Nuzhnyy, D.; Knizek, K.; Laufek, F.; Eckel, S.; Lamoreaux, S.K.; Sushkov, A.O.; Lezaic, M.; Spaldin, N.A.
A multiferroic material to search for the permanent electric dipole moment of the electron
Nature Materials, **9** (2010) 8, 649 – 654
5. Sasioglu, E.; Schindlmayr, A.; Friedrich, C.; Freimuth, F.; Blügel, S.
Wannier-function approach to spin excitations in solids
Physical Review B, **81** (2010) 5, 054434
6. Heinze, S.; von Bergmann, K.; Menzel, M.; Brede, J.; Kubetzka, A.; Wiesendanger, R.; Bihlmayer, G.; Blügel, S.
Spontaneous atomic-scale magnetic skyrmion lattice in two dimensions,
Nature Physics, **7** (2011) 713 – 718
7. Lorenz, B.; Persson, B. N. J.; Dieluweit, S.; Tada T.
Rubber friction: Comparison of theory with experiment
European Physical Journal E, **34** (2011) 12, 129
8. Wehling, T. O.; Sasioglu, E.; Friedrich, C.; Lichtenstein, A. I.; Katsnelson, M. I.; Blügel, S.
Strength of Effective Coulomb Interactions in Graphene and Graphite
Physical Review Letters, **106** (2011) 23, 236805.
9. Betzinger, M.; Friedrich, C.; Görling, A.; Blügel, S.
Precise response functions in all-electron methods: Application to the optimized-effective potential approach
Physical Review B, **85** (2012) 245124
10. Seemann, K.M.; Garcia-Sanchez, F.; Kronast, F.; Miguel, J.; Kakay, A.; Schneider, C.M.; Hertel, R.; Freimuth, F.; Mokrousov, Y.; Blügel, S.
Disentangling the Physical Contributions to the Electrical Resistance in Magnetic Domain Walls: A Multiscale Study
Physical Review Letters, **108** (2012) 7, 077201

Indicators

Quantitative Numbers

	2009	2010	2011
Peer-Reviewed Publications	40	53	74
Graduations			
Master/Diploma	1	2	4
Dissertation	0	1	8
Habilitation	0	0	0

Honours

Borchers Medaille der RWTH Aachen	Dr. Simon Woodford	2009
Springorum Denkmünze der RWTH Aachen	Markus Betzinger	2009
DAAD-JSPS-Stipendium für einen Forschungsaufenthalt in Japan	Paul Baumeister	2009
Doktorandenkurzstipendium des DAAD	Alexander Thiess	2010
Invitation Fellowship Programs for Research in Japan from Japan Society of Promotion of Science (JSPS)	Dr. Bo Persson	2010
Feodor-Lynen Fellowship from the Alexander von Humboldt Foundation	Dr. Samir Lounis	2010
Finalist of the Psi-k Volker Heine Young Investigator Award 2010 from the european Psi-k Network for outstanding research in computer simulation of electronic structures.	Dr. Samir Lounis	2010
Young Investigator Group from the Helmholtz Association of German Research Centers.	Dr. Samir Lounis	2011

Offers

2009	PD Dr. Erik Koch	German Research School for Simulation Sciences (GRS), Aachen/Jülich	W3-Professor auf Zeit
2011	Dr. Marjana Lezaic	RWTH Aachen	Junior Professor for Theoretical Physics
2011	Dr. Yuriy Mokrousov	RWTH Aachen	Junior Professor for Theoretical Physics

Selected Third Party Projects

- Alexander von Humboldt-Stiftung
Fellow: Dr. Irene Aguilera
Topological Insulators investigated by material specific ab initio theory
Funding period: 1.11.2012 – 31.10.2014
- Marie Curie Actions Intra-European Fellowships (IEF), FP7-PEOPLE-2011-IEF
Fellow: Dr. Zeila Zanolli
Graphene-Ferroelectric Interface for Electronic and Spintronic Technologies (GraFIEST)
Funding period: 1.09.2012 – 31.08.2014

3. EU Exzellenz Netzwerk, EU-FP7-NMP-2009-LARGE-3
IFOX: Interfacing Oxides
Coordinator: Prof. Georg Schmidt (Martin Luther Universität Halle)
Project leader: Prof. Dr. Stefan Blügel
Funding period: 01.12.2010-30.11.2014
4. DFG-SFB917 Nanoswitches, RWTH-Aachen
Local confinement of switching filaments in transition metal oxides in electrical, chemical, and mechanical gradients (Dr. Gustav Bihlmayer)
Correlation between the atomic structure and electronic states in resistively switching oxides (Prof. Dr. Marjana Lezaic)
Funding period: 2011-2015
5. DFG-Schwerpunktprogramm 1538 “Spin Caloric Transport (SpinCaT)”
Topological spin, charge and heat transport driven by temperature gradients in transition-metal compounds (Prof. Dr. Yuriy Mokrousov)
Computational design of spin-caloric nanostructures (Dr. Phivos Mavropoulos, Prof. Dr. Stefan Blügel)
Funding period: 01.07.2011-30.06.2014
6. EU Initial Training Netzwerk, FP7-PEOPLE-2007-1-1-ITN
Femtosecond opto-magnetism and novel approaches to ultrafast magnetism at the nanoscale (FANTOMAS)
Coordinator: Prof. Dr. Theo Rasing (Radboud University, Nijmegen, The Netherlands)
Project leader: Dr. A. Bringer, Prof. Dr. Stefan Blügel
Microscopic Description of the Inverse Faraday Effect at ultrafast time scale
Funding period: 01.10.2008-30.09.2012

PGI-2/IAS-3: Theoretical Nanoelectronics



The Institute PGI-2/IAS-3 - *Theoretical Nanoelectronics* pursues a diverse set of topics that further our theoretical understanding of electronic systems and devices at nano- and atomic scales, and in the application of these quantum worlds to new forms of information processing. Researchers have experience both in strongly- and weakly-correlated matter. Strong correlations result in the emergence of new kinds of spin- and orbital-ordering in compound crystals. Weakly correlated matter, including many of the materials that are vital in the information processing world today, give us the opportunity to develop computational techniques that permit simulations of unprecedented scale and realism. The group has a strong legacy in the macroscopic dynamics of crystalline matter.

The quantum properties of individual entities is an emerging theme in this department. Electron and spin transport through single-molecule structures, and thermoelectric behavior of highly correlated impurities, have been topics of current research. The institute has an emerging strong focus on quantum information science, in which quantum coherence is a vital resource for accomplishing qualitatively new tasks. In spin qubits, the spin of electrons in single-electron quantum dots can serve as a platform for quantum computing, and the group studies mechanisms for decoherence and recoherence in this system. Studies are done of other prospective qubits, including those available in superconducting devices; new multi-qubit architectural approaches are developed in close collaboration with experimentalists.

Head of Institute:

Prof. David DiVincenzo, email: d.divincenzo@fz-juelich.de, phone: +49-2461-61-9069.

Scientific Staff

On September 1st 2012, the staff of PGI-2/IAS-3 comprised 13 scientists, 0 technicians, 5 PhD students and 0 master students. The institute hosts 1 University-Helmholtz Young Investigator group.

Scientists

Brener, Dr., Efim
Costi, Dr., Theo
DiVincenzo, Prof., David
Dederichs, Prof., Peter H. (*Helmholtz Professor*)
Pavarini, Prof., Eva
Zeller, Dr., Rudolf

Junior Research Group Leader

Wegewijs, Junior Professor Dr., Maarten

Post-Docs

Catelani, Dr., Gianluigi
Gorelov, Dr. Evgeny
Misiorny, Dr., Maciek
Sapstov, Dr., Roman
Tabatabaei, Dr., Fatemeh
Zhang, Dr. Guoren

Guest Scientists

Boussinot, Dr., Guillaume

Research Highlights

Charge Kondo anomalies in PbTe doped with Tl impurities

T. A. Costi¹, V. Zlatić^{2,3}

¹ Peter Grünberg Institut and Institute for Advanced Simulation, Forschungszentrum Jülich

² Institute of Physics, 10001 Zagreb, Croatia

³ J. Stefan Institute, 1000 Ljubljana, Slovenia

We investigate the properties of PbTe doped with a small concentration x of Tl impurities acting as acceptors and described by Anderson impurities with negative onsite Coulomb energy. We show that the charge Kondo effect naturally accounts for the unusual low temperature and doping dependence of normal state properties, including the self-compensation effect in the carrier density and the non-magnetic Kondo anomaly in the resistivity. These are found to be in good qualitative agreement with experiment. Our results for the Tl s -electron spectral function provide a new interpretation of point contact data.

PbTe is a narrow gap semiconductor with a band gap of 190 meV at zero temperature [1]. Upon doping with Tl impurities [1,2] a number of striking anomalies appear in the low temperature properties, which have been attributed to Tl impurities acting as negative U centers, where $U < 0$ is an attractive onsite Coulomb energy. The resulting non-magnetic charge Kondo (CK) effect has been argued to explain many of the observed properties of $\text{Pb}_{1-x}\text{Tl}_x\text{Te}$ [3,4,5,6] which would then constitute the first physical realization of this effect.

A remarkable feature of $\text{Pb}_{1-x}\text{Tl}_x\text{Te}$ is that the low temperature properties depend sensitively on the Tl concentration, with two qualitatively different doping regimes. Below a critical concentration $x_c \approx 0.3\%$ Tl, $\text{Pb}_{1-x}\text{Tl}_x\text{Te}$ remains metallic-like and the Tl impurities act as a normal acceptors. In contrast, for $x > x_c$ the number of holes remains almost constant, the system exhibits “self-compensation” and the chemical potential is pinned to a value $\mu = \mu^* \approx 220$ meV [10,12]. Furthermore, the system exhibits a non-magnetic Kondo anomaly in its resistivity, and becomes superconducting with a transition temperature $T_c(x)$ increasing linearly with x and reaching 1.5 K at = 1.5 % Tl [7,4].

In order to explain these anomalous properties we consider a model of n Tl impurities in a PbTe crystal with N Pb sites with the impurities described by the negative- U Anderson model[8] and treated within Wilson’s numerical renormalization group method [9]. In addition, it is important to impose the charge neutrality condition $n_0 = x(n_s - 1)$ at each x and each

temperature, where n_0 is the number of holes created in the valence band by finite small concentration $x = n/N$ of Tl ions acting as acceptors (i.e. with a groundstate having preferentially $n_s = 2$ s -electrons and a charge splitting $\delta = E(\text{Tl}^{3+}) - E(\text{Tl}^{1+}) > 0$ to the next excited state with $n_s = 0$ s -electrons for negative U).

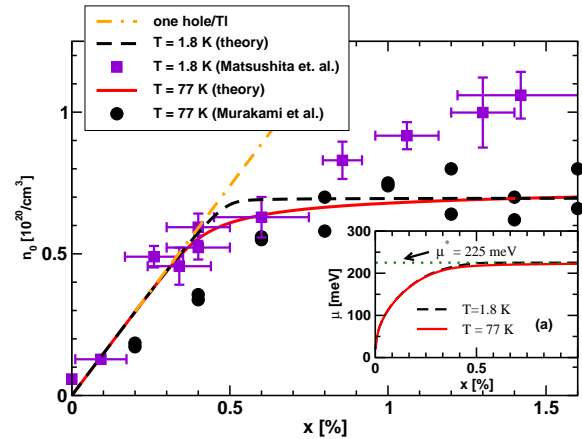


Figure 1. Hole density n_0 versus Tl doping x in % for $T = 1.8$ K and $T = 77$ K. Circles: experimental data at $T = 77$ K [10], squares: experimental data at $T = 1.8$ K [6], dot-dashed line: expected n_0 for one hole per Tl. Inset (a): chemical potential μ versus x at $T = 1.8$ K and $T = 77$ K (and hence $\delta(\mu) = \mu - \mu^*$).

Fig. 1 shows $n_0(x)$ versus x at $T = 1.8$ K and at $T = 77$ K and a comparison with experimental data on Hall number measurements [10,6]. At low dopings, n_0 is linear in x both in theory and in experiment, as expected for Tl impurities acting as acceptors (dot-dashed curve in Fig. 1). At higher dopings $n_0(x)$ saturates rapidly with increasing x for $T = 1.8$ K and more slowly at higher temperatures. The theoretical saturation density $n_0 \approx 0.7 \times 10^{20} / \text{cm}^3$ is close to the experimental value [10]. The self-compensation effect for $x \gg x^* \approx 0.5\%$ is a characteristic signature of the CK state: on entering this state the Tl ions fluctuate between Tl^{1+} and Tl^{3+} so the average valence is Tl^{2+} , which corresponds to no additional electrons being accepted or donated. The self-compensation effect can be seen also in the

pinning of the hole chemical potential μ for $x > x^*$, shown in Fig. 1a.

Fig. 2 shows the Tl s -electron spectral function $A(E, T = 0)$ for different dopings x . For $x < x^*$, the charge splitting $\delta(\mu) = \mu - \mu^*$, see Fig. 1a, is large resulting in a polarized spectral function so that its weight lies mostly below the Fermi level E_F [11]. For $x \geq x^*$, μ approaches μ^* and a CK effect develops. The spectral function develops a sharp asymmetric Kondo resonance close to, but below E_F (see Fig. 2a) and an upper Hubbard satellite peak appears above E_F . Early experiments for $x < 0.3\%$ showed only one resonant level below E_F [12], whereas more recent experiments for $x > 0.6\%$ show two “quasi-local” peaks [10], which we interpret as the Kondo resonance and the lower Hubbard satellite peaks in

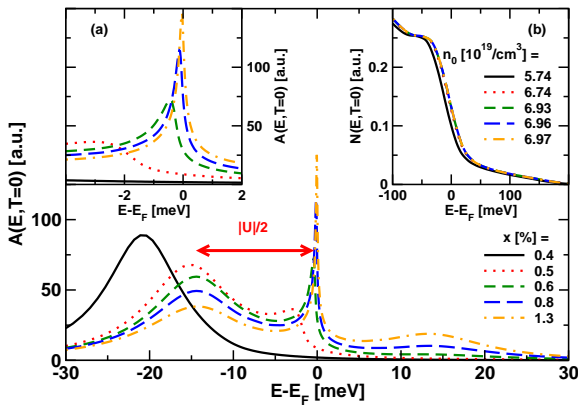


Figure 2. Tl spectral function $A(E, T = 0)$ versus $E - E_F$ for a range of Tl dopings x . Inset (a): region near $E - E_F$ showing the CK resonance. Inset (b): PbTe valence band density of states $N(E)$ versus $E - E_F$ for x as in the main panel [13].

The temperature and doping dependence of the

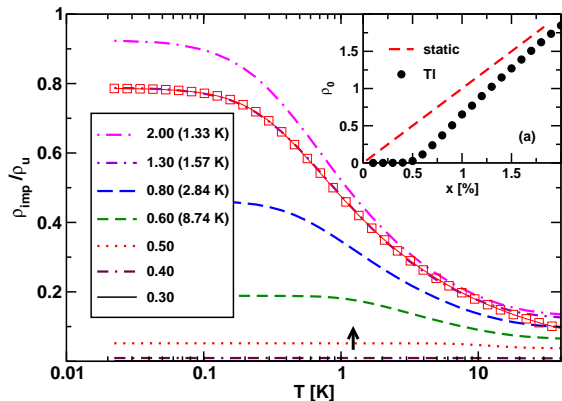


Figure 3. Impurity resistivity $\rho_{imp}(T)/\rho_u$ versus temperature T and a range of Tl concentrations x (in %, legend: column 1). For $x > x^*$, ρ_{imp} is well described by the usual spin Kondo resistivity [14] (open squares for $x = 1.3\%$), but with effective Kondo scales T_K^{eff} (legend: column 2). ρ_u is the residual resistivity for unitary scatterers. Vertical arrow: $T_K = 1.23\text{K}$. Inset (a): $\rho_0 = x\rho_{imp}(T=0)/\rho_u$ versus x (filled circles). Dashed line: ρ_0 for static unitary scatterers in place of Tl.

For $x < x^*$, Tl impurities act as acceptors with a well defined valence state (Tl^{1+}). They therefore act as weak potential scatterers and consequently the resistivity is much below the unitary value, as seen in Fig. 3. For $x > x^*$, dynamic fluctuations between the nearly degenerate Tl^{1+} and Tl^{3+} states leads to the CK effect and ρ_{imp} approaches the resistivity for unitary scatterers at $T = 0$. For $x > x^*$, ρ_{imp} is well described by the *spin* Kondo resistivity [14] (open squares, Fig. 3) Finally, Fig. 3a shows that the impurity residual resistivity is significant only when the CK effect is operative, i.e. for $x > x^*$, in qualitative agreement with experiment [4].

In summary, we investigated the normal state properties of $\text{Pb}_{1-x}\text{Tl}_x\text{Te}$ within a model of Tl impurities acting as negative U centers. Our NRG calculations support the suggestion that the CK effect is realized in $\text{Pb}_{1-x}\text{Tl}_x\text{Te}$ [4,5] and they explain a number of anomalies of $\text{Pb}_{1-x}\text{Tl}_x\text{Te}$, including the qualitatively different behavior below and above the critical concentration x^* , where $x^* \approx 0.5\%$ is close to $x_c \approx 0.3\%$ for the onset of superconductivity. Our results for the carrier density $n_0(x)$ are in good qualitative agreement with experiments [4,6,10], and those for the Tl s -electron spectral function provide a new interpretation of measured tunneling spectra [10], which could be tested by temperature dependent studies of tunneling or photoemission spectra.

- [1] S. A. Némov and Yu. I. Ravich, Phys. Usp. , 735 (1998).
- [2] B. A. Volkov, L. I. Ryabova, and D. R. Khokhlov, Phys. Usp. 45, 819 (2002).
- [3] T. A. Costi, and V. Zlatić, Phys. Rev. Lett. 105, 036402 (2012).
- [4] Y. Matsushita, H. Bluhm, T. H. Geballe, and I. R. Fisher, Phys. Rev. Lett. 94, 157002 (2005).
- [5] M. Dzero and J. Schmalian, Phys. Rev. Lett. 94, 157003 (2005).
- [6] Y. Matsushita, P. A. Wiancki, A. T. Sommer, T. H. Geballe, and I. R. Fisher, Phys. Rev. B 74, 134512 (2006).
- [7] I. A. Chernik and S. N. Lykov, Sov. Phys. Solid State, 23, 817 (1981).
- [8] P. W. Anderson, Phys. Rev. Lett. 34, 953 (1975).
- [9] K. G. Wilson, Rev. Mod. Phys. 47, 773 (1975); R. Bulla, T. A. Costi, and T. Pruschke, Rev. Mod. Phys. 80, 395 (2008).
- [10] H. Murakami, W. Hattori, Y. Mizomata, and R. Aoki, Physica C 273, 41 (1996).
- [11] S. Andergassen, T. A. Costi, and V. Zlatić, Phys. Rev. B 84, 241107 (2011).
- [12] V. I. Kaidanov, S. A. Rykov, and A. Rykova, Sov. Phys. Solid State 3, 1316 (1989)
- [13] D. J. Singh, Phys. Rev. B 81, 195217 (2010).
- [14] T. A. Costi, A. C. Hewson, and V. Zlatić, J. Phys.: Condens. Matter 6, 2519 (1994).

KKRnano: A Program for Large Scale Density Functional Calculations

R. Zeller¹, A. Thiess^{2,3}, S. Blügel^{3,4}

¹ IAS-3: Institute for Advanced Simulation, Forschungszentrum Jülich

² GRS: German Research School for Simulation Sciences

³ PGI-1: Quantum Theory of Materials, Forschungszentrum Jülich

⁴ IAS-1: Institute for Advanced Simulation, Forschungszentrum Jülich

KKRnano is a newly developed electronic structure code applicable to large insulating, semiconducting and metallic systems. It is massively parallelized for the efficient use of up to a hundred thousand processors and works with computing times which increase only linearly with the number of atoms in the systems. This opens the way to extend the limit for routine density functional electronic structure studies from a few hundred to many thousand atoms.

In the last three years we have developed a computer program for density-functional electronic-structure calculations for systems with many thousand atoms. This program is based on multiple-scattering theory within the Korringa-Kohn-Rostoker (KKR) formulation and can deal with systems extending over several nanometers. Consequently, we name it KKRnano.

KKRnano was designed from the outset to run efficiently on massively parallel supercomputers like the IBM Blue Gene/P available in Jülich. The second design aim was to avoid the unfavourable increase of the computing time proportional to the third power of the number of atoms which occurs if standard methods are used to solve the density-functional equations. In KKRnano the computing time increases linearly with the number of atoms if total energy changes of the order of meV per atom are tolerated compared to the standard full-potential KKR Green function (GF) method [1].

We obtain linear scaling of the computational effort as function of system size by an algorithm [2] based on the screened KKR method [3] which avoids wavefunctions and directly calculates the Kohn-Sham Green function by solving sparse systems of complex linear equations of dimension $N(l+1)^2$. Here N is the number of atoms and l depends on the angular spatial resolution around the atoms, usually $l=3$ is sufficient. We solve these equations iteratively by the quasi-minimal residual (QMR) method and calculate the electron density from the Green function by a contour integral in the complex energy plane using a few tenths of energy mesh points. Linear scaling for the computational effort is achieved by exploiting the concept of nearsightedness of electronic matter as it was called by Nobel Prize winner Walter Kohn. The concept means that in systems without long range electric fields the electronic density at a point in space insignificantly depends on potential changes far away. In KKRnano the nearsightedness is exploited by choosing a truncation region around each atom and neglecting

Green function contributions arising from the outside of the truncation region.

The increase of the computing time as function of system size and the effect of the truncation on the total energy accuracy are shown in FIG. 1 and FIG. 2 for two chosen example systems, Pd substitutionally doped with 3% Ni atoms and MgO with 5% of the oxygen atoms replaced by nitrogen atoms.

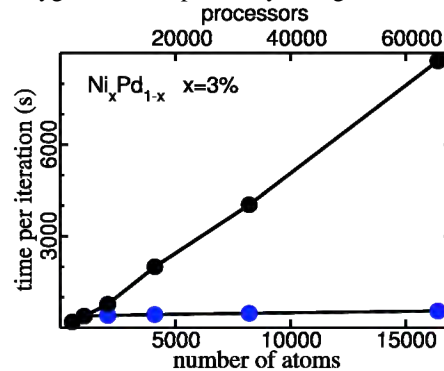


FIG. 1: Scaling behaviour of the wall clock time in one self-consistency step for dilute NiPd systems as function of system size using a truncation region of 959 atoms and no truncation (lower and upper curves). Four processors per atom are used.

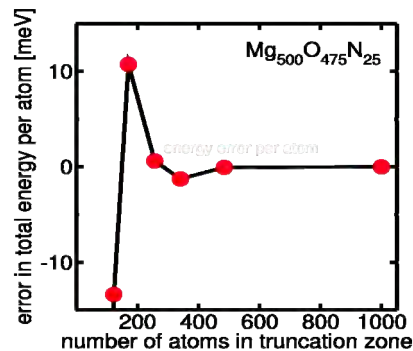


FIG. 2: Total energy error per atom as function of the number of atoms in the truncation region for a MgO system of 1000 atoms with 5% oxygen atoms replaced by nitrogen atoms.

Both example systems are of considerable physical interest, PdNi shows a quantum phase transition at about 2.5% Ni concentration and MgO doped with nitrogen is discussed as a transition metal free, room temperature ferromagnet with resistive switching properties useful for the next generation of nonvolatile memory. The electronic structure of these systems depends critically on defect distribution and interaction effects between defect atoms. The well established standard method for disordered systems, the KKR-CPA with its single-site mean-

field description fails here because neither short range order effects nor, in particular, the long range giant magnetic polarization clouds around Ni atoms in Pd can be described reasonably. In KKRnano such effects are accessible because large supercells can be treated with prescribed defect distribution.

FIG. 1 shows the wall clock time used in one density functional self-consistency step as function of the number of atoms in the system with and without spatial truncation of the Green function. Without truncation the time increases almost linearly if the number of processors is increased proportionally to the number of atoms. This means that the quadratically scaling total computational work is almost perfectly distributed over the increasing number of processors. If errors of the order of meV per atom are tolerated, the calculations can be speeded up by truncating the Green function, because then, the linear equations must be solved only in the truncation region. FIG. 1 shows for a truncation region of 959 atoms that the wall clock time only slightly increases with system size. This means that with truncation the total work increases only linearly and is again well distributed over the processors.

The good scaling behaviour can be explained from the multiple-scattering point of view of the KKRGF method [1]. In this method, space is divided into nonoverlapping cells around the atomic sites. For each cell, first a single-site scattering problem is solved using an angular momentum expansion of density, potential and wavefunctions. This part of KKRnano is straightforwardly parallelized using a simple matching between cells and processors. The complete multiple scattering is then obtained by solution of large systems of linear equations. Due to the iterative technique chosen in KKRnano the solution of the linear equations is also easily and efficiently parallelized because during the iterations no coupling between different cells occurs.

Because the linear scaling property of KKRnano is connected with total energy errors, it is important to know how large these errors are. Typical truncation errors are shown in FIG. 2 for the MgO:N system. The total energy error rapidly decreases with increasing size of the truncation region and is small enough if the truncation region contains more than a few hundred atoms. Similar accuracy for large metallic systems was found in a model study using periodic Cu and Pd supercells containing 131072 atoms [2].

For routine applications of KKRnano and for applications to even larger systems it is desirable to find ways to further reduce both wall clock time and computing time. Here we made considerable progress in the last year by developing a preconditioner for the linear equations and by using parallelization not only over the atoms, but also over the energy points, the two spin directions in magnetic systems and over the $L = (l + 1)^2 = 16$ angular momentum components.

The energy parallelization is dynamically load balanced by putting the energy points into two or three groups to deal with the considerably different

number of iterations at different energy points. The L parallelization, which is implemented presently only for the linear equation solver, but not for the rest of the program, is normally used with MPI message passing. Alternatively, for memory bound applications we use OPENMP to utilize the shared memory available in multicore CPUs. During the Blue Gene/P Extreme Scaling Workshop 2010 we were able to run a NiPd test system of 3072 atoms using from 3072 to 294912 processors, which means that KKRnano can use the entire Blue Gene/P. Increasing the number of processors from 147456 to 294912 gave a speedup of 1.6 for the wall clock time in the L parallelized part of KKRnano, whereas the time became larger for the remaining part. This part was fastest with 147456 processors.

It is well known that solving linear equations by iterative matrix multiplications can be accelerated by preconditioning. The preconditioner is a matrix which approximates the inverse of the original matrix as well as possible. Unfortunately, traditional preconditioners like ILU cannot be computed with the high degree of parallelization used in KKRnano. To overcome this difficulty, we developed a new preconditioner [4] that exploits the block structure of the original screened KKR matrix. In this matrix all blocks except for the ones on the diagonal only depend on the geometry of the system which is periodic or nearly periodic if relaxations of the atoms into their equilibrium positions are taken into account. As preconditioner we use a multilevel block-circulant matrix that is easy to compute and parallelize and leads to speedup factors between three and ten in applications of KKRnano for the systems we have studied so far. Another factor of two we gain by starting the QMR iterations with results from the previous self-consistency step.

With these recent improvements we anticipate that KKRnano, a full-potential all-electron program for large arbitrarily shaped supercells, can be widely applied to density functional electronic structure calculations for systems containing many thousand atoms.

-
- [1] N. Papanikolaou, R. Zeller and P. H. Dederichs, *J. Phys.: Condens. Matter* 14, 2799 (2002)
 - [2] R. Zeller, *J. Phys.: Condens. Matter* 20, 294215 (2008)
 - [3] R. Zeller, P. H. Dederichs, B. Újfalussy, L. Szunyogh, and P. Weinberger, *Phys. Rev. B* 52, 8807 (1995)
 - [4] M. Bolten, A. Thiess, I. Yavneh and R. Zeller, submitted to *Lin. Alg. Appl.*

Orbital-order melting in rare-earth manganites: the role of super-exchange

E. Pavarini¹, A. Flesch¹, G. Zhang¹, E. Koch²

¹ Institute for Advanced Simulation-3, Forschungszentrum Jülich

² German School for Simulation Sciences

We study the mechanism of orbital-order melting observed at temperature T_{OO} in the series of rare-earth manganites. We find that the purely electronic many-body super-exchange mechanism yields a transition temperature T_{KK} that decreases with decreasing rare-earth radius, and increases with pressure, opposite to the experimental T_{OO} . We show that the tetragonal crystal-field splitting reduces T_{KK} further increasing the discrepancies with experiments. This proves that super-exchange effects, although very efficient, in the light of the experimentally observed trends, play a minor role for the melting of orbital ordering in rare-earth manganites.

The role of orbital degrees of freedom in the physics of LaMnO_3 , and in particular the co-operative Jahn-Teller transition, is debated since long [1,2]. Ab-initio LDA+ U calculations show that Coulomb repulsion effects are key to understanding the orbitally-ordered antiferro-magnetic ground state. The purely electronic super-exchange mechanism alone [1], however, is not sufficient to explain the presence of co-operative Jahn-Teller distortions in nanoclusters up to $T \sim 1150$ K (orbitally disordered phase). Still, super-exchange effects are rather large: T_{KK} , the temperature at which super-exchange alone, i.e., in the absence of static Jahn-Teller distortions due to electron-phonon coupling, would drive the transition, is remarkably close to T_{OO} , the temperature at which the co-operative Jahn-Teller distortion disappears in resonant X-ray and neutron scattering. This fact could indicate that super-exchange, although insufficient to explain the persistence of Jahn-Teller distortions in the orbitally disordered phase, plays a major role in the orbital order-to-disorder transition (orbital order melting) observed at T_{OO} . Here we resolve this issue.

Remarkably, orbital-order melting has been observed in the full series of orthorhombic rare-earth (RE) manganites REMnO_3 . These systems are perovskites (Fig. 1) with electronic configuration $\text{Mn } 3d^4$ ($t_{2g}^3 e_g^1$). In the co-operative Jahn-Teller phase ($T < T_{OO}$), the MnO_6 octahedra are tilted and rotated, and exhibit a sizable Jahn-Teller distortion with long and short MnO bonds antiferro-ordered in the xy plane and ferro-ordered along z . Neutron and X-ray diffraction data show that T_{OO} increases from 750 K to ~ 1500 K with decreasing ionic radius IR ($\text{La} \rightarrow$

Dy); under increasing pressure eventually orbital order melts, while Jahn-Teller distortions still persist in nanoclusters.

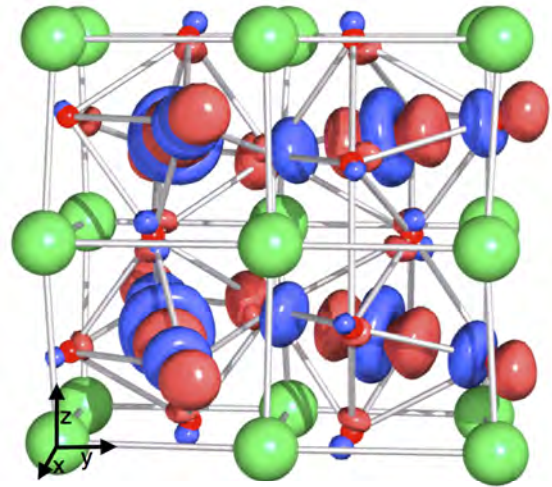


FIG. 1: Orbital-order in TbMnO_3 , as obtained by LDA+DMFT calculations. The pseudo-cubic axes pointing along Mn-Mn bonds are shown in the left corner.

In this work we [3] clarify the role of the purely electronic super-exchange mechanism in orbital-order melting. To do this, we perform ab-initio calculations based on the local density approximation (LDA) + dynamical mean-field theory (DMFT) method in the paramagnetic phase for fixed atomic position, explicitly setting to zero the static Jahn-Teller crystal-field splitting ϵ_{JT} , and excluding the effect of phonons. Apart from ϵ_{JT} , a tetragonal crystal-field splitting, ϵ_T , is present. We show that, in the absence of such crystal-field splitting, while in LaMnO_3 $T_{KK} \sim T_{OO}$, in all other systems T_{KK} is 2-3 times smaller than T_{OO} . Thus, while T_{OO} strongly increases with decreasing ionic radius, T_{KK} slightly decreases. Taking the tetragonal splitting into account, these trends are enhanced even further. This proves that, although very large, in view of the reported experimental trends, super-exchange plays a minor role in the orbital-order melting transition.

We solve the DMFT quantum impurity problem using a quantum Monte Carlo (QMC) solver, working with the full self-energy matrix in orbital space and a 4 Mn supercell with the Pbnm space

group; this ensures that we properly account for the point symmetries and the essential k -dependence. We construct the LDA Wannier functions via the downfolding procedure based on the N th-Order Muffin-Tin (NMTO) method. Additionally, we perform calculations based on the Linearized Augmented Plane Wave approach (LAPW) and construct maximally localized Wannier functions following the Marzari-Vanderbilt procedure. The band-structures and parameter trends obtained with the two methods are very similar.

Our results are shown in Fig. 2. While $T_{KK} \sim T_{OO}$ in LaMnO_3 , in all other systems T_{KK} is a factor 2-3 smaller than the experimental estimate for T_{OO} . Moreover, T_{KK} is maximum in LaMnO_3 , and roughly decreases with ionic radius from $\text{RE}=\text{La}$ to Tb , then increases again. T_{KK} also increases under pressure. These trends are opposite to those reported experimentally for the orbital melting temperature. They can be ascribed to the increasing distortions along the REMnO_3 series, and the decrease in volume and tilting/rotation with increasing pressure. Finally, for all systems super-exchange favors the occupation of the orbital $|\theta\rangle = -\sin\theta |x^2-y^2\rangle + \cos\theta |3z^2-r^2\rangle$, with $\theta = 90^\circ$, while experimentally $\theta \sim 108^\circ$ in LaMnO_3 increasing with decreasing ionic radius to 114° in TbMnO_3 . Due to the competition between the tetragonal crystal-field splitting ε_T and super-exchange (which favor the occupation of different orbitals), T_{KK} is reduced even further.

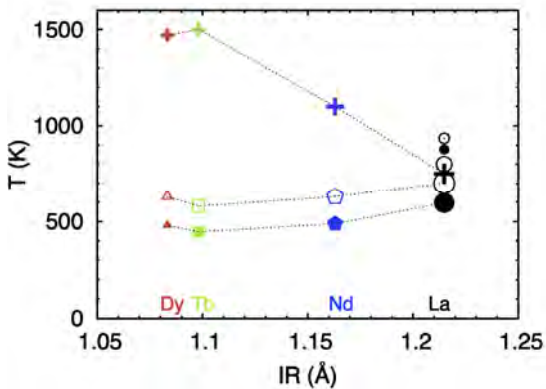


FIG. 2: Orbital-order transition temperature T_{KK} versus RE^{3+} radius in the REMnO_3 series, with $\text{RE}=\text{Dy}$ (triangles), Tb (squares), Nd (pentagons), La (circles). Full (empty) symbols: T_{KK} from LDA+DMFT total-energy (order parameter) calculations. Symbols of decreasing size: $P=0$ GPa, 5.4 GPa and 9.87 GPa. Crosses: Experimental values (ambient pressure).

In Fig. 3 we show the results for ε_T fixed at ~ 130 meV, sizable but smaller than for any of the considered systems. We find that at the reduced critical temperature, super-exchange rotates the orbital towards 90° . The change in T_{KK} is small for LaMnO_3 , but T_{KK} is reduced to 400 K for NdMnO_3 , and even more for DyMnO_3 and TbMnO_3 . Furthermore, in the zero temperature limit, the smaller T_{KK} , the closer is θ to 180° . Thus a fixed $\varepsilon_T \sim 130$ meV enhances the trend found for $\varepsilon_T = 0$: T_{KK} is

larger in LaMnO_3 , and decreases going to DyMnO_3 . Still, even for LaMnO_3 , θ is significantly larger than the experimental 108° . This means that a Jahn-Teller crystal-field splitting ε_{JT} is necessary to explain the experimental θ ; Fig. 3 shows that such splitting has to increase for the series $\text{RE}=\text{La, Nd, Dy, Tb}$.

Taking into account that tetragonal splitting actually increases with decreasing pressure, and substituting La with Nd , Tb , or Dy , this trend is enhanced even more. For ε_T corresponding to the real structures, down to 150 K we find no super-exchange transition for all systems but LaMnO_3 .

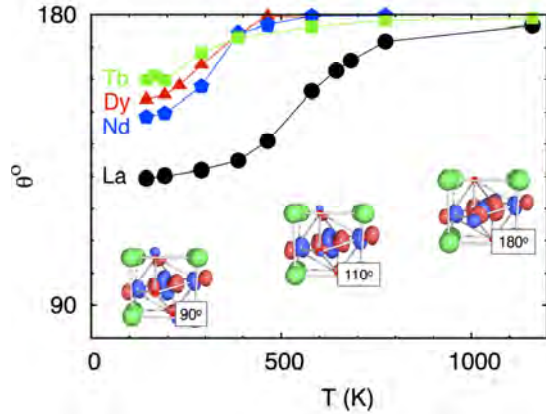


FIG. 3: Rotation of the most occupied state $|\theta\rangle$ as a function of temperature in the presence of a 130 meV tetragonal crystal field. The orbitals are shown for TbMnO_3 . The most occupied orbital remains well defined in the full temperature range; the orbital polarization is merely reduced by 30% at ~ 800 K.

In conclusion, for the orbital-melting transition in rare-earth manganites REMnO_3 , we find that many-body super-exchange yields a transition temperature T_{KK} very close to T_{OO} only in LaMnO_3 , while in all other systems T_{KK} is less than half T_{OO} . Moreover, we find that a tetragonal splitting ε_T reduces T_{KK} even further; ε_T increases when La is substituted with Nd , Tb or Dy and decreases under pressure, further enhancing the discrepancy with experiments. Finally, super-exchange effects become larger with increasing pressure, while experimentally orbital order eventually melts. Our work thus proves that, in the light of the experimentally observed trends, super-exchange plays a minor role in the orbital-melting transitions of rare-earth manganites.

We acknowledge financial support through the Deutsche Forschungsgemeinschaft through research unit FOR1346.

- [1] K.I. Kugel and D.I. Khomskii, Zh. Eksp. Teor. Fiz. 64, 1429 (1973) [Sov. Phys. JEPT 37, 725 (1973)].
- [2] J.B. Goodenough, Phys. Rev. 100, 564 (1955); J. Kanamori, J. Appl. Phys. Supp. 31, 148 (1960).
- [3] A. Flesch, G. Zhang, E. Koch, E. Pavarini, Phys. Rev. B 85, 035124 (2012).

Time-dependent transport: Interaction-induced adiabatic current

M.R. Wegewijs^{1,2}, F. Reckermann¹, J. Splettstoesser²

¹ PGI-2: Peter Grünberg Institute, Forschungszentrum Jülich

² Institute for Theory of Statistical Physics, RWTH Aachen University

We calculate the *time-dependent* transport current through a quantum dot *adiabatically driven* by a phase-shifted gate and bias voltage. We show that the additional dc current due to retardation of the quantum dot state is entirely generated by the electron-electron interaction. Lock-in measurement of this adiabatic dc current enables a “time-averaged” extension of non-linear transport spectroscopy which can probe effects of interactions, tunnel asymmetries and even the change in the ground state spin-degeneracy *without a magnetic field*.

Transport through nano-scale devices modulated by time-dependent applied electric fields is an active field of research important for transport spectroscopy and manipulation of the charge and spin degrees of freedom in nano-structures. A particularly gentle way of time-dependently probing a system is through “adiabatic pumping” [1]. Here a finite dc current is generated in the absence of an applied bias by a weak, low frequency periodic modulation of system parameters. Adiabaticity in a transport situation means that many electrons visit the system during one cycle of the driving with frequency Ω and that the modulation is too weak and too slow to excite the device by direct state-to-state transitions. In this report we analyze an interacting quantum dot in the single-electron tunneling (SET) regime, adiabatically driven by out-of-phase gate and bias potentials. In contrast to previous works, the applied bias can be arbitrary, i.e., we modulate the parameters around a *non-equilibrium steady state* supporting a finite dc current. We show that the strong local interaction *generates* an additional adiabatic dc current, which is identically zero without interaction for any value of the applied voltages and magnetic field. This adiabatic dc current can be measured using lock-in techniques and used for a new type of non-linear transport spectroscopy: plotted as function of the time-averaged gate and bias voltage, it gives rise to a new type of “stability diagram”, which is a central tool in quantum transport measurements. We consider a quantum dot weakly tunnel coupled to two electrodes and capacitively coupled to a gate in the common situation where a single orbital level with strong Coulomb interaction U is dominating the transport. The gate and bias voltage are modulated with frequency Ω around the working point specified by the voltages \bar{V}_g and \bar{V}_b :

$$V_x(t) = \bar{V}_x + \delta V_x \sin(\Omega t + \varphi_x), \quad x = b, g. \quad (1)$$

with $\varphi_b = 0$ and $\varphi_g = -\pi/2$. We denote the spin-resolved dot number operator by $n_\sigma = d_\sigma^\dagger d_\sigma$, where the spin $\sigma = \uparrow, \downarrow$ is quantized along the external magnetic field (if present). The Hamiltonian of the quantum dot reads $H_D(t) = \sum_\sigma \varepsilon_\sigma(t) n_\sigma + U n_\uparrow n_\downarrow$. The energy of an electron created by d_σ^\dagger equals $\varepsilon_\sigma(t) = -\alpha V_g(t) + \sigma B/2$ using the shorthand $\sigma = \pm 1$ for spin \uparrow, \downarrow . Importantly, the time-dependent gate voltage $V_g(t)$ capacitively modulates this energy with lever arm $\alpha < 1$. Furthermore, B is the Zeeman energy in units $e = \hbar = k_B = 1$. The many-body eigenstates of $H_D(t)$ are $|0\rangle$, $|\sigma\rangle = d_\sigma^\dagger |0\rangle$ with $\sigma = \uparrow, \downarrow$ and $|2\rangle = d_\uparrow^\dagger d_\downarrow^\dagger |0\rangle$ with energies 0 , $\varepsilon_\sigma(t)$, $\sum_\sigma \varepsilon_\sigma(t) + U$, respectively. The time-dependent bias $V_b(t)$ enters through the electro-chemical potentials $\mu_r(t) = \pm V_b(t)/2$ of electrodes $r = L, R$, which are described by $H_E(t) = \sum_{r,k,\sigma} (\varepsilon_k + \mu_r(t)) c_{rk\sigma}^\dagger c_{rk\sigma}$. Finally, $H_T = \sum_{r,k,\sigma} t_r d_\sigma^\dagger c_{rk\sigma} + H.c.$ describes the tunneling between the dot and the electrodes, with tunnel coupling strength $\Gamma_r = 2\pi\rho_r |t_r|^2$, where t_r is the amplitude and ρ_r the density of states of electrode $r = L, R$. We define $\Gamma = \sum_r \Gamma_r$. We consider here the important case where the transport is affected dominantly through the modulation of the energy level positions $\varepsilon_\sigma(t)$ and the bias energy window $\mu_L(t) - \mu_R(t)$. Since the total Hamiltonian $H(t) = H_E(t) + H_D(t) + H_T$ contains strong interaction on the dot, adiabatic time-dependence and a non-linear bias voltage we calculate the time-dependent occupation probabilities of the many-body dot states, $\mathbf{p}(t) = (p_0(t), p_\downarrow(t), p_\uparrow(t), p_2(t))$ from a master equation

$$\dot{\mathbf{p}}(t) = \int_{-\infty}^t dt' \mathbf{W}(t, t') \mathbf{p}(t'). \quad (2)$$

The kernel, $\mathbf{W}(t, t')$, accounts for changes of the dot occupations due to electron tunnel processes to/from the electrodes. Although it explicitly depends on both time arguments t and t' (in contrast to the time-independent case) it can be calculated perturbatively for slowly varying fields [2] and we restrict ourselves to the lowest order contributions in both the tunneling coupling (single-electron tunneling) and in the time-dependent perturbation of external system parameters (adiabatic driving). We consistently solve the time-dependent kinetic equation by expanding it around the instantaneous reference solution and account to first order for the actual delay suffered by the system due to the finite rate of sweeping the voltages. The time-dependent current flowing from lead $r = L, R$ into the dot is found in a similar way and can be decomposed into

two corresponding parts, $I_{i,r}^{(i)}$ and $I_{i,r}^{(a)}$. Averaging the two current contributions over a modulation cycle we obtain $\bar{I}_r^{(ia)} = \frac{\Omega}{2\pi} \int_0^{2\pi/\Omega} dt I_{i,r}^{(ia)}$. For small modulation amplitudes, $\bar{I}_r^{(i)}$ equals the dc current one would measure for time-independent voltages equal to \bar{V}_g and \bar{V}_b . Plotting $d\bar{I}_L^{(i)}/d\bar{V}_b$ as function of these voltages, one obtains the standard Coulomb blockade stability diagram. The adiabatic correction to this current, $I_{i,r}^{(a)}$, vanishes in the limit $\delta V\Omega \rightarrow 0$. The quantity of central interest here, $\bar{I}_r^{(a)}$, is the additional dc current component due to the retardation of the quantum dot state. This quantity can be obtained experimentally, e.g., by subtracting from the total measured time-averaged current its low frequency limit. The time-dependent adiabatic current can be expressed in terms of the rates of change of the average instantaneous charge, $\langle n \rangle_t^{(i)}$, and the spin polarization due to the magnetic field, $\langle S_z \rangle_t^{(i)}$:

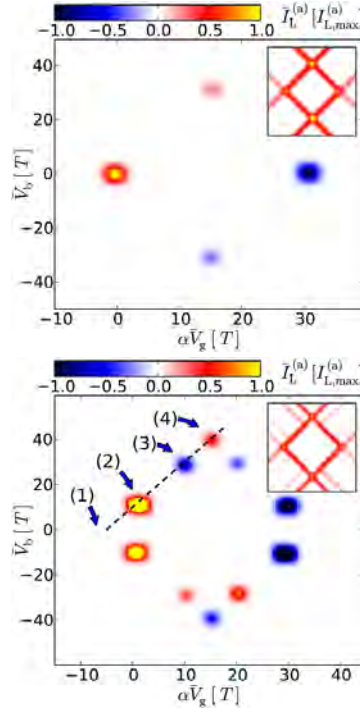
$$I_{i,r}^{(a)} = \frac{(\Gamma_r + \gamma_r)(\Gamma - \gamma) + \beta_r \beta}{\Gamma^2 - \gamma^2 + \beta^2} \frac{d}{dt} \langle n \rangle_t^{(i)} + 2 \frac{(\Gamma_r + \gamma_r)\beta - \beta_r(\Gamma + \gamma)}{\Gamma^2 - \gamma^2 + \beta^2} \frac{d}{dt} \langle S_z \rangle_t^{(i)} \quad (3)$$

where the prefactors in Eq. (3) contain

$$\gamma_r(t) = \frac{1}{2} \Gamma_r \sum_{\sigma} [f(\varepsilon_{\sigma r}(t)) - f(\varepsilon_{\sigma r}(t) + U)] \quad (4)$$

$$\beta_r(t) = \frac{1}{2} \Gamma_r \sum_{\sigma} \sigma [f(\varepsilon_{\sigma r}(t)) - f(\varepsilon_{\sigma r}(t) + U)] \quad (5)$$

and their sums $\gamma = \sum_r \gamma_r$, and $\beta = \sum_r \beta_r$, where $\sigma = \pm$ (corresponding to \uparrow, \downarrow) and $r = L, R$. All these quantities depend on time through the distance to resonance $\varepsilon_{\sigma r}(t) = \varepsilon_{\sigma r} - \mu_r(t)$ in the arguments of the Fermi-function $f(\omega) = (\exp(\omega/T) + 1)^{-1}$ with temperature T . From Eq. (3) we infer a necessary condition for a non-vanishing time-averaged adiabatic current which also holds for more complex systems: the adiabatic dc current $\bar{I}_L^{(a)}$ can only be non-zero if two resonance conditions for single-electron tunneling are satisfied *simultaneously*. If only a single resonance condition is satisfied (3) is a total time-derivative of a periodic function, resulting in a zero time-average. The resonances in $\bar{I}_L^{(a)}$ are thus located at resonance line *crossings* of the standard $d\bar{I}_L^{(i)}/d\bar{V}_b$ map. The prefactors in Eq. (3) reveal that the adiabatic dc current is *entirely induced by the Coulomb interaction U* : since the tunnel rates Γ_r and $\Gamma = \sum_r \Gamma_r$ are time-independent and $\gamma_r = \beta_r = 0$ for $U = 0$ the adiabatic current $I_{i,r}^{(a)}$ is a total time-derivative, which, integrated over a period, yields $\bar{I}_r^{(a)} = 0$. This result can in fact be proven rigorously for any order in the tunnel coupling Γ , i.e., beyond the weak coupling regime considered here.



In the experimentally important regime of strong local interaction $U \gg T \gg \Gamma$ the dependence on the time-averaged gate and bias voltage for zero magnetic field is plotted in the upper Figure as a *time-averaged* stability diagram. In contrast to the standard $(d\bar{I}_L^{(i)}/d\bar{V}_b)$ stability diagram shown in the inset this map of pumped current indeed shows resonant enhancements only at discrete points of size $\propto T$ where two SET resonances meet. The occurrence and sign of adiabatic dc current at a charge degeneracy point can be tied to the change in spin-degeneracy in the ground state: the sign is positive (negative) if the ground state spin-degeneracy increases (decreases) with the quantum dot charge and it vanishes if there is no change. The time-averaged stability diagram thus directly reveals non-degenerate ground states if $\bar{I}_L^{(a)}$ vanishes in the linear response regime. Indeed, in the lower panel for a magnetic field $B \gg T$ the adiabatic dc current is completely suppressed in the linear response regime $V_b \gg T$ marked by (1). The additional features marked (3-4) sensitively depend both in sign and magnitude on the asymmetry of the coupling Γ_L/Γ_R .

[1] P.W. Brouwer, Phys. Rev. B 58, R10 135 (1998)

[2] J. Splettstoesser et al., Phys. Rev. B 74, 085305 (2006)

From Majorana Fermions to Topological Order

Barbara M. Terhal¹, Fabian Hassler¹, and David P. DiVincenzo²

¹ Institute for Quantum Information, Physikzentrum RWTH Aachen University

² PGI-2: Theoretical Nanoelectronics, Forschungszentrum Jülich

While there is now striking evidence that Majorana Fermions exist in nanowire systems, there is no indication yet that they can make exceptionally coherent qubits. Our work starts with the premise that they will in fact permit us to realize “ordinary” qubits, which are susceptible to decoherence due to coupling to their environment. We propose here a network structure that will efficiently protect these qubits from decoherence, and will permit effective error correction. The nanostructured network that we propose permits a natural implementation of several equivalent many-body systems of interest for condensed matter physics: the Kitaev toric code model, and the transverse-field square-lattice Ising model with frustration.

We consider a physical system corresponding to a 2D network of links between Majorana fermions on superconducting islands. We show that the fermionic Hamiltonian modeling this system is topologically-ordered in a region of parameter space. More precisely we show how Kitaev’s toric code emerges in 4th-order perturbation theory. By using a Jordan-Wigner transformation we can map the model onto a family of signed Ising models in a transverse field where the signs (FM or AFM) are determined by additional sign or gauge qubits. Our mapping allows an understanding of the non-perturbative regime and

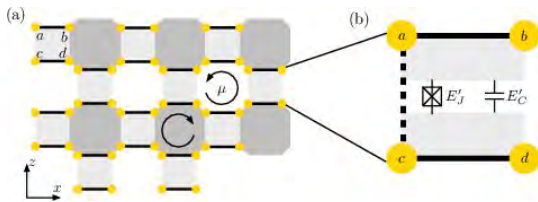


FIG. 1: (a) Toric code on a $L \times L$ lattice with $2L^2$ qubits on vertices and periodic boundary conditions in both directions. The Hamiltonian is a sum over white and grey plaquette operators $A_\mu = Z_{\mu+\hat{z}} Z_{\mu-\hat{z}} X_{\mu+\hat{x}} X_{\mu-\hat{x}}$. (b) The Hamiltonian in which the hatched plaquettes are omitted has ground space degeneracy of 8 in the topological phase, hence encodes an additional qubit. The logical operators of this qubit are depicted by the blue and red lines. We can call this a white hole qubit as it is obtained by omitting plaquettes in the Hamiltonian, i.e. making a hole in the lattice, which are centered on a white plaquette.

the phase-transition to a non-topological phase. We discuss the physics behind a possible implementation of this model and argue how it can be used for topological quantum computation by adiabatic changes in the Hamiltonian.

Kitaev’s well-known toric code [1] is a toy model Hamiltonian which demonstrates the concept of topological order in two dimensions; it features a 4-dimensional groundspace whose degeneracy is topologically-protected from sufficiently small perturbations. Thus one can imagine storing a qubit in this groundspace of such model such that at low temperature T compared to the gap, dephasing of such qubit is exponentially suppressed with growing lattice size. In the theory of quantum error correction this surface code architecture has emerged [2] as one of the more plausible routes towards fault-tolerant quantum computation. In this architecture the protection is due to the topological nature of the encoding and the sufficiently frequent error-correction. We consider the following fermionic Hamiltonian $H = H_0 + V$ where $H_0 = \sum_i^{2L^2} H_0^i$ and i labels the square islands in Fig. 1. For simplicity in the analysis, the lattice in Fig. 1 has periodic boundary conditions in both directions (see the end of the paper for a discussion of the model on a 2D surface).

Each H_0^i acts on two fermionic modes or four Majorana modes as

$$H_0^i = -\Delta \sum_i c_a^i c_b^i c_c^i c_d^i. \quad (1)$$

In addition we have $V = \lambda \sum_{i,j} V_{i,j}$ where i, j represents the interaction between two Majorana fermions on adjacent islands i and j , i.e. $V_{i=\mu\pm\hat{z}, j=\mu\pm\hat{x}}$ equals

$$\begin{aligned} V_{\mu+\hat{z}, \mu-\hat{x}} &= \pm i c_b^{\mu-\hat{x}} c_c^{\mu+\hat{z}}, V_{\mu-\hat{z}, \mu-\hat{x}} = \pm i c_a^{\mu-\hat{z}} c_d^{\mu-\hat{x}}, \\ V_{\mu-\hat{z}, \mu+\hat{x}} &= \pm i c_c^{\mu+\hat{x}} c_b^{\mu-\hat{z}}, V_{\mu+\hat{z}, \mu+\hat{x}} = \pm i c_d^{\mu+\hat{z}} c_a^{\mu+\hat{x}}. \end{aligned} \quad (2)$$

Clearly, all link operators $V_{\mu\pm\hat{z}, \mu\pm\hat{x}}$ mutually commute. The \pm signs of these terms will be fixed according to the consistent orientation in Fig. 1, i.e. the link on the top-left of a white plaquette μ represents the interaction $V_{\mu+\hat{z}, \mu-\hat{x}} = i c_b^{\mu-\hat{x}} c_c^{\mu+\hat{z}}$. Physically, the signs depend on the overlap of the wave function of the Majorana bound state and thus these signs are random but fixed. We can easily find an extensive set of operators which commute with all terms of H and which all mutually commute. These are, first of all, weight-8 fermionic plaquette operators $\{C_\mu^g, C_\mu^w\}$ (where g(w) stands for gray (white) plaquettes μ) which are the product of four link operators around a plaquette:

$$C_\mu^{g/w} = c_d^{\mu+\hat{z}} c_a^{\mu+\hat{x}} c_c^{\mu+\hat{y}} c_b^{\mu-\hat{z}} c_a^{\mu-\hat{x}} c_d^{\mu-\hat{y}} c_b^{\mu-\hat{x}} c_c^{\mu+\hat{z}}. \quad (3)$$

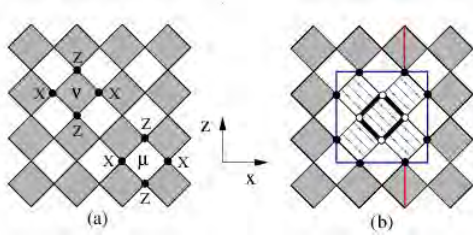


FIG. 2: (a) Toric code on a $L \times L$ lattice with $2L^2$ qubits on vertices and periodic boundary conditions in both directions. The Hamiltonian is a sum over plaquette operators $A_v = Z_{v+\hat{z}} Z_{v-\hat{z}} X_{v+\hat{x}} X_{v-\hat{x}}$. The lattice can be colored in checkerboard fashion so that we can speak of white and gray plaquettes. In Fig. (b) the dashed plaquettes represent plaquettes which have been omitted from the Hamiltonian, so that an additional qubit with logical operators depicted by the blue and red lines, can be encoded in the ground-space.

ial closed loops γ_1, γ_2 and the loop operators

$$C_{\gamma_{1/2}} = \prod_{(i,j) \in \gamma_{1/2}} V_{i,j} \text{ commute with all link } V_{i,j} \text{ and}$$

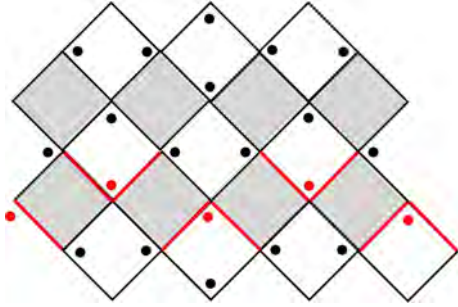


FIG. 3: The gauge qubits σ set the Ising interactions to FM (black edges) except for an AFM (red edges) loop around the torus. This AFM boundary will be felt in the FM phase, but not in the PM phase of the model leading to the topological degeneracy. A loop operator C_γ in the fermionic model becomes a product of Ising edges which winds around the torus; note that for the depicted sign pattern the loop operator which crosses this domain wall will have -1 eigenvalue.

island operators H_0^i . Thus the Hamiltonian is block-diagonal with respect to subspaces ('sectors') characterized by the eigenvalues $c_\mu^{g/w} = \pm 1$ of $\{C_\mu^{g/w}$ and $C_{\gamma_{1/2}} = \pm 1\}$. There is one linear dependency between the plaquette operators i.e. $C_{\text{all}} = \prod_\mu C_\mu^g = \prod_\nu C_\nu^w$ where C_{all} is the (properly ordered) product of all $8L^2$ Majorana operators. We can analyze the model in the perturbative regime where $\Delta \gg \lambda$ using a self-energy expansion or Schrieffer-Wolf perturbation theory. The groundspace of H at $\lambda=0$ is characterized by $\{c_a^i c_b^i c_c^i c_d^i = +1\}$, and thus the groundspace on each island is a two-dimensional subspace, a qubit. By a choice of convention one can define the logical X and Z operator on this island qubit as

$$X_i = ic_c^i c_a^i \equiv ic_d^i c_b^i, Z_i = ic_c^i c_d^i \equiv ic_b^i c_a^i. \quad (4)$$

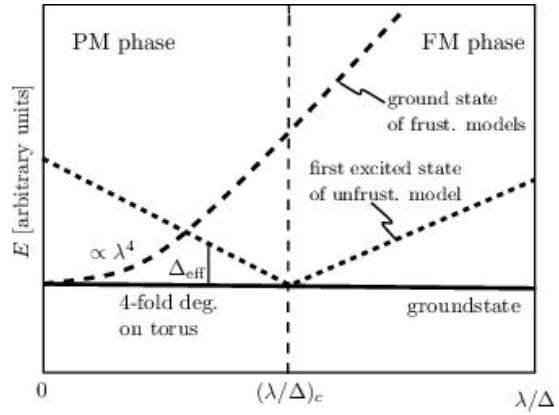


FIG. 4: Sketch of the spectrum of system as a function of λ/Δ . For small λ , the system is in a topological state with a four-fold groundstate degeneracy on the torus. In terms of the TF 2D Ising models, the topological phase corresponds to the paramagnetic side of the phase transition. The first excited states for small λ are Ising models with frustration labeled by the gauge qubits. All these models are degenerate for $\lambda = 0$ and the degeneracy lifts in fourth order perturbation theory in λ , see Eq. (5). The gap of the frustrated model increases monotonically for increasing λ . The phase transition towards a state without topological order happens at the transition point $(\lambda/\Delta)_c$ of the unfrustrated Ising model. At the point of the quantum phase transition the gap of the Ising model closes and the degeneracy of the topological states vanishes.

Let $P_- = 2^{-2L^2} \prod_{i=1}^{2L^2} (I + c_a^i c_b^i c_c^i c_d^i)$ be the projector onto this 2^{2L^2} -dimensional groundspace and $P_+ P_- = I$. Let $V_{\pm\mp} = P_\pm V P_\mp$ and let $G_+(z=0) = P_+ G_0(z=0) P_+ = -P_+ \frac{1}{H_0} P_+$ where we have redefined H_0 as $H_0 + 2\Delta L^2$ such its lowest-eigenvalue is 0. In the self-energy expansion all terms with odd number of perturbations V vanish. The second-order term $V_- G_+ V_-$ contributes a term proportional to I whereas the fourth-order term

$$V_- G_+ V_+ G_+ V_+ G_+ V_- = -\frac{5\lambda^4}{16\Delta^3} \sum_{\mu=1}^{2L^2} A_\mu, \quad (5)$$

where $A_\mu = Z_{\mu+\hat{z}} X_{\mu+\hat{x}} Z_{\mu-\hat{z}} X_{\mu-\hat{x}}$, i.e. the plaquette terms of the toric code in Fig. 2. Note that $P_- C_\mu^{g/w} P_- = A_\mu^{g/w}$ and hence the four-dimensional toric code groundspace of H when $\Delta \gg \lambda$ lies in the $\{c_\mu^{g/w} = +1\}$ sector. When $\Delta=0$ the ground-state of H is unique since we are in a state of fixed link parity $\{V_{ij} = -1\}$. Clearly this state also lies in the $\{c_\mu^{g/w} = +1\}$ sector since each $C_\mu^{g/w}$ is a product of four link operators V_{ij} .

Further details may be found in [3].

[1] A. Yu. Kitaev, Ann. Phys. (NY), 2 (2003).

[2] D. P. DiVincenzo, Phys. Scr. T, 014020 (2009).

[3] B. M. Terhal, F. Hassler, and D. P. DiVincenzo, "From Majorana Fermions to Topological Order," arXiv:1201.3757, Phys. Rev. Lett. **108**, 260504 (2012)

Selected Publications

1. Brener, E. A.; Marchenko, V.I.; Pilipenko, D.
Nonlinear Two-Dimensional Green's Function in Smectics
JETP Letters, **90** (2009) 10, 688 - 689
2. Costi, T. A.; Bergqvist, L.; Weichselbaum, A.; von Delft, J.; Micklitz, T; Rosch, A.; Mavropoulos, P.; Dederichs, P. H.; Mallet, F.; Saminadayar, L.; Bäuerle, C
Kondo Decoherence: finding the right spin model for iron impurities in gold and silver
Physical Review Letters, **102** (2009), 056802
3. Costi, T. A.; Zlatic, V.
Thermoelectric transport through strongly correlated quantum dots
Physical Review B, **81** (2010) 23, 235127
4. Gorelov, E.; Karolak, M.; Wehling, T.O.; Lechermann, F.; Lichtenstein, A.I.; Pavarini, E.
Nature of the Mott transition in Ca_2RuO_4
Physical Review Letters, **104** (2010) 22, 226401
5. Pavarini, E.; Koch, E.
Origin of Jahn-Teller distortion and orbital-order in LaMnO_3
Physical Review Letters, **104** (2010) 8, 086402
6. Reckermann, F.; Splettstoesser, J.; Wegewijs, M. R.
Interaction-Induced Adiabatic Nonlinear Transport
Physical Review Letters, **104** (2010) 22, 226803
7. Baumgärtel, M.; Hell, M.; Das, S.; Wegewijs, M.R.
Transport and accumulation of spin anisotropy
Physical Review Letters, **107** (2011) 8, 087202
8. Bouchbinder, E.; Barel, I.; Brener, E.A.; Urbakh, M.
Slow cracklike dynamics at the onset of frictional sliding
Physical Review Letters, **107** (2011) 23, 235501
9. Bravyi, S.; DiVincenzo, D.P.; Loss, D.
Schrieffer-Wolff transformation for quantum many-body systems
Annals of Physics, **326** (2011) 10, 2793 – 2826
10. DiVincenzo, D.P.
Toward Control of Large-Scale Quantum Computing
Science, **334** (2011) 6052, 50 – 51

Indicators

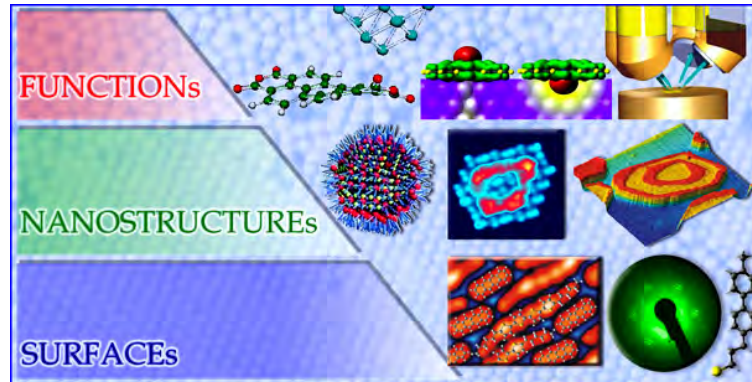
Quantitative Numbers

	2009	2010	2011
Peer-Reviewed Publications	12	12	27
Graduations			
Master/Diploma	1	1	2
Dissertation	1	2	2
Habilitation	0	0	0

Selected Third Party Projects

1. HGF-Nachwuchsgruppe Prof. Dr. Wegewijs
Projektleiter: Prof. DiVincenzo
Partner: HGF
Laufzeit: 01.04.2007-31.03.2013
2. Dynamical Mean-Field Approach with Predictive Power for Strongly Correlated Materials
PA 1950/1-1
Projektleiter: Prof. Pavarini
Partner: DFG
Laufzeit: 01.11.2010-01.11.2013
3. Nanoswitches SFB 917 TP: B7, Resistively Switching Chalcogenides for Future Electronics -
Structure, Kinetics and Device Scalability
Project leader: Dr. Brener
Partner: DFG
Funding period: 01.07.2011-30.06.2015
4. Psi-k Training
Projektleiter: Prof. Dederichs
Partner: EU
Laufzeit: 01.07.2006-30.06.2010

PGI-3: Functional Nanostructures at Surfaces



Research in surface science – this is our mission. A thorough understanding and mastering of surface properties and surface processes are absolutely essential for nanotechnology. Surface science has many methods, concepts and insights on offer that may teach us how to deal with the challenges of nanoscience and nanotechnology. Our research focuses on metal/molecule interfaces, thin organic films, molecular wires and switches, and semiconductor nanostructures. Overriding themes of our work are nanoscale structures and nanoscale charge transport.

A good illustration for the role of surface science in nanoelectronics research is provided by the field of molecular electronics. The idea of embedding the functions of an electronic device in the chemical structure of a single molecule is one of the most radical visions for the future of electronics. Formidable problems must be solved to develop this idea into a viable technology, many of them related to surface science. Examples are:

- (1) What are the properties of the contacts between a molecular device and the current leads that are used for input and output? In essence, this is a surface science problem: How do molecules and metals interact at their contact points? Insight into this question can be gained by systematic experiments on molecules that are adsorbed on single-crystalline metal surfaces.
- (2) Can we engineer molecular switches that perform well even if they are adsorbed on a surface and connected to leads? In solution or gas phase, many molecules undergo reversible changes if excited by an external stimulus (e.g. light). Such molecules are good candidates for switches in electric circuits. However, in many cases the switching functionality is lost if the molecule is adsorbed on a surface. Here, systematic surface science experiments can help to understand how the switching functionality can be preserved.
- (3) How can molecules be assembled into hierarchical structures in two or three dimensions? It is clear that a purpose-designed structural organisation is an important prerequisite for achieving desired functionalities. Surface science offers many tools to investigate the self-assembly of molecules into hierarchical structures.

Head of Institute:

Prof. Stefan Tautz, email: s.tautz@fz-juelich.de, phone: ++49-2461-61-4561.

Scientific Staff

On September 1st 2012, the staff of PGI-3 comprised 6 scientists, 1 junior research group leader, 6 technicians, 3 Post-Docs, 14 PhD students, and 1 Master student.

Scientists

Cherepanov, Dr. Vasily
Kumpf, Prof. Dr. Christian
Duden, Dr. Thomas
Soubatch, Dr. Sergey.
Tautz, Prof. Dr. F. Stefan
Voigtländer, Prof. Dr. Bert

Junior Research Group Leader

Temirov, Dr. Ruslan

Post-Docs

Bocquet, Dr. Francois
Sueyoshi, Dr. Tomoki
Wagner, Dr. Christian

Research Highlights

Energy – Entropy Cycle in Nanoscale Pit Formation at 2D Ge Layers on Si

K. Romanyuk, J. Brona, B. Voigtländer

PGI-3: Functional Nanostructures at Surfaces, Forschungszentrum Jülich

The structural stability of two-dimensional (2D) SiGe nanostructures is studied by scanning tunneling microscopy (STM). The formation of pits with a diameter of 2 – 30nm in one atomic layer thick Ge stripes is observed. The unanticipated pit formation occurs due to an energetically driven motion of the Ge atoms out of the Ge stripe towards the Si terminated step edge followed by an entropy driven GeSi intermixing at the step edge. Using conditions where the pits coalesce results in the formation of freestanding 8nm wide GeSi wires on Si(111).

The structural instability of nanostructures during annealing is an important issue which, along with the compositional instability, can be a serious threat to the functionality of nanodevices. Since the diffusion energies and intermixing barriers are particularly low at surfaces, the stability of surface nanostructures is most delicate. In the GeSi heteroepitaxial system there is a strong thermodynamic driving force for intermixing, since intermixing reduces strain and increases entropy [1, 2].

We have shown that the driving force for intermixing occurs to be so strong that it provokes drastic morphological changes during equilibration [3]. These structural changes are a way to bypass the kinetic barriers for direct intermixing. In particular, we show that one monolayer (ML) high Ge stripes grown at Si(111) step edges are unstable towards pit formation during annealing. The Ge leaving the stripe during pit formation attaches at the (Si covered) Ge stripe and intermixes with the subjacent Si (Fig. 1).

The pit formation arises by a concerted action of processes driven by an energy gain of the system and processes driven by an increase of the entropy of the system due to intermixing. The question arises why this rather complicated mechanism of pit formation is followed instead of the much simpler direct vertical intermixing of Ge with the subjacent Si. While the direct intermixing process results in a final state of even lower energy as the final state after pit formation, the kinetic barrier involved is much smaller than the barrier for direct vertical intermixing which favors the pit formation.

After submonolayer deposition Ge atoms attach to the step edges and form Ge stripes (Fig. 1(a)). It was found that the apparent height measured in STM is ~

1 Å higher on Bi terminated Ge areas compared to Bi terminated Si areas, allowing a distinction between Si and Ge on the nanoscale [4].

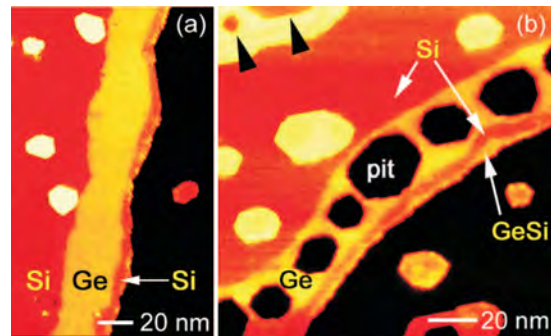


FIG. 1: (a) STM image of a one atomic layer high Ge stripe grown at a Si step edge. After Ge deposition a thin outer Si rim was grown. The apparent height contrast between Si and Ge is induced by the Bi termination of the whole surface. (b) After annealing at 733K unanticipated formation of pits and motion of the Ge originating from the pits to the outer Si rim is observed.

While attempting to grow alternating two-dimensional GeSi superlattices, we observed the formation of pits inside of Ge stripes for certain growth conditions. The unexpected formation of one atomic layer deep pits occurs if the growth of a Ge stripe is followed by the deposition of a Si stripe and subsequent annealing (Fig. 1(b)). In the following a model is described which explains the observed pit formation. In the first part of the pit formation process an initial amount of Ge is moving from the Ge stripe (pits) to the outer Si rim (Fig. 2(b)). For simplicity we leave out the actual nucleation event. The driving force for the first part of the pit formation process is bond energy gain. Ge-Ge bonds present in the Ge area are replaced by stronger Si-Ge bonds when Ge atoms attach to the Si terminated step edges. This process decreases the system energy and supplies an energetic driving force for Ge to form pits and to diffuse to the Si terminated step edge.

While the above reasoning can explain the initial pit formation, the pit formation should stop quickly if all Si step edges are terminated by Ge atoms (Fig. 2(b)). Subsequent Ge attachment at the step edges would not result in any bond energy gain. A further growth of pits, as observed in the experiment, would not be expected because it would only increase the step

energy. In a second step of pit formation the entropy driven GeSi intermixing acts at then outer step edge. The amount of GeSi intermixing can be close to 50% under usual conditions [5]. Due to the entropy driven intermixing at the step edge Ge is trapped and fresh Si is present at the outer step edge again (Fig. 2(c)). This Si starts the energy gain driven Ge diffusion from the pits towards the Si containing step edge again (Fig. 2(b)). The atomic processes shown in Fig. 2(b) and (c) can be considered as the subsequent energy driven and entropy driven parts of an energy–entropy cycle.

The question arises why the system takes the complicated pathway like the pit formation instead of the much simpler process of direct vertical intermixing with the underlying Si? During vertical intermixing high energy barriers have to be overcome in order to reach the intermixed low free energy configuration. The relevant barrier for direct vertical intermixing is the barrier for intermixing between the first and second layer which was recently measured for the Bi/Ge/Si(111) system as $U_{\text{step}}^{\text{terrace}} = 2.2$ eV [5]. The corresponding barrier at the step edge is lower ($U_{\text{step}}^{\text{step}} = 1.9$ eV) because the atoms are less confined by neighboring atoms at the step edges [5]. The pits are formed because their formation allows a path towards the minimum free energy configuration which involves a lower barrier than the direct exchange path. Due to the decreased energy barrier for GeSi exchange at the step edge, entropy can act more easily at the step edge while on the terrace the lower entropy intermixed state is not realized due to the large energy barrier involved with the GeSi exchange at the terrace.

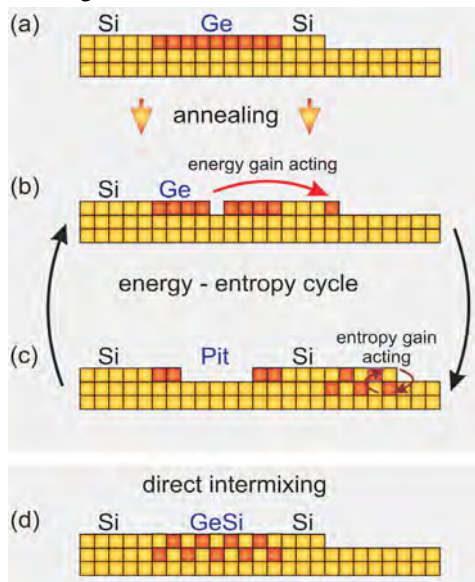


FIG. 2: In (a) and (c) the initial and final states before and after pit formation are shown. In the first part of the energy–entropy cycle (b) the energy is reduced by replacing Ge-Ge bonds (at the Ge stripe) through stronger Ge-Si bonds at the Si terminated step edge. The subsequent GeSi intermixing is driven by a gain in mixing entropy (c). Due to the intermixing Ge is trapped and the Si at the step edge is (partly) restored activating the energy driven part of the cycle again. An alternative simpler intermixing process without pit formation is direct intermixing with the Si from the lower layer (d).

The pit formation can be also used for nanostructuring. Using conditions at which pit formation is enhanced the fabrication of freestanding GeSi stripes with single digit nanometer width is possible. Fig. 3 shows an example of nanostructuring by pit coalescence.

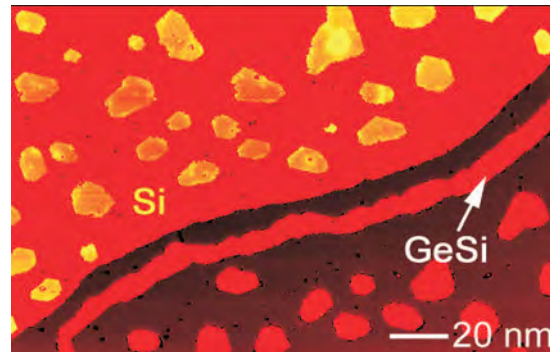


FIG. 3: Fabrication of a freestanding 8nm GeSi wire on the Si(111) substrate obtained by pit coalescence.

A continuous ~ 8 nm wide freestanding GeSi wire has been fabricated by pit coalescence. This wire is separated about $\sim 8 - 10$ nm from the step edge. Here the complete initial Ge stripe was removed. Such nanostructured templates can be used for next stage nanostructuring as for instance anchoring molecular nanostructures selectively at the wire or in the groove between the step and the freestanding nanowire.

- [1] M.S.Leite, A. Malachias, S.W. Kycia, et al. Phys. Rev. Lett. 100, 226101 (2008).
- [2] Rastelli, M. Stoffel, A. Malachias et al. Nano Lett. 8, 1404 (2008).
- [3] K. Romanyuk, J. Brona, and B. Voigtländer Phys. Rev. Lett. 103, 096101 (2009).
- [4] M. Kawamura, N. Paul, V. Cherepanov, and B. Voigtländer, Phys. Rev. Lett. 91, 096102 (2003).
- [5] N. Paul, S. Filimonov, V. Cherepanov, M. Cakmak and B. Voigtländer, Phys. Rev. Lett. 98, 166104 (2007).

Long range order of selfassembled structures of 4-methyl-4'-(n-mercaptoalkyl)biphenyls on Au(111) surfaces

M. Kazempoor¹, M. Müller¹, M. Homberger², U. Simon², G. Pirug¹

¹ PGI-3: Functional Nanostructures at Surfaces, Forschungszentrum Jülich

² Institute of Inorganic Chemistry, RWTH Aachen University

We investigate the long range ordering of 4-methyl 4'-(n-mercaptoalkyl)biphenyls (BPn) on Au(111) surfaces systematically for $n = 2 - 6$ applying Low Energy Electron Diffraction (LEED). Commensurate structures are deduced from sharp LEED patterns allowing the determination of unit cell sizes with intrinsic accuracy at variance with repeating units as deduced from topographical STM contrast. Consistent structure models are proposed within the limitations of STM based lateral distance and angle measurements. The comparison of LEED and STM results suggests that LEED reflects mainly the adsorbate substrate registry whereas the topographical STM contrast depends on the outer electronic structure strongly influenced by the intermolecular interaction.

The selfassembly of organic molecules is a promising bottom up approach for molecular electronics. Controlled charge transfer within π -conjugated aromatic phenyl groups indicates electronic functionality. The ordering of these selfassembled monolayers (SAM) depends not only on the intermolecular but also on the molecule substrate interaction. It turned out that the quality of these structures can be improved introducing alkene spacer chains between the thiol anchoring group and the aromatic system. Furthermore the sp^3 like configuration of the S adsorbed to the Au(111) surface and bound to the C of the alkane chains leads to different packing densities due to different tilt angles of the molecular axes for odd and even numbered BPn's. [1–4] Molecularly resolved STM pictures demonstrated the high perfection of these SAMs. Periodically repeating units seem to be related to commensurate structures. Whereas for the

odd numbered molecules an oblique $2\sqrt{3} \times \sqrt{3}$ is proposed [4] (Fig. 1) polymorphism with phase transitions between rectangular and oblique unit cells is observed for the even numbered molecules [5–8] (Fig. 2). Consistent with the molecular orientation as determined by NEXAF the odd numbered molecules are more densely packed than the even numbered molecules [6]. Common to all of these structures is the $2\sqrt{3}$ unit vector parallel to the $[11\bar{2}]$ except for the α -phase of BP4 which has been denoted as a rectangular $5\sqrt{3} \times 3$ structure. It should be mentioned, that the β -phase of BP4 has been controversially indexed as a $6\sqrt{3} \times 2\sqrt{3}$ [6] and $5\sqrt{3} \times 2\sqrt{3}$ [7] structure with two rows of 4 evenly spaced molecules in the $[11\bar{2}]$ direction with next nearest neighbor distances of 7.48 Å and 6.23 Å, respectively. This results with the same number of 8 molecules per unit cell in a significantly different packing density of 32.3 Å²/mol and 26.9 Å²/mol, respectively. This discrepancy should be resolved by LEED provided the adsorbed layer is stable against electron irradiation. Attempts with conventional LEED systems which require primary beam currents in the μA range failed. This problem can be solved using a micro channel plate (MCP) LEED system which allows a more gentle examination with a reduced electron dose in the pA range due to an amplification $> 2 \times 10^4$ of the diffracted electron beam.

In order to exclude preparation dependent differences the adsorbed layers are prepared under similar conditions as applied for the STM investigation although in situ characterization is not possible with LEED as a UHV based method.

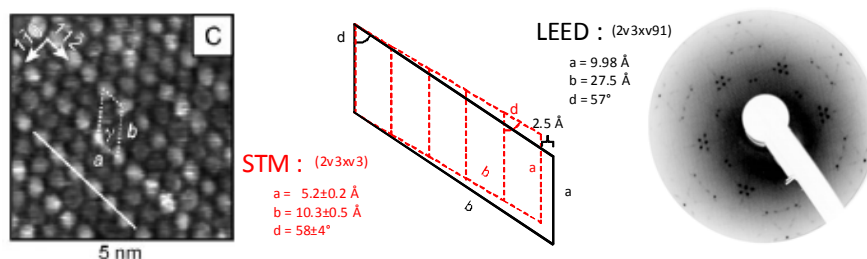


FIG. 1: Comparison of repeating units (STM) [7] and unit cells (LEED) for BP3 on Au(111)

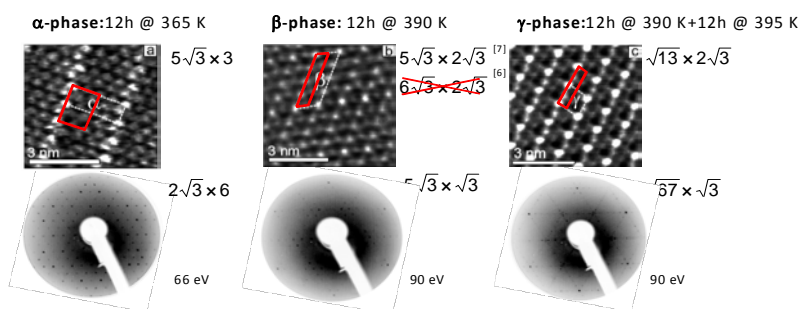


FIG. 2: Comparison of repeating units (-, STM) [4, 7] and unit cells (-, LEED) for BP4 phases on Au(111) after annealing as indicated

The BPn molecules are deposited in the gas phase or from solution, subsequently transferred into the UHV and annealed at different temperatures. In principal both methods yield the same results even though the structural quality of the gas phase deposited layers is higher.

The adsorption of BP3 has already been investigated in a combined STM and LEED study by Azzam et al. [4]. On the basis of the repeating units seen in STM images these authors proposed a $2\sqrt{3} \times \sqrt{3}$ structure which seems to be supported by a LEED pattern showing the corresponding but diffuse superlattice spots. The unit cell contains 2 inequivalent molecules due to different adsorption sites or azimuthal orientation. The LEED pattern which we obtained using a MCP LEED demonstrates that the diffuse spots seen by Azzam et al. can be better resolved into sharp clearly separated spots arising from a $2\sqrt{3} \times \sqrt{91}$ structure. While the angle between the unit vectors is with 57° only slightly smaller than 60° in a $2\sqrt{3} \times \sqrt{3}$ unit cell, the length of one unit cell vector differs by $\sqrt{91}/\sqrt{3} \approx 5.5$. This apparent discrepancy can be resolved within the typical accuracy achieved in lateral measurements from STM images comparing 5 repeating units with the unit cell as determined by STM and LEED, respectively (Fig. 1). The same structure has been found for BP5. In view of possible odd/even effects [1] we studied also BP4 as an example for even numbered BPn's which show after annealing more than one ordered phase. A comparison between the STM images [6, 7] and the LEED structures is shown in Fig. 2. The $5\sqrt{3}$ length for the repeating unit of the α -phase is not compatible with the symmetry of the corresponding LEED pattern. Instead a $4\sqrt{3}$ periodic length should be assumed. For the β -phase the $6\sqrt{3} \times 2\sqrt{3}$ structure [3, 5] can be safely excluded in favour of $5\sqrt{3} \times 2\sqrt{3}$ structure [7]. Combining the periodicity seen by STM and LEED common unit cells can be derived within the lateral accuracy generally expected for STM:

α -phase: $4\sqrt{3} \times 6$ β -phase: $5\sqrt{3} \times 2\sqrt{3}$ γ -phase: $\sqrt{67} \times 2\sqrt{3}$

The transition between these phases is schematically shown in Fig. 3. Assuming for the α -phase a non primitiv $4\sqrt{3} \times 2\sqrt{3}$ unit cell with 8 molecules which is consistent with the $4\sqrt{3} \times 6$ structure the phase transformations $\alpha \rightarrow \beta \rightarrow \gamma$ can be described by a

lateral extension followed by an azimuthal rotation and a slight compression. The resulting fractional coverages could be supported by XPS.

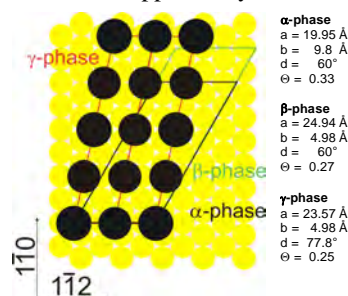


FIG. 3: Phase transitions for BP4 on Au(111)

The comparison of repeating units seen by STM with unit cells uniquely determined by LEED implies that these methods sense periodic overlayers in a differently. While the tunnelling current should depend much more on the outer electron density, the diffraction reflects the ordering of the main scatterers, namely the sulphur-gold complex next to the substrate surface. Stress release or intermolecular interactions within the self assembled layers may be responsible for the apparent differences. [9]

- [1] M. Zharnikov, S. Frey, H. Rong, Y.-J. Yang, K. Heister, M. Buck, and M. Grunze, *Physical Chemistry Chemical Physics* 2, 3359 (2000).
- [2] K. Heister, H.-T. Rong, M. Buck, M. Zharnikov, M. Grunze, and L. S. O. Johansson, *The Journal of Physical Chemistry B* 105, 6888 (2001).
- [3] P. Cyganik, M. Buck, W. Azzam, and C. Wöll, *J. Phys. Chem. B* 108, 4989 (2004).
- [4] W. Azzam, P. Cyganik, G. Witte, M. Buck, and C. Wöll, *Langmuir* 19, 8262 (2003).
- [5] P. Cyganik, and M. Buck, *J. Am. Chem. Soc.* 126, 5960 (2004).
- [6] P. Cyganik, M. Buck, T. Strunskus, A. Shaporenko, J. D. E. T. Wilton-Ely, M. Zharnikov, and C. Wöll, *J. Am. Chem. Soc.* 128, 13868 (2006).
- [7] G. J. Su, R. Aguilar-Sanchez, Z. Li, I. Pobelov, M. Homberger, U. Simon, and T. Wandlowski, *ChemPhysChem* 8, 1037 (2007).
- [8] B. Lüssem, L. Müller-Meskamp, S. Karthäuser, M. Homberger, U. Simon, and R. Waser, *J. Phys. Chem. C* 111, 6392 (2007).
- [9] P. Cyganik, M. Buck, J. D. E. T. Wilton-Ely, and C. Wöll, *J. Phys. Chem. B* 109, 10902 (2005).

Structure and Energetics of Azobenzene on Ag(111): Benchmarking Semiempirical Dispersion Correction Approaches

G. Mercurio¹, E.R. McNellis², I. Martin³, S. Hagen³, F. Leyssner³, S. Soubatch¹, J. Meyer², M. Wolf^{2,3}, P. Tegeder³, F. S. Tautz¹, and K. Reuter²

¹ PGI-3: Functional Nanostructures at Surfaces, Forschungszentrum Jülich

² Fritz-Haber-Institute of Max-Planck-Gesellschaft, Berlin

³ Fachbereich Physik, Freie Universität Berlin

We employ normal-incidence x-ray standing wave (NIXSW) and temperature programmed desorption (TPD) techniques to derive the adsorption geometry and energetics of the prototypical molecular switch azobenzene on Ag(111). This allows us [1] to assess the accuracy of semiempirical correction schemes as a computationally efficient means to overcome the deficiency of semilocal density-functional theory (DFT) with respect to van der Waals (vdW) interactions. The obtained agreement underscores the significant improvement provided by the account of vdW interactions, with remaining differences mainly attributed to the neglect of electronic screening at the metallic surface.

The potential of a molecular nanotechnology has motivated many studies of functional molecules at surfaces. In this context, a simulation platform for precise predicting of all relevant modes of the molecule-substrate interaction is required. The adsorption of organic molecules poses particular difficulties to theory, because the prevalence of dispersive interactions restricts the applicability of semilocal exchange and correlation (xc) functionals within DFT. Since high-level theories including vdW interactions by construction are still barely tractable for large surface-adsorbed molecules, computationally inexpensive semiempirical dispersion correction schemes to semilocal DFT (DFT-D) are appealing. In these approaches, vdW interactions are considered approximately by adding a pairwise interatomic C6R-6 term. At distances below a cutoff, motivated by the vdW radii of the atom pair, this long-range dispersion contribution is heuristically reduced to zero by multiplication with a short-range damping function. To verify the proposed simplification, accurate data from experiment for mindfully chosen prototype molecules are desired. In this report, we respond to this need by providing reference data on energetics and structure of the molecular switch azobenzene (Fig. 1a) adsorbed on Ag(111). We applied NIXSW technique to derive the structural data, i.e. adsorption height and molecular distortions. For the later, we

employed a novel analysis scheme which enabled us to overcome the challenge caused by a presence of

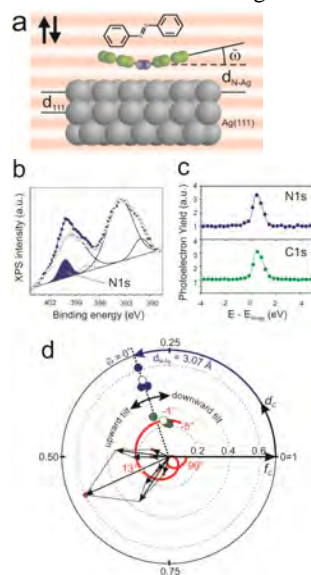


FIG. 1: (a) Adsorption model of azobenzene with key structural parameters ω and d_{N-Ag} . (b) Experimental photoemission spectra of azobenzene/Ag(111) (blue \varnothing) and clean Ag(111) (green \varnothing). For clean Ag(111), the three component lines of the fit are plotted as solid black lines. The fit of azobenzene/Ag(111) requires two additional components (shaded in blue (N1s) and displayed as a dashed line). (c) Extracted PEY as a function of photon energy relative to the Bragg energy (\varnothing) and the corresponding fits. (d) Argand diagram of dc and fc for N1s (blue \varnothing) and C1s (green \varnothing), and corresponding average points (\varnothing). The red spiral represents calculated dc and fc for C1s as ω sweeps from -5 to 90° . The vector sum of the six C atoms contributing to this is shown in the bottom left part (zoomed by a factor of 3) for $\omega = 13^\circ$.

spectroscopically identical carbon atoms at different heights. In short, the NIXSW exploits the fact that adsorbate atoms located at the positions of the antinode planes of a standing x-ray wave field induced by Bragg-reflection exhibit a maximum in the photoelectron yield (PEY). Scanning the photon energy through the Bragg energy shifts the position of the antinodes from the lattice planes to halfway positions between them. At different photon energies, the PEY thus probes different vertical locations of

adsorbate atoms relative to the substrate lattice planes. The NIXSW experiments were conducted at the ID32 ESRF beam line. The fits of measured PEY curves (i.e., integrated PE intensities vs. photon energy) for N1s and C1s core levels (Fig. 1c) provide two structural parameters for each species: the coherent position d_c and the coherent fraction f_c . The former is related to the average distance of the photoemitter from the relevant family of bulk lattice planes; the latter describes its actual distribution. For C, the fits yield $d_c = 0.28$ and $f_c = 0.24$. To quantify the N1s PEY at Ag(111), the N1s core level must be separated from plasmonic Ag3d satellites. After corresponding deconvolution, the fits of the PEY curve for N1s give the $d_c = 0.30$ and $f_c = 0.53$. This yields the height of N atoms as $d_{N-Ag} = 3.07\text{\AA}$. Coherent fraction and coherent position derived from C1s data represent a vector sum of individual contributions of single carbon atoms at the Argand diagram [1]. In the general case of nonplanar (tilted) geometry of azobenzene phenyl rings, this is not directly related to the actual average height of carbon atoms. To obtain the value of the tilt angle, we calculated the vector sum of contributions of individual carbon atoms for all possible tilt angles from $(-5$ to $90^\circ)$ for the height of N atoms fixed to experimentally found value of 3.07\AA . The intersection of the final curve (red spiral in Fig. 1d) with the average of experimentally found parameters for C1s core level uniquely defines the tilt of the phenyl ring as -1° . With accurate temperature programmed desorption experiments we also defined the desorption energy of azobenzene on Ag(111) as $1.08 \pm 0.05\text{ eV}$ (Fig. 2).

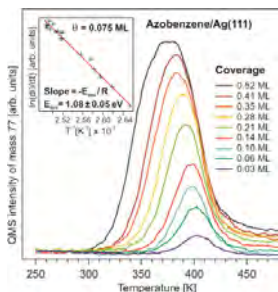


FIG. 2: Desorption spectra at different relative coverages Θ . The inset plots the desorption rate $\ln(d\Theta/dt)$ at $\Theta=0.075\text{ ML}$. The line slope determines the desorption energy.

We now compare the experimental data to the results obtained with the recent DFT-D schemes due to Grimme (G06) [2] and Tkatchenko and Scheffler (TS) [3]. In Fig. 3, the zero-point energy (ZPE) corrected desorption energies for different cases are displayed versus d_{N-Ag} . At the optimized adsorption heights, both bare DFT-PBE and the two DFT-D schemes yield an essentially planar molecule. This small variation indicates that the differential surface interaction within the extended molecule is too weak to overcome the molecular distortion cost. In contrast, the adsorption height is a very sensitive indicator of vdW interactions' strength. Indeed, bare DFT-PBE strongly overestimates this distance and produces only a weak binding; whereas both G06 and

TS lead to a sizable reduction of d_{N-Ag} (2.75\AA and 2.98\AA). Unfortunately, the improved structure goes hand in hand with a notable overbinding. Excluding other possible reasons, we conclude that the main source of the error in the predicted binding energies lies in the screening of dispersive attractions between the adsorbate atoms and the increasing number of more distant substrate atoms. By construction, such screening is not accounted for in the strictly pairwise evaluation of the dispersion interaction as inspired by Hamaker theory. Its anticipated effect, however, would primarily be a geometry-unspecific lowering of the binding energy. We mimicked this by reducing the number of substrate layers considered in the pairwise interaction C_6R^{-6} term and by even diminishing the C_6 coefficients of the Ag atoms in the topmost surface layer; this indeed shifts the computed binding energy curves in Fig. 3 up, but essentially without affecting the positions of their minima. Considering that the screening length in Ag is of the order of the interlayer distance, such a restriction of the considered terms to just the topmost layer is justified as a first step to improve the applicability of existing DFT-D schemes to adsorption at metal surfaces. The corresponding curve for the TS scheme (Fig. 3) comes indeed remarkably close to the experimental reference.

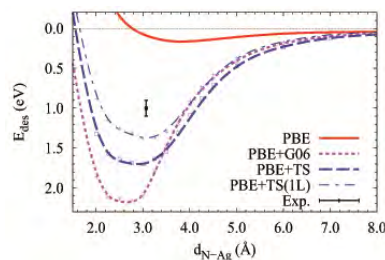


FIG. 3: ZPE-corrected desorption energy curves, computed with bare DFT-PBE and the two discussed DFT-D schemes. The black data point marks the experimental values and errors. Also shown is the curve computed with the TS correction reduced to the topmost layer Ag atoms.

In conclusion, we used the data on azobenzene adsorption on Ag(111) to assess the performance of two DFT-D schemes. The most recent TS scheme [3] is found to provide quite accurate structural properties, albeit at sizable overbinding. We assigned this geometry-unspecific overbinding primarily to the neglect of metallic screening of the dispersive interactions. This affirms that existing DFT-D schemes are not suitable to describe the role of vdW interactions in adsorption at metal surfaces comprehensively. However, the insight that the adsorption geometries are less sensitive to the neglect of screening suggests that these schemes may provide significantly improved structural data at zero additional computational cost.

-
- [1] G. Mercurio et al, Phys. Rev. Lett. **104**, 036102 (2010).
 [2] S. Grimme, J. Comput. Chem. **27**, 1787 (2006).
 [3] A. Tkatchenko and M. Scheffler, Phys. Rev. Lett. **102**, 073005 (2009).

Commensurate Registry and Chemisorption at a Hetero-organic Interface

Benjamin Stadtmüller, Tomoki Sueyoshi, Georgy Kichin, Ingo Kröger, Sergey Soubatch, Ruslan Temirov, F. Stefan Tautz, and Christian Kumpf

PGI-3: Functional Nanostructures at Surfaces, Forschungszentrum Jülich

We have investigated the hetero-organic interface between molecular layers of copper-II-phthalocyanine (CuPc) and 3,4,9,10-perylene-tetracarboxylic-dianhydride (PTCDA) that were stacked on Ag(111). A commensurate registry between the two molecular layers and the substrate, i.e., a common crystallographic lattice for CuPc and PTCDA films as well as for the Ag(111) surface, was found. It indicates that the growth of the upper layer is dominated by the structure of the lower. Photoemission spectroscopy clearly reveals a gradual filling of the lowest unoccupied molecular orbital of PTCDA due to CuPc adsorption. This finding proves a partly chemisorptive bonding between the single molecular layers.

The applicability of organic molecules as active materials in electronic devices such as organic light-emitting diodes, field-effect transistors, or solar cells strongly depends on the properties of the interfaces between different materials. While organic-metal contacts – model systems like PTCDA and Metal-Pcs in particular [1] – are intensively investigated in this context, organic-organic heterojunctions are characterized only seldom, even though such interfaces are at least of similar importance for organic electronic devices. Maybe this is due to the common belief that interfaces between different organic materials are generally dominated by very weak, van der Waals interaction, an assumption that will be proven to be incorrect.

We have investigated the geometric and electronic structure of the hetero-organic interface between the prototypical molecules CuPc and PTCDA [2]. The heterojunction is formed by adsorbing CuPc molecules on top of a closed layer of PTCDA on Ag(111). Figure 1 shows a high-resolution low-energy electron-diffraction (LEED) image of the so-called "stacked bilayer structure" (SB-structure). The image was recorded at 100 K for a CuPc coverage of 0.6 ML, but the same structure is observed at higher CuPc coverages (close to 1 ML) and room temperature (for details see [2]).

The LEED pattern of the SB structure can be explained unambiguously by one single structural model. In the upper right half of Fig. 1 the PTCDA diffraction spots are marked by red circles whereas in the lower left the spots stemming from the CuPc cell are indicated in blue. Note that all PTCDA spots

can also be indexed as CuPc spots. This immediately shows that the structure of the CuPc overlayer is commensurate with the PTCDA monolayer structure. Consequently, the superstructure matrices describing the unit cell of the CuPc/PTCDA stacked bilayer structure have integer numbers only:

$$\begin{pmatrix} \vec{A} \\ \vec{B} \end{pmatrix}_{SB} = \begin{pmatrix} 3 & 1 \\ -2 & 1 \end{pmatrix} \begin{pmatrix} \vec{A} \\ \vec{B} \end{pmatrix}_{PTCDA} = \begin{pmatrix} 3 & 16 \\ -12 & -9 \end{pmatrix} \begin{pmatrix} \vec{A} \\ \vec{B} \end{pmatrix}_{Ag}$$

The appearance of commensurate structures is usually an indication for a relatively strong interaction of organic molecules with the underlying substrate. Commensurability across an organic-organic heterojunction is therefore very unexpected and stands in contrast to the structure formation reported for such interfaces so far. However, in our case, commensurability is a very characteristic feature with important consequences for the formation of the CuPc film: In contrast to almost squared unit cells generally found for CuPc, and rectangular cells for PTCDA (both reflecting the fourfold or two-fold symmetry of the molecule), the SB structure has an oblique unit cell. This indicates that commensurability is not just the result of an arbitrary coincidence of similar lattices of the isolated PTCDA and CuPc layers. There must be a significant interaction across the heterojunction which dominates the structure formation and forces the CuPc layer in an unusual structure which otherwise would not be formed.

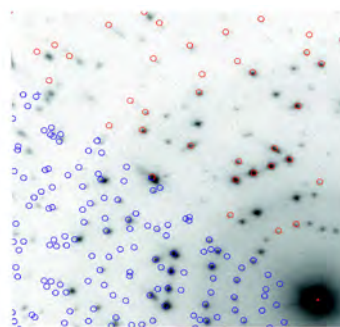


FIG. 1: High-resolution LEED image of 0.6 ML CuPc on a closed layer of PTCDA/Ag(111), recorded at 100 K. Red and blue circles mark calculated positions of diffraction spots from the PTCDA-monolayer structure and the CuPc/PTCDA stacked-bilayer (SB) structure, respectively.

We used low-temperature scanning tunneling microscopy (STM) in order to determine positions

and orientations of the molecules in the unit cell. Figure 2 shows constant-current images recorded at 10 K. In panel (a) the edge of a CuPc island on the PTCDA monolayer is visible with submolecular resolution in both regions: the PTCDA monolayer (lower part) and the CuPc island on top (upper part). It can be seen that CuPc homogeneously overgrows the PTCDA monolayer. The unit-cell dimensions obtained from SPA-LEED are confirmed by the STM images. Translating the well-known PTCDA superlattice (indicated by the red grid in the lower part of Fig. 2(a)) onto the CuPc island in the upper part and comparing it with the unit cell of that region (indicated by the blue grid) illustrates matching of the periodicities of the SB and PTCDA-monolayer phases.

CuPc molecules all show the typical crosslike STM contrast, even though their wings differ in apparent height. In Fig. 2(b), the positions of the underlying PTCDA molecules are marked as dotted ellipses. This plot reveals that the CuPc wings that appear bright are located directly above the PTCDA molecules, while dark wings are bridging the PTCDA molecules; i.e., they lie above the “gaps” in the lower layer. This finding indicates that the different contrast of the molecular wings is caused by an electronic coupling between the molecular layers. It appears as if the underlying PTCDA molecule facilitates electronic transport through that part of the CuPc molecule that lies exactly above the central part of the PTCDA molecule.

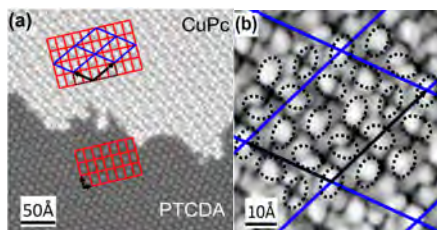


FIG. 2: STM images of the SB phase at 10 K (0.75 V, 18 pA). (a) A CuPc island (bright contrast) has condensed on a closed PTCDA monolayer on Ag(111). PTCDA and CuPc lattices are indicated by red and blue lines, respectively. (b) Dotted ellipses indicate the positions of PTCDA molecules under the CuPc layer. Bright STM contrast is found where CuPc wings lie above the PTCDA core.

We also used UPS to gain more insight into the electronic interaction between the substrate and the molecular layers. Figure 3 shows He I α UPS data recorded for different submonolayer CuPc coverages between 0 and 0.9 ML at RT. In the spectra of the bare PTCDA monolayer (lowest curves labeled “0.0 ML”), the highest occupied molecular orbital (HOMO) and a second state close to the Fermi level, the former lowest unoccupied molecular orbital (F-LUMO), can be seen. The F-LUMO is partially filled due to charge transfer from the substrate into the molecule. This directly indicates chemisorptive interaction between the Ag(111) substrate and the PTCDA molecule which is well-known for many organic molecules adsorbing on noble metal surfaces.

Upon adsorption of CuPc on top of the PTCDA layer, new peaks appear in the spectra (the HOMO and HOMO-1 states of CuPc) and some peak shifts are detected. However, the most important change in the spectra is the shift of the F-LUMO state of PTCDA. As illustrated by the vertical dashed lines in Fig. 3, this state shifts continuously by as much as 120 meV. This indicates an additional filling of the PTCDA F-LUMO induced by the adsorption of CuPc molecules, i.e., an increase of the charge transfer between substrate and adsorbate (and/or between both organic layers). This implies an enhancement of the chemisorptive interaction between the CuPc and PTCDA adsorbate layers and the substrate, and is in strong contrast to previous studies which reported only very weak interactions across organic-organic interfaces [3].

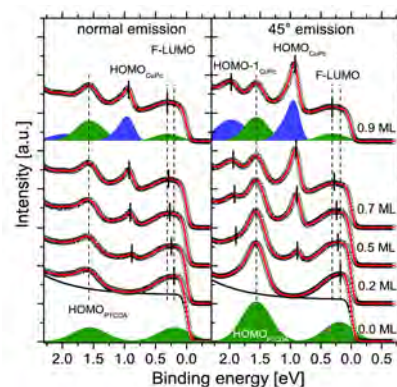


FIG. 3: UPS data of CuPc on PTCDA on Ag(111) for different CuPc coverages at RT. The red curves represent least-square fits to the data. For the lowermost and uppermost curves the fitting model consisting of up to four independent peaks is shown; PTCDA and CuPc states are displayed in green and blue, respectively. A background curve is shown as a black solid line with the lowermost curve.

In conclusion, we have presented evidence for an unexpectedly strong interaction (namely, a weak chemisorption) at the organic heterojunction between CuPc and PTCDA on Ag(111). The chemisorptive character is indicated (1) by the formation of a commensurate registry between the CuPc and PTCDA superstructures, consistently found by SPA-LEED and STM, (2) by the STM contrast of the CuPc benzene-wings which strongly depends on their position relative to the underlying PTCDA molecule, and (3) by the gradually increasing filling of the F-LUMO state of PTCDA upon adsorption of CuPc. Against common belief, these results prove that rather strong, chemisorptive interaction can occur also at hetero-organic interfaces. This aspect will have significant impact on the understanding and designing of molecular electronic devices.

- [1] F.S. Tautz, Prog. Surf. Sci. 82, 479 (2007); A. Hauschild et al., Phys. Rev. B 81, 125432 (2010); I. Kröger et al., J. Chem. Phys. 135, 234703 (2011); C. Stadler et al., Nature Phys. 5, 153 (2009); I. Kröger et al., New J. Phys. 12, 083038 (2010).
- [2] B. Stadtmüller et al., Phys. Rev. Lett. (2012).
- [3] M. Häming et al, Phys. Rev. B 82, 235432 (2010); W. Chen et al., J. Phys. Chem. C 112, 5036 (2008); F. Sellam et al., Surf. Sci. 478, 113 (2001).

Metal / Molecule Contacts: From Electronic Properties to Charge Transport

S. Soubatch¹, R. Temirov¹, P. Puschnig², E.-M. Reinisch², T. Ules², G. Koller², M. Ostler³, L. Romaner⁴, C. Toher⁵, F. Pump⁵, A. Greuling⁶, M. Kaczmariski⁶, M. G. Ramsey², C. Ambrosch-Draxl⁴, G. Cuniberti⁵, M. Rohlfing⁶, F. B. Anders⁷, F. S. Tautz¹

1 PGI-3: : Functional Nanostructures at Surfaces, Forschungszentrum Jülich

2 Universität Graz

3 Universität Erlangen

4 Montanuniversität Leoben

5 TU Dresden

6 Universität Osnabrück

7 TU Dortmund

Any progress toward the vision of molecular electronics requires a thorough understanding of current conduction through single molecules. For this reason, an intense effort has been focused recently on transport experiments in metal/molecule/metal junctions. However, before transport data can be understood quantitatively, a few prerequisites have to be fulfilled: The geometric and the electronic structures of the metal/molecule contact have to be known, and electron correlation effects have to be taken into account. Here we present new experimental and theoretical approaches to tackle these challenges. All experiments and simulations reported here have been carried out on the prototypical PTCDA molecule on silver surfaces.

Electronic structure of metal-molecule contacts

The valence bands of large conjugated molecules consist of a multiplicity of closely spaced molecular states, and their correct assignment is challenging both experimentally and theoretically. Experimentally, energy positions of molecular orbitals in organic molecular layers can be studied by ultraviolet photoemission spectroscopy (UPS). However, UPS spectra of thin molecular layers on metals often show only weak and rather broad features and are, therefore, not always conclusive. Also, UPS data depend on the experimental geometry, molecular orientation, and photon energy, which further complicates the assignment of the measured peaks. Therefore, calculated densities of states (DOSs) from *ab initio* electronic-structure calculations are commonly used to complement and interpret UPS data. However, this is problematic, for various reasons: For example, in density-functional theory (DFT) calculations, both the orbital energies and the orbital-energy order rely on approximations made for exchange-correlation effects, and thus the functional chosen. In ref. [1] we present a tomographic analysis of angle resolved

photoemission spectroscopy (ARPES) that provides a solution to the problem of assigning spectral features in UPS to specific molecular states.

We collect ARPES data in the full half-space above the sample surface. This data set contains a complete momentum- and energy-resolved DOS of the sample in the measured binding-energy range. To assign emissions to specific molecular states, we evaluate tomographic cross sections through the momentum-resolved data set and search for momentum space patterns that are characteristic for the corresponding molecular orbitals. This analysis is based on a simple plane-wave approximation for the final state in the photoemission process that has been shown to be appropriate for many π -conjugated organic molecules since scattering effects have been demonstrated to be negligible. In this approximation, the ARPES intensity distribution from a molecular state is related to the respective molecular orbital's Fourier transform.

The combination of these simulated momentum maps with experimental tomographs (Fig. 1) allows the quantitative deconvolution of a spectrum into contributions from individual molecular states beyond the limits of intrinsic line broadening and instrumental energy resolution, thus even if its deconvolution based on conventional peak fitting is impossible. This is achieved by carrying out the deconvolution in *k*-space, thereby making use of the full momentum space information of the molecular orbitals. The so-obtained orbital projected DOS provides a stringent test for electronic-structure theories including density functional calculations as well as wave-function-based approaches.

Comparison of *ab-initio* transport simulations to experiments in controlled geometries

Unfortunately, most single-molecule transport experiments to date do not allow the structural characterization of the junction independent of its transport properties. In this respect, STM-based approaches offer advantages. For example, in a

recent publication, we have shown that a surface-adsorbed molecule can be chemically bonded to an STM tip at a defined position within the molecule and peeled off the surface by tip retraction. Spectroscopic data recorded during tip retraction revealed a *mechanical gating effect*, in the sense that one of the molecular orbitals responds to the structural change and shifts with respect to the Fermi level of the substrate.

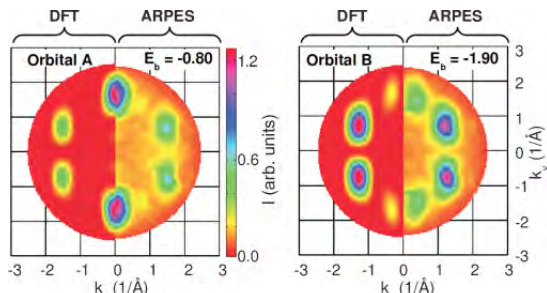


Fig. 1 Orbital Tomographs of PTCDA/Ag(110) [1].

In ref. [2] we present more comprehensive data of this experiment and compare the experimental data to an *ab initio* study of transport through this gated molecular wire. To describe the conduction through a molecule theoretically from first principles, three demanding quantum mechanical problems have to be addressed, namely, the geometric and electronic structures of the junction and the non-equilibrium current between two biased reservoirs across the molecular bridge. For the first two, we employ density functional theory (DFT), while the transport problem is solved by the non-equilibrium Green's function (NEGF) formalism.

Our analysis starts with a simulation of the contacting process during tip approach and the molecule-substrate bond-cleaving process during tip retraction. This yields structural and energetic data which can be compared to experimental results. In the second step, the transport calculations are carried out for the experimentally validated geometries and compared to experimental transport data. In this way, we can separately compare structure and transport simulations to experiment. Moreover, the comparison is not limited to a single point in the configuration space of the molecular junction, but includes a wide range of systematically and controllably varied configurations for each of which experimental transport data exist. The experiments thus provide a critical test of the theoretical methodology by effectively eliminating the possibility of fortuitous agreements between theory and experiments.

We find that DFT fully confirms structural aspects of the contacting and bond-cleaving scenarios deduced from experiment, while the transport simulations exhibit several differences compared to experiment. These can be understood as a failure of the DFT-NEGF platform with the local density approximation (LDA) to account for the dynamical nature of

electron-electron correlations in the transport orbital of the molecule.

The role of electron correlations in molecular transport

The interrelation between the structure of the junction and its transport spectra was studied in ref. [2] in terms of transport theory disregarding the dynamical correlation mechanisms. However, we concluded in ref. [2] that the mechanical gating is subject to subtle details of electronic correlation, e.g., screening of the intramolecular Coulomb repulsion by the electrodes, which is not described by conventional density functional theory (DFT). In ref. [3] we therefore apply the following strategy: DFT (in the local density approximation LDA) addresses the atomistic details of the junction structure but does not provide reliable, well-founded spectral data. To evaluate the electronic spectrum, we combine DFT with many-body perturbation theory (MBPT) for nonlocal correlation and with numerical renormalization group (NRG) theory for correlation dynamics beyond the mean-field level. Among these three approaches, MBPT constitutes the essential link between DFT and NRG. Most NRG studies so far have been based on empirical model parameters. MBPT spectra, on the other hand, provide better-founded NRG input data.

MBPT for large and complex systems such as, for example, the tip/PTCDA/Ag junction, which combines metallic with non-metallic screening and shows partial occupancy of the most important molecular level, is computationally very expensive. For such systems, the commonly employed GW approximation of MBPT thus requires further simplification. Here we introduce the so-called "LDA+GdW" as an efficient and systematic implementation of MBPT.

Within this framework of LDA + GdW + NRG, we can correctly describe the mechanical gating of the molecular wire, and we reproduce the evolution of a Kondo resonance in the initially non-magnetic molecule. Moreover, we have presented an approach to calculating electronic spectra that systematically includes nonlocal and dynamic correlation effects. Because of its computational efficiency, this state-of-the-art approach to electronic spectra should be widely applicable.

-
- [1] P. Puschnig, E.-M. Reinisch, T. Ules, G. Koller, S. Soubatch, M. Ostler, L. Romaner, F. S. Tautz, C. Ambrosch-Draxl, M. G. Ramsey, Phys. Rev. B 84 235427 (2011), Editor's Selection
 - [2] C. Toher, R. Temirov, A. Greuling, F. Pump, M. Kaczmarek, G. Cuniberti, M. Rohlfing, F. S. Tautz, Phys. Rev. B 83 155402 (2011), Editor's Selection
 - [3] A. Greuling, M. Rohlfing, R. Temirov, F. S. Tautz, F. B. Anders, Phys. Rev. B 84 125413 (2011)

Single Molecule and Single Atom Sensors for Atomic Resolution Imaging of Chemically Complex Surfaces

G. Kichin, C. Weiss, C. Wagner, F. S. Tautz, R. Temirov

PGI-3: Functional Nanostructures at Surfaces, Forschungszentrum Jülich

Individual Xe atoms as well as single CO and CH₄ molecules, adsorbed at the tip of a scanning tunnelling microscope (STM), function as microscopic sensors that change the tunnelling current in response to the forces acting from the surface. The STM equipped with any of these sensors images the short-range Pauli repulsion and so resolves the inner structure of large organic molecules. Differences in the performance of the three studied sensors suggest that the sensor functionality can be tailored by tuning the interaction between the sensor particle and the STM tip.

Recently we demonstrated that condensing molecular hydrogen or deuterium (H₂ or D₂) in the junction of a low-temperature scanning tunneling microscope (STM) it is possible to resolve the inner structure of molecular adsorbates [1,2] and directly image intermolecular interactions [3]. To explain the new imaging mechanism, named Scanning Tunneling Hydrogen Microscopy (STHM) it has been proposed that a single (H₂ or D₂) molecule in the tunneling junction acts as a static nanoscale force sensor and signal transducer [2]: Interactions with the sample surface change the position of the sensor molecule relative to the STM tip, thus varying the strength of Pauli repulsion between the tip and the molecule; this is the “sensor” action.

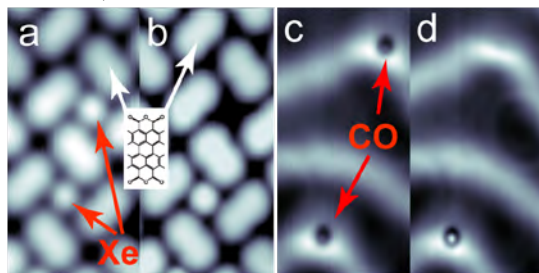


FIG. 1: (a). 5x2.5 nm² STM image of PTCDA/Au(111) with the two Xe atoms residing in the layer, measured with the clean Au tip. The chemical structure formula of PTCDA is shown in the inset. (b). The same as (a), but made after picking up the upper Xe atom with the tip. (c). 5x10 nm² STM image of the two CO molecules adsorbed on the clean Au(111) surface. (d). The same as (c), but made after picking up the upper CO molecule with the tip.

The “transducing” effect is based on the coupling of the Pauli force to the tunneling conductance; the coupling occurs because an increasing repulsion between tip and sensor molecule progressively

depletes the tip’s density of states close to the Fermi level.

However, since neither H₂ nor D₂ can be imaged in the STM, the assumed structure of the nanoscale force sensor was up to now inferred from the properties of the STHM contrast itself, rather than determined independently. In these circumstances, an unambiguous proof for the idea that a single molecule acts as the force sensor has remained elusive. In our latest experiments we used Xe, CO and CH₄ to demonstrate directly that a single atom or molecule that decorates the STM tip indeed produces an STHM-like resolution [4]. Utilizing known recipes we were able to transfer single Xe atoms and CO molecules between the tip and the surface reproducibly (Fig. 1a-d). This has allowed us to study the imaging properties of the decorated STM tips systematically.

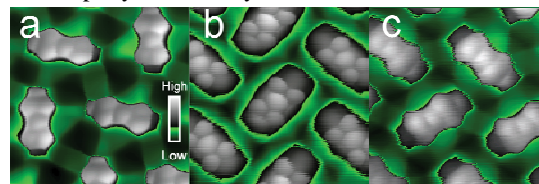


FIG. 2: (a). 2.5x2.5 nm² constant height image of the PTCDA/Au(111) recorded with the Xe-tip. The color palette is shown in the inset. Brightness scale: $I_{low} = -0.4$ nA, $I_{high} = -8$ nA. (b). The same as (a), but recorded with CO-tip. (c). The same as (a), but recorded with CH₄-tip.

When scanned at ordinary tunneling conditions, decorated tips yield a slight enhancement of spatial image resolution (Fig. 1b,d). However, when moved closer to the surface, these tips develop a new type of contrast (Fig. 2a-c). Comparing Fig. 2a to Fig. 1c from the ref. 3, we see that the contrast generated by the Xe-tip is almost identical to the STHM contrast obtained with D₂. Thus, the experiments with Xe allow significant progress in our understanding of STHM: Because the structure of the Xe-tip is known, it becomes unambiguously clear that the STHM-type contrast is produced by a single particle (Xe or D₂) which is bound to the apex of the STM tip, from where it interacts with the apex of the sample and thus senses the force exerted on it by the surface. The comparison between D₂-sensors and Xe-sensors shows that the mass of the involved particle has limited (if any) influence on the image contrast obtained. Therefore, also the static model of the STHM force sensor that was proposed in our earlier work is confirmed.

Study of different sensor particles (Xe, CO and CH₄) helped us to explore the possibility of tailoring the sensor properties by tuning the tip-particle interaction strength. Similar to Xe, all CO-terminated tips were able to resolve the inner structure of organic molecules (Fig. 2b). At the same time we found characteristic differences between the images recorded with different sensors: the CO-sensor yields better resolution of the aromatic backbone. On the other hand, the contrast in the spaces between the molecules, related to the intermolecular hydrogen-bond network [3], is much better reproduced with Xe and CH₄.

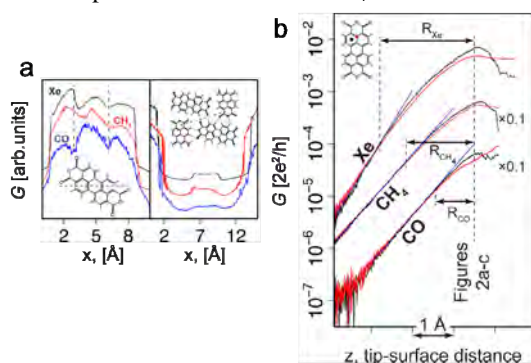


FIG. 3: (a). Conductance line profiles measured along the path marked by the dashed lines in the respective insets. The black curve was extracted from Fig. 2a measured with Xe, the red curve from Fig. 2c measured with CH₄, and the blue curve from Fig. 2b measured with CO. (b). The $G(z)$ spectra of the Xe, CO, and CH₄ sensors. The curves were shifted along the z -axis such that the tip-surface distances, at which the Fig. 2a-c were scanned, coincide.

Fig. 3a compares the contrasts obtained with different types of sensors. The left panel of Fig. 3a shows that the “Pauli repulsion images” recorded with the Xe- and CH₄-sensors are laterally distorted: e.g. in both cases, the three aromatic rings along the profile appear to have different sizes. This happens due to the deformations of the tip-sensor complex that occur during imaging. Notably, the contrast generated by the CO-sensor is much less distorted. This property of the CO-sensor may be rationalized by the stiffer bonding of CO to the tip, as compared to Xe and CH₄.

Looking at the signal above the hydrogen bonds (Fig. 3a, right), we see that the imaging performance is reversed: Here, the Xe- and CH₄-sensors provide a higher contrast than the CO-sensor. To rationalize this observation we inspect the conductance versus distance $G(z)$ spectra measured while the decorated tip approaches the surface. All $G(z)$ curves plotted in Fig. 3b exhibit pronounced non-exponential behavior at small tip-sample distances. Earlier we proposed that the observed deviation from the exponential behavior is related to the depletion of the tip DOS by

Pauli repulsion acting between the tip and the sensor molecule adsorbed at the apex.

Recording $G(z)$ spectra above a carbon atom (red curve) and a C₆ ring (black curve), we can directly observe that each sensor molecule indeed achieves its optimal imaging resolution of the carbon backbone (shown in Fig. 2a-c) at the distance where the difference between the red and the black $G(z)$ spectra is pronounced. At the same time the $G(z)$ behavior of all three sensors is slightly different manner: It is apparent that the tip-surface distance range in which the sensors are sensitive to any influence whatsoever from the sample surface (and thus their conductance deviate from exponent) differs substantially between the three sensor particles. This range can be quantified by the parameter R which is defined as the difference between the distance at optimal contrast and the distance at which the particular $G(z)$ curve starts to deviate from exponential growth.

According to Fig. 3b, the values R_{Xe} and R_{CH_4} are noticeably larger than R_{CO} , which means that the Xe- and CH₄-sensors produce detectable output in a wider range of tip-surface distances, while the sensitivity of the CO-sensor decays faster as the tip is moved away from the sample surface. Thus the CO-sensor has a substantially shorter sensitivity range than Xe- and CH₄-sensors and at the same time it yields the poorest hydrogen bond contrast. We suggest that this is not a mere coincidence, but that the shorter-range sensitivity of the CO-sensor is indeed the reason for its poor hydrogen bond resolution. Based on the fact that, in the area between the molecules where the hydrogen bond network is located, the effective tip-surface distance is larger than on top of PTCDA (we note again that all STHM images reported in this paper have been measured in constant height mode); because of their short-range sensitivity, the increased tip-surface distance above the interstitial areas must affect the performance of CO-sensors in a more pronounced way than of the Xe- and CH₄-sensors. This finding demonstrates the possibility of tuning the imaging performance of single atom and molecule sensors by tuning the interaction of the particle with the STM tip.

-
- [1] R. Temirov, S. Soubatch, O. Neucheva, A. Lassise, F.S. Tautz, *New J. Phys.* 10, 053012 (2008).
 - [2] C. Weiss, C. Wagner, C. Kleimann, F. S. Tautz and R. Temirov, *Phys. Rev. Lett.* 105, 086103 (2010)
 - [3] C. Weiss, C. Wagner, R. Temirov and F. S. Tautz, *J. Am. Chem. Soc.* 132, 11864 (2010)
 - [4] Kichin, C. Weiss, C. Wagner, F. S. Tautz, and R. Temirov, *J. Am. Chem. Soc.* 133, 16847 (2011)

Selective Adsorption of C₆₀ on Ge/Si Nanostructures

S. Korte¹, K. Romanyuk¹, B. Schnitzler¹, V. Cherepanov¹, B. Voigtländer¹, S. Filimonov²

¹ PGI-3: Functional Nanostructures at Surfaces, Forschungszentrum Jülich

² Department of Physics, Tomsk State University, Tomsk, 634050 Russia

Selective adsorption of C₆₀ on nanoscale Ge areas can be achieved, while neighboring Si(111) areas remain uncovered, if the whole surface is initially terminated by Bi. Fullerene chemisorption is found at Bi vacancies which form due to partial thermal desorption of the Bi surfactant [1]. The temperature dependence of the C₆₀ adsorption was measured using scanning tunneling microscopy (STM). The selectivity of the C₆₀ adsorption can be traced back to an easier vacancy formation in the Bi layer on top of the Ge areas compared to Si areas. Furthermore, it is also possible to desorb C₆₀ from Ge areas, allowing to use C₆₀ as a resist on the nanoscale.

Nanostructuring using epitaxial growth processes can lead down to sizes in the single digit nano-meter range or even ultimately to the single molecule/atom range which is not accessible by lithography. Serious challenges in these efforts are size fluctuations during the growth process and the ability to place self assembled nanostructures at desired positions. A great help in these nano-structuring attempts is the ability to directly inspect the nanostructure formation by chemically sensitive surface imaging techniques. For instance, in our previous studies it has been shown that the use of Bi as surfactant not only largely suppresses Si/Ge intermixing but also allows the distinction between Si and Ge on the nanometer scale [2]. Using step flow growth mode during Bi mediated Ge epitaxy on a vicinal Si(111) substrate we successfully fabricated an array of 4 nm wide one atomic layer high Ge nanowires. These nanowires could serve as templates for growth of even more complicated nanostructures based on different material combinations. However, attempts to either desorb Bi selectively from Ge areas or decorate the Ge nanowires by a metal failed so far. The fundamental reason for this lack of selectivity is that Si and Ge are, in fact, chemically very similar materials. To achieve the selectivity a physical mechanism has to be found that would enhance the material difference.

We show that the use of surfactants is a means to control the selectivity of C₆₀ adsorption and leads to new nanostructuring opportunities. Deposition of C₆₀ on a Bi terminated surface results in selective replacement of Bi by C₆₀ in Ge surface areas (Fig. 1 (a)). Our analysis shows that the high selectivity of C₆₀ adsorption is made possible due to a complex mechanism of C₆₀ adsorption, involving the formation of vacancies in the Bi layer followed by

vacancy mediated chemisorption of C₆₀ on Ge surface areas only [1].

Fig. 1 (a) shows an STM image of a Si(111) sample on which Ge nanowires have been grown at step

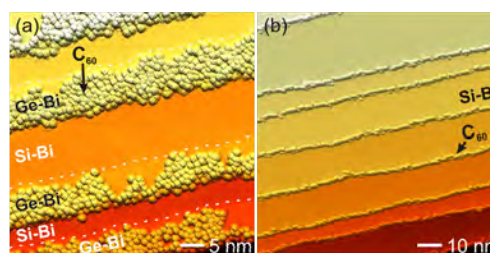


FIG. 1: (a) Selective growth of C₆₀ on Ge areas, while Si areas remain uncovered. The slight height difference between Si and Ge areas is highlighted by dashed lines at the Si/Ge boundaries. The C₆₀ are seen as round protrusions with intramolecular structure on the Ge areas. (5 ML C₆₀ deposited at 440°C during 10 min) (b) Selective adsorption of C₆₀ at Si step edges (2 ML C₆₀ deposited at 420°C during 10 min).

edges using Bi mediated epitaxy. The borders between the Si and the Ge areas (each with 1 ML Bi on top), which show different apparent heights in the STM images [2], are highlighted by dashed lines. Subsequently 5 ML of C₆₀ were deposited onto this Ge nanowire template at 440°C. Only a small fraction of the C₆₀ actually remains on the surface whereby C₆₀ adsorbs selectively on the Ge areas. The selectivity is perfect in the sense that virtually no C₆₀ adsorbs on the Si, however, the Ge nanowires are not completely covered by C₆₀. When no Ge area is present on the surface, deposition of C₆₀ on Bi:Si(111) leads to selective adsorption of C₆₀ at Si step edges (Fig. 1 (b)).

In order to identify the reason for the selective adsorption of C₆₀ on Ge areas we analyzed the C₆₀ adsorption as function of temperature, which shows a different behavior on the surfactant terminated surface than on clean Si or Ge [3]. The results are summarized schematically in Fig. 2. At room temperature C₆₀ adsorbs on top of the Bi layer and forms large two-dimensional islands consisting of well-ordered hexagonally arranged C₆₀ molecules. The observed height of the C₆₀ islands above the Bi layer of ~ 8 Å suggests a weak van der Waals bonding of C₆₀ to Bi:Ge/Si(111) and Bi:Si(111) surfaces. In this weakly bound physisorption state C₆₀ shows no selectivity and grows both on Si and on Ge areas. After short annealing at 200°C the physisorbed C₆₀ layer completely desorbs, restoring the Bi covered surface. Depositing C₆₀ in a

temperature range of 200-400°C does not lead to any adsorption of C_{60} (Fig 2 (b)).

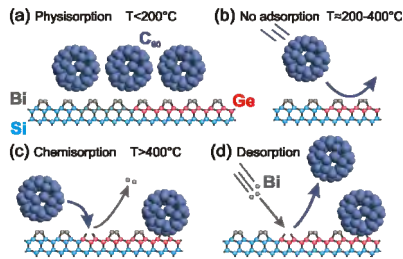


FIG. 2: Schematic of the C_{60} adsorption on Si(Ge) as function of temperature. (a) at room temperature C_{60} adsorbs in a weakly bound physisorption state on top of the Bi layer, (b) at 200-400°C no C_{60} adsorption occurs, (c) above 420°C chemisorption of C_{60} occurs at Bi vacancies on Ge. (d) under Bi flux C_{60} desorbs from the Ge surface.

At temperatures above 420°C adsorption of C_{60} could be seen on Ge, and starting from about 460°C also on Si terraces. At Si step edges the adsorption occurs already at somewhat lower temperatures, c.f. Fig. 1 (b). However, in this high temperature range the adsorption mechanism differs considerably from that observed at room temperature. At submonolayer surface coverages most of the C_{60} adsorb either as single molecules, or forming small irregular clusters. The measured apparent height of the C_{60} above the surrounding Bi layer is only 4 Å, suggesting that at elevated temperatures C_{60} adsorbs directly to Si (Ge), i.e. without Bi below C_{60} (Fig. 2 (c)). The irregular arrangement of the C_{60} clusters hints at strong covalent bonding of C_{60} to the underlying Si (Ge) surface, which also occurs for C_{60} adsorption on clean Si(111) and Ge(111) surfaces [3].

Direct bonding of C_{60} to Si and Ge surfaces may occur either at vacancies in the Bi layer or via displacement of Bi atoms by C_{60} . To experimentally prove the vacancy mediated chemisorption of C_{60} on the Bi terminated Si(111) surface, we deposited the same amount of C_{60} in two different ways. In the first experiment, 1.3 ML of C_{60} was deposited continuously for 5 min at 480°, while in the second experiment the sample was first annealed for 5 min at 480°C and then the same amount of C_{60} was deposited in a burst of only 10 sec at a low temperature of 350°C. Both the amount of C_{60} that actually stick to the surface (ca. 0.3 % of the deposited C_{60}) and the density of C_{60} clusters are almost identical in both cases. This indicates that the annealing phase, lasting the same time as the continuous deposition experiment, determines the island density and not the actual C_{60} deposition.

The major effect of the annealing is a partial desorption of Bi and formation of vacancies in the Bi layer which can be directly seen in STM images after annealing. Therefore, we conclude that the chemisorption of C_{60} occurs at vacancies in the Bi layer which are formed by thermal desorption of Bi. A more detailed analysis shows that a single vacancy where only one Bi trimer of the $\sqrt{3}\times\sqrt{3}$ Bi reconstruction has converted to a Bi monomer is not enough to trigger C_{60} adsorption, but larger vacancy

islands with reduced Bi coverage are needed as nucleation centers for C_{60} .

As an additional check for the proposed adsorption mechanism of C_{60} on Bi:Si(111) we have performed C_{60} deposition supplying a Bi flux to prevent Bi desorption. In this case the formation of Bi vacancies is inhibited (deposited Bi fills the vacancies), and the vacancy mediated C_{60} chemisorption should be suppressed, which is confirmed experimentally.

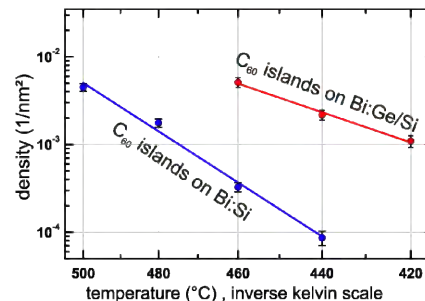


FIG. 3: Temperature dependence of the C_{60} island density on a 1ML Bi:Si(111) and on a Bi:Ge/Si(111) surface for deposition of 0.8 ML C_{60} during 2 min. The smaller slope indicates a lower vacancy formation energy for Bi on Ge than for Bi on Si.

An Arrhenius type temperature dependence was found for the C_{60} island density as shown in Fig. 3. From this data we obtain a much higher vacancy formation energy for Bi on Si (3.2 ± 0.3 eV) than for Bi on Ge (1.7 ± 0.3 eV). This explains the selectivity of the C_{60} chemisorption. One can tune the temperature so that Bi vacancies form readily at the Ge areas, which can serve as nucleation centers for C_{60} , while on the neighboring Si areas the activation energy for a Bi vacancy formation is so high that no Bi vacancies form. There might be additional factors that enhance C_{60} adsorption selectivity even further.

C_{60} can also be removed again from the Ge(1ML)/Si(111) surface. Annealing at 420°C in a flux of Bi leads to desorption of C_{60} according to the mechanism sketched in Fig. 2 (d). The Bi substitutes the C_{60} and fills the vacancies in the Bi termination layer. An almost complete C_{60} desorption from Ge can be achieved, leaving less than 1 % of the C_{60} bound to the surface.

In conclusion, selective adsorption of C_{60} at Ge areas and at Si step edges has been achieved. The mechanism for the selective adsorption is the nucleation and growth of C_{60} at Bi vacancies which form preferentially on Ge areas due to the lower vacancy formation energy compared to Si. It is possible to selectively cover Ge nanowire templates with C_{60} (and to remove it afterwards) in order to use C_{60} as a resist in further nanostructuring steps.

-
- [1] S. Korte, K. Romanyuk, B. Schnitzler, V. Cherepanov, B. Voigtländer, and S. Filimonov, Phys. Rev. Lett. 108, 116101 (2012).
 - [2] M. Kawamura, N. Paul, V. Cherepanov, and B. Voigtländer, Phys. Rev. Lett. 91, 096102 (2003).
 - [3] P.J. Moriarty, Surf. Sci. Rep. 65, 175 (2010).

Selected Publications

1. Romanyuk, K.; Brona, J.; Voigtländer, B.
Nanoscale Pit Formation at 2D Ge Layers on Si: Influence of Energy and Entropy
Physical Review Letters, **103** (2009) 9, 096101.
2. Soubatch, S., Weiss, C., Temirov, R. & Tautz, F. S.
Site-specific polarization screening in organic thin films.
Physical Review Letters **102**, 177405 (2009).
3. Stadler, C.; Hansen, S.; Kröger, I.; Umbach, E.; Kumpf, C.
Tuning intermolecular interaction in long-range ordered submonolayer organic films
Nature Physics, **5** (2009), 153 – 158.
4. Mercurio, G.; McNellis, E.R.; Martin, I.; Hagen, S.; Leyssner, F.; Soubatch, S.; Meyer, J.; Wolf, M.; Tegeder, P.; Tautz, F. S.; Reuter, K.
Structure and Energetics of Azobene on Ag(111): Benchmarking Semiempirical Dispersion Correction Approaches
Physical Review Letters, **104** (2010) 3, 036102.
5. Weiss, C.; Wagner, C.; Kleimann, C.; Rohlfing, M.; Tautz, F. S.; Temirov, R.
Imaging Pauli Repulsion in Scanning Tunneling Microscopy
Physical Review Letters, **105** (2010) 8, 086103.
6. Weiss, C., Wagner, C., Temirov, R. & Tautz, F. S.
Direct imaging of intermolecular bonds in scanning tunneling microscopy.
Journal of the American Chemical Society **132**, 11864-11865 (2010).
7. Kichin, G., Weiss, C., Wagner, C., Tautz, F. S. & Temirov, R.
Single molecule and single atom sensors for atomic resolution imaging of chemically complex surfaces.
Journal of the American Chemical Society **133** 16847–16851 (2011).
8. Wagner, C.; Fournier, N.; Tautz, F. S.; Temirov, R.
Measurement of the Binding Energies of the Organic-Metal Perylene-Teracarboxylic-Dianhydride/Au(111) Bonds by Molecular Manipulation Using an Atomic Force Microscope
Physical Review Letters, **109** (2012) 7, 076102
9. Puschnig, P.; Reinisch, E.-M.; Ules, T.; Koller, G.; Soubatch, S.; Ostler, M.; Romaner, L.; Tautz, F. S.; Ambrosch-Draxl, C.; Ramsey, M. G.
Orbital tomography: Deconvoluting photoemission spectra of organic molecules.
Physical Review B **84**, 235427 (Editor's suggestion) (2011).
10. Toher, C.; Temirov, R.; Greuling, A.; Pump, F.; Kaczmariski, M.; Cuniberti, G.; Rohlfing, M.; Tautz, F. S.
Electrical transport through a mechanically gated molecular wire.
Physical Review B **83**, 155402 (Editor's suggestion) (2011).

Indicators

Quantitative Numbers

	2009	2010	2011
Peer-Reviewed Publications	8	12	19
Graduations			
Master/Diploma	0	0	0
Dissertation	2	3	1
Habilitation	0	0	0

Honours

HGF Young Investigator Group	Ruslan Temirov	2009
AvH postdoctoral fellowship	Dr. Tomoki Sueyoshi	2010
ESRF poster prize	Martin Willenbockel	2011
Max-Auwärter-Prize	Guiseppe Mercurio	2012

Offers

2012	Dr. Crhristian Kumpf	RWTH Aachen	W2 Professor for Experimental Physics
------	----------------------	-------------	---------------------------------------

Selected Third Party Projects

1. “Complex Transport Regimes in Scanning Tunnelling Microscopy”
Helmholtz Young Investigator Group
Helmholtz-Gemeinschaft
Project leader: Dr. R. Temirov
Funding period: 01.02.2009 - 31.01.2014
2. “Tunable transport by controlling the structure of a STM molecular junction: Synchronizing theory and experiments”
DFG Priority Programme SPP 1243 (Quantum Transport Through Molecules)
Project leader: Prof. F. S. Tautz
Funding period: 01.01.2009 - 30.06.2011 und 01.07.2011 - 30.06.2013 (zwei Projekte)
3. „Ausgründungsinitiative mProbes“
Helmholtz-Gemeinschaft
Project leader: Prof. B. Voigtländer HGF
Funding period: 01.09.2012 - 31.08.2013

PGI-4/JCNS-2: Scattering Methods



Research of PGI-4/JCNS-2 - *Scattering Methods* is devoted to the understanding of strong electronic correlations as well as of magnetism on the nanoscale. To this end, we employ the complementary techniques of neutron scattering and scattering of synchrotron radiation in order to obtain a detailed microscopic understanding of structure and excitations on the atomic scale. The problems studied regularly push current neutron instruments to their limits and thus foster science driven instrumentation. In neutron instrumentation, PGI-4/JCNS-2 is a driver in the application of polarized neutron scattering techniques. While the method development, instrument construction and user operation are part of the programme “PNI: Research with Photons, Neutrons and Ions”, the institute brings the expertise in scattering methods to the programme “FIT: Fundamentals of Future Information Technology”. All systems studied within the institute have a potential for future applications either for information technologies or for energy technology.

Materials or materials systems studied at PGI-4 span the entire range from bulk via thin films and multilayers, laterally structured layered systems, nanoparticles and nanoparticle assemblies to molecular magnets. With JCNS being a user facility with outstations in Garching, Grenoble (France) and Oak Ridge (USA), we deliberately chose such a wide range of materials systems in order to provide topical scientific problems for all JCNS instruments and instrument scientists. In Jülich we operate laboratory equipment for sample preparation (oxide MBE, sputter chambers, floating zone mirror furnace) and sample characterization (Physical Property Measurement System, SQUID, x-ray scattering instruments).

The institute hosts two Young Investigator Groups, granted by the Helmholtz Association. The group „Complex Ordering Phenomena in Multifunctional Oxides“ led by Prof. Manuel Angst focuses on materials for information technologies, in particular multiferroics. The group “Lattice dynamics in emerging functional materials” led by Prof. Raphaël Hermann focuses on energy materials, in particular thermoelectric materials.

Head of Institute:

Prof. Thomas Brückel, email: t.brueckel@fz-juelich.de, phone: +49-2461-61-4699.

Scientific Staff

In September 2012, the institute encompasses 13 scientists, 8 technicians and engineers, 2 diploma and 15 Ph.D. thesis students.

Scientists

Brückel, Prof. Dr. Thomas
Friese, Dr. habil. Karen
Kentzinger, Dr. Emmanuel
Persson, Jörg
Petracic, PD Dr Oleg
Rücker, Dr. Ulrich
Schweika, PD Dr. Werner
Xiao, Dr. Yinguo

Junior Research Group Leader

Angst, Prof. Dr. Manuel
Hermann, Prof. Dr. Raphael

Post-Docs

Klobes, Dr. Benedikt
Nandi, Dr. Shibabrata
Weber, Dr. Alexander

Guest Scientists

Houben, Dr. Andreas
Waschk, Markus

Research Highlights

Phonon Dynamics in Parent and Superconducting FeAs Compounds

R. Mittal^{1,2,3}, Y. Su^{1,2}, L. Pintschovius⁴, M. Zbiri⁵, S. Rols⁵, Y. Xiao², H. Schober⁵, S. L. Chaplot³, T. Chatterji⁶, R. Heid⁴, A. Thamizhavel⁷, S. Matsuishi⁸, and Th. Brueckel^{1,2}

1 Jülich Centre for Neutron Science, IFF, Forschungszentrum Jülich, Outstation at FRM II, Lichtenbergstr. 1, 85747 Garching, Germany

2 PGI-4: Scattering Methods, Forschungszentrum Jülich

3 Solid State Physics Division, Bhabha Atomic Research Centre, Trombay, Mumbai 400 085, India

4 Forschungszentrum Karlsruhe, Institut für Festkörperphysik, P.O.B. 3640, 76021 Karlsruhe

5 Institut Laue-Langevin, BP 156, 38042 Grenoble Cedex 9, France

6 Jülich Centre for Neutron Science, Forschungszentrum Jülich

Outstation at Institut Laue-Langevin, BP 156, 38042 Grenoble Cedex 9, France

7 Tata Institute of Fundamental Research, Colaba, Mumbai 400 005, India

8 Frontier Research Center, Tokyo Institute of Technology, 4259 Nagatsuta-cho, Midori-ku, Yokohama 226-8503, Japan

We have carried out extensive measurements of the phonon dispersion relation and phonon density of states for the newly discovered parent and superconducting FeAs compounds using inelastic neutron scattering technique. The phonon spectra are analyzed using ab-initio and empirical model calculations giving density of states and dispersion relation. We found strong temperature dependence of some phonons in CaFe_2As_2 near the structural phase transition around 172 K, which may indicate strong electron phonon coupling and/or anharmonicity. Furthermore, measurement of phonon density of states in $\text{CaFe}_{1-x}\text{Co}_x\text{AsF}$ compounds ($x = 0, 0.06, 0.12$) support coupling of electrons and phonons in Co doped CaFeAsF compounds.

The discovery of superconductivity in fluorine-doped RFeAsO (R = rare earth) and K-doped BaFe_2As_2 has stimulated enormous interest [1-10] in the field of condensed matter physics. It is important to note that these compounds have high superconducting transition temperatures without requiring the presence of copper oxide layers. Electron or hole doping suppresses structural and magnetic phase transitions and induces superconductivity at lower temperatures. At present, it remains unclear whether the change of the electron concentration by doping is essential for achieving superconductivity or whether the suppression of the phase transition into a magnetically ordered state is the main effect.

Theoretical electronic structure calculations for FeAs compounds show that superconductivity in these compounds is mainly due to the structural and electronic states of the Fe-As layers. The mechanism of superconductivity, and in particular the role of lattice dynamics in superconducting pair formation in these newly discovered compounds is still to be

settled. Meanwhile it is necessary to study phonon dynamics carefully in these materials. This has motivated us to carry out measurements of phonon dynamics [4-10] in parent and superconducting FeAs compounds.

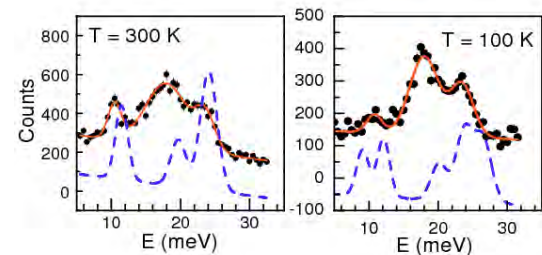


FIG. 1: Energy scans [4] taken at $Q = (2.5, 1.5, 0)$ at room temperature and at a temperature far below the structural phase transformation temperature of 172 K. The full lines are fit curves to the data. The dashed lines show phonon intensities calculated from density functional theory convoluted with the experimental resolution. The calculations were based on the experimental room temperature structure (which is non-magnetic, left hand side) and the orthorhombic low temperature structure (right hand side). For better visibility the calculated profiles (dashed lines) in the lower and upper panels are shifted down by 200 counts.

We have extensively carried out [4] inelastic neutron scattering measurements of phonons on a single crystal of CaFe_2As_2 . The measurements allowed us to establish a fairly complete picture of phonon dispersions in the main symmetry directions. The experiment was carried out on the 1T1 triple-axis spectrometer at the Laboratoire Léon Brillouin, Saclay. The phonon spectra were also calculated by density functional theory (DFT) in the local density approximation (LDA). There are serious discrepancies between calculations done for the optimized structure and experiment, because the optimised structure is not the ambient pressure

structure but is very close to the “collapsed” structure reached at $p = 3.5$ kbar. However, if the

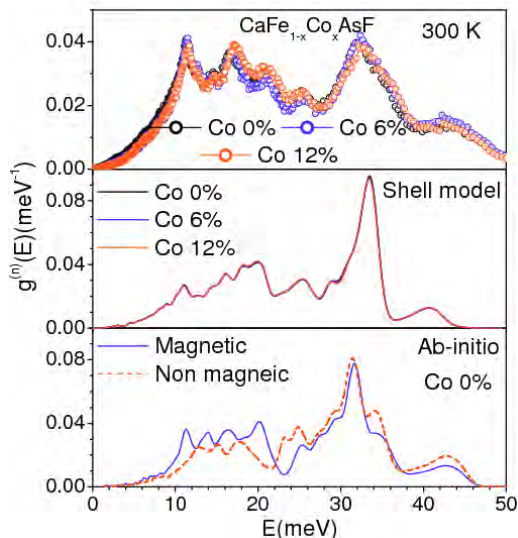


FIG. 2: Comparison of experimental phonon spectra [10] for $\text{CaFe}_{1-x}\text{Co}_x\text{AsF}$ ($x = 0, 0.06, 0.12$). The phonon spectra are measured with incident neutron wavelength of 5.12 \AA using the IN6 spectrometer at ILL. The calculated phonon spectra using the shell model and ab-initio are also shown. The calculated spectra have been convoluted with a Gaussian of FWHM of 5% of the energy transfer in order to describe the effect of energy resolution in the experiment.

experimental crystal structure is used the calculation gives correct frequencies of most phonons. We also observed strong temperature dependence of some phonons near the structural phase transition near 172 K. We have also carried out spin-polarized DFT-GGA calculations in the orthorhombic phase of CaFe_2As_2 . The calculated phonon spectra for non-magnetic/spin-polarized structures are shown as dashed lines in Fig. 1. It appears that the calculated line widths of phonon modes are larger in the orthorhombic phase because the orthorhombic distortion leads to a splitting of modes. The agreement between our experimental results and the calculation is poor, which further suggest anomalous phonons in CaFe_2As_2 . Our findings indicate that the interplay between magnetism and the lattice is in some way responsible for the anomalous phonons in CaFe_2As_2 . That is to say, the coupling of the vibrational and the electronic degrees of freedom is stronger than calculated by DFT, and hence phonons might play an important role in superconductivity in the doped compounds.

Further, we have measured [10] composition as well as temperature dependence of the phonon density-of-states in FeAs compounds with composition $\text{CaFe}_{1-x}\text{Co}_x\text{AsF}$ ($x = 0, 0.06, 0.12$). The electronic structure calculations for these compounds show that bands near the Fermi level are mainly formed by Fe 3d states, which is quite different from other 122 and 1111 FeAs compounds, where both Fe and As are believed to be related to superconductivity. The difference in electronic structure for fluorine based

compounds may cause phonon spectra to behave differently as a function of composition and temperature in comparison with our phonon studies [5,6,9] on parent and superconducting MFe_2As_2 ($\text{M}=\text{Ba}, \text{Ca}, \text{Sr}$). The composition as well as temperature dependence of phonon spectra for $\text{CaFe}_{1-x}\text{Co}_x\text{AsF}$ ($x = 0, 0.06, 0.12$) compounds have been measured (Fig. 2) using time of flight IN4C and IN6 spectrometers at ILL, France. The comparison of phonon spectra at 300 K in these compounds shows (Fig. 2) that acoustic phonon modes up to 12 meV harden in the doped compounds in comparison to the parent CaFeAsF . While intermediate energy phonon modes from 15 meV to 25 meV are also found to shift towards high energies only in the 12% Co doped CaFeAsF compound. The experimental results for $\text{CaFe}_{1-x}\text{Co}_x\text{AsF}$ ($x = 0, 0.06, 0.12$) are quite different from our phonon studies [5,6,9] on parent and superconducting MFe_2As_2 ($\text{M}=\text{Ba}, \text{Ca}, \text{Sr}$) where low-energy acoustic phonon modes do not react with doping, while the phonon spectra in the intermediate range from 15 to 25 meV are found to soften in these compounds. We argue that stronger spin phonon interaction play an important role for the emergence of superconductivity in these compounds. The lattice dynamics of $\text{CaFe}_{1-x}\text{Co}_x\text{AsF}$ ($x = 0, 0.06, 0.12$) compounds is also investigated using the ab-initio as well as shell model phonon calculations. We show that the nature of the interaction between the Ca and the Fe-As layers in CaFeAsF compounds is quite different compared with our previous studies on CaFe_2As_2 .

In conclusion, we have carried out extensive measurements of the temperature dependence of phonon spectra for parent and superconducting compounds using the inelastic neutron scattering technique. Our work on FeAs parent and superconducting compounds shows that electron-phonon coupling is present in these compounds but it can not be solely responsible for the superconductivity.

-
- [1] Y. Kamihara et al, J. Am. Chem. Soc. **130**, 3296 (2008).
 - [2] H. Takahashi et al, Nature **453**, 376 (2008).
 - [3] M. Rotter et al, Phys. Rev. Lett. **101**, 107006 (2008).
 - [4] R. Mittal, et al, Phys. Rev. Lett. **102**, 217001 (2009).
 - [5] R. Mittal et al, Phys. Rev. B **78**, 104514 (2008).
 - [6] R. Mittal et al, Phys. Rev. B **78**, 224518 (2008).
 - [7] R. Mittal et al., arXiv: 0911.1665.
 - [8] R. Mittal et al., arXiv:0912.1782.
 - [9] R. Mittal et al, Phys. Rev. B **79**, 144516 (2009).
 - [10] R. Mittal et al, Phys. Rev. B **79**, 214514 (2009).

Short-range Spin Correlations in Molecular Magnet $\{\text{Mo}_{72}\text{Fe}_{30}\}$

Z. Fu¹, P. Kögerler², U. Rucker¹, Y. Su³, R. Mittal³, Th. Brückel¹

¹ Jülich Centre for Neutron Science JCNS-2 and PGI-4, Forschungszentrum Jülich

² Institute für Anorganische Chemie, RWTH Aachen University

³ Jülich Centre for Neutron Science JCNS, Outstation at FRM II

The spin-frustrated molecular magnets have attracted intense interest. As a molecular analogue of the kagome lattice, $\{\text{Mo}_{72}\text{Fe}_{30}\}$ is one of the largest molecular magnets synthesized to date and represents a highly frustrated spin structure. We investigated the magnetic ground state of $\{\text{Mo}_{72}\text{Fe}_{30}\}$ by means of diffuse neutron scattering with polarization analysis. We explain the obtained magnetic diffuse scattering successfully within a three-sublattice spin model, which therefore proves to be a good approach to the magnetic ground state of $\{\text{Mo}_{72}\text{Fe}_{30}\}$.

As the smallest well-defined quantum magnets, molecular magnetic materials have attracted intense interest owing to their fascinating magnetic properties and potential applications in future quantum computing and massive data storage [1]. In molecular magnets, each molecule contains a relatively small number of paramagnetic ions, i.e. spins, interacting via superexchange interactions. The magnetic molecules are well isolated by ligands, so that intermolecular magnetic interactions can be neglected as compared to the dominating intramolecular interactions. Some of the molecular magnets are ideal systems to observe quantum magnetic phenomena, such as quantum tunneling and quantum coherence. Though most efforts in the field of molecular magnetism have been dedicated to synthesize magnets with high-spin ground states, molecular magnetism is branching out into new areas to explore new types of low-dimensional molecular-based magnets possessing attractive physical properties. In this context, the spin-frustrated molecular magnets allow exotic magnetic ground states and provide valuable test beds for the understanding to geometrical spin frustration from both experimental and theoretical points of view.

As one of the largest molecular magnets ever synthesized, the polyoxomolybdate $\{\text{Mo}_{72}\text{Fe}_{30}\}$ represents a highly frustrated spin structure with negligible intermolecular interactions. The $\{\text{Mo}_{72}\text{Fe}_{30}\}$ molecule is shown as the insert of FIG. 3. 30 Fe^{3+} ($S = 5/2$, $L = 0$) ions serve as magnetic centers and occupy the vertices of an icosidodecahedron, forming twenty corner-sharing triangles. The 30 spins are antiferromagnetically coupled among nearest neighbors [2]. Despite the difficulty in solving the complete Hamiltonian of this system, an approximate, diagonalizable effective Hamiltonian was adopted to explain the major low-

temperature properties of $\{\text{Mo}_{72}\text{Fe}_{30}\}$ [3]. The classical version of this effective Hamiltonian represents a frustrated ground state spin configuration called the three-sublattice model, where the 30 spins can be divided into three coplanar sublattices with angular spacing of 120° (see the insert of FIG. 3). In order to understand the magnetic ground state of $\{\text{Mo}_{72}\text{Fe}_{30}\}$, the spin correlations of $\{\text{Mo}_{72}\text{Fe}_{30}\}$ are investigated quantitatively by means of diffuse neutron scattering with polarization analysis.

The polarized neutron scattering measurements were carried out on deuterated $\{\text{Mo}_{72}\text{Fe}_{30}\}$ polycrystals at diffuse neutron spectrometer DNS, FRM II. The incident wavelength is 4.74 Å. Within the quasistatic approximation, the nuclear coherent, spin-incoherent and magnetic scattering cross sections are separated simultaneously with the full xyz -polarization method. The absolute scattering intensity from the sample is obtained by the calibration against the spin incoherent scattering from a Vanadium standard.

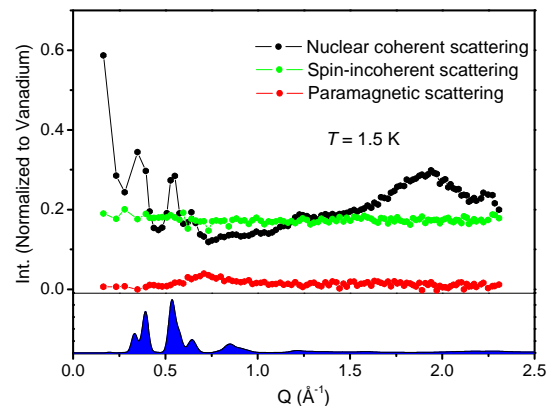


FIG. 1: Nuclear coherent (black circles), spin-incoherent (green circles) and paramagnetic (red circles) contributions to the total scattering of $\{\text{Mo}_{72}\text{Fe}_{30}\}$ at 1.5 K from xyz -polarization analysis on DNS. The blue area is the powder diffraction simulation convoluted with experimental resolution.

FIG. 1 shows the nuclear coherent, spin-incoherent and paramagnetic components separated from the total scattering by means of xyz -polarization method. The spin-incoherent scattering intensity is nearly constant, suggesting a successful separation of different scattering contributions. The nuclear coherent scattering shows a broad hump at high Q around 1.80 \AA^{-1} , which can be attributed to the scattering from amorphous crystal water. Several nuclear Bragg peaks are located within the Q range $0.25\text{-}1.00 \text{ \AA}^{-1}$, which are consistent with the

simulation of the powder diffraction pattern (marked as the blue line at the bottom of FIG. 1) of $\{\text{Mo}_{72}\text{Fe}_{30}\}$. The magnetic scattering obtained is almost 40 times smaller than the total scattering intensity, leading to long counting time to acquire reasonable statistics.

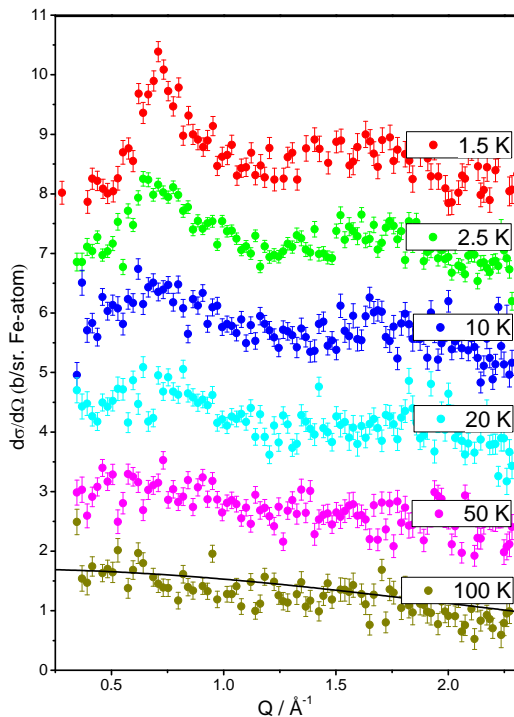


FIG. 2: Temperature evaluation of the differential magnetic scattering cross section $d\sigma/d\Omega$ obtained from DNS measurements on deuterated $\{\text{Mo}_{72}\text{Fe}_{30}\}$ polycrystals. The data at different temperatures are displaced vertically by 1.5 b sr^{-1} per Fe atom each for clarity. The solid line is the pure paramagnetic form factor of Fe^{3+} ($S = 5/2$).

FIG. 2 presents the differential magnetic cross section, $d\sigma/d\Omega$, extracted from the total scattering cross section at 1.5, 2.5, 10, 20, 50, and 100 K from DNS measurements. The magnetic scattering above 50 K agrees with the pure paramagnetic form factor of Fe^{3+} ions (black line in FIG. 2). Below 20 K, a diffuse peak at $Q \approx 0.70 \text{ \AA}^{-1}$ is seen to evolve and sharpen upon cooling, indicating the presence of short-range antiferromagnetic spin correlations. No long-range magnetic ordering can be detected even down to 1.5 K owing to the strong geometrical spin frustration of the individual molecules and the lack of intermolecular magnetic interactions.

In order to determine the nature of the short-range magnetic order for the magnetic ground state of $\{\text{Mo}_{72}\text{Fe}_{30}\}$, we compare our experimental data with a simulation based on a rigid three-sublattice spin model consisting of classical $S = 5/2$ Fe^{3+} spins. The analysis of the data starts with the equation given by I. A. Blech and B. L. Averbach in Ref [4] for the differential magnetic scattering cross section of spin pairs, which, already in powder average, can be written as,

$$\frac{d\sigma_{\text{mag}}}{d\Omega} = \frac{2}{3} S(S+1) \left(\frac{\gamma e^2}{mc^2} \right)^2 f^2(Q) + \left(\frac{\gamma e^2}{mc^2} \right)^2 \times \sum_n \left[a_n \frac{\sin Qr_n}{Qr_n} + b_n \left(\frac{\sin Qr_n}{Q^3 r_n^3} - \frac{\cos Qr_n}{Q^2 r_n^2} \right) \right],$$

where $(\gamma e^2/mc^2) = -0.54 \times 10^{-12} \text{ cm}$ is the magnetic scattering length, S is the spin quantum number of the scattering ion, $f(Q)$ is the magnetic scattering form factor, r_n is the distance from an atom at an arbitrary origin to the n th atom in the same molecule, and a_n and b_n are related to the probability of finding spin pairs with parallel components.

Only the spin correlations within individual molecules are considered in the simulation because the inter-molecular magnetic correlations are negligible. It should be noticed that actually every molecule in the sample could possess a specific ground state within the three-sublattice spin model, because the three spin sublattices can rotate as long as the 120° angle among their unit vectors is fulfilled. Therefore the final simulation should take a numerical average over all versions of the three-sublattice spin model, as shown by the blue line in FIG. 3. The simulation agrees well with the measured profile of the magnetic diffuse scattering.

-
- [1] D. Gatteschi, R. Sessoli and J. Villain, *Molecular Nanomagnets* (Oxford University Press, Oxford, 2006).
 - [2] A. Müller, *et al.*, *ChemPhysChem* **2**, 517 (2001).
 - [3] J. Schnack, M. Luban and R. Modler, *Europhys. Lett.* **56**, 863 (2001).
 - [4] I. A. Blech and B. L. Averbach, *Physics (N. Y.)* **1**, 31 (1964).

Magnetization distribution in the tetragonal phase of BaFe_2As_2

Y. Xiao¹, Y. Su², P. J. Brown³, T. Chatterji^{2,3}, Th. Wolf⁴, Th. Brückel^{1,2}

¹ Jülich Centre for Neutron Science JCNS-2 and PGI-4: Scattering Methods, Forschungszentrum Jülich,

² Jülich Centre for Neutron Science JCNS at FRM II

³ Institut Laue-Langevin, Grenoble, France

⁴ Karlsruhe Institute of Technology, Karlsruhe

The pnictide superconductors and their parent compounds have drawn extensive attention because they provide a new opportunity to investigate the mechanism of non-BCS exotic superconductivity [1,2]. Similar to high- T_c cuprates, superconductivity in iron pnictides is in proximity to magnetism. Scattering methods in particular neutron scattering have been playing an important role in the understanding of the interplay between superconductivity and magnetism. By using conventional neutron diffraction method, we have determined the magnetic structure of few representative parent compounds, such as BaFe_2As_2 [3], EuFe_2As_2 [4] and SrFeAsF [5]. Furthermore, investigation on the magnetization density distribution via polarized single-crystal neutron diffraction has been undertaken very recently on BaFe_2As_2 . The experimental results provide strong evidence that besides the spin and the lattice degrees of freedom, the orbital degree of freedom might also play an important role in iron pnictides [6].

All iron pnictides are found to be of layered structure in nature. For undoped iron pnictides, the chains of parallel Fe spins within the FeAs layers couple antiferromagnetically in the ab plane of the orthorhombic lattice with an antiparallel arrangement along the c axis. This antiferromagnetic order in the parent compounds is likely due to a spin-density-wave instability caused by Fermi-surface nesting. The undoped iron pnictides are not superconducting under ambient pressure, while the magnetic order is suppressed and superconductivity emerges concomitantly upon carrier doping.

The nature of magnetism and possible orbital order in iron pnictide compounds are still very controversial and therefore additional experimental information on these degrees of freedom for the parent compounds can be helpful in understanding the nature of superconductivity in these compounds. In order to get direct information about the electronic structure of the parent compound we have undertaken a polarized neutron-diffraction experiment on BaFe_2As_2 to determine the field-induced magnetization distribution. The structural parameters were determined from unpolarized neutron integrated intensity measurements made using the four-circle diffractometer D9 and flipping ratios were measured using the polarized neutron diffractometer D3. Both instruments are installed on

the hot neutron source of the high-flux reactor of the Institute Laue-Langevin in Grenoble. The sample was held at constant temperature in a closed-cycle refrigerator on D9 whereas on D3 it was oriented with a $[1\bar{1}0]$ axis parallel to the vertical field direction of a 9 T cryomagnet. The polarized neutron flipping ratios from the crystal were measured in the paramagnetic tetragonal phase at $T = 200$ K using a neutron wavelength 0.825 Å.

The flipping ratios measured for equivalent reflections and for repeated measurements of the same reflection were averaged together to give a mean value of R and used to calculate the magnetic structure factors F_M using the relationship

$$F_M = \frac{(R-1)F_N}{2(P^+ + P^-)},$$

where P^+ and P^- are the efficiencies of neutron polarization parallel and antiparallel to the applied field; F_N is the nuclear structure factor.

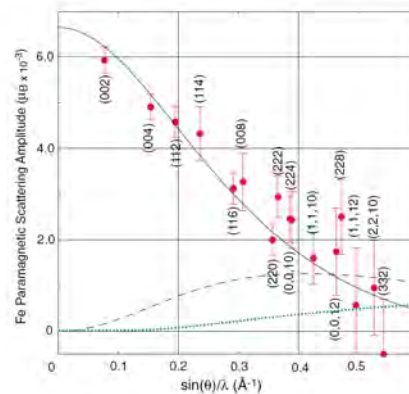


FIG. 1: Paramagnetic scattering amplitudes measured for Fe in BaFe_2As_2 at 200 K. The solid curve shows the $\langle J_0 \rangle$ form factor for neutral Fe, scaled to the paramagnetic magnetization of $6.65 \times 10^{-3} \mu_B/\text{Fe}$. The dashed and the dotted curves show $\langle j_2 \rangle$ and $\langle j_4 \rangle$ form factors, which multiply the anisotropic terms in the magnetic scattering on the same scale.

The magnetization induced in a crystal by a field of 9 T applied the (001) plane at 200 K was measured as $0.01 \mu_B/\text{f.u.}$ It is the sum of a paramagnetic part due to magnetic excitation of electrons near the Fermi surface and a diamagnetic part to which all electrons contribute. The diamagnetic volume susceptibility is given by the Langevin equation. The diamagnetic contribution to the magnetic structure factor is

$$F_{dia} = \frac{HC}{|k|} \sum_i \frac{df_i(k)}{dk} \exp ik \cdot r_i,$$

where $f_i(k)$ is the atomic form factor. The constant C has the value $1.52 \times 10^{-5} \mu\text{B} \cdot \text{\AA}^2$. The diamagnetic contribution to the magnetization calculated using the atomic form factors for Ba, Fe, As is $-0.0033 \mu\text{B}/\text{f.u.}$, the paramagnetic part of the magnetization is therefore $0.01 - (-0.0033) = 0.0133 \mu\text{B}/\text{f.u.}$. The diamagnetic contributions to the magnetic structure factors were calculated and values of F_{dia} were subtracted from the magnetic structure factor FM obtained from the flipping ratios to give the paramagnetic structure factors F_{para} .

An effective form factor for the Fe atom, obtained by dividing each F_{para} by the geometric structure factor of Fe for that reflection is shown in Fig. 1 where it is compared with the Fe 3d free atom curve scaled to $6.65 \times 10^{-3} \mu\text{B}$. The low-angle reflections fall on the curve with experimental error but at higher angles, at which the higher order form factors $\langle j_2 \rangle$ and $\langle j_4 \rangle$ become appreciable, significant scatter is apparent which may characterize an aspherical magnetization distribution.

The method of maximum entropy provides a model free method for reconstructing an image from sparse and noisy data. We have used this method to clarify the shape of the distribution. The maximization procedure coded was used to make the maximum entropy reconstruction of the magnetization distribution projected down $[1\bar{1}0]$ from the measured magnetic structure factors. The result of the reconstruction is shown in Fig. 2. The reconstruction shows clearly that the magnetization is confined to the region around the iron atoms and that there is no significant magnetization associated with either As or Ba atoms. The magnetization around the Fe atom is significantly nonspherical with a shape that appears to extend in the $[111]$ directions of the projection. Further clarification of the shape of the iron-atom magnetization was obtained by fitting the magnetic structure factors to a multipole model in which they are expressed as

$$F_M(k) = a_0 \langle j_0(k) \rangle + \sum_{l=2,4} \langle j_l(k) \rangle \sum_{m=-l}^{m=l} a_{lm} Y_l^m(lm \pm),$$

where the $\langle j_l(k) \rangle$ are the form factor integrals for a neutral Fe atom and the $Y_l^m(lm \pm)$ are the real combinations of spherical harmonic functions

$$Y_l^m(lm \pm) = \frac{1}{\sqrt{2}} \left[Y_l^m(\hat{k}) \pm (-1)^m Y_l^m(\hat{k}) \right]$$

In a site with fourfold symmetry the d-electron orbitals split into three singlet states: $d_{3z^2-r^2}$, $d_{x^2-y^2}$, and d_{xy} and a doublet combination of d_{xz} and d_{yz} . The first two singlet states are derived from the cubic e_g functions and the third singlet and the doublet form the t_{2g} ones. The occupancies of these four nondegenerate orbitals can be derived directly from the coefficients a_{lm} . However the parameters

obtained from the unconstrained fit lead to unphysical, negative occupancies for the two e_g -type orbitals but with large estimated standard deviations. A constrained fit in which the ratio between the a_{lm} was fixed to correspond to occupancy of the t_{2g} -type orbitals only, gave equally good agreement.

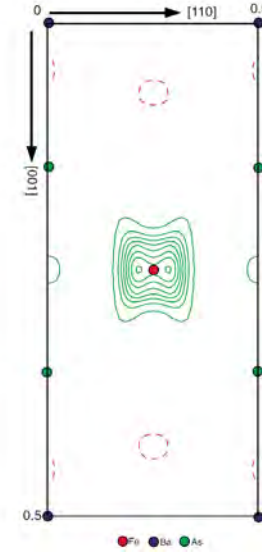


FIG. 2: Maximum-entropy reconstruction of the magnetization distribution in tetragonal BaFe_2As_2 at 200 K projected down $[1\bar{1}0]$. Contours are drawn at intervals of $10^{-2} \mu\text{B} \text{\AA}^{-2}$.

The results of the present experiment show that at least 96% of the electrons in BaFe_2As_2 , which give rise to the paramagnetic susceptibility, are localized on the Fe atoms with a radial distribution similar to that of a neutral Fe atom. Their angular distribution shows that they occupy the t_{2g} -type orbitals with a strong preference for the singly degenerate xy type which has its maxima in the $\langle 110 \rangle$ directions which are not those of any ligand atoms rather than the doubly degenerate xz and yz types which maximize in a cone containing directions nearly parallel to the Fe-As bond directions. If, as might be expected, there is strong hybridization between Fe and As atoms these hybridized bonding and antibonding states must lie well below and well above the Fermi level leaving narrow 3d nonbonding bands at the Fermi surface.

- [1] Y. Kamihara et al., J. Am. Chem. Soc. 130, 3296 (2008).
- [2] D. C. Johnston., Advances in Physics 59, 803(2010).
- [3] Y. Su et al., Phys. Rev. B 79, 064504(2008).
- [4] Y. Xiao et al., Phys. Rev. B 81, 220406(R)(2010).
- [5] Y. Xiao et al., Phys. Rev. B 81, 094523(2010).
- [6] P. J. Brown et al., Phys. Rev. B 82, 024421(2010).

Magnetism in the family of Fe-based super-conductors containing rare-earth elements

Y. Xiao¹, S. Nandi¹, Y. Su², S. Price¹, Th. Brückel^{1,2}

¹ Jülich Centre for Neutron Science JCNS-2 and PGI-4: Scattering Methods, Forschungszentrum Jülich

² Jülich Centre for Neutron Science JCNS at FRM II

The discovery of iron-pnictide superconductors has triggered extensive research on their physical properties and mechanism of high-temperature superconductors [1,2]. During last few years, we have investigated extensively on the lattice dynamics [3,4], magnetic order [5,6] and spin dynamics [7] of the family of Fe-based superconductors. Similar to high-Tc cuprates, superconductivity in iron pnictides is in proximity to magnetism. The magnetism is more complicated in compounds which contain both iron and rare earth elements. Scattering methods such as x-ray scattering and neutron scattering have played an important role in the understanding of the magnetism in superconducting systems. We have used x-ray resonant magnetic scattering (XRMS) and neutron scattering methods to disentangle the two magnetic moment sublattice contributions in the parent compounds SmFeAsO [8] and EuFe_2As_2 [9].

Most of the research on pnictide superconductors has focused on $\text{RFeAs}(\text{O}1-x\text{F}x)$ with $\text{R}=\text{La}, \text{Nd}, \text{or Sm}$, etc. and AFe_2As_2 with $\text{A}=\text{Ba}, \text{Ca}, \text{or Eu}$, etc., the so called “1111” and “122” families. These two families are closely related since both of them adopt a layered structure with a single FeAs layer in the unit cell of 1111 and two such layers in the unit cell of 122. The superconducting state can be achieved either by electron or hole doping of the parent compounds. Apart from carrier doping, the application of hydrostatic pressure or chemical pressure can also induce superconductivity. Considering that the electronic states near the Fermi surface are dominated by contributions from Fe and As, it is believed that the FeAs layers are responsible for superconductivity in these compounds.

Regarding to the SmFeAsO parent compound, XRMS experiments were performed for the Sm L_2 , L_3 and Fe K absorption edge. Below $T = 110$ K, both Sm and Fe magnetic moments order with a magnetic propagation vector $(1\ 0\ 1/2)$, as observed by the enhancement of XRMS intensities at Sm $L_{2,3}$ and Fe K edges, respectively. By exploiting the peculiar polarization dependence and site selectivity of XRMS we have determined the magnetic structure of the Sm sublattice, by collecting integrated intensities of a series of magnetic reflections measured at the Sm L_2 -edge. Similarly, the magnetic structure of Fe

sublattice was determined in the temperature range $5\ \text{K} \leq T \leq 110\ \text{K}$ and the final magnetic structure is shown in Fig. 1.

The temperature dependence of the sublattice magnetizations is represented in Fig. 2, where the Fe shows a typical magnetization curve and Sm follows a quite unusual behaviour, with a sharp increase of the intensity below 50 K, followed by a second magnetic phase transition at 5 K. This unusual temperature dependence of the Sm sublattice can be explained with a ground-state doublet crystal-field level, split by an exchange field, and can be modelled by taking into account only the ground-state doublet and a splitting $[\Delta(T)]$ proportional to the effective field $[\text{B}_{\text{eff}}(T)]$ produced by the Fe sublattice [see Fig. (2b), red line]. We obtained $\text{B}_{\text{eff}}(T=0) = 56.4 \pm 1.9$ Tesla characterising the strength of interaction between the two sublattices, which indicates a strong coupling between these two sublattices. Below 5 K a magnetic phase transition arises on both sublattices, as deduced by a drop of the Fe XRMS intensity [inset of Fig. 2(a)] and the switch of the XRMS intensities at Sm L_2 edge from $(3\ 0\ 7.5)$ reflection to the charge $(-2\ 0\ 6)$ reflection, signalling a change in the magnetic order of Sm with the magnetic unit cell equal to the chemical unit cell. Our finding reveals that the magnetisms of Sm and Fe in the SmFeAsO compound are strongly correlated.

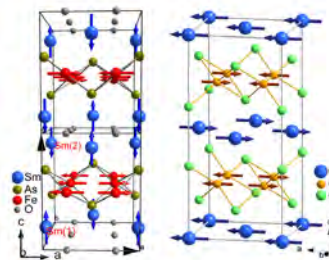


FIG. 1: Illustration of the magnetic structures of SmFeAsO in the temperature range $5\ \text{K} \leq T \leq 110\ \text{K}$ and EuFe_2As_2 at 2 K [5,8].

For EuFe_2As_2 , we have determined its low temperature magnetic structure by using neutron diffraction method [5]. Here we report a single-crystal neutron-diffraction study of the T-H phase diagram for EuFe_2As_2 under a magnetic field up to 3.5 T. As shown in Fig. 3(a), application of a field along a axis strongly weakens the (201) magnetic

reflection and suppresses it totally at the critical field H_{Crit}^{Eu} of 0.8 T at 2 K. On the other hand, the increase in intensity at (006) nuclear reflection indicates that the Eu spins gradually reorientate to the (100) direction. The field-induced magnetic phase transition takes place from antiferromagnetic, via a canted configuration, to the ferromagnetic structure. These results suggest that the Eu spins will orient to the direction of the applied magnetic field once the field strength is greater than the critical field. The temperature dependence of ferromagnetic reflections was measured afterwards to determine the ordering temperature of the Eu moments. According to the neutron measurement results, the magnetic phase transition temperatures are determined and plotted in Fig. 3(c).

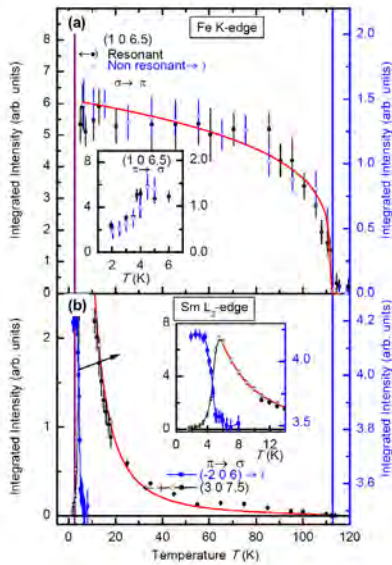


FIG. 2: (a) Temperature dependence of the (1 0 6.5) reflection measured in both resonant and nonresonant conditions near Fe K edge in polarization channel σ - π . The inset shows the change of Fe magnetic order below 5 K in π - σ channel. (b) Temperature dependencies of the (3 0 7.5) and (-2 0 6) reflections measured in resonant condition at the Sm L_2 edge. The inset shows the Sm phase transition below 5 K.

Besides of Eu order, we also examined the Fe order under the applied field along a axis. In contrast to the reorientation of the Eu spins, the antiferromagnetic spin density wave order of Fe is found to be robust and it persists till fields up to 3 T. Surprisingly, it is found that the integrated intensity of the (101) magnetic reflection decreases slightly and then sharply increases with increasing magnetic field, as shown in Fig. 3(b). It is known that a twinning structure may exist in orthorhombic EuFe_2As_2 phase due to the interchange of the orthorhombic a and b axes. The variation of (101) magnetic reflection exhibits the same behavior as (400) nuclear reflection, which indicated that the twin populations are redistributed with applying magnetic field. The critical fields for twin structure evolution are determined at different temperatures and plotted in Fig. 3(c). It is interesting that the critical field of the twin redistribution is closely correlated with the field that induces the antiferromagnetic to ferromagnetic

transition of Eu magnetic sublattice. The energy difference between two twins seems strongly related with the total energy of the Eu magnetism. Moreover, in-plane magnetotransport properties of EuFe_2As_2 are also investigated by angular dependent magnetoresistance measurement [10]. Strong anisotropy in magnetotransport properties is observed and it exhibits intimate correlation with the ordering states of both Eu and Fe spins in EuFe_2As_2 , which provides a direct evidence of the coupling between itinerant electrons and ordered spins.

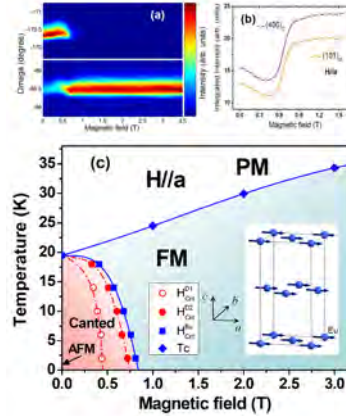


FIG. 3: (a) Magnetic field dependence of (201) magnetic and (006) nuclear reflections in two dimensional plots. (b) Field dependence of integrated intensities of (400) and (101) reflections. (c) Magnetic phase diagram for EuFe_2As_2 with applied field parallel to the crystallographic a axis. The inset shows the schematic view of the magnetic structure. Note that only Eu atoms are shown.

In summary, by using neutron and x-ray scattering methods, we found field induced spin reorientation and strong spin-charge-lattice coupling in EuFe_2As_2 compound. Surprisingly, we achieved detwinning in rather low external field without the need to apply uniaxial pressure. We also found an intricate interplay between the magnetism of Sm and Fe in the SmFeAsO compound, which sheds light on the currently debated importance of the rare-earth-iron interaction in the family of iron-based superconductors.

We would like to acknowledge our international collaborators for their valuable help and support on our research works. Lists of all collaborators are given as co-authors in our publications.

- [1] Y. Kamihara et al., J. Am. Chem. Soc. 130, 3296 (2008).
- [2] D. C. Johnston, Advances in Physics 59, 803(2010).
- [3] R. Mittal et al., Phys. Rev. Lett. 102, 217001(2009).
- [4] R. Mittal et al., Phys. Rev. B 79, 214514(2009).
- [5] Y. Xiao et al., Phys. Rev. B 81, 174424(2009).
- [6] Y. Xiao et al., Phys. Rev. B 81, 094523(2010).
- [7] Y. Su et al., to be submitted.
- [8] S. Nandi et al., Phys. Rev. B 84, 054419(2011).
- [9] Y. Xiao et al., Phys. Rev. B 81, 220406(R)(2010).
- [10] Y. Xiao et al., Phys. Rev. B 85, 094504(2012).

Magnetization Distribution and Self-Assembly of Magnetic Nanoparticles

S. Disch¹, R. P. Hermann^{1,2}, E. Wetterskog³, G. Salazar-Alvarez³, L. Bergström³, Th. Brückel¹

¹ JCNS-2: Jülich Centre for Neutron Science and PGI-4, Forschungszentrum Jülich

² Faculty of Science, University of Liège, B-4000 Liège, Belgium

³ Department of Materials and Environmental Chemistry, Arrhenius Laboratory, Stockholm University, S-10691 Stockholm, Sweden

The physical properties of magnetic nanoparticles are intensely investigated for both fundamental and technological reasons. A broad interest is attributed to their manifold possible applications in magnetic data storage, magnetic imaging, or biomedical applications. With regard to these applications, the two main aspects of fundamental interest are (i) the magnetic anisotropy and the related magnetization distribution in individual nanoparticles and (ii) the interparticle interactions leading to ordered assemblies of nanoparticles. Our study of the magnetization distribution in iron oxide nanoparticles as well as the shape induced symmetry in their assemblies using advanced X-ray and neutron scattering techniques aims at a better understanding of such fundamental nanoparticle properties.

The determination of the spatial magnetization distribution in magnetic nanoparticles represents a long standing challenge in nanomagnetism. Evidence for spin disorder at the particle surface was found by macroscopic measurements as well as simulations. Reduced magnetization values in nanoparticles as compared to the bulk material as well as excess susceptibility in high applied fields are commonly attributed to a magnetic dead layer at the nanoparticle surface. In order to determine the spatial distribution of the magnetization microscopically, we performed a polarized small-angle neutron scattering (SANS) study on iron oxide nanoparticles [1].

Well-dispersed solutions of non-interacting nanospheres and nanocubes with a 9 nm diameter and 8.5 nm edge length, respectively, were chosen as a model system. The excellent monodispersity of the samples with lognormal size distributions of 5.5(1) % and 7.2(2) % FWHM is an important requirement for the investigation of surface effects such as surface spin disorder. Polarized SANS experiments were performed at D22/ILL using 6 Å neutron wavelength and a horizontal magnetic field of ≤ 1.5 T. Polarized SANS gives quantitative access to the magnetic particle form factor, which is directly correlated with the spatially resolved microscopic magnetization distribution through Fourier transformation. We find a constant magnetization density in the nanoparticle core, which decreases

close to the nanoparticle surface (see Fig. 1), thus giving the first experimental evidence of surface spin canting in non-interacting nanoparticles.

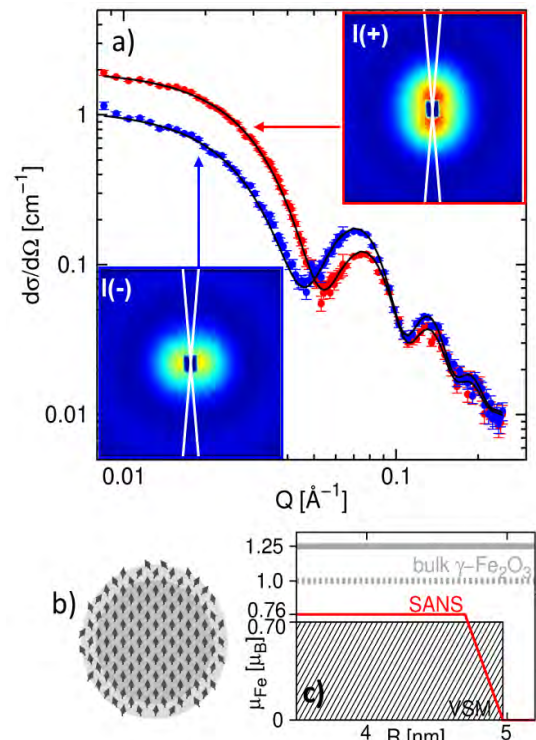


FIG. 1: Polarized SANS by iron oxide nanospheres a) Scattering cross sections obtained by magnetic contrast variation. Insets: 10° sectors used for integration. b) Schematic of the magnetization distribution model with surface spin canting. c) Quantitative magnetization distribution obtained by SANS compared to macroscopic measurements (VSM) and the bulk magnetization (dashed line).

Such spin canting may result from local structural deviations and broken symmetry at the particle surface. We further observe a substantial influence of the particle shape with a significantly larger surface thickness for the nanocubes. This is likely a direct consequence of the cubic shape anisotropy, related to a larger spin canting at the cube corners. Consequently, the magnetization decrease in the particle shell is attributed to a combination of both surface and shape anisotropies. Surface spin canting might be assumed to explain the reduced magnetization found macroscopically in nanoparticles. However, our quantitative analysis

reveals that even the atomic magnetic moments in the nanoparticle core are significantly lower than expected (see Fig. 1c). The lower magnetization density observed in nanoparticles as compared to the bulk material thus results partially from spin canting at the surface, but to a much larger extent from reduced magnetic moments inside the uniformly magnetized nanoparticle core.

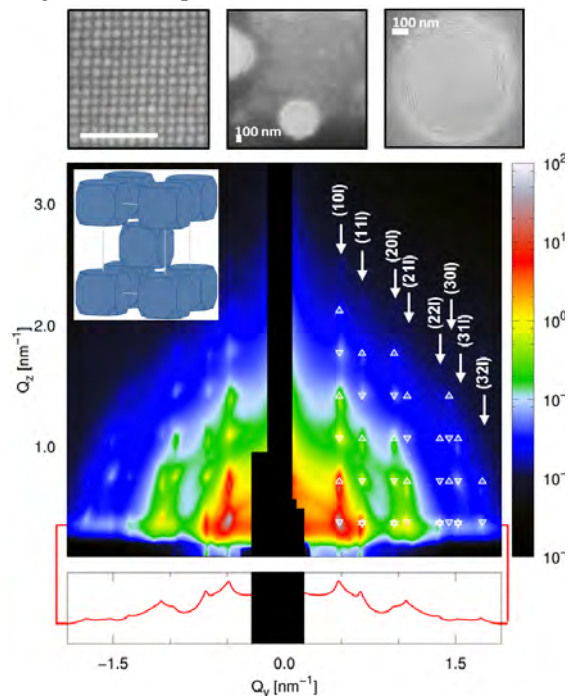


FIG. 2: GISAXS pattern of iron oxide nanocubes assemblies. Reflections are indexed according to a *bct* packing of nanocubes (inset). Bottom: In plane scattering intensities displayed on a logarithmic scale. Top: SEM images of the mesocrystal arrangements.

For investigation of interparticle interactions, nanoparticle assemblies provide suitable model systems. Self-assembly of nanocrystals is a widely investigated phenomenon, as its understanding promises new routes for the formation of large-scale ordered structures for nanotechnology. Most investigations focus on spherical nanoparticles or binary superlattices composed of different particle sizes or compositions. Because the interactions between the nanocrystal facets are important for self-assembly, slight variations in the nanocrystal shape

an influence their arrangements on the mesoscale. We have studied the self-assembly of iron oxide nanocubes with a slight degree of truncation of the cubes corners and report on the influence of the nanoparticle shape on the obtained structure [2].

Deposition in an applied magnetic field yields highly ordered mesocrystals with a micrometer lateral size and several hundred nm in height. A square lateral

order with face to face arrangement of the nanocubes is evident from scanning electron microscopy (SEM, see Fig. 2). Grazing-incidence small-angle X-ray scattering (GISAXS), performed at ID01/ESRF, allows for determination of the three dimensional mesocrystal structure. The in plane scattering contribution (red line in Figure 2) is in agreement with the square lateral order observed by SEM. By indexing of all *hkl* reflections in the GISAXS pattern shown in Figure 2, we derive a tetragonal body centered (*bct*) lattice with face to face arrangement of the nanocubes. This is different from the simple cubic (*sc*) arrangement reported for cubic Fe nanoparticles [3], which can also be inferred from the square symmetry observed by SEM.

Based on the precise knowledge of interparticle separation distances from GISAXS, TEM, and SEM, we were able to calculate the van der Waals energies for the different types of interparticle interactions found in the mesocrystal structure [2]. Comparing the energy needed to remove a nanocube from either *bct* or *sc* lattice revealed that the degree of truncation of the nanocubes corners is an essential parameter for the lattice type preference. The ratio between the interaction energies calculated for both lattice types indicates that the *sc* lattice is favoured at a low degree of truncation, whereas the *bct* lattice dominates at moderate truncation as observed for the nanocubes under study. The interaction energy estimates thus support the observed preference of a *bct* lattice and identify the degree of truncation to be crucial for the mesocrystal structure.

In combination, the presented studies contribute to the understanding of fundamental physical properties such as a possible spin canting close to the nanoparticle surface. The strong nanoparticle shape dependence of the observed mesocrystal structure types further illustrates the sensitivity of the interparticle interactions on nanoparticle shape anisotropy. With the structure-directing influence of the anisotropic nanoparticle shape as opposed to the spherical atoms in conventional crystal structures, a new dimension of crystallography has been established.

-
- [1] S. Disch, E. Wetterskog, R. P. Hermann, A. Wiedenmann, U. Vainio, G. Salazar-Alvarez, L. Bergström, Th. Brückel, *New J. Phys.* 14 (2012), 013025.
 - [2] S. Disch, E. Wetterskog, R. P. Hermann, G. Salazar-Alvarez, P. Busch, Th. Brückel, L. Bergström, S. Kamali, *Nano Lett.* 11 (2011), 1651.
 - [3] A. Demortière, P. Launois, N. Goubet, P. Albouy, C. Petit, *J. Phys. Chem. B* 112 (2008), 14583.

Lattice Dynamics in Thermoelectric Antimonides

A. Möchel^{1,2}, D. Bessas^{1,2}, W. Schweika¹, J. Voigt¹, Sergueev I.², and R. P. Hermann^{1,3}

¹ Jülich Centre for Neutron Science JCNS-2 and PGI-4, Forschungszentrum Jülich

² Faculty of Science, University of Liège, B-4000 Liège, Belgium

³ European Synchrotron Radiation Source

The lattice dynamics in several thermoelectric antimonides were studied by a combination of inelastic neutron scattering, synchrotron radiation nuclear inelastic scattering, and several macroscopic techniques. Combining the results obtained by these methods, detailed insights into microscopic vibrational properties were obtained. The different mechanisms which lead to the observed low thermal conductivity in skutterudites and in the thermoelectric Zintl phase $\text{Yb}_{14}\text{MnSb}_{11}$ were identified, and the calculations of the lattice properties including electron phonon coupling in the giant Seebeck coefficient material FeSb_2 were validated. The gained knowledge will prove useful in order to search for and enhance new efficient thermoelectric materials.

Direct conversion of thermal-to-electric energy and vice-versa by thermoelectric devices is attracting increasing interest in times where energy efficiency is a crucial issue. Advanced thermal management for future information technology or energy harvesting for processes where waste heat cannot be avoided are the main fields of application. Notably energy recovery from the exhaust gas system in the automotive industry is a strong driving force for research. Optimizing thermoelectric conversion efficiency is a balancing act involving improving the electric transport by doping and impeding the thermal transport by various mechanisms. Our research aims at an understanding on the atomic- and nanoscale of the influence on thermal transport for example of nanostructuring and grain boundary scattering, of inclusion of rattling guests in cage-like structures, and of complex large unit cell materials, with less effectively transporting modes.

Our investigations of the lattice dynamics are based essentially on the well known inelastic neutron scattering technique and on the phonon assisted nuclear resonant absorption by Mössbauer active nuclei. The recent development of this technique for new isotopes such as Sb or Te [1] has widened the technique and made it particularly attractive for investigating antimony based thermoelectrics, as it gives access to the element specific density of phonon states and a host of quantities such as the microscopic speed of sound, the force constants, and the vibrational entropy.

The lattice dynamics of the unfilled and filled skutterudites FeSb_3 , CoSb_3 and $\text{YbFe}_4\text{Sb}_{12}$ were studied and compared [2,3]. We have shown that the skutterudite FeSb_3 , a metastable compound that can

only be synthesized by thin film methods, is significantly softer than the isostructural compound

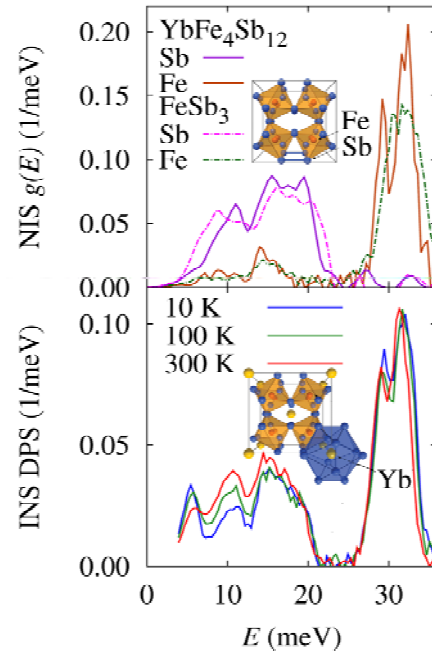


FIG. 1: Density of phonon states (DPS) in the filled $\text{YbFe}_4\text{Sb}_{12}$ and unfilled FeSb_3 skutterudites. Top: Sb and Fe element specific DPS (ESRF ID18 and ID22N), inset: unfilled structure. Bottom: neutron weighted DPS in $\text{YbFe}_4\text{Sb}_{12}$ (SNS, ARCS), inset: filled structure.

CoSb_3 . The phonon states are shifted towards lower energies and the velocity of sound is lower in FeSb_3 than in CoSb_3 [2]. Thus, beside the reduction of the thermal conductivity by the filler atoms, so called “rattlers”, the low thermal conductivity in filled $\text{RFe}_4\text{Sb}_{12}$ skutterudites, such as $\text{YbFe}_4\text{Sb}_{12}$, might more fundamentally be related to the soft $[\text{Fe}_4\text{Sb}_{12}]$ framework. We have also shown, that the lattice dynamics of the $[\text{Fe}_4\text{Sb}_{12}]$ framework is only slightly affected by filling the structure. Furthermore, our investigations have related the anomalous softening around 50 K of $\text{YbFe}_4\text{Sb}_{12}$ and the rearrangement of the spectral weight in the density of phonon states of $\text{YbFe}_4\text{Sb}_{12}$, a phenomenon that is very likely explained by the observed change in the Yb valence state[3].

Inelastic scattering by the new high temperature thermoelectric Zintl phase $\text{Yb}_{14}\text{MnSb}_{11}$ reveals that all phonon modes have energies below 25 meV. The low mean force constants, and the related low velocity of sound, have been identified as one reason

for its low thermal conductivity. Furthermore, $\text{Yb}_{14}\text{MnSb}_{11}$ has a very large unit cell, and thus the ratio of acoustic modes to optical phonon modes is quite small. As the number of modes that contribute to the thermal transport is thus small, the thermal conductivity is strongly reduced [4]. For comparison, in another Zintl phase, Zn_4Sb_3 , which exhibits similar thermal conductivity at room temperature, the low thermal conductivity in Zn_4Sb_3 is caused by a small phonon mean free path due to vibrational subunits [5] or Zn-interstitial disorder [6].

Finally, the density of phonon states and the elastic response was investigated in FeSb_2 , a material with a record Seebeck coefficient at low temperature that has been ascribed to electron phonon interactions. In a first study we have investigated the low temperature density of states in order to validate density functional theory calculations of the electronic and lattice dynamic properties. Our measurements reveal excellent agreement with calculations that include spin-orbit corrections and electron-phonon coupling. Further, our ultrasound spectroscopy measurements indicate that activation of the charge carries in this semi-conductor leads to a small lattice softening at 150 K [7].

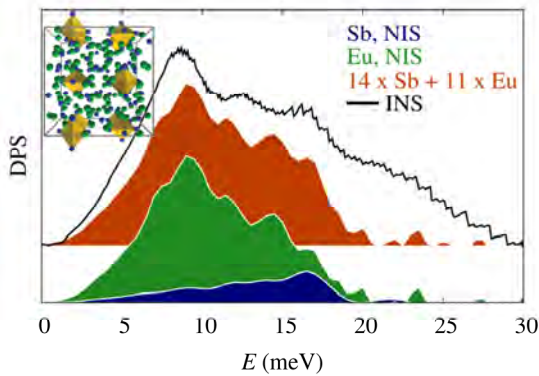


FIG. 2: Density of phonon states (DPS) in the $\text{Yb}_{14}\text{MnSb}_{11}$ Zintl phase, as obtained by inelastic neutron scattering (FOCUS, SINQ) and by nuclear inelastic scattering (NIS) by Sb and Eu (ID22N, ESRF). Eu is used as a substitute for Yb which is not accessible by NIS. Inset: $\text{Yb}_{14}\text{MnSb}_{11}$ body-centered unit cell with 208 atoms and a 6000 \AA^3 volume; Mn in yellow.

In summary, our measurements of the phonon properties in several antimonide thermoelectrics have revealed that a reduced lattice thermal conductivity in bulk materials can be achieved by several mechanisms. In cage structures, such as skutterudites, both the guests atoms and the framework dynamics play a role. In large volume cell structures an essential limitation comes from the number of effectively transporting modes. In the future we hope to improve on our understanding of the microscopic mechanisms at work including the interactions of the electronic and lattice degrees of freedom.

The European Synchrotron Radiation Facility, the Institut Laue-Langevin, the Spallation Neutron Source, and the Swiss Spallation Neutron Source, and the corresponding local contacts, are

acknowledged for provision of beamtime at ID18-ID22N, IN6, ARCS, and FOCUS, respectively.

The Helmholtz Association of German Research Centers is acknowledged for funding of the “Lattice Dynamics in Emerging functional Materials” Young Investigator Group.

-
- [1] Sergueev I., Wille H.-C., Hermann R. P., Bessas D., Shvyd'ko Yu.V., Zajac M., and Ruffer R., *J. Synchr. Rad.* 18, 802 (2011).
 - [2] Moechel A., Sergueev I., Nguyen N., Long Gary J., Grandjean F., Johnson D. C., and Hermann R. P., *Phys. Rev B* 84, 064302 (2011).
 - [3] Moechel A., Sergueev I., Wille H.-C., Juranyi F., Schober H., Schweika W., Brown S. R., Kauzlarich S. M., and Hermann R. P., *Phys. Rev B* 84, 184303 (2011).
 - [4] Moechel A., Sergueev I., Wille H.-C., Voigt J., Prager M., Stone M.B., Sales B.C., Guguchia Z., Shengelaya A., Keppens V., and Hermann R.P., *Phys. Rev B* 84, 184306 (2011). Editor's Suggestion.
 - [5] Schweika W., Hermann R. P., Prager M., Perßon J., and Keppens V., *Phys. Rev. Lett.* 99, 125501 (2007).
 - [6] Snyder G. J., Christensen M., Nishibori E., Caillat T., and Iversen B. B., *Nature Materials* 3, 458-463 (2004).
 - [7] Diakhate M. S., Hermann R. P., Moechel A., Sergueev I., Sondergaard M., Christensen M., and Verstraete M. J., *Phys. Rev. B* 84, 125210 (2011)

Competing Magnetic Phases and Absence of Ferroelectricity in LuFe_2O_4

J. de Groot¹, S. Adiga¹, T. Mueller¹, W.J.H. Borghols^{2,3}, K. Schmalzl^{2,4}, W. Schweika¹, Y. Su^{2,3}, M. Angst¹

¹ PGI-4 and Jülich Centre for Neutron Science, JCNS, Forschungszentrum Jülich

² Jülich Centre for Neutron Science JCNS, Forschungszentrum Jülich

³ JCNS Outstation at FRM II, D-85747 Garching,

⁴ JCNS Outstation at ILL, BP 156, 38042 Grenoble, France

Magnetolectric multiferroics with large electric polarizations and magnetolectric coupling are of strong interest for novel storage devices. Because the traditional mechanism of ferroelectricity is incompatible with magnetism, increasing attention is focused on various unconventional mechanisms, such as ferroelectricity originating from charge order (CO). In this field LuFe_2O_4 is often cited as a prototypical material for CO based multiferroic materials. Here both charge and (Ising) spin orders are localized at the Fe sites, which are contained in triangular Fe-O bilayers, a highly frustrated arrangement. Thus, this is an ideal system to study frustration effects. We identified two nearly degenerate spin structures by neutron and soft x-ray diffraction, establishing LuFe_2O_4 as a new model system for metamagnetic materials. Furthermore the crystal structure could be refined with a new CO configuration incompatible with ferroelectricity.

Above $T_{CO} \sim 320\text{K}$ observed diffuse x-ray scattering was linked to competing CO instabilities which could be addressed to geometrical frustration [1,2]. Similar frustration effects can also be expected for the magnetism. Below T_{CO} sharp CO reflections were interpreted as a CO configuration of Fe^{2+} and Fe^{3+} valences which renders the Fe-O bilayers polar, making LuFe_2O_4 ferroelectric or antiferroelectric [1,2]. Mainly for this reason, but also due to unrelated magnetic effects below $T_N \sim 240\text{K}$ [3] such as giant coercivity and various glassy states, this system is currently attracting increasing attention. Strong sample to sample variations in magnetic behavior are found, which could be attributed to tiny variations in oxygen stoichiometry. We focused our work on the type of samples showing the sharpest features in magnetization, where diffraction reveals sharp CO and magnetic reflections indicating 3D long range charge and spin orders, i.e. the best approximation for intrinsic defect-free magnetic behavior in LuFe_2O_4 .

The magnetic field (H) - temperature (T) phase diagram underlying the above unusual behaviors has now been established. In the following we focus on the region just below the magnetic ordering temperature T_N (Fig.1 [4]). Here, a sharp first-order

metamagnetic transition separates an antiferromagnetic (AFM) and a ferrimagnetic (fM) phase in low- H and high- H region, respectively. In a wide H - T region (hatched area) both phases can be stabilized, depending on the sample history.

In contrast to previous work we found by neutron and soft x-ray diffraction studies magnetic contributions on reflections where for the spin structure proposed in [3] no magnetic intensity should be present. Taking these additional reflections into account, the spin structures of both AFM and fM phases could be refined.

Interesting is the geometrical relation between the fM solution in Fig.2(a), which is identical to the AFM solution in Fig.2(b), except that all Ising-spins of one particular Fe-O bilayer flip their sign. This leads to the overall 2:1 configuration of \uparrow and \downarrow spins in the fM phase and zero net moment in the AFM phase, consistent with observations.

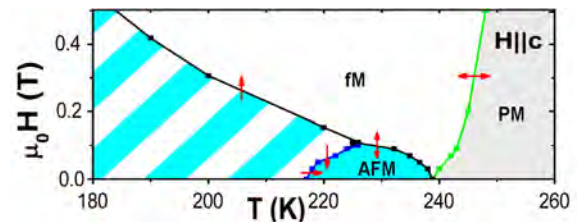


FIG.1: H - T phase diagram, which exhibits a para-magnetic (PM) an antiferromagnetic (AFM) and a ferrimagnetic (fM) phase, extracted from various $M(H)$ and $M(T)$ curves. The hysteretic region where either fM or AFM can be stabilized is hatched. Arrows across phase lines indicate for which measurement direction the particular transition is observed. After [4].

Phase competition and metamagnetic transitions between antiferro- and ferro-stacking of net bilayer moments are expected for layered magnets with very strong Ising-anisotropy. Such a behavior has already been observed in a few model systems at low temperatures [5]. Intriguingly, and in contrast to the expectations in the simple model systems, for LuFe_2O_4 the AFM-fM metamagnetic transition extrapolates to $H = 0$ for $T \rightarrow T_N$ as clearly seen in Fig.1. This means that at T_N and $H = 0$ the two phases seem to be essentially degenerate.

Given the particular differences between the two nearly degenerate spin-structures, just above T_N we may expect a random stacking of the net moments of bilayers that are still medium range ordered, i.e. a 2D-order. Magnetic diffraction would consequently result in a strong diffuse scattering line through $(\frac{1}{3} \ell)$ above T_N , still reasonably sharp in-plane, but featureless along the ℓ direction. This was indeed observed in Fig.3, visible even up to 280K.

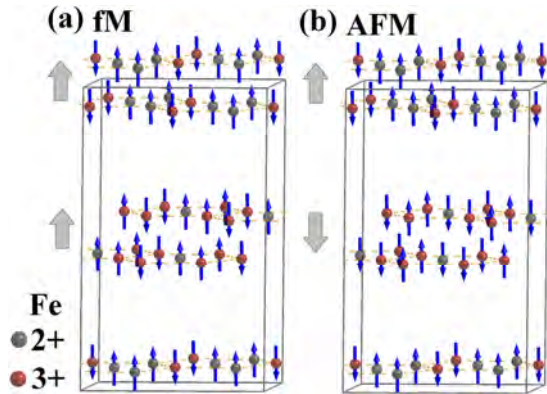


FIG.2: Charge order and Spin structure of the AFM (a) and fM phase (b). Gray arrows indicate bilayer net magnetization. For better visibility an additional Fe layer is shown above the unit cell.

The AFM / fM metamagnetism presented by us [4] is resolvable only in the highest quality samples but it has strong ramifications for all specimens of this material. For example, if disorder, e.g. due to oxygen off-stoichiometry, is added to the competing interactions, glassy freezing may be expected to replace long-range spin order at T_N , as observed in some samples.

Beside the spin structure we also refined the crystallographic structure in the charge ordered phase from which follows a totally new CO pattern involving charged bilayers (Fig.2). This new CO configuration is further collaborated by XMCD measurements [6] and moment-dependent spin structure refinements [4], which additionally provide a strict coupling between the charge and the spin order (Fig.2). The charged bilayers are *not polar* and this new CO is therefore incompatible with the generally accepted mechanism of CO-based ferroelectricity [1]. All these findings cast strong doubt on the CO based ferroelectric behavior of LuFe_2O_4 .

In summary, we have elucidated the magnetic phase diagram of LuFe_2O_4 close to T_N and determined a ferrimagnetic and an antiferromagnetic spin configuration which are almost degenerate at T_N in zero magnetic field. Such a phase competition was up to now not observed in classical metamagnetic materials. Therefore our results could establish LuFe_2O_4 as a simple model system for frustrated layered magnets. Furthermore, the charge order pattern for this material could be firmly established from crystal structure refinements. In contrast to the widely accepted charge order configuration with polar bilayers our new result exhibits charged bilayers coupled to the spin order. The absence of

polar bilayers casts strong doubt on the “ferroelectricity from charge order” scenario of

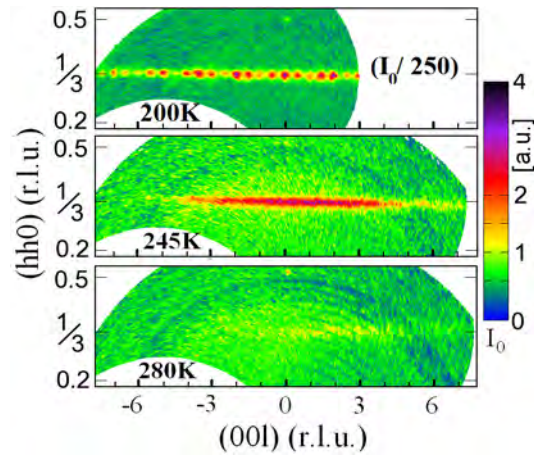


FIG.3: Reciprocal space map of the scattered intensity (logarithmic scale) in the (hhl) plane by polarized neutrons in the spin flip channel (DNS) at different T .

LuFe_2O_4 . Hence, a clear example of an oxide material with ferroelectricity originating from charge order has yet to be identified.

We would greatly acknowledge our collaborators: K. Marty, M.D. Lumsden, A.D. Christianson, S.E. Nagler, Z. Yamani, S. R. Bland, R. de Souza, U. Staub, R.A. Rosenberg, D.J. Keavney, Z. Islam, and J.-W. Kim.

-
- [1] N. Ikeda *et al.*, Nature 436, 1136 (2005).
 - [2] M. Angst *et al.*, Phys. Rev. Lett. 101, 227601 (2008).
 - [3] A. D. Christianson *et al.*, Phys. Rev. Lett. 100, 107601 (2008).
 - [4] J. de Groot *et al.*, Phys. Rev. Lett. 108, 037206 (2012).
 - [5] E. Strykowski *et al.*, Adv. Phys. 26, 487 (1977).
 - [6] J. de Groot *et al.*, Accepted for publication in Phys. Rev. Lett.; arXiv:1112.0978v1 (2012).

Selected Publications

- Mittal, R.; Pintschovius, L.; Lamago, D.; Heid, R.; Bohnen, K.-P.; Reznik, D.; Chaplot, S. L.; Su, Y.; Kumar, N.; Dhar, S. K.; Thamizhavel, A.; Brückel, T.
Measurement of Anomalous Phonon Dispersion of CaFe_2As_2 Single Crystals Using Inelastic Neutron Scattering
Physical Review Letters **102** (2009), 217001: 1 – 4
- Su, Y.; Link, P.; Schneidewind, A.; Wolf, Th.; Adelman, P.; Xiao, Y.; Meven, M.; Mittal, R.; Rotter, M.; Johrendt, D.; Brückel, T.; Loewenhaupt, M.
Antiferromagnetic ordering and structural phase transition in $\text{Ba}_2\text{Fe}_2\text{As}_2$ with Sn incorporated from the growth flux
Physical Review B **79** (2009), 064504: 1 – 6.
- Fu, Z.; Kögerler, P.; Rücker, U.; Su, Y.; Mittal, R.; Brückel, T.
An approach to the magnetic ground state of the molecular magnet $\{\text{Mo}_{72}\text{Fe}_{30}\}$
New Journal of Physics, **12** (2010), 083044: 1 – 15
- Disch, S.; Wetterskog, E.; Hermann, R.P.; Salazar-Alvarez, G.; Busch, P.; Brückel, T.; Bergström, L.; Kamali, S.
Shape induced symmetry in self-assembled mesocrystals of iron oxide nanocubes
Nano Letters (2011) **11** (4), 1651 - 1656
- Matsunaga, T.; Yamada, N.; Kojima, R.; Shamoto, S.; Sato, M.; Tanida, H.; Uruga, T.; Kohara, S.; Takata, M.; Zalden, P.; Bruns, G.; Sergueev, I.; Wille, H. C.; Hermann, R.; Wuttig, M.
Phase-Change Materials: Vibrational Softening upon Crystallization and Its Impact on Thermal Properties
Advanced Functional Material **21** (2011), 2232 - 2239
- Nandi, S.; Su, Y.; Xiao, Y.; Price, S.; Wang, X. F.; Chen, X. H.; Herrero-Martín, J.; Mazzoli, C.; Walker, H. C.; Paolasini, L.; Francoual, S.; Shukla, D. K.; Stempffer, J.; Chatterji, T.; Kumer, C. M. N.; Mittal, R.; Ronnow, H. M.; Rüegg, Ch.; McMorrow, D. F.; Brückel, T.
Strong coupling of Sm and Fe magnetism in SmFeAsO as revealed by magnetic x-ray scattering
Physical Review B **84** (2011), 054419: 1 - 8
- de Groot, J.; Müller, T.; Rosenberg, R. A.; Keavney, D. J.; Islam, Z.; Kim, J.-W.; Angst, M.
Charge Order in LuFe_2O_4 : An Unlikely Route to Ferroelectricity
Physical Review Letters **108** (2012), 187601: 1 - 5.
- de Groot, J.; Marty, K.; Lumsden, M. D.; Christianson, A. D.; Nagler, S. E.; Adiga, S.; Borghols, W. J. H.; Schmalzl, K.; Yamani, Z.; Bland, S. R.; de Souza, R.; Staub, U.; Schweika, W.; Su, Y.; Angst, M.
Competing Ferri- and Antiferromagnetic Phases in Geometrically Frustrated LuFe_2O_4
Physical Review Letters **108** (2012), 037206: 1 - 5.
- Disch, S.; Wetterskog, E.; Hermann, R.; Wiedenmann, A.; Vainio, U.; Salazar-Alvarez, G.; Bergström, L.; Brückel, T.
Quantitative spatial magnetization distribution in iron oxide nanocubes and nanospheres by polarized small-angle neutron scattering
New Journal of Physics **14** (2012), 013025: 1 - 11.
- L.-J. Chang, S. Onoda, Y. Su, Y.-J. Kao, K.-D. Tsuei, Y. Yasui, K. Kakurai & M. R. Lees
Higgs transition from a magnetic Coulomb liquid to a ferromagnet in $\text{Yb}_2\text{Ti}_2\text{O}_7$
Nature Communications **3**:992 (2012), DOI: 10.1038/ncomms1989

Indicators

Quantitative Numbers

	2009	2010	2011
Peer-Reviewed Publications	68	45	60
Graduations			
Master/Diploma	2	0	6
Dissertation	0	1	3
Habilitation	0	0	0

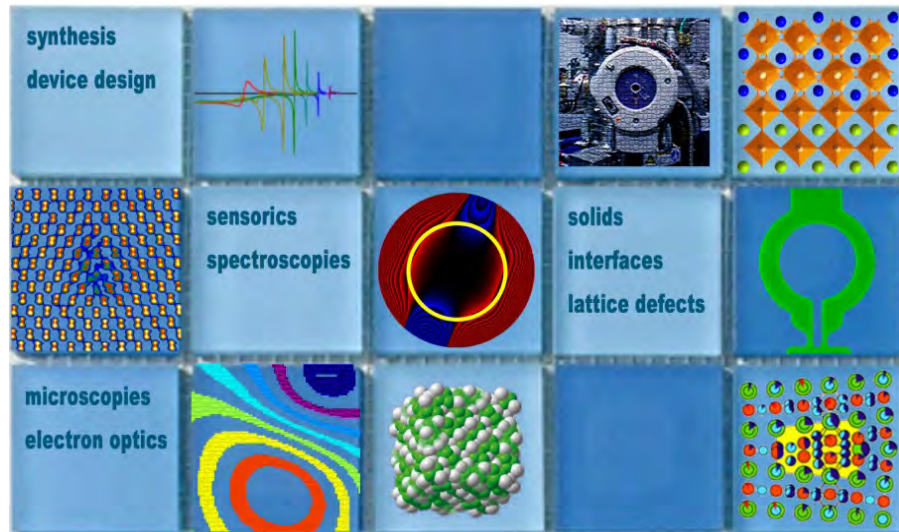
Honours

HGF Young Investigator Group	R. Hermann	HGF
HGF Young Investigator Group	M. Angst	HGF
DTG Young Researchers Award by the German Thermoelectric Society, 2011	Dr. Anne Möchel (JCNS-2)	Deutsche Thermoelektrik-Gesellschaft, DTG

Selected Third Party Projects

1. Lattice Dynamics in Emerging Functional Materials
Young Investigator Group (R. Herrmann)
2008 - 2013
2. Complex Ordering Phenomena in Multiferroic Oxides
Young Investigator Group (M. Angst)
2009 - 2014
3. Nanostrukturierte Thermoelectrika
DFG Priority Program (SPP 1386)
2009 – 2015
4. ESS Design Update Phase
BMBF Collaborative Project
2010 – 2013
5. High Intensity TOF Powder- and Texture Diffractometer POWTEX at FRM II
R. Dronskowski, RWTH Aachen & Th. Brückel, JCNS-2 & PGI-4
2007 - 2013

PGI-5: Microstructure Research



A major focus at *Microstructure Research* is the in-depth investigation of atomic-scale phenomena in crystalline solids with a special emphasis on electro ceramics, complex metal alloys, and nanostructured semiconductors for future applications in information technology as well as energy storage and power generation. Relevant issues cover the understanding of structural and electronic properties associated with heterointerfaces and lattice imperfections via a multidisciplinary research approach making use of a broad portfolio of microscopic and spectroscopic analysis techniques.

For the above purposes, PGI-5 continuously complements competence in the fields of single crystal growth, sputtering deposition technology, Josephson admittance and Hilbert spectroscopy as well as scanning tunnelling microscopy. In some of these fields, the competence covers the whole range from basic research via materials synthesis to the design and manufacturing of technical devices. In other fields, access to novel material classes and intricate problems are provided by qualified collaborations targeting on the application of ultra high-resolution transmission electron microscopy techniques accompanied by the development of novel analysis methods.

Over and above general solid state and technology-related activities, PGI-5 operates the Ernst Ruska-Centre for Microscopy and Spectroscopy with Electrons (ER-C) on a pari passu base with the Central Facility for Electron Microscopy (GFE) of RWTH Aachen University. Representing one of the world's foremost establishments in the field of electron optics research, ER-C features several unique tools for nanocharacterisation complemented by a strong expertise in the development of advanced methods provided also to external researchers within the framework of ER-C user services. Pushing the limits in the field of fundamental electron optical research is, hence, accompanied by the application of advanced techniques to the investigation of a variety of solid state phenomena taking place on the atomic scale.

Head of Institute:

Prof. Rafal E Dunin-Borkowski, e-mail: r.dunin-borkowski@fz-juelich.de, phone: +49-2461-61-9297.

Scientific Staff

On August 31st 2012, the staff of PGI-5 comprised 22 scientists (thereof 11 senior scientist, 7 junior scientists, and 4 guest scientists), 7.25 technicians, 5 PhD students, and 3 Master students.

Senior Scientists

Boothroyd, Dr. Christopher Brian
Divin, Dr. Yuri
Dunin-Borkowski, Prof. Dr. Rafal
Ebert, Dr. Philipp
Faley, Dr. habil. Michael
Feuerbacher, Dr. Michael
Houben, Dr. Lothar
Jia, Dr. Chun-Lin
Luysberg, Dr. Martina
Poppe, Dr. U.
Thust, Dr. Andreas
Tillmann, Dr. Karsten

Junior Scientists

Du, Dr. Hongchu [ext. funding]
Heggen, Dr. Marc [ext. funding]
Kovacs, Dr. Andras [ext. funding]
Jin, Dr. Lei
Lyatti, Dr. Matvey
Duchamp, Dr. Martial [ext. funding]
Stroppa, Dr. Daniel [ext. funding]

Guest Scientists

Barthel, Dr. Juri,
Chiu, Dr. Ya-Ping
Roitsch, Dr. Stefan
Wei Dr. Xiankui

Research Highlights

Elastic Energy of Metadislocations in Complex Metallic Alloys

M. Feuerbacher and M. Heggen

Ernst Ruska-Centre und PGI-5: Microstructure Research

A parameterized expression for the Burgers vectors of metadislocations is derived. We calculate the elastic line energy of metadislocations and demonstrate that the experimentally observed occurrence of Fibonacci relations between the members of a metadislocation series is due to energy minimization.

Complex metallic alloys (CMAs) are intermetallic compounds with a complex structure and a unit cell typically containing some hundred to some thousand atoms. As a result of the large lattice parameters, in these materials conventional dislocation-based mechanisms are prone to failure. The elastic line energy of a perfect dislocation would articulately exceed physically reasonable values. Metadislocations, first observed in the CMA ε -Al-Pd-Mn [1], are line defects mediating plastic deformation in a variety of CMAs. They have small Burgers vectors, hence low elastic line energies, and are accommodated in the lattice via the formation of a slab of phase that is different but closely related to the host. Fig. 1a and 1b depict metadislocations in the orthorhombic phases ε_6 and ε_{28} of the system Al-Pd-Mn, respectively. To date, metadislocations were further observed in monoclinic Al-Pd-Fe phases (Fig. 1c), in orthorhombic $\text{Al}_{13}\text{Co}_4$, and in orthorhombic Taylor phases (Fig. 1d).

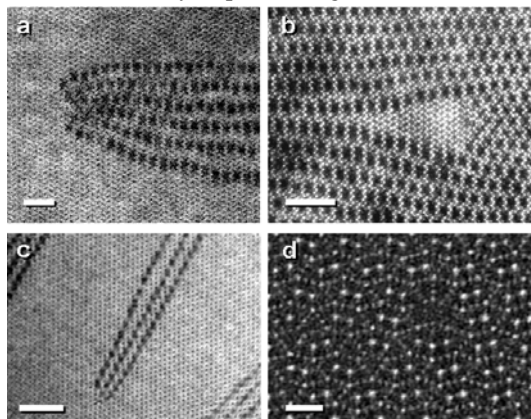


FIG. 1: Metadislocations with six associated phason halfplanes in ε_6 -Al-Pd-Mn (a) and in ε_{28} -Al-Pd-Mn (b). Metadislocations in ξ -Al-Pd-Fe (c) and in T-Al-Mn-Pd (d). Scale bar 10 nm for (a – c) and 1 nm for (d).

In a given CMA structure series of metadislocations with different Burgers vector lengths exist. Within a metadislocation series, the Burgers vectors of the

individual members are related by factors of τ , where is the golden mean. The latter comes into play due to the icosahedral local order occurring in CMA structures. Metadislocations with different Burgers vector length are associated with different quantities of related phase. It is experimentally found that the quantity of associated related phase within a metadislocation series follows a Fibonacci sequence. From a purely geometric point of view, however, it is not clear why the characteristic parameters of metadislocations are restricted to Fibonacci related numbers since other metadislocations, can be constructed equally well. In this paper, we calculate energy diagrams which show that the experimentally observed metadislocations are those of lowest elastic energy [2].

Fig. 2 depicts the tiling of a metadislocation in the ε_6 -phase. The metadislocation core is represented by the dark-grey tile, the ideal ε_6 -phase by flattened hexagons in alternating orientations, and the slab of related phase is realized by six phason halfplanes, represented by banana-shaped nonagons and regular pentagons (light grey). Superposed to the tiling is a Burgers circuit around the dislocation core starting at the solid point at the upper left and following the edges of the tiling in the direction of the arrows. The circuit yields a Burgers vector $\vec{b}_z = -c/\tau^4 [0 0 1]$, which, for ε_6 -Al-Pd-Mn corresponds to a Burgers vector length of 1.83 Å.

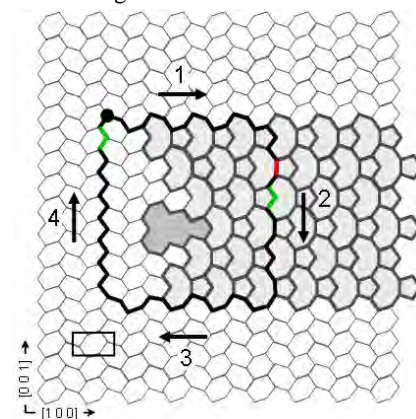


FIG. 2: Burgers circuit around a metadislocation in the ε_6 -structure.

In order to obtain an expression valid also for the other metadislocations in the series the expression is parameterized using parameters p and h chosen as

follows: p corresponds to the number of phason halfplanes the metadislocation is associated to and h corresponds to the number of hexagon planes on the left-hand side of the dislocation core. This yields the expression

$$b_\varepsilon = c \left(\frac{\tau^2}{2} p - h \right). \quad (1)$$

The parameterization implies the construction of a metadislocation according to a generalized Volterra process: a metadislocation is constructed by removing h hexagon halfplanes from an ideal ε -phase lattice, and filling the gap with p phason halfplanes. Since the thickness ratio of the hexagon and phason planes corresponds to an irrational number, the hexagon halfplanes can only be partially compensated or overcompensated. The resulting gap or overlap corresponds to the Burgers vector of the dislocation.

The elastic strain energy per unit length of dislocation can be approximated as $E_{el} \approx \mu b^2$, where μ is the shear modulus of the material. Inserting eq. (1) yields a parametrized expression for the elastic energy of a metadislocation, which can be represented in the form of an energy map in terms of the parameters p and h .

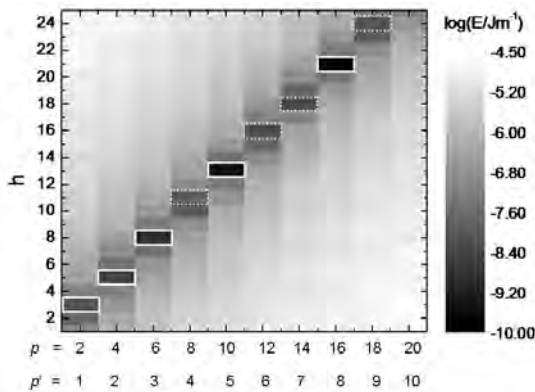


FIG. 3: Elastic energy of metadislocations in ε - and ξ -phases. Experimentally observed metadislocations in ε -Al-Pd-Mn are marked by boxes with solid white outline, further hypothetical metadislocations are marked by boxes with dashed outline. The upper abscissa (p) holds for orthorhombic ε -phases, the lower abscissa (p') for monoclinic ε -phases and ξ -phases.

Figure 3 shows the elastic energy for a wide range of (p,h) doublets, where $p/2$ and h are natural numbers. Each box represents the logarithm of the elastic energy of the corresponding metadislocation. The darkest grey represents the lowest energy values. We find a valley of low energies along a line, which is approximately diagonal in Fig. 3. The range of plotted (p,h) doublets contains five experimentally observed metadislocations, which correspond to particularly low energy values and are indicated by solid white boxes. There are further, hypothetical, metadislocations, which also possess relatively low energy, but which are not observed experimentally, for example those with 8, 12, or 14 associated phason halfplanes. These are indicated by boxes with dashed outline.

Following this approach, metadislocations with the highest number of associated phason halfplanes seem the most favorable. However there are additional factors which have not been accounted for, the most evident of which is the energy cost resulting from the inclusion of the associated phason halfplanes. Taking this into account by an additive linear term in the expression for the elastic energy, we find that metadislocations with six phason planes have the lowest energy. This is in agreement with the experimental observation frequency.

Following a similar approach, we can treat metadislocations in ξ -phases and monoclinic ε -phases (c.f. Fig. 1c). We find the expression

$$b_\xi = c' (\tau^2 p' - h'). \quad (2)$$

which has a very similar form as eq. (1). Substituting $p/2$ by p' , h by h' , and c by c' , Fig. 3 holds for metadislocations in the ξ -structure as well using the lower abscissa.

The energy diagram shown in Fig. 4 holds for metadislocations in Taylor-phases [3] (c.f. Fig. 1d), where s corresponds to the number of stacking faults the metadislocation is associated to and m corresponds to the number of c-lattice constants antagonizing the $[0\ 0\ 1]$ shift introduced by the s associated stacking faults. We can accordingly understand the construction of the metadislocation such that the $[0\ 0\ 1]$ shift introduced by s associated stacking faults is partially compensated or overcompensated by m “inserted” $(1\ 0\ 0)$ hexagon planes, and the difference corresponds to the Burgers vector of the dislocation. The same diagram also holds for metadislocations in orthorhombic $\text{Al}_{13}\text{Co}_4$, taking into account the parameter s' on the lower abscissa.

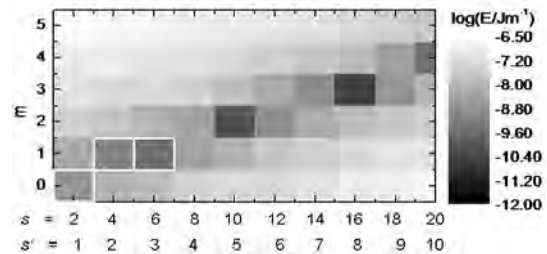


FIG. 4: Elastic energy of metadislocations in T -phases and in $\text{Al}_{13}\text{Co}_4$. Experimentally observed metadislocations in T -Al-Mn-Pd phase are marked by boxes. The upper abscissa (s) holds for T -phases, the lower abscissa (s') for $\text{Al}_{13}\text{Co}_4$.

In conclusion we find that metadislocation formation is not generally restricted to Fibonacci related construction parameters. Metadislocations with other, non-Fibonacci related construction parameters are generally possible, but do not form since they have higher elastic line energy.

-
- [1] H. Klein, M. Feuerbacher, P. Schall P, K. Urban, Phys. Rev. Lett. 82, 3468, 1999.
 - [2] M. Feuerbacher and M. Heggen, Acta Mat. 60, 1703, 2012.
 - [3] M. Heggen, L. Houben, M. Feuerbacher, Nature Mat. 9, 332, 2010.

Electric dipole rotation in flux-closure domains in ferroelectric $\text{Pb}(\text{Zr},\text{Ti})\text{O}_3$

C.L. Jia¹, K. Urban¹, M. Alexe², D. Hesse², I. Vrejoiu²

¹ PGI-5: Microstructure Research, Forschungszentrum Jülich and Ernst Ruska Centre

² Max Planck Institute of Microstructure Physics, Weinberg 2, D-06120 Halle

Low-dimensional ferroelectric structures are very promising for next generation ultrahigh density memory devices. Depolarizing fields, created by incompletely compensated charges at the surfaces and interfaces, depress the polarization of such structures. Theory suggests that with uncompensated surface charges local dipoles can organize in flux-closure structures in thin films and vortex structures in nano-size ferroelectrics, reducing depolarizing fields. By aberration-corrected transmission electron microscopy, we obtain experimental evidence for continuous rotation of the dipoles closing the flux of 180° domains in a ferroelectric perovskite thin film.

Ferroelectric thin films have demonstrated great potential for microelectronic applications [1]. In ferroelectric random access memories information is stored and read by switching and detecting the polarization orientation in the ferroelectric material. Microscopically polarization switching is realized through the motion of domain walls driven by an external electric field. Phenomenologically, domain arrangements are characterized by the angle between polarization directions in adjacent domains. In epitaxial thin-film systems, the domain pattern is determined by the growth conditions and by the mechanical interface strain and the electric boundary conditions related to the depolarization field at surfaces or interfaces. Ideally two such boundary conditions can be distinguished depending on whether the surface or interface charges are perfectly screened or unscreened.

Theoretical investigations have shown that in very small ferroelectric structures, of a size of a few nanometers, the local dipoles should organize in vortices rather than in domains with uniform polarization, due to the large depolarization fields [2]. The observations described below, in addition to giving evidence of the existence of flux-closure structures at a 180° domain wall, represent on atomic scale a direct experimental proof of continuous polarization rotation. Using atomic-resolution aberration-corrected transmission electron microscopy domain structures are studied of the epitaxial thin-film system $\text{PbZr}_{0.2}\text{Ti}_{0.8}\text{O}_3$ (in the following abbreviated by PZT) on SrTiO_3 (STO) [3]. We employ the negative spherical aberration imaging (NCSI) technique, which allows not only to locate all the atomic species but also to measure their positions, unit cell by unit cell, with a precision of a few picometers.

Figure 1 shows an atomic resolution image of an area including the interface between the PZT layer and the STO substrate. In Fig. 1 the structure (one projected unit cell) of PZT is indicated schematically in two regions (positions of Zr/Ti, PbO/SrO, and O atomic columns, seen end-on, are indicated by red, yellow and blue circles, respectively).

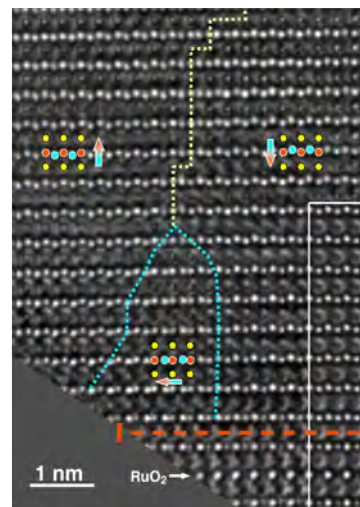


Fig. 1. Atomic-resolution image of a flux closure structure with continuous dipole rotation in $\text{PbZr}_{0.2}\text{Ti}_{0.8}\text{O}_3$ (PZT) close to the interface to the SrTiO_3 (STO) substrate. The interface is marked by a horizontal dashed line ("I"), which is determined based on a SrRuO_3 marker layer with a nominal thickness of 1.5 unit cells at the STO/PZT interface. The RuO_2 marker layer is also indicated. In the image recorded along the crystallographic $[\bar{1}\bar{1}0]$ direction, the atomic structure and the electric dipole direction (arrows) are given. In the image two larger domains with 180° orientation can be identified. The domain wall is indicated by a yellow dotted line. In the center of the lower half of the image an approximately triangular area (the domain wall is indicated by a dotted blue line) can be seen, where in the center, the dipole direction makes an angle of 90° with the two large domains. The inset on the right-hand side shows a calculated image demonstrating the excellent match between the atomic model and the specimen structure.

Due to the particular imaging conditions, dynamic electron scattering yields a sharp bright contrast in the approximately 11 nm thick sample for the Zr/Ti and the O atom columns, while the SrO and PbO atomic columns are relatively weak. The film-substrate interface was marked by depositing a nominally 1.5 unit cells thick layer of SrRuO_3 (SRO) on STO prior to the deposition of PZT. The interface, denoted by a horizontal dashed line, is then determined by observing the plane of RuO_2 serving as a marker.

The vertical shift in the Zr/Ti positions with respect to the adjacent O positions indicates that PZT is in a polarized state. On the left-hand side of Fig. 1, this shift is upward, while on the right-hand side, it is downward, resulting in the polarization-vector directions indicated by the arrows. This indicates the existence of two domains in a 180° orientation relation. By mapping the individual atom shifts, the position of the domain wall (dotted line) is localized. The horizontal width of this wall is about one $[\bar{1}\bar{1}0]$ projected crystal unit cell, which is in agreement with the results of earlier measurements [4]. At the bottom interface, in between the two 180° domains, *in-plane* displacements of the Zr/Ti positions with respect to the adjacent oxygen positions are observed.

Figure 2 displays an atomic displacement map superimposed on an image obtained by converting the grey-scale contrast of Fig. 1 into a false-colour scale to enhance contrast. The arrows located at the Zr/Ti column positions indicate the modulus and the direction of the “off-centre” displacement with respect to the middle point of the horizontal line connecting the two neighbouring O atom positions (taking the cubic structure with an inscribed oxygen octahedron in the non-polar state as a reference). The scale at the bottom left indicates a displacement of 40 pm. We note that a uniform atomic shift of this magnitude corresponds to an integral polarization of $108 \mu\text{C}/\text{cm}^2$ [4].

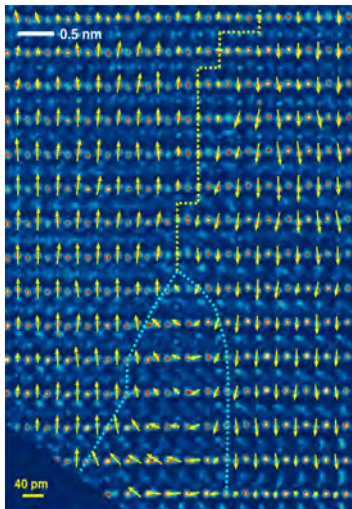


Fig. 2. Map of the atomic displacement vectors. The displacement of the Zr/Ti atoms (arrows) from the center of the projected oxygen octahedra is shown here superposed on the atomic image of Fig. 1. To enhance contrast, the grey scale is converted into a false-colour representation. The length of the arrows represents the modulus of the displacements with respect to the yellow scale bar in the lower left corner. The arrowheads point into the displacement directions. Note the continuous rotation of the dipole directions from “down” (right-hand side) to “up” (left) which closes the electric flux of the two 180° domains.

The displacement map provides direct evidence of a continuous rotation of the dipole direction from downward in the right-hand domain through a 90° orientation to upward in the left-hand domain, forming a particular type of flux-closure structure.

The reorientation of the dipoles occurs within a well-defined area of triangular shape with the maximum width at the interface of about 2.5 nm. The displacement vector modulus is small at the top, increasing towards the interface. The transition region from the downward orientation of the electric dipoles to the 90° orientation is about two projected unit cell widths on the right-hand side and up to about twice as wide on the left-hand side. No direct information is available on possible atom shifts along the $[\bar{1}\bar{1}0]$ viewing direction. However, the fact that we do not observe any in-plane elongation of the projected atom column contrast can be interpreted as evidence of the dipole rotation occurring exclusively in the image plane.

Our results provide direct experimental evidence for the continuous rotation of the atomic-scale polarization dipoles over a distance directly relevant for the formation of vortex structures as predicted by theory [2]. Our observations agree well with the results of calculations for thin-film epitaxial systems by first-principles techniques where it was found that, as observed in the present work, the lateral extension of the flux-closing area is quite narrow. Furthermore, theory yields a continuous rotation of the polarization direction rather than a closure domain with a 90° polarization orientation and relatively narrow domain boundaries, as known for ferromagnetics.

Our work demonstrates the unique capabilities of unit-cell-by-unit-cell mapping of the dipole vector by means of atomic-resolution transmission electron microscopy. This technique can therefore be employed to study further details of domain structures close to interfaces in ferroelectric heterostructures and of vortex-like structures in ferroelectric materials. Since these structures are sensitive to the balance between competitive interactions, even small changes in the interface properties could have substantial effects on the depolarization field behaviour. In fact, theory predicts quite dramatic effects for thicknesses of the order of a few nanometres in the PZT layer, where the top and bottom layers (metallic or insulating) cannot be treated separately [5]. In addition, unit-cell-thick “dead” layers, e.g. due to local deviations in permittivity caused by non-stoichiometry, are expected to change the flux-closure domain structure. Such investigations are also of potential significance for further progress in technology, in which thinner and thinner and smaller and smaller ferroelectric heterostructure systems are being considered for microelectronic applications.

-
- [1] N. Setter, R. Waser, *Acta Mater.* 48, 151 (2000).
 - [2] I. Naumov, L. Bellaiche, H. Fu, *Nature* 432, 737 (2004).
 - [3] C.L. Jia et al., *Science* 331, 1420 (2011).
 - [4] C.L. Jia et al., *Nat. mater.* 7, 57 (2008).
 - [5] S. Prosandeev, L. Bellaiche, *Phys. Rev. B* 75, 172109 (2007).

High Temperature Conductance of LaAlO₃ / SrTiO₃ Heterostructures

F. Gunkel¹, S. Hoffmann-Eifert¹, R. Dittmann¹, S. Mi², C. Jia², P. Meuffels¹, R. Waser¹

¹ PGI-7: Electronic Materials, Forschungszentrum Jülich

² PGI-5: Microstructure Research, Forschungszentrum Jülich

The interface conductance of LaAlO₃ / SrTiO₃ heterostructures was investigated under high temperature oxygen equilibrium, at a pO_2 range from 10–22 to 1 bar and a temperature of 800 to 1100 K. It is compared to the characteristic of SrTiO₃ single crystals, which is described in terms of a defect chemistry model. Up to 950 K the equilibrated heterostructures reveal an additional influence of a metallic-like conduction path with a very slight dependence on the oxygen partial pressure. Donor-type interface states are discussed as a possible origin for the exceptional interface conduction of LaAlO₃/SrTiO₃ heterostructures.

The discovery of the highly conducting interface between LaAlO₃ (LAO) films and SrTiO₃ (STO) substrates¹ has led to miscellaneous studies on the fundamental properties of LAO/STO-heterostructures grown by pulsed laser deposition (PLD) and has evoked extensive discussions about the physical mechanisms which underlie the high concentration of charge carriers in the interface region (10^{13} - 10^{17} cm⁻²)^{1,2}.

In this context, a strong impact of the oxygen atmosphere during PLD growth on the low temperature conductivity of LAO/STO-heterostructures with undefined defect configuration has been observed³ but no studies of the interface conductivity under equilibrium conditions have been reported so far. Therefore, we performed *in situ* measurements of the high temperature conductance (HTC) of LAO/STO-heterostructures under controlled oxygen partial pressure in order to gain more detailed insight into the defect structure of the LAO/STO-interface⁴.

8 unit cells of LAO were grown on TiO₂-terminated (100) STO substrates by means of PLD at a temperature of 970 K and a deposition oxygen pressure of 4×10^{-5} mbar. Clear reflection high energy electron diffraction intensity oscillations were observed during the process indicating layer-by-layer growth mode. Those samples exhibited a sheet conductance of about 0.03 mS at 300 K as determined by four-point-probe measurements in a van der Pauw configuration.

The perfect crystallinity and the heteroepitaxial character of the thin films were verified by high-resolution scanning transmission electron microscopy. Figure 1 shows a high angle annular dark field (HAADF) image of an interface region of a representative, as grown sample.

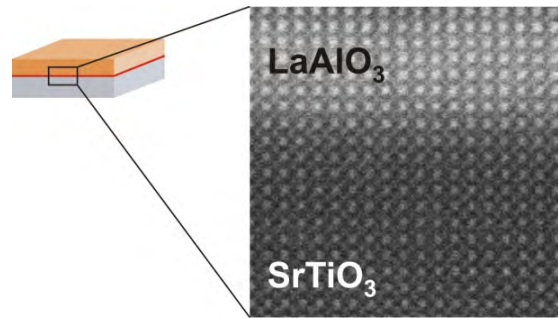


FIG. 1: HAADF image of the LAO/STO-interface region in an as-grown sample.

The brightness across the interface shows rather a gradual decrease than an abrupt, step-like change demonstrating A-site cation intermixing on a length scale of 2–3 unit cells at the interface in agreement with the findings of Nakagawa et al.⁵

The HTC measurements were performed at temperatures between 820 and 1250 K in an YSZ-oxygen-pump system which allowed to continuously adjust the oxygen partial pressure between 1 and 10^{-22} bar (for details see ref. 6).

The results of HTC measurements of a LAO/STO heterostructure under controlled oxygen atmosphere are illustrated in Figure 2 in comparison to the bare STO single crystal. In a simple model the dc characteristic of the heterostructure can be described by the sum of three parallel conductance contributions G_{STO} , G_{IF} , and G_{LAO} corresponding to STO single crystal, metallic interface, and LAO layer, respectively. Since the STO-substrate exceeds the thickness of the LAO thin film by a factor of 10^4 , one can deduce from reference measurements that the LAO film contribution is always small compared to the substrate contribution and can be neglected.⁴ The total conductance of the heterostructure G_{tot} is then given by

$$G_{tot} = G_{IF} + G_{STO} + G_{LAO} \approx G_{IF} + G_{STO} \quad (1)$$

At temperatures lower than 1100 K clear deviations between the conductance characteristic of the heterostructure and the single crystal are observed in the range 10^{-18} bar $\leq pO_2 \leq 10^{-5}$ bar. For the given temperature and pO_2 range it can be deduced that G_{IF} possesses a very weak pO_2 -dependence far beyond the (-1/4)-dependence of the STO single crystal.

The temperature dependence of the heterostructure's conductance measured under a controlled pO_2 of 10^{-18} bar is analyzed in more detail in Figure 3. Two temperature regimes can be distinguished: from 820 to 900 K, G_{tot} (black circles) decreases with increasing temperature down to a value of about 0.01 mS possessing to a metallic-type behavior. Above 900 K, G_{tot} increases with increasing temperature due to the exponentially rising conductance of the STO substrate. Hence, the decrease in the total conductance below 900 K has to be attributed to the interface contribution according to Eq. (1). This remarkable result indicates that the interface still exhibits a metallic-like conductance at 900 K under equilibrium conditions. The metallic-like behavior of G_{IF} implies the electronic nature of the charge carriers at the interface since ionic conduction possesses thermal activation. For the in-situ measurements it can be excluded that a mere reduction in the STO substrate during the PLD process is the main reason for the high electron density at the LAO/STO interface. Reduction would result in mobile oxygen vacancies which would strive for equilibration with the surrounding pO_2 when heating up the samples.

Furthermore, it is known from the research on defects in perovskite-type titanates that lanthanum donor doped STO bulk ceramics show a constant

region can be estimated directly from the conductance measurements adopting the values for the known electron mobility μ_{STO} in the STO bulk.⁷ Thereby, one obtains $n_S(850\text{ K}) = G_{IF} / e \mu_{STO} \approx 10^{13} - 10^{14} \text{ cm}^{-2}$ in accordance with published values.^{1,2}

In summary, the results of this study show that for a discussion on the nature of the interface conductivity in LAO/STO heterostructures one has to pay attention that the complex defect chemical state of the entire heterostructure is well defined.

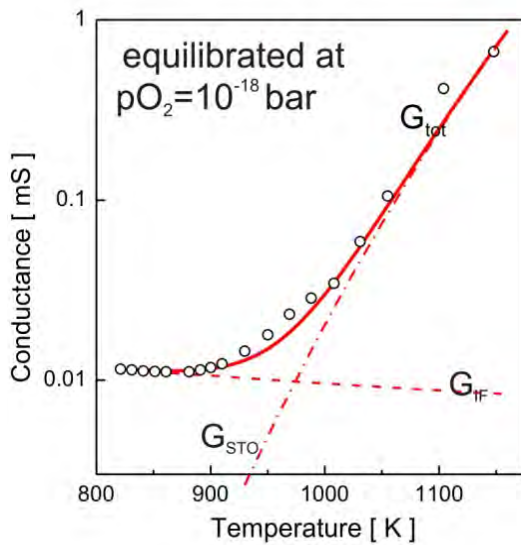


FIG. 3: Temperature dependence of the heterostructure's conductance equilibrated at $pO_2=10^{-18}$ bar. Expt. data (O); fits: metallic interface contribution $G_{IF} \sim 1/T$, substrate contribution $G_{STO} \sim \exp(-E_A/k_B T)$, and total conductance $G_{tot} = G_{STO} + G_{IF}$.

conductivity over a broad range of pO_2 in which the charge carrier density is determined by the fixed concentration of ionized dopants.⁷ Hence, the weak pO_2 -dependence of the interface conductivity might give hints for localized, donor-type defects in the interface region such as provided by A-site cation intermixing. Assuming this scenario of La-doping the sheet carrier density n_S within the interface

-
- [1] A. Ohtomo et al., Nature 427, 423 (2004).
 - [2] S. Thiel et al., Science 313, 1942 (2006).
 - [3] A. Brinkman et al., Nature Materials 6, 493 (2007).
 - [4] F. Gunkel et al., Appl. Phys. Lett. 97, 12103 (2010).
 - [5] N. Nakagawa et al., Nature Materials 5, 204 (2006).
 - [6] C. Ohly et al., J. Am. Ceram. Soc. 89, 2845 (2006).
 - [7] R. Moos et al., J. Am. Ceram. Soc 80, 2549 (1997).

Reconstruction of the Projected Crystal Potential Using HRTEM – Prospects for Materials Science Investigations

M. Lentzen¹, J. Barthel¹

¹ Ernst Ruska Centre and PGI-5: Microstructure Research, Forschungszentrum Jülich

The projected electrostatic crystal potential is reconstructed from an exit wave function, which has been reconstructed before from a through-focus series of atomic-resolution images recorded with a high-resolution transmission electron microscope (HRTEM). The potential reconstruction includes the self-consistent fit of object thickness, residual lens defocus, phenomenological absorption, and object tilt. The prospects of potential reconstruction are explored by investigating the microstructure of a BSCF crystal, which exhibits a polytype structure with closely spaced twin boundaries and a high concentration of oxygen vacancies.

In modern high-resolution electron microscopy various reconstruction methods have proven to be invaluable tools for materials science investigations. They comprise wave function reconstruction methods, which aim to eliminate unwanted imaging artifacts as non-linear contrast modulation and contrast delocalisation owing to the presence of lens aberrations. One of these methods, used also in this work, is the widely known focus-variation method [1, 2].

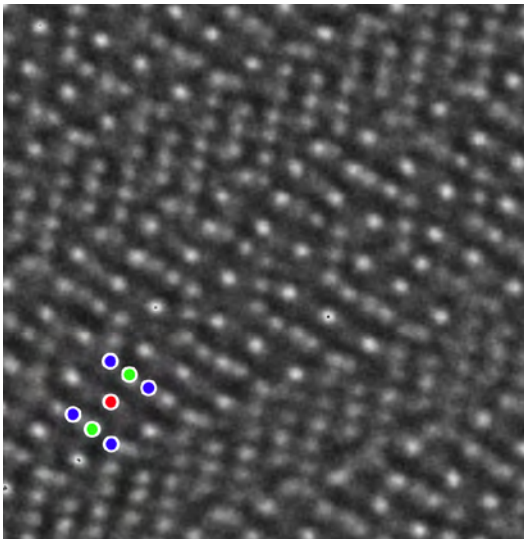


FIG. 1: High-resolution image of BSCF at bright-atom pass-band conditions, red: Ba/Sr, green: Co/Fe, blue: O. Frame size is 3.4 nm × 3.4 nm.

In the past two decades various forms of potential reconstruction methods have been proposed, which aim to eliminate the problems occurring in the

structural interpretation of reconstructed exit wave functions, imposed by the effects of dynamical electron diffraction. These effects give rise to a non-linear relation of scattering power and modulation of the wave function [3], and the local modulation can be further obscured by the presence of crystal tilt.

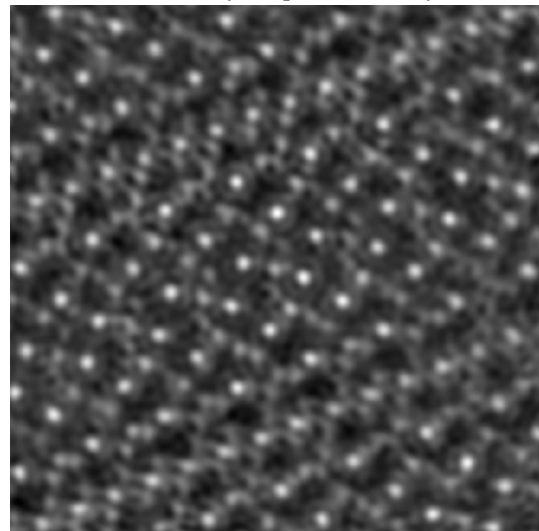


FIG. 2: Phase of reconstructed exit wave function of BSCF. Frame size is 3.4 nm × 3.4 nm.

Materials science investigations using potential reconstruction methods in combination with wave function reconstruction methods require knowledge beyond the idealised conditions for the reconstruction algorithms: in particular object thickness, crystal tilt, residual wave aberrations, and phenomenological absorption are often unknown in experiments. Extensive simulation studies using the channelling model of dynamical electron diffraction [3] and a rapid and stable potential reconstruction algorithm had revealed that the projected crystal potential can be determined for thick objects [4]. A breakthrough for the application in materials science investigations had been achieved by showing that object thickness, residual defocus, and phenomenological absorption can be fitted self-consistently together with the projected potential [5].

The last corner stone, preventing application of the potential reconstruction so far, has been added recently, namely the successful self-consistent fit of crystal tilt [6]. The prospects of potential reconstruction for materials science were explored by investigating the the microstructure of a $\text{Ba}_{0.5}\text{Sr}_{0.5}\text{Co}_{0.8}\text{Fe}_{0.2}\text{O}_3$ (BSCF) crystal, whose

perovskite unit cells can form a variety of polytype structures through rearrangement of oxygen octahedra. A through-focus series of 20 images was recorded from a thin specimen of BSCF with an aberration-corrected TITAN 80-300 operated at 300 kV.

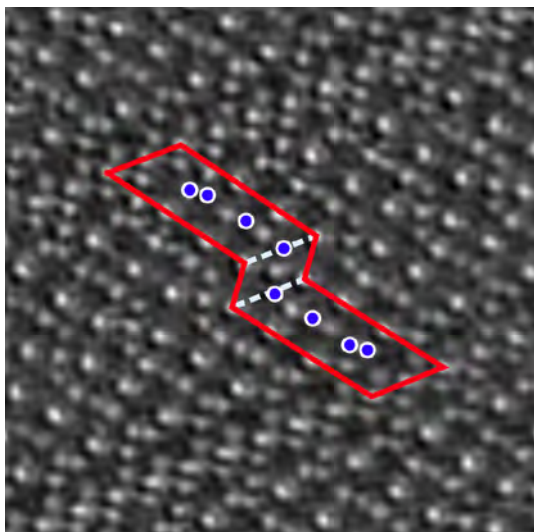


FIG. 3: Reconstructed projected potential of BSCF, frame 3.4 nm by 3.4 nm, red: projected unit cell, blue: oxygen columns used for histogram analysis, dashed: $\Sigma 3$ twin boundaries.

Next an exit wave function was reconstructed from the series using the TrueImage package (FEL, Eindhoven), which was then subjected to numerical correction eliminating residual aberrations up to the instrumental information limit of 0.08 nm. Finally the projected crystal potential was reconstructed from the corrected exit wave function using the methods described in [5, 6], and the following parameters were determined through self-consistent fit: 8.4 nm object thickness, 1.6 nm residual defocus, and 7.0 nm^{-1} crystal tilt. The final mismatch of model and experimental exit wave function was $S = 4.5\%$, which is a reasonably small value in view of nearly the same amount of mismatch between model and experimental images during the exit wave reconstruction.

The advantage of potential reconstruction over high-resolution imaging alone can be judged by comparing the structural information accessible through the image intensity (Fig. 1), through the phase of the reconstructed exit wave function (Fig. 2), or through the reconstructed projected potential map (Fig. 3). Although the image was recorded with a pass-band up to the information limit very fine

details cannot be seen owing to delocalisation. Investigation of the exit wave reveals such details; they are, however, slightly delocalised and corrupted by the presence of crystal tilt. In the potential map the effects of tilt are strongly reduced, and the non-linear distortion of the atomic contrast modulation owing to dynamical diffraction is eliminated.

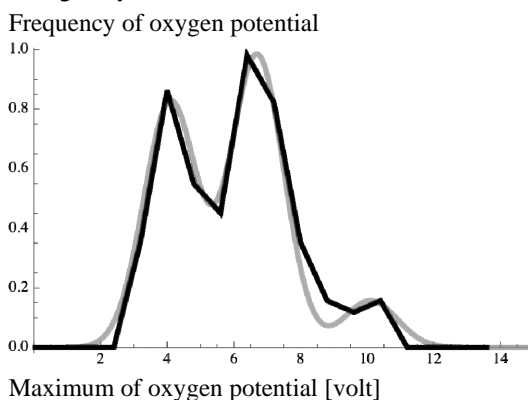


FIG. 4: Histogram analysis of oxygen columns, black: frequency of oxygen potential maxima, grey: fit of the distribution with three gaussians.

Numerical evaluation of the projected potential map allows a quantitative investigation of the projected crystal structure of the BSCF crystal, containing closely-spaced $\Sigma 3$ twin boundaries, in particular the disorder on the oxygen sublattice. Column-by-column measurement of the maxima of the projected oxygen potential reveals through a histogram of the potential maxima single oxygen atom precision of 2.6 volt per atom (Fig. 4). The three maxima of the potential distribution indicate the presence of a high concentration of oxygen vacancies.

One of us, J. B., gratefully acknowledges funding from the German Federal Ministry of Economics and Technology within the COORETEC initiative.

-
- [1] W. Coene, G. Janssen, M. Op de Beeck, D. Van Dyck, Phys. Rev. Lett. 20, 3743 (1992).
 - [2] A Thust, W. M. J. Coene, M. Op De Beeck, D. Van Dyck, Ultramicroscopy 64, 211 (1996).
 - [3] K. Kambe, G. Lehmpfuhl, F. Fujimoto, Z. Naturforsch. A 29, 1034 (1974).
 - [4] M. Lentzen, K. Urban, Acta Cryst. A 56, 235 (2000).
 - [5] M. Lentzen, Ultramicroscopy 110, 517 (2010).
 - [6] M. Lentzen, Proceedings MC2011 Kiel, IM2 P133 (2011).

Strain induced shift of the crystal-field splitting of SrTiO₃

M. Luysberg^{1,2}, D. Avila^{1,2,3}, M. Boese^{1,4}, L. Houben^{1,2}, J. Schubert⁵

¹ PGI-5: Microstructure Research, Forschungszentrum Jülich

² ER-C: Ernst Ruska Centre, Forschungszentrum Jülich

³ present address: Dep. de Química Inorgánica I, Fac. CC. Químicas, Universidad Complutense, Madrid

⁴ present address: CRANN, Trinity College Dublin, Dublin, Ireland

⁵ PGI-9: Semiconductor Nanoelectronics, Forschungszentrum Jülich

Strained SrTiO₃ layers have become of interest, since the paraelectric-to-ferroelectric transition temperature can be increased to room temperature. The effect of strain on the electron loss near edge structure of the Ti L_{2,3} edge in comparison to unstrained samples is investigated by electron energy loss spectroscopy. SrTiO₃ grown on DyScO₃ and GdScO₃, which is tensilely strained, shows a smaller crystal field splitting as observed for the unstrained case. Ab initio calculations of the Ti L_{2,3} and O K edge show a linear decrease of the crystal field splitting with increasing strain, i.e. the energy splitting of the fundamental transitions in the fine structure of Ti L_{2,3} and O K edges become smaller as the strain is increased. Calculated and experimental values of the crystal field splitting show a very good agreement [1].

Thin films with a ferroelectric to paraelectric transition near room temperature are the object of an intense development for their use in different devices such as gate dielectrics for metal semiconductor field-effect transistors (MOSFETs) [2]. SrTiO₃ (STO) is an incipient ferroelectric material but in its pure form at room temperature it exhibits a cubic structure and only at very low temperature its ferroelectric properties are observed. However, the transition temperature T_c can be adjusted by strain, e.g. by epitaxial growth on substrates with different lattice parameters [2]. Here we report on tensilely strained STO grown onto DyScO₃ (DSO) and GdScO₃ (GSO) substrates. Electron energy loss spectroscopy (EELS) is employed to measure the crystal field splitting of the Ti L₃ edge. Ab-initio calculations reveal that the crystal field splitting depends linearly on the strain. Hence, the crystal field splitting provides a measure of the strain in STO.

Multilayers of SrTiO₃/DyScO₃ and SrTiO₃/GdScO₃ were deposited by pulsed laser deposition on REScO₃ (RE: Gd, Dy) (110) substrates [3]. Previous studies revealed perfect epitaxial growth, which implies the formation of a domain structure within the REScO₃ layers [4]. EEL spectra were recorded in a probe aberration-corrected FEI Titan 80-300 scanning transmission electron microscope, equipped with a Wien-type electron monochromator and a Gatan GIF Tridiem 866 ERS post column energy filter. The titanium L₃ and oxygen K-edges were

calculated by means of real-space multiple scattering calculations, using the self-consistent version of this method implemented in the *ab initio* FEFF8.20 code [5].

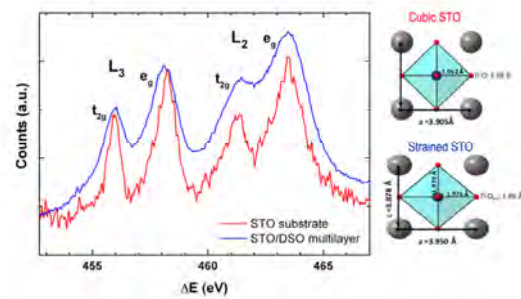


FIG. 1: EEL spectra showing the Ti L_{2,3} edges from unstrained and strained STO, which have been measured on a STO reference sample and STO grown onto DSO substrate. Clearly, the splitting of the L edges is reduced for the strained material. The schematic models on the right hand side display the effect of strain on the Ti-O bond lengths within the octahedra.

Figure 1 illustrates the experimental EEL spectra recorded in the multilayer system STO/DSO. The graph displays the features of the Ti L_{2,3} edge of strained STO grown onto a DSO substrate in blue and from a cubic STO reference sample in red. The two measurements were recorded with an energy resolution of 0.3 and 0.6 eV, respectively. The Ti L_{2,3} edge is formed by four well split peaks attributed to excitations of $2P_{3/2}$ and $2P_{1/2}$ sub-shells to unoccupied t_{2g} and e_g states. In cubic STO the Ti is surrounded by six oxygen atoms forming a regular octahedron with six equivalent Ti-O distances of 1.95 Å (see Figure 1). Under tensile strain this octahedron is distorted, with the four equatorial Ti-O distances being larger than the two apical ones, yielding an average distance Ti-O of 1.96 Å. This enlargement of the average bond length produces a weaker crystal field, which is traduced in a smaller line splitting as it is observed in the blue spectrum.

In order to evaluate the bonding effect, these situations were modeled by means of real-space full multiple scattering (FMS) calculations using the self-consistent version of this method implemented in the *ab-initio* FEFF8.20 code [5]. The FEFF calculations were done with the Hedin-Lungqvist self-energies to account for inelastic losses and it is found that a

cluster of about 50 atoms was sufficient to obtain well converged self consistent field (SCF) potentials. For two cases, i.e. a strain values of 0% and of 1.25%, calculations with larger clusters containing 150 atoms have been performed, which result in the same splitting of the Ti L_3 edge as obtained for a cluster of 50 atoms. For the FMS calculations, a cluster size of 185 atoms was used for both the titanium $L_{2,3}$ and oxygen K edges (not shown here, see [1] for details). The presence of final-state effects in the observed edges resulting from the core-level excitation is also taken into account. The core-hole effect is considered in the present FMS calculations with a fully relaxed potential in the presence of a core hole. The broadening of the theoretical spectra was implemented by measuring the FWHM of the zero loss peaks in the experimental spectra which gives the experimental resolution.

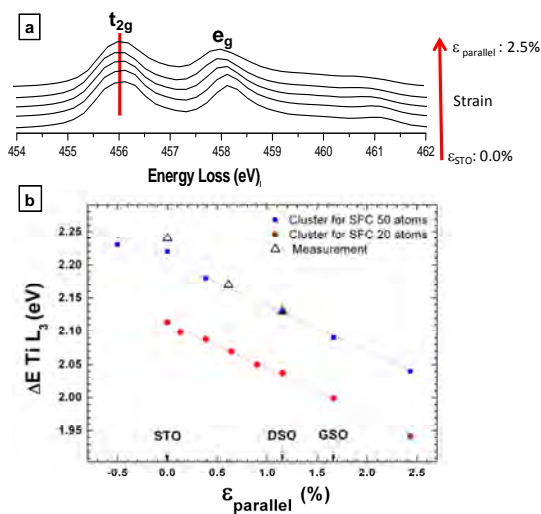


FIG. 2: a) Calculated Ti L_3 edges for different strain values for a cluster of 50 atoms b) The splitting of the L_3 edge calculated for different strain values (ϵ) and different cluster sizes (20 and 50 atoms) shows a linear decrease with increasing strain. Experimental values (triangles) show excellent agreement with calculations when the size of the cluster is 50 atoms.

Figure 2a represents the calculated titanium L_3 edges for different strain situations ranging from pure STO, where $\epsilon = 0$, to a large strain value of $\epsilon = 2.5\%$. The larger the biaxial strain represented by ϵ the smaller is the splitting of the L_3 edge. The plot of energy splitting of the L_3 edge against strain reveals a linear relationship. A cluster of only 20 atoms (circles in Fig. 2b) used in SCF calculations already reproduces the linearity. However, only for cluster sizes larger than 50 atoms (triangles in Fig 2b) the theoretical shift converges yielding an almost perfect agreement of calculated and experimental values. Two of the data points were measured from the spectra shown in Figure 1, where EEL spectra have been recorded

within unstrained STO substrate and STO grown onto a DSO substrate. The data agree very well with the splitting expected for a strain of 0% and 1.15%, respectively.

The ELNES of the O K edge gives also information about different coordination around the oxygen atom. It has been described that the first two peaks of the oxygen K edge are related to the hybridization of the titanium 3d orbitals with the oxygen 2p and their separation is related to the crystal field splitting. Therefore the calculated oxygen K edges should provide similar information as in the previously described case of Ti L edges. Indeed, a linear decrease of the separation between the two first peaks is observed upon increasing strain [1].

It is well known, that the Ti atom within a strained oxygen octahedron can be shifted with respect to central position, which causes ferroelectrical behavior of SrTiO_3 . Hence, it is expected, that the Ti atoms within the biaxially strained STO layers investigated here, may not be located at the central position of the octahedra. However, such a shift of the Ti atom is not likely to affect the splitting of the fundamental transitions in the Ti L edges and O K edge, because the average bond length is maintained. Indeed, ab initio calculations of such asymmetric octahedra (not shown here), did not reveal any change in the crystal field splitting.

So far only biaxially dilations of SrTiO_3 have been discussed, which match the experimental situation in scandate/STO multilayer systems. It is worth noticing, that also for compressive strain the linear relationship of crystal field splitting and strain is maintained, which can be deduced from the data point at a strain of -0.5% included into Figure 2. Hence, it is expected, that the crystal field splitting is a measure of biaxial compressive strain as well.

-
- [1] D. Avila, M. Boese, L. Houben, J. Schubert, M. Luysberg, submitted to ACS Applied Materials & Interfaces (2011).
 - [2] J. H. Haeni, P. Irvin, W. Chang, R. Uecker, P. Reiche, Y. L. Li, S. Choudhury, W. Tian, M. E. Hawley, B. Craigo, A. K. Tagantsev, X. Q. Pan, S. K. Streiffer, L. Q. Chen, S. W. Kirchoefer, J. Levy, D. G. Schlom, Nature 430, 758-761 (2004).
 - [3] T. Heeg, M. Wagner, J. Schubert, S. H. Buchal, M. Boese, M. Luysberg, E. Cicerella, J. L. Freeouf, Microelectron Eng. 80,150-153 (2005).
 - [4] M. Boese, T. Heeg, J. Schubert, M. Luysberg, J. Mater Sci 41, 4434-4439 (2006).
 - [5] A. L. Ankudinov, C. E. Bouldin, J. J. Rehr, J. Sims, H. Hung, Phys. Rev. B 65,104107/1-11 (2002).

Structure analysis of $\text{Cs}_{0.5}[\text{Nb}_{2.5}\text{W}_{2.5}\text{O}_{14}]$ with advanced HRTEM techniques

J. Barthel^{1,2}, Th. E. Weirich³, G. Cox⁴, H. Hibst⁵, A. Thust^{1,2}

¹ PGI-5: Microstructure Research, Forschungszentrum Jülich

² ER-C: Ernst Ruska-Centre for Microscopy and Spectroscopy with Electrons

³ Central Facility for Electron Microscopy, RWTH Aachen University

⁴ BASF SE, Polymer Physics Department, Ludwigshafen

⁵ BASF SE, Chemicals Research and Engineering, Ludwigshafen

The structure of the oxygen sub-lattice in $\text{Cs}_{0.5}[\text{Nb}_{2.5}\text{W}_{2.5}\text{O}_{14}]$ has been investigated for the first time by advanced electron-optical methods. Since the material resembles the crystal structure of the so-called M1 phase of Mo-V-Nb-Te-O, which is the best catalyst for the selective oxidation of propane to acrylic acid, the structure analysis of the oxygen sub-lattice can contribute substantially to a better understanding of this catalytic process.

The crystal structure of $\text{Cs}_{0.5}[\text{Nb}_{2.5}\text{W}_{2.5}\text{O}_{14}]$ resembles strongly the M1 phase of $\text{Mo}_{10}\text{V}_2^{4+}\text{Nb}_2\text{TeO}_{42-x}$, which is the active mass of the hitherto best heterogeneous catalyst for the partial and selective gas-phase oxidation of propane with molecular oxygen to acrylic acid [1]. The main difference between the crystal structures of $\text{Mo}_{10}\text{V}_2^{4+}\text{Nb}_2\text{TeO}_{42-x}$ and $\text{Cs}_{0.5}[\text{Nb}_{2.5}\text{W}_{2.5}\text{O}_{14}]$ is that the channels in the former compound contain Te-ions, while the channels in the latter compound are occupied by Cs-ions.

The crystal structure of $\text{Cs}_{0.5}[\text{Nb}_{2.5}\text{W}_{2.5}\text{O}_{14}]$ was first discovered and characterised by Lundberg and Sundberg in 1993 [2]. According to the latter study, the structure crystallises with a primitive orthorhombic cell with the approximate lattice parameters $a = 2.71$ nm, $b = 2.16$ nm, and $c = 0.394$ nm. The analysis of conventional high-resolution transmission electron micrographs recorded along the [001] direction allowed the previous authors to determine the positions of the heavy atoms within the projected unit cell. Later attempts to measure the so far only estimated oxygen positions by using precession electron diffraction and X-ray powder diffraction failed due to the difficulties to detect the light oxygen atoms in the vicinity of the heavier niobium and tungsten atoms.

Because of the strong interaction of electrons with matter, high-resolution transmission electron microscopy (HRTEM) offers the possibility to investigate the projected atomic structure in objects of extremely small volumes down to the length scale of a few nanometres. HRTEM is therefore a highly beneficial method for the structural analysis of very small crystals present in powder samples. In previous HRTEM studies oxygen columns could be resolved and quantitatively analysed in the proximity of heavier atom columns within perovskite ceramics

by employing spherical aberration correction, which is a hardware technique [3], together with focal-series reconstruction, which is mainly a software technique [4]. Using the reconstruction technique, the systematic errors in the quantification of atom positions, which are frequently caused by unavoidable residual lens aberrations persisting even after hardware correction, can be eliminated effectively by an a-posteriori numerical aberration correction of a reconstructed wave function. The combination of these two electron microscopy techniques is applied in the present investigation in order to determine the oxygen positions in the structure projection of $\text{Cs}_{0.5}[\text{Nb}_{2.5}\text{W}_{2.5}\text{O}_{14}]$ along the short c-axis. The phase of the finally resulting electron wave function at the exit plane of the object is displayed in Fig. 1.

In addition to these electron microscopy techniques two further techniques for the data evaluation are employed: In order to determine the average atom positions in the c-axis projection, the phase of the reconstructed and aberration-corrected electron wave function is subsequently used as input for the crystallographic image processing (CIP) procedure [5]. Within the CIP procedure the best fitting space-group symmetry is determined and finally imposed on a periodic part of the reconstructed wave function, as is shown in Fig. 2. In a further step, first-principles calculations [6] are used to check the consistency of the experimentally determined atom positions with theoretical values and to rule out the influence of surface relaxation effects, which might occur for the very small crystal thickness required by HRTEM in the 1 Ångström resolution regime.

By the application of the aforementioned techniques it is possible to determine the position of atomic columns with high accuracy. The average root-mean-square deviations of the x- and y- atom co-ordinates between experiment and the first-principles calculations amount to less than 9 pm for the nine heavy atoms, and to less than 13 pm for the 27 oxygen atoms of the unit cell [7]. In particular, the positions of the oxygen atoms in the vicinity of the strongly scattering metal atoms can be experimentally quantified, which has not been accomplished before. Additionally, it turns out that the phase of the reconstructed exit-plane wave function reveals remarkable deviations from the

periodic structure, including a possible splitting of oxygen columns [7]. Examples for different types of such deviations from the periodic crystal structure are highlighted in the phase image of Fig. 3.

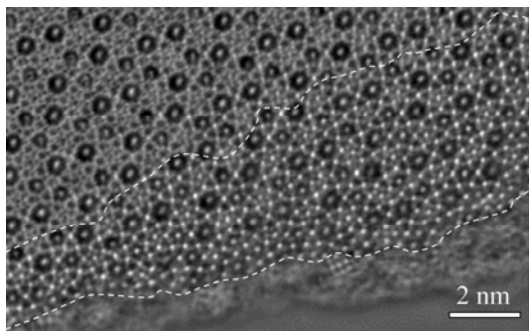


FIG. 1: Phase of the reconstructed and aberration-corrected wave function belonging to a thin region near the crystal edge. The average structure of $Cs_{0.5}[Nb_{2.5}W_{2.5}O_{14}]$ was determined from the area enclosed by the dashed curves. The area is 54.5 nm² large and contains approximately nine projected unit cells.

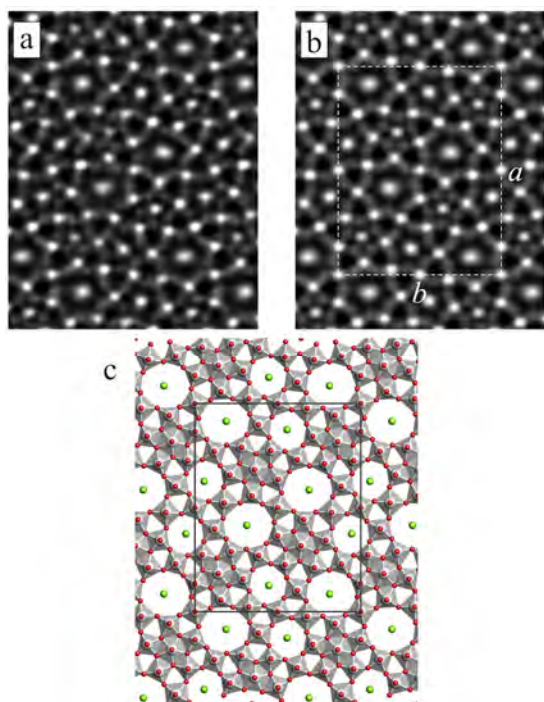


FIG. 2: Crystallographic image processing for $Cs_{0.5}[Nb_{2.5}W_{2.5}O_{14}]$. (a) Phase image obtained by averaging the unit cells within the area displayed in Figure 1. (b) Phase image obtained after imposing additionally p2gg symmetry. The prominent sharp maxima in the map show columns composed of niobium and tungsten atoms, whereas the broader and more diffuse maxima inside the 6- and 7-fold tunnels belong to columns of caesium atoms. The weakest peaks in the map indicate positions of oxygen columns. (c) Structure model as derived from the experimentally determined atom positions in projection along the [001] zone axis. Cs = green; Nb, W = light grey; O = red.

The present study describes a straightforward procedure for the acquisition of quantitative structural information by high-resolution transmission electron microscopy, which yields close-to-picometre accuracy for the determination of atom positions. The chosen combination of HRTEM techniques and data evaluation techniques constitutes a feasible alternative in experimental scenarios where traditional methods like XRD or neutron diffraction cannot be applied for structure analysis.

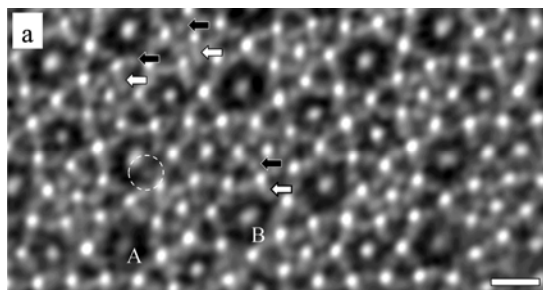


FIG. 3: Enlarged part of the reconstructed phase of Fig. 1 showing the defect structure of $Cs_{0.5}[Nb_{2.5}W_{2.5}O_{14}]$. Whereas the dark arrows point out symmetric and well-separated peaks belonging to oxygen columns, the white arrows highlight elongated peaks which are most likely caused by a splitting of the related oxygen columns. Further structural defects are additional or misplaced atoms in the tunnels, as can be seen in the encircled region. The lower peak height at the caesium position A indicates a site occupancy which is lower than the occupancy at the position B. The scale bar at the lower right corner corresponds to a length of 1 nm.

- [1] H. Hibst, F. Rosowski, G. Cox, Catalysis Today (2006), 117, 234 – 241.
- [2] M. Lundberg, M. Sundberg, Ultramicroscopy (1993), 52, 429 – 435.
- [3] M. Lentzen, B. Jahnen, C.L. Jia, A. Thust, K. Tillmann, K. Urban, Ultramicroscopy (2002), 92, 233 – 242.
- [4] A. Thust, W.M.J. Coene, M. Op de Beek, D. van Dyck, Ultramicroscopy (1996), 64, 211 – 230.
- [5] S. Hovmöller, A. Sjögren, G. Farrants, M. Sundberg, B.O. Marinder, Nature (1984), 311, 238 – 241.
- [6] M. Payne, M. Teter, D. Allen, T. Arias, J. Joannopoulos, Rev. Mod. Phys. (1992), 64, 1045 – 1097.
- [7] J. Barthel, Th. E. Weirich, G. Cox, H. Hibst, A. Thust, Acta Materialia (2010), 58, 3764 – 3772.

The benefit of negative- C_s imaging technique for quantitative HRTEM

C.L. Jia, L. Houben, A. Thust, and J. Barthel

PGI-5: Microstructure Research, Forschungszentrum Jülich and Ernst Ruska Centre

Employing an aberration corrector in a transmission electron microscope, the spherical aberration C_s can be tuned to negative values, resulting in a novel imaging technique: the negative C_s imaging (NCSI) technique. The image contrast obtained with the NCSI technique is compared quantitatively with the image contrast formed with the traditional positive C_s imaging (PCSI) technique. For the case of thin objects negative C_s images are superior to positive C_s images concerning the magnitude of the obtained contrast. As a consequence, the image signal obtained with a negative C_s is significantly more robust against noise caused by amorphous surface layers, resulting in a measurement precision of atomic positions which is by a factor of 2 to 3 better at an identical noise level. The quantitative comparison of the two imaging modes shows that the NCSI mode yields significantly more precise results than the traditional PCSI mode in quantitative high-resolution transmission electron microscopy of thin objects.

The availability of spherical aberration (C_s) correction has opened up a large field of applied materials research for high-resolution transmission electron microscopy (HRTEM). Based on the tunability of C_s , optimum imaging conditions were derived, which provide minimum contrast delocalization and maximum phase contrast at the same time [1]. Under such optimized conditions the point resolution is extended up to the information limit of the instrument. It was found that a high image contrast is obtained when employing a negative value of C_s in conjunction with an overfocus [2]. The related negative C_s imaging (NCSI) mode yields a bright atom contrast for thin objects, and leads to a substantially higher contrast compared to the dark atom images formed under the traditional positive C_s imaging (PCSI) mode.

For quantitative HRTEM it is mandatory to have on the one hand an adequate resolution in order to separate closely spaced atom columns, and to obtain on the other hand a sufficiently strong signal from these columns in order to achieve a high precision for the quantification of the atomic positions. Important conclusions on the selection of the appropriate imaging conditions for quantitative HRTEM can therefore be drawn from a quantitative comparison of the NCSI and the PCSI mode with respect to the obtained contrast and with respect to the resulting measurement precision of atomic column positions.

In the present study [3] we report on the benefit of the NCSI mode for quantitative HRTEM by a direct comparison with the traditional PCSI mode. The influence of the two imaging modes on the strength of the obtained image contrast is investigated quantitatively by means of image calculations. In addition, the precision obtained for the measurement of atom column positions is quantified including the effect of image noise caused by amorphous surface layers. Considering the technological relevance of perovskite materials, we select SrTiO_3 as an exemplary reference material for the image calculations.

Figure 1 shows a thickness series of images calculated for the two alternative imaging modes. The displayed atom symbols clarify that the NCSI mode leads to a bright atom contrast under a darker background. This bright atom contrast is preserved up to an object thickness of $t = 7.7$ nm. In contrast, the traditional PCSI mode results in a dark atom contrast for relatively thin objects ($t < 4.4$ nm), while bright peaks appear at the atom positions for an object thickness larger than 4.4 nm.

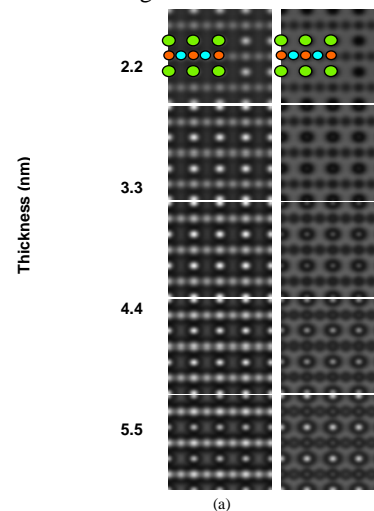


Fig. 1. Thickness series of [110] images of SrTiO_3 calculated for (a) the NCSI mode with $C_s = -15 \mu\text{m}$, defocus of $+6$ nm, and for (b) the PCSI mode with $C_s = +15 \mu\text{m}$, defocus of -6 nm, assuming a microscope information limit of 0.08 nm and an accelerating voltage of 300 kV.

The difference in image contrast between the NCSI and the PCSI mode is already evident from the visual inspection of the two image series of Fig. 1. A key requirement in quantitative HRTEM is the achievement of a good signal-to-noise ratio. The obtainable signal-to-noise ratio depends directly on the image intensity recorded at an atomic column

and determines finally the precision of position and occupancy determinations. The image intensity values for the three types of columns, SrO, Ti, and O are plotted in Fig. 2 for the images with a thickness of 3.3 nm. The solid-line profiles are taken from the images calculated for the NCSI mode and the dashed-line profiles are taken from the images calculated for the PCSI mode. The mean intensity is denoted by a dotted line.

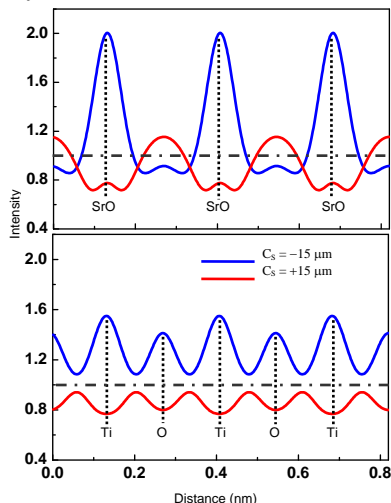


Fig. 2. Image intensity profiles belonging to SrO, Ti and O columns with a thickness of 3.3 nm resulting from the NCSI mode (blue lines) and from the PCSI mode (red lines). Images are normalized to a mean value of 1.

The SrTiO₃ images of Fig. 2 for a crystal thickness of 3.3 nm were selected for investigating the effect of an amorphous layer on the measurement precision. In order to evaluate the effect of different amorphous layer thicknesses, one up to five random phase object images were added to the selected images of the SrTiO₃ crystal as is illustrated in Fig. 3. The resulting precision of the column position determination is shown in Fig. 4 as a function of the number of amorphous layers. The displayed precision values represent twice the standard deviation of the scatter in the peak position of a Gaussian peak profile after a non-linear least squares fit. Overall, the precision obtained for the NCSI mode is by a factor of 2 to 3 better than the results of the PCSI mode.

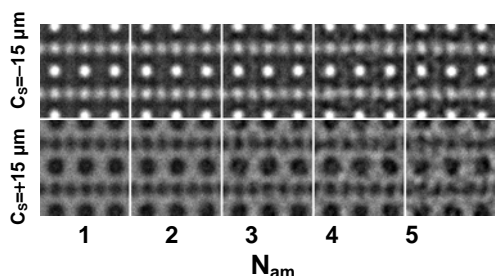


Fig. 3. Modelling of amorphous cover layers. The figure shows various thicknesses of fluctuating amorphous cover layers. The thickness of the amorphous cover layers is given as the number N_{am} of random phase object images added to the crystal image.

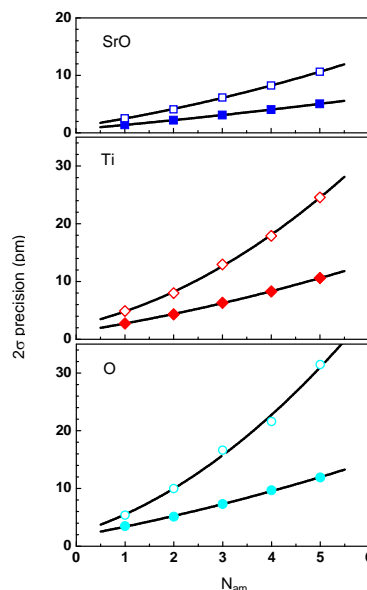


Fig. 4. Measurement precision for the position of SrO, Ti, and O atomic columns obtained with the NCSI mode (solid symbols) and the PCSI mode (open symbols). Each data point corresponds to the repeated measurement on a set of images of 3.3 nm thick SrTiO₃ [110] with stochastically modelled amorphous cover layers. The number N_{am} of random phase object images used to simulate the effect of amorphous cover layers is proportional to the thickness of these layers.

The images obtained by applying the NCSI mode exhibit extraordinary advantages with respect to the overall image contrast and the atom column intensity. In addition, for the NCSI mode the image intensity of all columns follows essentially a linear dependence on the total atomic number accumulated up to a thickness of at least 3.3 nm. Beyond this thickness the linearity is still valid for the lighter Ti- and O-columns, whereas the linearity is lost for the heavier SrO columns due to the shorter extinction length of the latter column type. In the case of the PCSI mode, the linearity between column intensity and the accumulated atomic number is already lost for all column types at a thickness of 3.3 nm.

The NCSI mode in aberration-corrected electron microscopy offers unique advantages for direct atomic imaging in HRTEM. Furthermore, the strong contrast offered by the NCSI mode provides also an excellent basis for quantitative measurements of various local structure properties at lattice defects such as grain boundaries, domain walls, interfaces, and dislocations in electroceramic materials [4,5].

[1] M. Lentzen *et al.*, Ultramicroscopy **92**, 233 (2002).
 [2] C.L. Jia, M. Lentzen, K. Urban, Science **299**, 870 (2003).
 [3] C.L. Jia *et al.*, Ultramicroscopy **110**, 500 (2010).
 [4] C.L. Jia *et al.*, Phys. Rev. Lett. **102**, 117601 (2009).
 [5] A.H. Heuer, C. L. Jia, and K.P.D. Lagerlöf, Science **330**, 1227 (2010).

Selected Publications

1. Chunlin Jia, Shaobo Mi, Knut Urban, I. Vrejoiu, Martin Alexe, and Dietrich Hesse:
Effect of a Single Dislocation in a Heterostructure Layer on the Local Polarisation of a Ferroelectric Layer,
Physical Review Letters **102** (2009) 117601.
2. Matvey Lyatti, Yuri Divin, Ulrich Poppe and Knut Urban:
Liquid identification by Hilbert spectroscopy,
Supercond. Sci. Technol. **22** (2009) 114005.
3. Marc Heggen, Lothar Houben, and Michael Feuerbacher:
Plastic deformation mechanisms in complex solids,
Nature Materials **9** (2010) 332-336.
4. Arthur H Heuer, Chunlin Jia, and K. Peter D. Lagerlöf:
The core structure of basal dislocations in deformed sapphire,
Science **330** (2010) 1227-1231.
5. Juri Barthel, Thomas E. Weirich, Gerhard Cox, Hartmut Hibst, and Andreas Thust:
Structure of Cs[NbWO] analysed by focal-series reconstruction and crystallographic image processing,
Acta Materialia **58** (2010) 3764-3772.
6. Kui Du, Frank Ernst, Michael C. Pelsozy, Juri Barthel, and Karsten Tillmann:
Expansion of interatomic distances in platinum catalyst nanoparticles,
Acta Materialia **58** (2010) 836-845.
7. Philip Ebert, Sarah Schaafhausen, A. Lenz, A. Sabitova, L. Ivanova, U. Dähne, Y.L. Hong, S. Gwo and Holger Eisele:
Direct measurement of the band gap and Fermi level position at InN(1120),
Applied Physics Letters **98** (2011) 062103.
8. Marc Heggen, Lothar Houben and Michael Feuerbacher:
Metadislocations in the complex metallic alloys T-Al-Mn-(Pd, Fe),
Acta Materialia **59** (2011) 4458-4466.
9. Chun-Lin Jia, Knut Urban, Marin Alexe, Dietrich Hesse and Ionela Vrejoiu:
Direct observation of continuous electric dipole rotation in flux-closure domains in ferroelectric Pb(Zr,Ti)O,
Science **331** (2011) 1420-1423.
10. Michael Feuerbacher and Marc Heggen:
Elastic Energy of Metadislocations in Complex Metallic Alloys,
Acta Materialia, **60** (2012) 1703 - 1711.

Indicators

Quantitative Numbers

	2009	2010	2011
Peer-Reviewed Publications	51	39	79
Graduations			
Master/Diploma	1	3	1
Dissertation	0	1	0
Habilitation	0	0	0

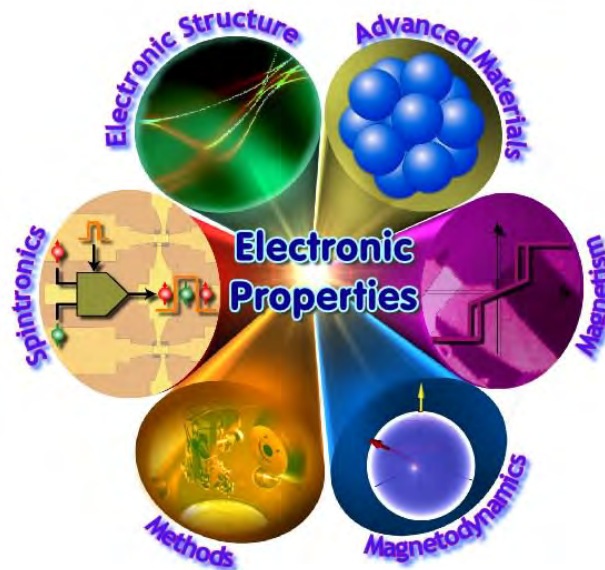
Honours

2011	Wolf Prize in Physics in Anerkennung um ihre Verdienste um die Weiterentwicklung der Elektronenmikroskopie	Knut Urban zusammen mit Harald Rose (TU Darmstadt) und Max Haider (CEOS GmbH Heidelberg)
------	--	--

Selected Third Party Projects

1. ERC (European Research Council)
ERC Advanced Grant INTIF – microstructure characterisation of inorganic fullerenes
Partner: Weizmann Institute et al.
Laufzeit: 2008–2013
2. DFG
Complex Metallic Alloys – Materials Production and Crystal Growth & Plasticity and Defects
Laufzeit: 2010–2013
3. EU-FP7
SILICON-Light – Improved material quality and light trapping in thin film solar cells
Partner: verschiedene
Laufzeit: 2010–2013
4. HGF Impuls- und Vernetzungsfond
Liquid identification by Hilbert spectroscopy for security screening
Partner: IRE der RAS Moskau
Laufzeit: 2011–2014
5. DFG Core Facility Projekt
Das ER-C: nationales Nutzerzentrum für ultrahochauflösende Transmissionselektronenmikroskopie
Partner: RWTH Aachen
Laufzeit: 2012–2015
6. EU-FP7
ESTEEM 2: Enabling Science and Technology through European Electron Microscopy
Partner: verschiedene
Laufzeit: 2012–2016

PGI-6: Electronic Properties



Electronic structures and properties are at the heart of many phenomena in condensed matter physics and material science, and largely determine functionalities in information technology, energy research, and related areas. The overarching theme in PGI-6 is on understanding spin-dependent effects in solid state physics and on advancing the field of spinoelectronics, i.e. exploiting the property spin for controlled transport and transfer processes. This goal is achieved on the basis of a broad portfolio of experimental techniques ranging from spin-resolved electron spectroscopies and microscopies without and with the use of synchrotron radiation to ultrafast laser pump-probe spectroscopies and electrical transport studies at low temperatures and high magnetic fields.

The systems of interest cover a wide range of length scales from magnetic thin film systems via nanostructures down to individual molecules, which are prepared by specialized thin film growth techniques, lithographic procedures and elaborate chemical syntheses. Materials include metal heterostructures, magnetic oxides, and carbon nanostructures. Spin-dependent transport concepts such as spin accumulation, spin-polarized tunneling, spin-transfer torque, pure spin currents, spin injection or spin effects in quantum transport are explored with regard to future spin-based devices. Tailoring magnetic and spin-dependent properties of these systems for spintronics applications requires a thorough understanding of the electronic and magnetic interactions and configurations. This includes particularly spin-dominated coupling phenomena between layers with different types of spin ordering or between molecules and magnetic substrates. With respect to charge/spin transport and transfer phenomena a specific emphasis is laid on the electronic, chemical and magnetic characterization of interfaces and buried layers. For this purpose, new experimental spectroscopy and microscopy techniques using hard x-rays are developed and employed.

Beyond the ground state the dynamic behaviour of spin systems plays a pivotal role. Our studies focus primarily on the nano- to femtosecond regime, thus covering both magnetization and spin dynamics. Particular emphasis lies on the element-selective dynamics in complex magnetic systems, which is addressed by both time-resolved spectroscopy and microscopy techniques. Priority objectives are an understanding of the influence of the various spin-dependent interactions on the spin dynamics, the investigation of optical spin switching themes, the exploration of the ultrafast dynamics in the exchange energy regime using sophisticated optical pump-probe methods and the study of spin excitations at surfaces and in thin films.

Head of Institute:

Prof. Claus M. Schneider, email: c.m.schneider@fz-juelich.de, phone: + 49-2461-61-4428

Scientific Staff

On September 1st 2012, the staff of PGI-6 comprised 10 scientists, 1 junior research group leader, 7 technicians, 7 Post-Docs, 18 PhD students, and 7 Master students.

Scientists

Adam, Dr. Roman
Baumgarten, Dr. L.
Bürgler, Dr. Daniel
Cramm, Dr. Stefan
Grünberg, Prof. Dr. Peter (*Helmholtz Professor*)
Matthes, Dr. Frank
Meyer, Dr. Carola
Schneider, Prof. Dr. Claus Michael
Wiemann, Dr. Carsten

Junior Research Group Leader

Müller, Dr. Martina

Post-Docs

Botar, Dr. Bogdan.
Feyer, Dr. Vitaliy
Kakay, Dr. Attila
Krug, Dr. Ingo
Plucinski, Lukasz
Seemann, Dr. Klaus Michael
Yan, Dr. Ming

Guest Scientists

Suga, Prof. Dr. Shigemasa (*A. v. Humboldt Awardee*)

Visiting Scientists

Besson, Dr. Claire.
Kögerler, Prof. Dr. Paul

Research Highlights

Beating the Walker limit with massless domain walls in cylindrical nanowires

Ming Yan¹, Attila Kakay¹, Sebastian Gliga² and Riccardo Hertel³

¹ PGI-6: Electronic Properties, Forschungszentrum Jülich

² Center for Nanoscale Materials, Argonne National Laboratory, Argonne, IL, USA

³ Institut de Physique et Chimie des Matériaux de Strasbourg, Université de Strasbourg

We present a micromagnetic study on the current-induced propagation of transverse domain walls (DWs) in thin soft-magnetic cylindrical nanowires. Due to the axial symmetry of the wire, these DWs are found to be effectively zero-mass micromagnetic objects. Consequently, they are able to travel arbitrarily fast without encountering the Walker limit, which all the massive DWs are subject to. The propagation of the DW is characterized by a spiraling motion around the wire. Our simulation data are confirmed by an analytical model.

A precisely controlled displacement of magnetic DWs by means of electric currents [1] is essential for the realization of the "race track memory" [2], a promising concept for future magnetic data storage devices. To achieve this, however, there exists a major obstacle, namely, the well-known Walker breakdown[3], which occurs when DWs are driven strongly enough to reach a critical velocity. The DW structure then collapses and undergoes a series of complex cyclic transformations. The Walker limit is thus the maximum velocity at which DWs can propagate without changing their structure. In a broader physical context, the Walker limit is connected to the mass of moving DWs [4]. This concept is based on the analogy between the energy increase of a moving DW, arising from the distortion of its structure, to kinetic energy of a moving object. Moving DWs in thin magnetic strips in fact display particle-like behaviour, including momentum and inertia. As the DW velocity increases, the energy continues to increase until it reaches a limit where Walker breakdown takes place. A DW would be massless if its structure did not change during its motion. We show that such massless DWs indeed exist, namely, transverse walls in thin cylindrical nanowires [5]. The vanishing DW mass leads to astounding dynamic properties, such as the absence of Walker limit and intrinsic pinning.

A transverse DW formed in a 10 nm diameter cylindrical Py wire compared to a transverse wall in a 100 nm wide strip of 10 nm thickness (up-right).

Using a finite-element method, we perform micromagnetic study on the dynamic properties of such DWs by numerically solving the Gilbert equation with additional spin transfer torque terms:

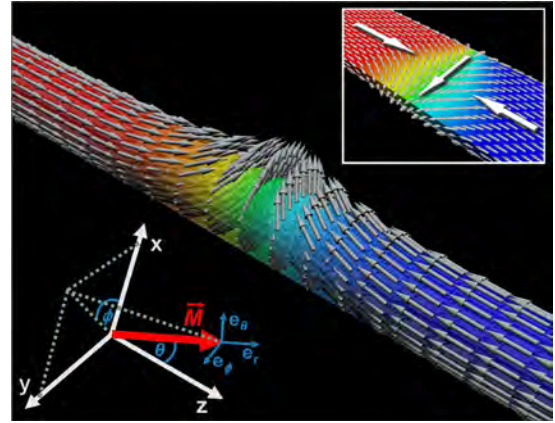


FIG. 1: A transverse DW formed in a 10 nm diameter cylindrical Py wire compared to a transverse wall in a 100 nm wide strip of 10 nm thickness (up-right).

$$\frac{d\vec{m}}{dt} = \gamma \vec{H}_{\text{eff}} \times \vec{m} + \frac{\alpha}{M_s} \left[\vec{m} \times \frac{d\vec{m}}{dt} \right] - (\vec{u} \cdot \vec{\nabla}) \vec{m} + \frac{\beta}{M_s} \vec{m} \times [(\vec{u} \cdot \vec{\nabla}) \vec{m}], \quad (1)$$

where \vec{m} is the normalized local magnetization, M_s the saturation magnetization, γ the gyromagnetic ratio, \vec{H}_{eff} the effective field, α the Gilbert damping factor, β the non-adiabatic spin transfer parameter. The vector \vec{u} is defined as $\vec{u} = -\frac{g \mu_B P}{2 e M_s} \vec{j}$, where \vec{j} is the current density, g is the Landé factor, μ_B the Bohr magneton, e the electron charge and P the polarization rate of the current. Typical material parameters of Permalloy (Py) are used in the simulation. Figure 1 shows the simulated configuration of a transverse wall in a 4 μm cylindrical wire with 10 nm diameter. Due to the axial symmetry, the structure of the wall and its energy are invariant with respect to rotations of the magnetization in the xy plane.

An electrical current along $+z$ displaces the DW towards the $-z$ direction, i.e., in the electron flow direction. In addition to the linear motion the DW rotates about the axis of the wire, as illustrated schematically in Fig. 2.

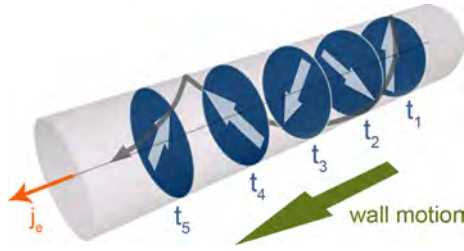


FIG 2. Schematic illustration of the current-driven DW motion. The blue cross-sections indicate the position of the wall plane at successive moments in time, while the arrows represent the orientation of the transverse magnetization.

In the simulations, α is set to 0.02 while the value of P varies. The DW velocity as a function of the current density J is plotted in Fig. 3a in a 10 nm diameter cylindrical wire for different values of β . The inset a_2 of Fig. 3 displays the lower range of J , as typically used in experiments. The results show that the velocity depends linearly on J and is independent of β . For comparison, we simulated the DW motion in a thin strip using the same parameters (inset a_1 of Fig. 3). The cylindrical wire displays several fundamental differences. First, there is no intrinsic pinning when $\beta=0$, while in the case of the strip a minimum (critical) current density must be injected to initiate the DW motion.

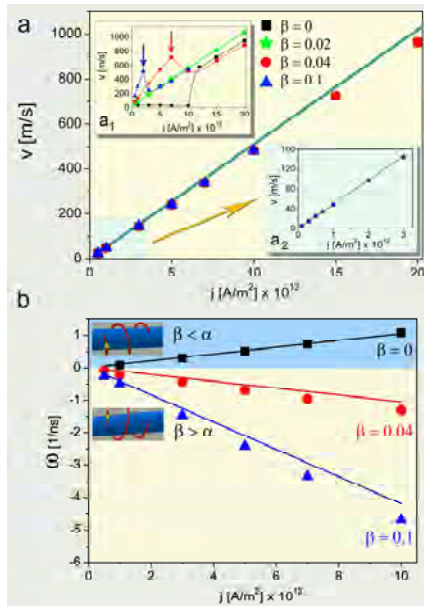


Fig. 3. Simulated DW linear velocity (a) and angular velocity (b) as a function of the current density j with $\alpha = 0.02$ and different values of β in the case of a 10 nm round Py wire. Inset (a1): Simulated DW dynamics in a 100 nm wide and 10 nm thick strip. Inset (a2): closeup of the data for lower values of j . The lines display analytic values.

Secondly, the DWs in the round wire behave like massless objects, i.e., their profile does not change during the motion. Correspondingly, there is no Walker breakdown in the case of the cylindrical wire. In the strip, however, the Walker limit occurs when $\beta > \alpha$, as indicated by the arrows in the inset a_1

of Fig. 3. Thirdly, the DW velocity does not depend on β in the cylindrical wire. The DW reaches a constant velocity immediately after the application of the current and stops immediately after the current stops, which is consistent with the absence of mass and inertia. The characteristics of the angular dynamics are summarized in Fig. 3b. The angular velocity shows a linear dependence on J and is found to be proportional to $(\beta - \alpha)$. We also adopt an analytical model to study the DW dynamics for this particular geometry. A spherical coordinate system is used as shown in Fig. 1. by the good agreement between the analytical model and simulations. For simplicity, we first consider the field-driven motion. In the case of the cylindrical wires, the demagnetizing field effect, which plays a significant role in DW dynamics in flat strips, vanishes due to the axial symmetry. The DW motion therefore can be easily solved, in the current-driven case yielding with

$$\dot{\theta} = -\frac{(1 + \alpha\beta)u_z}{1 + \alpha^2} \frac{\partial \theta}{\partial z} \Big|_{wc} \quad (2)$$

$$\dot{\phi} = \frac{(\beta - \alpha)u_z}{1 + \alpha^2} \frac{\partial \theta}{\partial z} \Big|_{wc}, \quad (3)$$

where the subscript WC denotes the DW center. The linear velocity of the DW, given by $v = \dot{\theta} \cdot \partial z / \partial \theta$, is basically equal to u [plotted as a line in Fig. 3a] and independent on β . The angular velocity of the DW, given by $\dot{\phi}$, is proportional to $(\beta - \alpha)$. Clearly, the non-adiabatic term only affects the rotational motion of the DW. Given the symmetry of the wire, the DW is free to rotate without any deformation, resulting the massless behaviour of the DW. The dependence of the frequency of the DW rotation on the difference between α and β provides a possibility for the measurement of the non-adiabatic spin transfer torque term β , which is generally difficult to determine. Also, the polarization rate P can be determined from the current-driven DW velocity, which in this case is almost exactly equal to u (cf. Fig. 3).

In conclusion, transverse DWs in cylindrical nanowires has a unique dynamic property, namely, being effectively massless. Such inertia-free DWs show particular dynamic properties which should allow one to precisely and efficiently control their position with electric currents and to extract important physical parameters.

- [1] L. Berger, Phys. Rev. B , 1572 (1986).
- [2] S.S.P. Parkin, M. Hayashi, and L. Thomas, Science , 190 (2008).
- [3] N.L. Schryer, and L.R. Walker, J. Appl. Phys. , 5406 (1974).
- [4] W. Döring, Z. Naturforsch. a, 373 (1948).
- [5] M. Yan, A. Kákay, S. Gliga, and R. Hertel, Phys. Rev. Lett. 057201 (2010).

Breathing-like modes in an individual multi-walled carbon nanotube

C. Spudat¹, M. Müller², L. Houben^{3,4}, J. Maultzsch², K. Goß¹, C. Thomsen², C. M. Schneider¹, C. Meyer¹

¹ PGI-6: Electronic Properties, Forschungszentrum Jülich

² Institut für Festkörperphysik, Technische Universität Berlin

³ PGI-5: Microstructure Research, Forschungszentrum Jülich

⁴ ER-C: Ernst Ruska-Centre

We studied collective vibrational breathing modes in the Raman spectrum of a multi-walled carbon nanotube. Correlating the results obtained by spectroscopy with high-resolution transmission-electron microscopy, we found that these modes have energies differing by more than 23% from the radial breathing modes of the corresponding single-walled nanotubes. This shift in energy can be explained with inter-shell interactions using a model of coupled harmonic oscillators. The strength of this interaction can be related to the coupling strength expected for few-layer graphene.

Multiwalled carbon nanotubes (MWCNTs) can be imagined as multiple graphene sheets rolled up in tubes, which are embedded into one another (inset FIG. 1). This material is interesting for application in nanoelectromechanical devices [1]. It is crucial for this purpose, however, to understand and measure the coupling between the nanotube shells. This coupling is caused by inter-shell interactions, and Raman spectroscopy is a versatile tool to study the nature of this coupling. Its strength shows up in the movement of the layers and shells against each other. Unfortunately, the corresponding inter-layer mode in graphite, the B_{2g} mode, is silent in infrared as well as in Raman spectroscopy. In multi-walled carbon nanotubes (MWCNTs), however, the corresponding vibrational motion has its origin in the radial breathing modes (RBMs) of the nanotube walls, which can be observed with Raman spectroscopy. Thus, carbon nanotubes can be seen as a model system for few-layer graphene.

Raman spectroscopy provides only indirect information of the atomic structure of CNTs. A correlation of aberration-corrected high-resolution electron-transmission microscopy (HR-TEM) and spectroscopy measurements on the same CNT significantly helps to interpret the low-frequency Raman spectrum experimentally observed [2].

MWCNTs were synthesized by chemical vapor deposition on a grid suitable for HR-TEM. The grid was prepared with a marker structure in order to identify individual tubes for the spectroscopic and microscopic measurements.

The HR-TEM image (inset FIG. 1) reveals that this MWCNT is composed of six walls. The shell

diameters of the tubes range from $d = 0.84$ nm for the innermost tube to $d = 4.34$ nm for the outermost tube. The distance between two shells is constant within the error of the measurements and $\Delta r = 0.35$ nm. We compare the diameters obtained in the HR-TEM measurement to the energy of the resonant Raman modes in the low-frequency spectrum. Usually, these resemble the RBMs of single walled carbon nanotubes and depend on the diameter of the tubes.

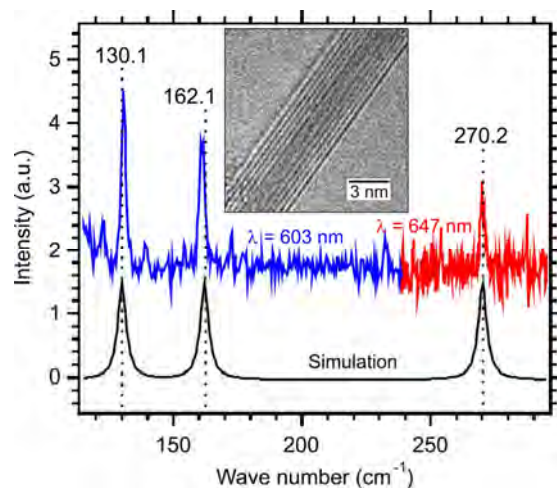


FIG. 1: Low-frequency Raman spectrum of the MWCNT measured at two different wavelengths (blue and red line) and its simulation. Inset: HR-TEM micrograph of the same MWCNT. The nanotube shells appear bright.

Frequency dependent Raman measurements of the same MWCNT are shown in FIG. 1. They were performed prior to the HR-TEM imaging in order to avoid any influence of defects that might be induced by electron irradiation. We observe three modes, which exhibit a strong resonance effect as expected for RBMs. Furthermore, their line width is 3-cm^{-1} , a typical value for RBMs of SWCNTs. Therefore, we assume that these peaks have their origin in the breathing modes of the tubes, which form the MWCNT.

The Raman shifts ω_{Raman} of the modes observed can be compared with the diameters obtained in the HR-TEM measurements using the relation

$$\omega_{\text{RBM}} = \frac{A}{d_{\text{T}} + B}$$

to convert the tube diameters d_{T} into Raman shifts ω_{RBM} as they would be expected for individual single-walled carbon nanotubes. A and B are sample-dependent constants, which are chosen to be $A = 223.75 \text{ cm}^{-1}$ and $B = 0$ for tubes without any additional interactions as suggested by Bandow et al. [3]. The results for the expected Raman shifts are listed in TAB. 1. Strong shifts toward higher wave numbers are found in the experiment for the second and especially for the third inner tube, where the mode is shifted by more than 23% with respect to the RBM position expected from the HR-TEM measurement.

tube no.	$d_{\text{T}}(\text{nm})$	$\omega_{\text{Raman}} [\text{cm}^{-1}]$	$\omega_{\text{RBM}} [\text{cm}^{-1}]$	$\omega_{\text{BLM}} [\text{cm}^{-1}]$
1	0.84	270	266.4	270.9
2	1.54	161	145.3	162.1
3	2.24	131	99.9	130.1
4	2.94		76.1	117.4
5	3.64		61.5	94.7
6	4.34		51.6	62.0

TAB. 1: Comparison of the measured Raman shifts and the simulated BLM-frequencies.

We have shown that the stiffening of the Raman modes can be explained by means of a coupling of the phonon modes due to van der Waals interactions between the walls of the MWCNT using a model of coupled harmonic oscillators [2].

In FIG. 1 the experimentally obtained spectra are compared with the position of the Raman modes obtained from the simulation. The best agreement between simulated and measured Raman shifts is found at a coupling frequency of $\Omega_{\text{c}} = 1.84 \text{ THz}$, which is a measure for the coupling strength. It will reach the inter-layer coupling of graphite $\Omega_{\text{c}} = 3.81 \text{ THz}$ for $d_{\text{T}} \rightarrow \infty$ and infinite number of shells. The

values obtained for the Raman shifts ω_{BLM} of the BLMs reflect the experimental data very well (see TAB. 1). And therefore, coupled breathing-like modes (BLMs) as predicted by Popov et al. [4] are observed rather than individual RBMs.

We could unambiguously attribute the Raman mode at $\omega_{\text{Raman}} = 270 \text{ cm}^{-1}$ to the counter-phase BLM, while the modes at $\omega_{\text{Raman}} = 161 \text{ cm}^{-1}$ and at $\omega_{\text{Raman}} = 131 \text{ cm}^{-1}$ are the first two BLMs of mixed modes. Three more modes are expected to be observed at $\omega_{\text{BLM}} = 117 \text{ cm}^{-1}$, at $\omega_{\text{BLM}} = 95 \text{ cm}^{-1}$ and at $\omega_{\text{BLM}} = 62 \text{ cm}^{-1}$ following the model. These modes do not show up in our measurements, because they are masked by the edge of the Rayleigh peak.

We conclude that the inter-layer coupling in MWCNTs cannot be neglected. The coupling strength we obtain from the model to be $\Omega_{\text{c}} = 1.84 \text{ THz}$ is smaller than expected. Calculations for few-layer graphene [5] predict values which are smaller than for graphite but $\Omega_{\text{c}} > 3 \text{ THz}$. In order to understand this deviation and also possible influences of the curvature, a model would be needed that includes the Van der Waals interaction explicitly.

-
- [1] Barreiro, R. Rurali, E. R. Hernández, J. Moser, T. Pichler, L. Forró, A. Bachtold, *Science* 320, 775 (2008)
 - [2] Spudat, M. Müller, L. Houben, J. Maultzsch, K. Goß, C. Thomsen, C. M. Schneider, C. Meyer, *Nano Lett.* 10, 4470 (2010)
 - [3] S. Bandow, S. Asaka, Y. Saito, A. M. Rao, L. Grigorian, E. Richter, P. C. Eklund, *Phys. Rev. Lett.* 80, 3779 (1998)
 - [4] V. Popov, L. Henrard, *Phys. Rev. B* 65, 235415 (2002)
 - [5] X. Q. He, S. Kitipornchai, K. M. Liew, *Nanotechnology* 16, 2086 (2005)

Dynamics of spin-torque oscillators in vortex and uniform magnetization state

R. Lehndorff¹, D. E. Bürgler¹, S. Gliga¹, R. Hertel¹, P. Grünberg¹, C. M. Schneider¹, Z. Celinski²

¹ PGI-5: Electronic Properties, Forschungszentrum Jülich

² Center for Magnetism and Magnetic Nanostructures, University of Colorado at Colorado Springs, USA

Current-driven magnetization dynamics in spintorque oscillators (STO) has a high potential for high-frequency (HF) applications. We experimentally study current-driven HF excitations of STOs in the vortex and uniform in-plane magnetized state. Our ability to switch between these two states in a given STO enables a direct comparison of the STO characteristics. We find that the vortex state maximizes the emitted HF power and shows a wider frequency tuning range.

Spin-torque oscillators (STO) based on ferromagnet/non-magnet/ferromagnet ($\text{FM}_{\text{fixed}}/\text{NM}/\text{FM}_{\text{free}}$) layered structures are an application of current-induced magnetization dynamics. They show a steady precession of the magnetization of FM_{free} under the action of a spin-polarized DC current. This precession generates via the giant or tunnel magnetoresistance (GMR, TMR) effect a HF voltage oscillation with frequencies in the GHz range, which can be tuned by the DC current amplitude and the external magnetic field strength. Still, one drawback of STOs is their low output power. Several groups work on the synchronization of arrays of STOs in order to achieve useful power levels. While this is a very promising approach, maximizing the output power of every single STO is undeniably the first step to do.

There are several possible arrangements for STOs, e.g. with in-plane, out-of-plane, or vortex-type magnetized FM_{fixed} and/or FM_{free} . Comparing the characteristics of HF excitations – especially output power – from different experiments is not conclusive, because impedance and absolute resistance variations of the samples strongly influence the detected power. Here, we study HF excitations in two mentioned arrangements that we are able to realize in the same STO. While FM_{fixed} is uniformly in-plane magnetized, FM_{free} is either uniformly in-plane magnetized or in a vortex state. The direct comparison shows some advantages of the vortex state for the application of STOs [1].

Samples are fabricated by depositing 150nm Ag/ 2nm Fe/ 6nm Ag/ 20nm Fe/ 50nm Au by molecular beam epitaxy on GaAs(100). The nanopillars are defined by electron beam lithography and ion beam etching and have a circular cross section with a diameter of 230 nm. Only the top magnetic layer (FM_{free}) is laterally confined, while the bottom layer (FM_{fixed}) In our study we applied the ALD technique to is extended with a typical width of 15 μm (see

inset in Fig. 1). The dimensions of FM_{free} are in a regime where a magnetic vortex and a uniform inplane magnetization are both stable states [2]. The 2 nm-thick FM_{fixed} is uniformly magnetized on length scales much larger than the pillar diameter as long as a small magnetic field suppresses domain formation.

Figure 1 shows current-perpendicular-plane (CPP) GMR curves at 10 K with the magnetic field applied in the sample plane. Starting from saturation at 150mT (blue curve) FM_{free} and FM_{fixed} undergo a gradual change from parallel to antiparallel alignment due to stray field interaction. The completely antiparallel alignment is reached at 0mT and results in a high resistance. FM_{free} shows a uniform in-plane magnetization in this field range. After field reversal at about -20mT in the formation of a vortex in FM_{free} results in a drop of the resistance. Upon further sweeping the field, the vortex core is moved from the center of the disk to the rim until it is expelled at about -100 mT. Micromagnetic simulations qualitatively reproduce this behavior as shown by the magnetization patterns in Fig. 1 (for more details see [1]).

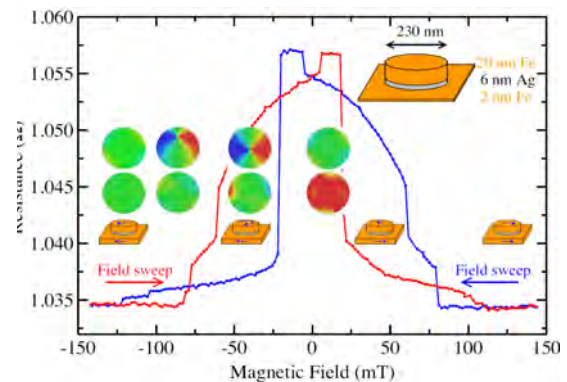


FIG. 1: CPP-GMR curves for increasing and decreasing field. Symbols and simulated micromagnetic magnetization patterns for FM_{fixed} (bottom) and FM_{free} (top) correspond to the decreasing (blue) sweep direction.

Figure 2 shows current-induced CPP resistance changes at 10 K and various field strengths. The initial states were prepared by magnetic field sweeps according to Fig. 1. We observe hysteretic switching of FM_{free} (e.g. green and red curves). The highresistive state at positive currents corresponds to uniformly and antiparallely aligned magnetizations in FM_{free} and FM_{fixed} , whereas the low-resistive state at negative currents is due to the vortex state in

FM_{free} . This is in agreement with previous experiments on Fe/Ag/Fe nanopillars [3], which have established that the spin-transfer torque due to a positive current acts towards an antiparallel alignment. The fact that we do not observe a switching to the vortex state at positive currents in Fig. 2 proves that the prevalent torque in the switching processes does not originate from Oersted fields. These circumferential fields tend to switch the magnetization of FM_{free} into a vortex state also at positive currents, just with the opposite vorticity compared to negative currents.

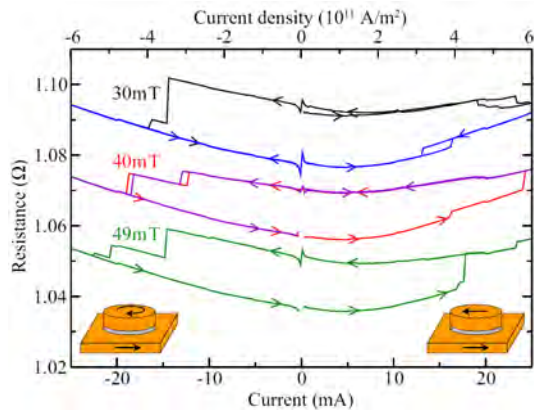


FIG. 2: Current-induced switching between the low-resistive vortex and high-resistive uniform state. The black and purple curves start in the uniform state, all others in the vortex state. For clarity the graphs measured at 40 and 30mT are offset by +20 and +40mΩ, respectively.

We measure DC current-induced HF excitations of the magnetization at room temperature by amplification and detection of voltage oscillations across the nanopillar using a microwave probe station. The voltage variation arises from the GMR of the Fe/Ag/Fe stack, which reaches 2% or 22mΩ in Fig. 1. The impedance of our sample was 11 Ω at 1.5 GHz. Figure 3(a) shows the HF response of a STO in the uniform state measured in an in-plane field of 82 mT. The low frequencies of the excitations are the result of the cancellation of the dipolar coupling field of about 80mT by the external field and the rather large size of the element, for which the standing-wave mode has a low frequency. The observed blue-shift behavior at low currents can be interpreted in terms of standingwave modes, which are deformed by the Oersted field. At higher currents the red-shift sets in that is explained by a predominantly homogeneous in-plane precession of the magnetization. Figure 3(b) shows representative HF excitations of a STO in the vortex state. Here, the gyrotropic mode [4] of the vortex is excited as previously reported by Pribiag et al. [5]. The gyrotropic mode is the lowest excitation mode of a magnetic vortex and consists of a circular motion of the vortex core around the equilibrium position. The radius of the trajectory is proportional to the excitation amplitude. When for increasing current the trajectory approaches the rim of the disk, the vortex experiences a stronger restoring force, increasing its precessional frequency. This results in a linear

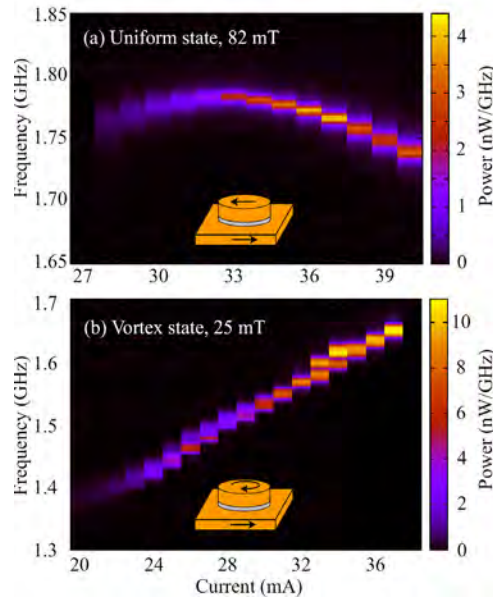


FIG. 3: Spin-transfer torque induced excitation of qualitatively different oscillatory modes in a STO: (a) Standingwave mode in the uniform state and (b) gyrotropic mode of the vortex state. The microwave power generated by the gyrating vortex for a given DC current in (b) is much higher than for the standing-wave mode in (a).

increase of the frequency yielding a mode agility of +17 MHz/mA [Fig. 3(b)]. At each spot within the trajectory of the vortex core, the magnetization rotates during one period of the gyrotropic cycle by full 2π about the sample normal. Thus, for a vortex core moving on a trajectory close to the rim of the sample the product of oscillation amplitude times area, where oscillations take place, is maximized. As a consequence, the emitted power of the STO in the vortex state is nearly three times the power emitted in the uniform state (Fig. 3).

In conclusion, we directly compared the characteristics of a STO in either the uniform state or the vortex state. Higher agility, wider tuning range, and higher output power are all advantageous for the application of the vortex state in STOs. Although this conclusion is derived from metallic, GMR-type STOs, our generic, micromagnetic arguments are also valid for the technologically more relevant TMR-based STOs.

- [1] R. Lehnorff, D. E. Bürgler, S. Gliga, R. Hertel, P. Grünberg, C. M. Schneider, and Z. Celinski, Phys. Rev. B **78**, 054412 (2009).
- [2] R. P. Cowburn, J. Phys. D: Appl. Phys. **33**, R1 (2000).
- [3] R. Lehnorff, M. Buchmeier, D. E. Bürgler, A. Kakay, R. Hertel, and C. M. Schneider, Phys. Rev. B **76**, 214420 (2007).
- [4] K. Y. Guslienko, B. A. Ivanov, V. Novosad, Y. Otani, H. Shima, and K. Fukamichi, J. Appl. Phys. **91**, 8037 (2002).
- [5] V. S. Pribiag, I. N. Krivorotov, G. D. Fuchs, P. M. Braganca, O. Ozatay, J. C. Sankey, D. C. Ralph, and R. A. Buhrman, Nature Physics **3**, 498 (2007)

Injection locking of the gyrotropic vortex motion in a nanopillar

R. Lehndorff¹, D. E. Bürgler¹, P. Grünberg¹, C. M. Schneider¹, Z. Celinski²

¹ PGI-6: Electronic Properties, Forschungszentrum Jülich

² Center for Magnetism and Magnetic Nanostructures, University of Colorado at Colorado Springs, USA

Spin-torque oscillators (STO) are a promising application for the spin-transfer torque effect. The major challenge is to increase the microwave output power by synchronizing an array of STOs. We study the effect of external high-frequency signals on the current-driven vortex dynamics and demonstrate injection locking of the gyrotropic mode as a prerequisite for STO synchronization.

The action of spin-polarized currents on a magnetic system – the spin-transfer torque – offers a novel handle on magnetization dynamics. One of the potential applications is seen in spin-torque oscillators (STO). These are pillar-shaped structures with a "fixed" magnetic layer acting as a polarizer for the electric current and a second "free" magnetic layer the magnetization of which oscillates under the impact of the spin-polarized current. The magnetoresistive response due to giant or tunnelling magnetoresistance (GMR, TMR) in the magnetic layered structure turns the nanometre-scaled STO structures into sources for high-frequency (HF) signals in the GHz range. The HF is tunable via the direct current (DC) and the external magnetic field. However, the HF output power of an STO is presently far too low for applications. Ongoing research aims at strategies to significantly increase the output power. The excitation of an array of STOs in a synchronized, phase-locked manner is believed to deliver a significant power increase, as N coherently coupled STOs emit up to the N^2 -fold power. The required STO-STO coupling can be achieved in two ways. The first mechanism involves spin waves in a common ferromagnetic layer. However, this interaction is short-range due to the fast decay of spin waves and requires a STO-STO separation clearly below $1\ \mu\text{m}$. The second coupling mechanism via microwaves propagating in common electrodes permits a larger STO separation, because electrical microwave signals propagate with negligible losses over long distances. Experimentally, this situation can be addressed by injection locking experiments [1], which study the interaction of a STO with an externally applied HF signal. Here we demonstrate phase-locking of the DC current-driven gyrotropic vortex motion in a vortex STO to external HF signals, and derive from the HF amplitude dependence of the locking criteria for the required STO output power for synchronization [2]. We fabricate cylindrical pillars of 230nm diameter by optical and e-beam lithography from multilayers of Ag 150 nm/Fe 2 nm/Ag 6 nm/Fe 20 nm/Au 50nm

grown by molecular beam epitaxy. The upper Fe layer and the Au cap form the pillar, while the remaining Ag/Fe/Ag layers constitute the bottom electrode (inset of Fig. 1). The electrode layout allows for contacting by two microwave probes via coplanar waveguides. One is used to inject a DC current and an HF current (f_{ext}) from a network analyzer. The second probe is connected to a 30 dB amplifier and a spectrum analyzer (see Fig. 2). In Fig. 1 we compare GMR measurements with corresponding micromagnetic simulations. The quasi-uniform onion state occurs when the field is reduced after saturation and the vortex state nucleates at low fields after field reversal. The magnetization of the extended layer is saturated along an easy axis for fields larger than 20 mT [3]. Thus, we are able to prepare a vortex state in the nanodisk while the magnetization of the extended layer is saturated along a magnetic easy axis of bcc Fe, e.g. by applying +25 mT after negative saturation. Positive DC currents (i.e. electron flow from the nanomagnet to the extended layer) excite the vortex state by spin-transfer torque into the gyrotropic mode that shows up as an HF voltage signal of about 1 GHz due to the GMR response of the Fe/Ag/Fe trilayer. By adding a HF component to the driving current we are able to demonstrate phase-locking of the DC current-

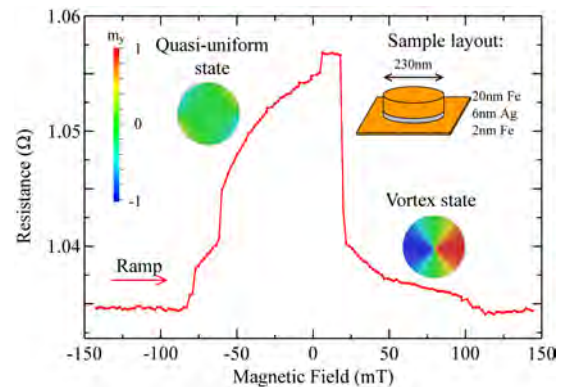


FIG. 1: CPP-GMR in comparison with micromagnetic calculations of the magnetization structure in the nanodisk. Inset: Sample layout.

induced gyrotropic motion to electric HF signals even if they are slightly out of tune. Figure 2 shows a measurement, where the vortex was excited by a current of 32 mA to a frequency of $f_{\text{osc}}=1.518\ \text{GHz}$, while an external signal of -17 dBm or 20 μW was swept from $f_{\text{ext}}=1.35$ to 1.7 GHz. This leads to a clear shift of the vortex frequency f_{osc} between 1.42 and

1.61 GHz. From 1.46 to 1.57GHz f_{osc} is completely locked to the external signal f_{ext} and is thus masked by it. In order to evaluate the synchronization behaviour we fit the frequency variation f_{osc} of the forced vortex motion with the frequency f_{ext} of the

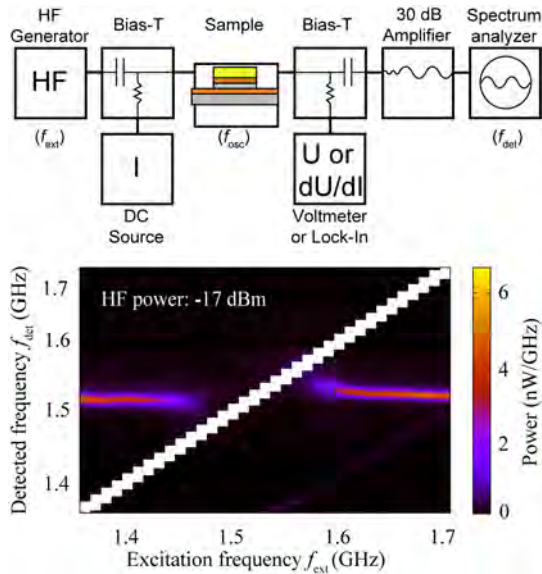


FIG. 2: Setup for injection locking and power spectra (f_{det} , vertical axis) of the current-induced gyrotropic mode as a function of HF excitation frequency (f_{ext} , horizontal axis). The power at f_{ext} exceeds the colour scale and appears as a diagonal white line.

injected HF signal to a formula derived by Slavin and Tiberkevich for nonlinear oscillators [Eq. (48b) of Ref. [4]]:

$$f_{osc} = f_{ext} + \text{sign}(f_0 - f_{ext}) \sqrt{(f_0 - f_{ext})^2 - \Delta^2}, \quad (1)$$

where $f_0 = f_{osc}(I_{HF}=0)$ is the frequency of the free-running vortex STO and Δ is the phase-locking range. An example of a fit is shown in the inset of Fig. 3. The main figure shows an increase of Δ with increasing amplitude of the external signal in accordance with the linear dependence predicted by Slavin and Tiberkevich [4]. However, the linear extrapolation to zero excitation amplitude (dashed line in Fig. 3) yields a non-vanishing locking range of about 18 MHz. This inconsistency may arise from the assumption of weak excitation in the theoretical model. Figure 4 shows the locking behaviour of the vortex STO when excited by a fixed DC current of 32 mA and an external 1.55 GHz signal of variable amplitude. For weak excitation the STO is not influenced and emits at its free-running frequency $f_0 \approx 1.52$ GHz. With increasing HF amplitude the STO tends to adjust to the external frequency and phase-locks for excitation amplitudes exceeding -18 dBm. We estimate the external HF power at -18 dBm reaching the pillar to be of the order of 1.3 μ W and the microwave power generated by the vortex STO to roughly 0.4 nW. This low value is related to the low absolute resistance and GMR ratio, which result in small resistance changes induced by the magnetization dynamics. Consequently, the output power of our GMR-based vortex STO is about 3

orders of magnitude too small to phase-lock another vortex STO.

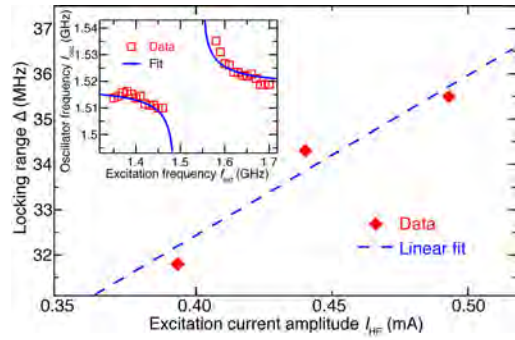


FIG. 3: Locking range Δ as a function of the external HF excitation amplitude. Inset: Fit of Eq. (1) to the locking behaviour for $I_{DC}=32$ mA and -16 dBm

Under these conditions synchronization of an array of vortex STOs seems unlikely, unless the output power of each single STO is significantly increased, e.g. by employing highly spin-polarized ferromagnetic electrode materials (Heusler alloys) or TMR structures with much larger MR ratios.

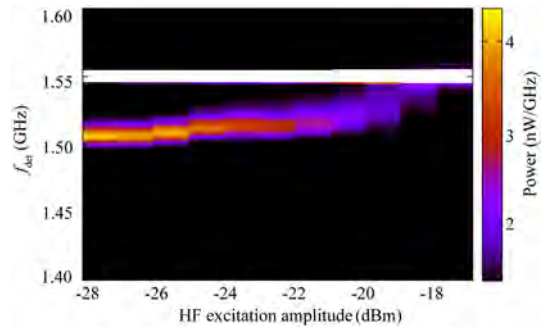


FIG. 4: Locking behaviour of a vortex STO as a function of the HF excitation amplitude at $f_{ext}=1.55$ GHz and $I_{DC}=32$ mA. Locking occurs at about -18 dBm.

In conclusion, we demonstrated phase-locking of the current-driven vortex motion in an STO to an external HF signal, being a prerequisite for the synchronization of vortex STOs. The relative locking range $2\Delta/f_0 \approx 5\%$ allows for a distribution of free-running frequencies in a STO array, which seems compatible with present fabrication technology. The power requirements for synchronization, however, call for STOs with much higher output power.

- [1] W. H. Rippard, M. R. Pufall, S. Kaka, T. J. Silva, S. E. Russek, and J. A. Katine, Phys. Rev. Lett. 95, 067203 (2005).
- [2] R. Lehdorff, D. E. Bürgler, C. M. Schneider, and Z. Celinski, Appl. Phys. Lett. 97, 142503 (2010).
- [3] R. Lehdorff, D. E. Bürgler, S. Gliga, R. Hertel, P. Grünberg, and C. M. Schneider, Phys. Rev. B 80, 054412 (2009).
- [4] A. Slavin and V. Tiberkevich, IEEE Trans. Magn. 45, 1875 (2009).

Electronic structure of a magnetic oxide directly on silicon

M. Müller¹, C. Caspers¹, A. X. Gray², A. M. Kaiser^{1,2}, A. Gloskowskii³, C. S. Fadley², W. Drube⁴, C. M. Schneider¹

¹ PGI-6: Electronic Properties, Forschungszentrum Jülich

² Department of Physics, University of California Davis, Davis, CA 95616, USA

³ Institut für Analytische und Anorganische Chemie, Johannes Gutenberg-Universität, 55128 Mainz

⁴ DESY Photon Science, Deutsches Elektronen-Synchrotron, 22603 Hamburg

We present an electronic structure study of a magnetic oxide/semiconductor model system, EuO on Silicon, which is dedicated for efficient spin injection and detection in silicon-based spintronics devices. A combined electronic structure analysis of Eu core levels and valence bands using hard x-ray photoemission spectroscopy was performed to quantify the nearly ideal stoichiometry of EuO “spin filter” tunnel barriers directly on silicon, and the absence of silicon oxide at the EuO/Si interface. These results provide evidence for the successful integration of a magnetic oxide tunnel barrier silicon, paving the way for the future integration of magnetic oxides into functional spintronics devices.

Accenting semiconductor electronics with spin functionality is a major thrust of current spintronics research. At present, considerable efforts are being made to replace conventional ferromagnet/semiconductor (FM/SC) or FM/oxide/SC contacts - which have hitherto been underlying many key experiments - with functional magnetic contact materials that could substantially alter the efficiency of spin injection and detection in semiconductor-based spintronics devices. In particular, magnetic oxides (MO) offer the unique combination of both generating almost fully spin polarized tunnel currents via a true “spin filter” effect and facilitating a conductance matched magnetic tunnel contact to a SC. Establishing MO tunnel contacts as efficient spin injectors and detectors bears large potential for ultimately realizing both high current transfer ratios *and* high magnetic sensitivities at the CMOS level, i. e. directly on Si.

With the goal to integrate ultrathin films of magnetic oxide as efficient spin-selective tunnel barriers directly on silicon, we present a study of the electronic properties of a MO/SC model system, Europium monoxide (EuO) on Si, that are dedicated for the use as spin injector and collector contacts. EuO is predicted to be chemically stable in direct contact with silicon. However, ferromagnetic EuO is very difficult to synthesize due to its large reactivity towards higher oxides, i. e. Eu_2O_3 . Furthermore, any excess oxygen may readily oxidize the Si surface, which can lead to a loss of tunneling spin polarization.

We succeeded in preparing high-quality EuO/Si(001) heterostructures with bulk-like magnetic properties. We used hard x-ray photoelectron spectroscopy (HAXPES) to probe the electronic structure of EuO tunnel barriers and the EuO/Si interface [1, 2]. Due to its large information depth—exceeding 10 nm at photon energies of 10 keV—HAXPES is a perfectly suited technique to probe the chemical quality of buried layers and interfaces (Fig. 1).

By studying photoemission spectroscopy from both core and valence levels, we obtain a comprehensive set of information on the electronic structure of EuO/Si(001). Fig. 2 (a)–(f) shows the Eu 4*s* and Eu 4*d* core levels, as well as the Eu 4*f* valence bands for stoichiometric EuO and O-rich Eu_2O_3 on Si [1, 2]. Eu cations in stoichiometric, ferromagnetic EuO are divalent, whereas Eu^{3+} antiferromagnetic contributions are expected in O-rich EuO. A quantitative peak analysis of the divalent and trivalent spectral contributions in the Eu 4*s*, 4*d* and 4*f* spectra is employed to extract the EuO chemical composition. We assign the individual spectral features observed in the Eu core level and valence spectra. Fig. 2 (a) and (b) shows the Eu 4*s* core level spectra for both EuO compounds. The prominent double-peak structure is caused by coupling of the 4*s* core level with the localized Eu 4*f* state, which leads to an exchange splitting $\Delta E = 7.4$ eV of the 4*s* inner shell.

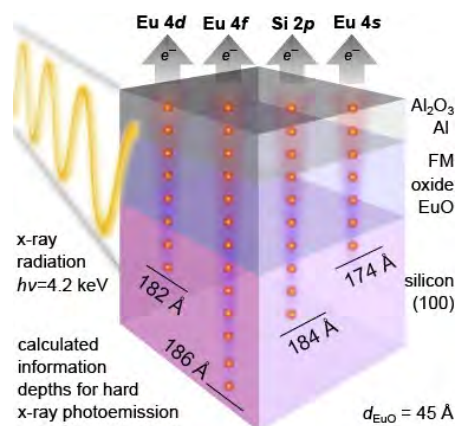


FIG. 1: Schematics of a hard x-ray photoemission spectroscopy (HAXPES) experiment of an Al/EuO/Si heterostructure probing the buried EuO thin film and the EuO/Si interface.

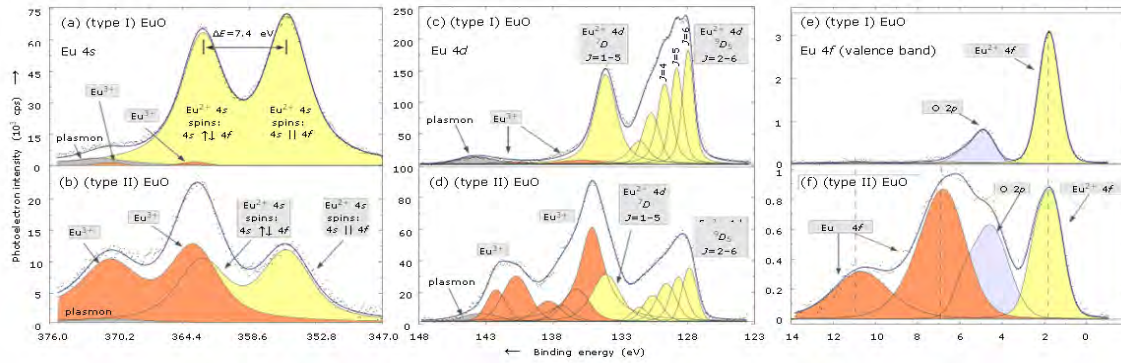


FIG. 2: Hard x-ray photoemission spectra from (a), (b) Eu 4s core levels and (c), (d) Eu 4d core levels, as well as (e), (f) Eu 4f valence bands, recorded at a photon excitation energy of 4.2 keV in normal emission geometry. A quantitative peak analysis yields a relative fraction of Eu^{3+} cations of only $(3.1 \pm 1.5)\%$ for stoichiometric EuO and of $(60.2 \pm 4.8)\%$ for O-rich Eu_2O_3 .

For (type I) EuO, the 4s double-peak is assigned to divalent Eu^{2+} spectral contributions, whereas an additional, overlapping trivalent Eu^{3+} double-peak feature appears in Fig. 2(b), that is chemically shifted by 8.1 eV towards higher binding energy.

The Eu 4d core level spectra are depicted in Fig. 2(c) and (d). They show a complex multiplet structure distributed in a wide energy range due to the strong 4d–4f exchange interaction and much weaker 4d spin-orbit splitting. Therefore, the 4d spectra cannot be separated into their $4d_{3/2}$ and $4d_{5/2}$ components. We can attribute the two main spectral contributions of the 4d spectra to a $J = L - S$ multiplet splitting caused by 4d–4f interaction, and assign the peaks to the 7D and 9D multiplets, respectively. The fine structure of the 7D final state is not resolved, whereas the $J = 2-6$ components in the 9D state is easily identified. Once more, we clearly observe a mainly divalent Eu^{2+} valency in EuO, but significant spectral contributions from Eu^{2+} cations in O-rich EuO.

We move on to the analysis of the Eu 4f valence bands in Fig. 2 (e) and (f). The pronounced peak located at 1.8 eV below EF displays the Eu^{2+} 4f final state multiplet. Spectral contributions up to 4.5 eV binding energy are attributed to valence bands of overlapping Eu^{2+} 4f and O 2p states. The chemically shifted Eu^{3+} 4f multiplet structure in O-rich EuO is located between 5 and 13 eV.

We finally performed a quantitative peak analysis by fitting the spectral contributions with convoluted Gaussian-Lorentzian curves. The result of the fitting procedure is shown by the solid lines in Fig. 2(a)–(f), which match the experimental data points very well. From the integrated spectral intensities of the divalent Eu^{2+} and trivalent Eu^{3+} components, we derive a relative fraction of Eu^{3+} cations of only $(3.1 \pm 1.5)\%$ for stoichiometric EuO and of $(60.2 \pm 4.8)\%$ for O-rich Eu_2O_3 .

The local chemistry and bonding at the EuO/silicon transport interface was probed via photoemission from the Si 2p core level recorded in normal and 45°

off-normal emission geometry at 4.2 keV. In this way, the information depth of the escaping photoelectrons is substantially varied, which allows one to distinguish spectral contributions from bulk and interface-like electronic states of the buried Si substrate. For stoichiometric EuO/Si(100), we confirm the chemical stability of the EuO/Si(001) interface as predicted by thermodynamic calculations, whereas in O-rich EuO/Si(100) features on the high binding energy side of $\text{Si}^{n+}2p$ states indicate the presence of interfacial SiO_x .

We presented an electronic structure study of a magnetic oxide/semiconductor model system, EuO on Silicon. We succeeded in stabilizing ultrathin EuO films on Si(001), and confirmed their nearly ideal stoichiometry using core-level and valence band hard x-ray photoemission spectroscopy. Moreover, we identified a chemically stable EuO/Si interface, with no signs of silicon oxide formation. With the aim to establish this novel class of spin injector/collector contacts on silicon, high-quality EuO magnetic oxide tunnel barriers will be integrated into silicon-based transport devices in the near future.

-
- [1] C. Caspers, M. Müller, A. X. Gray, A. M. Kaiser, A. Gloskovskii, W. Drube, C. S. Fadley, and C. M. Schneider, Electronic structure of EuO spin filter tunnel contacts directly on silicon, *Phys. Status Solidi RRL* 5, Vol. 12, 441 (2011)
- [2] C. Caspers, M. Müller, A. X. Gray, A. M. Kaiser, A. Gloskovskii, W. Drube, C. S. Fadley, and C. M. Schneider, Chemical stability the magnetic oxide EuO directly on silicon observed by high-energy photoemission spectroscopy, *Physical Review B* 84, 205217 (2011)

Probing the timescale of the exchange interaction in a ferromagnetic alloy

Roman Adam¹, Patrik Grychtol¹, Stefan Mathias², Chan La-O-Vorakiat³, Patrick Granitzka², Emrah Turgut³, Justin M. Shaw⁴, Hans T. Nembach⁴, Mark E. Siemens³, Steffen Eich², Claus M. Schneider¹, Thomas J. Silva⁴, Martin Aeschlimann², Margaret M. Murnane³, and Henry C. Kapteyn³

¹ PGI-6: electronic Properties & JARA-FIT, Forschungszentrum Jülich

² University of Kaiserslautern and Research Center OPTIMAS, 67663 Kaiserslautern

³ Department of Physics and JILA, University of Colorado and NIST, Boulder, CO, USA

⁴ Electromagnetics Division, National Institute of Standards and Technology, Boulder, CO, USA

The underlying physics of all ferromagnetic behavior is the cooperative interaction between individual atomic magnetic moments that results in a macroscopic magnetization. We use extreme femtosecond pulses of laser higher harmonics in the extreme ultraviolet spectral range as an element-specific probe of ultrafast, optically driven, demagnetization in a ferromagnetic Ni_{0.8}Fe_{0.2} (Permalloy). We show that for times shorter than the characteristic timescale for exchange coupling, the magnetization of Fe quenches more strongly than that of Ni [1]. Then, as the Fe moments start to randomize, the strong ferromagnetic exchange interaction induces further demagnetization in Ni, with a characteristic delay determined by the strength of the exchange interaction. We also show that we can further enhance this delay by lowering the exchange energy by diluting the NiFe with Cu. Our measurements probe how the fundamental quantum mechanical exchange coupling between Fe and Ni in magnetic materials influences magnetization dynamics in ferromagnetic alloys.

Progress in magnetic information storage and processing technology is intimately associated with complex materials that are engineered at the nanometer scale. Next-generation devices require that the magnetic state of materials is manipulated on fast timescales and at the nanometer level. However, a complete microscopic understanding of magnetization dynamics that involves the correlated interactions of spins, electrons, photons, and phonons on femtosecond timescales has yet to be developed.

In our work, we experimentally answered the fundamental question of whether the magnetization dynamics of individual elements in a ferromagnetic alloy can differ on ultrafast timescales [1]. This is a very important fundamental question that has not been addressed either theoretically or experimentally to date, the answer to which reveals how the exchange interaction affects the ultrafast dynamics of elemental spin subsystems in complex materials.

To answer this question, we rapidly excite permalloy with a train of ultrashort (≈ 25 fs) laser pulses and

probe the demagnetization dynamics with XUV pulses that allow to explore the involved spin dynamics *element specifically*.

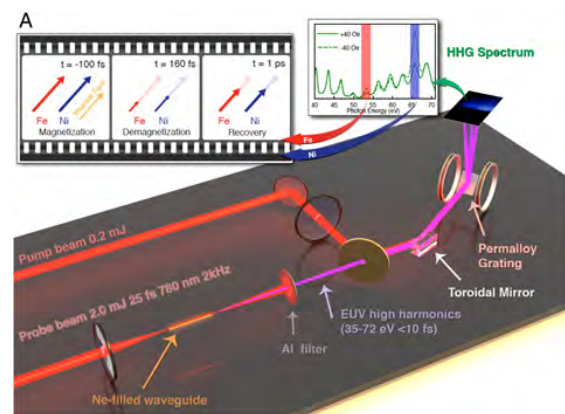


FIG. 1: Schematics of the experimental setup for XUV pump-probe measurement. XUV pulses (<10 fs) are reflected from a permalloy grating sample, forming a spectrum on a CCD camera. The reflected HHG intensity at the Fe and Ni M-shell absorption edges (red and blue) depends on the magnetization direction. After rapid excitation of the electron system by a femtosecond laser pulse, various scattering processes between electrons and phonons (with and without spin-flips) determine the dynamical response of the system. First, the strongly excited electron gas thermalizes by predominantly electron-electron scattering to a Fermi-Dirac distribution. The ferromagnet starts to demagnetize because of spin-flip scattering events during this thermalization process. Electron-phonon scattering processes transfer energy from the excited electron gas to the lattice, and thermal equilibrium is typically reached on picosecond timescales. Finally, on nanosecond timescales, the material cools by thermal diffusion. The red and blue arrows in the lower boxes show the observed distinct demagnetization dynamics of Fe and Ni in permalloy.

To reach the required temporal resolution in our experiment, sub-10 fs XUV light pulses from high-harmonic generation (HHG) are produced by focusing 2 mJ femtosecond laser pulses into a Ne-filled waveguide. The generated harmonic photon energies of 35 to 72 eV include the M absorption edges of Fe (54 eV) and Ni (67 eV).

In the transverse magneto-optical Kerr-effect (T-MOKE) geometry used for these measurements, the intensity of the reflected HHG light is directly

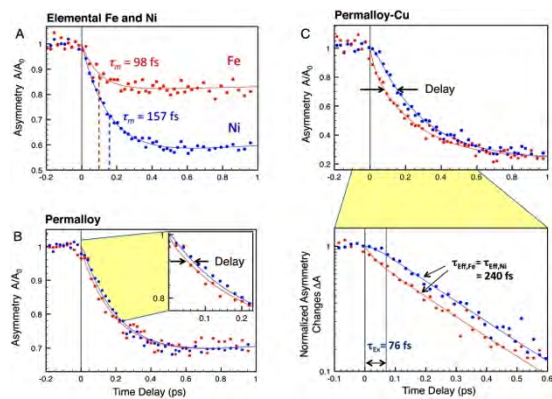


FIG. 2: Ultrafast demagnetization of Fe (red dots) and Ni (blue dots) for elemental Fe and Ni (A), in permalloy (B), and in permalloy-Cu (C). Fits to the model (solid lines) are used to extract the intrinsic demagnetization times for Fe and Ni in the alloys, τ_{Fe} and τ_{Ni} , as well as the exchange time τ_{Ex} after which the Fe and Ni spin baths return to equilibrium with respect to each other with an effective demagnetization time constant of τ_{eff} . The data for permalloy-Cu (C) is also shown in log-scale as a function of the normalized asymmetry changes $\Delta A(t) = (A(t) - A_{min}) / (A_0 - A_{min})$, where A_0 is the asymmetry amplitude and A_{min} the minimum asymmetry reached in the demagnetization process.

proportional to the sample magnetization transverse to the plane of incidence [6]. We probe the magnetization by reflecting the XUV beam from the sample, as shown in Fig.1. To gain insight into element sensitive dynamics, we used gratings patterned in three different ways: (i) alternating elemental Fe and Ni stripes to probe the behavior of the pure materials; (ii) permalloy (Ni0.8Fe0.2); (iii) permalloy-Cu ((Ni0.8Fe0.2)0.6Cu0.4). The HHG spectrum diffracted from the sample grating is focused onto an X-ray CCD camera. In order to determine the T-MOKE asymmetry, the change in reflected intensity of the XUV light at the M-absorption edges is monitored while the magnetization direction of the sample is reversed. After taking the spectra, the T-MOKE asymmetry parameter A is calculated from the experimental data as

$$A = \frac{I_r(H^\uparrow) - I_r(H^\downarrow)}{I_r(H^\uparrow) + I_r(H^\downarrow)}$$

where $I_r(H^\uparrow)$ and $I_r(H^\downarrow)$ denote the reflected XUV intensities for the two magnetization directions. More details of the measurement method can be found in Refs. [1-6]. We note that the demagnetization data for Fe and Ni are collected at the same time in this measurement, precluding any mismatch between the two elements in the determination of time-zero between pump and probe laser pulses.

The superior time resolution of our experiment allows us to observe that the magnetization dynamics of Fe and Ni are *transiently delayed* with respect to each other by about 18 fs in pure permalloy and 76 fs in Cu-diluted permalloy (Fig.2). We ascribe this

transient decoupling in the magnetic behavior to the finite strength of the fundamental quantum exchange interaction between Fe and Ni atoms in the material.

Specifically, for times shorter than the characteristic timescale for exchange coupling, the magnetization of Fe quenches more strongly than that of Ni. Then, as the Fe moments start to randomize, the strong ferromagnetic interatomic exchange interaction between Fe and Ni induces further demagnetization in Ni, with a characteristic delay determined by the strength of the Fe-Ni exchange interaction. Interatomic exchange energies of transition metal alloys are in the 10–100 meV range, yielding characteristic exchange times in the femtosecond range which corresponds to finite spin-flip scattering times of 10–100 fs. Our findings provide crucial information for open questions in femtosecond magnetization dynamics in the case of metallic, multispecies, exchange-coupled systems.

In summary, we explore the consequences of the fundamental quantum exchange interaction in strongly coupled ferromagnetic systems, showing that quantitatively *different magnetization dynamics of the individual elements can be observed on timescales shorter than the characteristic exchange timescale*. On longer timescales, the dynamics are dominated by the faster one of the two species. Analysis of our data indicates that the observed differences in demagnetization rate are primarily determined by intrinsic properties of the material. This fact has significant impact for fundamental models of ultrafast magnetism, and for the dynamical magnetic behavior for all types of exchange-coupled materials, including both the alloys and multilayer structures that are widely used for data storage.

-
- [1] Mathias, S., La-O-Vorakiat, C., Grychtol, P., Granitzka, P., Turgut, E., Shaw, J.M., Adam, R., Nembach, H.T., Siemens, M., Eich, S., Schneider, C. M., Silva, T., Aeschlimann, M., Murnane, M.M. & Kapteyn, H., PNAS **109**, 4792 (2012)
 - [2] La-O-Vorakiat, C., Turgut, E., Teale, C.A., Kapteyn, H.C., Murnane, M.M., Mathias, S., Aeschlimann, M., Schneider, C.M., Shaw, J., Nembach, H. & Silva, T., Physical Review X **2**, 011005 (2012)
 - [3] Adam, R., Grychtol, P., Cramm, S. & Schneider, C.M. Journal of Electron Spectroscopy and Related Phenomena **184**, 291 (2011)
 - [4] Grychtol, P., Adam, R., Valencia, S., Cramm, S., Bürgler, D.E. & Schneider, C.M., Phys. Rev. B **82**, 054433 (2010)
 - [5] La-O-Vorakiat, C., Siemens, M., Murnane, M., Kapteyn, H., Mathias, S., Aeschlimann, M., Grychtol, P., Adam, R., Schneider, C. M., Shaw, J., Nembach, H. & Silva, T., Phys. Rev. Lett. **103**, 257402 (2009)
 - [6] Hecker, M., Oppeneer, P.M., Valencia, S., Mertins, H.-Ch. & Schneider, C.M., Journal of Electron Spectroscopy and Related Phenomena **144–147**, 881 (2005)

Bulk Electronic Band Structure Measurements Using Hard X-ray Photoemission

L. Plucinski^{1,2}, J. Minar³, J. Braun³, A. X. Gray^{4,5}, S. Ueda⁶, Y. Yamashita⁶, K. Kobayashi⁶, H. Ebert³, C.S. Fadley^{4,5}, and C.M. Schneider^{1,2,7}

1 PGI-6:Electronic Properties, Forschungszentrum Jülich

2 Jülich Aachen Research Alliance - Fundamentals of Future Information Technologies (JARA-FIT)

3 Department of Chemistry, Ludwig Maximilian University, 81377 München

4 Department of Physics, University of California Davis, Davis, CA 95616, USA;

5 Materials Sciences Division, Lawrence Berkeley National Laboratory, Berkeley, CA 94720, USA;

6 NIMS Beamline Station at SPring-8, Nat. Inst. for Mat. Science, Hyogo 679-5148, Japan;

7 Fakultät für Physik, University of Duisburg-Essen, 47057 Duisburg

Traditional ultraviolet/soft X-ray angle-resolved photoemission spectroscopy (ARPES) may in some cases be too strongly influenced by surface effects to be a useful probe of bulk electronic structure. Going to hard X-ray photon energies and thus larger electron inelastic mean-free paths should provide a more accurate picture of bulk electronic structure. Special effects occurring in a higher-energy ARPES experiment must be considered, such as photon momentum, phonon-induced zone averaging effects, and the degree of cryogenic cooling required, which can be estimated via appropriate Debye-Waller factors.

ARPES is the most powerful tool to study the valence band electronic structure of solid, giving direct access to the k -resolved electronic bands in the direction parallel to the measured surface. In the widely used vacuum ultraviolet and soft x-ray regions ($h\nu = 10$ -1000 eV) photoemission is surface sensitive due to the electron mean free path of 10-20 Å. This surface sensitivity is advantageous in case one is interested in surface-related features, however, it commonly disturbs the interpretation of the bulk related properties such as the magnitude of the fundamental gap or the shape of three-dimensional Fermi surface. The only certain way to increase the electron mean free path, and in turn increase the bulk sensitivity, is to increase kinetic energy of the valence band electrons by increasing the photon energy.

We have pushed ARPES into the hard x-ray regime using photon energies 3-6 keV, which enhances the probing depth up to 30-60 Å [1], and such hard x-ray photoemission (HAXPES) results for (110) face of the W single crystal at $h\nu \sim 6$ keV are shown in Fig.1. Upper panel shows the raw data which contains contribution from direct and indirect transitions:

$$I_{\text{tot}} = e^{-|\mathbf{k}_f - \mathbf{k}_i|^2 \langle u^2 \rangle} I_{\text{DT}} + (1 - e^{-|\mathbf{k}_f - \mathbf{k}_i|^2 \langle u^2 \rangle}) I_{\text{NDT}}$$

where I_{DT} is the intensity of the wave-vector-conserving direct transitions, which gives the momentum dependent information of the band structure, and I_{NDT} describes indirect transitions,

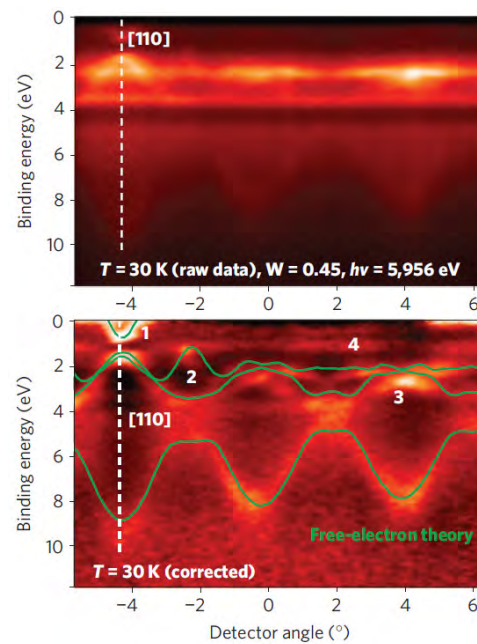


FIG. 1: HAXPES results for W(110) surface measured using 5956 eV photons at 20K [1]. Upper panel: raw data, Lower panel: data corrected for inelastic background and photoelectron diffraction effects, together with free-electron final state model simulation using DFT ab-initio bulk band structure.

where the creation or annihilation of phonons accompanies the photoemission process. The photoemission Debye-Waller factor $e^{-|\mathbf{k}_f - \mathbf{k}_i|^2 \langle u^2 \rangle}$ in this equation originates from the de-phasing of the initial and final state electron wave functions by lattice displacements, where $|\mathbf{k}_f - \mathbf{k}_i|$ is the electron wave-vector difference (equal to a reciprocal lattice vector

\mathbf{g} in the usual interpretation of ARPES), and $\langle u^2 \rangle$ is the mean-square thermal displacement of the atoms. This shows that reducing the temperature helps in improving the I_{DT}/I_{NDT} ratio. Furthermore $I(\text{angle})$ in the raw data in Fig. 1 is modulated by the photoelectron diffraction effects, and in the corrected spectra in the lower panel both of these effects are corrected by dividing the raw data image by averaged intensities in both energy and angular directions. The details of the band dispersions and spectral weights can be understood using a simple free-electron final state model, or accurate one-step photoemission calculations [1,2].

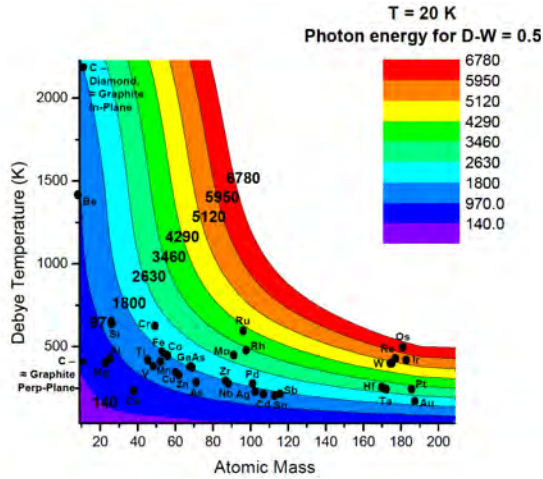


FIG. 1: Plot of the photon energies yielding valence-band Debye-Waller factors of 0.5, as a rough estimate of 50% direct-transition behavior, at a 20 K measurement temperature, as a function of atomic mass and Debye temperature. The points show various elements. This plot can be used to estimate the feasibility of high-energy ARPES experiments for other materials.

As an approximate way to assess the degree of phonon-induced Brillouin-zone averaging for various systems, we show in Fig. 2 the photon energies yielding Debye-Waller factors of 0.5 at 20 K (a reasonable measuring temperature for many current cryocooled sample holders) as a function of atomic mass and Debye temperature, with points for several elements indicated [3]. Other elements or compounds can be estimated from this plot. From this consideration of approximately 40 elements, we conclude that fruitful ARPES measurements should certainly be possible for many materials in the 1–3 keV range. For other materials, and/or with correction procedures such as this used for Fig. 1 (right panel), or better methods allowing more precisely for phonon effects, even higher energies up to 6 keV should be possible.

An additional consideration in hard x-ray ARPES (HARPES) measurements is the effects of recoil on energy positions and resolution. In the limit of free-atom recoil, the recoil energy can be estimated from

$$E_{recoil} = \frac{\hbar^2 k_f^2}{2M} \approx 5.5 \cdot 10^{-4} \left[\frac{E_{kin}(eV)}{M(amu)} \right]$$

where M is the effective mass of the atom(s) involved [3]. Here again, with typical resolutions of ~ 100 meV that can already be achieved with soft and hard x-ray ARPES systems, we find that most elements should be capable of study up to 4 keV, if not higher.

- [1] A. X Gray, C. Papp, S. Ueda, B. Balke, Y. Yamashita, L. Plucinski, J. Minar, J. Braun, E. R. Ylvisaker, C. M. Schneider, W. E. Pickett, H. Ebert, K. Kobayashi, and C. S. Fadley, “Probing Bulk Electronic Structure with Hard-X-Ray Angle-Resolved Photoemission: W and GaAs”, *Nature Materials* 10, 759 (2011),
- [2] L. Plucinski, J. Minar, B.C. Sell, J. Braun, H. Ebert, C.M. Schneider, and C.S. Fadley, “Band mapping in higher-energy x-ray photoemission: Phonon effects and comparison to one-step theory”, *Phys. Rev. B* 78, 035108 (2008),
- [3] C. Papp, L. Plucinski, J. Minar, J. Braun, H. Ebert, and C. S. Fadley, “Band mapping in x-ray photoelectron spectroscopy: an experimental and theoretical study of W(110) with 1.25 keV excitation”, *Phys. Rev. B* 85, 045433 (2011).

Selected Publications

1. C. La-O-Vorakiat, M. Siemens, M. M. Murnane, H. C. Kapteyn, S. Mathias, M. Aeschlimann, P. Grychtol, R. Adam, C. M. Schneider, J. Shaw, H. Nembach, and T. Silva:
Ultrafast Demagnetization Dynamics at the M-Edges of Magnetic Elements Observed Using a Tabletop High-Harmonic Soft X-Ray Source
Physical Review Letters **103** (2009) 257402
2. H. A. Dürr, T. Eimüller, H.-J. Elmers, S. Eisebitt, M. Farle, W. Kuch, M. Martins, F. Matthes, H.-C. Mertins, P. M. Oppeneer, L. Plucinski, C. M. Schneider, H. Wende, W. Wurth, H. Zabel:
A Closer Look into Magnetism: Opportunities with Synchrotron Radiation
IEEE Trans. Magn. **45** (2009) 15-57
3. C. Papp, A. X Gray, B. Balke, S. Ueda, Y. Yamashita, C. Sakai, H. Yoshikawa, S. L. He, L. Plucinski, J. Minár, J. Braun, H. Ebert, E. R. Ylvisaker, C.M. Schneider, K. Kobayashi, W. E. Pickett, and C. S. Fadley:
Determining Bulk Electronic Structure from Hard-X-Ray Angle-Resolved Photoemission
Nature Materials **10** (2011) 759.
4. K. M. Seemann, F. Freimuth, H. Zhang, Y. Mokrousov, S. Blügel, D. E. Bürgler, and C. M. Schneider:
On the Origin of the Planar Hall Effect in Nano-Crystalline $\text{Co}_{60}\text{Fe}_{20}\text{B}_{20}$
Physical Review Letters **107** (2011) 086603
5. Yan, M; Kakay, A; Gliga, S; Hertel, R
Beating the Walker Limit with Massless Domain Walls in Cylindrical Nanowires
Physical Review Letters **104**; (2010) 057201
6. Fu, ZD; Kogerler, P; Rucker, U; Su, Y; Mittal, R; Bruckel
An approach to the magnetic ground state of the molecular magnet $\{\text{Mo}_{72}\text{Fe}_{30}\}$
New Journal of Physics **12** (2010) 083044
7. R. Lehndorff, D. E. Bürgler, C. M. Schneider, and Z. Celinski
Injection Locking of the Gyrotropic Vortex Motion in a Nanopillar
Applied Physics Letters **97** (2010) 142503
8. S. Mathias, Ch. La-O-Vorakiat, P. Grychtol, P. Granitzka, E. Turgut, J. M. Shaw, R. Adam, H. T. Nembach, M. E. Siemens, S. Eich, C. M. Schneider, T. J. Silva, M. Aeschlimann, M. M. Murnane and H. C. Kapteyn:
Probing the Timescale of the Exchange Interaction in a Ferromagnetic Alloy
PNAS **109** (2012) 4792
9. Dennis Rudolf , Chan La-O-Vorakiat, Marco Battiato, Roman Adam, Justin M. Shaw, Emrah Turgut , Pablo Maldonado , Stefan Mathias , Patrik Grychtol, Hans T. Nembach, Thomas J. Silva, Martin Aeschlimann , Henry C. Kapteyn , Margaret M. Murnane , Claus M. Schneider & Peter M. Oppeneer:
Ultrafast magnetization enhancement in metallic multilayers driven by superdiffusive spin current.
Nature Communications 3:1037 DOI 10.1038/ncomms2029 (2012)
10. K. M. Seemann, F. Garcia-Sanchez, F. Kronast, J. Miguel, A. Kákay, C. M. Schneider, R. Hertel, F. Freimuth, Y. Mokrousov, and S. Blügel:
Multi-Scale Analysis of the Electrical Resistance in Bloch-Type Magnetic Domain Walls
Physical Review Letters **108** (2012) 077201

Indicators

Quantitative Numbers

	2009	2010	2011
Peer-Reviewed Publications	19	28	30
Graduations			
Master/Diploma	0	1	3
Dissertation	2	1	4
Habilitation	0	0	0

Honours

Gay-Lussac-Humboldt Award	Schneider	Franz. Wissenschaftsministerium
---------------------------	-----------	---------------------------------

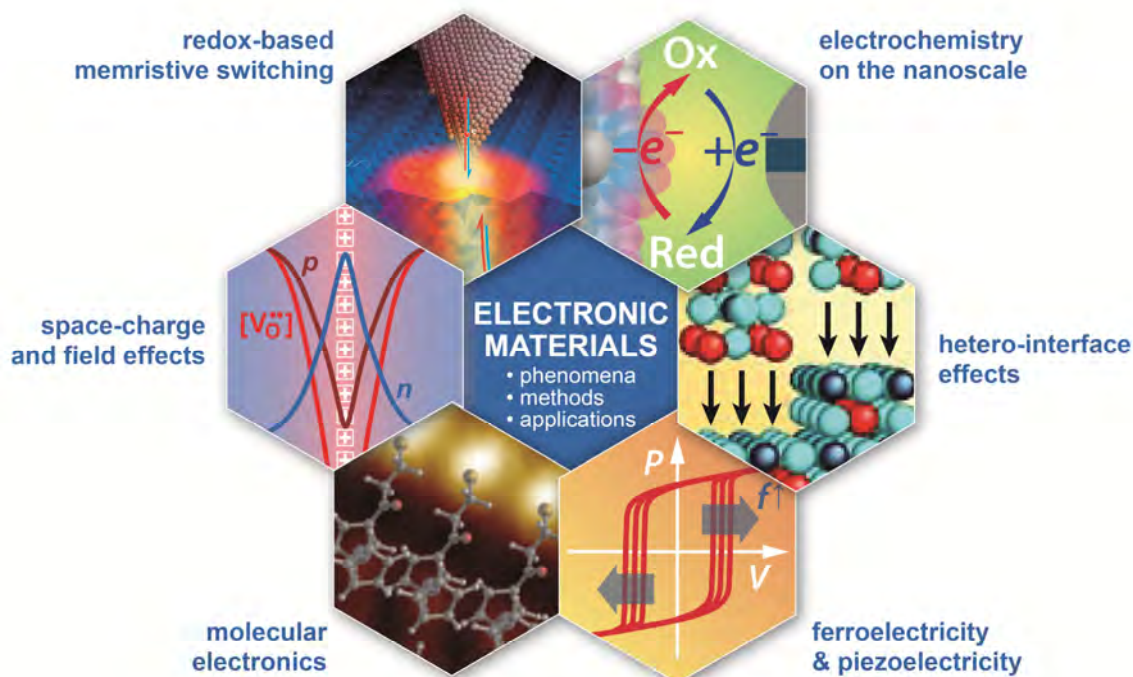
Offers

2010	Schneider	RWTH Aachen
2010	Hertel	CNRS Strasbourg

Selected Third Party Projects

1. Teilprojekt DFG-Forschergruppe 921
"Spinkohärenz"
2007 – 2013
2. Teilprojekt in der NRW Forschungsschule "Forschung mit Synchrotronstrahlung",
DELTA-Konsortium
2007 – 2012
3. Teilprojekt im SFB 917 „Nanoswitches“,
RWTH Aachen – FZ Jülich
2011 – 2015

PGI-7: Electronic Materials



Progress in information technology and fields such as energy storage, energy conversion, and sensors originates to a large extent from the findings of novel electronic phenomena in functional materials as well as advances in the processing technology of these materials.

In this sense, the Institute PGI-7 - *Electronic Materials* focuses on the physics and chemistry of electronic oxides and electronically active organic molecules which are promising for future device and systems application. Our research aims at the fundamental understanding of functional effects based on nano-scale electron transfer, electrochemical redox processes, resistive switching, space charge formation and field effects, as well as ferro- and piezoelectricity. In particular, we aim to apply our expertise in the area of lattice disorder thermodynamics and kinetics of transition metal oxides, surface and interface science, as well as electrochemistry in solid and liquid systems in order to explore the microscopic mechanism behind the electronic phenomena. The material systems and device concepts are selected for their potential in information storage, energy-efficient computing, energy conversion (e. g. in electrolysis, fuel cells, photoelectrochemical cells, piezoelectric actuators), and sensor functions.

In order to conduct our research, we utilize a broad spectrum of facilities ranging from atomically controlled film deposition methods for heteroepitaxial oxide thin films, and molecular self-assembly routes to dedicated integration technologies. In addition, our institute is equipped with tools for the characterisation of processes, structures, and electronic properties with atomic resolution. This is complemented by numerical simulation and modelling methods which aim to explain the electronic phenomena and materials under study as well as the corresponding devices.

Head of Institute:

Prof. Rainer Waser, email: r.waser@fz-juelich.de, phone: +49-2461-61-5811.

Scientific Staff

On September 1st 2012, the staff of PGI-7 comprised 12 scientists, 7 technicians, 13 PhD students, and 1 Master student.

Scientists

Hoffmann-Eifert, Dr. Susanne
Karthäuser, Dr. Silvia
Meuffels, Dr. Paul
Moors, Dr. Marco
Pithan, Dr. Christian
Rana, Dr. Vikas
Shkabko, Dr. Andrey
Szot, Prof. Dr. Kristof
Valov, Dr. Iliia
Waser, Prof. Dr. Rainer

Post-Docs

Lenser, Christian
Otsuka, Yusuke

Research Highlights

Coexistence of filamentary and homogeneous resistive switching in Fe-doped SrTiO₃ thin film memristive devices

R. Landrock¹, T. Menke¹, R. Dittmann¹, R. Waser^{1,2}

¹ PGI-7: Electronic Materials, Forschungszentrum Jülich

² Institute of Materials in Electrical Engineering 2, RWTH Aachen University

We have demonstrated that resistive switching in Fe-doped SrTiO₃ thin films can be either confined to a single strong filament or distributed over larger areas beneath the electrode, in the ideal case the whole junction area. Both types of switching coexist in one and the same sample and exhibit the opposite switching polarity. We suggest allocating those two switching types to areas of different defect density beneath the same electrode.

In the search for promising resistive switching oxide materials for future non-volatile memories [1], special attention has to be paid to their scaling capabilities. The issue of scaling is strongly linked to the question of, whether the switching current is distributed homogeneously across the device area or localized to one or a few conducting filaments [2]. In this work we used conductive AFM (LC-AFM) combined with a delamination technique to remove the top electrode of Fe-doped SrTiO₃ devices to gain insights into the nanoscale current distribution at the active switching interface

Figure 1a depicts the current-voltage (I-V) characteristic of a 1 at% Fe doped SrTiO₃ metal-insulator-metal (MIM) structure performed after an initial electroforming procedure (+12V, 50s). In the low bias regime, a stable resistive switching state, shown in green, is reached (“counter eightwise”). At higher negative voltage amplitude, a stable second type of switching can be achieved, shown in orange (“eightwise polarity”). Both types of switching occur in the same pad [3].

Figure 1b shows the topography and local current distribution of a junction after electroforming and top electrode removal. The inset covers the whole junction area, while the main topography and current images are magnifications of the lower right part of the junction area. Most of the interface is smooth and has not been structurally altered by the electroforming step. Only a small region in the lower right part of the junction shows some deformation as a result of the electroforming. The conductivity of the formed junction is shown on the right hand side

of Figure 1b and is confined to a section close to the crater. The crater itself is well conducting (marked in green) and a somewhat broadened area around the crater shows moderate conductivity (marked in orange).

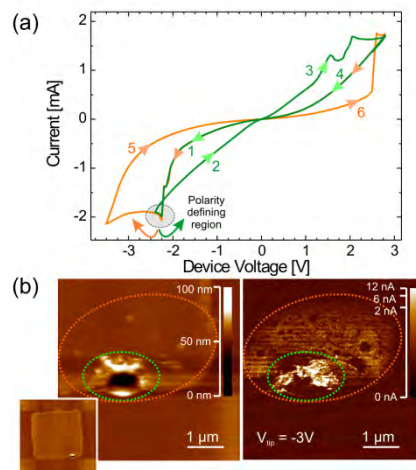


FIG. 1: (a) I-V-characteristics of a pulsed laser deposited 500nm thick 1at% Fe-doped SrTiO₃ thin film with 1 at% Nb-doped STO bottom electrode and Pt top electrode. (b) LC-AFM topography and current image of a junction after electroforming and top electrode removal recorded at -3V [3].

Fig. 2(a) shows a series of LC-AFM scans performed on the same sample. Starting from the conductivity image of an as-formed interface as shown Figure 1b, the tip was biased with -5 V, scanned across the surface, and afterwards another readout image at -3 V was recorded. This treatment step results in a conductivity decrease of the area marked in orange (upper left part of Figure 2a). A second scan with a reversed tip bias of +5 V recovers the conductivity of that region (upper right part of Figure 2a, recorded at -3 V again). In fact, not only this initial region but the complete junction area within the scan range has been switched on. A scan with -5V causes the conductivity to vanish again (with exception of the central crater), while yet another scan with +5 V switches it on again (lower right and lower left part

of Figure 2a). The polarity of this type of switching corresponds to the eightwise polarity (orange curve) in Figure 1a.

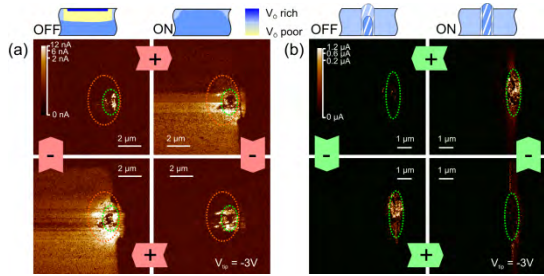


FIG. 2: Tip induced resistive switching of a delaminated MIM structure [3].

The crater region can be switched as well: a scanning voltage of +6 V decreases its conductivity (Figure 2b upper left to lower left), while a voltage of -6 V recovers it (Figure 2b lower left to lower right). The overall polarity of this type of switching corresponds to the green curve in Figure 1a (counter-eightwise). It is interesting to note that in this case only the crater region itself contributes to the switching, indicating a completely localized, filamentary process.

Supplementary to above experiments, two thin film MIM structures have been switched within the “eightwise” polarity and set to the LRS and HRS state before delamination. After delamination, the junction that has been left in the LRS state (Figure 3a) shows both a conducting crater region and a conducting surrounding region. The junction that has been switched to the HRS state, however, lacks the conducting surrounding region (Figure 3b). This experiment proves that eightwise resistive switching of takes place within an extended region surrounding the forming crater.

Concerning the underlying mechanisms, a standard DC forming step as described above results in the formation of a conducting filament (in our case the crater region) that locally bypasses the Schottky-like interface barrier between oxide material and top electrode [4] and that is a prerequisite for subsequent filamentary switching. The formation of this initial forming filament is aided by Joule heating. Due to heat conduction and a built up chemical gradient even a broadened area around this filament is reduced (extended region marked in orange in Figure 1- 3).

Both regions are involved in subsequent resistive switching steps. The crater (and the underlying forming channel) is a very defect-rich and slightly non-stoichiometric region, judging from its good conductivity and massive topography changes. The mobility of oxygen vacancies along this channel is expected to be quite high. Resistive switching within this channel relies on the attraction of oxygen vacancies into the upper interface and a corresponding lowering of the Schottky-like inter-

face barrier for negative voltages (LRS), and a repulsion of oxygen vacancies with a corresponding recovery of that barrier for positive voltages (HRS).

We suggest the following as one possible explanation for the eight-wise switching: due to slightly reducing deposition conditions, the overall film is n-conducting and contains a certain amount of distributed oxygen vacancies. If a negative voltage is applied to the upper interface, these vacancies migrate out of the lower regions and accumulate at the upper interface. Depending on the top electrode geometry (MIM electrode or AFM tip), this migration could ultimately result in an oxygen vacancy depleted region at the bottom electrode, where no further vacancies can be supplied from below (MIM structure), or in a depleted region at the penetration depth of the AFM tip’s electric field (see yellow region in inset in Figure 2a, Off state). Because of the low chemical mobility of oxygen vacancies in this structurally unperturbed region of the film (as opposed to the high mobility forming channel) a subsequent relaxing due to a chemical gradient is subdued and the overall resistance increases. A reversed voltage at the upper interface drives the oxygen vacancies out of the interface again and restores the completely n-type, well conducting film.

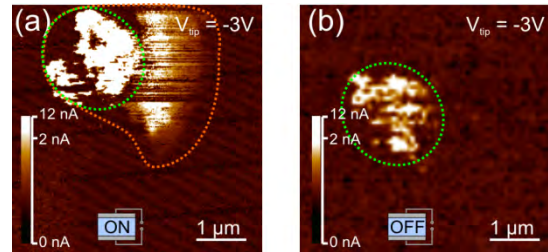


FIG. 3: Conductive AFM current images of a junction that has been set to On state (a) and a junction that has been set to the Off state before delamination. A vanishing of the broadened conducting area around the crater due to the Off switching can be seen [3].

Concerning device scaling, these results imply that resistive switching in SrTiO₃ thin films can in principle be extended over the whole junction area if the formation of thermally generated strong filaments is prevented during an appropriate electroforming process.

[1] R. Waser, R. Dittmann, G. Staikov, and K. Szot, *Adv. Mater.* 21, 2632 (2009).
 [2] A. Sawa, *Mater. Today* 11, 28 (2008).
 [3] R. Muenstermann, T. Menke, R. Dittmann, and R. Waser, *Adv. Mater.* 22, 4819 (2010).
 [4] T. Menke, P. Meuffels, R. Dittmann, K. Szot, and R. Waser, *J. Appl. Phys.* 105, 066104 (2009).

Complementary resistive switches for future memory devices

R. Rosezin¹, E. Linn², C. Kügeler¹, R. Bruchhaus¹, R. Waser^{1,2}

¹ PGI-7: Electronic Materials, Forschungszentrum Jülich

² IWE II: Institute for Electronic Materials II, RWTH Aachen University

Charge based non-volatile memory (Flash) approaches its physical limits. Thus, alternative concepts for the realization of highly scalable and area efficient memory devices are in the focus of research. In this report, a memory element, which is based on the very promising resistive switching effect, is introduced. The complementary resistive switch (CRS) is an anti-serial connection of two bipolar resistive switching devices and can be integrated into passive crossbar arrays while mitigating the sneak path problem. This makes high density memories based on CRS cells possible.

Charge based non-volatile memory devices face serious scaling challenges. With shrinking features sizes, memory levels in Flash transistors are only separated by a few 10 electrons. Thus, it becomes increasingly difficult to ensure data retention over 10 years. As an alternative non-volatile memory concept, ReRAM based on the resistive switching effect is in the focus of investigations [1-5]. In ReRAM, information is stored by a non-volatile resistance change of a simple metal/insulator/metal structure. This resistance can be toggled between at least two different values (high resistance state – HRS and low resistance state – LRS) by the application of a voltage stimulus. The simple device structure promotes the integration of resistive switching materials into high density architectures like passive crossbar arrays. However so far, the feasibility of this architecture was limited by sneak paths, which constrain the size of such a memory (Fig. 1). In the pattern shown in Fig. 1, the state of the high resistance memristive element shown in red color cannot be detected correctly, because the read current is dominated by the sneak current flowing through the adjacent cells. In the Figure only one of the possible paths is shown for simplicity.

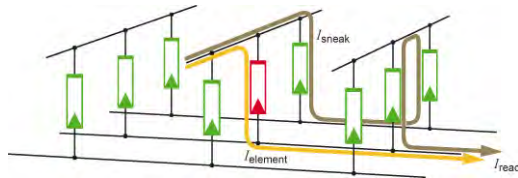


Fig. 1 Parasitic current paths

This figure shows a section of a crossbar array. In this example only the red element in the middle of the array is in HRS, the rest in LRS. In addition to the desired current path through the element in the middle, several other current paths (here is only marked one) occur and cause a large parasitic sneak current.

For bipolar memristive switches, we propose the CRS as a solution to the sneak path problem [6]. The schematic I-V-characteristic of such an element (here in form of an electrochemical metallization cell) is shown in Fig. 2. Important to note is that for switching to the HRS, a different voltage polarity is required than for the switching to the LRS.

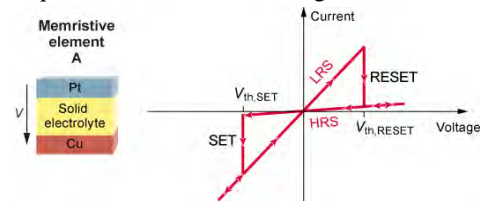


Fig. 2 Memristive element

Here the I-V-characteristic of a memristive element is shown. Initially, the memristive element is low resistive (LRS) and can be switch to the high resistive state (HRS) by applying a positive voltage $V > V_{th,RESET}$. For negative voltages ($V < V_{th,SET}$) the memristive element switches back to the LRS.

The complementary resistive switch (CRS) consists of two anti-serially (complementary) interconnected resistive switches, schematically shown in Fig. 3, together with a sketch of the resulting I-V-curve. A CRS cell is a two terminal device, just like a resistive switch, with four possible states (Table 1).

Tab. 1 CRS states

CRS	Memristive Element A	Memristive Element B	Overall resistance
0	HRS	LRS	\approx HRS
1	LRS	HRS	\approx HRS
ON	LRS	LRS	LRS + LRS
OFF	HRS	HRS	\gg HRS

The 'OFF' state is only found in uninitialized cells. It can be shown that the cells can be initialized into one of the operation states easily. The states '0' and '1' are the storage states. It is noteworthy that the resistances of the internal memory states '0' and '1' of a CRS cell are indistinguishable at low voltages because state '0' as well as state '1' exhibit a high resistance. Therefore, no parasitic current paths due to low resistance cells and no pattern dependencies can arise. Information is not stored by a resistance value but rather by a resistance combination of the two constituting elements. To determine the stored information of a single CRS cell the transient region of high current which can be seen in Fig. 3 is used. By choosing a read voltage $V_{th1} < V_{read} < V_{th2}$, the CRS cell will switch into the ON state only, if the cell originally stored a '1'. If the stored state was a '0', no change is induced and the current stays low. This difference can be detected easily, because it is

not disturbed by the adjacent cells. The destructive readout makes it necessary, to write back the previous state after reading.

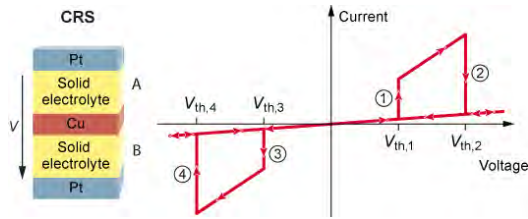


Fig. 3 I-V-characteristic of a CRS cell
 A CRS consists of two memristive elements which are connected antiseriially. If e.g. memristive element A is in the LRS and memristive element B in the HRS almost all voltage drops over memristive element B until $V_{th,1}$ is reached. At this point (1), element B switches to the LRS and element A remains in the LRS, because the potential drop at A is far below $V_{th,RESET}$. The CRS state is defined as 'ON' with now both memristive elements being low resistive and having an equal voltage drop. If the voltage reaches $V_{th,2}$ (2) memristive element A becomes high resistive, because this is equivalent to a voltage drop of $V_{th,RESET}$ over element A. This state is defined as '0'. For all applied voltages larger than $V_{th,3}$, the memristive element A stays high resistive and element B low resistive. If a potential V comes into the range $V_{th,4} < V < V_{th,3}$ (3), the high resistive element A switches to the low resistive state and both memristive elements in the CRS are in LRS (state 'ON'). If the negative potential exceeds $V_{th,4}$, element B switches back to HRS (4) and the resulting state is '1'.

In principle, every bipolar resistive switching material can be integrated into a CRS configuration. However, for an application, only elements which do not require a complicated dedicated forming procedure come into question. This is why we chose Cu/SiO₂/Pt bipolar resistive switches for a fully vertical integration [7]. A schematic cross section of the resulting CRS cell stack is depicted in Figure 4.

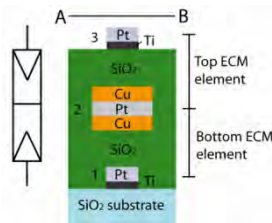


Fig. 4. Schematic cross section of the fabricated CRS stack. The constituting top and bottom ECM elements are marked. The final CRS device stack is (in order of deposition) 30 nm Pt/ 20 nm SiO₂/ 20 nm Cu/ 20 nm Pt/ 20 nm Cu/ 20 nm SiO₂/ 5 nm Ti/ 40 nm Pt.

The quasi-static electrical characterization, of these cells shows high resistance ratios ($R_{off}/R_{on} > 1500$), which allows for passive arrays of more than 106 elements, which is an improvement of more than 4 orders of magnitude compared to simple resistive switch based arrays. Furthermore, fast switching speed ($< 120 \mu s$) was proven (Figure 5). The results are one step further towards the realization of high-density passive nano-crossbar arrays based Gbit memory devices.

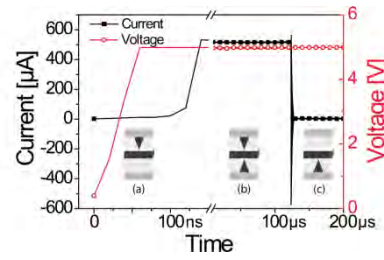


Fig. 5. High resolution pulse measurement of a CRS cell based on Cu/SiO₂ memristive elements showing the dynamics of the change of states. The CRS is initially in LRS/HRS, schematically shown in (a). About 120 ns after pulse application, the CRS cell switches to the LRS/LRS state (b), and a significant current flow through the device can be detected. After 125 µs the CRS cell switches to the HRS/LRS state (c), completing the write operation.

In summary, the use of CRS cells as memory element makes high density crossbar arrays feasible paving the way towards next-generation non-volatile memories.

- [1] J. Borghetti et al., *Nature* 464, 873-876 (2010).
- [2] D. Strukov et al., *Nature* 453, 80-83 (2008).
- [3] J. Green et al., *Nature* 445, 14-17 (2007).
- [4] R. Waser et al., *Nat. Mater.* 6, 833-840 (2007).
- [5] K. Szot et al., *Nat. Mater.* 5, 312-20 (2006).
- [6] E. Linn et al., *Nat. Mater.* 9, 403-406 (2010).
- [7] R. Rosezin et al., *IEEE EDL* 32, 191-193 (2011)

Cu-atom mediated bonding in close-packed benzoate/Cu(110)-systems

M.C. Lennartz¹, N. Atodiresei¹, S. Karthäuser¹, R. Waser^{1,2}, S. Blügel¹

¹ PGI-7: Electronic Materials, Forschungszentrum Jülich

² Institute for Materials in Electrical Engineering and Information Technology 2, RWTH Aachen University

Using UHV-STM investigations and density functional theory (DFT) calculations we prove the contribution of Cu-adatoms to the stabilization of a new high-density phase of benzoate molecules on a Cu(110) substrate. We show that two different chemical species, benzoate and benzoate Cu-adatoms molecules, build the new close-packed structure. Although both species bind strongly to the copper surface, we identify the benzoate Cu-adatoms molecules as the more mobile species on the surface due to their reduced dipole moment and their lower binding energy compared to benzoate molecules. Therefore, the self-assembly process is supposed to be mediated by benzoate Cu-adatom species, which is analogous to the gold-thiolate species on Au(111) surfaces.

In future technological applications, metals should act as electrodes or interconnectors to the CMOS world, whereas molecules with their functional groups and their effort to self-assemble in ordered layers are envisaged as the functional elements. Irrespective of the final circuit design, it is necessary to find suitable molecule/metal combinations that provide the desired functionality reliably. Because of its low resistance and its high heat capacity, copper combined with molecular materials is supposed to provide the prerequisites for developing integrated circuits with decreasing switching times, reduced heat dissipation, and higher reliability. Therefore, the carboxylate/copper system is a promising alternative to the intensively studied thiol/gold system.

First characterizations of benzoic acid (C_6H_5COOH) on Cu(110), done by Richardson et al. [1], showed that benzoic acid forms large domains of several well-ordered structures, depending on temperature and coverage. In this article, we present a UHV-STM experimental study and DFT calculations on the adsorption of benzoic acid on a Cu(110) surface [2]. We demonstrate the role of the copper adatoms in modifying the carboxylate/copper interface.

Straight forward vapor-deposition ($T_{\text{Sub}}=293$ K, $t=5$ min, $p=4.7 \cdot 10^{-4}$ mbar) with an additional annealing step at around 590 K results in a surface covered by a close-packed $c(8 \times 2)$ surface structure of standing molecules. The benzoate molecules bind usually on top of two copper atoms on the outermost surface layer rows, resulting in a surface coverage of 0.25 [1]. Furthermore, we found regions with a new high-coverage structure [2]. The latter has a smaller feature size of the spots displaying a row direction rotated by an angle of 35° with respect to the known

$c(8 \times 2)$ structure. Assuming commensurability and a standing-up configuration, high-resolution STM images and linescans along and between the molecular rows allow us to identify the unit cell of the new high-coverage phase as a $(1 \ 1; -4 \ 2)$ structure with two molecules in the unit cell (Fig. 1).

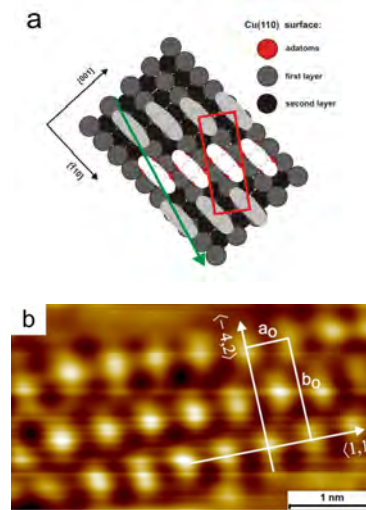


FIG. 1: a) Schematic of the new adatom-stabilized $(1 \ 1; -4 \ 2)$ structure of the benzoates on the Cu(110) surface. b) High-resolution STM image ($U_T=0.78$ V, $I_T=0.36$ nA) of the new close-packed structure with unit cell and substrate vectors.

Both the benzoates at the corners and the benzoates in the centers of the unit cell build rows in the $[112]$ direction. The molecules at the corner can be identified as chemisorbed on top of the copper atom rows of the outermost substrate layer, whereas this is not the case for the benzoate molecule in the center of the unit cell. A short bridge site at the center of the unit cell can only be provided by the incorporation of copper adatoms. This assumption is supported by the heights of our linescans from STM measurements and studies on flat-lying benzoate monolayers which can be interpreted by the incorporation of copper adatoms. Therefore, the new structure is described with a row of adatoms between the central benzoate molecule and the outermost copper layer so that all benzoate molecules of the unit cell bind on top of copper atoms and bridge the short lattice site (Fig. 1).

Our ab initio total-energy calculations have been performed in the framework of density functional theory (DFT) [3] by using the Perdew-Burke-Ernzerhof (PBE) [4] exchange-correlation energy functional as implemented in the VASP code [5, 6].

The molecule/metal system was modeled by a 3D repeated slab as described in detail for example in [7].

The theoretical calculations prove that the strong covalent interaction between the oxygen atoms of the carboxylate moiety and copper surface atoms favors the adsorption of molecules in the so-called bridge position. Neglecting the copper adatoms, we calculate a first structure where one benzoate is placed on two copper first-layer atoms and another benzoate molecule is placed on top of two copper second-layer atoms. During the geometry optimization, the second molecule relaxes to a configuration where it binds directly to copper atoms of the first layer due to a stronger covalent interaction, which can not be established with copper adatoms of the second layer. This relaxed structure does not agree with the one observed in the experiment. In a second configuration, one benzoate molecule is placed on top of copper first-layer atoms as before, but the second benzoate is substituted by a benzoate copper-adatom molecule placed on top of two copper second layer atoms. This configuration relaxes toward the experimentally observed (1 1; -4 2) structure with all benzoate molecules in bridge positions.

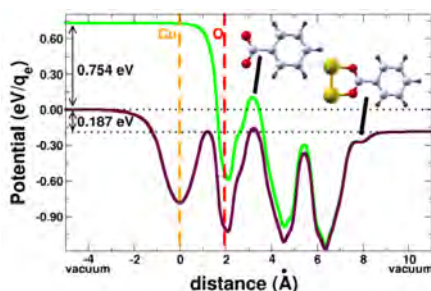


FIG. 2: Plane averaged electrostatic potential of the benzoate and the benzoate copper-adatoms molecules. The vertical dashed lines represent the positions of the copper and oxygen atoms.

Adsorption energy and enthalpy calculations demonstrate that two different chemical species, namely the benzoate and benzoate Cu-adatoms molecule, are strongly binding to the Cu(110) surface. The absolute value of the adsorption energy of the benzoate copper-adatoms molecule adsorbed on Cu(110) is 0.9 eV smaller than the one of the benzoate adsorbed directly on Cu(110) [2]. Therefore, the adsorption of the benzoate copper-adatoms molecule is weaker, the bonds formed between the copper-adatoms and the Cu(110) surface are easier to break and this suggests that the benzoate copper-adatoms molecules may have a higher surface mobility than the benzoate molecules.

In FIG. 2 we present the plane averaged electrostatic potential of the benzoate and the benzoate copper-adatoms molecule. The difference between the right and the left vacuum level shows the magnitude of the dipole moment and represents the change in the electrostatic potential along the molecule, when going from the right to the left. Based on frontier

molecular orbital interaction theory arguments, due to the huge decrease of the dipole moment together with the smaller adsorption energy of the benzoate copper-adatoms molecule as compared to benzoate, we conclude that the bonds between benzoate copper-adatoms molecules and the Cu(110) are much easier to break than those between benzoate molecules and the copper surface. The feature indicates that the chemical species with higher surface mobility are the benzoate copper-adatom molecules. This is not surprising, since for the well studied thiol/gold systems it has also been shown that gold-thiol complexes are more mobile on the metal surface than thiol molecules.

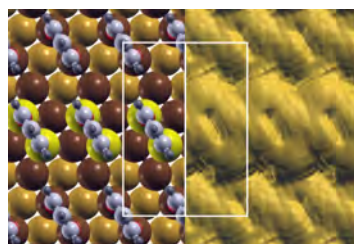


FIG. 3: Simulated constant-current STM image of the (1 1; -4 2) monolayer chemisorbed on Cu(110) for an applied bias voltage of $U_T = -0.78$ eV.

Finally we analyzed the real space topography of the (1 1;-4 2) structure by simulating STM images for an applied voltage of $U_T = -0.78$ eV (Fig. 3). Comparing the experimentally measured data, the surface schema and the simulated STM images, we conclude that the bright spots seen in experiment correspond to the spacing between the molecules. These spots represent the tail of the σ and π bonding wave functions, which have a maxima located at the anchoring carboxylate moiety. Although less obvious in the experimental STM image, the different highs of the molecular rows seen in the measured linescans are clearly visible in the simulated STM image.

This work was supported by the DFG Priority Program SPP1243. The theoretical calculations have been performed on the IBM Regatta and Blue Gene/L supercomputers in Jülich Supercomputing Centre (JSC).

- [1] B. G. Frederick, F. M. Leibsle, S. Haq, and N. V. Richardson, *Surf. Rev. Lett.* **3**, 1523–1546 (1996).
- [2] M. C. Lennartz, N. Atodiresei, L. Müller-Meskamp, S. Karthäuser, R. Waser, and S. Blügel, *Langmuir* **25**, 856 (2009).
- [3] P. Hohenberg and W. Kohn, *Phys. Rev.* **136**, B864 (1964).
- [4] J. P. Perdew, K. Burke, and M. Ernzerhof, *Phys. Rev. Lett.* **77**, 3865 (1996).
- [5] G. Kresse and J. Hafner, *Phys. Rev. B* **47**, 558 (1993).
- [6] G. Kresse and J. Furthmüller, *Phys. Rev. B* **54**, 11169 (1996).
- [7] N. Atodiresei, V. Caciuc, K. Schroeder and S. Blügel, *Physical Review B* **76**, 115433

Effect of Charge Compensation Mechanisms on the Conductivity at $\text{LaAlO}_3 / \text{SrTiO}_3$ Interfaces

F. Gunkel¹, P. Brinks², S. Hoffmann-Eifert¹, R. Dittmann¹, M. Huijben², J. E. Kleibeuker², G. Koster², G. Rijnders², and R. Waser¹

¹ PGI-7: Electronic Materials, Forschungszentrum Jülich

² MESA+ Institute for Nanotechnology, University of Twente, The Netherlands

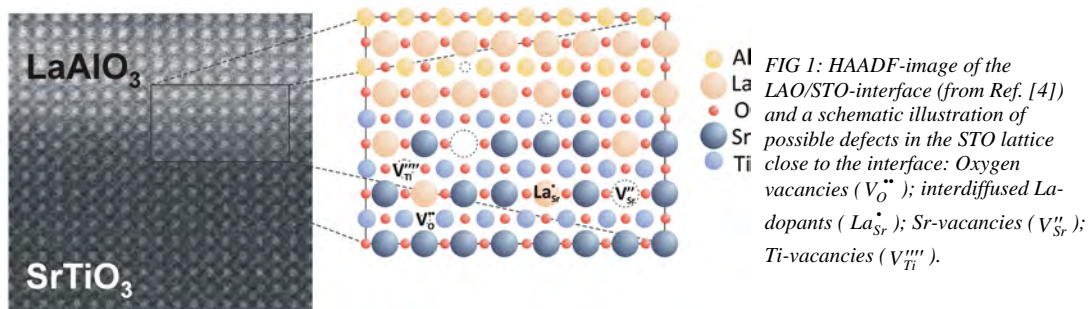
The equilibrium high temperature conductance (HTEC) of $\text{LaAlO}_3/\text{SrTiO}_3$ (LAO/STO)-hetero-interfaces was investigated as a function of ambient oxygen partial pressure ($p\text{O}_2$). Metallic conducting interfaces were obtained for LAO grown on STO single crystals as well as on STO-buffered LSAT substrates. For both structures, the high temperature sheet carrier density n_s of the LAO/STO-interface saturates at a value of about $1 \times 10^{14} \text{ cm}^{-2}$ for reducing conditions, which indicates the presence of interfacial donor states. A significant decrease of n_s is observed at high oxygen partial pressures. According to the defect chemistry model of donor-doped STO, this behavior for oxidizing conditions can be attributed to the formation of cation vacancies as charge compensating defects.

The role of defects is a focus of the ongoing discussion about the electronic properties of the conducting interface between the two insulators LaAlO_3 (LAO) and SrTiO_3 (STO). Besides the model of charge transfer due to the polar nature of LAO, it is generally accepted that defects in the vicinity of the LAO/STO interface can have a large impact on the electronic properties. At the extreme, the interdiffusion of La-ions on Sr-sites (La_{Sr}^+), and the creation of oxygen vacancies ($\text{V}_\text{O}^{\bullet\bullet}$) within the STO lattice, have even been considered as sole origin of the interface conduction.

In this study, the LAO/STO-interface is discussed from a defect chemical point of view [1]. Besides the above described defects, also cation vacancies in the STO lattice, i.e. Sr-vacancies ($\text{V}_{\text{Sr}}^{\bullet\bullet}$) and Ti-vacancies ($\text{V}_{\text{Ti}}^{\bullet\bullet\bullet}$), were considered in order to draw a complete picture of the LAO/STO-interface (see Fig. 1). The conducting LAO/STO-interfaces are fabricated by pulsed laser deposition (PLD) of LAO on TiO_2 -

terminated STO single crystal substrates, and by the heteroepitaxial growth of LAO and STO on LSAT ((La,Sr)(Al,Ta) O_3) single crystal substrates. Both types of heterostructures show metallic conductance behaviour at low temperatures as revealed by Hall measurements. In contrast to the standard LAO/STO-heterostructure, the electron mobility at the LAO/STO-interface on LSAT exhibits only a weak temperature dependence [2]. This indicates a more defective interface region originating from the STO growth process [3].

The particular defect structure of the LAO/STO-interface was investigated by means of high temperature conductance measurements in equilibrium with the surrounding atmosphere (HTEC). In the studied temperature range (950K-1100K), the decisive defect reactions at the LAO/STO-interface are activated, and hence, strive for a well-defined thermodynamic equilibrium state, which is related to the ambient oxygen pressure ($p\text{O}_2$). The resulting conductance characteristics contain information about the chemical reactions, which take place at the LAO/STO-interface, and the corresponding defect concentrations. Using this method, we could exclude that mobile oxygen vacancies are the sole origin of the electronic charge carriers at the interface [4]. In fact, the temperature- and oxygen partial pressure independent plateau region, which is found for reducing atmospheres, indicates the presence of immobile donor states (D^{\bullet}) close to the interface. In the $p\text{O}_2$ -independent plateau region, the sheet electron density n_s approaches a value of $1 \times 10^{14} \text{ cm}^{-2}$ for both samples (LAO/STO and LAO/STO/LSAT). This value is consistent with the carrier densities obtained from low temperature Hall measurements [2] as well as from spectroscopic investigations [5].



The HTEC measurements on LAO/STO systems grown on LSAT substrates additionally revealed a very interesting feature at oxidizing conditions. The observation of this effect was possible due to the low intrinsic conductance of the LSAT single crystal, while, for the standard LAO/STO-system, the interface behaviour under oxidizing conditions is mainly hidden by the large intrinsic conductance contribution of the SrTiO₃ single crystal [4].

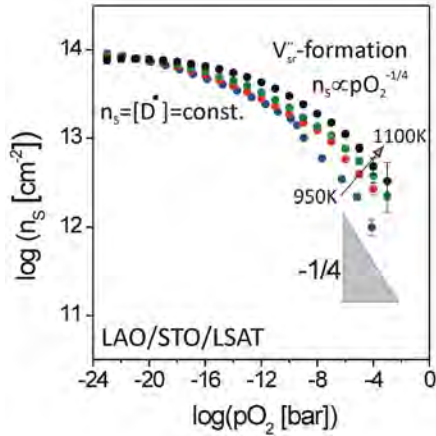


FIG 2: pO_2 -dependence of the sheet carrier density, n_s , of the LAO/STO interface on LSAT obtained from HTEC measurements (from Ref. [1]); A pO_2 - and temperature independent region is found for reducing conditions indicating the presence of interfacial donor states (D'). For oxidizing atmosphere, n_s decreases proportional to $pO_2^{-1/4}$ which can be attributed to the formation of acceptor-like Sr-vacancies.

Starting from the plateau region at low oxygen partial pressure (see Fig. 2), the interfacial electron density starts to decrease for increasing pO_2 . This decrease becomes proportional to $pO_2^{-1/4}$ for higher oxidizing conditions. In this region, n_s is no longer temperature independent. In contrast, n_s is thermally activated exhibiting an activation energy E_A of approximately 1eV. As will be discussed below, this change of behaviour can be seen as an indication for the formation of additional defects in the vicinity of the LAO/STO-interface.

The measured HTEC characteristics of the LAO/STO interfaces resemble in good agreement the HTEC behavior of donor-doped STO [6]. Therefore, the corresponding defect chemistry model was transferred to the LAO/STO heterostructures. In the pO_2 -independent region, each donor is compensated by a free electron which contributes to the interface conduction (full electronic compensation). This can be expressed by the charge neutrality condition $n=[D']$, whereas the concentration of extrinsic donors $[D']$ is considered as a pO_2 -independent parameter.

In order to maintain charge neutrality, the observed decrease of n below the donor level $[D']$ requires the formation of additional compensating defects which carry a negative net charge. This yields to the conclusion that cation vacancies, either Sr-vacancies (V''_{Sr}) or Ti-vacancies (V''''_{Ti}), have to be considered as acceptor-type electron traps in the vicinity of the

LAO/STO-interface [1]. Considering this scenario, the defect chemistry model of STO predicts a decrease of the electron density proportional to $pO_2^{-1/4}$ (in the limiting case of a full ionic compensation of the extrinsic donors). Hence, the observation of this characteristic behaviour can be regarded as an indication of the formation of cation vacancies in the vicinity of the LAO/STO-interface in oxidizing atmosphere.

The in-situ study of the HTEC of LAO/STO-heterostructures emphasizes the importance of crystal disorder for the electronic properties of the LAO/STO-interface. The observed pO_2 - and temperature-independence of the sheet electron density for reducing conditions supports the idea of a donor-type conduction mechanism at the LAO/STO-interface such as provided by cation-intermixing. Furthermore, the decrease of n_s in oxidizing conditions indicates a complex charge compensation mechanism in the vicinity of the interface, which involves the formation of cation vacancies at high oxygen partial pressures. This implies that oxygen annealing after the growth of LAO/STO-heterostructures - which is commonly thought to merely remove oxygen vacancies from the STO substrate - can also result in an increased cation vacancy concentration at the interface. These additional defects can reduce the electron density and, moreover, can act as scatter centers at low temperatures.

As pivotal result of this study, it has been shown that in the vicinity of the LAO/STO-interface exchange reactions in the cation sublattice, i.e., formation and annihilation of strontium vacancies take place at typical growth temperatures and have to be considered in the discussion of the LAO/STO interface.

This work was performed during a bilateral collaboration of the PGI-7 and the MESA+Institute of the University of Twente, Enschede.

-
- [1] Gunkel P. Brinks, S. Hoffmann-Eifert, R. Dittmann, M. Huijben, J. E. Kleibeuker, G. Koster, G. Rijnders, and R. Waser., Appl. Phys. Lett. 100, 052103 (2012).
 - [2] P. Brinks, W. Siemons, J. E. Kleibeuker, G. Koster, G. Rijnders, M.Huijben, Appl. Phys. Lett. 98, 242904 (2011).
 - [3] D. J. Keeble, S. Wicklein, R. Dittmann, L. Ravelli, R. A. Mackie, and W. Egger, Phys. Rev. Lett. 105, 226102 (2010).
 - [4] F. Gunkel, S. Hoffmann-Eifert, R. Dittmann, S. B. Mi, C. L. Jia, P. Meuffels, R. Waser, Appl. Phys. Lett. 97, 012103 (2010).
 - [5] G. Berner, S. Glawion, J. Walde, F. Pfaff, H. Hollmark, L. C. Duda, S. Paetel, C. Richter, J. Mannhart, M. Sing, and R. Claessen, Phys. Rev. B 82, 241405 (2010).
 - [6] R. Moos and K. H. Haerdtl, J. Am. Ceram. Soc. 80, 2549 (1997).

High density 3D memory architecture based on the resistive switching effect

C. Kügeler, M. Meier, R. Rosezin, S. Gilles, and R. Waser

PGI-7: Electronic Materials, Forschungszentrum Jülich

We demonstrate the fabrication of a 3D memory architecture based on the resistive switching effect. Resistive memory (RRAM) is under wide investigation since it is non-volatile, promises fast operation and can be integrated into high density architectures like crossbar arrays. Here, silver-doped methylsilsesquioxane (MSQ) is integrated in crossbar array structures providing good planarization properties so that emerging lithography techniques like nanoimprint lithography (NIL) are applicable. Furthermore, we could prove that silver-doped MSQ can be used as resistive switching material on the nano scale. Using this technique, crossbar arrays with a minimum feature size of only 100 nm are stacked on each other, which comprises the doubling of the memory density. Furthermore even higher integration is in principle not limited by this technique, while the CMOS overhead increases only slightly.

The resistive switching effect belongs to a new storage concept, which recently became very attractive, since it combines fast operation with non-volatile data storage [1]. A resistive switching memory is in principle comprised of two metal electrodes separated by a functional isolator (MIM structure). This device can exhibit two or more different ohmic resistances referred to in the simplest case as high resistance state (HRS) and low resistance state (LRS). The resistance states are non-volatile and can be toggled by simply exceeding threshold voltages $V_{th,SET}$ or $V_{th,RESET}$. Digital information like “0” can be defined by LRS and “1” by HRS. Stored information is retrieved by measuring the electrical current, when a small read voltage V_{read} is applied.

One benefit from resistive switching cells is that the concept deals with two terminal devices instead of three terminal devices like DRAM where always one access transistor is used. This offers the opportunity to invent novel and advanced architectures. Passive nano crossbar arrays on top of a conventional active CMOS infrastructure are one alternative approach [2]. In this architecture, a highly regular grid of parallel bottom electrodes and perpendicular top electrodes sandwiches the functional material in between and each crosspoint is equal to one memory cell with a size of $4F^2$. Recently we demonstrated the fabrication of nanocrossbar arrays with nanoimprint technology and the use of amorphous methylsilsesquioxane (MSQ) in combination with silver electrodes [3]. However, purely passive crossbar structures suffer from the drawback that sneak paths

will occur during the read/write process, if no non-linear elements like diodes are integrated with each resistive cell. Theoretical considerations show that dependent on the R_{OFF}/R_{ON} ratio passive crossbar arrays without rectifying elements will work, but the number of rows and columns is strongly limited, because error free operation, meaning a sufficient voltage swing for the CMOS periphery, is required even if a worst case pattern is stored in the memory. Using a three dimensional structure, where several crossbar arrays are stacked on top of each other, can circumvent the loss of lateral crossbar size.

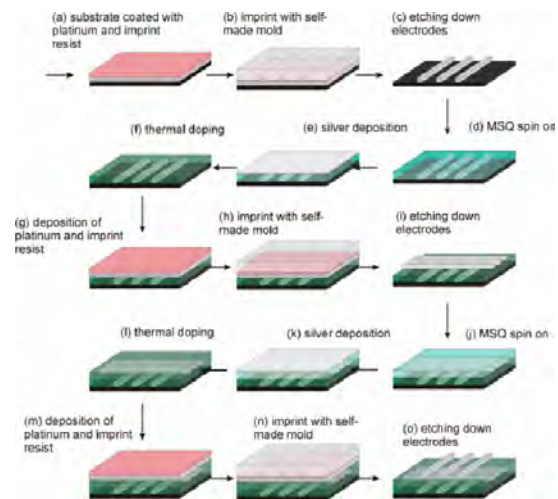


FIG. 1: Process flow of the fabrication procedure for silver-doped MSQ. The process starts with a platinumized SiO_2 substrate and imprint resist on top (a), which is then indented by a homemade mold (b). The patterns are transferred by etching (c). Afterwards, MSQ is spun on (d), covered by a thin silver layer (e), which is thermally doped into the material (f). By another imprint process, the top electrodes are created (g)–(i). The process is repeatable, creating multiple functional layers (j)–(o).

The fabrication of 3D crossbar arrays is shown in Fig. 1 and starts from a 30 nm thin platinumized Si/SiO_2 substrate with the structuring of the bottom electrode set (Fig. 1a). First, a resist is structured by nanoimprint lithography using a self-made quartz mold, which was made by electron beam lithography and dry etching (Fig. 1b). Next, the resist pattern is used to transfer the structures into the Pt layer by ion beam dry etching (Fig. 1c). This first bottom electrode set is covered by MSQ (Fig. 1d), which in this case fulfills two functions. First it provides good planarization properties and secondly it can be used as resistance switching matrix material [4]. After thinning the MSQ down to around 40 nm by Ar dry etching, the top electrodes can be applied.

Silver, as used in our previous work, cannot be chosen as electrode material, since our experiments have shown that during the curing of the MSQ film (1h, 425°C, nitrogen atmosphere) silver would diffuse uncontrolled into the film, leading to numerous defects in the electrode and thus destroying the memory array. So, for 3D crossbar arrays, temperature stable electrodes have to be used. To achieve the resistance switching property, silver has to be incorporated into the film, which is done thermally. A 15 nm thick silver film is evaporated on top of the sample (Fig. 1e), which is then treated at 450°C in N₂ for 5 min. A part of the silver diffuses into the MSQ and the remaining silver on top is removed by ion beam etching (Fig. 1f). Now, a Ti(5 nm)/Pt(25 nm)/Ti(5 nm) metal stack is sputtered on top for the second electrode layer (Fig. 1g). The process of imprint and dry etching is now repeated with a rotated mold (Fig. 1h) to form the top electrodes of the first crossbar array (Fig. 1i). One can repeat the procedure very often and fabricate a stack of many memory layers (Fig. 1j–o). Fig. 2 shows SEM images of some resulting nano crossbar and word structures. In Fig. 2a four metal layers with 16 parallel electrodes each (200 nm wide) are stacked on each other. The subsequent layers are rotated by 90°. In Fig. 2b two vertical word structures with a common single intermediate electrode are shown. This single electrode is 100 nm wide. A Focused Ion Beam (FIB) was used for cross section images (Fig. 2c). This cross section reveals the memory cell arrangement with four metal layers in the vertical direction whereby in this example every MSQ interlayer is Ag-doped and consequently defined as a functional layer. The presented solution to sandwich silver-doped MSQ between two inert Pt electrodes circumvents electrode degradation during the temperature treatment processes.

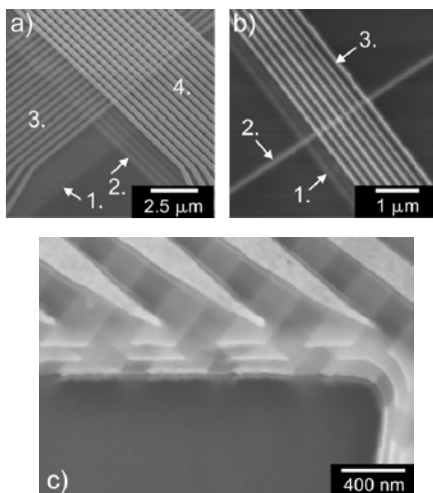


FIG. 2. (a) SEM images of multilayer crossbar memory structures with a half pitch of 200 nm. (b) Multilayer word structure with a half pitch of 100 nm. (c) FIB cross section of a four metal layer crossbar structure.

To prove that Ag doped MSQ will work the functionality in 3D nanocrossbar arrangements needs to be tested. The experiments are performed on a cell

in the corner of a crossbar array with an electrode width of only 200 nm, similar to that in Fig. 2c. Two superposed cells with one shared middle electrode (Fig. 3a) are contacted and then switching pulses are applied. The result for the top cell is presented in Fig. 3b. The cell is switched to the LRS by a voltage sweep and the resistance decreases to 10 kΩ followed by a RESET sweep, which turns the cell OFF to a resistance of 10 MΩ. Those switching characteristics are repeatable. The bottom cell exhibits similar properties and can be toggled between LRS and HRS achieving a good R_{OFF}/R_{ON} ratio > 100 (Fig. 3c).

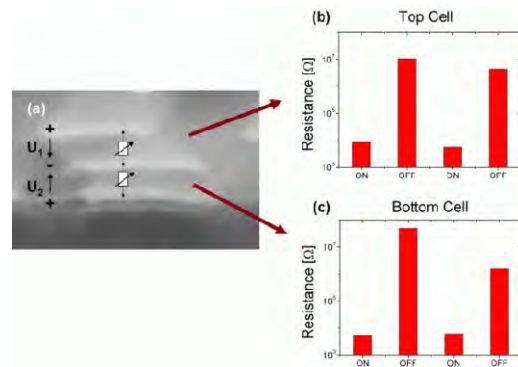


FIG. 3. (a) Two Pt/Ag doped MSQ/Pt memory cells on top of each other with applied voltages (magnification from Fig. 2c). (b) Resistances measured at the top cell during a SET and RESET sequence. (c) Resistances measured at the bottom cell during a SET and RESET sequence.

We present a new three dimensional multilayer stack architecture for future non-volatile high density memory applications. As core structures, passive crossbar arrays were fabricated with nano imprint lithography, offering immense scaling potential. The memory functionality is based on the resistive switching effect in silver-doped MSQ with inert Pt electrodes. The results suggest a method to fabricate a non-volatile memory with a dramatically increased memory density.

[1] R. Waser and M. Aono, *Nat Mater* **6**, 833 (2007).
 [2] D. Strukov and K. Likharev, *Nanotechnology* **16**, 888 (2005).
 [3] M. Meier, S. Gilles, R. Rosezin, C. Schindler, S. Trellenkamp, A. Ruediger, D. Mayer, C. Kuegeler, and R. Waser, *Microelectronic Engineering* **86**, 1060 (2009).
 [4] M. Meier, C. Schindler, S. Gilles, R. Rosezin, A. Ruediger, C. Kuegeler, and R. Waser, *IEEE Electron Dev Lett* **30**, 8 (2009).

Origin of the Nonlinear Switching Kinetics and Scaling Studies of Valence Change Memory Cells

S.Menzel², M. Waters¹, A. Marchewka², U. Böttger², R. Dittmann¹, R. Waser^{1,2}

¹ PGI-7: Electronic Materials, Forschungszentrum Jülich

² Institut für Werkstoffe der Elektrotechnik 2 – RWTH Aachen University

Experimental pulse length-pulse voltage studies of SrTiO₃ memristive cells which reveal nonlinearities in the switching kinetics of more than nine orders of magnitude were performed. The experimental results are interpreted using an electro-thermal 2D finite element model. The nonlinearity arises from a temperature increase in a few nanometer thick disc-shaped region at the Ti electrode and a corresponding exponential increase in oxygen vacancy mobility. Our model fully reproduces the experimental data and it provides essential design rules for optimizing the cell concept of valence change memories. The model is generic in nature: it is applicable to all those oxides which become n-conducting upon chemical reduction and which show significant ion conductivity at elevated temperatures.

Valence change memory (VCM) cells are a promising candidate for next generation non-volatile, high speed and highly scalable memory cells [1,2]. Particularly, a huge nonlinearity in the switching kinetics is needed to meet the demands posed by the voltage-time dilemma [2]. It is widely accepted that the drift of oxygen vacancies on the nanoscale and a subsequent electrochemical redox process are responsible for the VCM effect. Hereby, the movement of oxygen vacancies due to ion hopping is the limiting factor in the switching process. The mobility of ions can be either field accelerated or temperature activated. But, a detailed investigation of the dominating process has not been shown yet. Herein, we report on experimental switching kinetics studies on SrTiO₃ based VCM cells. The experimental results are interpreted using an electro-thermal 2D finite element model which allows for discriminating between the field and temperature contribution to the ion mobility enhancement. This electro-thermal model is subsequently employed to investigate the scaling potential of VCM cells.

The SrTiO₃ thin films with 1 at% Fe-doping of 50 nm thickness were grown by pulsed laser deposition (PLD) on (100)-oriented 1 at% Nb-doped SrTiO₃ (Nb:STO) single crystals serving both as substrate and bottom electrode. Subsequently, circular top electrodes of 50 μm diameter were prepared by magnetron sputtering of Pt (50 nm)-covered Ti (50 nm) through a shadow mask. By a wet-etching step using buffered HF solution a part of the bottom electrode was exposed. Al wire bonding of the

bottom electrode was used to achieve an ohmic contact. An initial quasistatic *I-V* sweep was used to electroform the VCM cell.

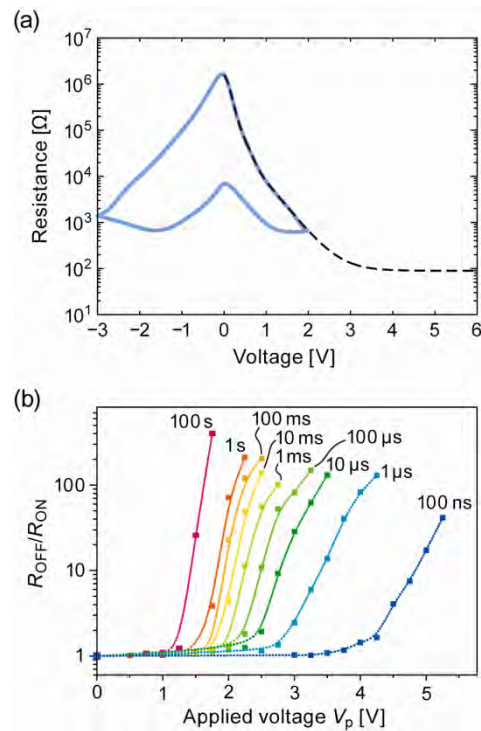


FIG 1: (a) *R-V* characteristic of a measured cell (blue curve) and in the simulation (black dashed curve). (b) SET switching dynamics of the corresponding sample for different pulse amplitudes and pulse widths, shown as the R_{OFF}/R_{ON} ratio as a function of the applied voltage amplitude of the pulse and the pulse duration..(Redrawn from [3]).

The fabricated VCM cells were electrically characterized by performing quasistatic *I-V* sweeps as well as by defined voltage pulses. Thereby, the voltage was always applied to the top electrode. The measured quasistatic *R-V* characteristic is shown in Figure 1a. Apparently, the low resistive state (ON state) and the high resistive state (OFF state) exhibit a nonlinear voltage dependence. A quasistatic resistance ratio $R_{OFF}/R_{ON} > 100$ is observed for moderate SET and RESET voltages of 2 V and -3 V, respectively. Pulse measurements with a pulse duration Δt_p ranging from 100 ns to 100 s and a pulse amplitude V_p ranging from 0.5-5 V were performed. Before and after a SET voltage pulse, the cell resistance was measured quasistatically to

determine the resistance change. The cell was subsequently RESET to its initial OFF state using a quasistatic I - V sweep. Figure 1b depicts the resulting resistance change. A highly nonlinear switching kinetics is visible. Changing V_p by a factor of 5 leads to a change of 9 orders of magnitude in the Δt_p required to SET the cell.

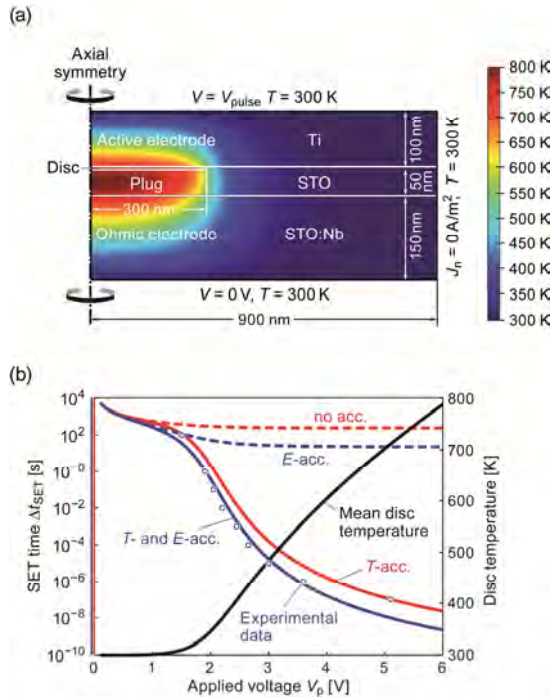


FIG. 2: (a) Cross section of the simulated cell. The temperature distribution for $V_p = 5$ V is shown in color. (b) Calculated SET time depending on the applied voltage for the four different cases in red and blue. The black line corresponds to the mean disc temperature used for the calculations. The experimental data are extracted from Figure 1(b) for a resistance ratio $R_{OFF}/R_{ON} = 30$ and shown as open circles. (Redrawn from [3]).

To interpret the experimental data we consider a 2D axisymmetric finite element simulation model of the VCM cell (see Figure 2(a)). The simulated cell comprises an n -conducting cylindrical region (“plug”) grown during electroforming in the SrTiO_3 film and a disc shaped region at the top electrode interface (“disc”). The conductivity in the disc region is fitted so that the experimental R - V characteristic is obtained (cf. Figure 1a). The movement of oxygen vacancies through this interfacial disc region triggers the switching event. The SET time can thus be estimated from the disc thickness and the drift velocity of oxygen vacancies as $\Delta t_{SET} = l_{disc}/v_{drift}$. The drift velocity is calculated according to the Mott-Gurney law of ion hopping as

$$v_{drift} \propto (T/K)^{-1} \exp(\Delta W_A/kT) \cdot E_0 \sinh(E_{disc}/E_0).$$

Here, the activation energy $\Delta W_A = 1.01$ eV, the characteristic field $E_0 = 1$ MV/cm, and $E_{disc} = V_{disc}/l_{disc}$. Hence, the SET time depends on the volt drop across the disc V_{disc} and the mean disc temperature T . These quantities are extracted from numerical FEM simulations of the field and temperature distribution with the VCM cell. For this,

the heat equation is solved for along with the continuity equation [3].

Figure 2a shows the simulated temperature distribution for an applied voltage $V_p = 5$ V. Apparently, the highest temperature emerges in the disc region. The resulting SET times (T - and E -acc.) are depicted in Figure 2b along with the mean disc temperature and the experimental data. Here, it is discriminated between the contributions of the field acceleration (E -acc.), the temperature acceleration (T -acc.). For comparison the non accelerated case for a purely linear drift (no-acc.) is shown. A best fit to the experimental temperature is obtained for a combination of field and temperature acceleration. Evidently, the latter is the dominating factor in interpreting the origin of the nonlinear switching kinetics. It has been shown that for all reasonable alternative scenarios, either the fitting procedure fails dramatically or unphysical parameter values have to be used [3].

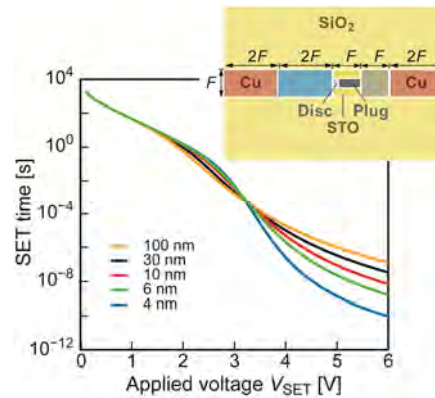


FIG. 3 Calculated SET time depending on the applied voltage for temperature and field accelerated switching. The cell geometry is shown in the inset. The feature size F has been used as a parameter for the set of calculations. The disc thickness is 3 nm in all simulations and the diameter of the filament is $0.4 F$.

To project the scaling potential of VCM cells the electro-thermal simulation model is applied to a nanosized axisymmetric VCM cell with an active electrode and an ohmic electrode as well as Cu interconnects and an adjacent SiO_2 layer (see inset in Figure 3), while the dimensions scale with F . Figure 3 shows the calculated SET times depending on the applied voltage. Apparently, the switching speed for $V_{SET} > 3.5$ V increases for smaller feature sizes F . This demonstrates that nanosized VCM cells are feasible.

[1] R. Waser, R. Dittmann, G. Staikov, K. Szot, Adv. Mater. 21, 2632 (2009).
 [2] A. Sawa, Mater. Today, 11, 28 (2008).
 [3] S. Menzel, M. Waters, A. Marchewka, U. Böttger, R. Dittmann, R. Waser, Adv. Funct. Mater., 21, 4487, (2011).

Resistive switching in 8 nm thin TiO₂ films grown by ALD

S. K. Kim¹, J. Zhang¹, C. Nauenheim¹, S. Mi², C. Kügeler¹, S. Hoffmann-Eifert¹, and R. Waser¹

¹ PGI-7: Electronic Materials, Forschungszentrum Jülich

² PGI-5: Microstructure Research, Forschungszentrum Jülich

We report on the development of a special atomic layer deposition (ALD) process for the growth of homogeneous and dense TiO₂ thin films from a stabilized titanium-isopropoxide precursor (Ti(O-i-Pr)₂(tmhd)₂) and water. Films deposited at 365 °C showed a nano crystalline structure and a surface roughness of about 1 nm. We integrated the films into cross point structures which represent the building blocks of future RRAM devices. Binary resistive switching was demonstrated on 100 x 100 nm² crosspoint structures containing ALD grown anatase type TiO₂ films with thicknesses as low as 8 nm.

Titanium oxide (TiO₂) films may act as functional layers in non-volatile resistive random access memories (RRAM). Titanium oxide shows binary stable electric resistance states, which can be switched from high to low resistance and vice versa by applying a certain voltage. This concept provides the benefit of a two-terminal device that permits the integration of electronic functions into crossbar structures with the ease of a moderate integration effort as compared to CMOS technology. Atomic layer deposition (ALD) is a surface-reaction controlled process and thereby allows homogeneity and excellent film thickness controllability to be achieved on complex structures. ALD is one of the most important technologies in today's DRAM and FLASH memory production.

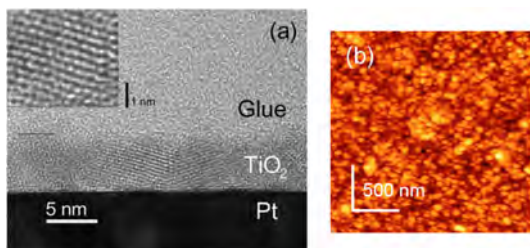


FIG. 1: a) Cross-sectional HRTEM image of a 5 nm thin TiO₂ film grown by ALD at 365 °C using Ti(O-i-Pr)₂(tmhd)₂ and H₂O as precursors. b) AFM image of a corresponding 25 nm TiO₂ film showing the homogeneous nano crystalline structure (taken from [1]).

In our study we applied the ALD technique to integration of dense TiO₂ films with thickness below 10 nm into sub-micron crosspoints as a pre-study for future integration into crossbar structures. For the ALD process we chose a liquid delivery injection technique which enables the use of a Ti-precursor with high thermal stability, Ti(O-iPr)₂(tmhd)₂

dissolved in ethylcyclohexane. The relatively high growth temperature during ALD of about 365 °C resulted in TiO₂ films which were crystallized in an anatase-type phase as deposited.[1] The obtained nano crystalline structure shows a dense morphology combined with a smooth surface structure for film thicknesses between 5 to 30 nm (see Figure 1). The residual carbon content in the films was below 3 at% as determined by XPS analysis.[1] The optimized ALD process was then integrated into the process line of crosspoint structures without any further modification. A schematic of the crosspoint structures is shown in Figure 2.

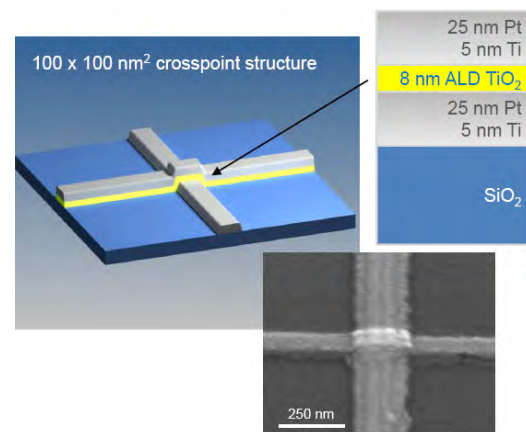


FIG. 2: Schematic and layer structure of a single crosspoint test structure. On one wafer thousand of crosspoints are fabricated for statistical characterisation. Each test device consists of an oxidized silicon substrate with a 5 nm Ti / 25 nm Pt bottom electrode, a 8 nm thin TiO₂ film grown by ALD and a Ti/Pt top electrode. The SEM picture shows the top view of a single 100 x 100 nm² crosspoint device.

Nano crosspoint devices were fabricated for the electrical characterization of the resistive switching properties. For this a combination of nanoimprint lithography (NIL), electron beam lithography, sputter deposition, e-beam evaporation, ALD and dry etching techniques was used. First, an oxidized silicon wafer was covered with an adhesion layer and a 30 nm Pt layer by sputter deposition. A subsequent structuring with UV-NIL and Ar plasma etching then defines the 100 nm wide bottom electrode together with the attached contact pad of 100 x 100 μm². [2] Next, the TiO₂ functional layer was deposited by the above described ALD process. Only the excellent step coverage of ALD in comparison to physical deposition techniques like

sputtering enabled us to reduce the film thickness of the functional TiO_2 layer below 10 nm. The homogeneity of the ultra thin ALD TiO_2 layer was obvious from the high yield of switching devices on the wafer of about 80 % which is a reasonable value for this type of laboratory devices. The 100 nm wide top electrode was made by e-beam lithography with a two layer resist system, which ensures an undercut so that after the evaporation of 5 nm Ti and 25 nm Pt a lift-off releases the metal electrode. A final dry etching step through the TiO_2 uncovers the bottom electrode contact pad to make contact for the electrical measurement set up. The scanning electron microscopic (SEM) picture in Figure 2 shows a slightly tilted top view onto a representative $100 \times 100 \text{ nm}^2$ test structure where both electrodes crosses each other with the 8 nm ALD TiO_2 layer in between.

The electrical characterization was performed with an Agilent 1500B semiconductor analyzer and a Suss probe station. A representative initial I-V characteristic measured at room temperature on a virgin Pt / 8 nm ALD TiO_2 / Ti / Pt crosspoint structure is shown in Figure 3a. Despite the film thickness of below 10 nm the TiO_2 films show a very good insulation behavior with values of the leakage current density in the range of 10^{-6} A/cm^2 at 1 V. This indicates the good quality of the functional layer with respect to coverage of the bottom electrode, homogeneity and absence of pinholes or voids. The asymmetric diode like behavior of the I-V characteristic is attributed to the difference of bottom and top contact, one Pt and one Ti, respectively. From previous work it is known that an electroforming process is mandatory to achieve resistive switching. A current driven process with negative polarity has been proofed to be the most reliable one.[3] The corresponding forming characteristic of the ALD TiO_2 film is shown in Figure 3b. Thereby, the current was increased in small steps and the voltage was measured. When the electrical breakdown field was exceeded the device resistance decreased dramatically, here from an initial value of $> 1 \text{ M}\Omega$ down to about 10 k Ω . The lower resistance level (LRS) was then defined as the 'ON' state. After the electroforming process the devices show stable resistive switching. Figure 3c presents five subsequent bipolar switching cycles with small currents and suitable switching voltages. The limiting current compliance was only 80 μA and the RESET performed without any current limitation at less than 100 μA .

Summarizing we produced Pt / TiO_2 / Ti / Pt nano crosspoint structures with functional ALD grown TiO_2 films as thin as 8 nm which exhibited reproducible bipolar resistive switching behavior with currents in the μA -regime.

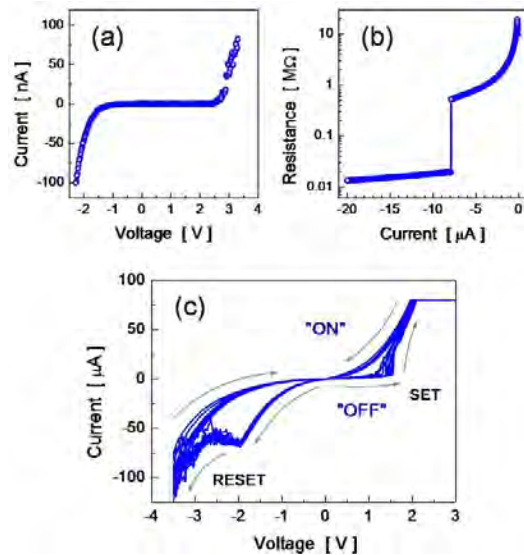


FIG. 3: Sequence of electrical measurements on a representative Pt/ TiO_2 /Ti/Pt crosspoint structure with an 8 nm ALD TiO_2 film. a) I-V characteristic of the test device in as deposited state; b) negative current driven electroforming characteristic; c) reproducible resistive switching behavior with currents in the μA regime.

The authors thank A. Besmehn (ZCH) for XPS analysis, R. Borowski and H. John (IFF) for technical support and M. Reiners (IFF) for fruitful discussions. S.K. Kim acknowledges the financial support from the Alexander von Humboldt foundation.

-
- [1] S. K. Kim, S. Hoffmann-Eifert, S. Mi, R. Waser, *J. Electrochem. Soc.* **156**, D296 (2009).
 - [2] C. Kügeler, M. Meier, R. Rosezin, S. Gilles, R. Waser, *Solid-State Electronics* **53**, 1287 (2009).
 - [3] C. Nauenheim, C. Kügeler, A. Rüdiger, R. Waser, A. Flocke and T.G. Noll, *Nanotechnology* (2008) **NANO** 08, Arlington, Texas, USA (2008)

Selected Publications

1. Schindler, C.; Staikov, G.; Waser, R.
Electrode kinetics of Cu-SiO₂-based resistive switching cells: overcoming the voltage-time dilemma of electrochemical metallization memories
Applied Physics Letters, **94** (2009), 072109
2. Waser, R.; Dittmann, R.; Staikov, G.; Szot, K.
Redox-based resistive switching memories - nanoionic mechanisms, prospects and challenges
Advanced Materials, **21** (2009) 25/26, 2632
3. Linn, E.; Rosezin, R.; Kügeler, C.; Waser, R.
Complementary resistive switches for passive nanocrossbar memories
Nature Materials, **9** (2010), 403 – 406
4. Münstermann, R.; Menke, T.; Dittmann, R.; Waser, R.
Coexistence of filamentary and homogeneous switching in Fe-doped SrTiO₃ thin film memristive devices
Advanced Materials, **22** (2010) 43, 4819 – 4822
5. Lennartz, M.C.; Baumert, M.; Karthäuser, S.; Albrecht, M.; Waser, R.
Dihydroxy (4-thiomorpholinomethyl) benzoic acids - From molecular asymmetry to diode characteristics
Langmuir, **27** (2011) 10312
6. Menzel, S.; Waters, M.; Marchewka, A.; Böttger, U.; Dittmann, R.; Waser, R.
Origin of the ultra-nonlinear switching kinetics in oxide-based resistive switches
Advanced Functional Materials, **21** (2011) 23, 4487 – 4492
7. Rosezin, R.; Linn, E.; Nielen, L.; Bruchhaus, R.; Waser, R.
Integrated complementary resistive switches for passive high-density nanocrossbar arrays
IEEE Electron Device Letters, **32** (2011) 2, 191 – 193
8. Szot, K.; Rogala, M.; Speier, W.; Klusek, Z.; Besmehn, A.; Waser, R.
TiO₂-a prototypical memristive material
Nanotechnology, **22** (2011) 25, 1 – 21
9. Tsuruoka, T.; Terabe, K.; Hasegawa, T.; Valov, I.; Waser, R.; Aono, M.
Effects of Moisture on the Switching Characteristics of Oxide-Based, Gapless-Type Atomic Switches
Advanced Functional Materials, **22** (2011) 70.
10. Valov, I.; Waser, R.; Jameson, J.R.; Kozicki, M.N.
Electrochemical metallization memories-fundamentals, applications, prospects
Nanotechnology, **22** (2011) 25, 254003

Indicators

Quantitative Numbers

	2009	2010	2011
Peer-Reviewed Publications	39	38	41
Graduations			
Master/Diploma	3	3	1
Dissertation	11	4	6
Habilitation	0	0	0

Honours

Feodor Lynen Scholarship	Dr. Martin Weides	Alexander von Humboldt
Promotionspreis	Dr. Björn Lüssem	VDE NRW
Promotion Prize	Dr. Keisuke Shibuya	Marubun Research Promotion Foundation
Ikeda Award	Prof. Rainer Waser	Ikeda Memorial Foundation (Japan)
Klaus Liebrecht Preis	Dr. Martin Weides	Universität Köln
Günther-Leibfried-Preis	Dr. Christina Schindler	Forschungszentrum Jülich
Friedrich-Wilhelm Preis	Dr. Christina Schindler	RWTH Aachen

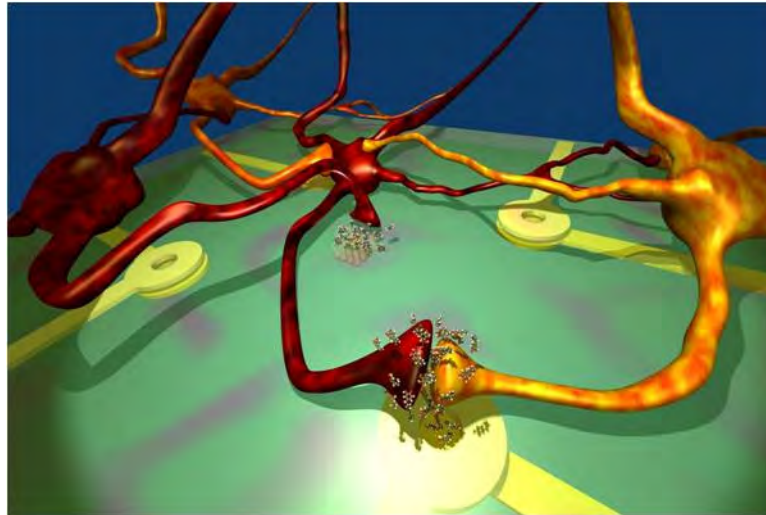
Offers

2009	Prof. Hermann Kohlstedt	Technische Fakultät Universität Kiel
2009	Prof. Kristof Szot	Verleihung des Prof.-Titels vom Präsidenten Kaczynski

Selected Third Party Projects

- EU
Interfacing Oxides (IFOX)
7th Framework Program, NMP Theme, Collaborative project,
01.12.2010-30.11.2013
- EU
ERANet – Matera- “Functional materials for resistive switching memories
23.12.2008–31.12.2011
- EU
Support for training and career development of researchers (Marie Curie) Networks for Initial Training (ITN ENHANCE)
“New Materials: Innovative Concepts for their Fabrication, Integration and Characterization”
01.10.2009–30.09.2013
- HGF Impuls- und Vernetzungsfonds
Virtuelles Institut « MEMRIOX » - Memory Effects in Resistive Ion-beam Modified Oxides
01.01.2011-31.12. 2013
- DFG
Sonderforschungsbereich SFB 917 “Resistively Switching Chalcogenides for Future Electronics (Nanoswitches)”
Sprecher: M. Wuttig, RWTH Aachen; Stellvertr. Sprecher: R. Waser
01.07. 2011-2015

PGI-8/ICS-8: Bioelectronics



In our research we focus on the functional connection of biological and electronic systems where we in particular examine the molecular, cellular and electronic and electro-chemical processes at this interface. This enables the development of electronic sensors for the detection of minute amounts of biochemicals in the environment and in body fluids or even exchange signals with cells. Magnetic sensors are developed for low field magnetic resonance imaging and detection of magnetic nanoparticle markers. For the detection of biomolecules in the environment and in body fluids, we focus on the development of devices that incorporate biological assemblies for analytical and biomedical research. In the Young Investigators Group on Nanotools for Cell-Chip Communication, we develop and investigate on-chip devices for bioelectronic applications based on nanofabrication technologies aimed at the establishment of tools for the communication with cells and cellular networks. In the field of Molecular Bioelectronics, we develop active bio-inorganic components for the investigation and control of charge transport phenomena in and across biomolecules. In Cellular Bioelectronics, we work on interfacing of electronics with cellular systems, including detection, stimulation, and characterization on the cellular and subcellular level. Together with University of Bonn, we work on Biomimetic Sensors towards understanding of processes found in nature and the transfer of the principles to technical systems. This research may lead to new approaches for the development of sensitive implants to replace destroyed sensory cells.

We operate onsite facilities for method developments, prototyping and testing bioelectronic systems, fabricating and measuring the performance of devices, and testing the interaction with biological materials. The Process Technology (PT) Group maintains micro- and nanoelectronics equipment, supports internal and external users of the cleanroom, and offer services for external clients.

Our Institute is embedded in two Helmholtz programmes of the research field “Key Technologies”: the programme FIT and the programme BioSoft: “Macromolecular Systems and Biological Information Processing”.

Head of Institute:

Prof. Andreas Offenhäusser, email: a.offenhaeusser@fz-juelich.de, phone: +49-2461-61-2330.

Scientific Staff

On December 31st 2011, the staff of PGI-8/ICS-8 (including Process Technology Group) comprised 14 scientists, 1 junior research group leader, 17 technicians, 3 Post-Docs, 12 PhD students, and 11 Diploma/Master/Bachelor students.

Scientists

Bousack, Dr. Herbert
Hollmann, Dr. Eugen
Krause, Dr. Hans-Joachim
Mayer, Dr. Dirk
Meffert, Dr. Simone
Mourzina, Dr. Youlia
Offenhäusser, Prof. Andreas
Pabst, Dr. Michael
Panaitov, Dr. Gregor
Vitusevich, Dr. Svetlana
Wördenweber, Prof. Roger
Zhang, Prof. Yi

Junior Research Group Leader

Wolfrum, Junior Prof. Bernhard

Post-Docs & Guest Scientists

Ghosh-Moulick, Dr. Ranjita
Maybeck, Dr. Vanessa
Zhu, Dr. Geng

Scientists working in the PT Group

Albrecht, Dr. Wolfgang
Trellenkamp, Dr. Stefan
Steffen, Alfred

Research Highlights

Axon guidance of rat cortical neurons by microcontact printed protein gradients

R. Fricke, P. Zentis, L. Rajappa, M. Papst, M. Prömpers, D. Saalfrank, M. Banzet, A. Offenhäusser, S. Meffert

PGI-8/ICS-8: Bioelectronics, Forschungszentrum Jülich & JARA-FIT: Jülich-Aachen Research Alliance

In this study, we constructed a discontinuous substrate-bound gradient to control neuronal cell position, pathway of neurite growth and axon directionality. Gradient patterns were fabricated by microcontact printing using laminin/ poly-L-lysine (PLL) or PLL alone. The gradients were tested on neurite growth and their impact on axon guidance effects of embryonic rat cortical neurons. The neurite length was determined and the axon was evaluated by Tau-1 immunostaining. We found that the microgradients of laminin/ PLL and PLL directed neurons adhesion, differentially controlled the neurite growth and guided up to 84% of the axons. Our approach proved to be very successful in guiding axons of single multipolar neurons with very high efficiency. It could thereby be useful to engineer defined neural networks for analyzing signal processing of functional circuits as well as to unravel fundamental questions of axon guidance mechanism.

All of the sophisticated and complex functions of the brain are based on highly ordered cell architecture and precisely wired neural circuits. This process is regulated by extrinsic guiding cues which are expressed as numerous spatio-temporal gradient patterns. Even though numerous techniques were already established [2] to construct substrate-bound gradients which affect axon guidance those procedures still fail to guide the axons of multipolar neurons. Thereby, the aim of this study was controlling 1) neuronal position, 2) pathway of neurite growth, 3) directionality of axon growth. Based on the study of Philipsborn et al. [2006] we fabricated a modified gradient and produced substrate-bound discontinuous patterns of laminin/ poly-L-lysine (PLL) and PLL alone. The gradient was tested for rat cortical neurons in respect to neurite outgrowth and axon guidance. We used laminin since it is the most commonly used ECM protein to foster neurite growth. Our results provide a simple and reproducible microstructuring method to guide axons and control neurite growth in neural networks with defined architecture. For the production of substrate-bound discontinuous gradients, a variety of micropatterns were designed with slight changes in slope, width, and length (Fig. 1). Microstamps were

produced by photolithographically generating a master and then casting Poly-(dimethylsiloxane) (PDMS) microstamps. The stamps were used to print discontinuous gradient patterns made of laminin/-PLL or PLL alone.

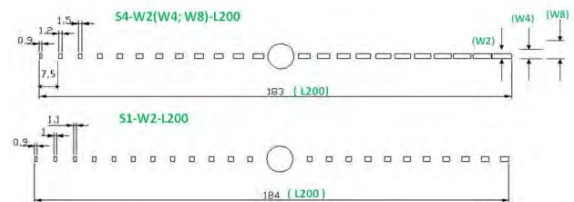


Fig. 1. Basic features of designs for the discontinuous gradient structures: Example of structures with different scopes. Measurements are given in μm .

For all experiments, the fluorescein isothiocyanate (FITC)-conjugated poly-L-lysine was used to visualize the printed protein. Dissociated cortical neurons were seeded in a low density ensuring localization of one single neuron per gradient structure and minimizing interference from trophic factors produced by neighboring neurons on neurite outgrowth. After three days in culture, cells were fixed and immunostained for MAP2- and TAU-1 to evaluate neurite growth and axon guidance effects. Fluorescence images were analyzed from structures where only one single neuron adhered with the soma directly on the node. Different gradients were analyzed for their ability to control the neurite growth and in more detail to differentially promote the growth of neurites towards one specific side of the guiding structure. The neurite growth direction along the increasing concentration was defined as the positive direction, while neurites growing along the decreasing concentration were defined as growing in the negative direction. Next to the effect on neurite growth, the gradients were also analyzed for their potential to guide the axon. After evaluating the axon by TAU-1 immunostaining (Fig. 2), the axon growth in the positive and negative direction was quantified. Comparing all gradients tested for their effects on axon-guiding pointed out that all patterns, independent of the different geometric parameters, evoked an effect on axon growth by

directing axons (>50%) in the positive direction along the gradient. The highest effect could be seen on PLL-S4-W4 (84%) and the lowest effect on the PLL-S1-W2 pattern, which did not reach significance. On the S1-W2 pattern where PLL induced nearly no effect on axon guidance, laminin/ PLL mediated a high and significant effect. This clearly shows that laminin mediates an additional effect on axon guidance in comparison to PLL alone, but the additional effect was restricted to the low slope and 2 μm wide structures. On the 4 μm and 8 μm width structures, the axon guiding effect of laminin was reversed. Whereas laminin/PLL mediated only a slight response, PLL triggered high and significant effects (8 μm width). Thereby, it could be shown for the first time that a discontinuous gradient of polycationic polymer is sufficient to induce axon guidance.

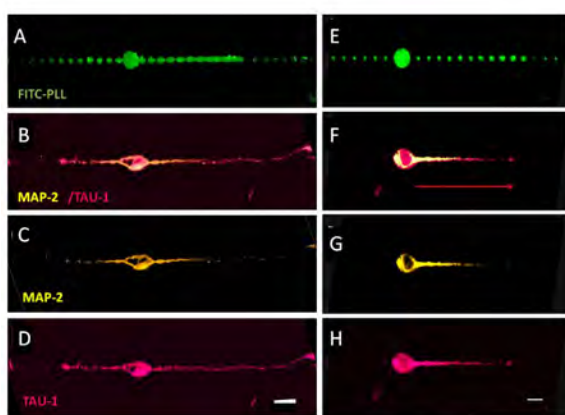


Fig. 2: Immunolabeling of neurons at DIV 3 with MAP2 and Tau-1 antibody. Neurons adhered onto the nodes and neurites grew out mostly along the pattern, forming bipolar neurons. The MAP2-TAU-1 immunostained neurons were used to determine the length of the neurites grown on the positive side of the gradient. Tau-1 positive neurites are the axons. (A-D): Laminin/PLL. (E-H): PLL pattern Tau-1 positive neurite grew in positive direction of the gradient. Scale bars 10 μm.

Discontinuous microgradients of laminin/ PLL, and PLL alone, direct neuron adhesion, controlling both neurite growth and axon guidance of single primary neurons. The potency of the structure to guide axons depends on the proteins used and geometric parameters (width and slope). The best results of axon guidance could be obtained by the structure with a slope of 0.04, a width of 4 μm and made of PLL. Similar effects could be obtained on structures with a shallower slope if they were made of laminin/PLL [1]. The data have shown that the growth cones can respond on gradients made of mixtures of extracellular guiding cues combined with positive charges, as well as on gradients of positive charges alone. This method proved to be very successful in obtaining discontinuous protein gradients, by which a model of in vivo protein gradient conditions was achieved in vitro.

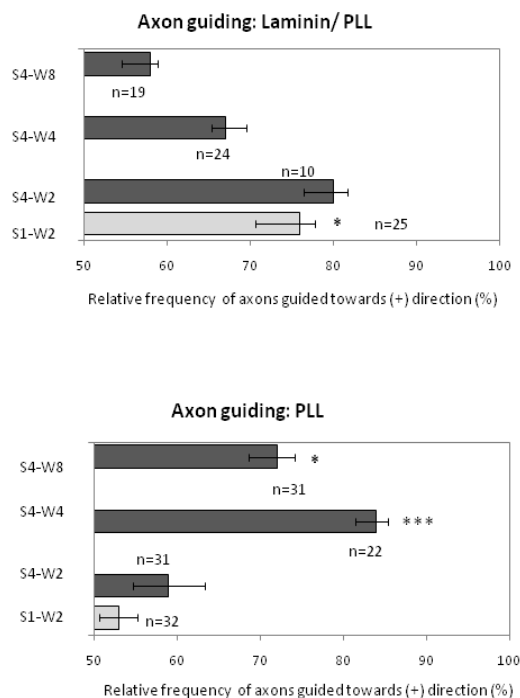


Fig. 3. Quantification of the axon guidance effect of the different patterns made of laminin/ PLL (A) and PLL (B). For statistical analysis, individual neurons were analyzed. Data represent the relative frequency of axons grown on the positive side of the gradients, error bars confidence intervals; *p < 0.05; p*** < 0.001.

The fabricated guiding structure is therefore useful to guide axons of single multipolar neurons with high efficiency in the design of defined neuronal networks in culture. Electrophysiological measurements may be used to confirm that these guiding structures could further be used to direct signal propagation.

[1] R. Fricke, P. D. Zentis, L. T. Rajappa, B. Hofmann, M. Banzet, A. Offenhäusser, S. H. Meffert. Axon guidance of rat cortical neurons by microcontact printed gradients. *Biomaterials* 32, 213 (2011).

[2] A. Offenhäusser, S. Böcker-Meffert, T. Decker, R. Helpenstein, P. Gasteier, J. Groll, M. Möller, A. Reska, S. Schäfer, P. Schulte, A. K. Vogt, Microcontact printing of proteins for neuronal cell guidance, *Soft Matter* 3, 290 (2007).

Light induced stimulation and delay of cardiac activity

V. Maybeck¹, B. Hofmann¹, S. Eick¹, S. Meffert¹, S. Ingebrandt^{1,2}, P. Wood³, E. Bamberg³, A. Offenhäusser¹

¹ PGI-8/ICS-8: Bioelectronics, Forschungszentrum Jülich & JARA-FIT: Jülich-Aachen Research Alliance

² Dep. of Informatics and Microsystem Technology, University of Applied Sciences Kaiserslautern, D-66482 Zweibrücken, Germany

³ Max-Planck-Institute of Biophysics, Max-von-Laue Strasse 3, D-60438 Frankfurt, Germany

A model system was developed in which light can be used to modify the activity of cardiac tissue. By introducing the ion channel Channelrhodopsin 2 (ChR2), cells can be depolarized with blue light. The behavior of the HL-1 cardiomyocyte-like cell line during manipulation with light was monitored using a custom built microelectrode array (MEA) measuring setup. The components of light induced current and action potentials (APs) could be distinguished in the MEA recordings, and kinetic characteristics of the light sensitive channel extracted. Using this system, the position of the cardiac pacemaker could be induced and furthermore, the exposure of spontaneously beating cell sheets to flashes of blue light could be used to delay beat rate.

The coupling of electrogenic cells to electronic devices is used to both measure and stimulate cells. Such electrically coupled extracellular systems allow good spatial resolution in combination with high temporal resolution. However, it is desirable to separate stimulation and recording modes to improve the quality of signal detection. Electrical stimulation from recording electrodes suffers from the drawbacks of scar formation, cell permeabilization, and blind time as the applied pulse dissipates from the electrode. Combining light based stimulation with MEA recordings maintains high accuracy in the recorded signal while increasing the available stimulation points and providing fast, non-invasive cell manipulation.

Channelrhodopsin 2 is a small protein from *C. reinhardtii*, which can be transfected into electrogenic cells. The protein binds trans-retinal to form ChR2, a directly gated cation channel activated by blue light [G. Nagel et al., Proc. Natl. Acad. Sci. 100, 13940-5 (2003)]. The flow of cations during illumination depolarizes electrogenic cells, and if depolarization exceeds threshold, the cell fires an AP. The cardiomyocyte-like cell line HL-1 [W. Claycomb et al., Proc. Natl. Acad. Sci. 95, 2979-84 (1998)] was transfected with this protein to allow us to manipulate the location of the pacemaker cell and beat rate using light.

HL-1 cells were transfected with a Channelrhodopsin 2-YFP construct with roughly 50% efficiency, creating a mixed network of light sensitive and light insensitive cells. Cells were cultured on MEAs for 2-4 days before measuring. The HL-1 cells divide until a confluent layer is formed, then build gap junctions between the cells, and finally become spontaneously active, sending waves of APs over the whole cell sheet. Fluorescence intensity was used to select presumed highly expressing cells for light based manipulation.

Our stimulation and recording setup is shown schematically in Fig. 1. A targetable laser spot, ~10 μm in diameter, couples into the microscope optics to apply flashes of 473 nm light from above with a pre-fiber intensity of 0-40 mW. From below, the cells are recorded by an 8x8 gold MEA.

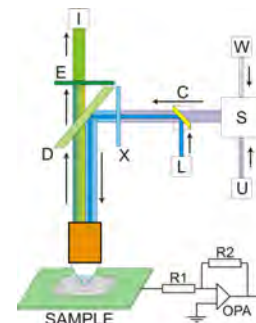


FIG. 1: Schematic of the laser stimulation & MEA recording setup. The cells grow on a MEA connected to a custom amplifier system [2,3]. The optical elements are; W- white light, U- fluorescence light source, S- light switch, L- 473 nm targeted laser, C- light coupling, X- excitation filter, D- beam splitter, E- emission filter, I- CCD imager, with beam paths indicated by the arrows

Comparison of the light induced AP and spontaneous APs on the same channel allows extraction of the light induced component of the recording. The isolated light induced component was fit with single exponentials for ChR2 opening and ChR2 closing. From this the time constants for the kinetics of ChR2 opening and closing were determined to be 11.3 ± 0.2 ms and 34.5 ± 0.2 ms, respectively.

In addition to being able to induce AP firing in a single cell, network effects were visible. Light induced APs propagated across the network at

propagation speeds equivalent to spontaneously generated APs. The location of a light generated pacemaker cell could be seen in the change in AP propagation direction across the MEA array. For example, in a culture with a naturally occurring pacemaker to the right of the array, a light induced pacemaker was generated near channel 55. The propagation of the AP was then observed to propagate in concentric rings from near channel 55 instead of from right to left, most clearly visible in the much later arrival of the AP in the top right corner of the array (see Fig. 2) [1].

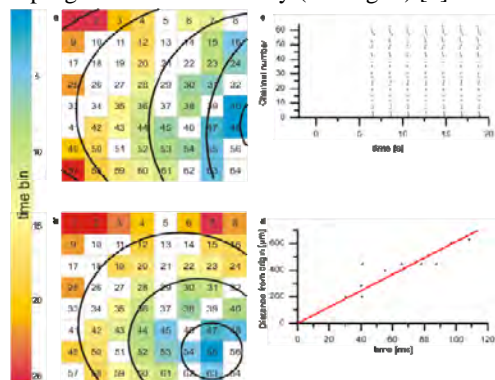


FIG. 2: APs arrival times are color coded on the array, white electrodes did not register an AP. All APs propagate regularly across the array, but the origin can be moved using light stimulation. a) Naturally occurring pacemaker to the right of the array. b) Light induced pacemaker near channel 55. Propagation lines are a guide to the eye. c) Propagating APs register on all functional channels. d) Propagation speed of light stimulated APs is normal at .61 cm/s, as determined by linear fit of the distance traveled vs. the time elapsed.

In cultures that were not mature, and showed no spontaneous APs, the frequency of AP firing did not always match the frequency of illumination. This failure to trigger an AP may occur when the subsequent flash arrives during the absolute refractory period of the cell. The Chr2 induced depolarization generates a light elongated refractory period (LERP) by extending the plateau phase of the cardiac action potential instead of triggering a new AP. Further evidence for this mode of action is provided by AP suppression when Chr2 depolarization is triggered immediately after a spontaneously occurring AP wave in mature cultures. In these mature cultures, extension of the plateau phase by light induced depolarization prevents spontaneous beating and slows beat rate. LERP may be a localized effect in the illumination area. However, when the cell captured by LERP is the naturally occurring pacemaker cell, the effect of suppression is global. If illumination is halted, the culture returns to its native spontaneous activity without any observable persistent effects of light induced modulation, see Fig. 3.

The generation of LERP in a non-pacemaker region of the culture would only locally suppress APs and provides a means of generating cardiac

cultures with inhomogenities in conduction. Such systems have become important models for cardiac disease, and currently rely on mixed cell type cultures or physical barriers within the tissue.

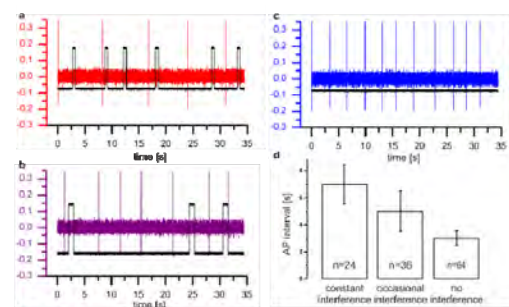


FIG. 3: Cell recordings plotted in color and the applied laser flashes in black. a) LERP at every AP results in a long inter-spike interval. b) When light flashes are less frequent, only individual spikes are delayed. c) In darkness the culture returns to its native spontaneous beat rate. d) Summary of inter-spike intervals with varying degrees of LERP.

A further application of light-controlled cardiac activity is the temporally precise determination of contraction for imaging studies. Since LERP prevents APs, and therefore prevents cell contractions, precise periods can be defined when cultures can be imaged without movement. This prevents use of chemical blocking agents that may alter other cell behaviors while blocking contraction. The optical systems of confocal microscopes would be sufficient for both the control of LERP and imaging during the non-contractile period.

The use of Chr2 to generate a light sensitive cardiomyocyte-like culture has been shown, without detectable alterations in AP firing or AP propagation in the dark. MEA recordings of APs occurring spontaneously in the dark and APs triggered by illumination with blue light propagate similarly through the tissue. Differences in signal shape allow the extraction of the light induced component of the recorded signal, and subsequent determination of channel kinetics of the Chr2. The light induced depolarization can be used to generate a pacemaker cell in immature cultures or to re-locate the pacemaker in mature cultures. It was furthermore shown that Chr2 activation by light not only allows the triggering of APs but also AP suppression by LERP in spontaneously beating cultures.

- [1] B. Hofmann, V. Maybeck, S. Eick, S. Meffert, S. Ingebrandt, P. Wood, E. Bamberg, A. Offenhäusser, Light induced stimulation and delay of cardiac activity, *Lab Chip*, 10, 2588 (2010)
- [2] M. Krause, S. Ingebrandt, D. Richter, M. Denyer, M. Scholl, C. Sprössler, A. Offenhäusser Extended gate electrode arrays for extracellular signal recordings. *Sensors and Actuators B-Chemical* 70(1-3) (2000) 101
- [3] H. Ecken, S. Ingebrandt, M. Krause, D. Richter, M. Hara, A. Offenhäusser, *Electrochimica Acta*, 48 (2003), 3355

Nanoelectronic devices for direct communication with cells

M. Jansen¹, V. Maybeck¹, J. Eschermann¹, S. Ingebrandt^{1,2}, L. Hess³, J. Garrido³, A. Offenhäuser¹

¹ PGI-8/ICS-8: Bioelectronics, Forschungszentrum Jülich & JARA-FIT: Jülich-Aachen Research Alliance

² Dep. of Informatics and Microsystem Technology, University of Applied Sciences Kaiserslautern, 66482 Zweibrücken

³ Walter-Schottky-Institute, Technical University Munich, Am Coulombwall 4, 85748 Garching

Si- based nanowire field-effect transistors (SiNW-FETs) were used to record the extracellular potential of the spontaneous activity of cardiac muscle HL-1 cells. Based on their sensitivity and interface with cell membranes large signals can be recorded. On the other side we used graphene as a nanoelectronic device. Here we used arrays of Graphene-field-effect transistors (G-FETs) for the detection of the electrical activity of electrogenic cells. The propagation of signals from cardiac myocytes across the layer was successfully tracked. Analysis of the recorded cell signals and the associated electronic noise of the transistors in the arrays suggest that both SiNW as well as G-FETs could open up unique opportunities in the field of bioelectronics.

Investigation of neuronal cell activity through interfacing with electronic devices is of great interest for many applications such as monitoring cell signal processing within neuronal networks, neuroprosthetic devices, and the use as a biosensor to monitor pharmaceutical agents, pollutants, etc. This requires the advancement of novel solid-state sensors and actuators with a further improvement in the signal detection capability, a superior stability in biological environments, and a more suitable compatibility with living tissue.

Silicon nanowire (NW) transistors had been used in recent times as biosensors for the detection of molecules such as DNA or proteins, antigens and viruses. We have fabricated Si-nanowires using nanoimprint lithography followed by anisotropic wet chemical etching of silicon-on-insulator substrates with tetramethylammonium hydroxide. The combination of these methods was highly reproducible, yielded very smooth surfaces (Fig. 1) and is suitable for a high integration density [1, 2].

These devices were used to record the extracellular potential of the spontaneous activity of cardiac muscle HL-1 cells. Their signals were measured by direct dc sampling of the drain current. An improved signal-to-noise ratio compared to planar field-effect devices was observed [3]. Furthermore, the signal shape was evaluated and could be attributed to different membrane currents. With these experiments, a qualitative description of the properties of the cell-NW contact was obtained and

the suitability of these sensors for electrophysiological measurements in vitro was demonstrated.

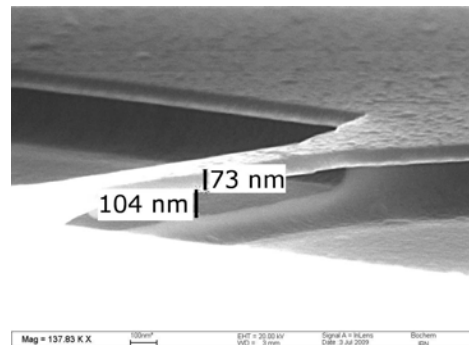


FIG. 1: Scanning electron microscopy image of a Si-NW fabricated by top-down process.

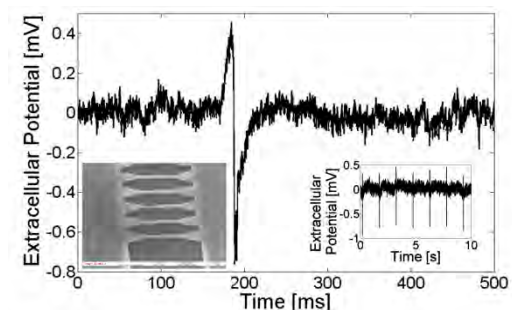


FIG. 2: Extracellular recordings from cardiac myocyte cell line using Si-Nanowire sensor. The left inset shows the six Si-NW used for the recording of the signal. The right inset shows a series of recorded action potentials.

Another interesting nanomaterial that bridges between one-dimensional NWs and conventional planar electronics is graphene. As the charge carriers in graphene are confined to an atomically-thick plane, the electrical conductance of graphene is extremely sensitive to its surroundings, making graphene an ideal sensing material for label-free chemical and biological detection.

G-FETs were used for the detection of the electrical activity of electrogenic cells. The arrays were fabricated at the Walter-Schottky-Institute in Munich using large-area graphene films grown by CVD on copper foil. Cardiomyocyte-like HL-1 cells were cultured on these arrays and exhibited a

healthy growth. After characterizing the transistors in an electrolyte, the action potentials of these cells could be detected and resolved by the G-FETs under the cells (Fig. 3a). Using the complete transistor array, the propagation of the cell signals across the layer was successfully tracked. Analysis of the recorded cell signals and the associated electronic noise of the transistors in the arrays confirms that graphene FETs surpass the performance of state-of-the-art commercial devices for bioelectronic applications.

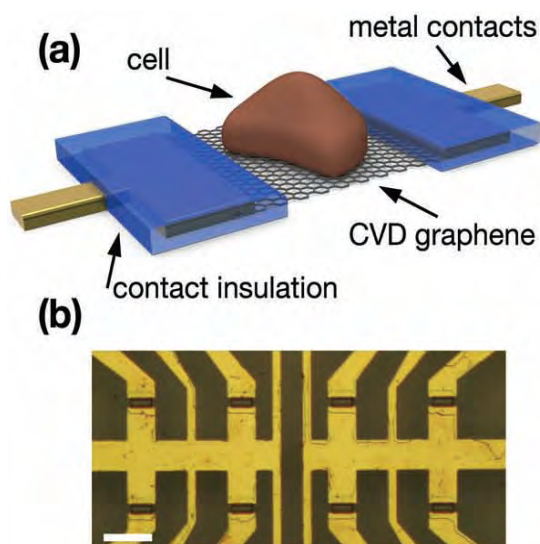


FIG. 3: a) Schematic view of a G-FET with a cell on the gate area. The graphene is shown between the drain and source metal contacts, which are protected by a chemically resistant layer. b) Optical microscopy image showing eight transistors in the central area of a G-FET array. The transistor active area between the drain and source contacts is $10 \times 20 \mu\text{m}^2$. The scale bar is $100 \mu\text{m}$ [4].

The HL-1 cells seeded on the transistor arrays exhibited healthy growth and formed a densely packed layer covering the entire sample surface including the open transistor areas after several days. Figure 4a depicts a differential interference contrast (DIC) microscopy image of an array with the HL-1 cells, combined with a fluorescence image of the same region, where the confluent layer of healthy cells is revealed by calcein staining. Figure 4b shows the current response of eight graphene transistors measured simultaneously on one sample. The transistor bias was chosen such that the transconductance was maximized for all of the transistors. Repeated spikes can be seen for all working transistors at similar times, which can be attributed to the propagation of action potentials across the cells. By using the transistor transconductance, the current spikes can be converted to gate voltage spikes and reach values up to $900 \mu\text{V}$ with a root mean square (RMS) noise level of $50 \mu\text{V}$ (Figure 4d).

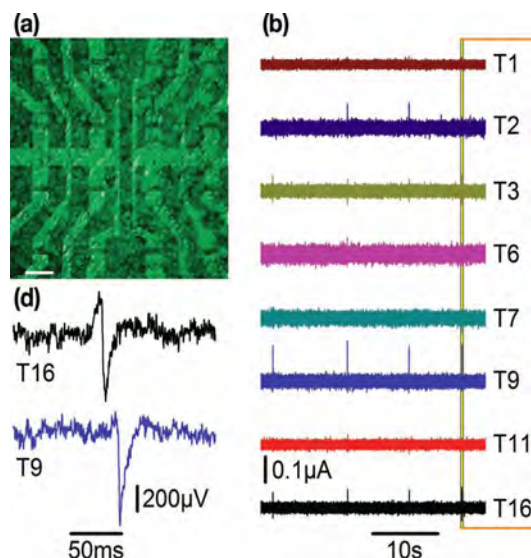


FIG. 4: a) Combination of an optical microscopy image of a transistor array and a fluorescence image of the calcein-stained cell layer on the same array. The scale bar is $100 \mu\text{m}$. b) Simultaneous current recordings of eight transistors in one FET array over tens of seconds. d) Exemplary single spikes. The current response has been converted to an extracellular voltage signal. The upper spike resembles a capacitive coupling followed by the opening of voltage-gated sodium channels whereas in the bottom one the ion channels dominate over the capacitive coupling. [4].

Signals recorded from cardiomyocytes with SiNW and with G-FET indicate that both devices are suitable for extracellular recordings and that a stable interface between cells and electronic device is formed. In addition, comparisons of peak-to-peak recorded signals with G-FET devices versus NW-FETs will allow in future an assessment of relative resolution in extracellular recording.

The complementary of G- and NW-FETs could open up interesting opportunities in the field of bioelectronics in the future.

- [1] X. T. Vu, J. F. Eschermann, R. Stockmann, R. Ghosh Moulick, A. Offenhäusser, S. Ingebrandt, Top-down processed silicon nanowire transistor arrays for biosensing *Physica Status Solidi A*, 206 (2009) 3, 426 – 434
- [2] X. T. Vu, R. Ghosh Moulick, J. F. Eschermann, R. Stockmann, A. Offenhäusser, S. Ingebrandt, Fabrication and application of silicon nanowire transistor arrays for biomolecular detection, *Sensors and Actuators B*, 144 (2010) 2, 354 - 360
- [3] J.F. Eschermann, R. Stockmann, M. Hüske, X.T. Vu, S. Ingebrandt, A. Offenhäusser, Action Potentials of HL-1 Cells Recorded With Silicon Nanowire Transistors *Applied Physics Letters*, 95 (2009) 8, 083703
- [4] L. H. Hess, M. Jansen, V. Maybeck, M. V. Hauf, M. Seifert, M. Stutzmann, I. D. Sharp, A. Offenhäusser, J. A. Garrido, Graphene Transistor Arrays for Recording Action Potentials from Electrogenic Cells, *Adv. Mater.* (2011) 23, 5045–5049

Development and characterization of carbon nanotube sensors

V. Sydoruk¹, M. Petrychuk², F. Gasparyan³, A. Offenhäusser¹, S. Vitusevich¹

¹ PGI-8/ICS-8: Bioelectronics, Forschungszentrum Jülich & JARA-FIT: Jülich-Aachen Research Alliance

² Taras Shevchenko National University, Kiev, Ukraine

³ Yerevan State University, Yerevan, Armenia

The main aim of the project “Development and characterization of carbon nanotube sensors” is developing low-noise high-speed test device structures on the basis of single-wall carbon nanotubes(SWNTs) for biosensor applications. The noise spectroscopy results allow us to analyze the mechanisms of conductivity in fabricated carbon nanotube structures. Furthermore, we showed that functionalization of the electrolyte-insulator-semiconductor (EIS) structure with multilayers of polyamidoamine dendrimer and single-walled carbon nanotubes leads to an essential reduction of the 1/f noise compared with noise in a bare EIS device. Thus the control of molecular architecture is important to obtain the enhanced performance of multilayer structures interfacing with electrolyte.

Carbon nanotubes (CNTs) are unique materials due to the high degree of ordering of carbon atoms on the surface of the tube, which represents a very uniform channel for high-speed electron transport. Therefore CNTs are very promising for various applications, including extremely sensitive biosensors. Noise spectroscopy is a powerful method for studying the transport properties, performance, and reliability of material structures, especially scaled down to the nanoscale [1]. The fluctuation phenomena contain important information on the material performance and may be utilized as a valuable method for the characterization of nanoscaled materials and devices.

We studied the phenomena of charge transport in structures consisting of bundles of carbon nanotubes [2] prepared by applying uniaxial pressure. The Raman spectra data demonstrate that the bundles mainly consist of single-walled nanotubes. Low-frequency noise and transport properties of the structures were studied for samples fabricated in the form of dumbbells, containing a constriction with a characteristic size of $100 \times 100 \mu\text{m}^2$ in cross-sectional area and a length of about $200 \mu\text{m}$. In the temperature range from 20K to 200K, the measured data demonstrate the characteristic for Luttinger liquid temperature dependence of resistance $R \sim T^{-\alpha}$ with exponent of $\alpha = 0.4$. At the temperatures higher than 200K, the measured dependence deviates from this simple function. At lower temperatures, $T \approx (4.2 - 20) \text{K}$ the resistance follows an exponential function $R \sim \exp(T_0/T)^{0.25}$ Exponential dependence of the resistance versus the sample temperature with an

exponent of 0.25 indicates the hopping mechanism of conductivity with variable hopping length. The noise spectra of the sample have $1/f$ dependence, which is a characteristic function of flicker noise. To analyze the nature of the noise current in the nanotube bundles, we measured the spectral density of current noise, as a function of the current, $S_I \sim I^\beta$, at different temperatures in the range from 4.2K to 300K. Based on these results, we found the dependence of the coefficient β on the temperature (Fig.1).

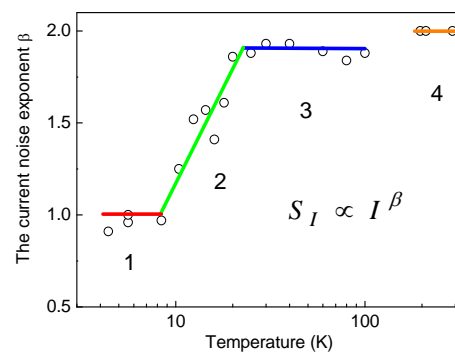


FIG. 1: The current noise exponent β of power function $S_I \sim I^\beta$ determined from measured noise spectra as a function of temperature, corresponding to: (1) hopping mechanism of conductivity; (2) transition region (see for details see Ref.[2]); (3) Luttinger liquid conductivity; (4) diffusion conductivity.

A transition region is recorded in the temperature range $T = (8 - 25) \text{K}$, which indicates the transition from hopping conductivity to Luttinger liquid conductivity. Our experiment showed that the conductivity of Luttinger liquid is less "noisy" than the conductivity of the Fermi liquid. A sharp increase of noise in this latter region can be explained by increased phonon scattering and, as a result, a decrease in the mean free path of carriers. At the same time, the conductivity of Luttinger liquid up to the temperature $T \approx 200 \text{K}$ is of a ballistic nature and is characterized by a low noise level, weakly dependent on temperature.

On the other hand, noise spectroscopy is a very sensitive method for the analysis of the semiconductor/insulator interface quality as well as for characterization of the quality of functionalization/

passivation layers in liquid environments. We studied the low-frequency noise properties of a capacitive field-effect EIS structure functionalized with polyamidoamine (PAMAM) dendrimer/SWNT multilayers (Fig.2) and compared with noise of a bare EIS device [3].

In contrast to transistor structures, capacitive EIS sensors are simple in layout and cost-effective in fabrication (usually, no photolithographic process steps or complicated encapsulation procedures are required). Capacitive Al-p-Si-SiO₂-Ta₂O₅ structures with a 30 nm thermally grown SiO₂ and a 55 nm Ta₂O₅ layer were fabricated. The Ta₂O₅ layer has been prepared via electron-beam evaporation of 30 nm Ta followed by thermal oxidation at 515 °C for about 30 min. As the contact layer, a 300 nm Al film was deposited on the rear side of the Si wafer and then, the wafer was cut into single chips of 10 mm x 10 mm size. The EIS sensor was mounted into a home-made measuring cell and sealed by an O-ring to protect the side walls and backside contact of the chip from the electrolyte solution. The contact area of the EIS sensor with the solution was about 0.5 cm²

The LF noise spectra were measured in buffer solutions of pH 3, pH 7, and pH 11 in accumulation, depletion, and inversion regions of the EIS structure by applying different gate voltages. We have observed that the pH value of the buffer solution did not significantly influence the noise spectral density. This is in agreement with results obtained on pH ion sensitive field-effect transistors (ISFETs) previously. It has been reported that the gate-referred 1/f noise in a channel current of pH ISFETs is also independent of the pH, and the origin of LF noise in these ISFET devices is the trapping/detrapping of carriers at the Si-SiO₂ interface. Moreover, it has been discussed that the ionic strength of the solution does not affect the noise magnitude of liquid-gated SWNT transistors. These results may suggest that the interface between the solution and the gate insulator does not or not significantly contribute to the 1/f noise. It has been observed that the gate current noise in EIS structures with thin gate oxides is increased with increasing the gate voltage or leakage current. This has been attributed to the more slow-trap states available for a trap-assisted tunneling with increasing gate voltage. The noise spectral density exhibits an 1/f^γ dependence with the power factor γ of 0.8 and γ(0.8 – 1.8) for the bare and functionalized EIS sensor, respectively.

It has been revealed that functionalization of the EIS structure with multilayers of polyamidoamine dendrimer and single-walled carbon nanotubes leads to considerable reduction of the 1/f noise.

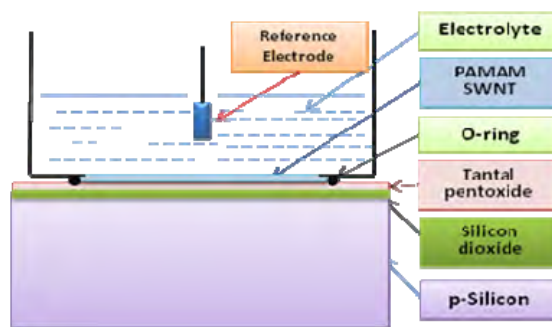


FIG. 2: Electrolyte-insulator-semiconductor (EIS) bio-sensor functionalized with a multilayer of polyamidoamine (PAMAM)/SWNTs. See details in [3].

The gate-current noise behavior in bare and functionalized EIS devices has been modelled. The experimentally observed gate-voltage dependence of the noise in capacitive EIS structures is explained by the gate-voltage-dependent changes in the occupancy of the oxide trap levels resulting in a modulation of the conductivity of current paths or charge carriers passing through the EIS structure. Physical processes in the semiconductor, insulator, and electrolyte medium responsible for low-frequency charge fluctuations are discussed based on an electrical equivalent scheme for the capacitive EIS structure [4].

Thus, CNTs offer new perspectives for development of biosensors. We demonstrated that noise can be used to investigate transport phenomena and factors determining the performance of electrolyte-insulator-semiconductor structures. Biomolecules and biological objects contain a backbone carbon atoms. Therefore, interfacing living systems with nanocarbon materials is promising direction for biosensor applications.

-
- [1] S.Vitusevich, F.Gasparyan: Low-frequency noise spectroscopy at nanoscale: carbon nanotube materials and devices. in "Carbon Nanotubes Applications on Electron Devices", edited by J.M.Marulanda, InTech publisher, ISBN 978-953-307-496-2, (2011) 257-298
 - [2] B.A.Danilchenko et al.: 1/f noise and mechanisms of the conductivity in carbon nanotube bundles. Carbon, 49 (2011) 5201-5206
 - [3] F.V.Gasparyan et al.: Low-frequency noise in field-effect devices functionalized with dendrimer/carbon nanotube multilayers. IEEE Sensors Journal, 11 (2011) 142-149
 - [4] F.V.Gasparyan, S.A.Vitusevich, A.Offenhäusser, M.J.Schöning: Modified charge fluctuation model for electrolyte-insulator-semiconductor devices. Modern Physics Letters B, 25, 11, (2011), 831-840

Nanotechnology tools for cell-chip communication

E. Kätelhön, B. Hofmann, M. Hüske, A. Yakushenko, P. Rinklin, A. Offenhäusser, B. Wolfrum

PGI-8/ICS-8: Bioelectronics, Forschungszentrum Jülich & JARA-FIT: Jülich-Aachen Research Alliance

The project on “nanotechnology tools for cell-chip communication” deals with the investigation of functional nanostructures for detecting cellular signals *in vitro*. This includes the development of new chip-based devices for electrical and electrochemical recording. Our main focus has been directed at studying techniques based on nanocavity redox cycling. This approach allows one to detect minute quantities of redox-active molecules down to the single-molecule level by boosting the electrochemical signals exploiting fast diffusion on the nanoscale. We applied the nanocavity redox cycling technique in a sensor array design and demonstrated that concentration gradients of the neurotransmitter dopamine can be mapped on the chip. Furthermore, we showed that the nanocavity approach can be used for highly localized recording of electrical activity inside a cellular network.

Redox cycling amplification is a powerful tool for increasing the sensitivity of electrochemical detection. Molecules that can undergo reversible redox reactions are repetitively oxidized and reduced at independently biased electrodes which are located in close proximity to each other (see sketch in Fig. 1). Since the oxidation state is “recycled” after exchanging electrons with the electrodes, this approach allows multiple reactions of a single molecule at the same electrode, resulting in an amplified electrochemical signal.

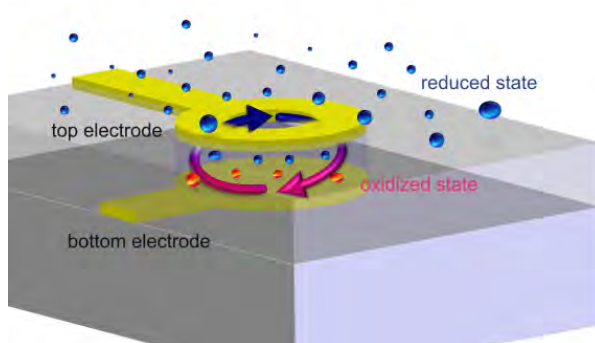


FIG. 1: Sketch of the redox cycling principle at a nanocavity device. Molecules are repetitively oxidized and reduced at two closely spaced electrodes, leading to an effective amplification of the electrochemical current.

The efficiency of this recycling method depends on the average number of cycles a molecule performs before it escapes and the time it takes to undergo a complete

redox cycle. Thus, it is strongly influenced by the geometry and size of the device.

Very efficient redox cycling can be performed in confined geometries where the electrode distance is well below 100 nm. Nanofluidic channels with integrated electrodes have especially demonstrated an increase in molecular sensitivity by several orders of magnitude compared to conventional voltammetry. The distinct advantages of confined redox cycling make this technique an interesting candidate for biosensing applications. One application is the on-chip spatiotemporal detection of redox-active neurotransmitters with the prospect to investigate localized release of neurotransmitters from neuronal networks with high sensitivity. In the last years, we have developed arrays of circular nanocavities [1] as well as dual-electrode nanopore sensor platforms [2], which were structured by means of optical and template-based lithography, respectively. We have demonstrated the redox cycling efficiency of these sensors and their applicability for the detection of redox active compounds such as hexacyanoferrate and the neurotransmitter dopamine. Furthermore, we have shown that chemical gradients and changes in the local concentration can be spatiotemporally characterized on-chip using our array-based nanocavity approach [1]. This feature is a crucial requirement for future applications such as mapping neurotransmitter release from chemical synapses in a cellular network.

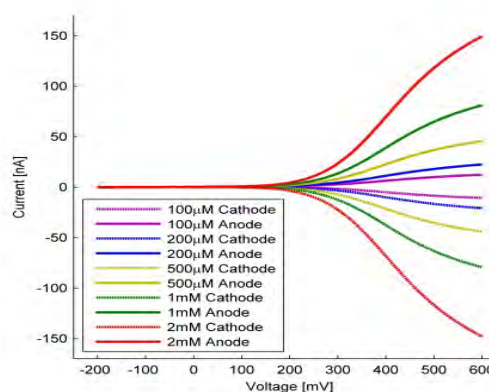


FIG. 2: Electrochemical current of a nanocavity sensor in response to different concentrations of hexacyanoferrate [1]. During the measurement, one electrode is kept constant at -200 mV vs. Ag/AgCl while the second electrode is swept from -200 mV to 600 mV. The anticorrelation of anodic and cathodic currents reveals a redox cycling efficiency close to 100%.

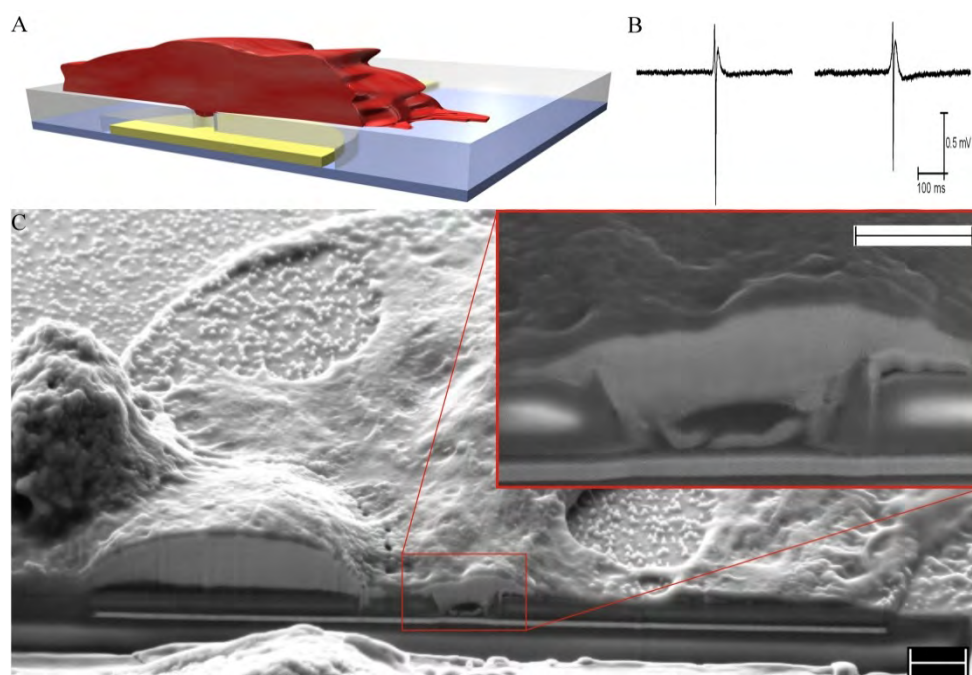


FIG. 3: Nanocavity device for recording electrophysiological activity of individual cells in a network. A) Schematics of cell-chip coupling. B) Action potential recordings from HL-1 cells. C) SEM image of a FIB cross section at the cell sensor interface. The scale bars in the main and enlarged image are 2 μm and 1 μm , respectively. See details in [5].

Another interesting feature of nanocavity redox cycling sensors is the anticorrelation of the anodic and cathodic current, which is useful for the discrimination of interfering signals (see Fig. 2). The high amplification gain in combination with the anticorrelation signatures make nanocavity redox cycling devices powerful tools for a variety of electrochemical investigations. Applications range from investigations of rapid electron transfer kinetics [3] to single-molecule studies [4].

Furthermore, we could show that nanocavity array devices can be used for highly localized on-chip detection of electrophysiological activity from individual cells in a network (see Fig. 3). We have demonstrated this by monitoring action potential propagation in a cardiomyocyte-like cell line (HL-1) at μm -sized spots [5]. There are obvious advantages of this new concept for extracellular microelectrode array recordings. As the overall impedance is dominated by the size of the electrode-electrolyte interface, the liquid filled nanocavity effectively reduces the impedance of the sensor. In contrast, the spatial resolution of the sensor is not affected and is only determined by the aperture connecting to the nanocavity. The high resolution provided by small apertures allows the exact assignment of individual cells to the respective recording electrodes. Furthermore, single cells are able to completely cover the apertures leading to an increased seal resistance and consequently a better cell-electrode coupling.

The strong coupling in combination with a low electrode impedance now enables the analysis of individual cells, that are integrated into dense clusters. Our results demonstrate the versatility of the

nanocavity approach. The next goal is to advance cell-chip communication employing simultaneous stimulation and recording techniques at high temporal and spatial resolution.

-
- [1] E. Kätelhön, B. Hofmann, S.G. Lemay, M. Zevenbergen, A. Offenhäusser, and B. Wolfrum: Nanocavity Redox Cycling Sensors for the Detection of Dopamine Fluctuations in Microfluidic Gradients. *Analytical Chemistry*, 82 (2010) 8502-8509
 - [2] M. Hüske and B. Wolfrum: Fabrication of a nanoporous dual-electrode system for electrochemical redox cycling. *Physica Status Solidi A*, 208 (2011) 1265-1269
 - [3] M.A.G. Zevenbergen, B.L. Wolfrum, E.D. Goluch, P.S. Singh, S.G. Lemay: Fast electron-transfer kinetics probed in nanofluidic channels. *JACS*, 131 (2009) 11471-11477
 - [4] M.A.G. Zevenbergen, P.S. Singh, E.D. Goluch, B.L. Wolfrum, S.G. Lemay: Stochastic Sensing of Single Molecules in a Nanofluidic Electrochemical Device. *Nano Letters*, 11, 7, (2011), 2881-2886
 - [5] B. Hofmann, E. Kätelhön, M. Schottdorf, A. Offenhäusser, and B. Wolfrum: Nanocavity electrode array for recording from electrogenic cells. *Lab Chip*, 11 (2011) 1054-10583.

Electrochemically transduced logic gate on molecular level

Y. Liu, A. Offenhäusser, D. Mayer

PGI-8/ICS-8: Bioelectronics, Forschungszentrum Jülich & JARA-FIT: Jülich-Aachen Research Alliance

Organic molecules that are able to generate a detectable response to an external stimulus are of great scientific interest since they can be used for data processing, as for instance information storage, transformation, and communication. Logic gates such as AND, OR, INHIBIT, XOR, XNOR, and NOR Boolean functions have been realized on the molecular level and are able to process information and to perform arithmetic operations. In the scope of the sub topic “molecular bioelectronics” we have realized electronic functions typically performed by solid state devices like current rectification and logic operations by electrochemical means. A surface confined redox mediator is tethered to the electrode surface which controls the charge transfer between soluble redox probes and electrode.

Although numerous molecular systems performing different computing operations have been developed so far, this research is still in a very early experimental and theoretical stage. In order to achieve practical applications, the future of molecular logic elements is strongly related to the successful linkage of molecules onto a conductive or semi-conductive support. However, logic gate functions performed by molecule functionalized electrodes are relatively rare. Here, we make use of a reaction scheme that is widely used in nature to regulate biological charge transfer and to realize a unidirectional current. Therefore, a number of redox species is arranged such that the electrons pass through these locally separated redox compounds in a defined order. The driving force of these processes is the release of energy when electrons are transferred from redox species with low redox potentials to species with higher anodic potentials. Based on this concept, we demonstrated the realization of different functions with electrical readout by immobilizing robust, redox-active (bio-) molecules on a solid-state surface and applying different redox probes as input signals. The different functional units presented here have in common that they are all based on electrochemical rectifiers (ECR). An electrochemical rectification is characterized by a unidirectional redox current which is transferred between redox probes in solution and a metal electrode functionalized with the molecular redox mediator. Therefore, the electrode is modified by an insulating layer (typically alkanethiols) inhibiting the direct electron transfer between redox probe and electrode [1,2].

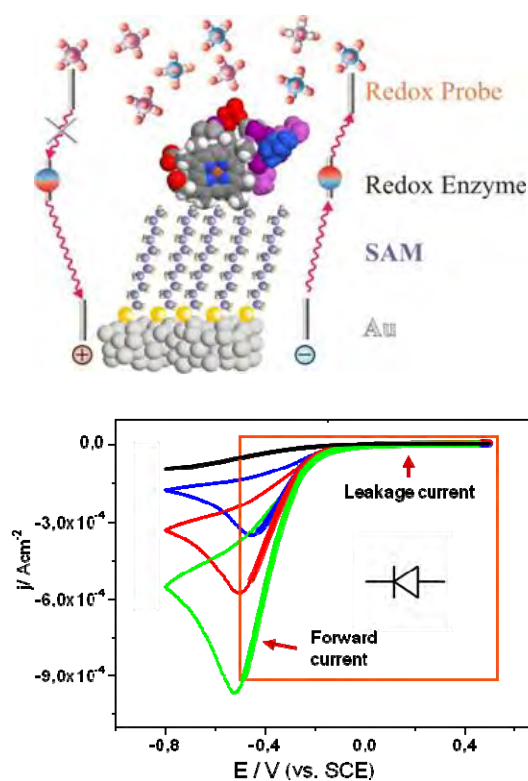


FIG. 1, top: Scheme of the electrochemical current rectification. SAM and MP-11 (enzyme) act as insulating layer and electron transfer mediator, respectively. Considering the relative redox potential of MP-11 (-0.36 V) and redox probe (ferri/ferrocyanide, 0.18 V), MP-11 receives an electron from the Au electrode and then transfers it to ferricyanide when the reduction potential of MP-11 is reached (right side). In the reverse scan, the electron transfer between ferrocyanide and MP-11 is thermodynamically unfavorable (left side). Bottom: Cyclic voltammogram of on a Au/UDT/MP-11 electrode in ferricyanide of different concentrations showing electrochemical current rectification. An electrochemical current rectification with a pronounced cathodic forward current is generated due to a directionally-dependent electron transfer.

Furthermore, an enzymatic redoxmediator (microperoxidase, MP-11) is attached to the insulating surface layer. The unidirectional current develops due to selective electron transport from the functionalized gold electrode to the redox probe (ferri/ferrocyanide) or vice versa such that the redoxmediator controls the read-out of the coupled redox system. A high forward current can be observed if electrons are continuously

transferred from the source to the drain via states of lower energy, Fig. 1 top right. If one state has a higher energy than the source state then only marginal leakage currents can be observed (reverse direction, Fig. 1 top left). The relative position of donor, mediator, and acceptor redox potentials defines the charge transport and hence the potential-dependent electrochemical current rectification.

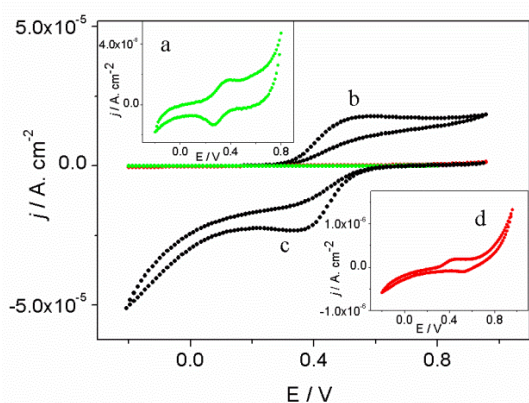


FIG. 2: Cyclic voltammograms of a HDT / ferrocenylthiol functionalized gold electrode in a) PBS (input 0,0), b) 0.5 mM ferrocyanide (input 1,0), c) 0.5 mM iridate(IV) (input 0,1), and d) a mixture of 0.5 mM ferrocyanide and 0.5 mM iridate(IV) ions (input 1,1). b) and c) are representing an anodic and cathodic electrochemical rectifier response.

Electrochemical rectifiers do not only have electrical / electrochemical characteristics similar to conventional diode rectifiers, they also can be combined to perform higher logic operations. Therefore, we linked a cathodic and anodic ECR together to realize a XOR logic gate [3]. Redox active ferrocenylthiol is attached to a gold electrode acting as redox mediator for two different redox inputs. If the redox potentials of the redox probes are clearly separated (ferrocyanide 0.23 V, hexachloroiridate 0.71 V) and the redox potential of the mediator is located in between (0.34 V) then one obtains two linked ECRs of opposite sign, Fig. 2 b,c. To perform the XOR operation, binary encoding of information contained in electrical signals is required. Therefore, the redox probes are considered as inputs and the absolute electrochemical outputs which are assigned to 0 and 1.

As can be seen in Fig. 2, a strong current signal at 0.50 V was present (output: 1) when either ferrocyanide or iridate(IV) ions were added (input: b:1,0 or c:0,1). A pronounced current signal was absent (output: 0) when neither or both of the inputs were applied (input: a:0,0 or d:1,1). Figure 3 shows the current responses of the modified electrode with respect to different input signals. By summarizing input and output signals in a truth table, it becomes obvious that an XOR logic gate function was realized with high switching ratio between output signals “1” and “0”. Additionally, the modified electrode can be used to successively perform XOR logic gate functions (Fig. 3) without renewing the system (electrode and solution) after finishing the first operation of the XOR logic gate function. The

total level of the output signal encodes additional information of the input signal history. This property will allow application of several input cycles, thus underlining the reproducibility of the system and is a prerequisite for many electronic applications. It is worth noting that an XOR logic gate can also be operated as a comparator, which distinguishes whether the input signals have the same value or not.

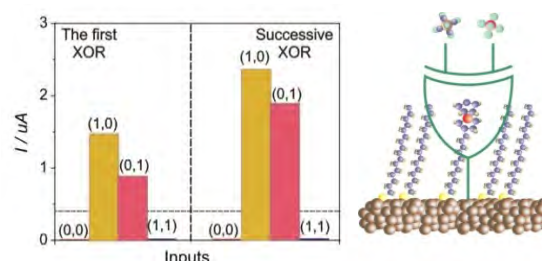


FIG. 3, left: Current responses (output signals) of a modified electrode corresponding to various input signals at the potential of 0.50 V. Here, the current is shown as absolute value independent of current direction during first and subsequent operations. Right: schematic of a molecular XOR logic gate based on two linked electrochemical rectifiers.

The strategy to link different surface bound and unbound redox centers to electrified interfaces can be further expanded to the development of other molecular logic gates with electrical readout, which might pave the way to integrate logic and sensing operations for advanced sensor performance. The opportunity to use different sensory inputs being processed by a logic gate will improve the reliability of sensor responses by suppressing cross sensitivity and linking the signal of several (bio)-markers together. Furthermore, it can be envisioned that this XOR logic gate is operated as switch triggered by redox probe inputs.

- [1] Y. Liu, A. Offenhäusser, and D. Mayer, Electrochemical current rectification at bio-functionalized electrodes, *Bioelectrochemistry*, 77 (2010) 89-93.
- [2] Y. Liu, A. Offenhäusser, and D. Mayer, An Electrochemically Transduced XOR Logic Gate at the Molecular Level, *Angewandte Chemie-International Edition*, 49 (2010) 2595-2598.
- [3] Y. Liu, A. Offenhäusser, D. Mayer, Rectified tunneling current response of bio-functionalized metal-bridge-metal junctions, *Biosens. Bioelectron.*, 25 (2010) 1173-1178.

Intermolecular electron transport investigated by break junctions

X. Dong, Z. Yi, Y. Zhang, F. Pyatkov, A. Offenhäusser, D. Mayer

PGI-8/ICS-8: Bioelectronics, Forschungszentrum Jülich & JARA-FIT: Jülich-Aachen Research Alliance

Theoretical and experimental investigations of charge transport through (bio) molecules have attracted considerable attention driven by the interest in fundamental aspects of charge transport and the vision of future applications in molecular electronics and biosensors. Within the sub-topic “molecular bioelectronics” we address open mechanistical questions of electron transport in model systems which are relevant for protein charge transport. We investigated the relation between inter- and intramolecular electron transport, considered the role of metal ions in metal-organic complexes, and showed that electrostatically bridged molecules have a lower conductance than the same molecules bridged by covalent bonds.

Within this project period, we established a mechanically controllable break junction (MCBJ) which facilitates electrical addressing of individual molecules. A micro-fabricated metal wire is bent in a mechanical bending apparatus until it breaks, resulting in two closely spaced nanoelectrodes (Fig. 1). The molecule of interest is anchored between the electrodes and subsequently electrically characterized by recording I/s and I/V responses. The current-voltage characteristics of alkanes typically exhibit a transition from direct tunneling to field emission as the applied bias exceeds a threshold voltage. This voltage is proportional to the effective tunneling barrier and shifts to lower values as the distance between the nanoelectrodes decreases. Previously, this shift was assigned to an enhanced intermolecular electron transport between parallel molecules. With MCBJ experiments we demonstrated that also for single molecules an enhanced field emission can be observed as the molecular junction was compressed [1]. I/V measurements with various numbers of molecules in the junction at a given gap size revealed that intermolecular electron transport between adjacent molecules was of minor importance and alkanedithiols can be considered as individual transport channels.

Furthermore, we have used MCBJ for the investigation of the influence of metal ions on conductivity of metal complexes. Metal complexes play an important role for many biochemical redox processes and their charge transport depends on the nature of anchored metal ions. We have investigated metal-molecule-metal junctions which were built from aminooligocarboxylic acids (C_2 -NTA), a general sequestering agent. Breaking a gold junction modified by (C_2 -NTA) generated a clear peak

in the conductance histogram (Fig. 2). After addition of metal ions, a second set of peaks at lower conductance values was observable in the histogram. The position of these peaks shifts depending on the kind of entrapped metal ion. A statistical analysis of the recorded conductance traces revealed that the complex conductance depends strongly on the type of coupling ion with the order: $Ca^{2+} \gg Zn^{2+} > Ni^{2+}$ [2].

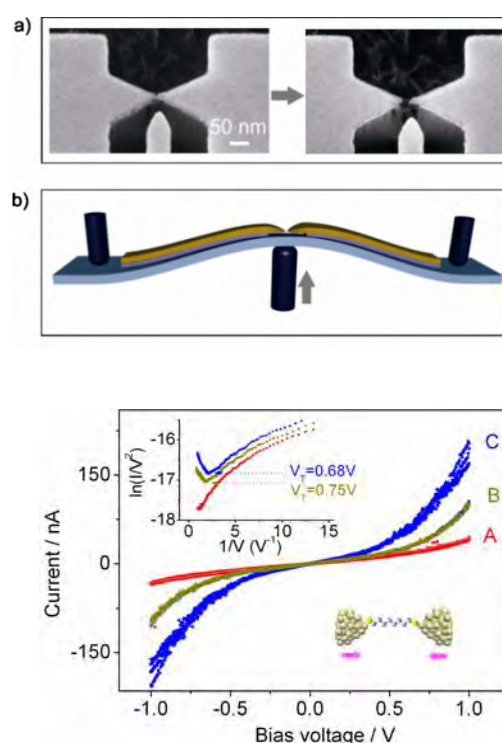


FIG. 1: Working principle of the mechanically controllable break junction (MCBJ). a) Scanning electron microscopy images of micro-fabricated MCBJ consisting of a freestanding metal bridge with a central constriction. Left) before and right) after breaking of the constriction. b) Schematic of the MCBJ mounted into a three-point bending configuration. Bottom: I/V curves of single octane dithiol junctions with three different gap sizes. Curves B and C were recorded after the gap size was decreased by approximately 0.2 and 0.4 nm compared to the gap of curve A, respectively. The insert shows corresponding $\ln(I/V)$ versus $1/V$ characteristics. An inflection point can be observed, which shifts to lower biases as the gap size decreases.

The conductance was found to be reciprocally dependent on the complex stability. The observed relation between type of metal ion and conductivity of molecular junctions helps us to understand in detail the

role of metal ions in biological charge transport. Furthermore, it may pave the way for novel design strategies of molecule based devices.

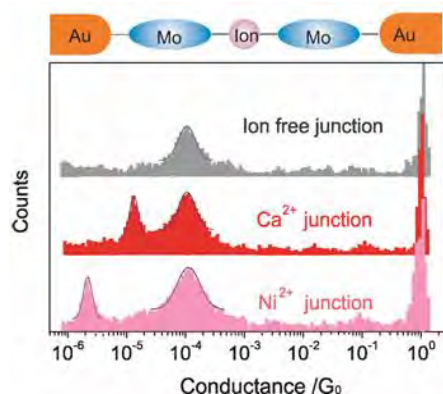


FIG. 2: Log-histograms of measured conductance values obtained from successive opening cycles after: top) dithiobis (C2-NTA) was applied to the junction. Here, only one peak can be clearly observed. Middle and bottom) Molecules bridged by Ca^{2+} and Ni^{2+} , respectively. All histograms possess a peak at $10^{-4}G_0$ which can be assigned to the conductance of metal-(C2-NTA)-metal junctions. Additional peaks located at lower conductance values indicate that metal-molecule-ion-molecule-metal junctions were formed.

To investigate charge transport processes on a single molecule level in aqueous solution, an electrochemical break junction setup was established (Fig. 3). Pairs of facing nanoelectrodes were fabricated and encapsulated on a silicon chip. The two electrodes were initially separated by a submicron gap and subsequently narrowed by electrochemical deposition until a gold junction was formed. We tuned the electrode surface morphology by the deposition potential to generate a dendritic surface, which results in high junction stability and small contact area between the electrodes [3]. The electrochemical break junction setup was used to electrostatically bind ferrocene dicarboxylic acid (FDA) to cysteamine modified electrodes. This coupling is possible only within a small pH range, where the two molecules are oppositely charged. However, within this pH range, it was possible to bridge two opposing nanoelectrodes by electrostatically linked cysteamine(+)/(-)FDA(-)/(+)cysteamine junctions in aqueous solution and to determine corresponding conductance histograms. The obtained single molecule conductance of the electrostatically linked junction was one order of magnitude smaller than the conductance of covalently linked cysteamine-FDA-cysteamine, which indicates that the intermolecular electron transport through electrostatic interfaces has lower efficiency compared to intramolecular electron transport [4].

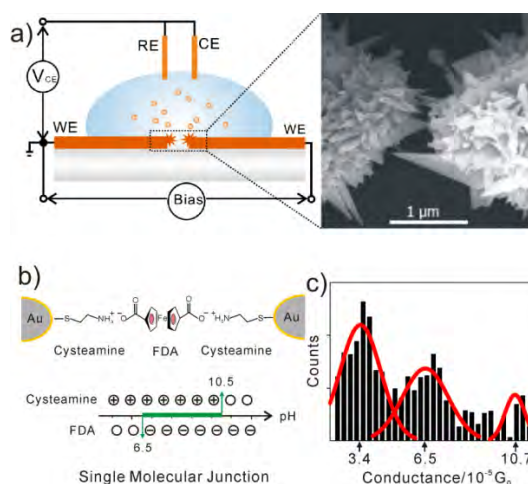


FIG. 3: (a) Scheme of an electrochemical mechanical break junction setup. SEM image of electrodeposited gold nanojunction from a template nanogap. (b) Assembling molecular junctions based on electrostatic interactions. Illustration of the appropriate pH range (green) where FDA is deprotonated and cysteamine is protonated. (c) Conductance histograms constructed from breaking cysteamine modified gold junctions in FDA containing buffer at pH 8.0.

This finding is of relevance to re-evaluate the role of electrostatically linked complexes for interprotein charge transport.

In summary, the obtained results show that biologically relevant questions of charge transport can be investigated by means of MCBJ on the level of individual molecules. The synthetic model molecules used so far will be substituted in the next step by more complex oligopeptides, the building blocks of proteins [5].

- [1] D. Xiang, F. Pyatkov, Y. Zhang, A. Offenhusser, D. Mayer, Gap size dependent transition from direct tunneling to field emission in single molecule junctions, *Chem. Commun.*, 47 (2011) 4760-4762.
- [2] D. Xiang, F. Pyatkov, Y. Zhang, A. Offenhusser, D. Mayer, Molecular Junctions Bridged by Metal Ion Complexes, *Chem. Eur. J.*, 17 (2011) 13166-13169.
- [3] Z. Yi, M. Banzet, A. Offenhusser, D. Mayer, Fabrication of nanogaps with modified morphology by potential-controlled gold deposition, *Phys. Status Solidi (RRL)*, 4 (2010) 73-75.
- [4] Z. Yi, S. Trelenkamp, A. Offenhusser, D. Mayer, Molecular junctions based on intermolecular electrostatic coupling, *Chem. Commun.*, 46 (2010) 8014-8016.
- [5] Y. Liu, A. Offenhusser, D. Mayer, Rectified tunneling current response of bio-functionalized metal-bridge-metal junctions, *Biosens. Bioelectron.*, 25 (2010) 1173-1178.

Strained SrTiO₃ films on sapphire

R. Wördenweber¹, T. Grellmann¹, K. Greben¹, J. Schubert², R. Kutzner¹, E. Hollmann¹

¹ PGI-8/ICS-8: Bioelectronics, Forschungszentrum Jülich & JARA-FIT: Jülich-Aachen Research Alliance

² PGI-9: Semiconductor Nanoelectronics, Forschungszentrum Jülich

Owing to the strong connection between strain and ferroelectricity, large shifts of the Curie temperature and polarization are observed in strained ferroelectric material. In this work, the effects of lattice-mismatch induced stress upon the crystallographic structure, strain, and generation of different types of defects in epitaxial SrTiO₃ films on CeO₂ buffered sapphire are examined and discussed in context with the resulting impact of strain on the polarization of the ferroelectric layers. Depending on the thickness of the SrTiO₃ layer, characteristic changes in their structural perfection and crystallographic orientation with respect to the substrate system are observed. For thin films, misfit dislocations partially compensate the stress in the SrTiO₃ layer, whereas cracks develop in thicker SrTiO₃ films. The structural modifications and the formation of defects can be explained in a model based on lattice misfit induced stress and energy considerations. It is demonstrated that intrinsic mismatch and thermal mismatch must be considered to explain strain dependent effects such as induced ferroelectricity and modifications of the permittivity of these complex heteroepitaxial layer systems

Pseudomorph strained-layer epitaxial growth has quickly turned from a mere curiosity into a major technology for advanced semiconductor devices and structures for solid state research. It has been demonstrated that mechanical strain can have dramatic effects on the electromagnetic properties of thin films. The most significant effect has been observed in the incipient ferroelectric oxide SrTiO₃ (STO) where a ferroelectric transition can be induced and an enhancement of the transition temperature T_c up to room temperature has been reported [1,2]. For epitaxially grown thin films, the strain is naturally induced by the underlying substrate (clamping effect). The strain is caused by the lattice mismatch and the differences in thermal expansion coefficients between the substrate and the STO film. Therefore the development of strained epitaxial STO films on suitable substrates and the analysis of their ferroelectric and structural properties are of large interest for various applications in the semiconductor technology, ranging from high-frequency devices to specific sensor applications.

Here we report on induced ferroelectricity of STO films grown on different substrates. We will focus on epitaxially grown films on the microwave suitable substrate sapphire. For this system, ferroelectricity is observed up to $T_c \approx 200\text{K}$ which cannot be explained

by standard structural analysis obtained from room temperature XRD measurements.

A series of STO films is grown on NdGaO₃ (110) (NGO), DyScO₃ (110) (DSO), and CeO₂ buffered r-cut sapphire (Al₂O₃) via pulsed laser deposition and magnetron sputter technology. Due to the lattice mismatch, STO films on DSO substrates are expected to be exposed to tensile strain, whereas NGO would lead to compressive strain parallel to the film surface (in-plane). As demonstrated in fig. 1b, the STO films on NGO and DSO behave as expected. The in-plane lattice parameter a_{\parallel} is elongated or distorted for STO on DSO or on NGO, respectively, and compensated by the out-of plane parameter a_{\perp} . As a consequence and in agreement with the theory [3], in-plane ferroelectricity is induced in STO on DSO, whereas no ferroelectricity is measured in STO on NGO (see fig. 1a).

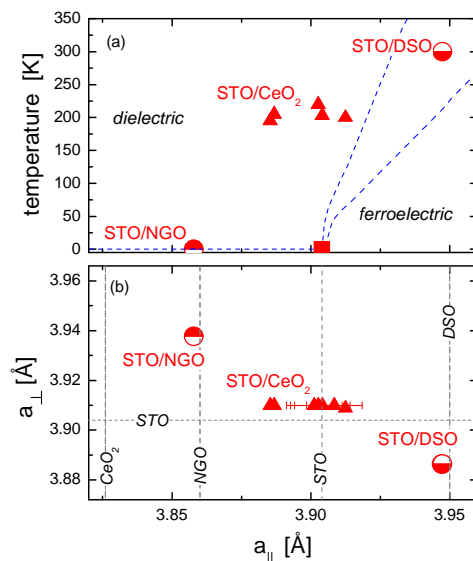


Fig. 1: Ferroelectric transition temperature T_c (a) and out-of-plane lattice parameter (b) for STO on different substrates as function of in-plane lattice parameter. The dashed lines represent the theoretical predictions for the regime of the phase transition from ferroelectric to dielectric behavior according to [3] in (a) and the nominal lattice parameter for the different substrate systems in (b).

The STO films on CeO₂ buffered sapphire behave quite differently. The lattice mismatch between the CeO₂ and STO does not seem to affect the in-plane lattice parameter of the STO in the same way observed for the other systems (STO on NGO and DSO). STO

films on CeO₂/sapphire seem to be nearly unstrained at room temperature (Fig. 1b). However, the ferroelectric properties of the films are affected. In contrast to the theoretical predictions [3], in-plane ferroelectricity is induced in STO on sapphire, and T_c values up to 200K are observed. In order to understand this unexpected behavior, we analyzed the structural and mechanical properties of STO films on sapphire in more detail.

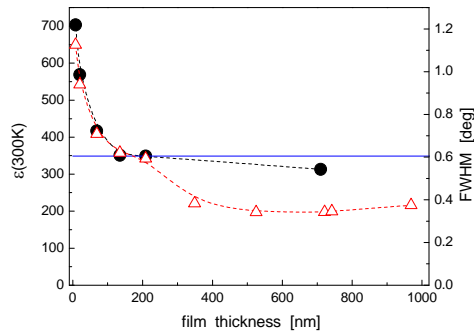


Fig. 2: Thickness dependence of the permittivity (circles) and FWHM of the STO (200) XRD rocking curve (triangles) of the STO layers on CeO₂ buffered sapphire. The solid line indicates values for the room temperature permittivity of a STO single crystal.

A first indication that stress is also imposed on the films on sapphire and results in a modification of structural and dielectric properties is provided by a comparison of XRD and permittivity data for films of different thicknesses (Fig. 2). A clear indication is given by the observation of crack formation in thick STO films on sapphire (fig. 3).

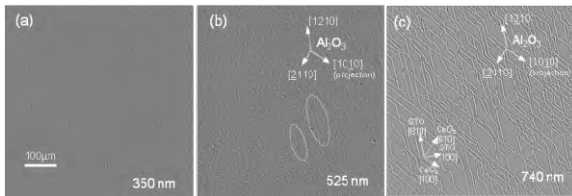


Fig. 3: Microscope images (area: 590 μm x 587 μm) of the surface of STO films of thickness $d_{\text{STO}}=350\text{nm}$ (a), 525nm (b), and 740nm(c). The crystallographic orientations of the substrate, CeO₂ buffer and STO layer are determined via XRD diffraction experiments; they are identical for all images as indicated. The dashed ellipses in (b) mark hardly visible cracks in the STO film of medium thickness.

All samples with a thin STO layer ($d_{\text{STO}} \leq 350\text{nm}$) show a smooth surface and no cracks. In contrast, all thick STO films ($d_{\text{STO}} \geq 525\text{nm}$) reveal cracks. As shown in fig. 3b ($d_{\text{STO}}=525\text{nm}$), first a few cracks with finite lateral extension (typically $< 200\mu\text{m}$) are present. All cracks point in the same crystallographic direction, i.e. the [010] direction of STO which is identical to the [1210] direction of r-cut sapphire. With increasing thickness, a ‘network of cracks’ develops (see fig. 3c). The cracks are oriented along two crystallographic directions, i.e. along the [1210] and the [1010] direction of the r-cut sapphire. Since there is no distinguished crystallographic orientation of the STO and CeO₂ layers equivalent to the [1010] direction of the r-cut sapphire, this indicates that the cracks are generated by the difference in the expansion coefficients of sapphire and STO, and that the (in-

plane) expansion coefficient of sapphire is slightly anisotropic.

Heteroepitaxial strained-layer growth signifies a major technology for use in advanced semiconductor and correlated devices, as well as for other structures in solid state research. The most fundamental questions in strained-layer growth are, (i) up to what thicknesses are heteroepitaxial layers stable, (ii) which type of misfit defects will develop and (iii) what happens upon modifications to the misfit (for instance due to cooling of the film)? It is generally believed that below a critical thickness the strained state is the thermodynamic equilibrium state, and above a critical thickness a strained layer may be metastable or it may relax [4]. Different critical thicknesses might be associated to different types of misfit defects, e.g., dislocations, misalignments, or even cracks [5]. Stress in heteroepitaxially grown films results from both an *intrinsic* and a *temperature-dependent* component. The main reason for the development of intrinsic stress in heteroepitaxially grown films is given by the nominal lattice mismatch $\varepsilon_0 = (a_{\text{film}} - a_{\text{substrate}})/a_{\text{film}}$ at growth conditions [4,5], where a represents the lattice parameter of the film and substrate. The thermal contribution to the stress arises from the difference in thermal expansion coefficients of the film and the underlying substrate. These two (intrinsic and extrinsic (here temperature-dependent)) contributions generate defects (ranging from misfit dislocations to cracks) in our heteroepitaxial STO films. A detailed description of the model is given in ref. [6].

The importance of *intrinsic* and *thermal induced* stresses for the understanding of structural modifications, the formation of defects, and the resulting ferroelectric properties of heteroepitaxially grown STO films is demonstrated. A model (details in ref. [6]) is developed to describe (i) the generation of misfit dislocations during growth and (ii) the crack formation during cooling of the sample. In general, the misfit in lattice constant and thermal expansion can be a very powerful tool to engineer the properties of heteroepitaxial films and, in particular, the ferroelectric properties of STO, suitable for various applications in semiconductor technology ranging from tunable high-frequency devices to microwave sensor concepts.

- [1] J. H. Haeni et al., Nature 430, 758 (2004).
- [2] R. Wördenweber et al., J. Appl. Phys. 102, 044119 (2007).
- [3] N. A. Pertsev et al., Phys. Rev. B 61, R825 (2000); 65, 219901(E) (2002).
- [4] J. R. Downes et al., Semicond. Sci. Technol. 9, 1265 (1994).
- [5] A.G. Zaitsev et al., Appl. Supercond. 1997, Inst. of Phys. Conf. Ser. 158, 25 (1997).
- [6] E. Hollmann et al., J. Appl. Phys. 105, 114104 (2009)

Low field magnetic resonance imaging with tuned high- T_c SQUID

C. Liu^{1,3}, Y. Zhang^{1,3}, L. Qiu^{2,3}, H. Dong^{2,3}, H. J. Krause^{1,3}, X. Xie^{2,3}, A. Offenhäusser^{1,3}

¹ PGI-8/ICS-8: Bioelectronics, Forschungszentrum Jülich & JARA-FIT: Jülich-Aachen Research Alliance

² State Key Laboratory of Functional Materials for Informatics, Shanghai Institute of Microsystem and Information Technology (SIMIT), Chinese Academy of Sciences (CAS), Shanghai 200050, China

³ Joint Research Laboratory on Superconductivity and Bioelectronics, Collaboration between CAS-Shanghai and Forschungszentrum Jülich

In order to improve low-field (LF) Magnetic Resonance Imaging (MRI) measurements with a tuned high- T_c radio-frequency (rf) Superconducting Quantum Interference Device (SQUID) as a signal detector, we use a permanent magnet pair for sample pre-polarization. MRI images are acquired by using filtered back projection reconstruction. The projections are obtained by recording free induction decay (FID) or spin echo (SE) signals with the gradient field applied at different angles. For every projection, the sample is first pre-polarized in the gap of the PM pair and then mechanically transported to the measuring position underneath the tuned SQUID. Taking 12 projections, two-dimensional LF-MRI images of two water phantoms are obtained without averaging, exhibiting a spatial resolution of about 0.2 mm.

Recently, LF-MRI using a SQUID as a signal detector was demonstrated [1] at low measurement field B_m in the μT range. The magnetization M of the sample is proportional to the pre-polarization field B_p while B_m determines the Larmor frequency f_L . The precession of signals scale only with B_p when a SQUID is employed as the detector because of its frequency-independent sensitivity. However, the technical relevance of MRI at low field is usually limited by the relatively low signal-to-noise ratio.

It is very difficult to generate a polarization field B_p larger than 50 mT using copper-wire-wound coils at room temperature [2] because of the dissipated heat due to the large coil current, the difficulty to switch off B_p quickly because of the large coil inductance, and flux trapping in the SQUID. In order to overcome this, we use sample pre-polarization by a permanent magnet (PM). Two NdFeB disk magnets are integrated with a soft iron yoke, generating a B_p field of about 1 T. A tuned high- T_c (HTS) rf SQUID is used as the signal detector. The MRI images are acquired by using filtered back projection reconstruction. Each measurement is performed by first pre-polarizing the sample in the gap of the PM pair and then mechanically transporting it to the measuring position. Because of the strong polarizing field

and the high sensitivity of the tuned SQUID, the FID and SE signals can be recorded without averaging.

Our LF-MRI measurement setup, schematically shown in Fig. 1, is designed for small-size samples. It consists of four parts: a coil system, a tuned HTS rf SQUID, a PM pair with yoke, and a mechanical transport system.

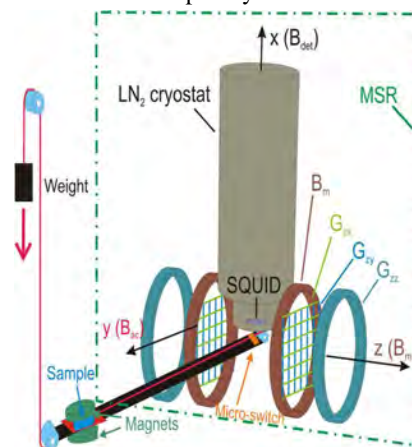


FIG. 1: Schematic of the LF-MRI setup. Labels are defined in the text.

The 2-D MRI coil system includes a Helmholtz coil pair for the generation of the measurement field B_m , three coil pairs generating the gradient field components G_{zx} , G_{zy} , and G_{zz} , and an excitation field B_{ac} coil pair to generate the $\pi/2$ or π pulse.

A Helmholtz coil pair of 22 cm diameter provides a B_m of 212 μT along the z -direction. An excitation field B_{ac} in the y -direction is produced by a coil pair (not shown in Fig. 1). The gradient field $G_{zz} = dB_z/dz$ is generated by a Maxwell coil, whereas the other two gradient fields, $G_{zx} = dB_z/dx$ and $G_{zy} = dB_z/dy$ are produced by planar multi-loop gradient coils. When the filtered back projection reconstruction is utilized to create 2-D MRI images, the direction of the gradient field in the y - z plane can be rotated stepwise by adjusting the strength of G_{zz} and G_{zy} .

The tuned HTS rf SQUID combines an rf SQUID magnetometer and a LC resonant circuit, which is inductively coupled to the SQUID [3]. The tuned rf SQUID not only improves the sensitivity to 6 ~

7 fT/Hz at $f_L \approx 9$ kHz but also provides the large detection area of the L coil which is 40 mm in diameter [3].

Once the sample arrives at the measuring position, a micro-switch produces a TTL pulse to start the measurement sequence shown in Fig. 2. First, a $\pi/2$ pulse of B_{ac} is applied to tilt the sample magnetization M perpendicular to B_m . A Q-switch circuit damps the ringing in the LC circuit induced by the ac pulse [4] before the FID signal is recorded. Subsequently, a π pulse of B_{ac} is applied to obtain a SE signal. After the recordings, the sample is transported back to the gap of the PM pair for pre-polarization and the gradient field is rotated to acquire the next projection.

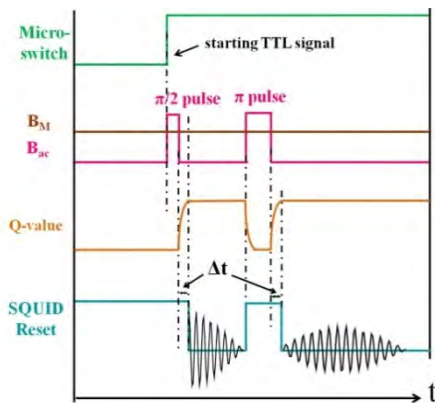


FIG. 2: Pulse sequence used in the measurements.

The filtered back projection reconstruction was utilized for 2-D MRI measurements [5]. In the y - z plane, each projection corresponded to a gradient field $G_{z(y-z)}$ of about 20 Hz/cm, with its direction rotated step by step to cover 180° . For all projections, both FID and SE signals were recorded without averaging.

We performed LF-MRI measurements with water phantoms [6]. Image quality generally increases with increasing number of projections. To illustrate this effect, images were reconstructed from 6 and from 12 projections, as shown in Fig. 3 (a). Here, sample #1 with five isolated cylinder-shaped bores filled with tap water (1×0.2 ml with diameter of 6 mm in the center and 4×0.35 ml with diameter of 8 mm around it) was utilized. The MRI image reconstructed from 6 projections was distorted because of the low number of projections. When the number of projections was increased to 12, the image quality was clearly improved. Usually, the echo signal is utilized to reconstruct the image. Here we make a comparison between the images of sample #2 reconstructed from FID and Echo signals. The sample #2 is a plexiglass slab with two cylinder-shaped bores, 7.5 mm in diameter, filled with tap water (0.35 ml each), and separated by a distance of 13 mm. The photo of the sample #2 and its reconstructed 2-D MRI images with 12 projections are shown in Fig. 3 (b). Geometrical shapes of the

images reconstructed from both FID and SE signals are in good agreement with the dimensions of the sample.

The spatial resolution Δx of MRI in one dimension can be expressed as $\Delta x = 2\pi\delta/\gamma G$, where δ is the linewidth of the NMR spectrum, γ the gyromagnetic ratio of proton ($\gamma/2\pi = 42.58$ MHz/T), and G the applied gradient field strength ($47 \mu\text{T/m}$). For the measured 0.4 Hz linewidth of sample #2, a spatial resolution of about 0.2 mm was reached.

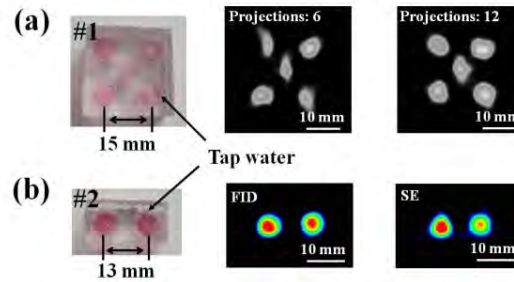


FIG. 3: Sample photos and their 2-D LF-MRI images. The tap water in the sample photos was pink-colored and the sample substrates were made from plexiglass. (a) Photo of sample #1 and its 2-D MRI images reconstructed from FID signals for different numbers of projections. (b) Photo of sample #2 and its 2-D MRI images reconstructed from FID and SE signals.

The quality of the images demonstrates that it is feasible to image small-sized samples with 1 T pre-polarization, sample movement and a tuned SQUID detector [6]. The performance was significantly improved over pre-polarization by a copper coil. MRI images were reconstructed from 12 projections without averaging. In our present scheme, a relatively long relaxation time T_2 of the sample on the order of seconds is required. In the future, not only the homogeneity of B_m should be improved to reduce the distortions of the reconstructed MRI image, but also the sample transport time should be shortened to lower the requirement on the sample's T_2 .

-
- [1] R. McDermott et al., Proc. Natl. Acad. Sci. 101, 7857-61 (2004)
 - [2] V.S. Zotev et al., IEEE Trans. Appl. Supercond. 17, 839-42 (2007)
 - [3] L.Q. Qiu, Y. Zhang, H.-J. Krause, A.I. Braginski, A. Usoskin, Rev. Sci. Instrum. 78, 054701 (2007)
 - [4] H. Dong, Y. Zhang, H.-J. Krause, X. Xie, A.I. Braginski, A. Offenhäusser, SUST 22, 125022 (2009)
 - [5] H. Dong, Y. Zhang, H.-J. Krause, X. Xie, A. Offenhäusser, IEEE TAS 21 (2011) 509-13 (2011).
 - [6] C. Liu, Y. Zhang, L. Qiu, H. Dong, H.-J. Krause, X. Xie, A. Offenhäusser, SUST 25, 075013 (2012).

Selected Publications

1. Wördenweber, R.; Hollmann, E.; Schubert, J.; Kutzner, R.; Kumar Ghosh, A.
Pattern induced phase transition of vortex motion in high-T_c films
Applied Physics Letters **94** (2009), 202501 – 202503
2. Kisner, A.; Lenk, S.; Mayer, D.; Mourzina, Y.; Offenhäusser, A.
Determination of the Stability Constant of the Intermediate Complex during the Synthesis of Au Nanoparticles Using Arous Halide
Journal of Physical Chemistry C **113** (2009) 47, 20143- 20147
3. Eschermann, J. F.; Stockmann, R.; Hüske, M.; Vu, X. T.; Ingebrandt, S.; Offenhäusser, A.
Action Potentials of HL-1 Cells Recorded With Silicon Nanowire Transistors
Applied Physics Letters **95** (2009) 8, 083703
4. Hofmann, B.; Maybeck, V.; Eick, S.; Meffert, S.; Ingebrandt, S.; Wood, P.; Bamberg, E.; Offenhäusser, A.
Light induced stimulation and delay of cardiac activity
Lab on a Chip **10** (2010), 2588 – 2596
5. Kätelhön, E.; Hofmann, B.; Lemay, S.G.; Zevenbergen, M.A.G.; Offenhäusser, A.; Wolfrum, B.
Nanocavity Redox Cycling Sensors for the Detection of Dopamine Fluctuations in Microfluidic Gradients
Analytical Chemistry **82** (2010) 20, 8502 – 8509
6. Liu, Y.; Offenhäusser, A.; Mayer, D.
An Electrochemically Transduced XOR Logic Gate at the Molecular Level
Angewandte Chemie-International Edition **49** (2010) 14, 2595 – 2598
7. Xiang, D.; Zhang, Y.; Pyatkov, F.; Offenhäusser, A.; Mayer, D.
Gap size dependent transition from direct tunneling to field emission in single molecule junctions
Chemical Communications **47** (2011) , 4760 – 4762
8. Hofmann, B.; Kätelhön, E.; Schottdorf, M.; Offenhäusser, A.; Wolfrum, B.
Nanocavity electrode array for recording from electrogenic cells
Lab on a Chip **11** (2011) , 1054-1058
9. Fricke, R.; Zentis, P. D.; Rajappa, L. T.; Hofmann, B.; Banzet, M.; Offenhäusser, A.; Meffert, S. H.
Axon guidance of rat cortical neurons by microcontact printed gradients
Biomaterials **32** (2011) 8, 2070 – 2076
10. Yakushenko, A.; Schnitker, J.; Wolfrum, B.
Printed Carbon Microelectrodes for Electrochemical Detection of Single Vesicle Release from PC12 Cells
Analytical Chemistry **84** (2012) , 4613 – 4617

Indicators

Quantitative Numbers

	2009	2010	2011
Peer-Reviewed Publications	58	44	61
Graduations			
Master/Diploma	9	10	7
Dissertation	4	5	6
Habilitation	0	0	0

Honours

Special Award of the President of CAS for doctoral studies	Hui Dong	Chinese Academy of Sciences (CAS), 2011
Poster prize	Philipp Rinklin	“Engineering of Functional Interfaces” conference in Linz (A), 2011
Visiting professorship	Hans-Joachim Krause	Université Pierre et Marie Curie, 2011
Guest Professorship	Andreas Offenhäusser	Shanghai Institute of Microsystem and Information Technology, Chinese Academy of Sciences , 2012
Young Investigator Group	Bernhard Wolfrum	HGF 2009
Postdoctoral fellowship	Jaydeep Bhattacharya	Alexander von Humboldt, 2008 – 2010

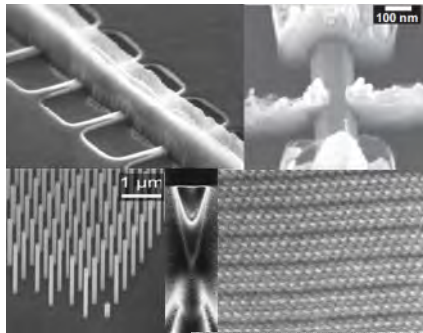
Offers

2009	Norbert Klein	Imperial College London	Chair in Electromagnetic Nanomaterials
2010	Roger Wördenweber	Universität zu Köln	APL, Mathematisch-Naturwissenschaftliche Fakultät

Selected Third Party Projects

1. Nanotools for Cell-Chip Communication
HGF, Helmholtz Young Investigators Group
Jun 2009 – May. 2014
2. BiMEA: Bidirektionale Kommunikation zwischen Retina-Stimulatoren und Netzhaut
DFG,
Coll. Project, Dec 2010 – Nov 2012
3. CILIA - Customized Intelligent Life-inspired Arrays
EU, frame work programme 6
Integrated Project, Sep 2005 – Feb 2010
4. Netzwerk: The Human Brain Model
Helmholtz-Allianz Systembiologie
Impuls- und Vernetzungsfonds, HGF
1.1.2008 – 31.12.2012

PGI-9: Semiconductor Nanoelectronics



The omni-presence of IT products in our daily life and its corresponding energy consumption reaching almost 10% of the total electrical power production in modern societies will change the importance of individual technology drivers. Over the past decades aggressive downscaling of Si-CMOS devices was the main driver to fulfil increasing demands of computing power. With this approach running out of pace, energy efficiency will become the technology driver of the future. Smart, ultra-light and grid independent portable devices may guard our life. This will require the integration of efficient energy harvesting and storing devices, data sensing and processing devices as well as antennas for data transmission. Within this framework the institute of semiconductor nanoelectronics studies alternative routes for energy efficient transistors, new concepts for nanostructured photovoltaic and thermoelectric elements, nanowire based optoelectronic as well as THz devices. Our research approach includes the introduction of new materials and device concepts as well as alternative technologies. The combination of strained Si nanowires, high-k gate dielectrics and gate all-around technology has resulted in a significant performance boost towards energy efficient C-MOS transistors. Innovative paths to further increase the strain in these devices are under investigation. Moreover, the developed technology is transferred to Schottky-Barrier-MOSFets as well as to Tunnel-FETs providing concepts to significantly reduce the power consumption of transistors. The technology of these nanowire transistors remains challenging, the control of the strain on a nanometer scale, the silicide source/drain contact resistivity, carrier injection, parasitic capacities and gate control as well as thermal stability are critical subjects of investigation. On a long-term basis, novel concepts beyond the Si-CMOS technology are to be addressed. This implies low-dimensional nanotransistor designs with new geometries and material combinations as well as revolutionary approaches. A series of alternative processes for realization of such structures were developed. In the conventional GaAs material system, well ordered arrays of nanowires (NW) that were controllable in diameter and length were grown selectively by MOVPE on pre-patterned substrates. Growth of III/V NW exhibiting axial and radial heterostructures has been successfully implemented. Magneto-transport are used to unravel the fundamental properties, such as the free mean path and the spin coherence length of electrons in NW. Based on the insights, new device designs using quantum mechanical properties of these structures are under investigation. Strengthening this concepts, expertise in the material systems of topological insulators (Bi_2Te_3 , Bi_2Se_3 and Sb_2Te_3) as well as in the growth of NW composed of phase change materials such as GeSb has been build up. The first one may pave the road towards conceptually new spintronics or quantum information devices, whereas the later may permit the design of NW based circuitry combining logic and memory elements on the nanoscale.

The research activities of PGI-9 are well embedded in the general framework of the JARA-FIT section in very close collaboration with several groups at the RWTH. The latter is manifested in the foundation of the JARA institute of "Green-IT" merging activities of the Institute of Physics (IA) of RWTH, PGI-7 and PGI-9.

Our work has successfully addressed the technology and physics of nanoscale devices. The achieved results, spanning the regime of advanced state-of-the-art CMOS technology to future device concepts contribute to close the gap between forefront research and today's developments. In doing so, the research team has become a preferred partner for industrial collaborations of a national as well as European level.

Head of Institute:

Prof. Detlev Grützmacher, email: d.gruetzmacher@fz-juelich.de, phone: +49-2461-61-2340.

Scientific Staff

On September 1st 2012, the staff of PGI-9 comprised 15 scientists, 1 young research group leader, 3 Post Docs, 13 technicians, 25 PhD students, and 6 Master/Diploma students.

Senior Scientists

Dr. Martina von der Ahe
Dr. Yulieth Arango (*Alexander von Humboldt*)
Dr. Dan Mihai Buca
Dr. Beata Dunin-Borkowska
Prof. Dr. Detlev Grützmacher
Dr. Hilde Hardtdegen
Dr. Bernd Holländer
Dr. Mihail Ion Lepsa
Prof. Dr. Siegfried Mantl (*Helmholtz Professor*)
Dr. Jürgen Moers
Dr. Gregor Mussler
Prof. Dr. Thomas Schäpers
Dr. Jürgen Schubert
Dr. Toma Stoica
Dr. Qing-Tai Zhao

Young Research Group Leader

Prof. Dr. Christoph Stampfer (JARA Junior Prof., RWTH Aachen)

Post Docs

Dr. Svetlana Borisova
Dr. Nataliya Demarina
Dr. Martin Mikulics

Visiting Scientists

Prof. Dr. H. Lüth (Emeritus)
Dr. Igor Batov

Research Highlights

Phase-Coherence and Spin-Orbit Coupling in InAs Nanowires

S. Estévez Hernández¹, M. Akabori¹, K. Sladek¹, Ch. Volk¹, S. Algha¹, H. Hardtdegen¹, M. G. Pala², J. Schubert¹, M. Schnee¹, N. Demarina¹, D. Grützmacher¹, Th. Schäpers¹

¹ PGI-9: Semiconductor Nanoelectronics, Forschungszentrum Jülich

² IMEP-LAHC, UMR 5130, MINATEC, Grenoble INP, 3 Parvis Louis Néel, BP 257, 38016 Grenoble, France

The phase-coherence and spin-orbit coupling in InAs nanowires is investigated by means of interference experiments, i.e. universal conductance fluctuation and weak anti-localization measurements. The InAs nanowires were grown by selective area metal-organic vapor-phase epitaxy. Control of the electron interference is achieved by applying a magnetic field or by using a top- or back-gate electrode. For the phase-coherence length a values of several 100nm was found at temperatures below 1 K, while for the spin-orbit scattering length a value of 70nm was extracted from the comparison with theoretical calculations.

Due to their small dimensions, semiconductor nanowires offer an exciting route to study charge or spin related interference effects in the low-temperature electron transport [1]. By choosing the narrow-band-gap semiconductor InAs as a material for the nanowire, the common problem connected with carrier depletion at the surface can be avoided. In fact, due to the Fermi level pinning within the conduction band at the surface an electron accumulation layer is formed. In addition, the strong electric field, resulting from the modulation of the potential profile at the surface is expected to lead to a pronounced Rashba spin-orbit coupling. The latter effect is interesting for spinelectronic devices, since it would allow the control of the spin orientation by electrical means, i.e. by a gate electrode. Here, we investigated the phase-coherence and spin-orbit coupling in InAs nanowires by means of electron interference experiments.

The InAs nanowires were selectively grown on a patterned GaAs (111)B substrate by low-pressure metal-organic vapor phase epitaxy in an N₂ atmosphere at a temperature of 650 °C. The wires have a diameter d of approximately 100nm. For the transport measurements the nanowires were contacted individually by Ti/Au electrodes using electron-beam lithography. Gate control was achieved either by using the highly-doped Si substrate as a back-gate or by using additional top-gate electrodes defined by electron beam lithography. In the latter case, a novel approach was

utilized for the gate isolation by employing GdScO₃ and LaLuO₃ as a high- k dielectric [2,3]. The advantage of GdScO₃ and LaLuO₃ is their high dielectric constant, i.e. $k = 22$ and 30 , respectively, which is expected to allow a gate control at lower gate voltages compared to more common dielectrics, e.g. SiO₂, with comparable layer thickness. For a complete coverage of the nanowire by the high- k dielectric, pulsed laser deposition was employed.

In Fig. 1(a) a scanning electron micrograph of an InAs nanowire covered by a 1.6 μ m long gate is shown. As illustrated in Fig. 1(b) for gate isolation a 10nm thick LaLuO₃ layer was used. As can be seen from the output characteristic shown in Fig. 1(c), an efficient gate control of the nanowire conductance is achieved by this approach [3].

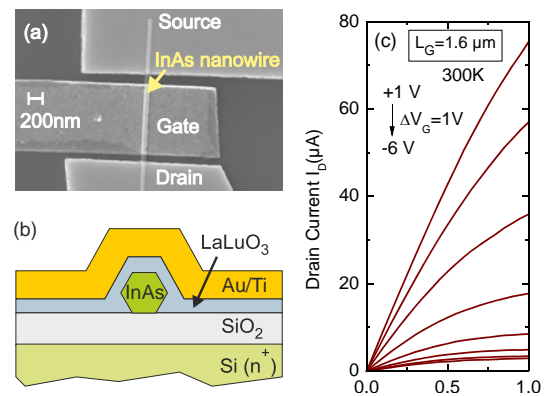


FIG. 1: (a) Scanning electron beam micrograph of an InAs nanowire field-effect transistor with a 1.6 μ m long gate. (b) Schematics of the transistor cross-section. (c) Output characteristics of the field-effect transistor with a 1.6 μ m long gate at room temperature.

Information on the spin-orbit scattering length l_{so} , which is a measure for the strength of spin-orbit coupling, can be obtained from weak antilocalization measurements. The signature of this effect is a conductance maximum at zero magnetic field.

However, as can be seen in Fig. 2(b), the pronounced conductance fluctuations prevent to observe any

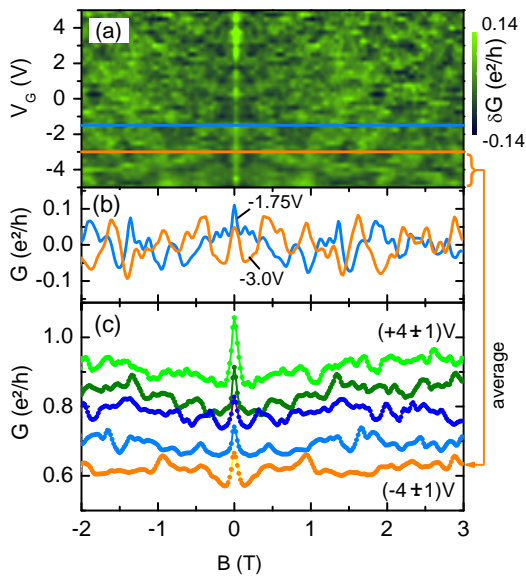


FIG. 2: (a) Color-scaled conductance as a function of magnetic field and gate voltage at 0.5 K. The trace of the conductance fluctuations shown in (b) are indicated by the horizontal lines. (b) Magnetoconductance at 0.5K at $V_G = -1.75V$ (light blue curve) and at $-3.0V$ (orange curve). (c) Averaged magnetoconductance corrections for fluctuation measurements within a 2V wide gate-voltage interval.

antilocalization effect. Nevertheless, by averaging the conductance fluctuations over a gate voltage range of 2V, these conductance fluctuations can be suppressed. As can be seen in Fig. 2(c), now a clear conductance peak is resolved at zero magnetic field, indicating the presence of weak antilocalization.

So far, no theoretical model is available, which describes the weak antilocalization effect in conductors of circular geometry. In order to obtain information on the phase coherence length l_ϕ and the spin orbit scattering length l_{so} , simulations based on a recursive two-dimensional Green's-function approach were performed. The corresponding simulation results can be seen in Fig. 3. From the comparison with the experimental data one finds that the spin-orbit scattering length is relatively short, i.e. 70nm, indicating a strong spin-orbit coupling.

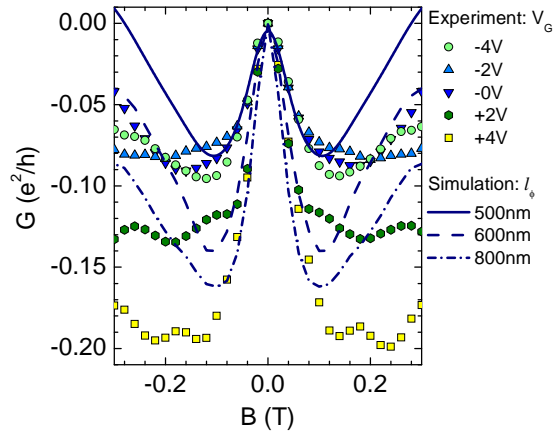


FIG. 3: Averaged magnetoconductance corrections for fluctuation measurements within a 2V wide gate-voltage interval (dots). The center-gate voltages of the intervals are: +4, +2, 0, -2, -4V. The lines represent the corresponding simulations.

Our results show that InAs nanowires are interesting candidates for the realization of nanoelectronic devices based on electron interference as well as on spin-related effects.

-
- [1] C. Thelander, P. Agarwal, S. Brongersma, J. Eymery, L. Feiner, A. Forchel, M. Scheffler, W. Riess, B. Ohlsson, U. Gösele, and L. Samuelson, *Mater. Today* 9, 28 (2006).
 - [2] C. Volk, J. Schubert, K. Weis, S. Estévez Hernández, M. Akabori, K. Sladek, H. Hardtdegen, and Th. Schäpers, *Appl. Phys. A*, 100, 305 (2010)
 - [3] C. Volk, J. Schubert, M. Schnee, K. Weis, M. Akabori, K. Sladek, H. Hardtdegen, and Th. Schäpers, *Semicond. Sci. Technol.* 25, 085001 (2010)
 - [4] S. Estévez Hernández, M. Akabori, K. Sladek, Ch. Volk, S. Alagha, H. Hardtdegen, M. G. Pala, N. Demarina, D. Grützmacher, and Th. Schäpers, *Phys. Rev. B* 82, 235303 (2010)

Supercurrent in Nb/InAs-Nanowire/Nb Josephson junctions

H. Y. Günel¹, I. E. Batov¹, H. Hardtdegen¹, K. Sladek¹, A. Winden¹, K. Weis¹, G. Panaitov², D. Grützmacher¹, and Th. Schäpers¹

¹ PGI-9: Semiconductor Nanoelectronics, Forschungszentrum Jülich

² PGI-8/ ICS-8: Bioelectronics, Forschungszentrum Jülich

Planar mesoscopic Josephson junctions are formed by InAs nanowires coupled to superconducting Nb terminals. The properties of the junctions are tuned by the Si-doping of the InAs-nanowires. The junction characteristics are studied as a function of temperature, gate voltage, and magnetic field. Josephson supercurrent values up to 100 nA are found for junctions with high doping concentrations.

The Josephson coupling persists up to 4 K. In all junctions the critical current monotonously decreased with the magnetic field, in accordance with the model of the proximity effect in ultra-small Josephson junctions. In low-doped Josephson junctions the critical current can be controlled by the gate voltage. The observed strong conductance fluctuation amplitude is attributed to phase-coherent Andreev reflection as well as to the large number of phase-coherent channels due to the large superconducting gap of the Nb electrodes.

Modern nanofabrication techniques provide a possibility to fabricate planar multi-terminal Josephson structures relevant for the realization of different types of hybrid superconductor/semiconductor nanoscale devices.^{1,2} Josephson field effect transistors,³ superconducting quantum point contacts⁴ and injection current controlled Josephson junctions⁵ were realized with high-mobility 2-dimensional electron gases in semiconductor heterostructures. Recently, the Josephson effect was also observed in nanoscale devices formed by semiconductor nanowires coupled to superconducting terminals.^{1,6} Moreover, semiconductor nanowires have been used for experiments dedicated to confirm the existence of Majorana fermions.⁷

In our study we investigated the Josephson effect in Nb/InAs-nanowire/Nb hybrid structures. By using InAs-nanowires with two different bulk carrier concentrations we were able to vary the properties of the nanoscale weak link Josephson junction to a large extent, i.e. in the junctions with the highly doped InAs nanowires a relatively large Josephson supercurrent is observed, whereas for junctions with low doped nanowires I_c is reduced but here a gate control of the superconducting switching currents is possible. We devoted special attention to effects which originate from the small size of the junctions, in particular the magnetic field dependence of the

critical current as well as the gate voltage dependent conductance and supercurrent fluctuations. The field dependence of the critical current and the fluctuation phenomena are compared to recent theoretical models.

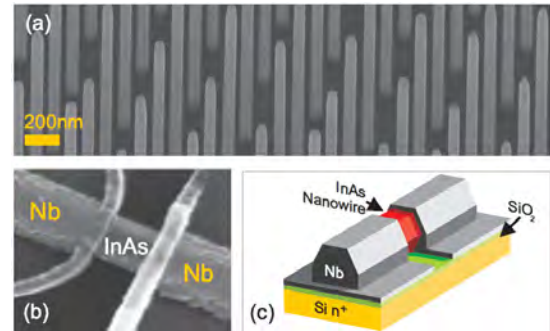


FIG. 1: (a) Scanning electron micrograph of the as grown highly doped nanowires. (b) Scanning electron micrograph of sample L2. (c) Schematic illustration of the junction layout.

The n-type doped InAs nanowires were grown by selective area metal organic vapor phase epitaxy (MOVPE) without using catalyst material. Disilane has been employed for n-type doping, In Fig. 1(a) depicts a scanning electron micrograph of the as-grown nanowires.

In order to contact the nanowires with Nb electrodes they were transferred from the growth substrate to an n+-Si/SiO₂ substrate with predefined electron beam markers. The Nb electrodes were defined by electron beam lithography and lift-off. The 100 nm thick Nb layer was deposited by sputtering. The highly doped n-type substrate was used for back-gating of the nanowires. A scanning electron micrograph of a typical junction is shown in Fig. 1(b), while a schematics of the junction layout can be found in Fig. 1(c).

The transport measurements were performed at temperatures down to 0.3K in a He-3 cryostat equipped with a superconducting solenoid with a magnetic field up to 7 T. The DC and differential current-voltage characteristics were measured using a four-terminal current-driven measurement scheme.

In Fig. 2 the current-voltage (IV) characteristics at various temperatures between 0.4 and 4.8K are shown for a sample with a highly doped nanowire. At temperatures $T \leq 4K$ and small bias, a clear Josephson supercurrent is observed in the junction. As the bias current exceeds a certain value I_{sw} , the Josephson junction switches from the

superconducting to the normal state. The switching current I_{sw} measured at 0.4K is about 100 nA.

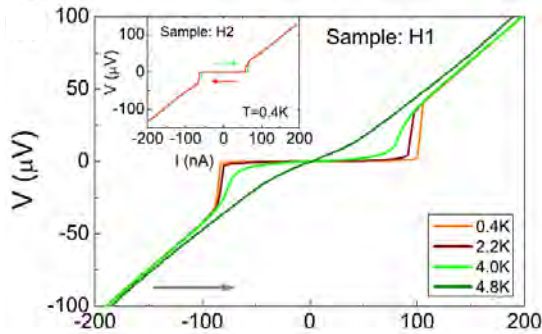


FIG. 2: (a) IV-characteristics of a highly doped device (sample H1) at various temperatures. The inset shows the IV-characteristics of a second highly doped device (sample H2) at 0.4 K.

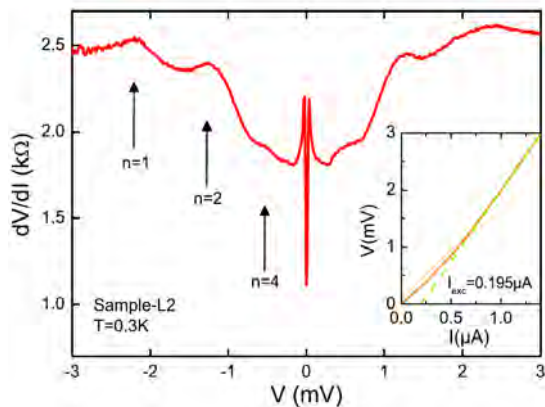


FIG. 3: Differential resistance dV/dI versus bias voltage using a low doped nanowire at 0.3 K. The subgap features are indicated by arrows. The inset shows a high bias range IV-characteristic of the device (solid line) and the linear fit of the IV-curve at $V > 2\Delta$ (dashed line) to show the excess current value I_{exc} .

In Fig. 3, the differential resistance dV/dI vs bias voltage of a sample with a low doping level in the nanowire is shown. The measurement temperature was 0.3 K. The peaks in dV/dI at finite bias voltages can be associated with subharmonic energy gap structures caused by multiple Andreev reflections. Fitting the peak positions yields a superconducting energy gap $\Delta = 1.2\text{meV}$ in the Nb. The contact transparency in this device can be estimated from the excess current I_{exc} (cf. Fig. 3, inset) to $T_n \approx 0.6$. From the electron-phonon coupling strength and assuming $\Delta=1.2\text{meV}$ for the superconducting gap at $T = 0$, we obtain a critical temperature $T_c = 7.2\text{K}$ for the Nb electrodes.

Owing to the large critical field of Nb a Josephson supercurrent is maintained up to relatively large magnetic fields. At 0.4 K a magnetic field was applied perpendicular to the substrate. A monotonous decrease of the measured critical current I_c with magnetic field B is found. A complete suppression of I_c occurred at about 0.2 T. The monotonous decrease of I_c with increasing B can be explained by a recently developed theoretical model for the proximity effect in diffusive narrow-width Josephson junctions. Here, the decrease of I_c is explained by the magnetic pair breaking effect in

narrow-width Josephson junctions. In the junctions with the lower doped nanowires the Josephson supercurrent I_c as well as the conductance fluctuates when the gate voltage is varied. The measured average amplitude of supercurrent fluctuations is smaller than the theoretically expected value. The large difference between both values is attributed to the presence of a barrier at the Nb/nanowire interface. The average conductance fluctuation amplitude for the Nb/InAs-nanowire samples is considerably larger than the corresponding value for a reference sample with normal conducting Au/Ti contacts. We attribute this enhancement to the contribution of phase-coherent Andreev reflection.

Finally, we would like to address the possibility of Majorana fermions that can be created by using a structure based on a superconducting electrode and a semiconductor nanowire. In fact, nanowires based on InAs comprise the necessary strong spin-orbit coupling and a large g -factor. Furthermore, by using Nb as a superconducting electrode a sufficiently large gap can be induced in the nanowire. Majorana fermions can be observed only at moderate magnetic fields, therefore superconducting Nb electrodes offer an advantage due to its high critical magnetic field. Thus, InAs nanowires combined with Nb electrodes can be regarded as a suitable system for the creation of Majorana fermions.

In summary, we have successfully fabricated and characterized Nb/InAs-nanowire/Nb Josephson junctions. By taking advantage of Nb as a superconductor, we could demonstrate that the junctions comprising a highly doped InAs nanowire show a clear Josephson supercurrent up to relatively high temperatures of 4 K. For the junctions with the lower doped nanowire, gate control of the Josephson supercurrent was achieved. The measurements of I_c as a function of magnetic field show that a Josephson supercurrent can be maintained up to a field of 0.2 T.

-
- [1] S. De Franceschi, L. Kouwenhoven, C. Schönberger, and W. Wernsdorfer, *Nature Nano* 5,703 (2010).
 - [2] Th. Schäpers, *Superconductor/Semiconductor Junctions*, vol. 174 (Springer Tracts on Modern Physics, 2001).
 - [3] T. Akazaki, H. Takayanagi, J. Nitta, and T. Enoki, *Appl. Phys. Lett.* 68, 418 (1996).
 - [4] H. Takayanagi, T. Akazaki, and J. Nitta, *Phys. Rev. Lett.* 75, 3533 (1995).
 - [5] Th. Schäpers, V. A. Guzenko, R. P. Müller, A. A. Golubov, A. Brinkman, G. Crecelius, A. Kaluza, and H. Lüth, *Phys. Rev. B* 67, 014522 (2003).
 - [6] Y.-J. Doh, J. A. van Dam, A. L. Roest, E. P. A. M. Bakkers, L. P. Kouwenhoven, and S. D. Franceschi, *Science* 309, 272 (2005).
 - [7] V. Mourik, K. Zuo, S. M. Frolov, S. R. Plissard, E. P. A. M. Bakkers, and L. P. Kouwenhoven, *Science* 336, 1003 (2012).

Electron and hole mobilities of Ω -gated Si NW-array MOSFETs

S. Habicht, Q.T. Zhao, D. Buca, S. Mantl

PGI 9: Semiconductor Nanoelectronics, Forschungszentrum Jülich

Non-planar CMOS concepts such as FinFETs and nanowire (NW) MOSFETs are intensively studied for sub-20nm FETs. These devices can take advantage of mobility enhancement by choosing the optimum crystal orientation for current transport. It is, therefore, interesting to study the integration of novel materials into such multigate devices.

The electrical characteristics of Ω -gated n - and p -NW array FETs on (001) strained/unstrained silicon-on-insulator (S/SOI) substrates are investigated. NW MOSFETs consisting of 1000 parallel NWs with cross sections of $20 \times 20 \text{ nm}^2$ and 4 nm SiO_2 gate oxide were fabricated along $\langle 110 \rangle$ and $\langle 100 \rangle$ crystal directions (Fig.1). The devices presented here have a channel length of $2 \mu\text{m}$. Electron and hole mobilities were extracted employing the split C-V method to determine the gate capacitance and to eliminate parasitic capacitances. The devices feature excellent I-V characteristics: off-currents (I_{off}) as low as 10^{-14} A , ideal subthreshold swings of 60 mV/dec and maximum $I_{\text{on}}/I_{\text{off}}$ ratios of 10^{11} for both n and p -type transistors on SOI and SSOI substrates (Fig.1). The C-V characteristics as well as the ideal inverse subthreshold swings indicate high quality of the gate oxide and low interface state density.

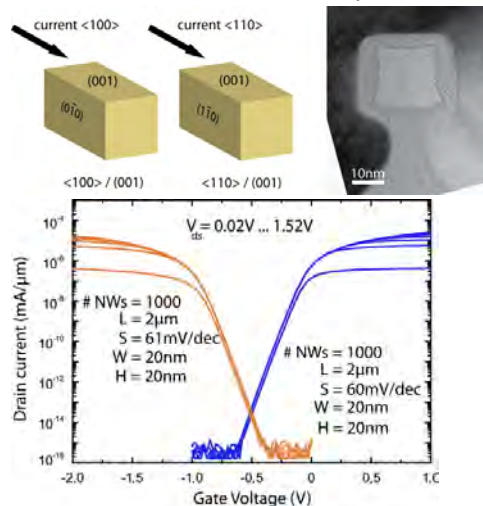


Fig.1 (top) Schematic view of NW devices fabricated on (001)Si. Compared to planar devices three surfaces contribute to carrier transport. TEM image of a Ω -gated $20 \times 20 \text{ nm}^2$ NW. (bottom) Transfer characteristic of n - and p -NW FETs with $\langle 110 \rangle$ channel direction.

P -type NW-array FETs aligned along $\langle 110 \rangle$ direction showed 1.4 times larger on-currents and 1.3 times higher transconductances compared to devices oriented along $\langle 100 \rangle$ direction. This improvement is explained by the 40% higher hole mobility measured on $\langle 110 \rangle$ p -FETs compared to $\langle 100 \rangle$ devices

(Fig.2) [1]. Decreased band splitting between the HH- and LH sub-bands due to the electric quantum confinement degrades mobility of (100) at high gate electric fields (high values of N_{inv}). Moreover, reduced scattering, originating from surface roughness and interband scattering, results for $\langle 110 \rangle$ p -FETs, due to the linear dependence of the scattering rate on the electric field. The hole mobility gain as a function of inversion carrier density N_{inv} for $\langle 110 \rangle$ p -FETs is presented in Fig 2.

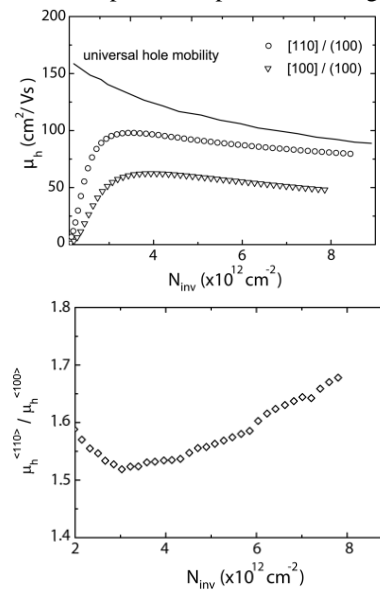


Fig. 2: Hole mobilities of $\langle 110 \rangle$ and $\langle 100 \rangle$ NW-array p -FETs (top) and the hole mobility gain as a function of inversion carrier density N_{inv} for $\langle 110 \rangle$ p -FETs (bottom).

N -FETs NW devices fabricated along $\langle 100 \rangle$ crystal direction show 1.3 times enhanced on-currents and 45% increased electron mobility compared to $\langle 110 \rangle$ channel direction (Fig.3). These enhancements are ascribed to the anisotropy of electron mobility and to re-population of conduction sub-bands along the Si NW [2]. The mobility gain for n -FETs along $\langle 100 \rangle$ saturates with increasing inversion carrier density N_{inv} (Fig.3) as a further increase of the gate voltage does not change the occupancy of the Δ_2 sub-bands.

Similar NW devices were fabricated using SSOI substrates. It is known that biaxial tensile strain efficiently improves the electron mobility in Si. The initial stress in the SSOI layer was 1.5 GPa. Lateral strain relaxation through patterning is employed to transform biaxial tensile strain into uniaxial tensile strain along the NW [2, 3]. The electrical characteristics of uniaxially tensile strained NW-array FETs with channels oriented along $\langle 110 \rangle$ and

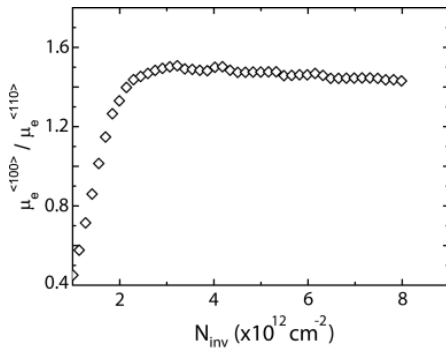


Fig. 3: The mobility gain for <100> n-FETs saturates with increasing inversion carrier density N_{inv} .

<100> are compared. Similarly to unstrained Si NW array n-FETs, the on-current of <100> uniaxial tensile strained channels increases by a factor of 1.2 compared to strained <110> channels. (Fig.4). The comparison of strained and unstrained n-FETs along <110> and <100> clearly demonstrates improved electron mobilities for strained channels of both, <110> and <100> channel orientations [5].

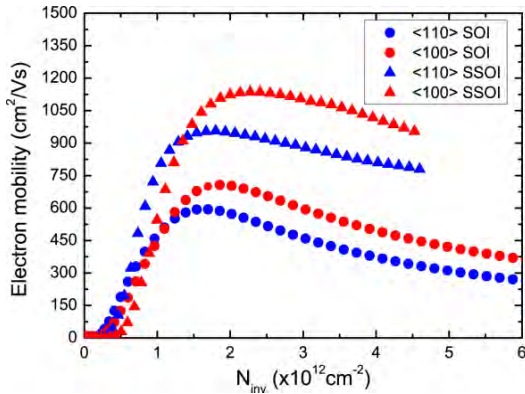


Fig. 4: Electron mobilities for NW-array n-FETs aligned along <110> and <100> for SOI and SSOI substrates.

Low temperature I-V characterization of strained and unstrained NW array n-FETs, at temperatures ranging from 4K to 280K, was performed. The inverse subthreshold swing, $S(T)$, follows perfectly the theoretical predicted behavior (Fig.5). An increase of the threshold voltage, $V_{th}(T)$, with decreasing temperature of -0.6 mV/K for strained Si and -0.85 mV/K for unstrained Si devices was measured. The off-currents of the NW array MOSFETs are independent on the channel orientation, the strain within channel, as well as the type of the device (n- or p-type).

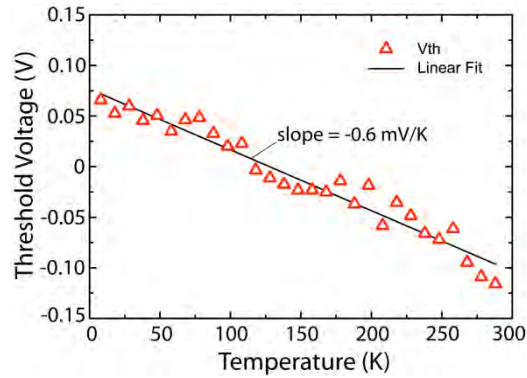
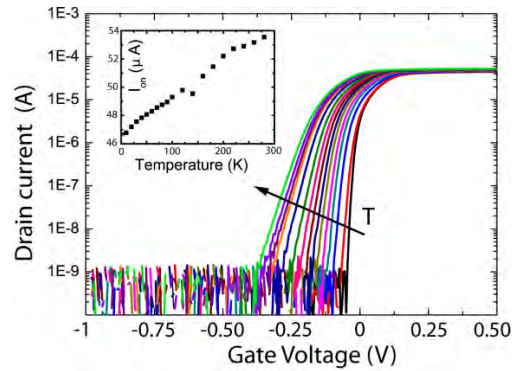


Fig. 5: Transfer characteristics and on current (inset) of <110> strained NW n-FET for T ranging from 4K to 280K ($\Delta T=20\text{K}$). The lower graph shows the threshold voltage $V_{th}(T)$ -dependence for <110> strained Si device.

In conclusion, $20 \times 20 \text{ nm}^2$ NW array transistors with 1000 parallel wires show excellent performance with inverse subthreshold slopes close to 60 mV/dec and very large I_{on}/I_{off} ratios up to 1012. Optimum results were obtained with nanowires oriented along <110> for n-FETs and <100> for p-FETs on (100) Si.

- [1] S. Habicht, S.F. Feste, Q.-T. Zhao and S. Mantl, ESSDERC 2010, Seville, 372 (2010)
- [2] J. Chen, T. Saraya, K. Miyaji, K. Shimizu and T. Hiramoto, Jpn. Jour. Appl. Phys., 48, 011205 (2009)
- [3] S.F. Feste, J. Knoch, S. Habicht, D. Buca, Q.-T. Zhao and S. Mantl, Solid State Electron, 53, 1257 (2009)
- [4] R.A. Minamisawa, S. Habicht, D. Buca, R. Carius, S. Trellenkamp, K.K. Bourdelle and S.Mantl, J. Appl. Phys., 108, 124908 (2010).
- [5] M. Chu, T. Nishida, X. Lv, N. Mohta and S. E. Thompson, J. Appl. Phys., 103, 113704 (2008)

Self-organized MBE growth of Ge quantum dots directed by extreme ultraviolet interference lithography

S. Danylyuk¹, G. Mussler², S. Brose¹, L. Juschkin^{1*}, G. Panaitov², D. Grützmacher², P. Loosen¹

¹ Chair for Technology of Optical Systems, RWTH Aachen University

² PGI-9 : Semiconductor Nanoelectronics, Forschungszentrum Jülich

*on leave at University College Dublin, Ireland

Quantum dot arrays (QDs) based on Si/Ge heterosystem are highly interesting objects with unique electronic and optical properties. Creating a dense and well-ordered array of these structures allows the realisation of a novel type of solid matter - “artificial crystals” - with energy band distributions not existing in nature. In this work we report about realisation of ordered Ge quantum dot arrays fabricated by means of extreme ultraviolet interference lithography (XIL) and molecular-beam epitaxy (MBE).

Quantum dots are quasi-zero dimensional semiconductor structures on the nanometer scale, which provide a confining potential for charge carriers in all three dimensions. Hence, these artificial atoms have a completely different energy structure compared to bulk material or other semiconductor nanostructures, such as quantum wells or quantum wires. Therefore, novel device applications based on QDs in the field of electronics, optoelectronics, spintronics or even quantum computation are envisioned. Currently, the main method to create large arrays of QD is self-organised growth in Stranski Krastanov mode. Main drawbacks of the self-organised QDs are the strong variation in shape and size as well as the random position of the QDs. For device applications, it is mandatory to control exactly the position of the Ge QDs in order to address individual QDs. In addition, the uniformity of the QDs regarding size and shape is of utter importance to ensure the identical energy structure of all QDs.

One of the most promising methods to create an ordered QD arrays with high resolution is the self-organisation of QDs on substrates, prepatterned by the XUV interference lithography. It is currently the only technique that can realistically achieve the sub-20 nm resolution for large and dense arrays of nanostructures. XIL relies upon soft x-ray / extreme ultraviolet light at wavelengths of 10 – 15 nm, so that highly accurate patterns with a spatial resolution of typically 5 – 10 nm are obtained. In addition, interaction of light with matter maximises in this spectral range (absorption lengths lie in the range of 100 nm), which ensures photochemical sensitivity, very efficient use of photons and independence of substrate material. Further benefits over traditional

electron-beam lithography include no charging effect, negligible proximity effect and moderate to high throughput. This method is being used already with synchrotron radiation sources with great success. In this work we demonstrate the possibility to perform the patterning using a laboratory EUV source.

The high-power laboratory sources of short-wavelength radiation based on gas discharge pinch plasmas are actively developed in Aachen for more than 10 years. These thermal sources are not inherently coherent, however, they can be tuned to radiate in a limited bandwidth from a rather small (down to 250 μm) region (pinch), thus providing a required partial coherence. We have shown recently that one can obtain a highly intensive radiation around 11 nm efficiently filtered to $\Delta\lambda/\lambda \sim 3\text{-}4\%$ [1], which is a requirement for achromatic Talbot interference [2].

In this approach a so-called Talbot self-imaging is utilised. Classically, a grating, or any structure with periodic transmission profile will form self-images in certain near-field planes after the grating when illuminated by monochromatic light. Recently it was shown that allowing the light not to be perfectly monochromatic, i.e. with a bandwidth of the order of few percent, one can obtain not only direct images of the grating, but also an image with a half of the period of the grating. Both, monochromatic and achromatic Talbot effects can be used for patterning with XUV light. The benefits, in comparison with other techniques, include a mask error correction, large depth of focus and a relatively simple optical setup. A frequency doubling effect with achromatic Talbot images allows to reduce requirements of the mask fabrication, e.g., to obtain a 20 nm period on a wafer, only a 40 nm period transmission mask is necessary.

In addition, the required spatial coherence length reduces with the period of structures, which makes the Talbot approach suitable for sub-20 nm periods. On the other hand, the contrast of achromatic images does not exceed a quarter of initial contrast of the mask and depends on the spatial coherence of the source. As a result, successful sub-20 nm structuring in this regime require rigorous simulation of Talbot patterns to determine an optimum coherence length

and a suitable transmission mask design. Another challenge is caused by the fact that for short-wavelength radiation and sub-100 nm periods, the distance from the grating to a Talbot plane is between 1 and 100 micrometer. This means that illuminated wafers needs to be in the proximity of the mask, and the distance should be controlled with sub-micrometer precision.

Taking into account these considerations, we have realised a laboratory-scale setup for XUV interference patterning with transmission masks for structuring on a sub-100 nm scale. The system is designed to accept up to 2" substrates with single illumination fields exceeding 100 $\mu\text{m} \times 100 \mu\text{m}$. Three capacitive sensors are used to control not only the distance between mask and wafers, but also a relative tilt. Double polished Si wafers with a total thickness variation (TTV) below 1 μm are used to guarantee sub-1 μm distance precision in all illuminated area. A special type of transmission mask was developed together with FZJ to provide us necessary flexibility with wavelength choice. Our masks use niobium membranes that are known for their mechanical stability [3] and have a high transmission at 11 nm. The transmission grating design is shown in Fig. 5. As an absorbing material, chromium or nickel is used, which allow us not only to match the efficiency of standard 13.5 nm SiNx-based gratings but also to exceed it in a wavelength range between 8 and 15 nm. We have achieved membranes with areas up to 1000 $\mu\text{m} \times 1000 \mu\text{m}$ and with sub-100 nm e-beam patterned structures. The masks demonstrate excellent contrast (>1:20) and in addition also act as a spectral filter, effectively blocking all radiation above 15 nm.

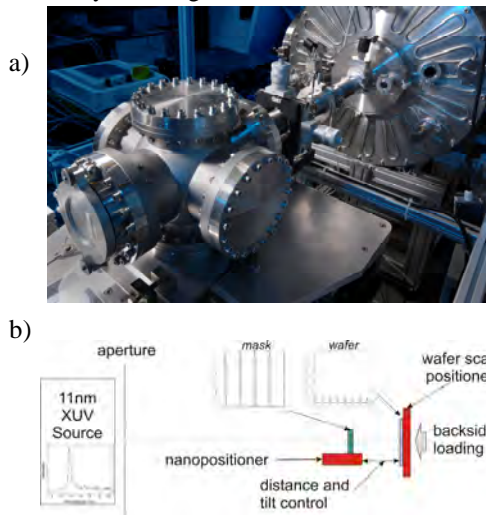


FIG. 1: XUV-IL illumination set-up realised at TOS with a wafer loading chamber and a source behind (a). The principal scheme of the XUV-IL nano-patterning system (b).

High-resolution e-beam resists, such as HSQ, PMMA and ZEP are used with typical exposure times between 2 and 10 min, depending on thickness and type of the resist.

To demonstrate the feasibility of the achromatic Talbot interference method, we have modelled and manufactured a mask with a series of line and space

(L/S) patterns with periods down to 200 nm. The results of the exposure of the positive ZEP520A resists are shown in Fig. 2.

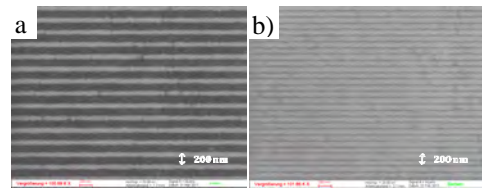


FIG. 2: SEM images of lines/space pattern produced by proximity printing (a) and achromatic Talbot interference lithography (b) with the same mask. The period reduction is demonstrated.

The predicted frequency doubling is clearly visible, allowing us to create patterns with 100 nm period with 200 nm period on the mask.

Subsequently, the same mask has also allowed us to create a patterns with a crossed double exposure of lines/spaces array. By a careful optimization of the exposure, development and etching parameters, we have obtained high-quality templated Si substrates. Using these templated substrates, we succeeded in growing Ge QD arrays with a good degree of ordering over a large spatial extend (300 $\mu\text{m} \times 300 \mu\text{m}$), as shown in Fig. 3. In this case the hole diameter was 100 nm, that led to nucleation of 4 Ge QDs in each patterned hole.

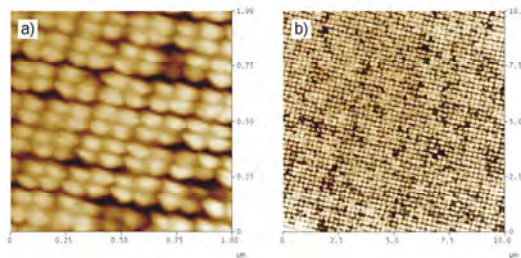


FIG. 3: AFM images of a Ge QD array realized on a Si substrate, templated by means of XIL at RWTH-TOS. The hole period amounts to 200 nm. Each hole is filled with 4 Ge QDs that nucleate at the corners.

Further work on optimisation of the quality of the masks, improving of vibration isolation and quality of the pattern transfer should allow to decrease the periodicity of the patterns to the target size of 20 nm, enabling lateral coupling of QDs.

[1] K. Bergmann, S. V. Danylyuk, L. Juschkun, Optimization of a gas discharge plasma source for extreme ultraviolet interference lithography at a wavelength of 11 nm, J. Appl. Phys. 106, 073309 (2009)

[2] H. H. Solak, Y. Ekinici, Achromatic spatial frequency multiplication: A method for production of nanometer-scale periodic structures, J. Vac. Sci. Technol. B 23 (6), 2705 (2005).

[3] S.V. Danylyuk, R. Ott, G. Panaitov, G. Pickartz, E. Hollmann, S.A. Vitusevich, A.E. Belyaev and N. Klein, Aluminium nitride-niobium multilayers and free-standing structures for MEMS, Thin Solid Films 515, 489 (2006)

Strained Silicon Nanowire Array and Si/SiGe Heterostructure Tunneling Field-Effect Transistors

S. Richter¹, M. Schmidt¹, L. Knoll¹, S. Lenk¹, J.-M. Hartmann², A. Schäfer¹, R. Luptak¹, K. K. Bourdelle³, Q. T. Zhao¹, S. Manti¹

¹ PGI-9: Semiconductor Nanoelectronics (PGI 9-IT), Forschungszentrum Jülich

² CEA-LETI, MINATEC, 17 rue des Martyrs, 38054 Grenoble, France

³ SOITEC, Parc Technologique des Fontaines, 38190 Bernin, France

TFETs with strained Si nanowire channels and HfO₂/TiN gate stacks were fabricated and analyzed. Inverse subthreshold slopes down to 76 mV/dec were observed. Temperature dependence of the subthreshold slope was investigated and compared to MOSFET devices. In addition, heterostructure TFETs with SiGe source and Si channel/drain were fabricated with a stepped gate structure. These devices exhibit $S = 65$ mV/dec with an applied back gate voltage and decreased ambipolar behavior.

Tunneling field-effect transistors (TFETs) are promising devices to overcome the switching slope limitation of conventional MOSFETs of 60mV/dec. Devices with a steep switching slope are necessary in order to lower supply voltage in integrated circuits and thus lower the power consumption. In TFET devices excellent electrostatic control is crucial in order to increase the band-to-band tunneling current. As illustrated in the SEM image in Fig. 1 (a), the fabricated TFET devices feature an

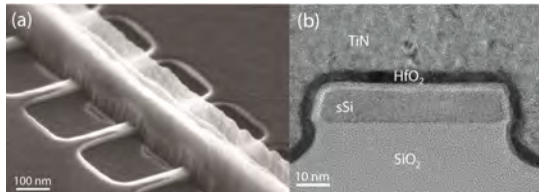


FIG. 1: (a) Scanning electron micrograph of nanowire array with a 100 nm gate length TiN metal gate. (b) Cross-sectional transmission electron micrograph of a single nanowire with HfO₂/TiN gate stack.

array of trigated nanowires with a HfO₂ high- κ gate dielectric in combination with a TiN metal gate, as shown in the cross-section TEM image of Fig. 1 (b). The devices were fabricated on strained silicon on insulator (SSOI) substrates using a gate first process [1]. Self aligned ion implantation was used in order to form the n-doped source and the p-doped drain region. Fig. 2 shows the transfer characteristics of a p-channel TFET with 100 nm gate length. The p-channel transfer-characteristics are measured with a negative voltage applied to the p-doped drain region and a negative voltage applied to the gate, while the n-doped region is grounded as source. The transfer characteristics exhibit point slopes down to 76 mV/dec and an average slope of 97 mV/dec over four orders of magnitude of I_D at $V_{DS} = -0.3$ V. The

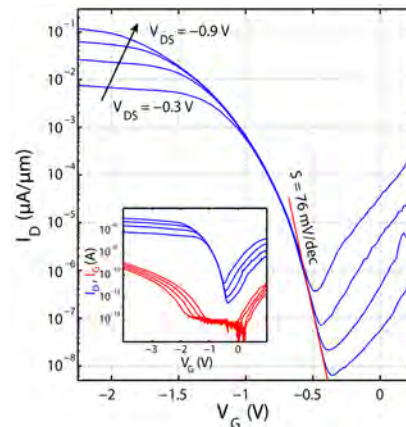


FIG. 2: Transfer characteristic of a strained Si nanowire array TFET with 100 nm gate length. The inset shows both, drain current I_D and gate leakage current I_G vs. gate voltage V_G . Inset in Fig. 2 shows the gate leakage current I_G which is at least two orders of magnitude lower than I_D , showing that the best obtained slopes are not caused by gate leakage effects. Fig. 3 illustrates the temperature dependence of the transfer characteristics between 100 K and 350 K. The inset

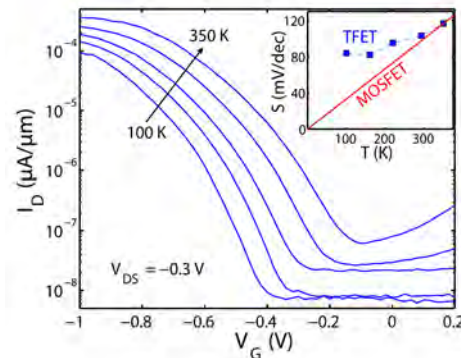


FIG. 3: Transfer characteristic of nanowire array TFET measured between 100 K and 350 K. The inset shows the measured temperature dependence of S for the TFET and the linear $S(T)$ for a MOSFET.

depicts the inverse subthreshold slope in dependence of the temperature. In comparison with the theoretically expected linear dependence of $S(T)$ for a MOSFET the change of S with temperature is much smaller for a TFET.

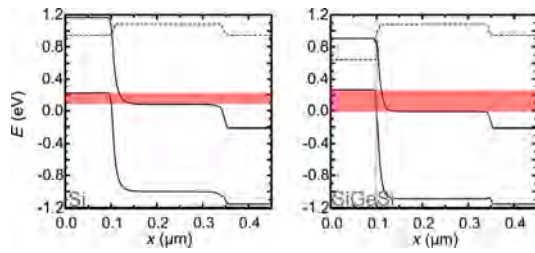


FIG. 4: Comparison of the simulated band structure of an all-Si TFET (left) and $\text{Si}_{0.5}\text{Ge}_{0.5}/\text{Si}$ heterostructure TFET (right). The energy regions where BTBT may occur is colored.

The band structure of TFET devices can be optimized for band-to-band tunneling (BTBT) by employing heterostructures [2].

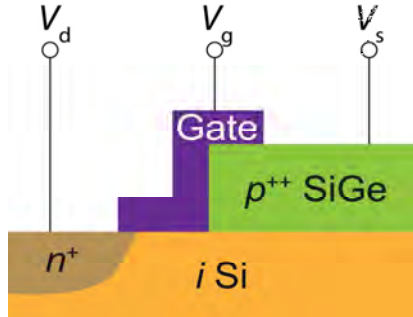


FIG. 5: Scheme of a step-like SiGe/Si heterostructure TFET.

Fig. 4 shows the simulated p-i-n band structure of an all-Si TFET (left) and a TFET with $\text{Si}_{0.5}\text{Ge}_{0.5}$ source and Si channel/drain (right) with an applied gate voltage $V_{gs} = 0.5$ V and drain voltage $V_{ds} = 0.1$ V. The energy range where band-to-band tunneling is enabled is larger for the SiGe/Si heterostructure and the tunneling distance is decreased. These simulations indicate that the BTBT current should be higher in a TFET with $\text{Si}_{1-x}\text{Ge}_x$ source, due to decreased bandgap E_g and smaller effective mass m^* of $\text{Si}_{1-x}\text{Ge}_x$, with increasing Ge concentration x . A schematic layout of such a heterostructure device with p-SiGe source, an intrinsic Si channel and an n-implanted Si drain is shown in Fig. 5. We fabricated TFETs on fully strained 12 nm $\text{Si}_{0.5}\text{Ge}_{0.5}$ layers, which were grown on thinned-down SOI substrates (20 nm Si/145 nm buried oxide) at 550 °C by reduced pressure chemical vapor deposition (RP-CVD). The $\text{Si}_{0.5}\text{Ge}_{0.5}$ layer was in-situ doped during growth with B which resulted in a homogeneous impurity concentration of about $N_A = 2 \times 10^{20} \text{ cm}^{-3}$ of this layer. It was subsequently capped with 10 nm of Si to prevent large-area oxidation of the SiGe. After thinning down the Si cap mesa structures were etched, followed by the removal of SiGe on the drain side by highly selective wet etching. The structure was cleaned by subsequent H_2SO_4 and HCl, immediately followed by conformal 2.6 nm HfO_2 atomic layer deposition (ALD) and ~ 80 nm TiN atomic vapor deposition (AVD). The gate was patterned by standard optical lithography and reactive ion etching (RIE). The gate length amounts to 25 μm . The drain side was implanted with 3 keV

As^+ ions at a dose of $1 \times 10^{15} \text{ cm}^{-2}$. The activation was carried out at a low temperature of 650 °C for 1 min, to avoid B and Ge interdiffusion into the SOI layer, which would have degraded the junction significantly. After passivation of the structure by plasma-enhanced chemical vapor deposition (PE-CVD) of SiO_2 , the devices were metalized with Cr/Al. For further improvement of the gate oxide quality, a forming gas anneal (FGA) was carried out at 450 °C for 10 min under N_2/H_2 atmosphere, to saturate the interfacial Si/ $\text{SiO}_x/\text{HfO}_2$ dangling bonds.

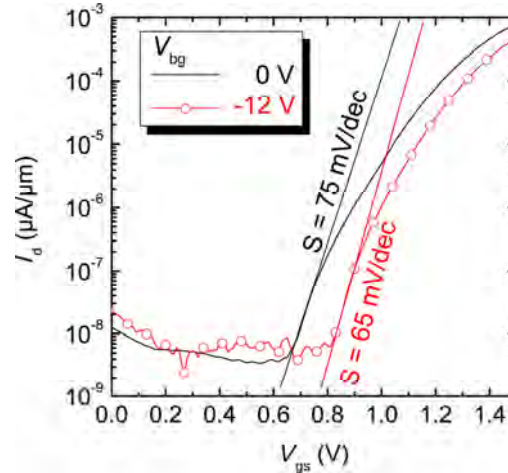


FIG. 6: Transfer characteristics of a SiGe source/Si channel/Si drain heterostructure TFET for applied $V_{ds} = 0.5$ V and $V_{bg} = -12$ V.

For electrical characterization, the gate voltage was swept from $V_{gs} = 0$ to 1.5 V. The devices showed a sub-threshold point slope of $S = 75$ mV/dec, which could be improved to 65 mV/dec by applying a backgate voltage of $V_{bg} = -12$ V. From C-V measurements an EOT of ~ 1 nm was extracted. The key to understand the improvement of S and I_{on}/I_{off} lies in the understanding of the impact of the device parameters on these characteristics. A steeper tunneling junction, provided by the in-situ doped source, combined with a good electrostatic control, achieved by use of a high- k gate stack, positively impacts the device performance. However, the high resistance on the drain side limits the on-current. In future, the S/D resistance will be reduced by silicidation.

This work was financially supported by the FP7 EU STREP project STEEPER.

[1] S. Richter, M. Schmidt, S. Trellenkamp, R. Luptak, K. K. Bourdelle, Q. T. Zhao, S. Mantl, EDL-2012-02-0248, unpublished (2012).

[2] M. Schmidt, L. Knoll, S. Richter, A. Schäfer, J.-M. Hartmann, Q. T. Zhao, S. Mantl; Proceedings of the 13th International Conference on Ultimate Integration on Silicon 2012, p.237-240 (2012).

Advances towards future III-nitride based THz OEICs in the UV range

M. Mikulics¹, H. Hardtdegen¹, A. Winden¹, R. Adam¹, D. Gregušová², P. Kordoš²,
M. Marso³, R. Sobolewski⁴, H. Lüth¹, D. Grützmacher¹

¹ Peter Grünberg Institute 9, Forschungszentrum Jülich, 52425 Jülich

² Slovak Academy of Science, 84101 Bratislava, Slovakia

³ Université du Luxembourg, 1359 Luxembourg

⁴ University of Rochester, Rochester NY14627-0231, USA

A group III-nitride based MSM photodetector integrated with a MESFET in an OEIC circuit is presented exhibiting an exceptionally high 3 dB-bandwidth of 410 GHz. Advances towards circuit improvement by the future implementation of a gate recessed AlGaIn/GaN HEMT device are reported. μ -PL is used directly on the processed device to optimize processing with respect to processing related strain and damage effects. It is demonstrated that μ -PL allows insight into device and material optimization which are the strategic key to improved future III-nitride based UV-optoelectronic integrated circuits (OEIC) operated up to the THz range.

THz sources are of utmost importance for spectroscopy since they can be employed for material production control, the detection of safety relevant chemicals as well as in the analysis of food and the environment. In the past it has been demonstrated that semiconductor materials and especially group III group V alloys are very well suited for the generation of THz radiation especially due to their tunability in the low THz range. The sources can be integrated into sophisticated circuits which allow the amplification of the signals. Further improvements with respect to the signal to noise ratio would increase the efficiency of the sources and are in the focus of this report. The starting point for our investigations were our recent achievements in the field of UV-sensitive and visible-light-blind

metal-semiconductor-metal photodetectors (MSM PDs) and their integration with MESFET structures [1].

Figure 1 presents both devices which form an optoelectronic integrated circuit (OEIC). The PD is excited by a train of 100-fs-wide and 360-nm-wavelength laser pulses. Its photoresponse transient is amplified by the MESFET device. The frequency response of our MSM PD yields a 3 dB-bandwidth of 410 GHz that is the highest bandwidth ever reported for a GaN-based PD (Figure 1). It should be also noted that the MSM signal amplified by the MESFET exhibits a higher amplitude than the actual input MSM PD signal of up to 150 GHz. These results show that our device is a very promising candidate for future THz operated UV optoelectronic integrated circuits.

Further improvements of the amplifier performance could be obtained by substituting the GaN MESFET layer by an optimized AlGaIn/GaN or InAlN/GaN [2] high electron mobility transistor (HEMT), which is known reduce the noise and is also faster leading to a decrease of the amplified signal's FWHM. The usability of the circuit in this material system at high powers and its thermal and radiative robustness makes it attractive for future satellite and wireless communication at high data transfer rates. To this end the performance of the AlGaIn/GaN HEMT calls for improvement with respect to the threshold voltage towards a normally off device

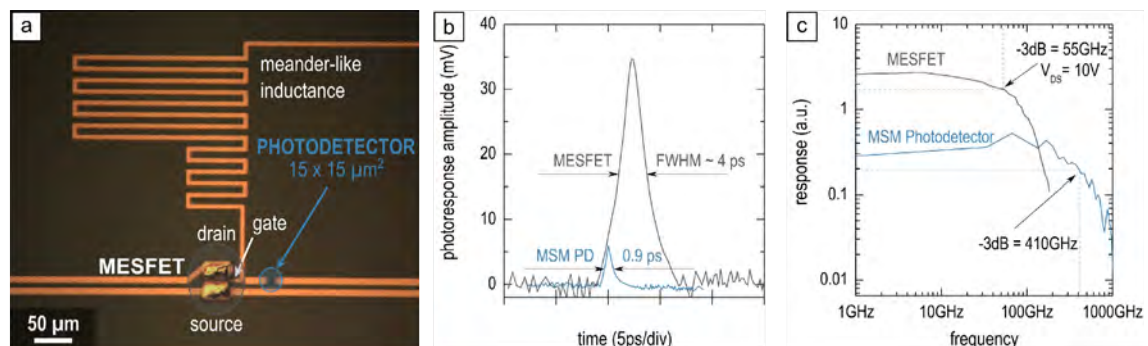


FIG. 1: (a) OEIC circuit containing an MSM PD integrated with MESFET in a CPS line layout fabricated on GaN/AlN/SiC. The meander structure that biases the gate acts as an inductor to block the high-frequency signal from the PD. (b) Time-resolved photoresponse transients of just the MSM PD and the amplified signal at the drain side of the MESFET. (c) Optoelectronic frequency response of the MSM PD (bottom trace) and of our entire OEIC (top trace). (Fast Fourier transform of the time domain measurements of (b)).

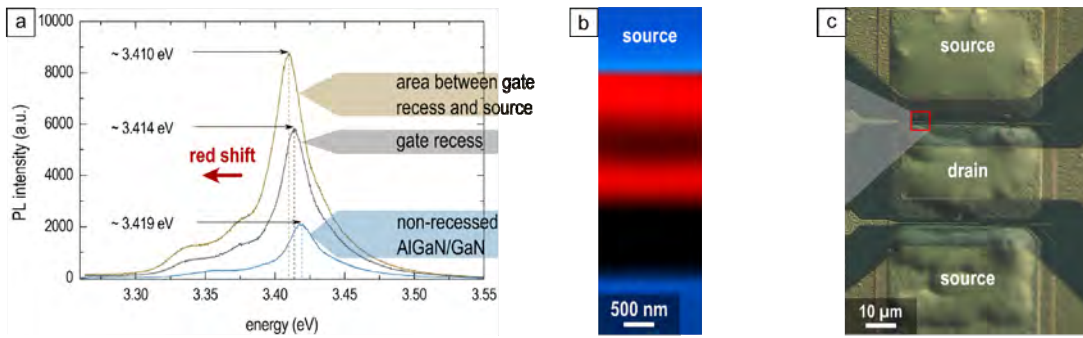


FIG. 2: (a) Photoluminescence spectra of three regions of a 6 nm recessed AlGaIn/GaN heterostructure. (b) PL intensity mapping across the recessed gate at an emission wavelength of 363 nm. (c) Micrograph of a transistor. It becomes clear that strain and defects are non-uniformly distributed.

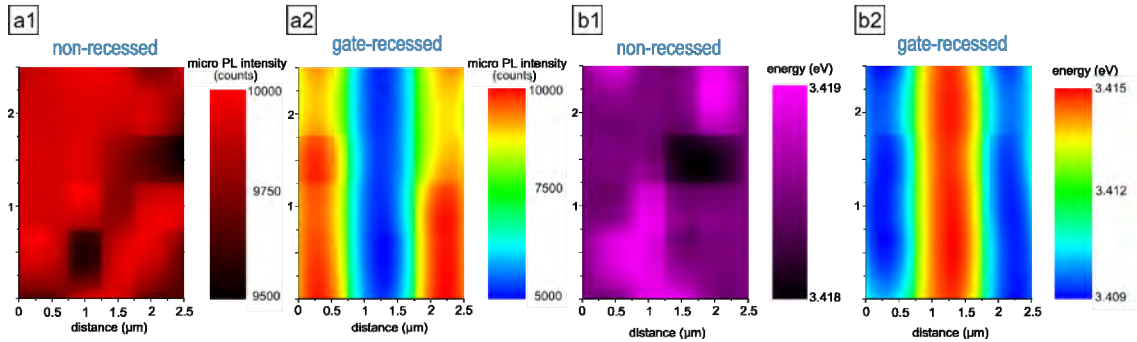


FIG. 3: Mapping of (a) micro PL intensity and (b) band edge PL energy for (1) a non-recessed and (2) its 6nm gate-recessed HFET counterpart.

and to the aspect ratio for improved DC and high frequency performance. Gate recessing was developed to address both topics [3] necessitating the employment of dry etching technology. This technology calls for careful etching parameter optimization to minimize surface roughening / damage and to reduce detrimental in-depth defects due to channelling. Additionally, the influence of recessing on strain in the device needs to be carefully monitored since strain distribution/relaxation will eventually affect the channel properties and therefore the device characteristics. Micro photoluminescence (μ -PL) studies are particularly suited as a powerful and non-destructive technique for the study of induced strain and damage after gate recess etching. The high lateral resolution of μ -PL studies allowed the observation of a non-uniform band edge luminescence energy – related to strain – and of the PL-intensity – related to differences in non-radiative recombination centers (defects) – in the device region [4].

The AlGaIn/GaN layer system deposited on 6H-SiC substrates was comparatively investigated for a recessed and a non-recessed device. Typical micro PL spectra of the non-recessed and < 6 nm recessed HFET structures are shown in Figure 2. The peak emission energy for non-recessed structures is recorded at a wavelength of < 362.7 nm (3.419 eV) which is in good agreement with the energy reported recently for GaN on 6H-SiC substrates [5]. A closer look at the spectra recorded of the recessed device reveals (see the inset of Fig. 2) a slight red-shift of the band edge emission (3.414 eV). It is well known

that GaN layers are not fully relaxed and exhibit residual strain. The strain depends on many device process factors and especially on the layer thickness. The energy shift $\Delta E = 5$ meV observed after 6 nm recessing corresponds to a slight decrease of the in-plane stress from about -0.9 GPa to -0.68 GPa [5]. This indicates that the thickness change of the AlGaIn barrier layer leads to a partial strain relaxation in the underlying GaN buffer layer. Due to the reduction of strain, the polarization charge should be lower in recessed structures compared to non-recessed ones. Additionally, the lateral intensity distribution of the luminescence over the device structure for the recessed device is not uniform as presented in detail also in Figure 3.

All these factors need to be taken into account to further fine tune the device performance. In future these optimized HEMTs will be integrated into the optoelectronic integrated circuit (OEIC) reported above allowing a high power operation at harsh environment conditions in the THz range.

[1] M. Mikulics et al., IEEE Photonics Technology Lett., vol. 23, no. 17, 1189 (2011).
 [2] M. Mikulics et al., Appl. Phys. Lett. 97, 173505 (2010).
 [3] Y. Pei et al., IEEE Electron Device Lett. 29, 300 (2008).
 [4] M. Mikulics et al., Phys. Status Solidi C 9, no. 3–4, 911 (2012).
 [5] D. G. Zhao et al., Appl. Phys. Lett. 83, 677 (2003)

Molecular-Beam Epitaxy of Topological Insulator Bi_2Te_3 Thin Films

G. Mussler¹, J. Kampmeier¹, J. Krumrain¹, S. Borisova¹, L. Plucinski², M. Luysberg³, D. Grützmacher¹

¹ PGI-9: Semiconductor Nanoelectronics, Forschungszentrum Jülich

² PGI-6: Electronic Properties, Forschungszentrum Jülich

³ PGI-5: Microstructure Research, Forschungszentrum Jülich

We report on molecular-beam epitaxy (MBE) of Bi_2Te_3 thin films on Si(111) substrates. At carefully optimized MBE growth parameters, atomically smooth, single-crystal Bi_2Te_3 films with large areas of single quintuple layers (QLs) on top are obtained. Angular-resolved photoelectron spectroscopy reveals a linear energy dispersion of charge carriers at the surface, evidencing topologically insulating properties of the Bi_2Te_3 epilayers. Further analyses show that in the very beginning of the growth, two different domains, in-plane rotated by 60° , are formed. After the growth of a few QLs an overlapping occurs, causing one domain to prevail.

Recently a new state of matter called the topological insulator (TI) has been theoretically predicted and experimentally observed in a number of materials, such as $\text{Bi}_{1-x}\text{Sb}_x$, Bi_2Se_3 , Sb_2Te_3 , and Bi_2Te_3 . The main feature of TIs lies in its band structure, which is depicted in figure 1a. The bulk of TIs is an insulator with conduction and valence band, separated by a band gap. The surface, however, hosts gapless states with a linear energy dispersion, in a similar way as graphene. Hence, carriers at the surface of TIs are expected to have unparalleled properties, such as extremely high mobilities and a spin-locked transport behavior. Consequently, these features may lead to new applications in the field of spintronics, or quantum computing [1].

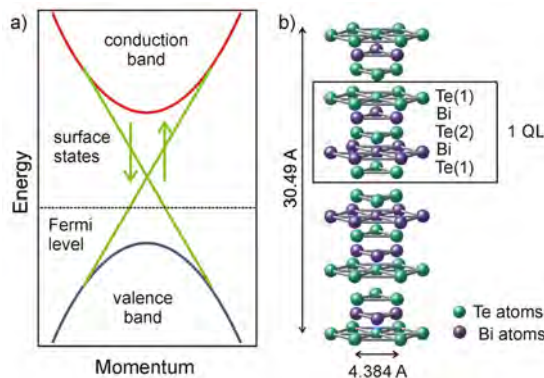


FIG. 1: a) The TI energy dispersions of bulk and surface states. b) The unit cell of Bi_2Te_3 .

The TI behavior in Bi_2Te_3 is based on the crystalline structure (Fig. 1b), which includes a sequence of five atomic layers Te(1)-Bi-Te(2)-Bi-Te(1), so called quintuple layer (QL). A unit cell consists of three

QLs, and there are only weak van der Waals bonds between the QLs.

Concerning the MBE growth of Bi_2Te_3 , very important parameters are the Bi and Te effusion cell temperatures. We have found that a Te overpressure condition is mandatory for the growth of single-crystal Bi_2Te_3 epilayers. In order to investigate the influence of the Bi and Te effusion cell temperatures on the growth rates, x-ray reflectivity (XRR) scans were performed. Figure 2a shows XRR curves of three Bi_2Te_3 layers, grown with different Te effusion cell temperatures. Same layer thickness of 31 nm is obtained for all three samples, evidencing that for Te overpressure and the used substrate temperature of 400°C , the growth rate of Bi_2Te_3 does not depend on the Te partial pressure. In contrast, fig 2b shows XRR curves of three Bi_2Te_3 epilayers grown with different Bi effusion cell temperatures. We can see that there is an increase in thickness from 15 to 55 nm for higher Bi fluxes. Hence, the growth rate is solely determined by the Bi flux. The Te overpressure condition has a consequence on the growth of Bi_2Te_3 , whereas the surface is always Te-terminated, in a similar fashion as the MBE growth of GaAs [2].

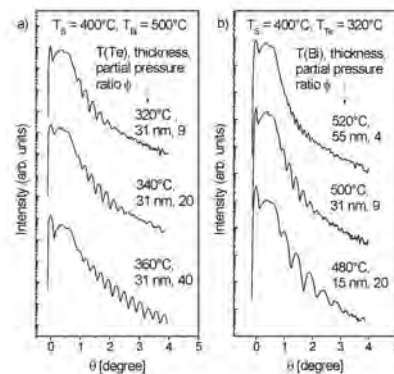


FIG. 2: XRR curves for series of Bi_2Te_3 samples grown with different Te (a) and Bi (b) effusion cell temperatures.

In order to prove the stoichiometry of the grown Bi_2Te_3 films, scanning tunneling electron microscopy (STEM) measurements were carried out. Figure 3a shows a cross-sectional image of the epilayer. The bright and dark spots show the Bi and Te atoms, respectively. The image reveals the correct order sequence of the QL (cf. figure 1b). Moreover, the data reveal that the Bi_2Te_3 epilayer is of single-

crystal nature and the out-of-plane direction is the c-axis, which was also confirmed by x-ray diffraction. Figure 3b shows a color-coded atomic force microscopy (AFM) image of the Bi_2Te_3 surface, showing three different atomically smooth plateaus, whereas one QL covers more than 75% of the surface. Figure 3c illustrates the step height analysis along the dashed line in figure 3b. The step heights are always an integer of 1 nm, which represents the height of 1 QL, evidencing the QL by QL growth mode. Figure 2d shows an ARPES scan. The Dirac cone is clearly seen, proving the linear energy dispersion at the surface of the Bi_2Te_3 layer. From the slope, a Fermi velocity $v_F = 4.28 \cdot 10^5$ m/s is determined [3], which is in agreement with theoretical calculations. Besides, the hexagonal-shaped rim is seen, which is typical of Bi_2Te_3 due to an interaction of the surface states with the bulk bands in reciprocal space.

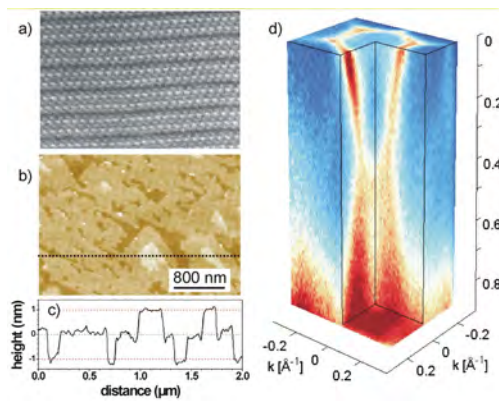


FIG. 3: a) Cross-sectional STEM image of the Bi_2Te_3 layer. The bright and dark spots are Bi and Te atoms, respectively. b) AFM image of the Bi_2Te_3 surface. c) Height profile along the dashed line in b). d) ARPES scan showing the Dirac cone.

The choice of substrate is of high importance for realizing single-crystal Bi_2Te_3 epilayers. We have used Si(111) substrates because of their hexagonal arrangement of the surface atoms, which match the hexagonal crystal structure of Bi_2Te_3 . It was found that the large lattice mismatch ($\sim 14\%$) is not crucial for the growth of the Bi_2Te_3 epilayers, as the epilayers are only weakly bonded to the substrates via van der Waals forces. However, the substrate determines the in-plane crystal orientation of the Bi_2Te_3 epilayers. Figure 4a shows a pole figure measurement around the (105) reflection of the Bi_2Te_3 epilayer and around the (311) and (221) reflections of the Si substrate. Evidently, the peaks of the Bi_2Te_3 epilayer have same angular orientation of the Si substrate peaks, indicating the same in-plane orientation of substrate and epilayer. Despite the three-fold symmetry of this reflection, six peaks of the (105) reflection are seen. This can be explained by the formation of domains, in-plane rotated by 60° , in the early stage of growth. In fact, the Bi_2Te_3 crystal may nucleate on the Si(111) substrate in two different orientations, as depicted in figure 4b. Here crystal 1 and 2 cannot be transformed into each other by a translation, but a 60° rotation is necessary. Consequently, when these

crystalline domains coalesce, grain boundary defects are formed. An example of such domain boundary is given in the STEM image of Fig. 4c, where a Fourier-filtered image shows the contributions of two reflections belonging to two different domains. Domain II (green), which extends over about 60 nm, is encapsulated by domain I (red). It has to be noticed that the presence of two domains is found by STEM only within the first 5-6 monolayers. At a later stage, when the growth mode is QL by QL, only one domain dominates. Fig. 4d displays the domain wall at right side of domain II in a higher resolution image. The vertical wall reveals small facets.

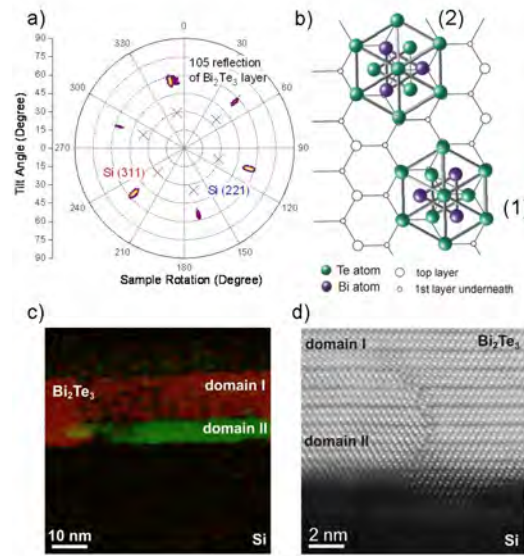


FIG. 4: a) Pole figure scans of the Bi_2Te_3 epilayer and the Si substrate. b) Sketch of the two different Bi_2Te_3 crystals that can nucleate on the Si(111) surface. c) Fourier-filtered STEM image shows the contributions of two reflections, which belong to two different domains. d) Magnification of the domain boundary.

Future works will be devoted on transport measurements. Preliminary results show a large contribution of the bulk electrons, hiding the surface electronic transport. The possible origin of the high bulk electron concentration might be attributed to the observed domain boundary defects. Hence special emphasis will be put on reducing the amount of bulk carriers, for example by doping the TI epilayers. The goal is to minimize the impact of bulk carriers, and obtain a dominant transport of the surface carriers with the expected high mobilities and spin-resolved transport features. We can however conclude that the MBE-grown TI materials of high crystalline quality may be harnessed for device applications, as well as for very interesting fundamental researches.

- [1] J. E. Moore, Nature 464, 194 (2010).
- [2] J. Krumrain, G. Mussler, S. Borisova, T. Stoica, L. Plucinski, C. M. Schneider, D. Grützmacher, J. Crystal Growth 324, 115 (2011).
- [3] L. Plucinski, G. Mussler, J. Krumrain, A. Herdt, S. Suga, D. Grützmacher, C.M. Schneider, Appl. Phys. Lett. 98, 222503 (2011).

Selected Publications

1. S. Estevez Hernandez; M. Akabori; K. Sladek K.; Ch. Volk, S. Alagha, H. Hardtdegen, M.G. Pala, N. Demarina, D. Grützmacher, Th. Schäpers:
Spin-orbit coupling and phase coherence in InAs nanowires
Physical Review B **82**, 235303 (2010) DOI: 10.1103/PhysRevB.82.235303
2. Q.T. Zhao, J-M. Hartmann, S. Mantl
An Improved Si Tunnel Field Effect Transistor With a Buried Strained Si_{1-x}Ge_x Source
IEEE Electron Device Letters **32**, 1480 (2011) DOI: 10.1109/LED.2011.2163696
3. Ch. Blömers, M. Lepsa, M. Luysberg, D. Grützmacher, H. Lüth, Th. Schäpers,
Electronic Phase Coherence in InAs Nanowires
Nano Letters **11**, 3550 (2011) DOI: 10.1021/nl201102a
4. M. Mikulics, P. Kordos, D. Gregusova, R. Adam, M. Kocan, S. Wu, J. Zhang, R. Sobolewski, D. Grützmacher, M. Marso
Monolithic Integration of Ultrafast Photodetector and MESFET in the GaN Material System
IEEE Photonics Technology Letters **23**, 1189 (2011) DOI: 10.1109/LPT.2011.2157816
5. L. Plucinski, G. Mussler, J. Krumrain, A. Herdt, S. Suga, D. Grützmacher, C.M. Schneider
Robust surface electronic properties of topological insulators: Bi₂Te₃ films grown by molecular beam epitaxy
Applied Physics Letters **98**, 222503 (2011) DOI: 10.1063/1.3595309
6. N.V. Demarina; D.A. Grützmacher
Electrical properties of rolled-up p-type Si/SiGe heterostructures
Applied Physics Letters **98**, 192109 (2011) DOI: 10.1063/1.3584869
7. N.P. Stepina, E.S. Koptev, A.V. Dvurechenskii, A.I. Nikiforov, J. Gerharz, J. Moers, D. Grützmacher,
Giant mesoscopic photoconductance fluctuations in Ge/Si quantum dot system
Applied Physics Letters **98**, 142101 (2011) DOI: 10.1063/1.3574022
8. Ch. Blömers, J.G. Lu, L. Huang; C. Witte, D. Grützmacher, H. Lüth, Th. Schäpers
Electronic Transport with Dielectric Confinement in Degenerate InN Nanowires
Nano Letters **12**; 2768 (2012) DOI: 10.1021/nl204500r
9. W.Yu; B. Zhang; Q.T. Zhao, D. Buca, J.-M. Hartmann, R. Luptak, G. Mussler, A. Fox, K.K. Bourdelle, X. Wang, S. Mantl
Hole Mobilities of Si/Si_{0.5}Ge_{0.5} Quantum-Well Transistor on SOI and Strained SOI
IEEE Electron Device Letters **33**, 758 (2012) DOI: 10.1109/LED.2012.2190035
10. S. Wirths, M. Mikulics, P. Heintzmann, A. Winden, K. Weis, Ch. Volk, K. Sladek, N. Demarina, H. Hardtdegen, D. Grützmacher, Th. Schäpers
Preparation of Ohmic contacts to GaAs/AlGaAs-core/shell-nanowires
Applied Physics Letters **100**, 042103 (2012) DOI: 10.1063/1.3678639

Indicators

Quantitative Numbers

	2009	2010	2011
Peer-Reviewed Publications	58	43	51
Graduations			
Master/Diploma	9	5	9
Dissertation	4	2	5
Habilitation	1	0	0

Honours

Ehrendoktorwürde	Prof. Dr. Hans Lüth	University Mulhouse
Ernennung zu APL Professor	Thomas Schäpers	RWTH
Jülicher Exzellenzpreis 2010	Sebastian Feste / Prof. Mantl	FZJ
Best paper award ULIS 2009	Sebastian Feste / Prof. Mantl	ULIS

Offers

2009	Thomas Schäpers	apl. Prof., RWTH Aachen
2011	Thomas Schäpers	interim professorship, RWTH Aachen

Selected Third Party Projects

1. GaAs und GaN basierte Quantenpunkt-Halbleiteremitter und optimierte Nachweiselektroniken für Systemuntersuchungen zu Quantenkryptographie-Übertragungsprotokollen – QPENS
Prof. Grützmaker
BMBF
01.07.2008 – 31.12.2011
2. DECISIF
Prof. Mantl
BMBF/VDI
01.08.2008 – 31.07.2011
3. STEEPER
Prof. Mantl
EU
01.06.2010 – 31.05.2013
4. KZWEI
Prof. Mantl
AMD
5. Coherent spin transport and spin manipulation III-V semiconductors
Prof. Schäpers
DFG Sch835/6-2
01.07.2011 – 30.06.2014

V. Major Facilities and Scientific-Technical Infrastructure

Helmholtz Nanoelectronic Facility

Ernst Ruska-Centre

Jülich Centre for Neutron Science

Jülich Synchrotron Radiation Laboratory

Scientific Infrastructure of the PGI

Helmholtz Nanoelectronic Facility (HNF)

The Helmholtz Nanoelectronic Facility is proposed to combine advanced patterning and characterization methods for nanoelectronic technologies. HNF will be operated as a typical Helmholtz user facility within the Helmholtz Programme Fundamentals for Future Information Technology open to academic and industrial partners. It will be a unique facility in Germany with its combination of technologies, processes and experts over a broad range of materials for nanoelectronic research and technologies.

Timeline:

Building closed	Aug. 2012
Cleanroom/technical installations	Jun. 2012 – Dez. 2012
Final Acceptance test	Feb. 2013
Hook up	Mar. 2013 – Jun. 2013

Status:

The facade of the cleanroom wing was closed according to the schedule. The technical installations have begun and will last until end of the year.

View of HNF:



Cleanroom area and technical installations for air condition

The HNF consists of a front building and a clean-room wing. The front building is visible in the foreground covered with white concrete slabs. It includes media access to the grid of Forschungszentrum Jülich and the offices of the operating teams.

The clean room wing is seen in the background. Its facade consists of gray fins.



Getting access

Access is proposal driven and equivalent to internationally accepted rules. The HNF Office manages the access and the efficient operation of the devices, instruments and technologies available within HNF. The office is the primary contact for users regarding scientific and technological questions. It organizes the proposal procedure, including publishing calls, acceptance of scientific proposals, and the assessment of scientific and technical feasibility. A technology expert commission assesses the proposals and decides how to implement the proposals or not.

For more information, see www.hnf.fz-juelich.de

Available Technology

Technology	HNF Equipment
Deposition	MBE- Molecular Beam Epitaxy MOMBE – Metal Organic Molecular Beam Epitaxy MOCVD- Metal Organic Chemical Vapour Deposition ALD- Atomic Layer Deposition CVD & PVD Laser ablation EBID-electron beam induced Deposition (JARA-FIT) Nano-Cluster for in situ deposition of different materials in combination with in situ structuring and modification
Lithography	Optical lithography Large area/high resolution electron beam writing Nanoimprint XUV-lithography (JARA-FIT)
Pattern transfer	FIB - Focused Ion Beam RIE - Reactive Ion Etching IBE/Sputtering Wet etching
Fabrication	Ion Implanter RTA - Rapid Thermal Annealing LP/PECVD – Low Pressure/Plasma Enhanced CVD Annealing and Oxidation Wafer Bonding
Analysis	HTEM/ High resolution transmission electron spectroscopy STM- Scanning Tunnelling Microscopy/Low Temperature AFM- Atomic Force Microscopy SEM Magnetic Transport Layer characterization (LEEM/PEEM, ESCA, SIMS, etc.) Ellipsiometry Particle Scattering Methods Spectroscopy (RAMAN, FS Spectroscopy, etc.) Device Characterization (HF-Characterization)
Simulation	CAD; Finite element methods, ANSYS, etc.; Ab initio calculation, Many Body and Transport calculations
General	Wafer Cleaner (automatic standard wafer cleaning 200/300mm) Wafer Scriber Bonder Dicing Saws CMP

Nano-epitaxy laboratory (Nano-Cluster)

The nano-epitaxy laboratory of HNF consists of a new kind of epitaxy cluster for future applications with the highest requirements. The complex cluster units comprise different deposition procedures (MBE), combined with procedures for pre-structuring and a chamber for surface and interface analysis. The system is designed to be modular and flexible. The goal is to enhance the material basis to flexibly respond to scientific progress and to integrate complex structures and systems in current research. Our approach is clearly different to existing clusters in Europe, Japan or the USA (Motorola concept), which have been designed for the integration of classical III/V semiconductor (GaAs-based) and germanium technology into the standard CMOS technology, performing the next step of the IRTS Roadmap. The approach will use templated self-assembly for the design of new nanostructures as the basis of new concepts for nanoelectronic devices.

The cluster will integrate a III-V(As) MBE-chamber, a III-V (Sb) MBE-chamber, an ALD-system, a Metal MBE-System, a PCM-MBE-System, a sputter system for Oxides, a sputter system for magnetic materials, an Metal Oxide MBE-Chamber, and two chamber for surface and interface analysis.

The cluster system is open to external equipment. External users are offered the opportunity to connect their own equipment to the cluster for the duration of the project or in addition to other users or projects.

Ernst Ruska-Centre (ER-C)

Ernst Ruska-Centre
for Microscopy
and Spectroscopy
with Electrons

ER-C

The mission of the ER-C is defined by three topic areas: (i) the development of advanced transmission electron microscopy methods for condensed matter research, (ii) the application of these techniques to topical issues in

solid state research and (iii) making instrumental resources and expertise available to external users from academia and industry from home and abroad. The ER-C presently operates three aberration corrected transmission electron microscopes, four standard instruments and equipment for the fabrication of electron transparent specimens. Access to ER-C resources is granted to microscopists whose research proposals have been positively evaluated by an external committee appointed by the Germany Research Foundation (DFG). The ER-C is both a frontier research platform and a user facility that is open to external microscopists and provides valuable guidance to visiting scientists.

A unique next generation transmission electron microscope, referred to as the PICO, was inaugurated on 29 February 2012. This instrument allows further advances to the physical limits of electron optics and is one of two electron microscopes of this type worldwide capable of correcting chromatic aberration. PICO enables atomic structures to be imaged with a spatial resolution of 50 pm combined with electron energy loss spectroscopy measurements at an energy resolution of 100 meV. The improved spatial resolution also increases the precision of measuring atomic distances from 5 pm to merely 1 pm, allowing measurements of local lattice distortions in the vicinity of lattice imperfections or the polarisation of solids on the atomic scale. PICO also permits chemically sensitive energy filtered electron microscopy (EFTEM) analysis at atomic resolution.

The ER-C has considerably extended the limits of electron optics by developing a wide bunch of quantitative methods for atomic resolution electron microscopy during the past few years. To fully exploit the capabilities of the PICO microscope, several fundamental methodological problems have been addressed by ER-C scientists: (1) the development of advanced strategies for aberration measurement in scanning transmission electron microscopy, (2) the precise determination of the information limit of ultra-high resolution transmission electron microscopes and the development of techniques for the measurement and control of instrumental transfer properties sufficient for achieving 50 pm resolution, (3) the development of reconstruction algorithms for the determination of atomic crystal potentials from experimentally measured wave functions, (4) advances in electron energy-loss spectroscopy on the atomic scale with sub-electronvolt resolution for local spectrometry of the chemical and electronic structure of heterointerfaces, lattice defects and nanomaterials, and (5) developing 3D electron tomographic reconstruction towards atomic resolution dimensions. Patents were granted in 2011 (European Patent Nos. 2102886 and 205236) for developments in the field of electron optics which have been carried out in close cooperation with the manufacturers FEI Company (Eindhoven) and CEOS GmbH (Heidelberg). A major methodological breakthrough has been achieved in the reconstruction of the projected crystal potential from the electron exit plane wavefunction (Ultramicroscopy 110 (2010) 517).



Ernst Ruska-Centre (ER-C)

For the operation of the PICO microscope an advanced new laboratory annexe to the ER-C being characterised by virtually vibration and stray field free conditions was put up during the past four years with a total sum of about five million Euros having been invested. This improved infrastructure facilitates the position of the ER-C as a leading centre in advanced electron microscopy.

The commissioning of a Titan “HOLO” microscope in 2012 – equipped with a double biprism for electron holography measurements and a significantly larger pole piece gap for in situ observations of dynamic events over a wide range of operating conditions – and a Titan “ChemiSTEM” microscope in 2013 – a state-of-the-art analytical instrument equipped with a specialised energy dispersive x-ray spectroscopy (EDS) system providing superior sensitivity and read out speed – provides a further increase in the instrumental portfolio of the ER-C. The start-up of both microscopes will permit a diversity of experiments related to interface, lattice defect and surface properties of solids beyond pure atomic resolution structure analysis. In the medium term, both instruments will be made available to the electron microscopy and nanoscience communities through the ER-C’s user services.



Research Highlights

High-resolution transmission electron microscopy on an absolute contrast scale

A. Thust^{1,2}

¹ IFF-8: Microstructure Research

² ER-C: Ernst Ruska-Centre for Microscopy and Spectroscopy with Electrons

A quantitative approach to high-resolution transmission electron microscopy requires a satisfactory match between image simulations and experiments. While an almost perfect image match is routinely achieved on a relative contrast level, a huge mutual discrepancy in the absolute image contrast by a factor of three has been frequently reported. It is shown that a major reason for this well known contrast discrepancy, which is called Stobbs-factor problem, lies in the neglect of the correct detector modulation-transfer-function in image simulations.

The technique of high-resolution transmission electron microscopy (HRTEM) offers nowadays the possibility to study the atomic configuration of solid state objects with a resolution of around 0.08 nm. Highly accurate information about atomic positions and chemical occupancies at lattice defects and interfaces can be obtained by the quantitative use of this technique.

Due to the quantum-mechanical nature of the electron diffraction inside the object and due to the subsequent electron-optical imaging process, any quantitative extraction of object information from HRTEM images requires a justification by accompanying image simulations. Since the introduction of digital image comparison to HRTEM in the early 1990s, a satisfactory agreement between simulation and experiment could be established only on a relative basis by disregarding the absolute magnitude of the image contrast. The reason for this still common practice was first published by Hýtch and Stobbs in 1994, who found a remarkably strong discrepancy between the magnitude of the simulated and the experimental image contrast [1]. In their experiment, the image contrast was found to be by a factor of three too low when compared to image simulations. Since the image motifs were nevertheless widely consistent between simulation and experiment, the problem was regarded mainly as a scaling problem, and became prominent as Stobbs-factor problem, factor-of-three problem, or contrast-mismatch problem. An explanation for this prominent and long standing problem, which has

been meanwhile frequently reproduced and investigated, has not been found so far.

The electron microscopic imaging process can be subdivided into three stages, of which each can be potentially responsible for the contrast-mismatch problem: (i) the diffraction of the incoming electron wave by the object, (ii) the subsequent electron optical transfer of the diffracted wave by the electromagnetic lenses, and (iii) the final image acquisition by a camera. Concerning the diffraction part, plasmon and phonon scattering were explicitly ruled out as a reason for the problem, and moreover,

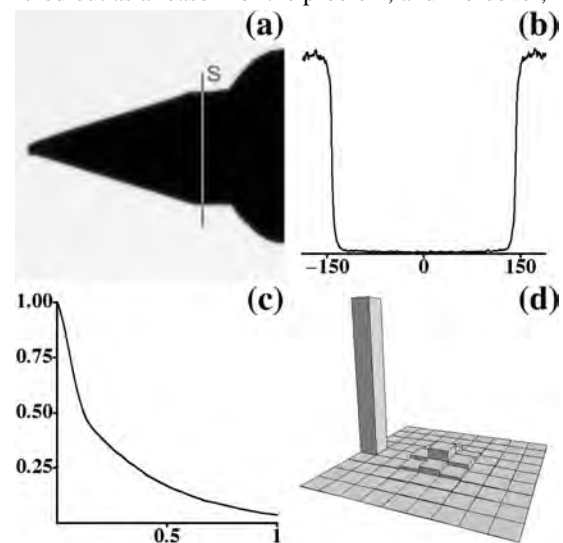


FIG. 1: (a) Shadow image of beam stop acquired with 300 kV electrons by a Gatan UltraScan 1000 camera. (b) Linescan through the vertical section labeled by "S" in the shadow image. Abscissa in pixel units. (c) 1-dim. section of modulation transfer-function MTF derived from shadow image. Abscissa in units of the Nyquist frequency. (d) Central 9×9 "pixels" of the related point-spread function PSF. The bar at the edge shows the height of an ideal δ -like PSF.

a remarkable discrepancy between measured and simulated diffraction data was not found. Concerning the electron optical part, the measurement of coherent aberrations and of partially coherent contrast dampening functions is possible with high accuracy and did not reveal inconsistencies. However, little attention has been paid to the final

image recording step, which involves the frequency-transfer properties of the image recording device.

In the work of Hýtch and Stobbs the modulation transfer-function (MTF) of the photographic film plates used at that time was not considered [1]. It is also remarkable that the most popular image simulation software packages, EMS and MacTempas, do not allow to incorporate actually measured MTFs. In all, the actual MTFs of the meanwhile used CCD (charge coupled device) cameras were often not considered in the literature related to the Stobbs-factor problem. Concerning the very rare implementation of actually measured MTFs into image simulations, criticism is allowed: Earlier MTF measurements were often based on the so-called noise method, which is known to yield too optimistic results when compared to the knife-edge method, which is the state-of-the art technique for MTF measurement.

A generalization of the knife-edge method towards a 2-dimensional evaluation of the MTF was developed for this work [2]. This improved method uses as input a shadow image of the microscope's beam stop and is designed to avoid artifacts due to image noise, aliasing, and periodic continuation. Fig. 1 displays (a) the shadow image of the beam stop, (b) a line scan through the shadow image, (c) the rotationally symmetric part of the MTF, and (d) the corresponding point-spread function. The strong fall-off of the measured MTF, which is reflected by a considerably low and broad point-spread function, indicates a strong contrast-dampening effect of the CCD camera in use.

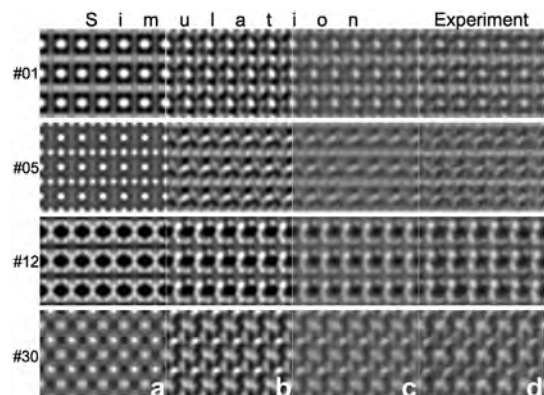


FIG. 2: Image patches comprising 3×3 SrTiO₃ unit cells projected along the [110] zone axis. The patches 1, 5, 12, and 30, belong to different focal values and are shown exemplarily for a series of 30 images. All patches are displayed on the same grey scale extending between intensity values 0.35 (black) and 2.2 (white). (a) Simulation for an object thickness of 2.8 nm, (b) simulation including additionally residual lens aberrations, (c) simulation including residual aberrations and additionally the measured MTF, (d) experimental images.

A focal series of [110]-oriented SrTiO₃ was acquired with a spherical-aberration corrected FEI Titan 80-300 microscope operated at 300 kV and is compared with image simulations including the measured MTF. The series of 30 images was acquired with a spherical aberration of $C_s = -25 \mu\text{m}$ at an excessively high sampling rate of 9.71 pixels/Å.

The main steps of the accompanying image simulation are visualized in Fig. 2, which highlights four exemplary images belonging to the focal series of 30 images. Column (a) shows ideal images simulated for an object thickness of 2.8 nm. In column (b) residual optical aberrations, which cannot always be avoided during experiment, have been added to the simulation. Column (c) displays the simulated images after the additional application of the measured MTF, and column (d) shows the experimentally acquired images. Simulation (c) and experiment (d) are displayed on the same grey level scale, and are in almost perfect agreement, not only with respect to the similarity of the image motifs, but – what is most important here – also with respect to the occupied absolute contrast range.

A quantitative contrast comparison for the complete series is shown in Fig. 3. It can be seen that the residual aberrations, which change the image motifs in a drastic way, have a comparatively small impact on the simulated image contrast. The major contrast reducing effect is clearly due to the MTF. Only after the application of the correctly measured MTF in simulation (dashed line in Fig. 3) an almost perfect absolute contrast match to experiment (squares in Fig. 3) is possible.

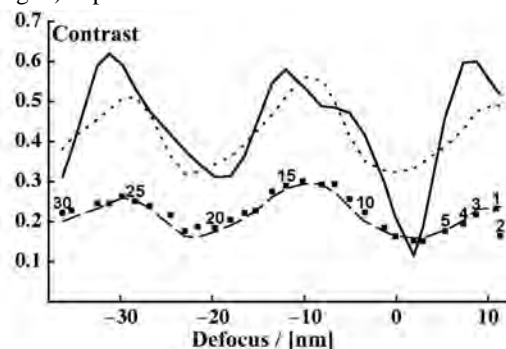


FIG. 3: Solid line: Image contrast simulated for an object thickness of 2.8 nm and for the focal values of the experimental SrTiO₃ series. Dotted line: Simulated contrast including additionally residual lens aberrations. Dashed line: Simulated contrast including residual aberrations and additionally the MTF. Squares: Experimental image contrast. Image numbers within focal series are indicated.

In summary, the existence of a general contrast-mismatch problem of remarkable size in HRTEM can not be confirmed. On the contrary, an almost perfect consistency between simulation and experiment is found when including the correct detector MTF in image simulations.

[1] M. J. Hýtch and W. M. Stobbs, Ultramicroscopy 53, (1994) 191.

[2] A. Thust, Phys. Rev. Lett. 102, (2009) 220801.

Monolayer resolved EEL spectroscopy for high-resolution interface analysis

M. Heidelmann^{1,3}, J. Barthel^{2,3}, L. Houben^{1,3}

¹ IFF-8: Microstructure Research

² Gemeinschaftslabor für Elektronenmikroskopie, RWTH Aachen

³ ER-C: Ernst Ruska-Centre for Microscopy and Spectroscopy with Electrons

The physical properties of materials can be controlled by compositional and bonding fluctuations on the nanoscale. Resolving such fluctuations on the atomic scale has been a long standing challenge in analytical microscopy. Electron energy loss (EEL) spectroscopy with a high-energy electron probe focussed to atomic size in a scanning transmission electron microscope (STEM) is an essential approach to this problem. Here, a simple and powerful technique for monolayer resolved spectrometry of interfaces or 1-dimensional nanostructures is demonstrated. Contrary to the common approach, a precise synchronization of measurement location and spectral information is possible. Electron dose control in combination with atomic-scale resolution and quantitative accuracy opens unique possibilities for studying the local composition of chemically abrupt interfaces.

The commonly used technique for gathering spatially resolved EEL data in a STEM is to record spectra for a series of raster points. If this is done in one spatial dimension it is called the line profile technique while spectrum imaging (SI) refers to a mapping over two dimensions. For each raster point, either full EEL spectra are available for fine structure analysis or elemental maps can be extracted by spectrum integration over an energy window at the onset of a characteristic core-loss. The EEL spectrum acquisition is disrupted periodically to take a high-angle annular dark-field (HAADF) image of a reference area. The image of the reference area is

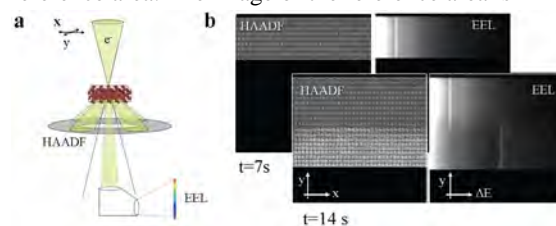


FIG. 1: StripeSTEM measurement. High-resolution HAADF data and EEL data are recorded isochronously while the electron probe with a diameter of less than 1 Å scans the sample. The HAADF image reveals the spatial origin of the energy-loss signal alongside any distortions related to unavoidable specimen and beam drift. The corresponding EEL spectrum stack image reveals the chemical composition as a function of one spatial coordinate.

used to counteract the unavoidable specimen and beam drift by applying a compensating shift of the scan frame. The SI and the line profile technique

share disadvantages: The recording of an EEL spectrum with a sufficient signal-to-noise ratio (SNR) usually requires a dwell time during which instrumental instabilities are hardly negligible, even for a single beam position. The consequential loss of control over the measurement position due to inherent specimen and beam drift becomes most perceivable at atomic resolution. Small probe displacements on the Ångstrom scale sensitively affect the excitation probability of an inelastic core-loss scattering event, meaning that quantitative spectroscopic data must be considered with caution.

In order to overcome the inherent uncertainties connected with the common procedures we propose a simple technique which is most suited for atomic scale spectroscopy of 1-dimensional nanostructures or planar interfaces [1]. The technique, named

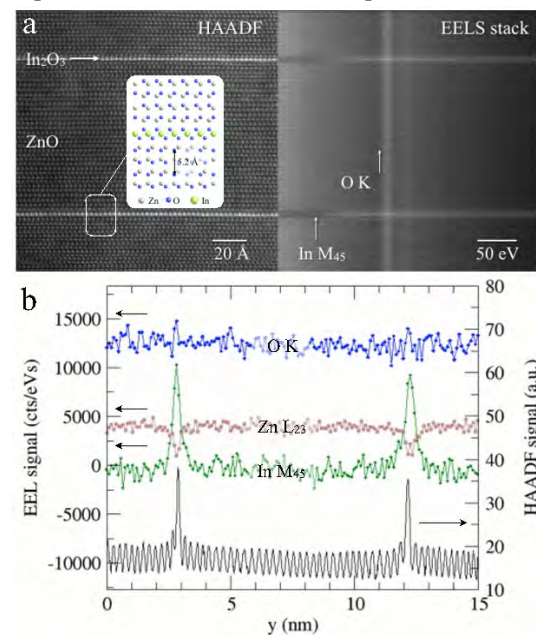


FIG. 2: Monolayer resolution in a StripeSTEM measurement on a reference sample containing monolayer precipitates of In_2O_3 in a ZnO matrix. (a) StripeSTEM data, a model of the defect is superimposed onto the HAADF image. (b) HAADF and EEL chemical profiles orthogonal to the basal plane precipitates.

StripeSTEM, is based on an isochronous collection of a series of EEL spectra while an HAADF image is taken in a continuous, uninterrupted scan. Fig. 1 shows the schematic procedure for the case of a crystalline sample. While the electron probe scans successively

along lattice planes aligned to the x-direction, EEL spectra are recorded in sequence as a function of the y-coordinate of the scan. Spectrometer readout times are set such that several EEL spectra are recorded per traversed lattice plane and that each spectrum relates to several scan lines along the y-direction.

Since specimen and beam drift during the experiment, the raw spectral intensity collected shows variations even for equivalent lattice planes in a crystalline sample. However, in a StripeSTEM experiment the effective beam dwell time for a certain monolayer can be calculated using the HAADF-image as a log of the instabilities. Details of the according signal normalization and a practical example are described in [1]. The post-correction of signals leads to an improved accuracy of compositional data compared to the commonly used techniques.

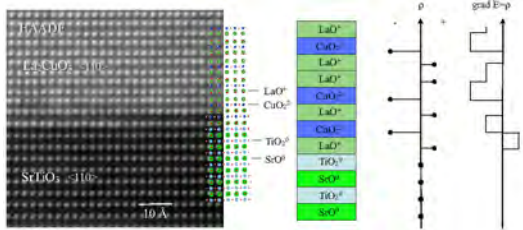


FIG. 3: Atomic coordination at the SrTiO₃/La₂CuO₄ interface ([001]STO || [001]LCO). Left: The multiexposure HAADF image shows two intermediate perovskite blocks. A tentative model is depicted. Right: According to the ionic model an abrupt chemical termination would give rise to a net electrostatic field and diverging potential in the LCO.

Monolayer resolution is achieved for core loss EEL signals. An experimental proof is shown in fig. 2. Monolayer precipitates of octahedrally coordinated In₂O₃ in ZnO served as an atomically sharp reference structure. In the StripeSTEM experiment, the In₂O₃ monolayers are resolved with a spatial resolution of 1.8 Å in the HAADF profile and 2.7 Å in the In M45 core loss signal.

The spatial resolution of the energy loss data is affected by three principal factors: (1) the delocalization of the inelastic scattering process, for core-losses this is typically 1-2 Å, (2) the dynamical dispersion of the electron beam in the sample, and (3) the "geometrical source width" of the probe at high beam current [1]. The first two factors are of physical nature and represent the ultimate limit for the attainable resolution. The last factor is connected to the brightness of the electron emitter. With modern Schottky field emitter microscopes in combination with aberration corrected probe formation the ultimate limit of the spatial resolution can be achieved for strong energy loss signals, like the white lines of transition metals. For weak signals, e.g. the core loss of oxygen, it is necessary to adjust for a high beam current in order to achieve a sufficient SNR for accurate quantification, on the expense of spatial resolution.

StripeSTEM was applied to the analysis of an interface between La₂CuO₄ and SrTiO₃. The

interface is of the polar/non-polar type and structural or electronic reconstruction is required to avoid a 'polar catastrophe' [2]. The HAADF image in fig. 3 reveals two perovskite blocks in the atomic coordination at the interface. According to the ionic model an abrupt chemical termination would give rise to a net electrostatic field. Previous work based on the quantification of the phase of a reconstructed wavefunction in high-resolution TEM suggested intermixing in the cation sub-lattice, in contrast to electronic reconstruction and free charge carrier accumulation [3]. The StripeSTEM experiment

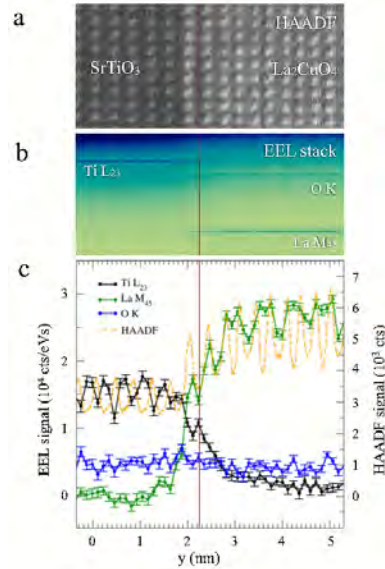


FIG. 4: StripeSTEM analysis of the chemical composition of the interface between STO and LCO. (a) HAADF image and (b) stack of EEL spectra. (c) Quantitative signal of core losses of Ti, O, and La after background subtraction. Error bars indicate the 1 σ uncertainty due to noise and background extrapolation. The HAADF signal is displayed for comparison. The substitution of Cu by Ti in the interfacial perovskite layer introduces an excess positive charge which aids in avoiding a fictional 'polar catastrophe'.

shown in fig. 4 now proves that a considerable Ti concentration is present in the intermediate perovskite-like La(Cu,Ti)O₃ layers. The substitution of Cu²⁺ in the CuO₂²⁻ plane with a high fraction (50%) of Ti⁴⁺ provides the extra positive charge required to avoid an interface charge: Accumulation of free charge carriers is not a necessity, ionic reconstruction averts a diverging electrostatic potential.

- [1] M. Heidelmann, J. Barthel, and L. Houben, *Ultramicroscopy*, **109** (2009) 1447 – 1452.
- [2] N. Nakagawa, H. Y. Hwang, and D. A. Muller, *Nature Materials* **5** (2006), 204 – 209
- [3] L. Houben, *J. Mater. Sci.* **41** (2006), 4413–4419

Selected Literature

1. Yu R, Lentzen M and Zhu J:
Effective object planes for aberration-corrected transmission electron microscopy,
Ultramicroscopy **112** (2012) 15–21.
2. Bar-Sadan M, Barthel J, Shtrikman H and Houben L:
Direct imaging of single Au atoms within GaAs nanowires,
Nano Letters **12** (2012) 2352-2356.
3. Urban K:
Electron Microscopy – The challenges of graphene,
Nature Materials **10** (2011) 165–166
4. Beleggia M, Kasama T, Dunin-Borkowski RE, Hofmann S and Pozzi G:
Direct measurement of the charge distribution along a biased carbon nanotube bundle using
electron holography,
Applied Physics Letters, **98** (2011) 243101.
5. Barthel J and Thust A:
Aberration measurement in HRTEM: Implementation and diagnostic use of numerical procedures
for the highly precise recognition of diffractogram patterns,
Ultramicroscopy **111** (2010) 27-46.
6. Lentzen M:
Reconstruction of the projected electrostatic potential in high-resolution transmission electron
microscopy including phenomenological absorption,
Ultramicroscopy, **110** (2010) 517–526.
7. Jia C, Houben L, Thust A and Barthel J:
On the benefit of the negative-spherical-aberration imaging technique for quantitative HRTEM,
Ultramicroscopy, **110** (2010) 500–505.
8. Heidelmann M, Barthel J, and Houben L:
StripeSTEM – a technique for the isochronous acquisition of high angle annular dark-field images
and monolayer resolved electron energy loss spectra,
Ultramicroscopy **109** (2009) 1447.
9. Thust A:
High-Resolution Transmission Electron Microscopy on an Absolute Contrast Scale,
Physical Review Letters **102** (2009) 220801.
10. Urban K:
Is science prepared for atomic resolution electron microscopy?,
Nature Materials **8** (2009) 260.

Jülich Centre for Neutron Science (JCNS)

Within the programme structure of the Helmholtz Association, Forschungszentrum Jülich participates in the topic “Neutrons” of the programme “Research with Photons, Neutrons and Ions” (PNI) in the research field “Structure of Matter”. Inside the Forschungszentrum, research with neutrons is carried out by the institute “Jülich Centre for Neutron Science” (JCNS) [<http://www.fz-juelich.de/jcns/>]. For the vibrant German and international neutron scattering communities, Jülich Centre for Neutron Science is a novel user access platform. It facilitates access to unique infrastructures and experimental facilities and promotes the development of state-of-the-art neutron techniques.

JCNS operates instruments at leading national and international sources: at the FRM II research reactor in Garching, Germany, at the high-flux reactor at the Institut Laue-Langevin (ILL) in Grenoble, France, and at the first megawatt-class (MW) spallation source, SNS, in Oak Ridge, Tennessee, USA. These instruments are made available for external users to conduct experiments by means of a procedure whereby proposals are reviewed by an independent group of experts. Thus, JCNS offers its users access to state-of-the-art neutron instruments under consistent conditions at the neutron source, affording the best conditions for each individual experiment undertaken. In addition, JCNS serves as the organizational framework for Forschungszentrum Jülich's development programme for methods and instruments, as well as for its own research programmes in the field of Key Technologies.

The scientific use of the FRM II, the most up-to-date continuous neutron source, is governed by a cooperation agreement between the Technical University Munich, TUM, on the one hand, and the Helmholtz centres FZJ, HZG and HZB on the other. By the operation of a majority of 11,5 scattering instruments, the Helmholtz involvement is clearly led by JCNS. This engagement broadens the basis for the scientific use of FRM II and ensures that it is jointly organized by equal partners as expressed by the fact that the scientific directorate of FRM II consists of one director from TUM and one director from FZJ.

With its involvement in the instrumentation and user operation at three instruments of the SNS, JCNS gained experience in building instruments at MW spallation sources, and opened access for the German user community to the unique opportunities offered there. JCNS is proactive in preparing the future of neutron research in Europe by leading the German contribution to the design update study of the European Spallation Source ESS, to be built in Lund, Sweden.

At the world's highest flux neutron research reactor of the ILL in Grenoble, Forschungszentrum Jülich has the role of the German associate. Based on a long standing collaboration with French partners from the CEA Grenoble, JCNS makes three instruments available to the German community.

In terms of user statistics, 2734 beam days were requested and 1358 beam days were allocated during the period 2009 to 2011 (Note: not all instruments and sources were fully available during the reporting period). About 40 % of the users came from Europe, with the largest share from France (7.3 %) and the United Kingdom (4.3 %). Usage from overseas include the United States (4.8 %), Japan (2.8 %) and Australia (1.5 %).

List of instruments

From 2009 to 2012, JCNS operated a total of 14 neutron scattering instruments at three different sources. Two additional instruments are currently under construction.

Outstations:

Research Reactor FRM II (Forschungs-Neutronenquelle Heinz Maier-Leibnitz) in Garching, Germany

High Flux Reactor at the Institut Laue-Langevin in Grenoble, France

Spallation Neutron Source at the Oak Ridge National Laboratory, Oak Ridge, USA

	<u>Diffraction</u>
	BIODIFF Single crystal diffractometer for biological macromolecules (collaboration with Technical University Munich)
	D23 Thermal neutron two-axis diffractometer for single-crystals (CEA instrument, access for German users through JCNS)
	HEIDI Hot single crystal diffractometer (operated by RWTH Aachen)
	POLI POLarisation Investigator using HEIDI monochromator (operated by RWTH Aachen)
	POWGEN Powder diffractometer (SNS instrument, access for German users through JCNS)
	POWTEX POWder and TEXture – High intensity time-of-flight diffractometer (under construction)
	<u>Reflectometry</u>
	MARIA MAGnetic Reflectometer with high Incident Angle
	<u>Small Angle Scattering</u>
	KWS -1 Small Angle Neutron Scattering diffractometer
	KWS-2 Small Angle Neutron Scattering diffractometer for soft matter and biology
	KWS-3 Ultra Small Angle Neutron Scattering diffractometer
	<u>Spectroscopy</u>
	BASIS Backscattering spectrometer (SNS instrument, access for German users through JCNS)
	DNS Diffuse Neutron Scattering spectrometer with polarisation analysis
	IN12 Cold neutron three-axis spectrometer with polarisation analysis
	IN22 Thermal neutron three-axis spectrometer with polarisation analysis (CEA instrument, access for German users through JCNS)
	J-NSE Jülich Neutron Spin Echo spectrometer
	SPHERES Backscattering SPectrometer for High Energy RESolution
	SNS-NSE Spallation Neutron Source - Neutron Spin Echo spectrometer
TOPAS Time-Of-flight with Polarisation Analysis Spectrometer (under construction)	
Photos: W.Schürmann/TUM	

Research Highlights

Unravelling Complex Magnetic Correlations in Spin Ice $\text{Ho}_{2-x}\text{Y}_x\text{Ti}_2\text{O}_7$

L. J. Chang¹, Y. Su², Y. J. Kao³, Y. Z. Chou³, R. Mittal², H. Schneider², Th. Brückel⁴, G. Balakrishnan⁵, M. R. Lees⁵

¹ Department of Physics, National Cheng Kung University, Taiwan

² JCNS: Jülich Centre for Neutron Science

³ Department of Physics, National Taiwan University, Taiwan

⁴ JCNS: Jülich Centre for Neutron Science and Peter Grünberg Institute

⁵ Department of Physics, University of Warwick, UK

Magnetic monopoles may appear in frustrated magnets as fractional particles carrying the magnetic charges and thus obeying the magnetic Coulomb law. Recent neutron scattering [1-2] and magneticity experiments [3] have identified the low-temperature state of the dipolar spin ice pyrochlore compounds $\text{Ho}_2\text{Ti}_2\text{O}_7$ and $\text{Dy}_2\text{Ti}_2\text{O}_7$ as the magnetic Coulomb phase, which hosts the emergent magnetic monopoles. In order to shed the lights on the effect of impurity doping on the magnetic correlations in the magnetic Coulomb phase, we have carried out comprehensive diffuse neutron scattering measurements with polarization analysis on the single crystals of the diluted spin ice $\text{Ho}_{2-x}\text{Y}_x\text{Ti}_2\text{O}_7$ ($x = 0, 0.3$, and 1) at DNS [4]. At low temperature, the spin flip patterns are characteristic of a dipolar spin ice and are unaffected by Y doping. At 2 K, the spin flip scattering patterns are typical of a nearest-neighbour spin ice and the effects of Y doping are seen in the widths of the pinch points. In the non-spin flip channel, we observe the signature of strong antiferromagnetic correlations at the same temperature as the dipolar spin ice correlations appear in the spin flip channel.

The spin ice compound $\text{Ho}_2\text{Ti}_2\text{O}_7$ exhibits a local $\langle 111 \rangle$ Ising-like anisotropy and an effective ferromagnetic interaction between the magnetic moments. The organizing principles of the magnetic ground-state, or the “ice rules”, require that two spins should point in, and two out of each elementary tetrahedron in the pyrochlore lattice. The minimal model for the system is the dipolar spin ice model (DSM) with the nearest-neighbor exchange and long-range magnetic dipole interactions, given by the following Hamiltonian,

$$H = -J \sum_{\langle ij \rangle} \mathbf{S}_i \cdot \mathbf{S}_j + Da^3 \sum_{i>j} \left[\frac{\mathbf{S}_i \cdot \mathbf{S}_j}{r_{ij}^3} - \frac{3(\mathbf{S}_i \cdot \mathbf{r}_{ij})(\mathbf{S}_j \cdot \mathbf{r}_{ij})}{r_{ij}^5} \right]$$

where a is the nearest neighbor distance, $\mathbf{S}_i = \sigma_i \hat{z}_i$ is a spin of unit length along the $\langle 111 \rangle$ Ising orientation \hat{z}_i . At high temperatures, the low energy physics can be adequately described by the nearest-neighbor spin ice model (NNSM), which is the DSM Hamiltonian truncated at the nearest-neighbor interactions, as a result of the self-screening of the dipolar interactions on the pyrochlore lattice. The magnetic correlations have the spatial dependence of a dipolar form, resulting in characteristic pinch-point features in the neutron scattering data.

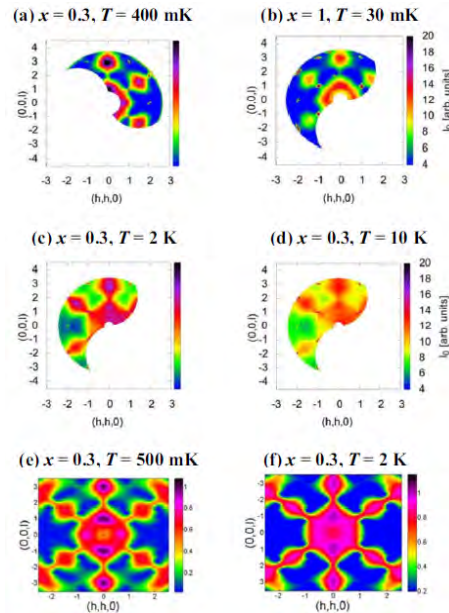


FIG. 1: Experimental neutron spin-flip scattering patterns for the $\text{Ho}_{2-x}\text{Y}_x\text{Ti}_2\text{O}_7$ compounds [4] for (a) $x = 0.3$ at 400 mK, (b) $x = 1.0$ at 30 mK, (c) $x = 0.3$ at 2 K, and (d) $x = 0.3$ at 10 K; Monte-Carlo simulations made using the DSM for (e) $x = 0.3$ at 500 mK, and (f) $x = 0.3$ at 2 K.

We have carried out a comprehensive investigation of the magnetic diffuse scattering in the (h, h, l) reciprocal plane for single crystals of $\text{Ho}_{2-x}\text{Y}_x\text{Ti}_2\text{O}_7$ ($x = 0, 0.3, \text{ and } 1$) via neutron polarization analysis to study the short-range magnetic correlations in these materials. A neutron wavelength of 4.74 \AA was chosen for all the experiments. The $[1, -1, 0]$ direction of the crystals was aligned perpendicular to the horizontal scattering plane so that the (h, h, l) reciprocal plane can be mapped out by rotating the samples. The neutron polarization at the sample position was aligned along the $[1, -1, 0]$ direction of the sample, i.e. the z -direction of the chosen experimental coordinate system. Within this setup, the spin flip (SF) and non-spin flip (NSF) scattering cross sections are,

$$\left(\frac{d\sigma}{d\Omega}\right)_z^{\text{SF}} = M_{\perp y}^* M_{\perp y} + \frac{2}{3} I_{SI}$$

$$\left(\frac{d\sigma}{d\Omega}\right)_z^{\text{NSF}} = M_{\perp z}^* M_{\perp z} + N^* N + \frac{1}{3} I_{SI}$$

where $M_{\perp y}^* M_{\perp y}$ and $M_{\perp z}^* M_{\perp z}$ are the components of the magnetic scattering cross section in and out of the (h, h, l) scattering plane respectively. I_{SI} is the total nuclear spin incoherent scattering cross section, and $N^* N$ is the nuclear coherent scattering cross section. In the neutron SF scattering, we observe a crossover at $T \sim 2 \text{ K}$ in the diffuse scattering from patterns that are typical of a NNSM at high-temperature to those representatives of a DSM at low temperature. In the NSF channel, diffuse scattering corresponding to apparent short-range AFM correlations is observed at the zone boundaries below 2 K .

Figure 1 shows the experimental SF scattering patterns for the $\text{Ho}_{2-x}\text{Y}_x\text{Ti}_2\text{O}_7$. The low- T results (see Fig. 1(a-b)) show clearly a distinct DSM scattering pattern with four intense regions around $(0, 0, 0)$, and the spread of the broad features connecting $(0, 0, 0)$ to regions of intensity around $(0, 0, 3)$ and $(3/2, 3/2, 3/2)$. The pinch points, which are associated with dipolar correlations in real space, are clearly observed at the $(0, 0, 2)$ position in as bow-tie shapes. The experimental results, however, show that the Y dilution does not alter the scattering patterns significantly even with $x = 1.0$, i.e., half of the spins removed.

Meanwhile, we observe a crossover from the magnetic correlation pattern of the DSM at 400 mK to that of the NNSM at 2 K (Fig. 1(c)). The NNSM pattern exists up to 10 K (Fig. 1(d)). Monte-Carlo simulations of the DSM at 500 mK (Fig. 1(e)) and 2 K (Fig. 1(f)) confirm these results. At high- T , the energy difference between states in the quasi-degenerate manifold is irresolvable due to the thermal fluctuations, and the DSM is projectively equivalent to the NNSM. At low- T , the residual energy scales become relevant and it is necessary to include the full dipolar interaction to account for the details of the scattering pattern.

It has also been observed that at low- T the widths of the pinch point are not affected by dilution. However, at 2 K , the effects of Y dilution are evident [4]. These results show that doping reveals the temperature regime where the “projective

equivalence” between the DSM and NNSM is a valid description of the system. At 2 K , although the microscopic Hamiltonian is given in the above master equation, the low-energy physics is described by the NNSM, and doping with Y can effectively destroy the singular behavior at the pinch point. At lower temperature, one needs to take into account the full long-range dipolar interactions as the simpler NNSM description is no longer valid.

Figure 2 shows the NSF scattering for $x = 0.3$ at 400 mK . The pattern in Fig. 2 corresponds to the component of the magnetic correlations perpendicular to the (h, h, l) scattering plane, and is only observed when the dipolar spin ice pattern appears in the SF channel. Signatures of strong AFM correlations along $(0, 0, 1)$ and $(h, h, 0)$ are observed for all the compounds. One of the possible antiferromagnetic configurations is depicted in the inset of Fig. 2(a).

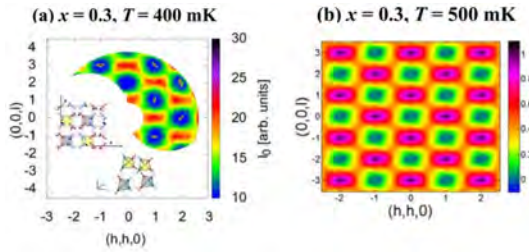


FIG. 2: Non-spin flip scattering for $x = 0.3$ at 400 mK . The inset shows one of the possible antiferromagnetic configurations (x - y plan projection and in three dimensions, \pm indicates that the moment is along $\pm z$ - z direction) predicted; (b) MC simulation results using DSM for $x = 0.3$ at 500 mK ;

In conclusion, we have studied the complex magnetic correlations in Y doped single crystals of the spin ice $\text{Ho}_2\text{Ti}_2\text{O}_7$ using diffuse neutron-scattering with polarization analysis. For all the specimens studied, at temperatures between 2 K and 10 K the magnetic correlations produce SF neutron scattering patterns that can be described using a nearest-neighbor spin ice model. Below $\sim 2 \text{ K}$ the scattering patterns can be described by a dipolar spin ice model. At low- T , the widths of the pinch points are not affected by dilution, while at 2 K , the effects of Y dilution become significant. These results show that doping reveals the regime where the DSM and NNSM are valid descriptions of the system. The signature of AFM correlations, which are observed along the zone boundary in the NSF scattering, and at positions $(0, 0, 1)$, $(0, 0, 3)$, $(3/2, 3/2, 3/2)$ in the SF channel, may be the precursor of the predicted long-range order in the spin ice.

-
- [1] T. Fennell, et al., *Science* **326**, 415 (2009).
 - [2] D.J.P. Morris, et al., *Science* **326**, 411 (2009).
 - [3] S.R. Giblin, et al., *Nature Physics* **7**, 252 (2011).
 - [4] L.J. Chang, et al., *Phys. Rev. B* **82**, 172403 (2010).

Hydrogen Release from Sodium Alanate Observed by Time-resolved Neutron Backscattering

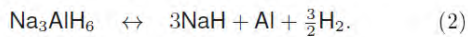
Aline Léon¹, Joachim Wuttke²

¹ Karlsruhe Institute of Technology, Institute of Nanotechnology

² JCNS: Jülich Centre for Neutron Science

Time-resolved quasielastic measurements on the backscattering spectrometer SPHERES were used to monitor the decomposition kinetics of sodium alanate, $\text{NaAlH}_4 \rightarrow \text{Na}_3\text{AlH}_6 \rightarrow \text{NaH}$. Both reaction steps were found to be accelerated by autocatalysis, most likely at the surfaces of Na_3AlH_6 and NaH crystallites.

Sodium alanate NaAlH_4 is widely studied as a model system for hydrogen storage. Hydrogen release through the reaction steps



is very slow and irreversible in undoped bulk material, but the desorption and absorption kinetics can be improved decisively by doping [1] and nanostructuring [2]. Further improvement requires a detailed understanding of the reaction mechanism.

Neutron scattering offers promising ways to observe structural changes in situ while the hydrogen is being released. In this project, we use intermolecular dynamics, probed by quasielastic scattering, as a very sensitive proxy for structural changes. So far, we have completed a series of measurements on hydrogen release from pure bulk alanate [3].

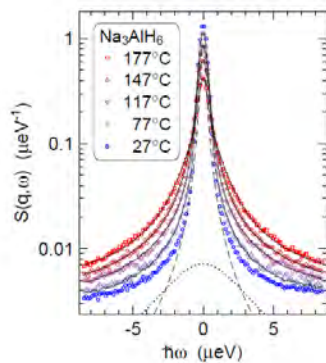


Fig. 1: Neutron scattering spectra of Na_3AlH_6 . The 27°C data represent the resolution function. The other data are fitted with a delta line and two Lorentzians, convoluted with the measured resolution. The dashed and the dotted line show the two Lorentzians for 117°C separately and in unconvoluted form.

To obtain reasonable statistics within short time slices we choose an energy window of $\pm 8.6 \mu\text{eV}$ out of the full energy range of SPHERES of $\pm 31 \mu\text{eV}$. Within our window, NaAlH_4 and NaH only show

elastic scattering. Therefore, the intermediate reaction product Na_3AlH_6 can be clearly identified from its strong quasielastic scattering, fitted in Fig. 1 by two Lorentzians.

In a good first approximation, the Lorentzians have temperature-independent amplitudes $a(q)$ and wavenumber-independent linewidths $\Gamma(T)$, which is the signature of localized processes. We see no scattering by long-ranged diffusion: Most probably, diffusion of H_2 is too fast and diffusion of heavier species is too slow to be observed within the dynamic window of SPHERES.

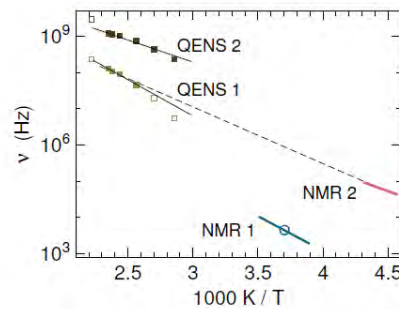


FIG 2: Rotation frequencies in Na_3AlH_6 as determined by quasielastic neutron scattering (QENS) and by nuclear magnetic resonance (NMR) [4,5]. The dashed suggests that NMR 2 and QENS 1 are one and the same process.

The temperature dependence of the $\Gamma(T)$ is compatible with an Arrhenius law, and at least for one of the two Lorentzians it is consistent with NMR observations of thermally activated rotational jumps of AlH_6 octahedra around C_4 axes in Na_3AlH_6 below room temperature (Fig.2). On this base, the amplitude of the dominant Lorentzian can be used as a well understood measure of the amount of Na_3AlH_6 present in a transforming sample.

Time-resolved measurements were performed with four fresh NaAlH_4 samples. After measuring the resolution at room temperature, the sample was quickly heated to 170, 180, or 185°C, and kept there at constant temperature for 2 days or more. Initially, no quasielastic scattering is observed. It takes several hours before a quasielastic signal appears above the wings of the resolution function. The signal continues to grow, until a maximum is reached about 30 h after the start of the measurement. Then, the quasielastic intensity decreases and about 65 h after the start of the measurement we are left with purely

elastic scattering, which however is only half as strong as in the beginning.

The time-resolved spectral data are binned in time slots covering 20 minutes each, and fitted with a delta line plus a Lorentzian with a fixed linewidths obtained for each experimental temperature from the Arrhenius law of Fig.2, yielding the amplitudes shown in Fig.3. Solid lines are fits with a quantitative kinetic model.

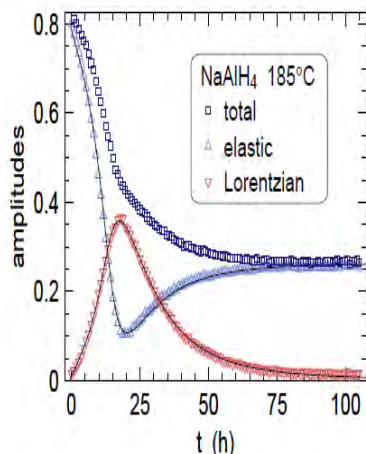


FIG 3: Transformation of NaAlH_4 at 185°C : Total backscattering intensity I , fitted elastic amplitude a_8 , and fitted Lorentzian amplitude a_1 versus time. Solid lines are fits with a kinetic model described in the text.

We now abbreviate the two-step reaction (1), (2) as $A \rightarrow B \rightarrow C$, where A stand for NaAlH_4 , B for $1/3 \text{Na}_3\text{AlH}_6$, and C for NaH , ignoring side products that do not significantly contribute to the observed spectra. Writing concentrations as dimensionless mol/mol fractions, normalized to a pure NaAlH_4 sample, the initial composition is $[A] = 1$, $[B] = [C] = 0$. Since our scattering signal is almost exclusively due to bound hydrogen, we set

$$a_1(t) = \frac{1}{2}[B]f_B, \quad (3)$$

$$a_8(t) = [A]f_A + \frac{1}{4}[C]f_C, \quad (4)$$

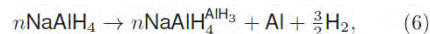
Where the f are Lamb-Mössbauer factors.

On this base, we searched for rate equations that reproduce the observed time series $a_1(t)$ and $a_8(t)$. It turned out that the relatively sharp peak in $a_1(t)$ can only be reproduced if some autocatalysis is assumed. To improve the agreement with the experimental $a_8(t)$ and $a_1(t)$, we admitted concentration dependences with fractional exponents. In this heuristic way, we found that the following simple kinetic model to be compatible with the measured amplitudes $a_8(t)$ and $a_1(t)$:

$$\begin{aligned} d[A]/dt &= -k_{00}[A] - k_{01}[A][B]^2, \\ d[B]/dt &= -d[A]/dt - d[C]/dt, \\ d[C]/dt &= k_{10}[B]^{4/3} + k_{11}[B]^{4/3}[C]^{2/3}, \end{aligned} \quad (5)$$

The exponents, multiples of $2/3$, are suggestive of an autocatalytic reaction at a surface; that k_{j_0} stands for nucleation and k_{j_1} for crystallite growth.

Our model is perfectly compatible with the reaction pathways proposed in a density-functional study [6]. Based on first-principles calculations, the migrating species were suggested to be AlH_3 and NaH vacancies. The lowest activation energy was found for AlH_3 vacancies, leading to the following pathway for reaction (1):

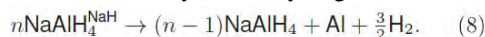


where the superscript denotes one vacancy, and n indicates an arbitrary amount of bulk material. The proposed diffusion mechanism also involves an AlH_5^{2-} ion. Anyway, the vacancy ultimately reaches a NaAlH_4 - Na_3AlH_6 boundary, where it annihilates, releasing an excess Na^+ that aggregates with the growing Na_3AlH_6 phase.

An alternate pathway starts with the unassisted release of Na^+ and H^- at the boundary of the growing Na_3AlH_6 according to



The two ionic vacancies migrate together to the Al - NaAlH_4 boundary, where hydrogen is released:



Using positron annihilation, it was confirmed experimentally that vacancies are formed in NaAlH_4 during dehydrogenation [7].

In these pathways, hydrogen release is limited by processes at boundaries: The NaAlH_4 - Na_3AlH_6 boundary as a sink for AlH_3 vacancies and as a source for NaH vacancies, and the Al - NaAlH_4 boundary as a sink for NaH vacancies and as the location of H_2 release. This is in accordance with the autocatalytic terms of our kinetic model.

-
- [1] Bodganović B and Schwickardi M (1997) J. Alloys Comp. 253-254 71.
 - [2] Zaluski L, Zaluska A and Ström-Olsen J O (1999) J. Alloys Comp. 290 71.
 - [3] Léon A and Wuttke J (2011) J. Phys. Condensed Matt. 23 254214.
 - [4] Senegas J, Villepastour A M and Bonnetot B (1981) J. Phys. Chem. Solids 42 1061.
 - [5] Verkuijlen M H W, van Bentum P J M, van Eck E R H, Lohstroh W, Fichtner M and Kentgens A P M (2009) J. Phys. Chem. C 113 15467.
 - [6] Gunaydin H, Houk K N and Ozoliņš V (2008) Proc. Natl. Acad. Sci. USA 105 3673.
 - [7] Sakaki K, Nakamura Y, Akiba E, Kuba M T and Jensen C M (2010) J. Phys. Chem. C 114 6869.

Selected Literature

1. Aliouane, N.; Schmalzl, K.; Senff, D.; Maljuk, A.; Prokes, K.; Braden, M.; Argyriou, D. N.
Flop of electric polarization driven by the flop of the Mn spin cycloid in multiferroic TbMnO₃
Physical Review Letters **102** (2009), 207205: 1 - 4
2. Chatterji, T.; Schneider, G. J.; Perbon, J.
Low-energy nuclear spin excitations in NdAl₂
Physical Review B **79** (2009), 132408: 1 - 4
3. Ehlers, G.; Mamontov, E.; Zamponi, M.; Kam, K. C.; Gardner, J. S.
Direct observation of a nuclear spin excitation in Ho₂Ti₂O₇
Physical Review Letters **102**, 016405 (2009)
4. Fennell T., Deen P.P., Wildes A.R., Schmalzl K., Prabhakaran D., Boothroyd A.T., Aldus R.J.,
McMorrow D.F., Bramwell S.T.,
Magnetic Coulomb phase in the spin ice Ho₂Ti₂O₇
Science **326**, 415-417 (2009)
5. Rheinstädter M. C., Schmalzl K., Wood K., Strauch D.,
Protein-protein interaction in purple membrane
Physical Review Letters **103**, 128104-1 – 128104-4 (2009)
6. Voigt, J.; Babcock, E.; Brückel, T.
Beam transport and polarization at TOPAS, the thermal time-of-flight spectrometer with
polarization analysis
Journal of Physics: Conference Series **211** (2010), 012032: 1 - 6
7. Arndt, J.; Stockert, O.; Schmalzl, K.; Faulhaber, E.; Jeevan, H. S.; Geibel, C.; Schmidt, W.;
Loewenhaupt, M.; Steglich, F.
Spin fluctuations in normal state CeCu₂Si₂ on approaching the quantum critical point
Physical Review Letters **106**, 246401 (2011)
8. Babcock, E.; Mattauch, S.; Ioffe, A.
High level of ³He polarization maintained in an on-beam ³He spin filter using SEOP
NIM A, **625**, 43-46, (2011)
9. Stockert O., Arndt J., Faulhaber E., Geibel C., Jeevan H.S., Kirchner S., Loewenhaupt M.,
Schmalzl K., Schmidt W., Si Q., Steglich F.
Magnetically driven superconductivity in CeCu₂Si₂
Nature Physics **7**, 119-124 (2011)
10. Houben, A.; Schweika, W.; Brückel, T.; Dronskowski, R.
New neutron-guide concepts and simulation results for the POWTEX instrument
Nuclear Instruments and Methods in Physics Research A **680** (2012), 124 - 133

Jülich Synchrotron Radiation Laboratory (JSRL)



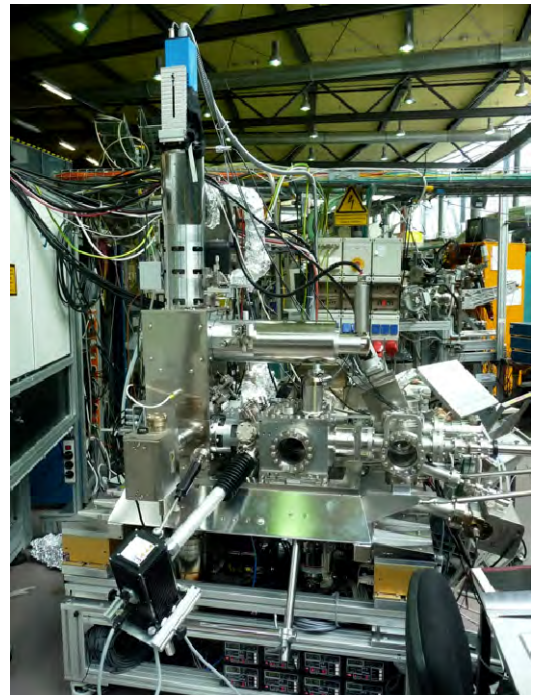
Synchrotron radiation with its unique properties such as wide range tunability, polarization characteristics, coherence, and time structure has become an indispensable tool in condensed matter physics and materials research. It is the mission of the Jülich Synchrotron Radiation Laboratory (JSRL) to develop state-of-the-art spectroscopy, microscopy and scattering experiments and operate them at the best synchrotron radiation sources world-wide to address contemporary problems in solid state physics and information technology. These instruments are not only used

for our in-house research, but also open to external user groups .

At present, the JSRL operates proprietary instruments and beamlines at the synchrotron radiations sources DELTA (Dortmund), HZB-BESSY (Berlin) and Elettra (Triest, Italy).

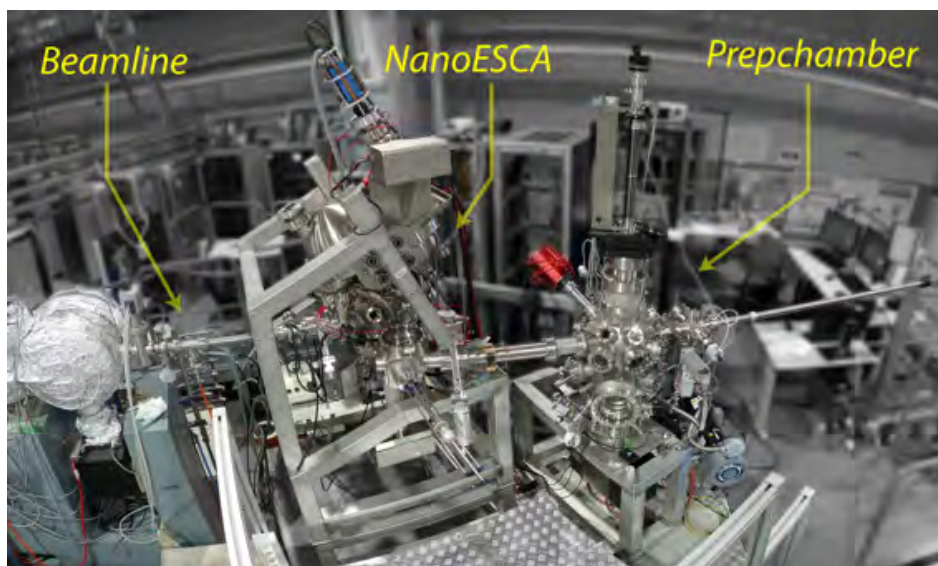
Our engagement at DELTA is focused on photoemission spectroscopy and magnetic resonant scattering experiments. For this purpose, we have constructed a PGM beamline (BL5) to disperse the linearly polarized light from a planar electromagnetic undulator. The endstation of BL5 is a unique spin- and angle-resolved photoelectron spectrometer dedicated to spin-polarized band mapping studies of materials systems in spintronics, such as magnetic layers, topological insulators or Heusler phases. In addition, we have 30% of the beamtime at the PGM beamline (BL2) which is connected to a linear permanent magnet undulator and is used for XPS and XSW investigations.

At HZB-BESSY we maintain our own SGM beamline at the undulator UE56-1, covering the soft x-ray range with variable light polarization. The endstation comprises a unique aberration-corrected and energy-filtering PEEM/LEEM instrument coined as the Nano-Spectroscopy Facility (NSF). The NSF represents the backbone for our static and time-resolved microscopy studies within the research programme FIT. The instrument has been opened to external users in 2011.



Aberration-corrected PEEM/LEEM experiment at the variable polarization beamline at HZB-BESSY (Berlin).

At the soft x-ray nanofocus beamline BL1.2 of Elettra we have located a novel energy-filtered photoemission microscope (NanoESCA), which is dedicated to nanospectroscopy. The variable light polarization permits studies on nonmagnetic and magnetic material systems. A particular feature of the microscope is an additional diffraction lens, which permits a very efficient Fermi surface mapping. Also this instrument is open to external users since 2011.



NanoESCA experiment at the nanospectroscopy beamline at Elettra (Trieste, Italy).

The PGI-4 has contributed to the instrumentation at the Advanced Photon Source APS in Argonne, USA, a high energy undulator beamline, which is now operated by the APS.

Further activities within the JSRL concern the development of hard x-ray photoemission towards high lateral resolution, the development of time-resolved experimental schemes in the femtosecond regime for the future use of FEL sources, and the implementation of novel electron spin-detection principles for the study of spin-based effects and spin structures/textures in novel materials.

Beamline	photon energy	polarization	experiment	light source
BL5	10 – 700 eV	linear	ARUPS, SP-ARUPS	DELTA
BL2	60 – 1500 eV	linear	XPS, XPD, XSW	DELTA
UE-56/SGM	60 – 1500 eV	linear, circular	PEEM/LEEM	HZB-BESSY
BL1.2	60 – 1200 eV	linear, circular	NanoESCA	Elettra

Research Highlights

Development of a gating technique for time-resolved synchrotron experiments based on electrostatic deflection

C. Wiemann, A.M. Kaiser, C.M. Schneider

Peter Grünberg Institut PGI-6, Research Center Jülich, 52425 Jülich, Germany

In this report, a newly developed gating technique for a time-resolving photoemission microscope is presented. The technique makes use of an electrostatic deflector within the microscope's electron optical system for fast switching between two electron-optical paths, one of which is used for imaging, while the other is blocked by an aperture stop. The system can be operated with a switching time of 20 ns and shows superior dark current rejection. We report on the application of this new gating technique to exploit the time structure in the injection bunch pattern of the synchrotron radiation source BESSY II for time-resolved measurements in the picosecond regime.

Synchrotron-based pump-probe experiments form an important approach to investigate dynamic processes in magnetic systems. A typical experimental setup consists of an excitation (pump) by a pulsed magnetic field, which is synchronized by a variable time delay to the synchrotron pulse serving as photoemission probe. In particular, photoemission microscopy (PEEM) utilizing x-ray magnetic circular dichroism (XMCD) as contrast mechanism to map magnetic domains is commonly used by a number of groups worldwide. Being a pump-probe technique, this kind of experiment relies on repetitive events which are sampled over typically 10^6 - 10^9 times in a stroboscopic manner. The time scales involved in magnetic system, in particular the magnetic system's recovery times, limit these experiments to single-bunch mode or other low-current modes of operation of the synchrotron especially dedicated to time-resolved experiments.

Our approach lifts this restriction by making use of the time structure the standard bunch injection pattern at the synchrotron facility BESSY-II (bottom graph of Fig. 1). By dynamically time-gating the detection system of a Focus-IS-PEEM on the single bunch which is always present in a 100ns wide gap in the multi-bunch sequence, we can use the associated synchrotron light pulse for

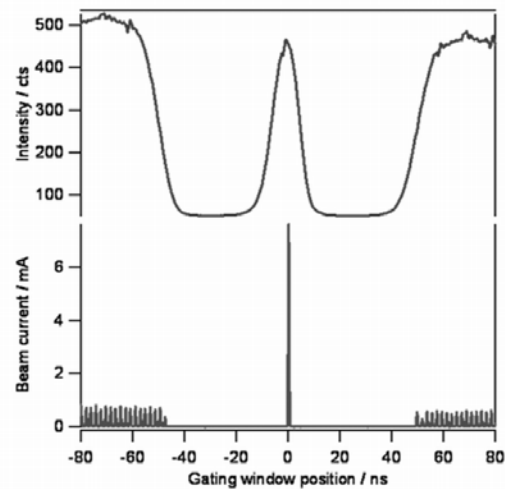


Figure 1: Integrated photoemission signal (top) vs. gating window position matches the BESSY II injection pattern (bottom).

time-resolved experiments in the same way as in genuine single bunch operation, with the additional benefit that the full intensity of the synchrotron light can be used alternatively at any time to adjust the microscope's optic. In contrast to the known gating methods relying on a gain-switch of the multi-channel plate which serves as variable gain amplifier in the microscope's imaging unit, we make use of an electrostatic deflector in the electron optics to temporarily redirect the photoelectrons used for imaging. The principle of operation is sketched in Fig. 2. The deflector used for gating is situated near the first image plane of the microscope. During OFF state of the gate, a static voltage is applied, resulting in an electric field perpendicular to the optical axis of the microscope. The field deflects the electrons in such a way that they are blocked by a small aperture placed in the second focal plane. The gate is temporarily set to ON state by coupling an electric pulse to the deflector plates which compensates the static voltage and therefore the

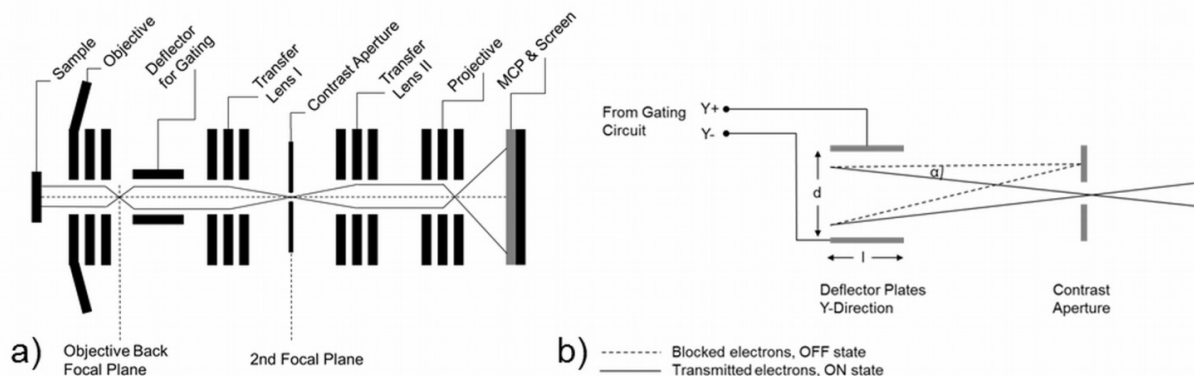


Figure 2: (a) Sketch of the PEEM lens system. The deflector used for gating is located in the first image plane. The aperture separating the deflected part is located in the second focal plane, behind the first transfer lens. (b) Schematic of the gating operation. Dashed lines: trajectories of electrons while gate is in “OFF” state; solid lines: trajectories of electrons while gate is in “ON” state

deflecting field. During ON state, the electrons can pass through the aperture and subsequently form an image on the microscope’s screen. The timing performance of the gate can be judged from the top graph in Fig. 1. Here, the temporal position of the gate opening was swept vs. the storage ring’s 1.25MHz timing signal marking the single bunch. The resulting photoemission signal from the microscope was integrated over the image detector. Around zero time delay, only photons generated by the single bunch pass the gating window, which is our desired mode of operation. From the rise time of the signal we can estimate a switching time of 20ns for the entire timing circuit of our setup, which consists of a commercial variable delay generator (Highland Technology P400), a custom-build pulse generator and an inductive coupling circuit to add the pulse to the static voltage.

To check the influence of the gating setup on the image quality, we compare XMCD-images taken on the same sample during single bunch operation and standard multi-bunch operation with gating in Fig. 3.

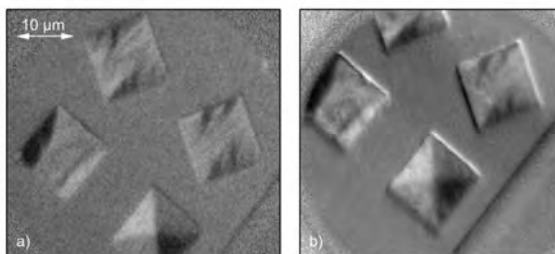


Fig. 3: Comparison of images of magnetic domains, taken during single-bunch operation (a) and gated multi-bunch mode (b), respectively. Both images show calculated asymmetry between images taken at opposite light helicities at Fe L3 edge ($h\nu = 709.25 \text{ eV}$).

Qualitatively, there is no difference between the images, which have been calculated as asymmetry between images taken at opposite light helicities. From a practical point of view, it has to be pointed out that the gated mode allows using the full intensity of the multi-bunch operation for the adjustment of the microscope’s optic, which considerably speeds up this procedure in comparison to genuine single bunch operation. The gating is switched on after finishing the adjustment procedure for the time-resolved experiments only. Further details on technical issues can be found in [1].

Recently, a similar gating setup has been incorporated into the SPECS P90 AC-LEEM/PEEM instrument serving as a permanent end-station at the FZJ beamline UE56-1/SGM at BESSY-II. A publication on first time-resolved results from this instrument is currently in preparation.

[1] Wiemann, C.; Kaiser, A. M.; Cramm, S.; Schneider, C.M.: Deflection gating for time-resolved x-ray magnetic circular dichroism–photoemission electron microscopy using synchrotron radiation
Review of Scientific Instruments, 83 (2012) 6, 063706

A Hemispherical Photoelectron Spectrometer with Two-Dimensional Delay-Line Detector and Integrated Spin-Polarization Analysis

L. Plucinski^{1,2}, M. Escher³, N. B. Weber³, A. Oelsner⁴, M. Merkel³, C. M. Schneider^{1,2}

¹ Peter Grünberg Institut PGI-6, Research Center Jülich, 52425 Jülich, Germany

² Jülich Aachen Research Alliance - Fundamentals of Future Information Technologies (JARA-FIT)

³ FOCUS GmbH, Neukirchner Str. 2, Hünstetten, D-65510, Germany

⁴ Surface Concept GmbH, Staudingerweg 7, D-55099 Mainz, Germany

Photoelectron spectrometers usually allow detection of either spin-resolved energy-distribution curves (EDCs) at single emission angle, or 2D angle-versus-energy images without spin-resolution. We have combined the two detection schemes into one spectrometer system which permits simultaneous detection of a 1D spin-resolved EDC and a 2D angular map. A state-of-the-art VG Scienta SES2002 analyzer is used as an energy filter. Its original scintillator detector has been replaced by a delay-line-detector (DLD), and part of the electron beam is allowed to pass through to reach the spin-polarized low energy electron diffraction spin-detector mounted behind a 90° deflector to feature simultaneous detection of in-plane and out-of-plane spin components. The planned upgrade with an exchange-scattering based spin detector which allows high energy resolution in spin-polarized mode is also discussed.

A full experimental characterization of an electronic state and its symmetry requires the determination of the photoelectron wave vector and its spin character. Most commercial spectrometers are nowadays based on hemispherical capacitors and provide a two-dimensional (2D) detection scheme which captures a sizable part of the angular variation of the spectral distribution $E(\vec{k})$ in a single measurement. Spin detection schemes range from high-energy Mott scattering ($\sim 10^4$ eV), to spin-orbit scattering phenomena at low (~ 100 eV), and to exchange scattering processes at very low energies (~ 10 eV) and the respective spin detectors usually have a well-defined working point in terms of scattering angle and energy in order to obtain maximum spin sensitivity.

Figure 1 presents the schematic view of our setup [1], which is built around a commercial VG Scienta SES2002 hemispherical spectrometer, and is located permanently at the synchrotron laboratory DELTA in Dortmund. In order to integrate 2 detectors into our system we have

retrofitted a delay-line detector (DLD) instead of the standard multichannel plate (MCP) scintillator-CCD design, mainly because it operates without the need for a viewport and a CCD camera. This makes it more convenient to fit into the area crowded with the MCP and the electron transfer optics for the spin-detector. A spin-polarized low energy electron diffraction (SPLEED) detector is used for the spin-detection purpose [3].

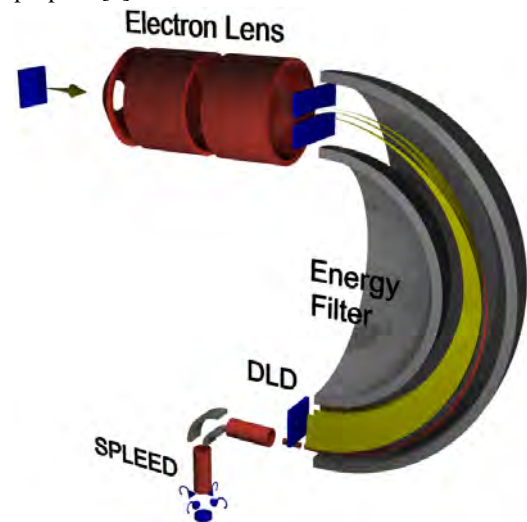


FIG. 1: Schematic representation of the spectrometer system in DELTA/Dortmund [1]. Currently used SPLEED detector will be replaced by the FERRUM [2] to combine the spin-polarization capability with the high energy resolution on the routine basis.

Its advantages are a high spin asymmetry, and no need to use very high, or very low electron energies – which is convenient for the electron optics. The SPLEED is connected through an additional 90° deflector operating at a high pass energy which enables the access to both the in-plane and out-of-plane spin polarization components. The W(100) single crystal is used as a scattering target with four channeltrons positioned to capture each of the four {2,0} LEED beams. The design has been optimized for a constant 104.5 eV scattering energy.

Figure 2 shows a combination of ARPES and spin-resolved data for a 10ML Ni film evaporated on Cu(100). The two-dimensional ARPES map shows emission around 15° off-normal angle at $h\nu = 50$ eV. In this region one can see the spin-split sp-band of Ni(100), with the exchange splitting of approx. 0.2 eV. For 10ML Ni/Cu(100) the easy axis of magnetization lies out-of-plane, however, the spin-polarized data reveal non-zero spin-polarization components for both orthogonal directions measured by the SPLEED. This is due to the vectorial character of the quantity \vec{P} . In our geometry the full separation between the in-plane and out-of-plane components is only possible in normal-emission geometry, and spin-polarization (if any present) is always expected in both directions in off-normal emission data. Taking this into account the data in Fig. 2 shows that the investigated 10ML Ni/Cu(100) system has high total spin polarization of above 40% oriented fully perpendicular to the surface of the film.

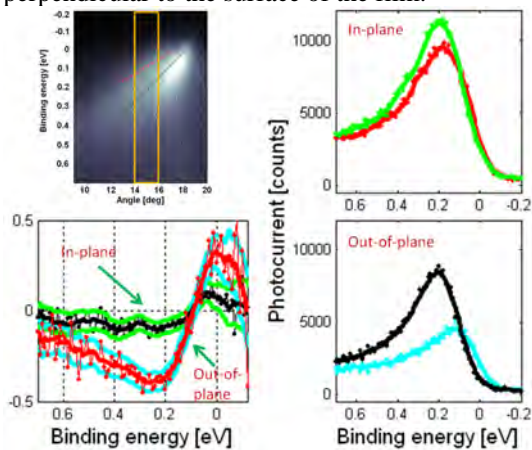


FIG. 2: ARPES and spin-polarized data for 10ML Ni/Cu(100) at $h\nu = 50$ eV. Spin-polarized spectra are measured at an emission angle of 15° and represent approximately the angle-integrated intensity from the area marked by the rectangle in top-left panel.

A spin detector based on the exchange scattering of electrons at a magnetized target has been described by Hillebrecht et al. [4]. Depending on the relative orientation of the electron-spins and the target magnetization, the reflected electron intensity shows a high asymmetry at low kinetic electron energies. However, ferromagnetic scattering targets must be prepared as thin films and are quite sensitive to surface contamination by adsorbates. A breakthrough has been achieved recently by Bertacco et al. [5] by passivating an iron film with oxygen which extends the time period between preparations up to one week or longer. Based on the above principles we have constructed the *FERRUM* spin detector [2], which shows the figure of merit of $8.8 \cdot 10^{-3}$, more than one order of magnitude higher than the one of SPLEED. The layout of *FERRUM* is shown in Fig. 3.

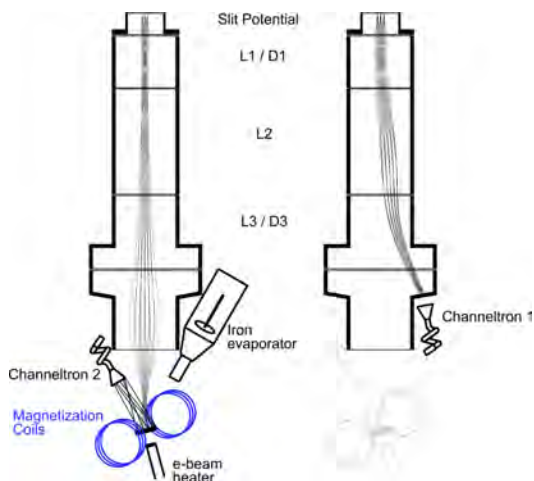


FIG. 3: Operational scheme of the *FERRUM* spin-polarimeter. Left: spin-resolved measurement mode. An iron film is evaporated onto the scattering target and magnetized by one of two orthogonal pairs of coils. Electrons are focused from the analyzer exit slit onto the scattering target and counted by the channeltron 2. Right: integral intensity measurement. The electron beam is deflected and focused into the off-axis channeltron 1 by two deflectors integrated into the transfer lens.

The similarity in the physical construction allows to directly exchange the SPLEED polarimeter with the *FERRUM* in our current setup, which in the future will allow to perform spin-polarized experiments at the high energy resolution to reveal the details of the spin-polarization near the Fermi level at unprecedented accuracy. Foreseen applications are in revealing the complex helical spin texture in three-dimensional topological insulators and in measuring the details of spin polarization of quantum well states in perfectly ordered ultrathin ferromagnetic films.

- [1] L. Plucinski, A. Oelsner, F. Matthes, and C. Schneider: A Hemispherical Photoelectron Spectrometer with Two-Dimensional Delay-Line Detector and Integrated Spin-Polarization Analysis, *Journal of Electron Spectroscopy and Related Phenomena* **181**, 215 (2010).
- [2] M. Escher, N. B. Weber, M. Merkel, L. Plucinski, and C. M. Schneider: *FERRUM*: A New Highly Efficient Spin Detector for Electron Spectroscopy, *e-Journal of Surface Science and Nanotechnology* **9**, 340 (2011).
- [3] D. Yu, C. Math, M. Meier, M. Escher, G. Rangelov, and M. Donath: Characterisation and application of a SPLEED-based spin polarisation analyser, *Surface Science* **601**, 5803 (2007).
- [4] F. U. Hillebrecht, R. M. Jungblut, L. Wiebusch, C. Roth, H. B. Rose, D. Knabben, C. Bethke, N. B. Weber, S. Manderla, U. Rosowski and E. Kisker: High-efficiency spin polarimetry by very-low-energy electron scattering from Fe(100) for spin-resolved photoemission, *Review of Scientific Instruments* **73**, 1229 (2002).
- [5] R. Bertacco, D. Onofrio, and F. Ciccacci: A novel electron spin-polarization detector with very large analyzing power, *Review of Scientific Instruments* **70**, 3572 (1999).

Selected Literature

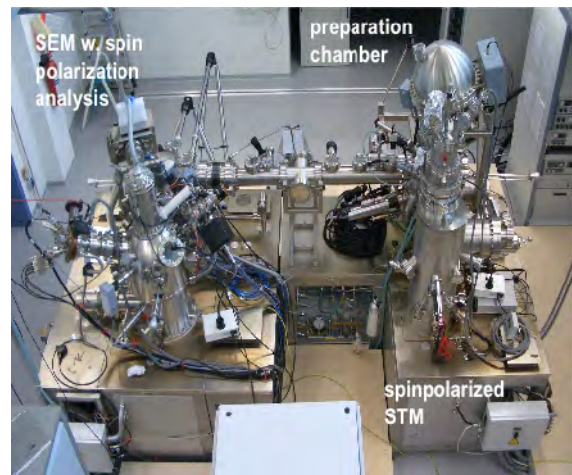
1. C. Wiemann, A. Kaiser, S. Cramm, and C. M. Schneider
Deflection Gating for Time-Resolved XMCD-PEEM using Synchrotron Radiation
Rev. Sci. Instrum. **83** (2012) 063706
2. C. Wiemann, M. Patt, S. Cramm, M. Escher, M. Merkel, A. Gloskovskii, W. Drube, and C. M. Schneider
Probing Buried Layers by Photoelectron Spectromicroscopy With Hard X-Ray Excitation
Appl. Phys. Lett. **100** (2012) 223106
3. M. Gilbert, H.-Ch. Mertins, M. Tesch, O. Berges, H. Feilbach, and C.M. Schneider
TetraMag: A Compact Magnetizing Device Based on Eight Rotating Permanent Magnets
Rev. Sci. Instrum. **83** (2012) 025109
4. C. Wiemann, M. Patt, I. P. Krug, N. B. Weber, M. Escher, M. Merkel, and C. M. Schneider
A New Nanospectroscopy Tool with Synchrotron Radiation: NanoESCA@Elettra
e-J. Surf. Sci. Nanotech. **9** (2011) 395
5. M. Escher, N. B. Weber, M. Merkel, L. Plucinski, and C. M. Schneider
FERRUM: A New Highly Efficient Spin Detector for Electron Spectroscopy
e-J. Surf. Sci. Nanotech. **9** (2011) 340
6. S. Suga, A. Sekiyama, G. Funabashi, J. Yamaguchi, M. Kimura, M. Tsujibayashi, T. Uyama, H. Sugiyama, Y. Tomida, G. Kuwahara, S. Kitayama, K. Kimura, K. Fukushima, T. Yokoi, K. Murakami, Y. Saitoh, L. Plucinski, and C. M. Schneider
High-Resolution, Low-hv Photoelectron Spectroscopy with Use of a Microwave-Excited Rare-Gas Lamp and Ionic Crystal Filters
Rev. Sci. Instrum. **81** (2010) 105111
7. L. Plucinski, A. Oelsner, and C.M. Schneider
A Hemispherical Photoelectron Spectrometer with Two-Dimensional Delay-Line Detector and Integrated Spin-Polarization Analysis
J. Electron Spectrosc. Rel. Phenom. **181** (2010) 215
8. A. Gray, F. Kronast, C. Papp, S.-H. Yang, S. Cramm, I. Krug, F. Salmassi, E. M. Gullikson, D. M. Hilken, E. H. Anderson, P. Fischer, H. A. Dürr, C. M. Schneider, and C. S. Fadley
Standing-Wave Excited Soft X-Ray Photoemission Microscopy: Application to Co Microdot Magnetic Arrays
Appl. Phys. Lett. **97** (2010) 062503

Scientific Infrastructure of the PGI

In order to meet the challenges brought about by contemporary condensed matter physics, the Peter Grünberg Institute has set up a variety of dedicated medium-sized facilities and specialized laboratory instruments outside the HNF, ER-C, JCNS and JSRL.

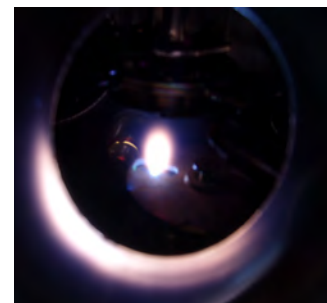
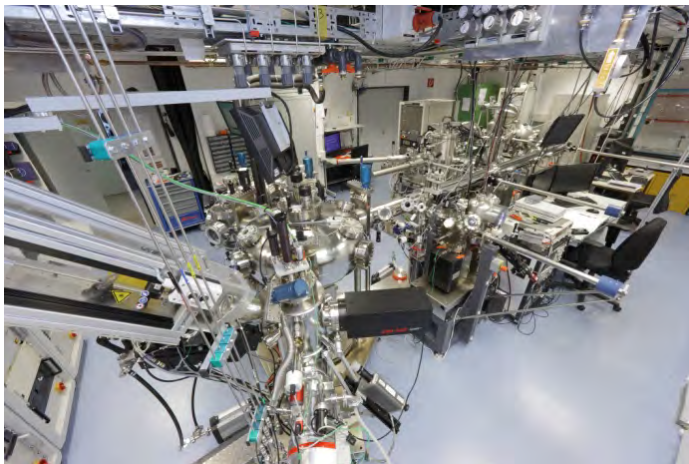
In order to foster collaboration in the field of semiconductor nanoelectronics with national and international academic and industrial partners a line of new tools was installed. Putting emphasis on industrial relevant processes, 12" tools for SiGe epitaxy and deposition of high-k dielectrics and gate metals as well as for ion implantation, rapid thermal processing and wafer cleaning were installed. The set of instruments puts PGI in the unique position to combine cutting edge research at the forefront of modern technology with today's manufacturing processing making PGI a preferred partner on European and National level.

The research on spintronics and magnetic systems has a focus on small length and short time scales. Small length scales are addressed by a suite of scanning microscopes. The main facility is the **Nanospintronics Facility** which combines mesoscopic domain imaging by means of a scanning electron microscope with spin polarization analysis (SEMPA) with a low-temperature spin-polarized scanning tunneling microscope. Short time scales are important in the studies of magnetization and spin dynamics which employ a set of ultrashort pulsed laser pump-probe techniques. The use of higher harmonic energy conversion schemes permits even an element-selective approach to spin dynamics on the femtosecond scale.



NanoSpintronics Cluster Tool at PGI-6

Complex transition metal oxides and their heteroepitaxial interfaces exhibit a large variety of exciting physical properties, some of which could be employed in novel nanoelectronic devices. Therefore, these materials are under investigation in several groups within the PGI and JARA-FIT. In order to tailor the physical properties of complex oxides, one has to gain precise control over lattice defects as well as over the valence state of the partially multivalent components. In order to tackle this challenging problem, we built up a **UHV cluster-tool** at the PGI-7 in which we combine a variety of complementary surface analysis tools *in-situ* with **oxide-specific deposition methods** e.g. pulsed laser deposition and sputtering in order to prevent surface contamination. In particular, the analysis part of the cluster comprises scanning probes techniques (AFM, STM, LC-AFM, PFM), photoelectron spectroscopy (XPS) as well as photoelectron microspectroscopy (NanoESCA). Besides the growth of atomically tailored complex oxide thin films, the cluster tool provides the opportunity to gain a deeper understanding e. g. of nanoscale redox-processes which occur in oxides under electrical stimulus and are the topic of the JARA-FIT SFB 917. Preparation capabilities of the oxide cluster are complemented by the oxide MBE at the PGI-4, which features 6 effusion cells, 2 electron beam evaporators, an oxygen plasma source and in-situ REED, LEED and Auger capabilities.



Plasma plume within the PLD system

Oxide cluster system (June 2012)

Scientific Infrastructure of the PGI

The studies addressing the physics of molecules on surfaces employ a variety of highly specialized microscopy techniques. In October 2010 a new **Aberration Corrected Low Energy Electron Microscope (AC-LEEM) and Photo Electron Emission Microscope (PEEM)** was installed in the labs of PGI-3. Although it is a commercial instrument delivered by Elmitec GmbH (Clausthal-Zellerfeld, Germany), it can be considered as a prototypical microscope, since it is only the second Elmitec AC-LEEM which has been delivered so far. Worldwide there are only about 5 other comparable microscopes in operation (Jan 2011). It reaches a world-record lateral resolution of 2 nm in AC-LEEM mode. The microscope has the potential to boost many of our ongoing research projects, e.g. regarding the growth of organic thin films on metal substrates, since it enables in situ investigations in real time.

Scanning tunnelling microscopes (STM) can not only be used to image surfaces with atomic resolution, but also to record spectra from single atoms. With an STM, it is even possible to move individual atoms and molecules at will. How does this work? A sharp metal tip is scanned across the sample surface, thereby recording a profile of the surface structure and revealing information about its local electronic properties. If the interaction between tip and sample is strong enough, the tip can move single atoms at the sample surface.

After three years of construction, in March 2011 a state-of-the-art **ultra-low vibration laboratory for precision scanning tunnelling microscopy (STM)** has been completed in PGI-3. STM experiments require ultimate mechanical stability of the microscope. The smallest vibration of the tip against the surface will disturb the experiment. Although scanning tunnelling microscopes are constructed in a way to minimize their susceptibility to mechanical vibrations, for the most demanding applications it is still necessary to shield the microscope from the detrimental influence of sound and floor vibrations, as well as electromagnetic radiation. For this purpose we have designed two specially shielded rooms in our Ultra-Low Vibration STM Laboratory.

The Ultra-Low Vibration STM Laboratory is based on a room-in-room concept. Two sound-proof and electromagnetically shielded rooms that house one STM each are located in a hall from where the microscopes are operated. Each room is built on a 100-ton concrete foundation that floats on passive air dampers and is therefore decoupled from the surrounding building. The large mass of the foundations ensures a low mechanical resonance frequency (below 1 Hz), thereby offering optimum vibration-insulation of the microscopes in the rooms.

Low-temperature scanning tunneling microscope in the Ultra-Low Vibration STM Laboratory.



The PGI-3 also developed a new type of ultra-compact piezoelectric motor, the so-called **Koala drive**, which has a diameter of less than 2.5 mm. The Koala drive operates in ambient conditions as well as in ultra-high vacuum, at low temperatures (4 K) and in magnetic fields. The Koala drive serves as the heart of a new STM design: Due to its compactness, a 4-tip STM or nanoprobe with an outer diameter of only 50 mm can be built. The Koala drive will be commercialized by the newly founded spin-off company mProbes GmbH.



Integrating the KoalaDrive™ nanopositioner as coarse approach inside a tube scanner pushes the design of SPMs towards ultra compact instruments. A minimal size leads to improvements of the key figures of merit in scanning probe microscopy. A smaller size leads directly to a smaller thermal drift and increases the eigenfrequencies, leading to a better damping of external vibrations.

Cover images

Top image: Spatial distribution of local density of states for a $\text{Ge}_{512}\text{Vac}_{512}\text{Sb}_{1024}\text{Te}_{2048}$ supercell. In the left lower part the chemical information, in the upper right part the value of the LDOS is displayed. Large (small) radii of the spheres correspond to high (low) DOS values. For both parts of the plot Ge, Vac, Sb, and Te are shown in white, transparent, light blue, and dark blue, respectively.

From: A. R. Thieß; Development and application of a massively parallel KKR Green function method for large scale systems; Dissertation (2011).

Small images from left to right:

- Section through the electronic state distribution within tungsten observed with hard X-ray photo electron spectroscopy.
From: A.X. Gray et al.; Probing bulk electronic structure with hard X-ray angle-resolved photoemission; Nature Materials 10, 759-764 (2011), DOI:10.1038/nmat3089.
- Graphic representation of an electrochemical sensor (green with yellow conductors) that detects neurotransmitter molecules. These molecules are secreted by neurons (dark red).
- Orbital order in TbMnO_3 , as obtained by LDA+DMFT calculations.
From: A. Flesch et al.; Orbital-order melting in rare-earth manganites: Role of superexchange; Physical Review B 85, 035124 (2012), DOI: 10.1103/PhysRevB.85.035124.
- Aberration-corrected high-angle annular dark-field scanning transmission electron micrograph of a tetragonal Ga-Mn nanocrystal at the end of a GaMnAs nanowire.
Acknowledgments: A. Kovács, C. Boothroyd, T. Kasama, I. Dódy, J. Sadowski, R. Dunin-Borkowski.
- Contacted InN nanowire with two gate fingers for quantum transport experiments.
G. Petersen et al.; Spin-orbit coupling and phase-coherent transport in InN nanowires; Physical Review B 80, 125321 (2009), DOI:10.1103/PhysRevB.80.125321.

www.fz-juelich.de/pgi/